

DISSERTATION

INDEPENDENT MEASUREMENT OF THE T2K NEAR DETECTOR CONSTRAINT  
USING THE OFF-AXIS PI-ZERO DETECTOR

Submitted by

Matthew Gregory Hogan

Department of Physics

In partial fulfillment of the requirements

For the Degree of Doctor of Philosophy

Colorado State University

Fort Collins, Colorado

Fall 2019

Doctoral Committee:

Advisor: Walter Toki

Robert Wilson

Norman Buchanan

Wen Zhou

Copyright by Matthew Gregory Hogan 2019

All Rights Reserved

## ABSTRACT

# INDEPENDENT MEASUREMENT OF THE T2K NEAR DETECTOR CONSTRAINT USING THE OFF-AXIS PI-ZERO DETECTOR

The Tokai to Kamioka (T2K) experiment is a long-baseline neutrino oscillation experiment hosted in Japan searching for electron neutrino appearance in a high purity muon neutrino beam. In order to constrain the systematic uncertainties in the oscillation analysis, a dedicated near detector (ND) complex called ND280 is located 280 meters from the neutrino production source in line of the beam. To date, the Fine Grain Detector (FGD) in ND280 has provided the ND constraint using a binned maximum likelihood estimate fit. This thesis describes the effort to validate the ND constraint using the same framework, but with an independent data set from the ND280 pi-zero detector (PØD). Expanding on previously developed PØD selections, new selections have been developed to select neutrino and antineutrino events in one and multiple track topologies on water and carbon. These selections are shown to have similar sensitivity to the T2K flux and cross section systematic uncertainties. Using the same parameterization as the official ND constraint result, a hypothesis test was conducted between the PØD-only and FGD-only data fit results. A p-value of 0.2865 was obtained indicating the two data sets are likely describing the same population of neutrinos and their interactions in T2K.

## ACKNOWLEDGEMENTS

I would like to first thank Elliott Forney for making a publicly accessible L<sup>A</sup>T<sub>E</sub>X template. I also thank the T2K collaboration and the Beam and Near Detector Flux Task Force in T2K for supporting this analysis. I give thanks to my loving wife Hannah who has supported me through my graduate career. I want to acknowledge the support from my family and friends. I could not have made it this far without them.

I acknowledge the support of the following agencies and individuals. I acknowledge the United States Department of Energy under Grant Contracts DEFG0293ER40788 and DESC0017740 to support my research. I acknowledge my advisers Robert Wilson and Walter Toki for guiding me on my journey through graduate school. Finally, I acknowledge Shaila Parashar, Jeff Penn, and the rest of the Engineering Technology Services team at Colorado State University for supporting my high performance computing requirements.

## TABLE OF CONTENTS

ABSTRACT . . . . .	ii
ACKNOWLEDGEMENTS . . . . .	iii
TABLE OF CONTENTS . . . . .	iv
LIST OF TABLES . . . . .	vii
LIST OF FIGURES . . . . .	ix
Executive Summary . . . . .	1
Chapter 1 Introduction . . . . .	3
1.1 Introduction to Neutrinos . . . . .	3
1.2 The T2K Experiment . . . . .	28
1.3 Summary . . . . .	54
Chapter 2 The BANFF Fit Likelihood . . . . .	55
2.1 Conditional Probability Density Functions . . . . .	56
2.2 The BANFF Fit Test Statistic . . . . .	57
2.3 Summary . . . . .	62
Chapter 3 The PØD Selections and Samples . . . . .	63
3.1 The ND280 Global Reconstruction . . . . .	65
3.2 Selection Cuts . . . . .	65

3.3	Selection Kinematics . . . . .	72
3.4	Summary . . . . .	94
Chapter 4	The BANFF Fit Parameters . . . . .	96
4.1	Fit Binning . . . . .	96
4.2	Systematic Uncertainties and Penalty Terms . . . . .	100
4.3	Summary . . . . .	136
Chapter 5	Validation of the BANFF Fit Procedure . . . . .	139
5.1	Asimov Data Fit . . . . .	139
5.2	Fake Data Fits . . . . .	149
5.3	Summary . . . . .	155
Chapter 6	Results of the BANFF Fit Using the PØD Samples . . . . .	160
6.1	Prefit Sample Distributions . . . . .	160
6.2	Postfit Results . . . . .	161
6.3	Statistical Significance of Parameter Agreement Between the PØD and FGD BANFF Fits . . . . .	190
6.4	Summary . . . . .	201
Chapter 7	Discussion . . . . .	203
7.1	Prediction of the T2K Oscillation Analysis Samples . . . . .	204
7.2	Analysis Improvements . . . . .	207
7.3	Future Prospects: Joint PØD+FGD Fit . . . . .	214
Bibliography	. . . . .	218
Appendix A	PØD CC- $\pi$ Analysis . . . . .	228
A.1	The PID Tools . . . . .	229
A.2	Momentum Reconstruction . . . . .	232

Appendix B	Bin Normalizations . . . . .	239
Appendix C	Toy Experiment Variations . . . . .	258
Appendix D	Cross Section Variations . . . . .	285
Appendix E	Log-Likelihood Sample Scans . . . . .	302
Appendix F	Log-Likelihood Penalty Scans . . . . .	316
Appendix G	Computing Resources . . . . .	328
Appendix H	Postfit Parameters . . . . .	330
Appendix I	Postfit ROC Curves . . . . .	354
Appendix J	Cross-Validated Fit . . . . .	365

## LIST OF TABLES

1.1	Sensitivity of Different Oscillation Experiments . . . . .	22
1.2	Global Best Fit for the Oscillation Parameters . . . . .	25
1.3	PØD Water Target Mass Composition . . . . .	46
2.1	Parameters that Affect the Analysis Bins . . . . .	59
3.1	The PØD Water Target Fiducial Volume and Veto Corridor Definitions . . . . .	68
3.2	T2K Data-Taking Periods and Collected POT Used in the Analysis . . . . .	72
3.3	Enumeration of NEUT Interaction Modes . . . . .	74
4.1	Flux Binning and Uncertainties . . . . .	104
4.2	List of Detector Systematics in the Analysis . . . . .	112
4.3	Eigenvalues of the Sample Covariance . . . . .	128
4.4	Cross Section Model Fit Parameters in the BANFF Fit . . . . .	135
5.1	Event Rate Table for Asimov Set . . . . .	142
6.1	Neutrino-Nucleon Exposure on Target Elements . . . . .	188
7.1	Oscillation Parameters Used as Inputs for Studies of Simulated Data . . . . .	205
7.2	Number of Events Expected in the SK CCQE-enriched Samples . . . . .	205
7.3	Neutrino-Nucleon Exposure on Target Elements in a PØD+FGD Joint Fit . . . . .	216
A.1	Selection Statistics for the PØD CC- $1\pi$ Analysis . . . . .	232

B.1 Observable Normalization Fit Bins . . . . .	239
D.1 Event Rate Variations Per Cross Section Parameter Variation . . . . .	286
G.1 Computing Resources Used in this Thesis . . . . .	328
H.1 Prefit and Postfit Parameters with Errors . . . . .	331

## LIST OF FIGURES

1.1	The Elementary Particles of the Standard Model of Particle Physics . . . . .	5
1.2	The CC and NC $\nu_e e^- \rightarrow \nu_e e^-$ Interaction . . . . .	8
1.3	Helicity of the Neutrino . . . . .	9
1.4	A Schematic of $\theta$ in $\nu_e e^-$ Scattering . . . . .	13
1.5	A $\nu_\mu$ -Induced CCQE Interaction . . . . .	14
1.6	Illustration of a Mixing Matrix in Two Dimensions . . . . .	18
1.7	Survival and Disappearance Probability . . . . .	20
1.8	Semi-logarithmic Plot of the Two Flavor Survival Probability . . . . .	21
1.9	Neutrino Mass Hierarchy Problem and MNSP Representation . . . . .	24
1.10	The Matter and Energy Content of the Universe . . . . .	27
1.11	Birds Eye View of the T2K experiment on the Japanese Archipelago . . . . .	29
1.12	The Unoscillated $\nu_\mu$ Flux at Super-Kamiokande . . . . .	30
1.13	Bird's Eye View of the J-PARC Laboratory . . . . .	31
1.14	Schematics of the J-PARC Accelerators . . . . .	32
1.15	The Neutrino Beamline at J-PARC . . . . .	33
1.16	Photographs of the T2K Target Station . . . . .	34
1.17	Accumulated Protons on Target for T2K . . . . .	35
1.18	Schematic of the INGRID Detector . . . . .	38
1.19	Photographs of the T2K MPPC . . . . .	39
1.20	The T2K On-Axis Beam Profile . . . . .	39

1.21	The INGRID Detector Event Rate . . . . .	40
1.22	Schematic of the Off-Axis Near Detector ND280 . . . . .	42
1.23	The ND280 Detector Magnetic Field Measurement . . . . .	43
1.24	Schematic of the PØD . . . . .	45
1.25	Cross Section of a PØD Scintillating Bar . . . . .	46
1.26	Cut-Away Drawing of a TPC Volume in ND280 . . . . .	48
1.27	Diagram of the Super-Kamiokande Detector . . . . .	49
1.28	Representative T2K Events in Super-Kamiokande . . . . .	50
1.29	Predicted and Best Fit Measurements for the T2K Flux at SK . . . . .	51
1.30	Predicted CCInc Cross Section at T2K Energies . . . . .	52
3.1	The PØD $\nu_\mu$ and $\bar{\nu}_\mu$ CC-0 $\pi$ Selection Kinematics . . . . .	64
3.2	Frequently Used Legends in the Analysis . . . . .	74
3.3	Reconstructed Kinematics of the $\nu_\mu$ in FHC Mode CC 1-Track Selection Categorized by CCQE and Non-CCQE Interactions . . . . .	76
3.4	Reconstructed Kinematics of the $\nu_\mu$ in FHC Mode CC 1-Track Selection Categorized by the True Particle Matched to the Main Track . . . . .	77
3.5	Reconstructed Vertex Z Position of the $\nu_\mu$ in FHC Mode CC 1-Track Selection .	78
3.6	Efficiency and Purity of the $\nu_\mu$ in FHC Mode CC 1-Track Selection . . . . .	78
3.7	True Kinematics of the $\nu_\mu$ in FHC Mode CC 1-Track Selection . . . . .	79
3.8	Reconstructed Kinematics of the $\nu_\mu$ in FHC Mode CC N-Tracks Selection Categorized by CCQE and Non-CCQE Interactions . . . . .	80
3.9	Reconstructed Kinematics of the $\nu_\mu$ in FHC Mode CC N-Tracks Selection Categorized by the True Particle Matched to the Main Track . . . . .	81
3.10	Reconstructed Vertex Z Position of the $\nu_\mu$ in FHC Mode CC N-Tracks Selection Categorized by the True Target Nucleus . . . . .	81
3.11	Efficiency and Purity of the $\nu_\mu$ in FHC Mode CC N-Tracks Selection . . . . .	82
3.12	True Kinematics of the $\nu_\mu$ in FHC Mode CC N-Tracks Selection . . . . .	83

3.13	Reconstructed Kinematics of the $\bar{\nu}_\mu$ in RHC Mode CC 1-Track Selection Categorized by CCQE and Non-CCQE Interactions . . . . .	84
3.14	Reconstructed Kinematics of the $\bar{\nu}_\mu$ in RHC Mode CC 1-Track Selection Categorized by the True Particle Matched to the Main Track . . . . .	85
3.15	Efficiency and Purity of the $\bar{\nu}_\mu$ in RHC Mode CC 1-Track Selection . . . . .	85
3.16	True Kinematics of the $\bar{\nu}_\mu$ in RHC Mode CC 1-Track Selection . . . . .	86
3.17	Reconstructed Kinematics of the $\bar{\nu}_\mu$ in RHC Mode CC N-Tracks Selection Categorized by CCQE and Non-CCQE Interactions . . . . .	87
3.18	Reconstructed Kinematics of the $\bar{\nu}_\mu$ in RHC Mode CC N-Tracks Selection Categorized by the True Particle Matched to the Main Track . . . . .	87
3.19	Efficiency and Purity of the $\bar{\nu}_\mu$ in RHC Mode CC N-Tracks Selection . . . . .	88
3.20	True Kinematics of the $\bar{\nu}_\mu$ in RHC Mode CC N-Tracks Selection . . . . .	89
3.21	Reconstructed Kinematics of the $\nu_\mu$ Background in RHC Mode CC 1-Track Selection Categorized by CCQE and Non-CCQE Interactions . . . . .	90
3.22	Reconstructed Kinematics of the $\nu_\mu$ Background in RHC Mode CC 1-Track Selection Categorized by the True Particle Matched to the Main Track . . . . .	91
3.23	Efficiency and Purity of the $\nu_\mu$ Background in RHC Mode CC 1-Track Selection . . . . .	91
3.24	True Kinematics of the $\nu_\mu$ Background in RHC Mode CC 1-Track Selection . . . . .	92
3.25	Reconstructed Kinematics of the $\nu_\mu$ Background in RHC Mode CC N-Tracks Selection Categorized by CCQE and Non-CCQE Interactions . . . . .	93
3.26	Reconstructed Kinematics of the $\nu_\mu$ Background in RHC Mode CC N-Tracks Selection Categorized by the True Particle Matched to the Main Track . . . . .	93
3.27	Efficiency and Purity of the $\nu_\mu$ Background in RHC Mode CC N-Tracks Selection . . . . .	94
3.28	True Kinematics of the $\nu_\mu$ Background in RHC Mode CC N-Tracks Selection . . . . .	95
4.1	Main Track Momentum Resolution for the $\nu_\mu$ in FHC Mode CC 1-Track Sample . . . . .	98
4.2	Main Track Angular Residuals for the $\nu_\mu$ in FHC Mode CC 1-Track Sample . . . . .	99
4.3	The BANFF Prefit Flux Covariance Matrix . . . . .	102

4.4	Neutrino Flux Prediction at SK and Flux Bin Edges . . . . .	103
4.5	Vertex Distribution Showing Evidence of PØD Bulging . . . . .	114
4.6	Bin Normalizations Edges for the $\nu_\mu$ in FHC Mode Samples . . . . .	120
4.7	Bin Normalization Edges for the $\bar{\nu}_\mu$ in RHC Mode Samples . . . . .	121
4.8	Bin Normalizations for the $\nu_\mu$ Background in RHC Mode Samples . . . . .	122
4.9	Event Variations in Observable Normalization Bins . . . . .	123
4.10	Detector Penalty Covariance Matrix . . . . .	126
4.11	Principal Component for the Sample Variance . . . . .	128
4.12	Cross Section Parameters Prefit Covariance and Correlation Matrices . . . . .	137
5.1	Complete Prefit Correlation Matrix for the BANFF Fit. . . . .	140
5.2	Test Statistic Scans for Variations of Fit Parameters in the Asimov Set . . . . .	144
5.3	Asimov Fit Results for the Flux at ND280 . . . . .	145
5.4	Asimov Fit Results for the Flux at Super-K . . . . .	146
5.5	Asimov Fit Results for the Bin Normalization Parameters . . . . .	147
5.6	Asimov Fit Results for the Cross Section and FSI Parameters . . . . .	148
5.7	Complete Postfit Correlation Matrix for the Asimov Data Fit . . . . .	149
5.8	Flux and Cross Section Postfit Correlation Matrix for the Asimov Data Fit . . .	150
5.9	Neutrino Energy Distributions in the High Energy Neutrino Flux Variation Fake Data Set . . . . .	152
5.10	Neutrino Energy Distributions in the High Energy Neutrino Flux Variation Fake Data Set (Continued) . . . . .	153
5.11	Postfit Parameters for the High Energy Neutrino in FHC Flux Fake Data fit . .	154
5.12	Lepton Candidate Momentum Distributions in the Single Pion Event Rate Variation Fake Data Set . . . . .	156
5.13	Lepton Candidate Momentum Distributions in the Single Pion Event Rate Variation Fake Data Set (Continued) . . . . .	157
5.14	Postfit Parameters for the $C_A^5$ Fake Data Fit . . . . .	158

6.1	Prefit for the Water-In $\nu_\mu$ in FHC Mode CC 1-Track Sample . . . . .	162
6.2	Prefit for the Water-In $\nu_\mu$ in FHC Mode CC N-Tracks Sample . . . . .	163
6.3	Prefit for the Water-In $\bar{\nu}_\mu$ in RHC Mode CC 1-Track Sample . . . . .	164
6.4	Prefit for the Water-In $\bar{\nu}_\mu$ in RHC Mode CC N-Tracks Sample . . . . .	165
6.5	Prefit for the Water-In $\nu_\mu$ in RHC Mode CC 1-Track Sample . . . . .	166
6.6	Prefit for the Water-In $\nu_\mu$ in RHC Mode CC N-Tracks Sample . . . . .	167
6.7	Prefit for the Water-Out $\nu_\mu$ in FHC Mode CC 1-Track Sample . . . . .	168
6.8	Prefit for the Water-Out $\nu_\mu$ in FHC Mode CC N-Tracks Sample . . . . .	169
6.9	Prefit for the Water-Out $\bar{\nu}_\mu$ in RHC Mode CC 1-Track Sample . . . . .	170
6.10	Prefit for the Water-Out $\bar{\nu}_\mu$ in RHC Mode CC N-Tracks Sample . . . . .	171
6.11	Prefit for the Water-Out $\nu_\mu$ in RHC Mode CC 1-Track Sample . . . . .	172
6.12	Prefit for the Water-Out $\nu_\mu$ in RHC Mode CC N-Tracks Sample . . . . .	173
6.13	Postfit for the Water-In $\nu_\mu$ in FHC Mode CC 1-Track Sample . . . . .	175
6.14	Postfit for the Water-In $\nu_\mu$ in FHC Mode CC N-Tracks Sample . . . . .	176
6.15	Postfit for the Water-In $\bar{\nu}_\mu$ in RHC Mode CC 1-Track Sample . . . . .	177
6.16	Postfit for the Water-In $\bar{\nu}_\mu$ in RHC Mode CC 1-Track Sample . . . . .	178
6.17	Postfit for the Water-In $\nu_\mu$ in RHC Mode CC 1-Track Sample . . . . .	179
6.18	Postfit for the Water-In $\nu_\mu$ in RHC Mode CC N-Tracks Sample . . . . .	180
6.19	Postfit for the Water-Out $\nu_\mu$ in FHC Mode CC 1-Track Sample . . . . .	181
6.20	Postfit for the Water-Out $\nu_\mu$ in FHC Mode CC N-Tracks Sample . . . . .	182
6.21	Postfit for the Water-Out $\bar{\nu}_\mu$ in RHC Mode CC 1-Track Sample . . . . .	183
6.22	Postfit for the Water-Out $\bar{\nu}_\mu$ in RHC Mode CC N-Tracks Sample . . . . .	184
6.23	Postfit for the Water-Out $\nu_\mu$ in RHC Mode CC 1-Track Sample . . . . .	185
6.24	Postfit for the Water-Out $\nu_\mu$ in RHC Mode CC N-Tracks Sample . . . . .	186
6.25	Postfit ND280 Flux Parameters for the PØD-only BANFF Fit . . . . .	191
6.26	Postfit SK Flux Parameters for the PØD-only BANFF Fit . . . . .	192
6.27	Postfit Cross Section Parameters for the PØD-only BANFF Fit . . . . .	193

6.28	Prefit and Postfit Bin Normalization Parameters . . . . .	194
6.29	The 2p2h Shape Mirrored Spline . . . . .	195
6.30	Postfit Correlation Matrix . . . . .	196
6.31	Prefit and Post Flux and Cross Section Parameter Correlations . . . . .	197
6.32	Prefit and Post Flux and Cross Section Parameter Correlations . . . . .	198
6.33	P-Value for the PØD vs FGD ND Constraint . . . . .	201
7.1	Reconstructed $\nu_\mu$ and $\bar{\nu}_\mu$ CCQE-enriched Energy Distributions at SK . . . . .	206
7.2	Reconstructed $\nu_e$ CCQE-enriched Energy Distribution at SK . . . . .	206
7.3	Reconstructed $\nu_e$ CCQE-Enriched Energy Distribution at SK . . . . .	207
7.4	Cross-Validation Curve for the BANFF Fit Regularization Strength. . . . .	210
7.5	The Lasso vs Elastic Net Constraint . . . . .	213
A.1	Topological Features Developed for CC-1 $\pi$ Analysis . . . . .	231
A.2	Momentum Calibration for PØD Fully Contained Muon Tracks . . . . .	237
A.3	Resolution Function for PØD Fully Contained Muon Tracks . . . . .	238
E.1	Corrected 2p2h Shape Location Scans . . . . .	315

# Executive Summary

Neutrinos are the most abundant particles in the Universe, yet their properties are least well understood. The observation of neutrinos changing from one type (flavor) to another have provided evidence of flavor mixing, also called flavor oscillations, and nonzero neutrino masses. The framework describing neutrino oscillations involves a phase parameter,  $\delta_{\text{CP}}$ , that is related to charge parity (CP) violation between neutrino and antineutrino mixing. Such an observation provides direct evidence of physics beyond the Standard Model of particle physics.

The Tokai to Kamioka (T2K) experiment is currently making critical measurements of  $\delta_{\text{CP}}$  and other properties that describe neutrino oscillations. Using a long-baseline of 295 km, a beam of muon-type neutrinos (or antineutrinos) are detected to change flavor at the Super-Kamiokande (SK) detector. By counting the number of oscillated neutrinos and antineutrinos, measurements on the oscillation parameters can be made.

The largest sources of systematic uncertainty in the oscillation analysis are related to the flux of neutrinos and the neutrino-nucleus cross section. Using data collected at the T2K near detector, ND280, stronger constraints are placed on those systematic uncertainties in the analysis. The process for constraining these uncertainties uses a binned maximum likelihood fit based on neutrino interaction topology. This thesis provides an independent measurement of the constraint using data collected using the T2K pi-zero detector (PØD) in ND280.

The thesis is organized as follows. The history of the neutrino physics, neutrino oscillations, and the T2K experiment are described in Chapter 1. The binned likelihood procedure

is described in Chapter 2 followed by the data selections described in Chapter 3. The systematic uncertainties in the analysis and the fit parameterization are described in Chapter 4. The validation of the fit procedure will be shown in Chapter 5, which is followed by the results of the likelihood fit shown in Chapter 6. Finally, Chapter 7 provides some concluding remarks and discussion on the results and possible analysis improvements.

This thesis was typeset using L<sup>A</sup>T<sub>E</sub>X. It was written in the LyX document processor with the unofficial Colorado State University L<sup>A</sup>T<sub>E</sub>X template graciously provided by Dr. Elliott Forney. The L<sup>A</sup>T<sub>E</sub>X template is available at <https://github.com/idfah/csuthesis> and the LyX layout is available at <https://github.com/hoganman/graduateDissertation>.

# Chapter 1

## Introduction

*Chose trop vue n'est chère tenue*

A thing too much seen is little prized – French proverb

### 1.1 Introduction to Neutrinos

The history of the neutrino can be traced back to the electron energy spectrum observed in neutron  $\beta$ -decay. While measurements of the  $\alpha$ - and  $\gamma$ -decay of atomic nuclei showed discrete spectral lines, the electron ( $\beta$  particle) exhibited a continuous energy spectrum. Experimentally, there were two observed particles in each decay process and classical physics dictated that the outgoing daughter particles should have discrete energies. The fact that the  $\beta$ -decay spectrum was very different posed a fundamental problem for physicists in the mid-1910s, which was that energy was not conserved. Two solutions were postulated: either the “energy conservation law is only valid statistically in such a process [...] or an additional undetectable new particle [...] carrying away the additional energy and spin [...] is emitted” [90]. The latter solution was proposed by Wolfgang Pauli in a letter dated 4 December, 1930, to a group of physicists meeting in Tübingen, modern Germany, where he first proposed the

neutrino<sup>1</sup>. Pauli's solution also predicted that the undetected neutrino would have half-integer spin, a quantum mechanical property of matter, since the observed particles in  $\beta$ -decay did not conserve angular momentum. The existence of the neutrino and validation of Pauli's predictions would not be experimentally verified for another 20 years.

The neutrino was first observed in 1953 by Clyde Cowan and Frederick Reines using a nuclear reactor in South Carolina, United States of America. Since then, three types or “flavors” of neutrinos and antineutrinos have been observed using accelerators and also from unique sources like the Sun and a supernova. Neutrino physics continues to be an active area of fundamental research since the neutrino is a truly unique probe to subatomic processes. For example they are observed to originate from the depths of the Sun’s core (over  $10^7$  degrees Kelvin) where fusion occurs.

Neutrinos rarely interact with normal matter, meaning that they travel essentially unimpeded towards one’s particle detector. The rarity of such interactions can be illustrated by the fact that over a typical human lifetime, only one solar neutrino interaction with an individual is expected out of the  $7.0 \times 10^{10}$  neutrinos/cm<sup>2</sup>/sec incident on the Earth<sup>2</sup>. So this begs the question: how does one detect a neutrino? The short answer is that one requires a large enough flux of neutrinos passing through a large dense volume of matter just to detect a single neutrino with today’s technology.

Scientists continue to be interested in neutrinos due to the unusual properties they exhibit. One of the more recent and surprising aspects of neutrinos is their ability to undergo “flavor oscillations” where a neutrino of definite flavor (type) is created and later observed as a different flavor. The impact of differences between neutrino and antineutrino oscillations

---

<sup>1</sup>In W Pauli’s December 1930 letter, he referred to his proposed particle as the “neutron”, and not the neutrino. It was Enrico Fermi who would coin the particle as a “neutrino” meaning in Italian *little neutral one*.

<sup>2</sup>To give some perspective to this number, this means 70 billion neutrinos are traveling every second through an area similar to one’s own thumb nail.

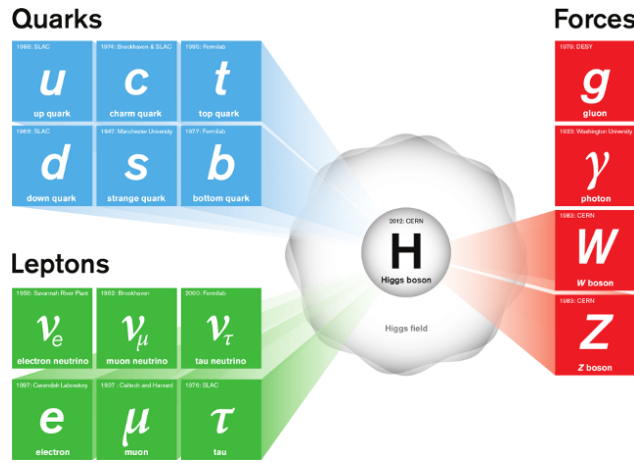


**Figure 1.1:** The Standard Model of particle physics consists of six quarks (up, down, strange, charm, bottom, and top), six leptons (electron, muon, tau, electron neutrino, muon neutrino, and tau neutrino), four force propagating bosons (gluon, photon, W, and Z), and the Higgs boson. The quarks, electron, muon, tau, W, and Z all gain mass through the Higgs field. The focus of this thesis are the neutrinos which are classified according to their charged, more massive lepton cousins. Image taken from [14].

could help explain the observed matter-antimatter asymmetry in the Universe which one of the most profound mysteries in physics today.

### 1.1.1 Neutrinos in the Standard Model

The Standard Model (SM) of particle physics is the theory of elementary or fundamental particle constituents and the forces between them. These forces are the electromagnetic, the weak, and the strong. String theory, which is not yet tested, attempts to incorporate the gravitational force. The SM forces and the gravitational force constitute the four *known* fundamental forces of the Universe. Each force in the SM has at least one “force carrier” particle that mediates the interactions between the matter particles. The force carriers are formally called “gauge bosons”, which indicates that they are particles with integer ( $0, 1, 2, \dots$ ) spin that mediate the interaction. The weak nuclear gauge bosons, the charged  $W^\pm$  and the neutral Z, couple to neutrinos as well as the other fermions, particles with half-integer ( $\frac{1}{2}, \frac{3}{2}, \frac{5}{2}, \dots$ ) spin, in the SM. All of the elementary particles of the SM are shown in Figure 1.1 on page 5.

Neutrinos in the SM are electrically neutral, massless particles categorized into three generations based on their more massive charged lepton cousins. In the SM, the three neutrinos and the three antineutrinos are the only neutral charge, spin  $1/2$  particles that experience only weak interactions. The neutrino and its associated charged cousin of the same flavor pair into a “weak isospin doublet” in the SM. These doublets are locally gauge invariant under a  $SU(2) \otimes U(1)$  symmetry which leads to the postulated existence of the photon, the  $W^\pm$  and  $Z$  bosons. They are necessary to enable local gauge invariance<sup>3</sup>.

What follows is a brief introduction to weak interactions. This is followed by a exploration on the nature of neutrino handedness. Then this is followed by a discussion on neutrino scattering with matter.

#### 1.1.1.1 Weak Interactions

The name “weak force” comes from the fact that this force is much weaker than the electromagnetic and strong nuclear forces. This is due to the weak mediating bosons, the  $W^\pm$  and  $Z$ , being massive particles unlike the massless gluon ( $g$ ) and photon ( $\gamma$ ). The  $W^\pm/Z$  have masses of  $80/90 \text{ GeV}/c^2$ , which is more massive than all the other elementary particles except for the top quark.

For weak interactions to occur at energies far below the rest mass (also called “off-shell”) of the  $W^\pm$  and  $Z$ , the interaction time must be infinitesimally small as dictated by the Heisenberg Uncertainty Principle

$$\Delta E \Delta t \gtrsim \hbar \quad (1.1)$$

<sup>3</sup>A gauge theory describes ways to measure physical forces or fields through interactions between elementary particles. The electric or magnetic fields for example can only be probed by charged particles. In the realm of quantum field theories, fields are postulated to permeate everywhere and it is excitations of these fields that produce experimental observables. Fields are constructed using the Lagrangian formalism and altered using gauge transformations. If altering the Lagrangian in some way does not affect the observables, this is referred to as a gauge invariance. Local gauge invariance means that under the constraints of the experiment, certain gauge transformations do not affect the observables. The allowed locally gauge invariant transformations require knowledge of its underlying Lie, or symmetry, group. With the weak isospin doublets, the Lie groups are  $SU(2) \otimes U(1)$  where  $SU(2)$  is the special unitary group of  $2 \times 2$  unitary matrices, and  $U(1)$  is the unitary (circle) group consisting of complex numbers of magnitude 1.

where  $\Delta E$  is the energy of the particle and  $\Delta t$  is the time during which the particle exists. As an example, consider a neutrino emitting a Z-boson as shown in Figure 1.2a on page 8. If the energy of the neutrino is 1 GeV, the lifetime of the  $Z$  boson is about  $10^{-25}$  seconds according to (1.1). In general, the probability that a massive particle of mass  $M$  will be created from the collision of two particles is given by a relativistic Breit–Wigner distribution

$$f(M) \propto \frac{1}{(M^2 - M_0^2)^2 c^4 + M_0^2 \Gamma^2}, \quad (1.2)$$

where  $M_0$  is the rest mass and  $\Gamma$  is the decay width of the particle. For  $M \ll M_0$ , the probability of creating that particle will be infinitesimally small. Therefore to observe a single weak interaction requires a large number of weakly interacting particles incident on a target.

Weak interactions are classified into two classes: charged current (CC) and neutral current (NC). The CC interaction involves a charged W boson and changes the incident neutrino into an electrically charged lepton of flavor  $l$  as shown Figure 1.2a on page 8. It is through the CC interaction where the flavor of the neutrino is inferred from the charged lepton. For instance, an electron type neutrino,  $\nu_e$ , is inferred to have interacted with matter if an electron is observed. The same is not true for NC interactions, since those interactions are flavor agnostic. The NC interaction involves a neutral Z boson and does not change the neutrino's flavor as shown in Figure 1.2b on page 8.

### 1.1.1.2 Chirality: How Neutrinos are Left Handed

Neutrinos are observed to have their spin direction vectors  $\boldsymbol{\sigma}$  opposite to their momentum  $\mathbf{P}$  and this is reversed for antineutrinos. This property is called helicity and is given by

$$\mathcal{H} = \frac{\boldsymbol{\sigma} \cdot \mathbf{P}}{|\mathbf{P}|}. \quad (1.3)$$

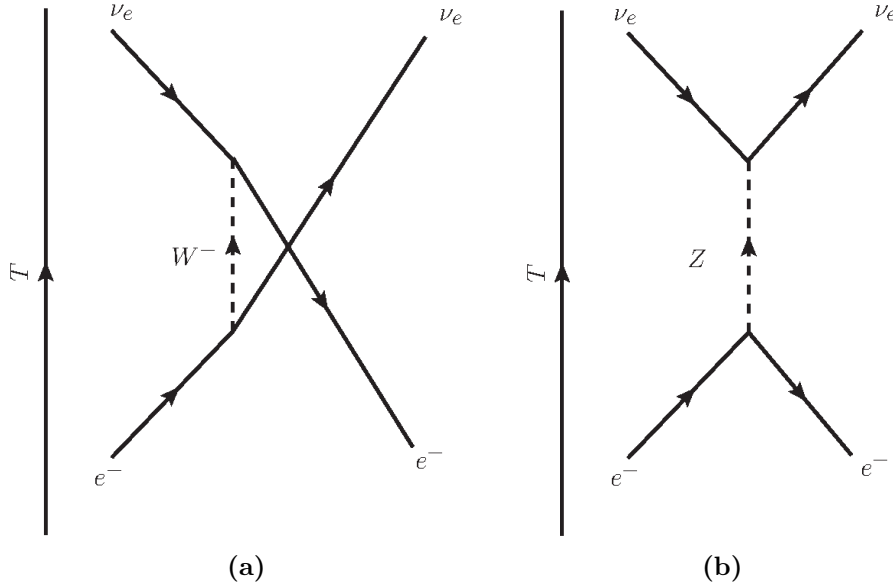


**Figure 1.2:** The CC and NC  $\nu_e e^- \rightarrow \nu_e e^-$  interaction

Although neutrino detection is difficult, the neutrino helicity is readily inferred from the daughter muon's helicity in pion decay,  $\pi^+ \rightarrow \mu^+ \nu_\mu$ . The  $\mu^+$  has negative helicity ( $\mathcal{H} = -1$ ) and to conserve spin, the neutrino's helicity must also be negative as shown in Figure 1.3 on page 9. The antineutrino's helicity is positive (+1) as shown in Figure 1.3 on page 9 through use of the charge (C) conjugation and parity (P) transformations. A C conjugation is a linear transformation that transforms all particles into their corresponding antiparticles while the P transformation inverts all spatial coordinates. Thus neutrinos are referred to as *left-handed* (LH) particles while antineutrinos are referred to as *right-handed* (RH) particles. It turns out that helicity is a useful quantum number to describe neutrinos and coincides with a property called chirality. To understand chirality and its relationship to helicity requires an analysis of the Dirac Lagrangian and Dirac equation.

The Dirac Lagrangian for a free particle field  $\psi(x)$  with half-integer spin can be written as

$$\mathcal{L} = \bar{\psi}(x) \left[ \frac{i\hbar}{2} \sum_{\mu=0}^3 \gamma^\mu \left( \overrightarrow{\partial_\mu} - \overleftarrow{\partial_\mu} \right) - mc \right] \psi(x), \quad (1.4)$$

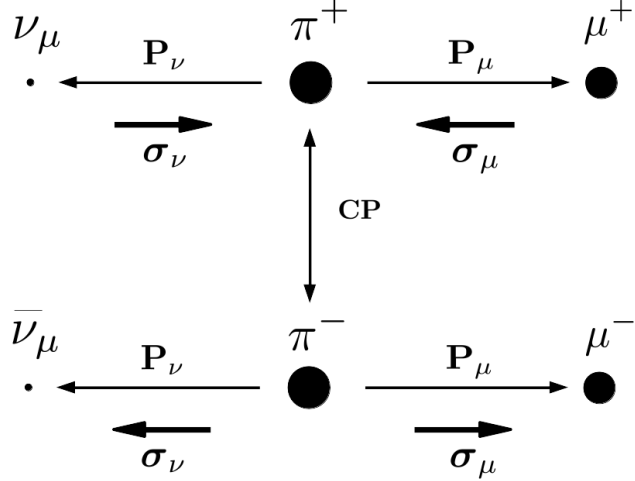


**Figure 1.3:** The helicity of the neutrino as inferred from pion decay. Since a pion at rest has zero (0) angular momentum, the system of daughter particles must have also net zero angular momentum. By measuring the muon's helicity, the helicity of neutrino is inferred. A neutrino (antineutrino) is a left-handed (right-handed) helicity particle since its spin is anti-parallel (parallel) to its momentum.

where  $\psi(x)$  is a four-component vector (spinor) describing a particle field and  $\gamma^\mu$  are a set of four 4x4 matrices. The adjoint field  $\bar{\psi}(x)$  is defined as

$$\bar{\psi}(x) \equiv \psi^\dagger(x) \gamma^0, \quad (1.5)$$

where  $\dagger$  denotes the conjugate and transpose operations. The  $\overrightarrow{\partial}_\mu$  operator is a four-vector defined as

$$\partial_0 = \frac{1}{c} \frac{\partial}{\partial t}, \partial_1 = \frac{\partial}{\partial x}, \partial_2 = \frac{\partial}{\partial y}, \partial_3 = \frac{\partial}{\partial z}, \quad (1.6)$$

that acts only to the right while  $\overleftarrow{\partial}_\mu$  only acts to the left (i.e.  $\overleftarrow{\psi} \overleftarrow{\partial}_\mu = \partial_\mu \overleftarrow{\psi}$ ). The  $\gamma^\mu$  matrices are not unique and different representations are more appropriate for different kinematic regimes. The field equations are extracted from the Lagrangian using the Euler-Lagrange procedure. In general for a set of  $M$  fields, the field equations are given by

$$\partial_\mu \frac{\partial \mathcal{L}}{\partial (\partial_\mu \psi_r)} - \frac{\partial \mathcal{L}}{\partial \psi_r} = 0 \quad (r = 0, 1, 2, \dots, M-1, M). \quad (1.7)$$

For the Dirac Lagrangian, the field equation for  $\psi$  is given by

$$\partial_\mu \frac{\partial \mathcal{L}}{\partial (\partial_\mu \bar{\psi})} - \frac{\partial \mathcal{L}}{\partial \bar{\psi}} = 0, \quad (1.8)$$

which yields the Dirac equation

$$\left[ i\hbar \sum_{\mu=0}^3 \gamma^\mu \partial_\mu - mc \right] \psi(x) = 0. \quad (1.9)$$

The representation of the  $\gamma^\mu$  matrices that is useful to describe neutrinos is the *Chiral representation* (also called the *Weyl representation*) where

$$\gamma^0 = \begin{bmatrix} 0 & I_2 \\ I_2 & 0 \end{bmatrix}, \gamma^1 = \begin{bmatrix} 0 & \sigma_x \\ -\sigma_x & 0 \end{bmatrix}, \gamma^2 = \begin{bmatrix} 0 & \sigma_y \\ -\sigma_y & 0 \end{bmatrix}, \gamma^3 = \begin{bmatrix} 0 & \sigma_z \\ -\sigma_z & 0 \end{bmatrix}, \quad (1.10)$$

$I_2$  is the  $2 \times 2$  identity matrix,  $\sigma_{x,y,z}$  are the Pauli Spin matrices given by

$$\sigma_x = \sigma_1 = \begin{pmatrix} 0 & 1 \\ 1 & 0 \end{pmatrix}, \quad \sigma_y = \sigma_2 = \begin{pmatrix} 0 & -i \\ i & 0 \end{pmatrix}, \quad \sigma_z = \sigma_3 = \begin{pmatrix} 1 & 0 \\ 0 & -1 \end{pmatrix}.$$

Using the Chiral representation, the chirality matrix,  $\gamma^5$  (the fifth gamma matrix), is defined as

$$\gamma^5 = i\gamma^0\gamma^1\gamma^2\gamma^3 = \begin{bmatrix} -I_2 & 0 \\ 0 & I_2 \end{bmatrix}, \quad (1.11)$$

which is diagonal as well as Hermitian, meaning that its eigenvalues are real and observable. Let the eigenfunctions of the chirality matrix be denoted with subscripts  $P$  and  $M$  such that the eigenvalue equations are

$$\begin{aligned} \gamma^5 \psi_P &= +1 \psi_P, \\ \gamma^5 \psi_M &= -1 \psi_M. \end{aligned} \quad (1.12)$$

The field equation solutions to (1.9) can be decomposed into  $\psi_P$  and  $\psi_M$  projections using two chiral projection operators  $\hat{O}_{P,M}$  where

$$\psi = (\hat{O}_P + \hat{O}_M) \psi = \psi_P + \psi_M. \quad (1.13)$$

The chiral operators are explicitly given by

$$\begin{aligned} \hat{O}_M &= \frac{1}{2} (I_4 - \gamma^5) = \begin{pmatrix} 0 & 0 \\ 0 & I_2 \end{pmatrix}, \\ \hat{O}_P &= \frac{1}{2} (I_4 + \gamma^5) = \begin{pmatrix} I_2 & 0 \\ 0 & 0 \end{pmatrix}, \end{aligned} \quad (1.14)$$

where  $I_4$  is the  $4 \times 4$  identity matrix. Taken together (1.13) and (1.14) indicate the free neutrino field is a vector  $\psi$  minus axial vector  $\gamma^5\psi$ , also referred to as V-A, under P transformations. This feature is what allows for the weak force to violate P-symmetry and CP-symmetry. Referring back to (1.4) and (1.7), the Dirac equation becomes a set of coupled equations

$$\begin{aligned} i\hbar \sum_{\mu=0}^3 \gamma^\mu \partial_\mu \psi_P &= mc\psi_M \\ i\hbar \sum_{\mu=0}^3 \gamma^\mu \partial_\mu \psi_M &= mc\psi_P, \end{aligned} \quad (1.15)$$

where dynamics are set by the mass.

Since the chiral projection operators are decompositions of the identity matrix, the simplest nontrivial solution to  $\psi$  is

$$\psi = \begin{pmatrix} \chi_P \\ \chi_M \end{pmatrix} \quad (1.16)$$

where  $\chi$  represents two-component spinors. Using 1.16 the Dirac equation in (1.15) can again be rewritten as

$$\begin{aligned} i\hbar \left[ \frac{1}{c} \frac{\partial}{\partial t} + \boldsymbol{\sigma} \cdot \boldsymbol{\nabla} \right] \chi_P &= -mc\chi_M \\ i\hbar \left[ \frac{1}{c} \frac{\partial}{\partial t} - \boldsymbol{\sigma} \cdot \boldsymbol{\nabla} \right] \chi_M &= -mc\chi_P, \end{aligned} \quad (1.17)$$

where

$$\boldsymbol{\sigma} \cdot \boldsymbol{\nabla} = \sigma_x \frac{\partial}{\partial x} + \sigma_y \frac{\partial}{\partial y} + \sigma_z \frac{\partial}{\partial z}. \quad (1.18)$$

In the limiting case of vanishing mass ( $m \rightarrow 0$ ), as is in the SM, the free particle field equations in (1.17) decouple into

$$\begin{aligned} \left( \frac{E}{c} + \boldsymbol{\sigma} \cdot \boldsymbol{P} \right) \chi_P &= 0, \\ \left( \frac{E}{c} - \boldsymbol{\sigma} \cdot \boldsymbol{P} \right) \chi_M &= 0, \end{aligned} \quad (1.19)$$

where the differential operators have been evaluated as the particle's energy  $E$  and momentum three-vector  $\boldsymbol{P}$ . For massless neutrinos,  $\chi_P$  and hence  $\psi_P$ , describe particles of negative energy  $E = -|\boldsymbol{P}|c$  which in the context of quantum field theory are interpreted as antiparticles traveling backwards in time. Conversely,  $\psi_M$  have positive energy  $E = |\boldsymbol{P}|c$  and which means they are particles traveling forward in time.

If one also multiplies (1.15) by  $\gamma^5 \gamma^0$  and uses the fact that the spin operator  $\boldsymbol{\sigma}$  is given by

$$\boldsymbol{\sigma} = i(\gamma^2 \gamma^3, \gamma^3 \gamma^1, \gamma^1 \gamma^2) = \gamma^0 \gamma^k \gamma^5 \quad (k = 1, 2, 3), \quad (1.20)$$

each decoupled equation becomes

$$\frac{\boldsymbol{\sigma} \cdot \boldsymbol{P}}{|\boldsymbol{P}|} \psi_{P,M} = \gamma^5 \psi_{P,M} = \pm \psi_{P,M}, \quad (1.21)$$

where one recognizes that the helicity and chiral states are the same for  $m \rightarrow 0$  only. Thus the labels  $M$  and  $P$  actually are identical to the LH and RH helicity labels, respectively. Using the results above, a neutrino is always observed as a LH particle while the antineutrino is always observed as a RH antiparticle.

The observation of only LH neutrinos and RH antineutrinos is an important feature in the SM. However, since neutrinos are known to have mass and given that neutrinos oscillate, it is theoretically possible to observe a RH neutrino and a LH antineutrino. That would require boosting to a highly relativistic reference frame with respect to the laboratory.

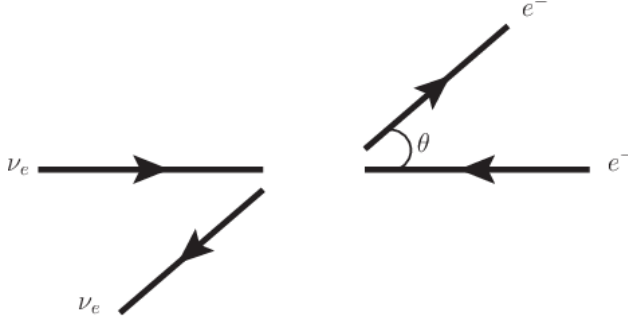


**Figure 1.4:** A schematic of  $\theta$  in  $\nu_e e^-$  scattering. The same diagram is used to describe  $\bar{\nu}_e + e^-$  scattering with  $\nu_e \rightarrow \bar{\nu}_e$ .

### 1.1.1.3 Neutrino Scattering with Matter

Charged current (CC) neutrino interactions on nuclear particles are the interactions investigated in this thesis. These interactions produce an outgoing charged lepton and a variety of hadronic states. While interactions with valence electrons are possible, they are far less common in large, subatomic particle detectors. However, the physics of neutrino-electron scattering is very similar to neutrino-nucleus scattering.

Consider neutrino-electron scattering, the cross section for  $\nu_e e^-$  is given by

$$\frac{d\sigma}{d\Omega} = \left( \frac{G_F \hbar c}{2\pi} \right)^2 s, \quad (1.22)$$

where  $G_F$  is the Fermi constant and  $s$  is the center of mass energy squared. Due to the V-A nature of the weak force, neutrinos couple to LH particles and to RH antiparticles. The outgoing particles are isotropically distributed in the center-of-mass frame since the initial and final spin state of the system is  $J = 0$ . Compare Eqn. (1.22) with the cross section for

$\bar{\nu}_e e^-$

$$\frac{d\sigma}{d\Omega} = \left( \frac{G_F \hbar c}{4\pi} \right)^2 (1 - \cos \theta)^2 s, \quad (1.23)$$

where  $\theta$  is the observed scattering angle of the electron as shown in Figure 1.4 on page 13. Since the total spin of the  $\bar{\nu}_e e^-$  system is  $J = 1$  with z-projection  $J_z = 1$ , the antineutrino is preferentially forward scattered. Integrating over all angles, the cross sections are related

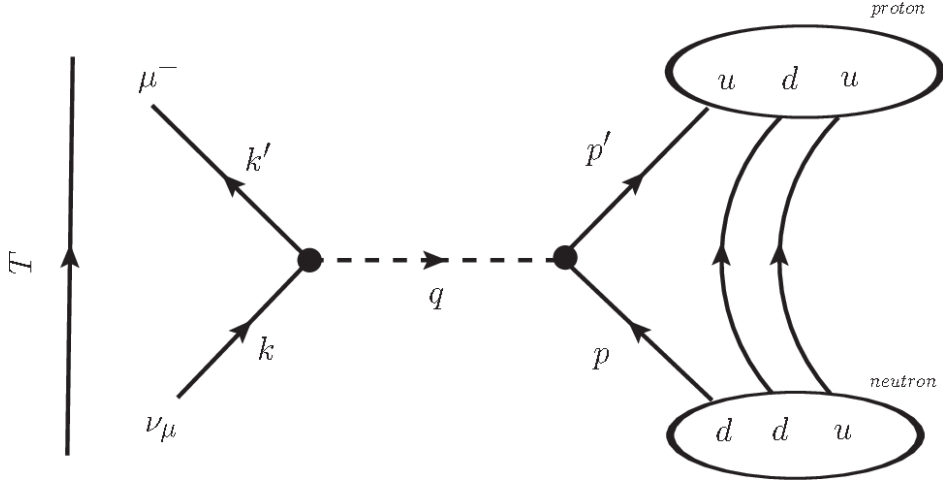


**Figure 1.5:** A  $\nu_\mu$ -induced CCQE interaction.

to each other by

$$\sigma(\bar{\nu}_e e^-) = \frac{1}{3} \sigma(\nu_e e^-).$$

The factor  $1/3$  arises from the fact that angular momentum conservation forbids the  $J_z = -1$  and  $0$  states for  $\bar{\nu}_e e^-$  scattering. The same  $1/3$  factor arises between  $\nu_\mu d \rightarrow \mu^- u$  and  $\bar{\nu}_\mu u \rightarrow \mu^+ d$  scattering.

In neutrino-nuclear scattering, the simple picture of free quarks must be replaced with the reality of the nuclear medium. Interactions with a single quark are still possible, but nuclear effects can alter the products of the interactions. The kinematics of the particles involved can be altered as well depending on the initial state of the nucleus. Distinctions must be made in neutrino physics between observables from primary interactions like  $\nu_e + e^-$  and nuclear “final state interactions” (FSI).

There are three neutrino-nuclear scattering classes presented in this thesis: quasi-elastic (CCQE), deep inelastic scattering (CC-DIS), and single pion production (CC-1 $\pi$ ). The  $\nu$  CCQE interaction refers to the process where an incoming neutrino and neutron ( $udd$ ) scatter to produce a charged lepton and proton ( $uud$ ) as shown in Figure 1.5 on page 14. For  $\bar{\nu}$  CCQE, the proton is converted to a neutron instead. The CCQE interaction is the lowest energy CC interaction with a nucleon and has approximate mass conservation between

the proton-neutron states ( $\Delta m = 1.29 \text{ MeV}/c^2$ ). The CC-DIS interaction is a high energy transfer process that shatters the nucleus apart. Finally, CC- $1\pi$  interactions refer to processes where a post-FSI charged pion is experimentally observed presumably from the decay of resonance state like the  $\Delta(1232)$  baryon. These interactions are not well understood currently since they occur in the transition between CCQE and CC-DIS interaction modes.

### 1.1.2 Neutrino Oscillations

Neutrino oscillations is the physical process of a neutrino produced with a particular, definite flavor is later observed as a different flavor. This phenomenon was first observed as a deficit of neutrinos for a number of atmospheric and solar neutrino experiments. The deficit also seemed more pronounced for atmospheric neutrinos as the distance from their source increased. For neutrino oscillations to occur, at most one neutrino can be massless. This observation firmly established that the SM is incorrect with its assumption of massless neutrinos.

The first indication of neutrino oscillations was from the Ray Davis Homestake Mine experiment [33] which began operation in the 1960s. Ray Davis was an expert chemist and designed a radiochemical experiment to measure the flux of neutrinos from the sun. The purpose of this experiment was to test John Bahcall's prediction of the fusion rate in the Sun and neutrino flux from it as well. Davis' experiment would need to operate for many years to collect enough statistics due to the expected low capture rate. Measurements continued into the 1980s and showed that the flux of neutrinos was about one-third the expected rate and this became known as the "Solar Neutrino Problem." The primary explanations were either that the solar model was incorrect or the neutrino capture cross section was incorrect. The Sudbury Neutrino Observatory (SNO) was able to resolve this problem by making a model-independent measurement of the solar neutrino flux. The SNO experiment observed a  $\nu_e$  CC-to-NC ratio of  $0.301 \pm 0.033$ , which confirmed that only about 30% of neutrinos

arrive as  $\nu_e$  flavors on Earth. In other words, the majority of neutrinos arrive as the wrong flavor [90].

Another outstanding problem emerged with measurements of atmospheric neutrinos, which are the muon and electron types. Atmospheric neutrinos are produced when high energy cosmic rays strike atmospheric particles. These cosmic ray collisions generate mostly pions and kaons that decay into neutrinos. When trying to measure the  $\nu_\mu/\nu_e$  ratio, there was another significant deficit. This was particularly apparent for the Super-Kamiokande (SK) experiment, which is a 50 kt tank of pure water lined with thousands of photomultiplier tubes designed to observe solar and atmospheric neutrinos. It was the first experiment to perform a neutrino oscillation analysis that successfully and definitely explained the deficit.

The observation of neutrino oscillations is a relatively new discovery. Bruno Pontecorvo [66] first proposed such a mechanism in 1957 between neutrinos and antineutrinos much like known neutral K-mesons oscillations. However, oscillations between flavored neutrinos was not expected since it requires the neutrino to have mass. The reasons why are explained in the next subsection.

### 1.1.2.1 Two Flavor Derivation of Neutrino Oscillations

The phenomenon of neutrino oscillations can be described with elementary, non-relativistic quantum mechanics using the Schrödinger Equation

$$-\frac{\hbar}{i} \frac{d}{dt} |\nu(\mathbf{r}, t)\rangle = \hat{H} |\nu(\mathbf{r}, t)\rangle, \quad (1.24)$$

where  $\hat{H}$  is the Hamiltonian for the physical system. Here we consider massive neutrinos of mass  $m_j$  in its rest frame (free particle). The Hamiltonian is diagonal in this case, which acting on  $|\nu_j\rangle$  results in the eigenvalue equation

$$\hat{H} |\nu_j(\mathbf{r}, t)\rangle = E_j |\nu_j(\mathbf{r}, t)\rangle, \quad (1.25)$$

where  $E_j$  is the energy of the neutrino  $|\nu_j\rangle$ . Substituting (1.25) into (1.24) and solving for  $|\nu(\mathbf{r}, t)\rangle$ , one obtains

$$|\nu_j(\mathbf{r}, t)\rangle = e^{-iE_j t/\hbar} |\nu_j(\mathbf{r}, t=0)\rangle, \quad (1.26)$$

where  $|\nu_j(\mathbf{r}, t=0)\rangle$  is created with momentum  $\mathbf{p}$  at the origin  $\mathbf{r}=0$ . The time-independent solution to (1.24) is a plane-wave given by

$$|\nu_j(\mathbf{r}, t=0)\rangle = e^{i\mathbf{p} \cdot \mathbf{r}/\hbar} |\nu_j\rangle. \quad (1.27)$$

Before being able to describe neutrino oscillations, the basis states must be defined. For this example, consider that there are only two eigenstates, labeled  $\nu_1$  and  $\nu_2$ , in the “mass” basis with definite mass  $m_1$  and  $m_2$ , respectively. However, experiments can produce neutrinos, as well as probe them, only in a definite flavor state, denoted by a Greek letter subscript. Let the generated neutrino, which is a linear superposition of mass states 1 and 2, have momentum  $\mathbf{p}$  and flavor  $\alpha$ . Since both mass eigenstates share the same momentum  $\mathbf{p}$  (but not energy!), the exponential term in (1.27) is an overall phase that will cancel out later. One can postulate a linear transformation,  $U$ , between the basis states given by

$$\begin{bmatrix} \nu_\alpha \\ \nu_\beta \end{bmatrix} = \begin{bmatrix} U_{11} & U_{12} \\ U_{21} & U_{22} \end{bmatrix} \begin{bmatrix} \nu_1 \\ \nu_2 \end{bmatrix} \quad (1.28)$$

This linear transformation must be a unitary matrix ( $U^{-1} = U^\dagger$ ,  $\dagger$  = transpose conjugate) since the states  $\nu_{1,2}$  constitute a complete orthonormal basis in the mass basis. With this unitary property,  $U$  can be written as a rotation matrix

$$\begin{bmatrix} \nu_\alpha \\ \nu_\beta \end{bmatrix} = \begin{bmatrix} \cos(\theta) & \sin(\theta) \\ -\sin(\theta) & \cos(\theta) \end{bmatrix} \begin{bmatrix} \nu_1 \\ \nu_2 \end{bmatrix}, \quad (1.29)$$

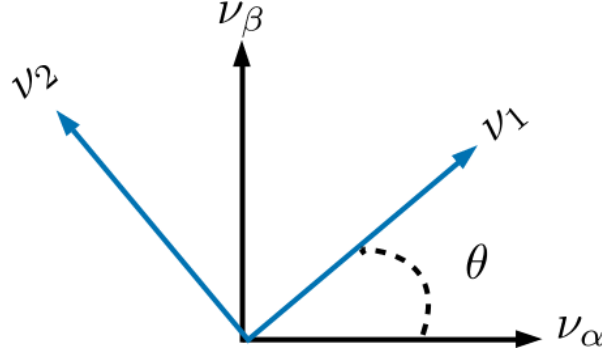


**Figure 1.6:** Illustration of a mixing matrix in two dimension.

where  $\theta$  is the angle between the two bases. One can imagine this transformation between bases as shown in Figure 1.6 on page 18. The probability of creating a neutrino of flavor  $\alpha$  and later observing it as flavor  $\beta \neq \alpha$  at time  $t = T > 0$  is given by

$$\begin{aligned} \mathcal{P}(\nu_\alpha \rightarrow \nu_\beta) &= |\langle \nu_\alpha(t=0) | \nu_\beta(t=T) \rangle|^2 \\ &= |\{\cos(\theta) \langle \nu_1(t=0) | + \sin(\theta) \langle \nu_2(t=0) |\} \\ &\quad \times \{-\sin(\theta) |\nu_1(t=T)\rangle + \cos(\theta) |\nu_2(t=T)\rangle\}|^2. \end{aligned} \quad (1.30)$$

Evaluating all inner products and simplifying terms in (1.30) results in the following equation

$$\mathcal{P}(\nu_\alpha \rightarrow \nu_\beta) = \sin^2(2\theta) \sin^2\left(\frac{E_1 - E_2}{2\hbar}T\right). \quad (1.31)$$

The terminology of “neutrino oscillations” should be more apparent now since (1.31) demonstrates that the probability changes sinusoidally as a function of time  $T$ . This equation is not, however, terribly useful in the laboratory frame since it is hard to design an experiment where the travel time an individual neutrino is actually measured. Since neutrinos are nearly massless, they travel very close to the speed of light. Therefore time  $T$  is replaced with  $L/c$  where  $L$  is the distance between the neutrino origin and detection. One can also approximate the energy of the mass eigenstate as

$$\begin{aligned}
E_j &= \left( m_j^2 c^4 + p_j^2 c^2 \right)^{\frac{1}{2}} = p_j c \left( 1 + \frac{m_j^2 c^2}{p_j^2} \right)^{\frac{1}{2}} \\
&\approx p_j c \left( 1 + \frac{m_j^2 c^2}{2p_j^2} + \mathcal{O} \left( \frac{m_j c}{p_j} \right)^4 \right) \\
&\approx E_\nu + \frac{m_j^2 c^4}{2E_\nu},
\end{aligned} \tag{1.32}$$

where for oscillation experiments  $p_j \gg m_j c$  and  $p_j c \approx E_\nu$  where  $E_\nu$  is the neutrino energy as measured in the laboratory. Substituting these assumptions in (1.31), the oscillation probability is given by

$$\mathcal{P}(\nu_\alpha \rightarrow \nu_\beta) = \sin^2(2\theta) \sin^2 \left( \frac{\Delta m^2 c^3}{4\hbar} \frac{L}{E_\nu} \right), \tag{1.33}$$

where  $\Delta m^2 = m_2^2 - m_1^2$  is the mass-squared difference between the mass states.

For a moment consider evaluating all the physical constants in natural units ( $c = \hbar = 1$ ), the  $\Delta m^2$  in eV<sup>2</sup>,  $L$  in km, and  $E_\nu$  in GeV. The oscillation probability from between states  $\nu_\alpha$  to  $\nu_\beta$  is given by

$$\mathcal{P}(\nu_\alpha \rightarrow \nu_\beta) = \sin^2(2\theta) \sin^2 \left( 1.27 \frac{\Delta m^2}{[\text{eV}^2]} \frac{L/E_\nu}{[\text{km}/\text{GeV}]} \right) \text{ [natural units]} \tag{1.34}$$

which more clearly illustrates the physics of neutrino oscillations. The oscillation probability has an amplitude of  $\sin^2(2\theta)$  and varies with frequency inversely proportional to  $\Delta m^2$  as shown in Figure 1.7 on page 20. Since  $L$  and  $E_\nu$  are the only controllable parameters for an oscillation experiment, probing  $\theta$  or  $\Delta m^2$  can be difficult unless the experiment can probe a large range of  $L/E_\nu$  as shown in Figure 1.8 on page 21.

### 1.1.2.2 Three Flavor Oscillations

In the general case of oscillations using a  $n \times n$  mixing matrix, the unitary transformation can be written as a rotation matrix with  $\frac{n}{2}(n-1)$  weak mixing angles with  $\frac{1}{2}(n-2)(n-1)$  Charge-Parity (CP) violating phases. In addition, oscillations are dictated by a total of  $n-1$

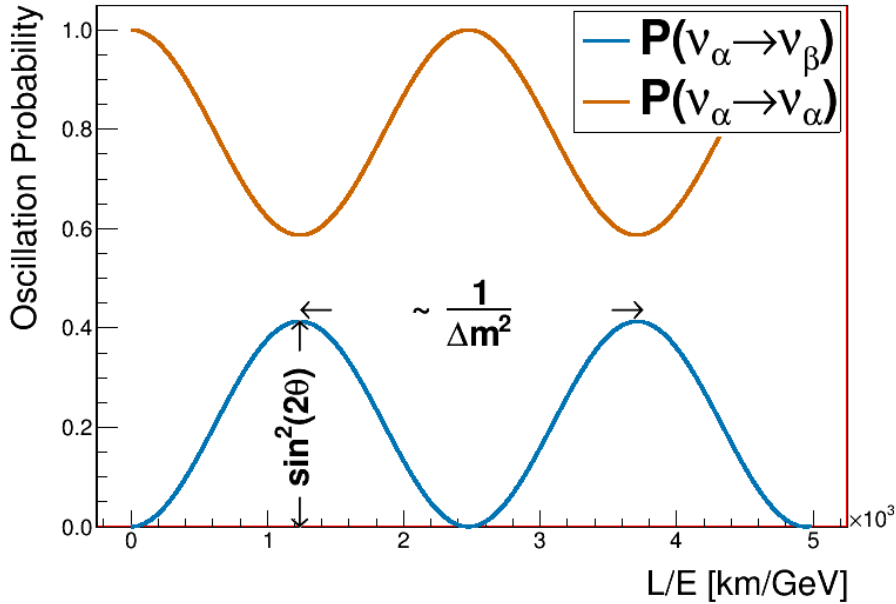


**Figure 1.7:** Two flavor oscillation probability as a function  $L/E$  is shown using  $\theta = 20^\circ$  and  $\Delta m^2 = 10^{-3} \text{ eV}^2/c^4$ . The spacing between adjacent peaks/troughs is proportional to the inverse of  $\Delta m^2$ . Note that  $\mathcal{P}(\nu_\alpha \rightarrow \nu_\alpha) = 1 - \mathcal{P}(\nu_\alpha \rightarrow \nu_\beta)$  since the oscillation probability must always sum to 1.

mass-squared splittings [90]. This all assumes that neutrinos obey the Dirac Equation, or that they are not their own antiparticles. The favored mixing model is a  $3 \times 3$  matrix since there are three known neutrino flavors,  $\nu_e$ ,  $\nu_\mu$ , and  $\nu_\tau$ . This means that there are three (3) mixing angles, one (1) CP violating phase, and three (3) mass-squared splittings.

The most frequently used matrix parameterization is the MNSP (MNSP: Maki-Nakagawa-Sakata-Pontecorvo) matrix. Pontecorvo is credited with first conceiving of neutrino oscillations, albeit between neutrino and antineutrinos [65]. It was Maki, Nakagawa, and Sakata who conceived of the parameterization based on the ideas of Pontecorvo [60]. The MNSP matrix is decomposed into separate rotation matrices as given by (1.35)

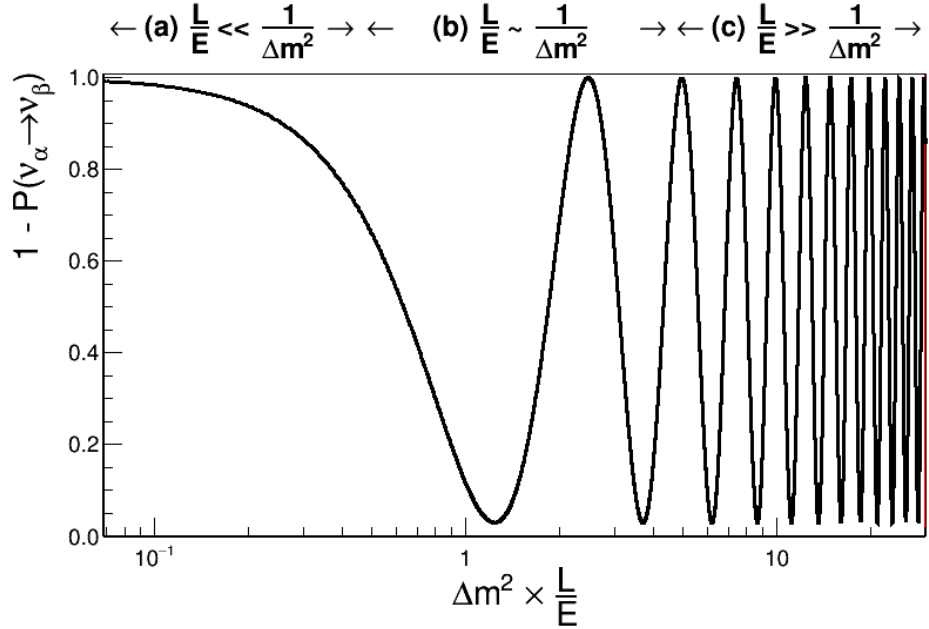


**Figure 1.8:** Semi-logarithmic plot of the survival probability of flavor  $\alpha$  ( $1 - \mathcal{P}(\nu_\alpha \rightarrow \nu_\beta) = \mathcal{P}(\nu_\alpha \rightarrow \nu_\alpha)$ ) over a wide range of  $L/E$  values for  $\theta = 40^\circ$ . The arrows above the plot coarsely denote three possible cases: (a) no oscillations ( $L/E \ll 1/\Delta m^2$ ); (b) sensitivity to oscillations ( $L/E \sim 1/\Delta m^2$ ); (c) only average measurement ( $L/E \gg 1/\Delta m^2$ ). Image originally inspired by reference [75].

$$U_{\text{MNSP}} = \underbrace{\begin{bmatrix} 1 & 0 & 0 \\ 0 & c_{32} & s_{32} \\ 0 & -s_{32} & c_{32} \end{bmatrix}}_{U_{32}=U_{\text{atm}}} \times \underbrace{\begin{bmatrix} c_{31} & 0 & s_{31}e^{i\delta_{\text{CP}}} \\ 0 & 1 & 0 \\ -s_{31}e^{-i\delta_{\text{CP}}} & 0 & c_{31} \end{bmatrix}}_{U_{31}=U_{\text{rea}}} \times \underbrace{\begin{bmatrix} c_{21} & s_{21} & 0 \\ -s_{21} & c_{21} & 0 \\ 0 & 0 & 1 \end{bmatrix}}_{U_{21}=U_{\text{sol}}}, \quad (1.35)$$

where

$$c_{ij} = \cos \theta_{ij}, \quad s_{ij} = \sin \theta_{ij}, \quad (1.36)$$

and  $\delta_{\text{CP}}$  represents the CP violating phase. Each rotation matrix  $U_{ij}$  represents the different sources for neutrino oscillations experiments with “atm”, “rea”, and “sol” representing atmospheric  $\nu$ ’s, nuclear reactor  $\nu$ ’s, and solar  $\nu$ ’s, respectively. The sensitivity of neutrino oscillations for different sources is given in Table 1.1 on page 22.

**Table 1.1:** Sensitivity of different oscillation experiments originally published in reference [81].

Source	Species	Baseline [km]	Mean Energy [GeV]	$\min(\Delta m^2) [\text{eV}^2]$
Reactor	$\bar{\nu}_e$	1	$\sim 10^{-3}$	$\sim 10^{-3}$
Reactor	$\bar{\nu}_e$	100	$\sim 10^{-3}$	$\sim 10^{-5}$
Accelerator	$\nu_\mu, \bar{\nu}_\mu$	1	$\sim 1$	$\sim 1$
Accelerator	$\nu_\mu, \bar{\nu}_\mu$	$10^3$	$\sim 1$	$\sim 10^{-3}$
Atmospheric $\nu$ 's	$\nu_{e,\mu}, \bar{\nu}_{\mu,e}$	$10^4$	$\sim 1$	$\sim 10^{-4}$
Sun	$\nu_e$	$1.5 \times 10^8$	$\sim 10^{-3}$	$\sim 10^{-11}$

If neutrinos are their own antiparticles, they are not described by the Dirac Equation but instead are described the Majorana Equation. This adds two (in general  $n - 1$ ) more CP violating Majorana phases,  $\alpha$  and  $\beta$ , to the MNSP matrix

$$U_{\text{MNSP}} \rightarrow U_{\text{MNSP}} \times \underbrace{\begin{bmatrix} 1 & 0 & 0 \\ 0 & e^{i\alpha} & 0 \\ 0 & 0 & e^{i\beta} \end{bmatrix}}_{U_{\text{Majorana}}} . \quad (1.37)$$

Unfortunately, neutrino oscillations are not able to probe the Majorana phases since the Majorana matrix is diagonal. The question of as to whether neutrinos are Majorana ( $\nu = \bar{\nu}$ ) or Dirac ( $\nu \neq \bar{\nu}$ ) particles is an open question that is being explored by neutrino-less double beta decay experiments [74].

The full three flavor oscillation probability is given by

$$\begin{aligned} \mathcal{P}(\nu_\alpha \rightarrow \nu_\beta) = & \delta_{\alpha\beta} - 4 \sum_{j=1}^3 \left[ \sum_{i>j}^3 \text{Re}(K_{\alpha\beta,ij}) \sin^2(\phi_{ij}) \right] \\ & + 4 \sum_{j=1}^3 \left[ \sum_{i>j}^3 \text{Im}(K_{\alpha\beta,ij}) \sin(\phi_{ij}) \cos(\phi_{ij}) \right], \end{aligned} \quad (1.38)$$

where

$$K_{\alpha\beta,ij} = U_{\alpha i} U_{\beta i}^* U_{\alpha j}^* U_{\beta j} \quad (1.39)$$

encapsulates the MNSP matrix elements and

$$\phi_{ij} = \frac{\Delta m_{ij}^2 c^3}{4\hbar} \frac{L}{E_\nu}. \quad (1.40)$$

Since CP violation means that  $\mathcal{P}(\nu_\alpha \rightarrow \nu_{\beta \neq \alpha}) \neq \mathcal{P}(\bar{\nu}_\alpha \rightarrow \bar{\nu}_{\beta \neq \alpha})$ , CP violating terms must be odd function of  $\delta_{\text{CP}}$ . Consider the following two examples, muon neutrino survival and muon neutrino to electron neutrino appearance.

**Muon Neutrino Survival** The probability of a muon type neutrinos (antineutrinos) surviving is given by

$$\begin{aligned} \mathcal{P}\left(\overset{(-)}{\nu}_\mu \rightarrow \overset{(-)}{\nu}_\mu\right) &= 1 - 4s_{23}^2 c_{13}^2 \left(V_{\cos \delta_{\text{CP}}}\right) \sin^2 \phi_{31} \\ &\quad - 4s_{23}^2 c_{13}^2 \left(Z_{\cos \delta_{\text{CP}}}\right) \sin^2 \phi_{32} \\ &\quad - 4 \left(V_{\cos \delta_{\text{CP}}}\right) \left(Z_{\cos \delta_{\text{CP}}}\right) \sin^2 \phi_{21}, \end{aligned} \quad (1.41)$$

where

$$V_{\cos \delta_{\text{CP}}} = s_{12}^2 c_{23}^2 + s_{13}^2 s_{23}^2 c_{12}^2 + 2s_{12}s_{13}s_{23}c_{12}c_{23} \cos \delta_{\text{CP}}, \quad (1.42)$$

$$Z_{\cos \delta_{\text{CP}}} = c_{12}^2 c_{23}^2 + s_{13}^2 s_{23}^2 s_{12}^2 - 2s_{12}s_{13}s_{23}c_{12}c_{23} \cos \delta_{\text{CP}}, \quad (1.43)$$

and  $\overset{(-)}{\nu}_\mu$  represents either  $\nu_\mu$  or  $\bar{\nu}_\mu$ . If a definitive measurement of  $\mathcal{P}(\nu_\mu \rightarrow \nu_\mu) \neq \mathcal{P}(\bar{\nu}_\mu \rightarrow \bar{\nu}_\mu)$  in vacuum occurs, it implies that the combined C, P and time (CPT) symmetry is violated<sup>4</sup>.

**Electron Neutrino Appearance** The previous subsection briefly explored the muon disappearance probability, which is not tested as a channel for CP violation. Electron neutrino appearance, however, does provide insight into CP violation in the lepton sector. The appearance probability of electron neutrino types from muon neutrino types is given by

<sup>4</sup>When going to through matter however, the oscillation probability is affected. This is explained more in Section 1.1.2.3.

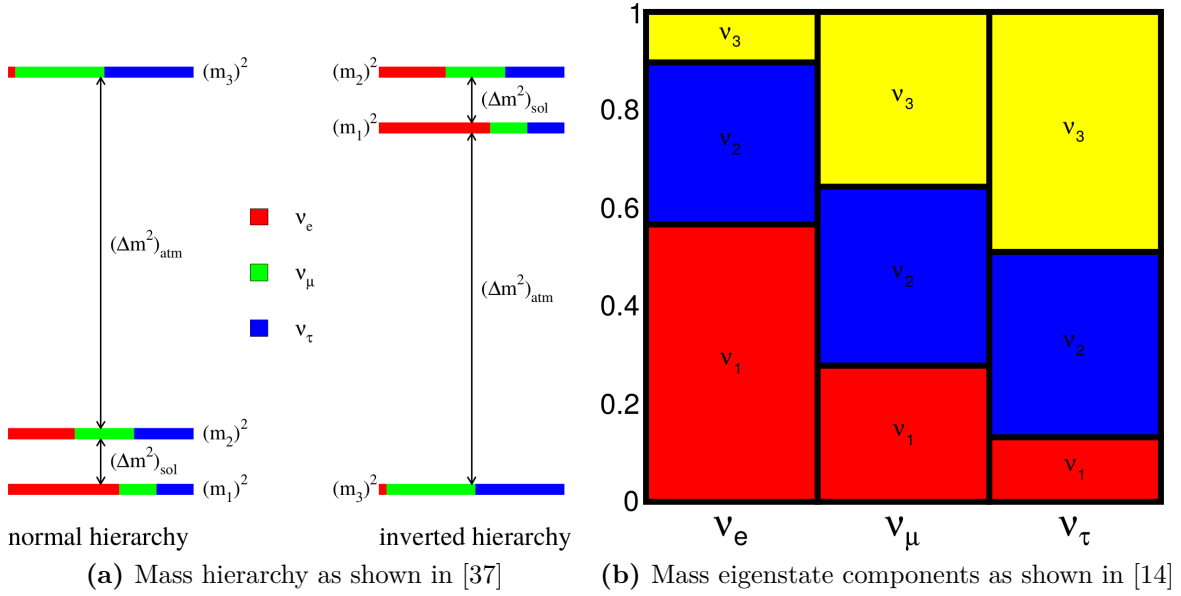


**Figure 1.9:** Neutrino mass hierarchy problem and MNSP representation. Left: the mass hierarchy problem is shown. The colored bars for each mass eigenstate correspond to the approximate flavor content of the neutrino. For example, state “2” has about equal three portions of all three flavors. Right: the mass eigenstate components of each flavor eigenstate. This is a complementary demonstration of the MNSP matrix.

$$\begin{aligned}
\mathcal{P} \left( \overset{(-)}{\nu}_\mu \rightarrow \overset{(-)}{\nu}_e \right) = & 4 c_{13}^2 s_{13}^2 s_{23}^2 \sin^2 \phi_{31} \\
& + 8 \left( X_{\cos \delta_{\text{CP}}} \right) \cos \phi_{23} \sin \phi_{31} \sin \phi_{21} \\
& - \underbrace{8 \left( Y_{\sin \delta_{\text{CP}}} \right)}_{\text{CP violating}} \sin \phi_{32} \sin \phi_{31} \sin \phi_{21} \\
& + 4 \left( Z_{\cos \delta_{\text{CP}}} \right) s_{12}^2 c_{13}^2 \sin^2 \phi_{21}, \tag{1.44}
\end{aligned}$$

where

$$X_{\cos \delta_{\text{CP}}} = c_{13}^2 s_{12} s_{13} s_{23} (c_{12} c_{23} \cos \delta_{\text{CP}} - s_{12} s_{13}), \tag{1.45}$$

$$Y_{\sin \delta_{\text{CP}}} = \frac{1}{8} \sin (2\theta_{12}) \sin (2\theta_{13}) \sin (2\theta_{23}) c_{13} \sin \delta_{\text{CP}}, \tag{1.46}$$

and (+) represents the sign change from neutrinos to antineutrinos. The CP violating term (1.46) is also known as the Jarlskog Invariant and is a measure of CP violation independent

**Table 1.2:** Global best fit for the oscillation parameters. All values except for  $\delta_{\text{CP}}$  are combined values from the Particle Data Group and  $\delta_{\text{CP}}$  is from the 2018 NuFit analysis [38,81].

Parameter	Normal Hierarchy	Inverted Hierarchy	Units
$\Delta m_{32}^2$	$2.51 \pm 0.05$	$-2.56 \pm 0.04$	$10^{-3}$ eV $^2$
$\Delta m_{21}^2$	$7.53 \pm 0.18$		$10^{-5}$ eV $^2$
$\sin^2(\theta_{21})$	$0.307^{+0.013}_{-0.012}$		1
$\sin^2(\theta_{32})$	$\begin{cases} 0.417^{+0.025}_{-0.028} & \theta_{32} \in (0, \frac{\pi}{2}) \\ 0.597^{+0.024}_{-0.030} & \theta_{32} \in (\frac{\pi}{2}, \frac{\pi}{4}) \end{cases}$	$\begin{cases} 0.421^{+0.033}_{-0.025} & \theta_{32} \in (0, \frac{\pi}{2}) \\ 0.592^{+0.023}_{-0.030} & \theta_{32} \in (\frac{\pi}{2}, \frac{\pi}{4}) \end{cases}$	1
$\sin^2(\theta_{31})$	$2.12 \pm 0.08$		$10^{-2}$
$\delta_{\text{CP}}$	$217^{+40}_{-28}$	$280^{+25}_{-28}$	degrees

of the mixing parameterization [54]. This oscillation channel is of primary importance in current and future proposed accelerator and atmospheric neutrino oscillation experiments.

Current and next generation experiments aim to improve knowledge of the mixing parameters. There are a couple of degeneracies to unravel as well as precise measurement of  $\delta_{\text{CP}}$ . While the two defined mass-squared splittings  $\Delta m_{21}^2 = \Delta m_{\text{sol}}^2$  and  $\Delta m_{32}^2 = \Delta m_{\text{atm}}^2$  are known, it is unknown which eigenstates are more massive. This problem is known as the mass hierarchy problem and is illustrated in Figure 1.9a on page 24. Normal hierarchy refers to the case where  $m_3 > m_2 > m_1$  whereas the inverted hierarchy has  $m_2 > m_1 > m_3$ . Also distinguishing if  $\theta_{23}$  is in the first octant  $\theta \in (0, \pi/2)$  or second octant  $\theta \in (\pi/2, \pi/4)$  of the unit circle requires large statistics. Finally the value of  $\delta_{\text{CP}}$  is quite uncertain with values in the 3rd and 4th quadrants. Best fit measurements of the oscillations parameters are given in Table 1.2 on page 25.

### 1.1.2.3 Matter Effects

Traveling through matter has the potential to increase the sensitivity of neutrino oscillation measurements if the baseline is long enough. Known as the Mikheyev-Smirnov-Wolfenstein (MSW) effect [85], all oscillations are affected by coherent forward scattering

of neutrinos with electrons in the media. Taking the example of  $\overset{(-)}{\nu}_\mu \rightarrow \overset{(-)}{\nu}_e$  from (1.41), the MSW effect to first order is

$$\begin{aligned} \mathcal{P}\left(\overset{(-)}{\nu}_\mu \rightarrow \overset{(-)}{\nu}_e\right) &\rightarrow \mathcal{P}\left(\overset{(-)}{\nu}_\mu \rightarrow \overset{(-)}{\nu}_e\right) + \frac{8\alpha}{\Delta m_{31}^2} \left(c_{13}^2 s_{13}^2 s_{23}^2\right) \left(1 - 2s_{13}^2\right) \\ &\times \left( \sin^2 \phi_{31} \overset{(+) \text{ under } \phi_{31}}{-} \underbrace{\left(\frac{\Delta m_{31}^2 c^3}{4\hbar} \frac{L}{E_\nu}\right)}_{\phi_{31}} \cos \phi_{32} \sin \phi_{31} \right), \end{aligned} \quad (1.47)$$

where

$$\alpha = 2\sqrt{2}G_F n_e E_\nu, \quad (1.48)$$

and  $n_e$  is the average electron density of the Earth through which the neutrinos travel [17]. Carefully studying (1.47) reveals that the MSW effect alters the oscillation probability as a function of the electron density and increases in magnitude with baseline.

### 1.1.3 CP Violation: Origins of Matter

The observation of CP violation in the lepton sector might provide critical insight into the origins of the matter. CP violation dictates that certain interactions behave differently between matter or antimatter like  $\mathcal{P}(\nu_\mu \rightarrow \nu_e) \neq \mathcal{P}(\bar{\nu}_\mu \rightarrow \bar{\nu}_e)$ . The Big Bang Theory suggests that in the first fractions of a second of the Universe, equal amounts of matter and antimatter were created. However, observational evidence shows the Universe consists of only 4.5% baryonic matter (i.e. protons and neutrons) from cosmological models as shown in Figure 1.10 on page 27. The anti-baryonic fraction of the baryonic matter is infinitesimally low from external constraints on data from gamma-ray telescopes like Fermi-GLAST [21]. This problem is known as the Baryon Asymmetry of the Universe (BAU).

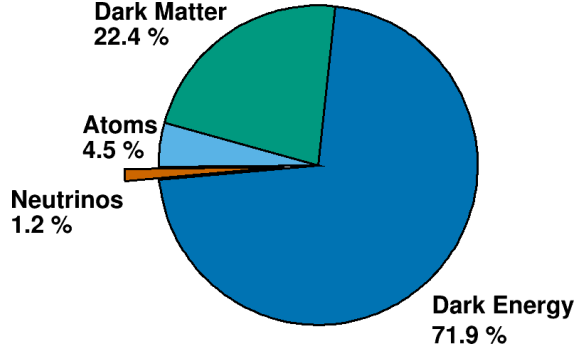


**Figure 1.10:** The matter and energy content of the Universe. The observable Universe contains about 4.5% of atoms (baryons and electrons) and an estimated neutrino content less than 1.2%. The rest of the Universe consists of Dark Matter at 22.4% and a form of energy called Dark Energy at 71.9%. These inferred parameters are taken from the  $\Lambda$ CDM model, the simplest model that describes the cosmos [56].

The process of Baryogenesis<sup>5</sup> is a favored model to explain the BAU and lacks a necessary precursor mechanism. One of the necessary conditions for Baryogenesis [72] is C symmetry violation and CP violation. Evidence of CP violation has been experimentally confirmed in the quarks, but not to the level which resolves the BAU. Baryogenesis can be achieved by having Leptogenesis<sup>6</sup> occur first through the decay of very heavy, right handed Majorana neutrino ( $\nu = \bar{\nu}$ ) through the *see-saw* mechanism. Detailed discussions on Leptogenesis and the *see-saw* mechanism can be found in the following reference [14].

#### 1.1.4 Long-Baseline Neutrino Oscillation Experiments

The KEK to Kamioka (K2K) experiment was the first neutrino oscillation experiment where researchers controlled the production and observation of neutrinos. In K2K, a beam of muon neutrinos were directed from the 12 GeV proton synchrotron at KEK to the Kamioka Observatory at a distance of 250 km. While traveling through the Earth, the neutrinos

<sup>5</sup>Baryogenesis is the mechanism by which matter and antimatter baryons are created in the early Universe.

<sup>6</sup>Leptogenesis is the mechanism by which leptons and anti-leptons are created in the early Universe.

oscillate before they are observed at Kamioka. Prior to K2K, neutrino sources only included the atmosphere, the Sun, and one supernova.

The K2K experiment established the experimental methods for current and planned next generation long-baseline neutrino oscillation experiments from accelerators. The accelerator neutrinos are produced when a high energy proton beam hits a target. The secondary particles are then forward focused using electrically pulsed magnets and allowed to decay in a large decay volume. This generates a highly pure muon neutrino beam with order 1% electron neutrino contamination. Prior to any oscillations, a “near” detector is used to measure the neutrino flux as function of neutrino energy and study detector systematic uncertainties associated at the “far” detector at Kamioka. The successor experiment to K2K called Tokai to Kamioka (T2K), closely followed this design methodology. Other notable accelerator-based long-baseline experiments include MINOS [90] and NO $\nu$ A [13], both in the United States.

## 1.2 The Tokai to Kamioka Experiment

The Tokai to Kamioka (T2K) experiment is a long-baseline, neutrino oscillation experiment hosted in Japan [1] as shown in Figure 1.11 on page 29. It is the successor experiment to the K2K neutrino oscillation experiment that was also hosted in Japan. The T2K experiment produces a high intensity, relatively pure muon neutrino beam at the Japan Proton Accelerator Complex (J-PARC) which is a world class particle accelerator facility. The beam is directed at the Super-Kamiokande (SK) [43] detector, which is 295 km away from the source. Additionally, the beam is designed to maximize the  $\nu_\mu \rightarrow \nu_e$  probability at the far detector  $L = 295$  km baseline using a neutrino energy spectrum sharply peaked at  $E_\nu = 0.6$  GeV as shown in Figure 1.12 on page 30. This spectrum is achieved by directing the center of the beam axis 2.5 degrees off center from SK. Along the beamline at 280 m from the beam source is the near detector facility called ND280 [40], whose data is used in thesis.

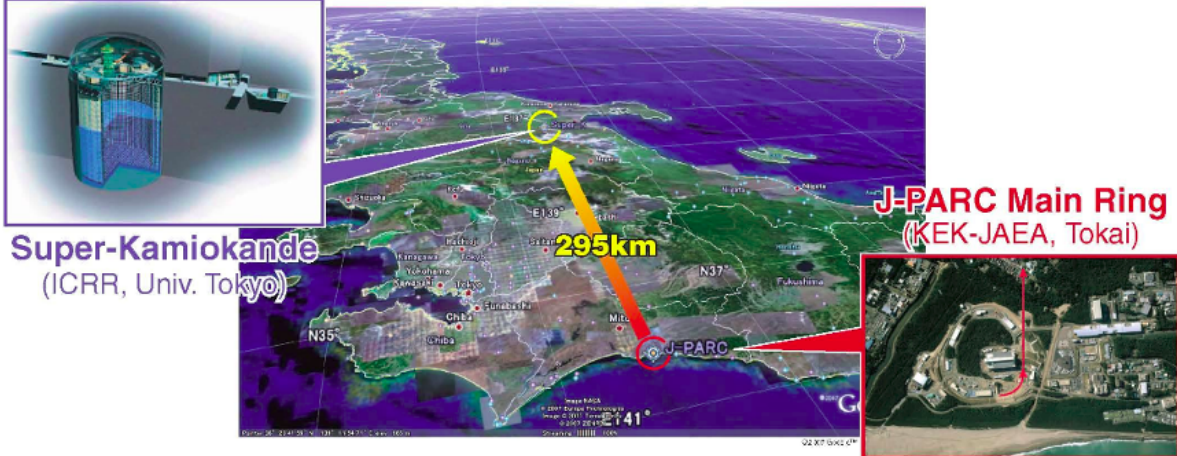


**Figure 1.11:** Birds eye view of the T2K experiment on the Japanese archipelago. An intense beam of neutrinos is produced at the J-PARC site (bottom right red box) using high energy protons. The beam is directed towards the Super-Kamiokande detector (top left blue box) at a distance of 295 km away from J-PARC.

The ND280 facility is designed to observe and characterize the unoscillated neutrino beam. There are two detectors at ND280: the primary, off-axis detector and on-axis detector. The measurement in this thesis uses data collected from the off-axis near detector.

The T2K experiment was primarily designed to measure the last unknown MNSP mixing angle  $\theta_{13}$ , which was thought to be nearly zero, via the  $\nu_\mu \rightarrow \nu_e$  channel. In addition it aims to make a precision measurement the atmospheric mixing parameters,  $\theta_{23}$  and  $\Delta m_{23}^2$  via the  $\nu_\mu \rightarrow \nu_\mu$  channel. An early landmark for the T2K experiment was a  $7.3\sigma$  measurement excluding non-zero  $\theta_{13}$  in 2013 [3]. It continues to be a world leader in oscillation physics and as of 2018 rejects CP conserving values ( $\delta_{\text{CP}} = 0, \pi$ ) at the  $2\sigma$  level [9].

The following topics will be discussed in the following order. First a look how neutrinos are produced at J-PARC. Next a detailed look at the T2K near detectors which are used in this thesis. This is followed by a discussion on Super-Kamiokande, the T2K far detector. The final topic is an examination of the near detector constraint and its importance in the oscillation analysis.

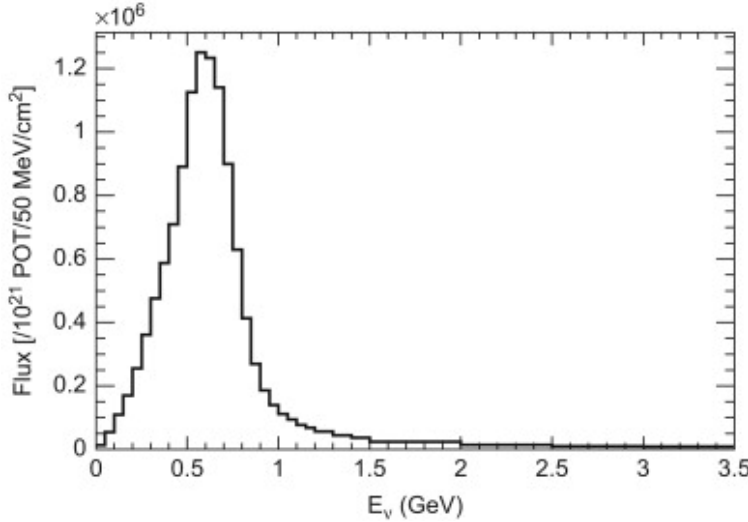


**Figure 1.12:** The T2K experiment’s unoscillated  $\nu_\mu$  flux at Super-Kamiokande at the off-axis angle of  $2.5^\circ$ .

### 1.2.1 Neutrino Production at J-PARC

To facilitate the high intensity neutrino beam requirements for T2K, the J-PARC site generates a high intensity proton beam through a series of particle accelerators. A bird’s eye view of J-PARC can be seen in Figure 1.13 on page 31 which highlights its accelerators and other facilities. For this section, note that all beam energies are kinetic energies.

Protons for the T2K beamline are first accelerated in the J-PARC linear accelerator<sup>7</sup> (linac) and then the rapid cycle synchrotron<sup>8</sup> (RCS). Hydrogen ions ( ${}_1^1\text{H}^-$ ) are extracted from plasma in a electrical discharge chamber and fed through a series of linac elements as shown in Figure 1.14a on page 32. Each linac element, except for the initial quadrupole magnet, accelerates the ions using carefully synchronized oscillating electric fields generated by radio frequency pulses. After traveling 240 m along the linac, the ions have been boosted to 181 MeV of kinetic energy and transported into the RCS. While in transit to the RCS, the

<sup>7</sup>A linear accelerator accelerates particles using time varying electric fields along a one direction, terminal beamline. Linear accelerators are also used in the medical field to generate X-rays.

<sup>8</sup>A synchrotron is cyclic particle accelerator that relies on time varying magnetic fields to accelerate particles. Since they require many magnets and large spaces to operate, they are usually operated at national laboratories for others uses like material and life sciences.

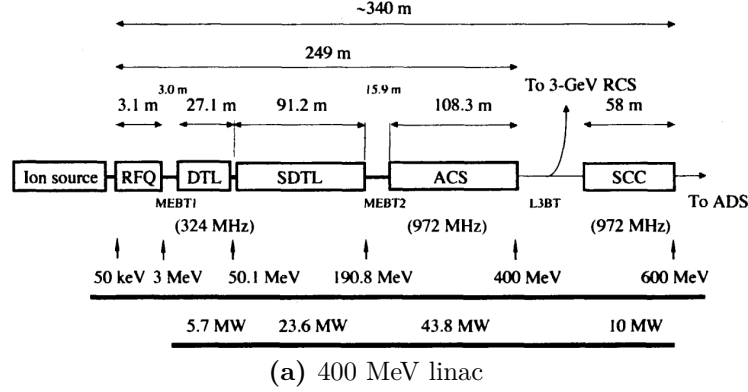


**Figure 1.13:** Bird's eye view of the J-PARC laboratory showing the primary components of its accelerator programs. To generate the high intensity neutrino beam, first the linear accelerator (Linac, red) accelerates protons into the 3 GeV Synchrotron (also red) called the rapid-cycle synchrotron (RCS). The RCS then injects some of its protons into the 50 GeV Synchrotron (yellow) called the main ring (MR), which currently runs at 30 GeV. Finally the MR protons are directed into a target material along the neutrino beamline (teal) [30].

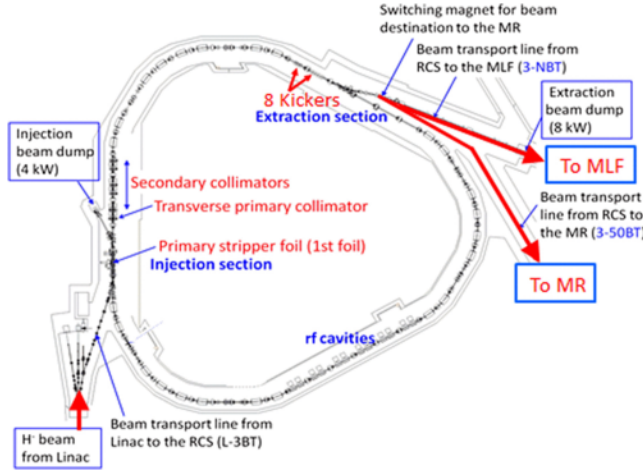
ions are stripped of their electrons via charge stripping foils. The 348 m circumference RCS then further boosts the protons to 3 GeV at an operating frequency of 25 Hz. While being accelerated, protons are aggregated into two bunches and focused using particle collimators as shown in Figure 1.14b on page 32.

The next stage for the protons intended for the neutrino beamline is the much larger main ring (MR) synchrotron as shown in Figure 1.14c on page 32 which has a circumference of 1567 m. While nominally designed to boost protons to 50 GeV, it currently operates at 30 GeV. Protons are injected into the MR to form eight proton bunches (spill), initially six when T2K first ran, before entering the neutrino beamline. The total temporal width of the spill is approximately  $0.5 \mu\text{s}$  [1]. At a spill cycle frequency of 0.5Hz, the bunches are extracted from the MR into the neutrino beamline.

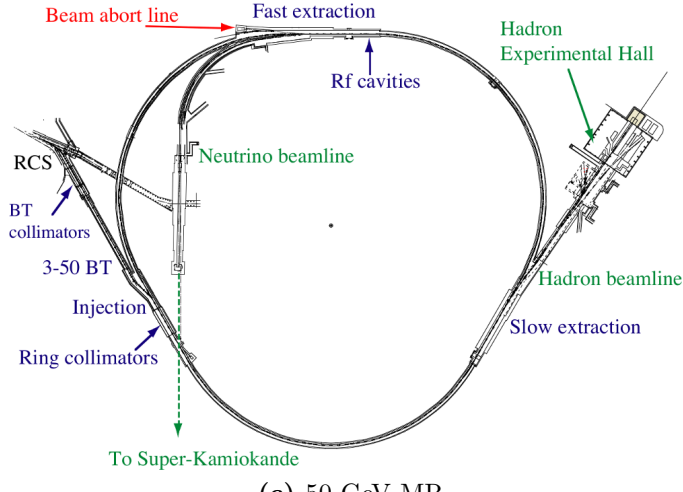
The neutrino beamline is designed to direct the protons toward SK and generate neutrinos by striking them into the end of a cylindrical target. Figure 1.15a on page 33 shows the process of proton extraction from the MR for both primary and secondary neutrino beamlines. In the primary beamline, a series of normal and superconducting magnets steer the



(a) 400 MeV linac

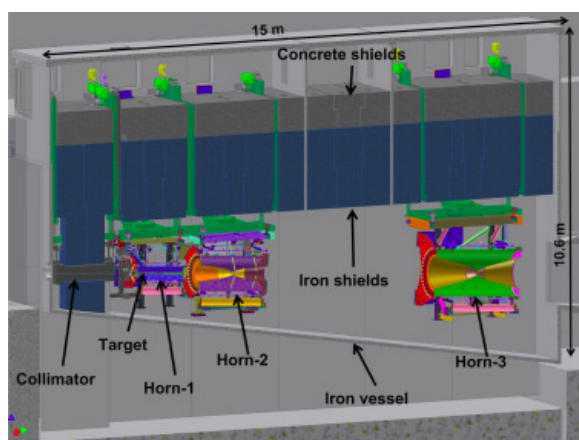
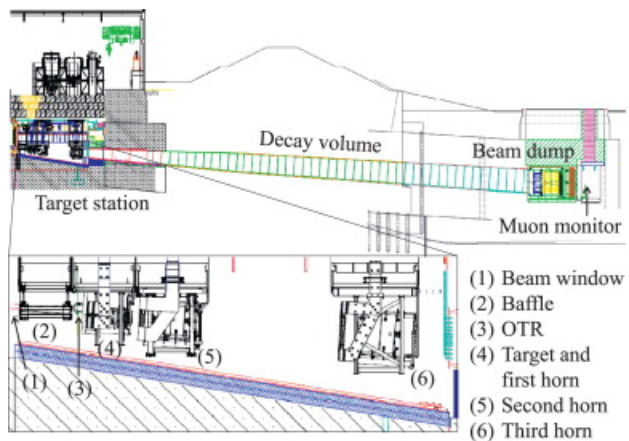
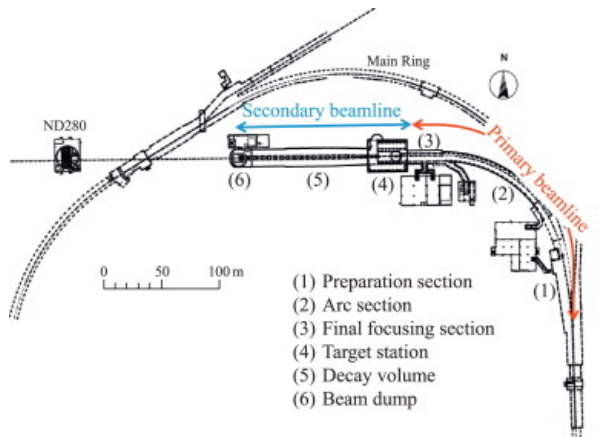


(b) 3 GeV RCS



(c) 50 GeV MR

**Figure 1.14:** Schematics of the J-PARC accelerators. (a) The linac accelerates hydrogen ions to 181 MeV of kinetic energy, designed for 400 MeV, from the ion source [87]. (b) Protons from the linac are collected into the RCS and accelerated to 3 GeV [71]. (c) Protons from the RCS are injected into the MR synchrotron. While the MR is designed for 50 GeV, it currently operates at 30 GeV.



(c) Beamlime horns

**Figure 1.15:** The neutrino beamline at J-PARC consists of a primary and secondary beamline. (a) The primary beamline redirects the protons towards the secondary beamline [1]. (b) In the secondary beamline, the protons are impinged on a cylindrical target producing mostly pions. The pions are focused using in sequence horns and decay in a long decay volume. Any non-decayed particles are stopped at the beam dump. (c) A further zoomed in cross section of the target station showing the target and focusing horns [78].



(a) A graphite target at the target station



(b) A magnetic focusing horn

**Figure 1.16:** Photographs of the T2K target station. (a) The graphite rod being extracted from the target station is shown in the black-dashed box. (b) One focusing horn in T2K.

proton beam away from the MR first along a 54 m preparation section and then a 147 m arc section to bend the beam towards SK. A final focusing section in the primary beamline focuses the protons into the secondary beam while directing it downwards  $3.637^\circ$  with respect to the local horizontal. Since a well-tuned and stable proton beam is necessary for neutrino production, numerous beam monitors are installed along the primary beamline to measure any losses.

The secondary beamline marks the end of the proton beam and production of a neutrino beam as shown in Figure 1.15b on page 33. It consists of a target station, a decay volume for the outgoing particles from the target station, and a beam dump for any remaining particles. The target station houses a 91.4 cm long, 2.6 cm diameter, and  $1.8 \text{ g/cm}^3$  graphite rod, which corresponds to 1.9 radiation lengths. When the protons strike the target, strong (nuclear) interactions produce  $\pi(\pi)$ -mesons (pions) and K-mesons (kaons) like those produced from cosmic ray collisions in the upper atmosphere. To enhance the flux of neutrinos, a series of three current pulsed, focusing magnets called horns<sup>9</sup> as shown in Figure 1.15c on page 33 are used to focus the mesons of the correct charge towards SK. Photographs of a graphite

---

<sup>9</sup>The name horn derives from the fact that the focusing magnets are shaped like brass horns in a music ensemble or marching band. One can think of these horns like a focusing lens for charged particles.

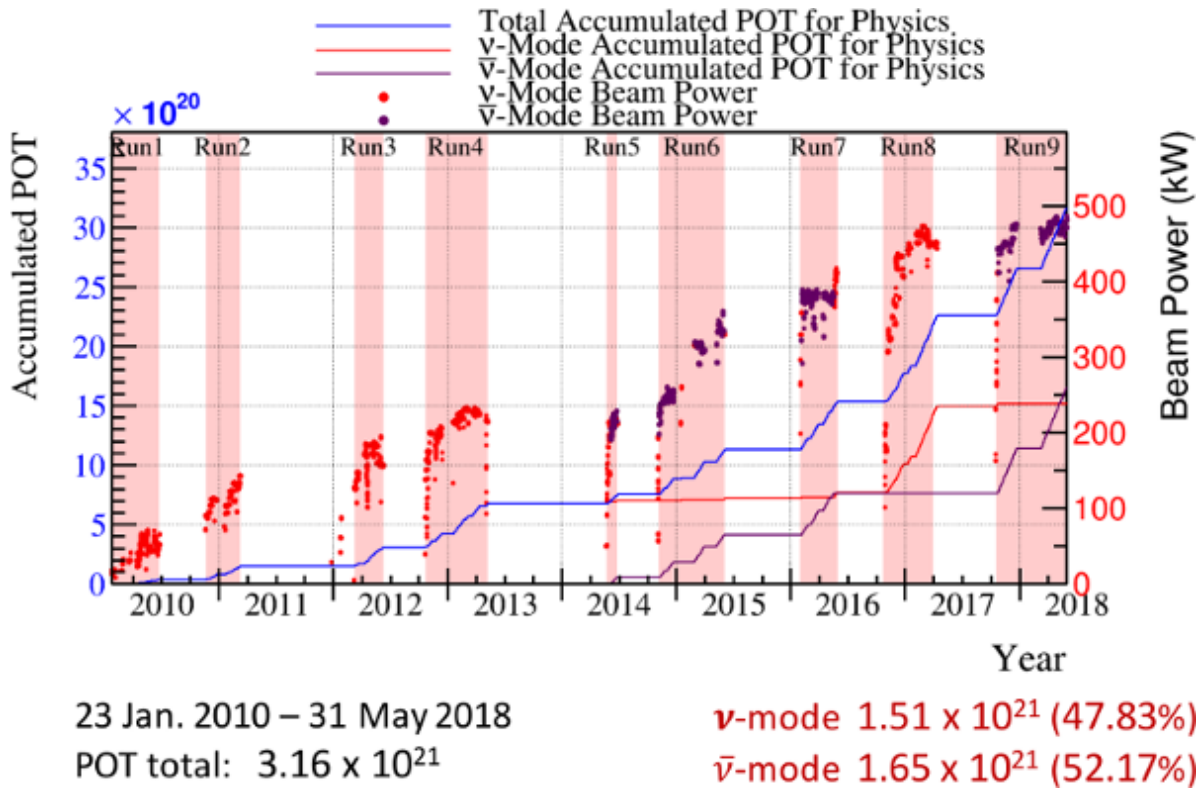


**Figure 1.17:** The accumulated protons on target for the T2K experiment since 2010 shows a steady increase in beam power over time.

target and focusing horn are shown in Figure 1.16 on page 34. The horns are pulsed at +250 kA (-250 kA) to select positively (negatively) charged pions. The focused pions then decay in the 96 m long decay volume creating a neutrino beam boosted along the secondary beamline direction. For safety reasons, the decay volume is filled with gaseous helium at 1 atm of pressure which has a low pion absorption rate. A beam dump is placed at the end of the decay volume to stop particles like muons that have not yet decayed from contaminating the beam with their decay neutrinos.

Along both beamlines are numerous monitors and timing systems to ensure stable production of neutrinos. Proton beam monitors are placed along the primary beamline to ensure the proton beam is properly steered into the secondary beamline. An optical transition radiation monitor is situated around the target to observe any protons not intersecting with the target region itself. The last monitor along the secondary beamline is the a muon mon-

itor (MUMON), which is placed downstream of the beam dump to characterize the flux of daughter muons of  $> 5$  GeV/c momentum [1].

In order to provide timing information for the neutrino beam at SK, a global positioning system (GPS) is used to synchronize clocks at SK and J-PARC. Any event outside the beam timing window is rejected in the T2K oscillation analysis, and so having precise timing information for the neutrino beam is critical for the experiment. The GPS has an internal accuracy of 50 ns, or about  $\sim 150$  m assuming that the neutrinos are traveling near the speed of light. This is well within the time it takes for a neutrino to travel the 295 km between J-PARC and SK.

J-PARC continues to improve the proton delivery and neutrino flux intensity since T2K began in 2010. The T2K experiment has run in two horn current modes:  $\nu$ -mode and  $\bar{\nu}_\mu$ -mode. Focusing positively charged pions with +250 kA horn current is called forward horn current (FHC) mode. Similarly, using -250 kA horn current is called reverse horn current (RHC) mode. The aggregate running of T2K for both FHC and RHC modes is shown in Figure 1.17 on page 35 in units of protons on target (POT).

In addition the proton beam intensity, as measured in kW, has been increased over time which increases the number of neutrino interactions observed at SK. Note that while  $\pm 250$  kA is the preferred horn current in both FHC and RHC modes, the horns were run briefly at +205 kA when operations resumed after 2011 Tohoku earthquake.

### 1.2.2 Neutrino Near Detectors: ND280

The T2K experiment has a near detector (ND) site at J-PARC that is designed specifically to observe the neutrino beam in flight aimed at Super-K. The primary purpose of a ND site is to *constrain the neutrino flux and interaction rate* at SK in order to reduce the impact of their systematic uncertainties on the oscillation analysis. The analysis in this thesis uses the data collected by the off-axis ND. The site is called ND280 and is located 280 m away from the production target. The primary detector is an off-axis, magnetized tracking

detector consisting of different subdetectors. A separate detector array called the Interactive Neutrino Grid (INGRID) measures the neutrino beam profile.

The following subsections begin with a description of INGRID and its purpose at ND280. This is followed by a general description primary off-axis, magnetized detector. The last two subsections are descriptions of two primary subdetectors in the off axis detector. The first and second being the pi-zero detector (PØD) and time projection chamber (TPC), respectively.

From here on, unless specified, INGRID will refer only to the on-axis ND and ND280 will refer only to off-axis ND.

### 1.2.2.1 On-Axis Detector

The on-axis near detector called the Interactive Neutrino Grid (INGRID) is a tracking scintillator detector designed to directly measure the neutrino beam profile. As shown in Figure 1.18 on page 38, it is a grid of tracking modules in the shape of a cross centered at the designed neutrino beam center ( $\theta = 0$ ). The INGRID detector is capable of measuring the on-axis neutrino beam in a  $10\text{ m} \times 10\text{ m}$  transverse area. Each module consists of alternating layers of iron plates and scintillator bars except for the two most downstream scintillating layers which lack iron plates. To monitor any beam asymmetry, two separate modules are placed off the grid axis.

Each scintillating bar consists of scintillator-doped polystyrene, which emits light when a charged particle deposits energy in the medium. Each bar contains a single wavelength-shifting (WLS) fiber to collect and shift the light to a different wavelength. The light trapped in the fiber is then collected by a device called a multipixel photon counter (MPPC) and converted into an electrical signal. A MPPC is a compact device containing many sensitive avalanche photodiode pixels that act as Geiger micro-counters as shown in Figure 1.19 on page 39. The MPPCs are well matched with the spectral emission of the WLS fibers and operate in a strong magnetic fields, unlike traditional photomultiplier tubes. In order to enhance the collection efficiency, a reflective  $\text{TiO}_2$  doped polystyrene shell surrounds each

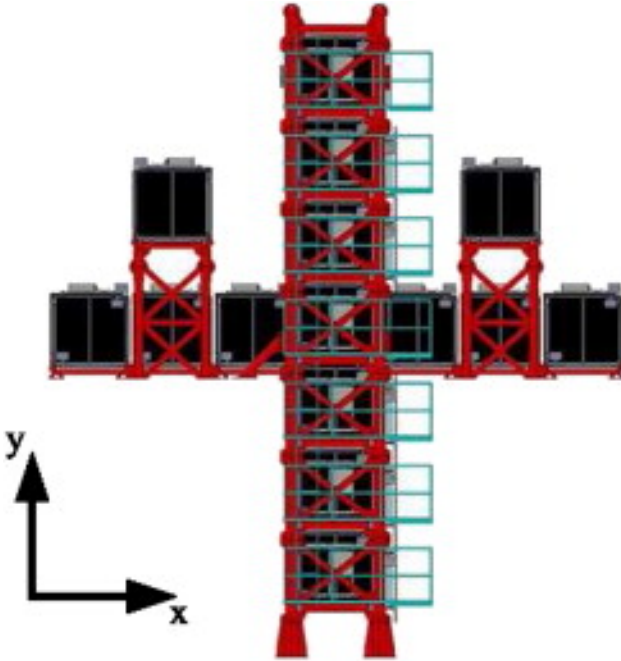


**Figure 1.18:** A schematic of the INGRID detector showing the arrangement of the tracking scintillating modules. There are 16 identical modules total with seven in the vertical row, seven in the horizontal row, and two at off-axis positions. With the vertical row upstream of the horizontal row, the designed beam center intersects each row's center module [2].

bar. The bars are assembled into planes to provide tracking capabilities. Veto planes also surround each module to prevent false signals to trigger.

The INGRID detector is continuously operated to check that the neutrino beam center was properly aligned at its designed center. Diagnostic plots such as Figure 1.20 on page 39 are collected on a monthly basis to ensure that the neutrino flux at Super-Kamiokande (SK) is consistent with T2K’s requirements. A history of the beam profile and event rate on INGRID between January 2010 and October 2016 is shown in Figure 1.21 on page 40.

### 1.2.2.2 Off-Axis Detector

The primary ND used for T2K is ND280, which is an off-axis, magnetized tracking detector. It is a collection of different detector technologies designed to facilitate three primary measurements:

1. The flux of  $\nu_\mu$  at SK,

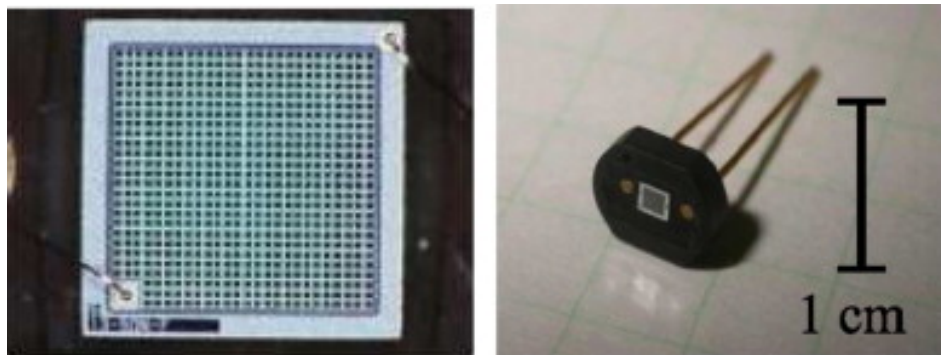


**Figure 1.19:** Photographs of the specially designed MPPC in T2K. A magnified face view is shown on the left with an entire unit shown on the right. Each device has 667-pixel sensors with an effective area of  $1.3 \text{ mm} \times 1.3 \text{ mm}$  [1].

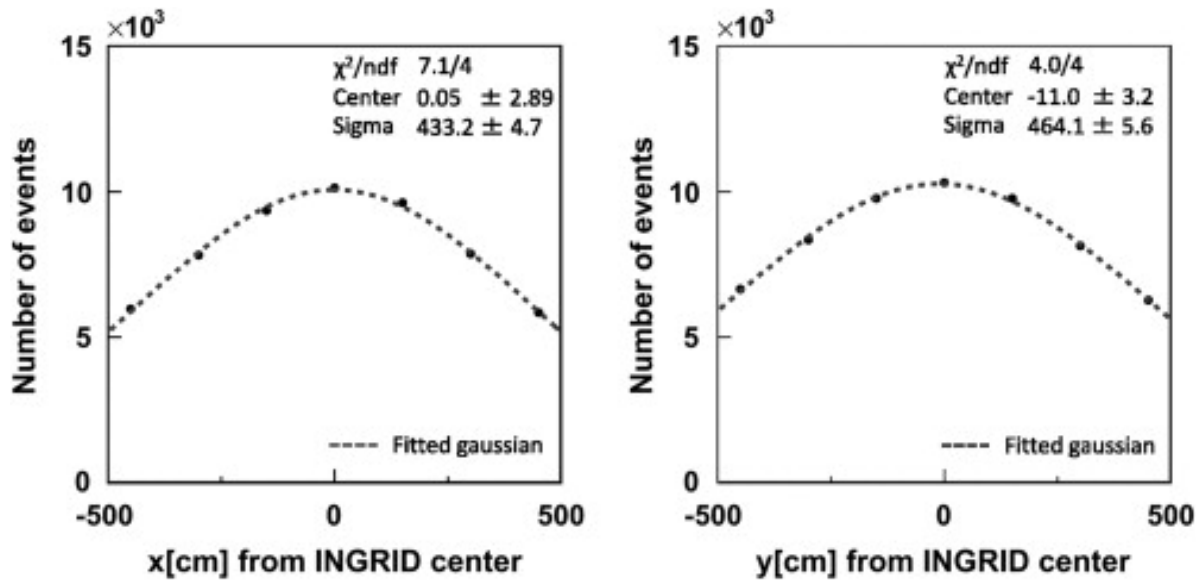


**Figure 1.20:** A beam profile taken with INGRID in April 2010 shows the Gaussian nature of the beam. The errors on the data points are about 1%. [2]

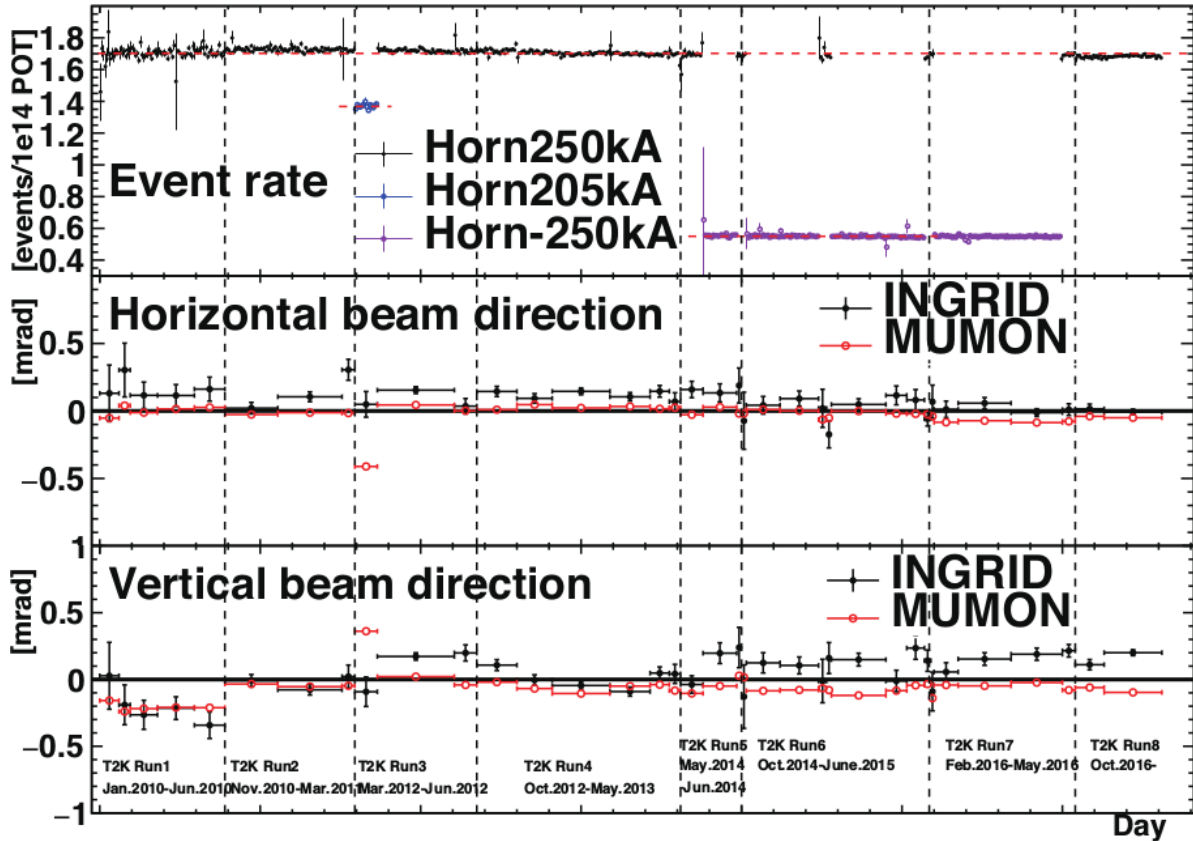


**Figure 1.21:** The INGRID detector interaction event rate and beam profiles are shown. The top panel shows the event rate for the three different horn currents. The middle and bottom panels show the horizontal and vertical beam directions with respect to the beam center, respectively. A deviation of 1 mrad corresponds to a little under 30 cm. The error bars shown are the statistical errors on the mean.

2. The irreducible  $\nu_e$  background flux at SK, and
3. The rate of background  $\nu_\mu$  interactions and cross sections for the  $\nu_\mu \rightarrow \nu_e$  search.

The ND280 detector consists of a pi-zero detector (PØD), a tracker region consisting of a fine grain detector (FGD) and a time projection chamber (TPC), an electromagnetic calorimeter (ECal), and a side muon range detector (SMRD). The ND280 subdetectors are instrumented inside the UA1/NOMAD magnet, that was recycled from the European Organization for Nuclear Research (CERN), with the SMRD in the magnetic field return yoke itself. All but the FGD are instrumented with the same MPPC technology mentioned above. A schematic of the different detector components of ND280 is shown in Figure 1.22 on page 42.

The analysis in this thesis uses measurements from the PØD and the TPC subdetectors. The PØD serves as a massive target for the incident neutrino beam and the TPC serves to measure the charge and momentum of the outgoing particles.

The ND280 magnetic field is generated using electrical current fed through solenoid coils to generate a dipole field of strength  $0.2\text{ T}^{10}$  in the x direction. The field is highly uniform near the center of the detector which is where the majority of the TPC system is located. However, it has significant deviations from 0.2 T near the solenoid edges. In order to fully understand the field inside ND280, a precise 3D model was generated using a machine controlled Hall probe. The operating field strength during the mapping process was 0.07 T due to power restrictions at the time. The model was then compared with measurements in the TPC region as shown in Figure 1.23 on page 43. After scaling the model to the nominal operating strength of 0.2 T, a fractional uncertainty of  $10^{-3}$  or uncertainty of 2 Gauss in each direction was obtained.

The ND280 magnetic field permits the measurements of particle charge and momentum. A particle of charge  $q$ , rest mass  $m_0$ , and velocity  $\mathbf{v}$  under the influence of an external electric

---

<sup>10</sup>This is a powerful magnetic field. According to the The US/UK World Magnetic Model for 2015-2020, the magnetic field strength on the surface of the Earth is about 0.294385 Gauss or  $2.94385 \times 10^{-5}\text{ T}$ . So the field inside ND280 is about 6800 times more forceful than the Earth's influence [32].

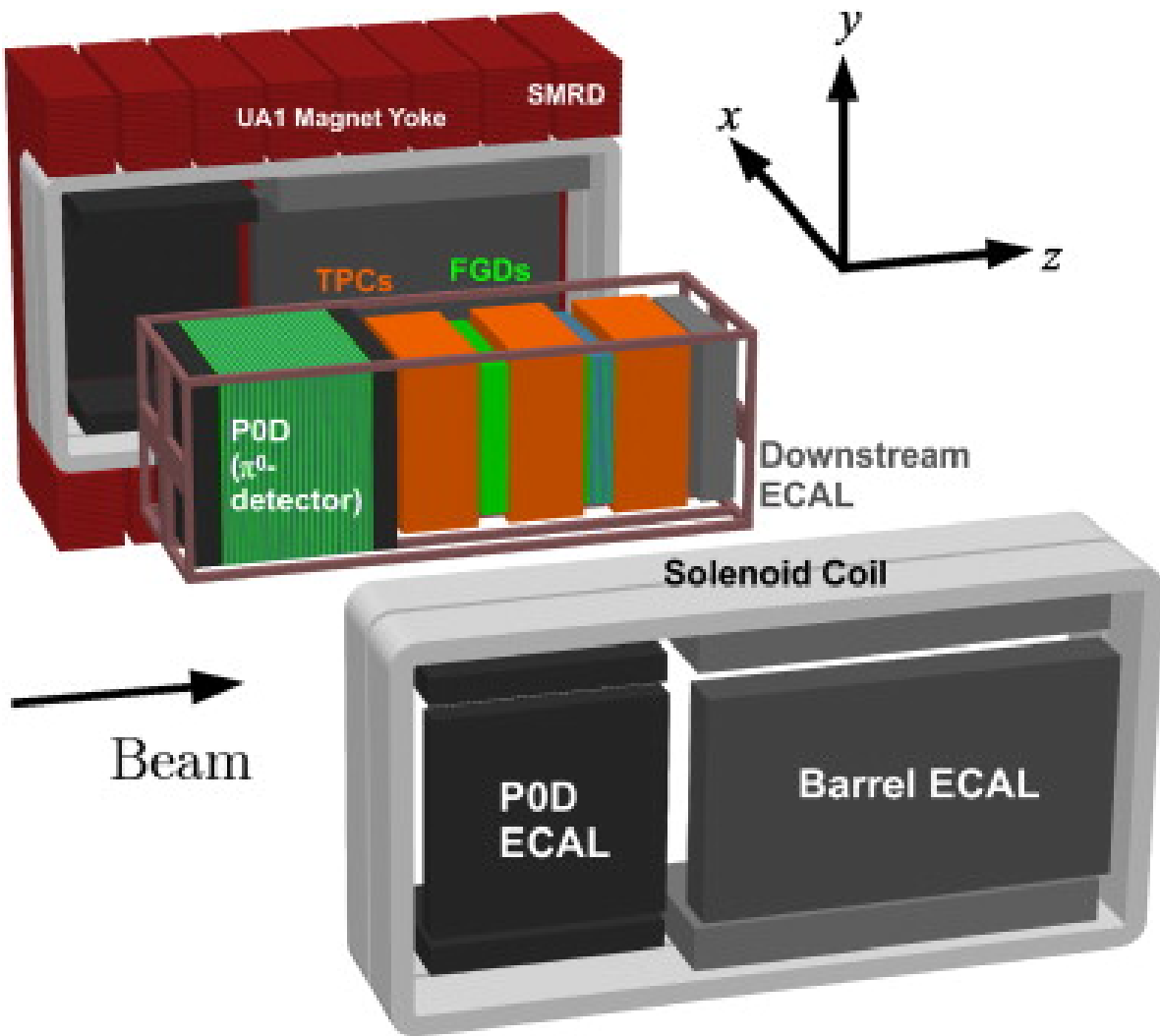


**Figure 1.22:** An exploded view of the ND280 off-axis detector. The magnetic field is generated from the Solenoid Coil via an electrical current which produces a dipole magnetic field of strength 0.2 T. The field is designed to return to the Magnetic Yoke.

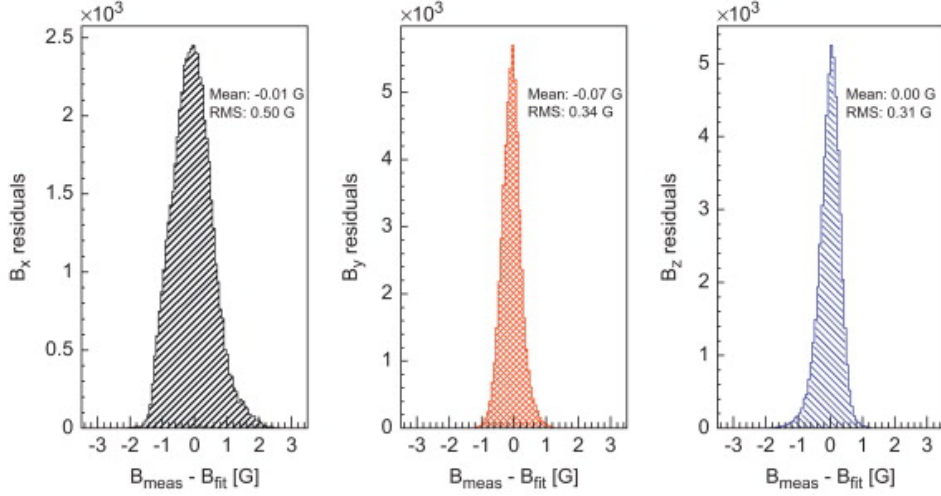


**Figure 1.23:** The ND280 detector magnetic field measurement in all three directions. Each of the magnetic field components are compared between a fit of the data and the actual measurements near the center of ND280. The systematic uncertainty on the field is extracted from the RMS of the mapping [1].

and magnetic fields,  $\mathbf{E}$  and  $\mathbf{B}$ , respectively, experiences a force  $\mathbf{F}$  given by the Lorentz force equation

$$\mathbf{F} = q(\mathbf{E} + \mathbf{v} \times \mathbf{B}). \quad (1.49)$$

Assuming for now that there is no external electric field, the force on the particle is

$$\mathbf{F} = q\mathbf{v} \times \mathbf{B}, \quad (1.50)$$

which is both orthogonal to  $\mathbf{v}$  and  $\mathbf{B}$ . Since the mechanical work performed on a particle in a magnetic field is zero, the particle's energy is unchanged ( $|\mathbf{v}| = v = \text{constant}$ ). Newton's Second Law allows us to rewrite the force as an change in momentum  $\mathbf{P}$

$$\begin{aligned}
\mathbf{F} &= \frac{d\mathbf{P}}{dt} \\
&= \frac{d}{dt} (\gamma(v)m_0\mathbf{v}) \\
&= m_0\mathbf{v} \left( \frac{d\gamma(v)}{dt} \right) + \gamma(v)m_0 \left( \frac{d\mathbf{v}}{dt} \right) \\
&= m_0\mathbf{v} \left( \frac{d\gamma(v)}{dv} \right) \left( \frac{dv}{dt} \right)^0 + \gamma(v)m_0\mathbf{a} \\
&= \gamma(v)m_0\mathbf{a},
\end{aligned} \tag{1.51}$$

where  $\mathbf{P} = \gamma(v)m_0\mathbf{v}$  is the relativistic momentum and  $\gamma(v) = (1 - (v/c)^2)^{-1/2}$  is the Lorentz factor. For uniform circular motion, the magnitude of the acceleration is given by

$$|\mathbf{a}| = v^2/R, \tag{1.52}$$

where  $R$  is the radius of curvature for the circle. Combining Eqn. (1.52) and Eqn. (1.51) with some algebra yields

$$R = \frac{\gamma(v)m_0v}{q|\mathbf{B}|\sin\theta_{\mathbf{v}\mathbf{B}}}, \tag{1.53}$$

where  $\theta_{\mathbf{v}\mathbf{B}}$  is the angle between  $\mathbf{v}$  and  $\mathbf{B}$ . The numerator of Eqn. (1.53) is recognized as the magnitude of the momentum  $|\mathbf{P}|$ . Some further rearrangement yields

$$|\mathbf{P}| = q|\mathbf{B}|R\sin\theta_{\mathbf{v}\mathbf{B}}, \tag{1.54}$$

and thus measuring the direction and radius of curvature inside the field provides the charge and momentum, respectively, as desired.

### 1.2.2.3 Off Axis pi-zero detector (PØD)

The PØD is the primary detector used as the neutrino target in this thesis. It is a plastic scintillator-based tracking calorimeter inside the ND280 magnet region. It was designed to measure the neutral current (NC) process  $\nu_\mu + N \rightarrow \nu_\mu + N + \pi^0 + X$  on water, where  $N$  is

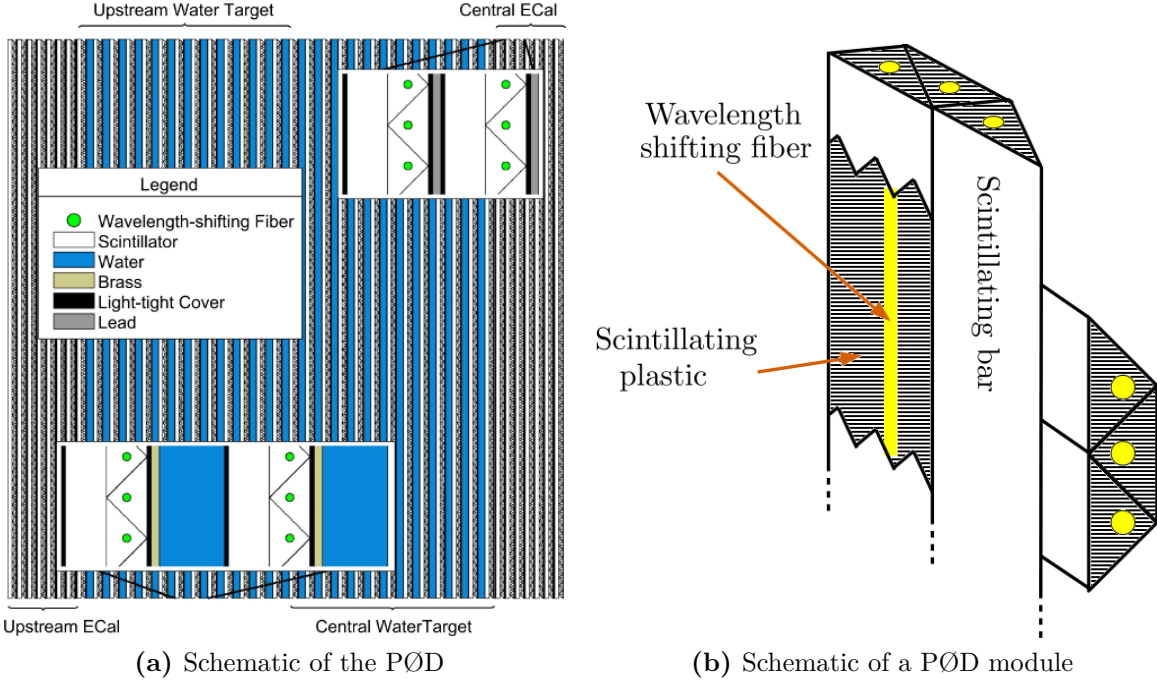


**Figure 1.24:** Schematics of the PØD. Left: insets detail the Water Target and ECal layers. Right: A view of a PØD module illustrating the orthogonal layout of the scintillating planes. Both: the neutrino beam is coming from the left.

a nucleus and  $X$  is any set of final state particles. The NC  $\pi^0$  process was expected to be a significant background in the  $\nu_e$  appearance search in the likelihood that  $\theta_{13} \approx 0$  since a pi-zero decay can mimic a  $\nu_e$ -like signal. The PØD can be operated with or without water, enabling the determination of water target (WT) cross sections by comparing water-in data with water-out data.

A representation of the PØD is shown in Figure 1.24 on page 45. The active detector components are very similar to INGRID's design with the primary difference being that each bar is triangular in shape as shown in Figure 1.25 on page 46. A plane of 134 horizontal and 129 vertical bars together form a PØD module (PØDule) as shown in Figure 1.24b. The purpose of the triangular bar design is that particle tracks (muons and pions) are likely to deposit energy in only two bars for each layer crossed. This would not be true for electromagnetic shower events which would deposit energy in many bars. These differences provide a discriminant between particle tracks and electromagnetic showers.

**Table 1.3:** Elemental composition of PØD water target region. The table is sorted from top to bottom by fraction of mass. This table was originally produced in reference [7].

Element	Symbol	Fraction [%]
Carbon	C	45.0
Oxygen	O	29.9
Copper	Cu	14.3
Hydrogen	H	8.0
Zinc	Zn	1.6
Chlorine	Cl	1.1
Titanium	Ti	0.1

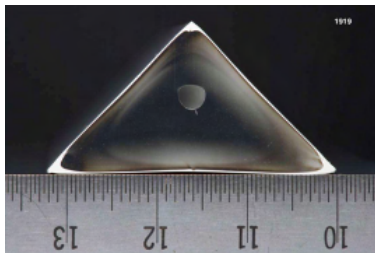


**Figure 1.25:** A cross section of a PØD scintillating bar. The base and height is 33 mm long and 17 mm high. The wavelength shifting fiber is inserted in the bored hole which is half-way between the base and tip.

The PØD dimensions are  $2.298 \times 2.468 \times 2.350 \text{ m}^3$ , in XYZ respectively, with a fiducial mass of  $\sim 1900 \text{ kg}$  for water and  $3570 \text{ kg}$  for other materials. The total mass of the PØD is approximately 15,800 kg when the bags are full of water. The PØD is arranged into three regions: a water target (WT) region and two ECals. The WT region contains 26 PØDules interleaved between bags of water 2.8 cm thick when filled and a 1.3 mm thick brass sheets designed to help contain  $\pi^0$  decay photons. The last two regions are the upstream ECal and central ECal, each with seven PØDules interleaved with steel sheets clad with lead between them [7]. An elemental composition of the WT is shown in Table 1.3 on page 46.

The readout electronics for the PØD is based on the Trip-T application specific integrated circuit (ASIC) shared among the SMRD, ECals, and INGRID. Signals from 64 MPPCs are routed to Trip-T front end boards (TFB) that each house four Trip-T ASICs. Each Trip-T collects the MPPC charge in 23 programmable integration cycles.

The TFBs are readout to back-end electronics which control the TFBs and synchronize clocks. A total of six readout merger module (RMM) electronics receive the TFB data and control each TFB ASIC. The RMM internal timing clocks are synchronized with a cosmic trigger module and a slave clock module (SCM), both of which are synchronized with a master clock module from the beamline. Synchronizing the RMMs with the SCM allows for the Trip-T ASIC integration windows to match with the beam. The RMMs are responsible for distributing the TFB data to the data acquisition (DAQ) system for storage.

The ND280 DAQ consists of a MIDAS framework to monitor and control data collection. The primary purpose of the DAQ system is to merge data and package it for long term storage. In conjunction with the DAQ system is the Global Slow Control (GSC) system which measures temperatures, voltages, and other physical quantities. Together the DAQ and GSC help scientists consistently produce high quality data and maintain the overall stability of the detector [1].

#### 1.2.2.4 Off Axis Time Projection Chamber (TPC)

The ND280 TPC is designed to provide momentum measurements of charged particle tracks and high resolution particle counting capabilities. The TPC is divided into three volumes separated by the two FGD volumes. Each volume ( $2.3 \times 2.4 \times 1.0 \text{ m}^3$ ) consists of an inner box that holds an argon-based gas and an outer box that holds an insulating  $\text{CO}_2$  gas. The inner gas mixture is 3000 L of  $\text{Ar:CF}_4:\text{C}_4\text{H}_{10}$  (95:3:2) gas. It was selected for its high speed, low diffusion, and good performance with a bulk micromegas detector [1]. A simplified schematic of the TPC is shown in Figure 1.26 on page 48.

A TPC works by measuring the ionization electrons left in the gaseous medium as charged particles through it. The electron drift acceleration is rapid due to the strong 5 kV/cm electric field present. Drift electrons are multiplied and sampled by micromegas detectors that line the sides of the TPC, providing nearly  $3 \text{ m}^2$  of active surface coverage. Arrival times of the electrons provide timing information to give a full three dimensional portrait of the events.

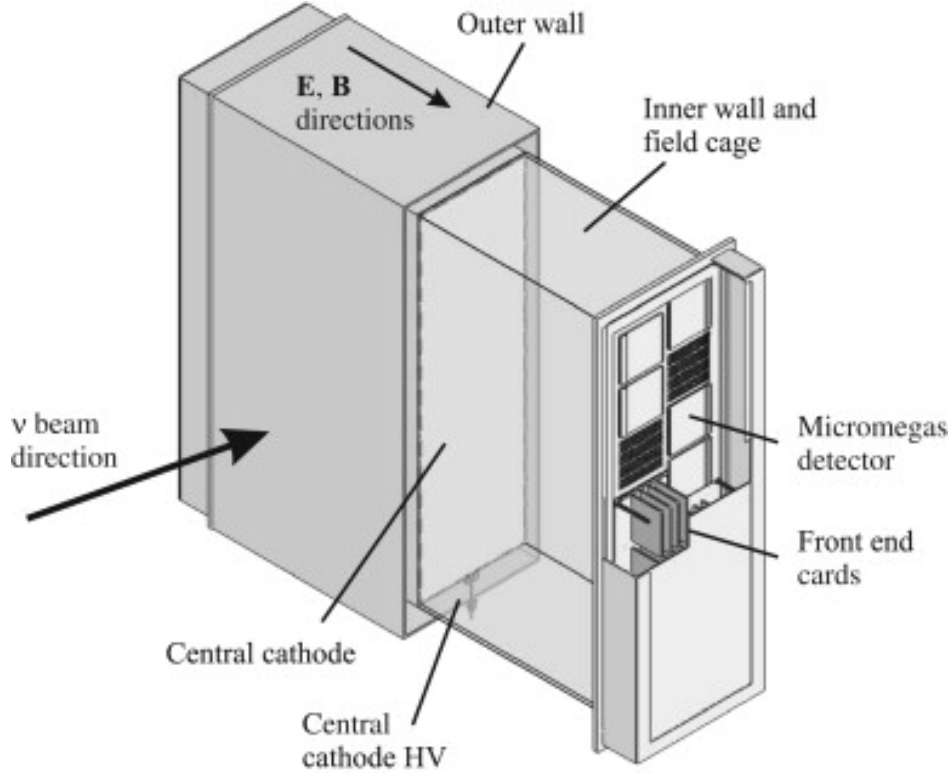


**Figure 1.26:** Cut-away drawing of a TPC volume in ND280 [1].

#### 1.2.2.5 Track Reconstruction in ND280

The goal of track reconstruction software is to capture the shape and history of energy deposited in the detector. Since ND280 is collection of different technologies, highly specific algorithms and models are used to identify track-like patterns. Since this analysis uses neutrino events incident in the PØD and cross into the TPC, a unified and coherent reconstruction model is needed. A reconstruction package called “Global” is designed to combine all ND280 information for this purpose.

### 1.2.3 Neutrino Far Detector: Super-Kamiokande

The Super-Kamioka neutrino detection experiment, abbreviated as Super-Kamiokande (SK), is the dedicated far detector for the T2K experiment. Positioned at 295 km away from the neutrino source with a 1 km overburden, it is well designed to detect the elusive neutrino.

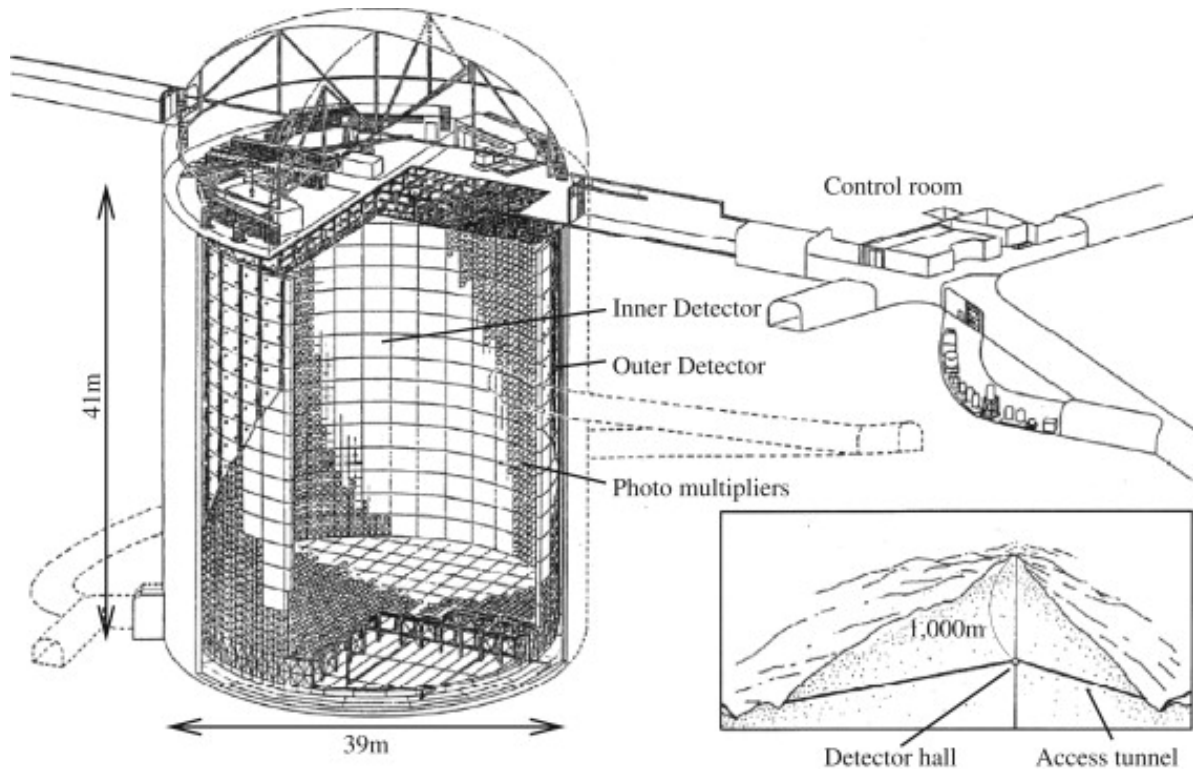


**Figure 1.27:** Diagram of the Super-Kamiokande detector consisting mainly of the inner and outer detector segments. The boundary between the two segments is cylindrical scaffolding used to mount the PMTs and optically isolate the segments.

Containing about 50 kt of pure water, it is lined with photomultiplier tubes (PMTs) in both an inner and outer detector as shown in Figure 1.27 on page 49.

When charged particles travel through the water, a Cherenkov radiation cone is produced. The sharpness of the cone edge is a unique identifier for the particle species that produced it. An electron produces a fuzzy edge since it experiences many large multiple scatterings off the water molecules. A muon on the other hand produces a sharp edge since it is much more massive and thus is less perturbed by the water molecules. Both types of events are shown in Figure 1.28 on page 50. By identifying the sharpness of the cone, the particle species is deduced. If a cone is coincident with the T2K neutrino beam, it can be used to infer the neutrino flavor.

While events from SK are not used in this analysis, the goal is to try to improve T2K's oscillations parameters which depend on comparing the ND neutrino measurements to the

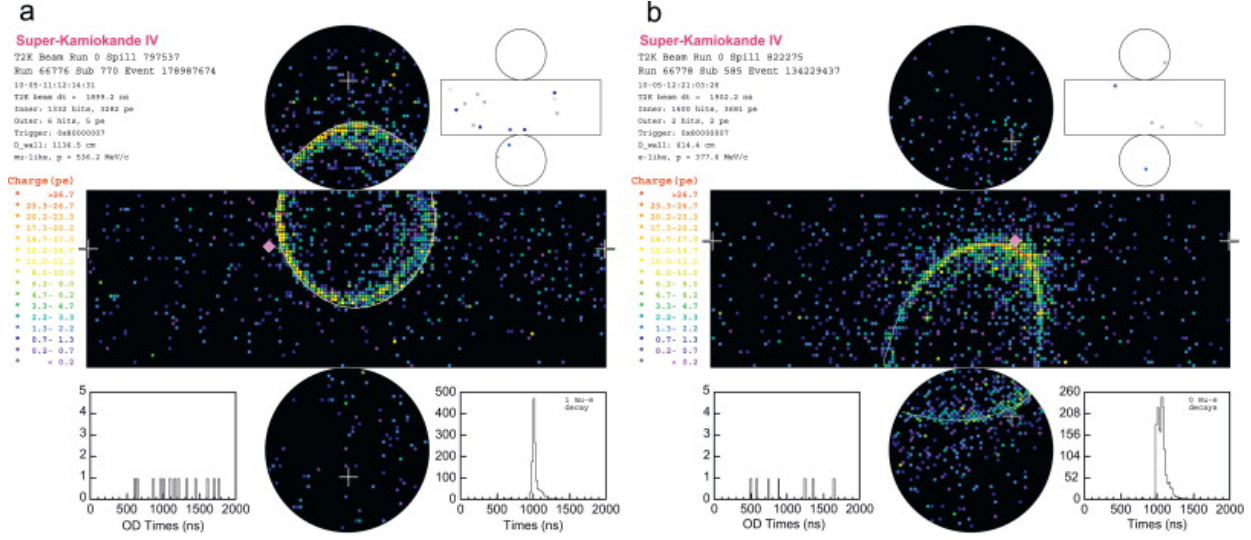


**Figure 1.28:** Representative T2K events in Super-Kamiokande for (a) a muon-like ring and (b) an electron-like ring. Both figures show Super-Kamiokande unrolled onto a plane with each colored point representing a PMT. The color of each PMT corresponds to the amount of charge collected. In upper right corner shows the same unrolled hit map for the veto outer detector. White crosses indicate the location of the reconstructed vertex. A solid diamond marks the location where a ray parallel to the beam would intersect the detector wall starting from the vertex.

far detector neutrino measurements. Therefore a discussion on the T2K ND constraint on the oscillation analysis is warranted.

### 1.2.4 Oscillation Analysis ND Constraint

As stated before, the primary goals of T2K are measure to measure the oscillation parameters  $\theta_{13}$ ,  $\theta_{23}$ ,  $\Delta m_{23}^2$ , and nonzero  $\delta_{\text{CP}}$ . This is performed by fitting the oscillation parameters to the number of observed flavored neutrinos at SK. The number of observed neutrino events,  $N_{\nu_\alpha}$ , of flavor  $\nu_\alpha$  is

$$N_{\nu_\alpha} = B + S_{\nu_\alpha} \quad (1.55)$$

where  $B$  is the number of all misidentified  $\nu_\alpha$  events and  $S_{\nu_\alpha}$  is the number of true events. The expected neutrino appearance rate is given by

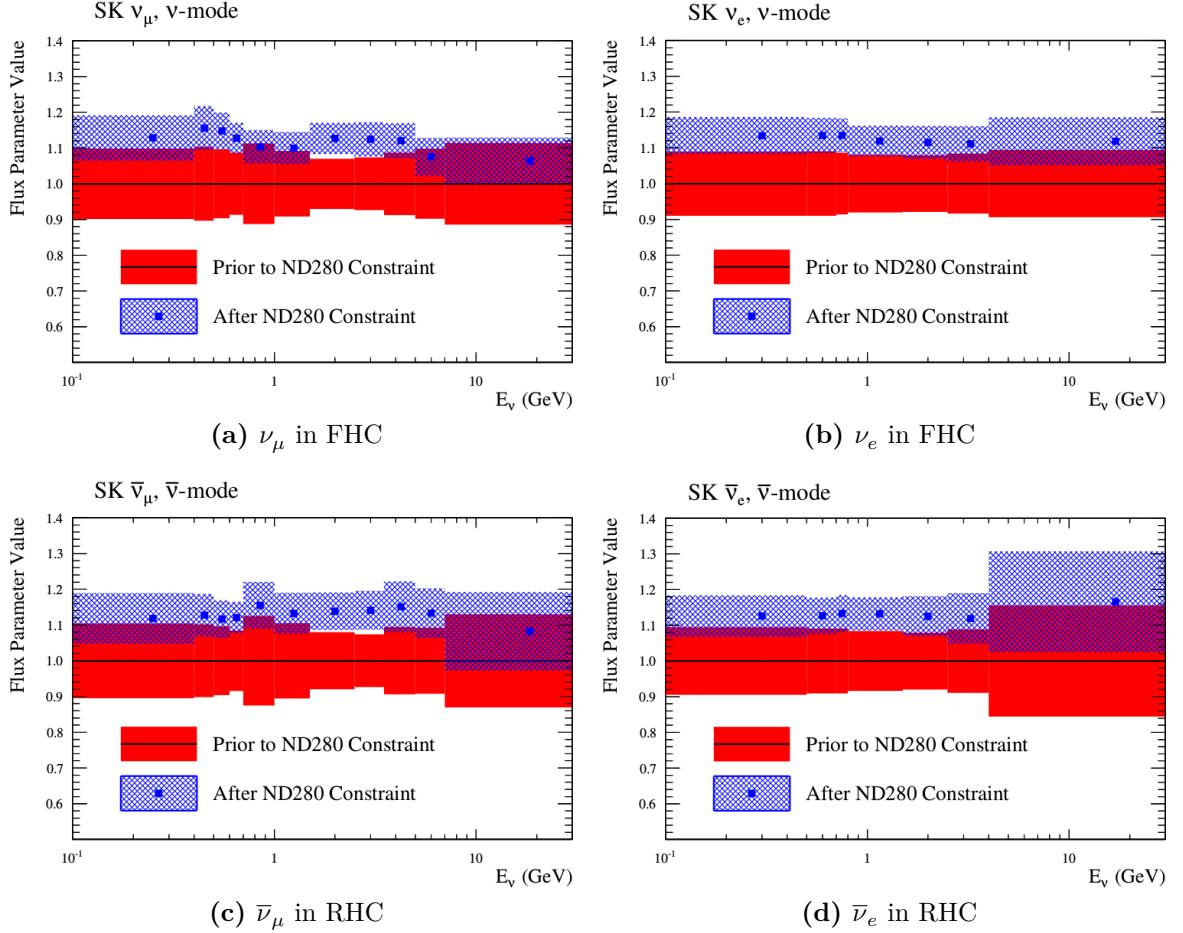


**Figure 1.29:** Predicted and best fit measurements for the T2K flux at Super-Kamiokande. The horizontal axes are the neutrino energy and the vertical axes are the fractional change in the flux normalization. These figures were taken from the 2017 T2K oscillation analysis [6]. A value 1.1 corresponds to a 10% increase in the number of predicted events.

$$S_{\nu_\alpha} = \sum_{\lambda=e,\mu} \left[ \mathcal{P}_{\nu_\lambda \rightarrow \nu_\alpha} (E_\nu; \vec{\sigma}) \right] \times \sum_t \left[ \sigma_{\nu_\alpha}^t (E_\nu) \cdot t_N \right] \\ \times \Phi_{\nu_\alpha} (E_\nu) \times \epsilon(p_\alpha, \theta_\alpha), \quad (1.56)$$

where  $\vec{\sigma}$  is a vector of the oscillation parameters from Eqn. (1.38),  $\sigma_{\nu_\alpha}^t$  is the cross section for  $\nu_\alpha$  on target  $t$ ,  $t_N$  is the number of targets of type  $t$ ,  $\Phi_{\nu_\alpha}$  is the flux of neutrinos, and  $\epsilon(p_\alpha, \cos \theta_\alpha)$  is the efficiency of reconstructing and correctly categorizing the event as a function of momentum  $p$  and angle  $\theta$ .

Having a large, sensitive off-axis ND like ND280 provides a tool to determine the oscillation analysis constraints. This includes the oscillation channel  $\nu_\mu \rightarrow \nu_e$ , but also the

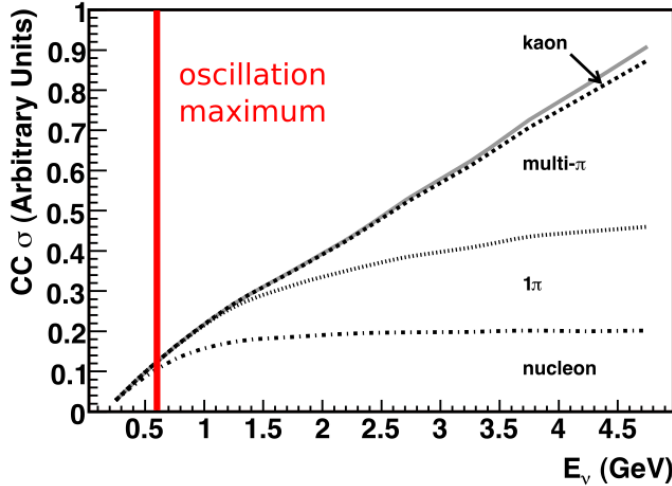


**Figure 1.30:** Predicted CC inclusive scattering cross section at T2K relevant energies. Only the most common final state modes are shown. A thick, red line indicates the T2K  $\nu_e$  appearance probability maximum. For CCQE-like interactions (nucleon), a single nucleon is struck. Higher energy interactions like resonance ( $1\pi$ ) and DIS (multi- $\pi$ ) interactions produce pion and kaon final states as well. All combined, the inclusive cross section increases linearly with energy. This image was edited and originally produced by Formaggio and Zeller [41].

intrinsic  $\nu_e$  background in the T2K beam. These neutrinos interact the same way an oscillated neutrino would at SK. Without ND280, the fractional uncertainty on the flux rate is about  $\sim 10\%$  per energy bin. These constraints are obtained from the MUMON detector discussed above and the NA61/SHINE experiment [12]. Adding the ND constraint reduces the uncertainty to about  $\sim 5\%$  as seen in fig. 1.29 on the preceding page.

T2K uses the NEUT<sup>11</sup> [52] program library to simulate neutrino interactions with nucleons and the nucleus. It was originally designed to simulate atmospheric neutrinos for the Kamioka Nucleon Decay Experiment (Kamiokande), the predecessor to the Super-Kamiokande experiment. Included in NEUT are numerous models for neutrino interactions on matter and intra-medium hadron spatial transport within the nucleus.

Using the ND280 constraint tunes the NEUT cross section model to best match the T2K data. The canonical T2K cross section model in NEUT is problematic due to dependence on effective models describing neutrino-nucleus scattering. In particular, large model and data

---

<sup>11</sup>NEUT is neither an initialism nor acronym.

disparities exist within recent, high statistics CCQE measurements [41]. This forces T2K to constantly explore other physics models, some of which are employed in this analysis.

### 1.2.5 Contributions to the T2K Experiment

Since joining the T2K experiment five years ago, I have played a critical role in an analysis that is currently in preparation for publication [76]. This analysis was a second generation measurement of the  $\nu_\mu$  CC single pion production cross section on water in the PØD. I am a co-author of that paper and its internal T2K technical document that outlines the analysis procedure and studies. In particular, I helped develop the momentum calibration and event selection using machine learning. Further details on my contributions are found in Appendix A.

In addition to analysis work, the majority of my contributions to the experiment include on-site expertise for the ND280 detector. I was involved in the 2015 work to replace two PØD water bags when they showed evidence of leaking. Additionally, I helped measure the PØD water mass and deformations in the PØD structure due to the internal stresses from the water mass. I am certified as a Trip-T ASIC expert, PØD water system and calibration expert, and experienced DAQ shifter. As an expert in these areas, I was solely responsible for daily reporting and monitoring for the SMRD, ECal, and PØD detectors during beam taking periods. This included being the first point-of-contact, 24/7 for those electronic systems and the PØD water target whenever problems arose.

My most recent contribution was participating in the 2018 SK open tank work at the Kamioka Observatory. My work had three primarily goals:

- Cleaning the support structures, walls, and PMTs of non-water contaminants. This includes using clean wipes to remove diesel fume residue on the support structures from the initial construction and rust removal using electrolysis,

- Collecting glass shards remaining in the tank after a major multi-PMT implosion in 2001, and
- Replacing the light-tight insulation that separates the inner and outer detectors.

These tasks helped the Kamioka Observatory identify external water leaks and remove contaminants in the SK detector. This is all in preparation for adding gadolinium (Gd), a rare earth metal, to the pure water in the detector which will enhance the antineutrino capture cross section.

### 1.3 Summary

The neutrino is an elusive particle to detect. The relatively new neutrino oscillation phenomenon has opened up the further possibilities of exploring fundamental questions of the Universe like CP violation. In the T2K experiment, some of the uncertainties associated with neutrino oscillations are being explored. To facilitate these goals, constraining all forms of uncertainty in neutrino-nuclear interactions and flux help improve its sensitivity to the oscillation predictions.

The next chapters in this thesis are presented in the following order. First is the ND280 constraint on the flux and cross section models using the beam and near detector flux task force (BANFF) maximum likelihood fit. Next is the description of the analysis samples that are used in the BANFF fit. With the samples defined, the parameterization of the fit bins and penalty terms are defined for this analysis. This is followed by the validation of the BANFF fit in a few scenarios. Then the BANFF postfit results are analyzed in relation to previous analyses. The final chapter is a discussion of the results and prospects for the future.

# Chapter 2

## The BANFF Fit Likelihood

The T2K experiment has organized a task force dedicated to provide the near detector constraint for the oscillation analysis. This task force is called the “Beam And Near detector Flux task Force (BANFF)<sup>12</sup>. The BANFF group has implemented a binned likelihood maximization fit of the ND280 data for the oscillation analysis [4].

The BANFF near detector (ND) constraint fit is done separately from fitting the Super-Kamiokande (SK) data. In a joint fit, the measurements from both detectors are considered to estimate the oscillation parameters. This joint-fit approach is more computationally expensive since it must include all parameters that affect the both the ND and SK systematic uncertainties, also called nuisance parameters. Also the time to perform a fit increases non-linearly with increasing the number of fit parameters. Therefore the separate BANFF likelihood maximization, hitherto referred to as the “BANFF fit”, must include parameters that affect the measurement of the oscillation parameters. Then those fit parameters and their respective covariances are used as inputs in the oscillation analysis. This “divide-and-conquer” approach allows for more rapidly completed studies on the effects of model parameters and biases present. However, information encoded in the ND280 measurements for shared nuisances such as the neutrino flux is inevitably lost in the BANFF fit.

---

<sup>12</sup>Banff is a national park in Canada.

The modern BANFF fit is described in detail in the following reference [6]. To summarize the details, the BANFF fit uses a frequentist approach to find the best parameter set to maximize a binned likelihood. Subsequent updates to the BANFF fit have increased the sample sizes and systematic uncertainty parameterizations.

This chapter describes the BANFF fit and overview of the fitting procedure. First we introduce the concept of likelihood functions in Section 2.1. Then we explore the mechanics of the BANFF fit using likelihood functions in Section 2.2. The final topic is a chapter summary in Section 2.3.

## 2.1 Conditional Probability Density Functions

Consider the problem of extracting physics parameters  $\vec{y}$  given some data vector  $\vec{N}$ . The conditional probability density function (PDF)  $\mathcal{P}$  to measure these parameters is given as

$$\mathcal{P}(\vec{y}|\vec{N}) = \frac{\mathcal{L}(\vec{N}|\vec{y})\mathcal{P}(\vec{y})}{\int \mathcal{L}(\vec{N}|\vec{x})\mathcal{P}(\vec{x})d\vec{x}}, \quad (2.1)$$

where everything on the right of the vertical lines represents a condition on the probability.  $\mathcal{L}(\vec{N}|\vec{y})$  is the likelihood of the model with parameters  $\vec{y}$ ,  $\mathcal{P}(\vec{y})$  is the probability for the model, and the denominator is the normalization. A frequentist interpretation of the PDF is a proportion of outcomes of repeated trials or experiments. A likelihood function is an expression of the probability of observing data as a function of the model parameters in their appropriate ranges.

One arrives at Eqn. (2.1) by using the definition of compound probabilities

$$\mathcal{P}(A, B) = \mathcal{P}(B|A)\mathcal{P}(A), \quad (2.2)$$

to evaluate  $\mathcal{P}(\vec{y}|\vec{N})$  as

$$\mathcal{P} \left( \underbrace{\vec{y}}_B \middle| \underbrace{\vec{N}}_A \right) = \frac{\mathcal{P}(\vec{N}, \vec{y})}{\mathcal{P}(\vec{N})}, \quad (2.3)$$

where the denominator is the normalization of the PDF. The compound PDF  $\mathcal{P}(\vec{N}, \vec{y})$  can be expanded using Bayes' theorem which states

$$\mathcal{P}(A|B)\mathcal{P}(B) = \mathcal{P}(B|A)\mathcal{P}(A), \quad (2.4)$$

and combined with Eqn. (2.2) yields

$$\mathcal{P} \left( \underbrace{\vec{N}}_A, \underbrace{\vec{y}}_B \right) = \mathcal{P}(\vec{N}|\vec{y}) \times \mathcal{P}(\vec{y}), \quad (2.5)$$

where the PDFs to the left and right of the  $\times$  operator are the likelihoods and priors, respectively. Combining resulting in Eqn. (2.3) and Eqn. (2.5) reproduces the original expression of Eqn. (2.1).

## 2.2 The BANFF Fit Test Statistic

Curve fitting is commonly used in particle physics in order to constrain unknown model parameters using histograms. This procedure seeks to find the “best” set of the model predictions,  $\theta$ , that match the data, as is the case for the BANFF fit. This analysis uses a chi-squared test to provide a goodness of fit metric, a parameter estimation (also referred to as “best fit parameters”), and a error estimation for the BANFF fit.

The BANFF fit is an attempt to maximize the agreement between the measured and predicted data curves at the ND280 detector. This is equivalent to maximizing a binned likelihood function  $\mathcal{L}$  of the ND280 data given a set of parameters in the likelihood function that predict the measured rate. The use of likelihood functions in fits to histograms is explained further in reference [20] and the PDG review on statistics. By invoking Wilks’

theorem, also known as the likelihood ratio theorem, the likelihood maximization procedure is converted into a minimization problem involving a test statistic denoted as a chi-squared. Below is an explanation of the BANFF test statistic and the model terms.

### 2.2.1 Log-Likelihood Ratio

Consider many binned samples that select different charged current topologies. A convenient choice of observables for all the samples is the outgoing charged lepton  $l$  momentum  $P_l$  and angle  $\cos \theta_l$  as measured in the ND280 detector [49]. For each  $(P_l, \cos \theta_l)$  analysis bin  $i = 1, 2, \dots, M - 1, M$ , the likelihood is given by

$$\mathcal{L}(\vec{N}^d | \vec{N}^p) = \prod_{i=1}^M \frac{(\vec{N}_i^p)^{\vec{N}_i^d} \exp(-\vec{N}_i^p)}{\vec{N}_i^d!} \quad (2.6)$$

where  $\vec{N}_i^d$  is the number of observed data events in the  $i$ th bin and  $\vec{N}_i^p$  is the number of predicted events as a function of the fit parameters in the same bin. One recognizes the likelihood function in Eqn. (2.6) as a product of Poisson distributions, since this is counting data measured in  $M$  analysis bins. The parameters that affect the predicted event rate are:

- The cross section physics models, labeled as “xsec”,
- The neutrino flux, and
- The detector biases and inefficiencies.

We use these parameters to calculate the number of predicted charged current (CC) events  $N^{\nu_l}$  from any neutrino flavor  $\nu_l$  at ND280 as

$$N^{\nu_l} = \underbrace{\Phi_{\nu_l}}_{\text{Flux}} \times \left[ \sum_t \underbrace{(\sigma_{\nu_l}^t M^t)}_{\text{Effective area}} \right] \times \underbrace{\epsilon_{\nu_l}}_{\text{Efficiency}}, \quad (2.7)$$

where  $\Phi_{\nu_l}$  is the flux of  $l$  flavor neutrinos,  $\sigma_{\nu_l}^t$  is the cross section of the interaction for neutrino flavor  $l$  on target  $t$ ,  $M^t$  is the number of  $t$  targets, and  $\epsilon_{\nu_l}$  is the total efficiency

**Table 2.1:** Parameters that affect the analysis bins. The top three parameters are fit while the others are constants set by the input data and bookkeeping.

Description	Symbol	Fit?
Fit bin normalizations	$\vec{d}$	Yes
Flux normalizations	$\vec{b}$	Yes
Cross section weights and norms.	$w(\vec{x})$	Yes
POT weight for the MC	$w^{\text{POT}}$	No
Flux bin selector	$\delta_{j,k}^{\text{Flux}}$	No
Number of flux parameters	$N^{\text{Flux}}$	No
Number of cross section parameters	$N^{\text{xsec}}$	No
Number of MC events	$N^{\text{MC}}$	No

to reconstruct and properly identify the event as  $\nu_l$ CC interactions. Since the cross section is a measure of interaction probability in units of area, multiplication of  $M_t$  represents the effective cross sectional area of material  $t$  in the detector. Each term in Eqn. (2.7) is modeled carefully using Monte Carlo (MC) simulations. For the efficiency term, control samples are used to constrain detector systematic uncertainties effects.

The number of events in a given analysis bin is varied in the BANFF fit using weight functions. The total number of predicted events in the  $i$ th analysis bin is given by

$$\vec{N}_i^p(\vec{b}, \vec{x}, \vec{d}) = \sum_{j=1}^{N_i^{\text{MC}}} \left\{ w_i^{\text{POT}} \sum_{k=1}^{N^{\text{Flux}}} (\delta_{j,k}^{\text{Flux}} \vec{b}_k) \times \left[ \prod_{l=1}^{N^{\text{xsec}}} w_{j,l}(\vec{x}_l) \right] \times \vec{d}_i \right\}, \quad (2.8)$$

where the parameters are described in Table 2.1 on page 59. While Eqn. (2.8) looks complicated as expressed in the T2K model, it is functionally the same as Eqn. (2.7). Since the flux bins are categorized by neutrino energy, neutrino flavor, and horn current mode, the  $\delta_{j,k}^{\text{Flux}}$  term is needed to select the correct flux normalization bin for the  $j$ th MC event. Also the number of neutrino targets  $M$  in the detector is treated as a detector systematic uncertainty.

Using the likelihood ratio test theorem, a test statistic is defined as taking -2 times the natural logarithm of the ratio of predicted to observed likelihoods from Eqn. (2.6). This test statistic is given as

$$\begin{aligned}\chi_{\text{LLR}}^2 &= -2 \log \frac{\mathcal{L}(\vec{N}^d | \vec{N}^p)}{\mathcal{L}(\vec{N}^d | \vec{N}^d)} \\ &= 2 \sum_{i=1}^M \left[ \vec{N}_i^p - \vec{N}_i^d + \vec{N}_i^d \log \left( \frac{\vec{N}_i^d}{\vec{N}_i^p} \right) \right],\end{aligned}\tag{2.9}$$

where this obeys a true chi-squared distribution for asymptotically large sample sizes. The denominator in Eqn. (2.9) is the MC predicted probability, which assumes the best maximum likelihood estimate is the number of observed events.

### 2.2.2 External Constraints on the Fit

Since the BANFF ND constraint is a predictive model fit to data, it is subject to the bias-variance problem. This problem basically states that for a set of samples  $s \in \mathcal{S}$ , a predictive model  $f_1 \in \mathcal{F}$  would have larger variance and smaller bias compared to a constrained or shrunken model  $f_2 \subseteq f_1$  of which has larger bias but smaller variance. We wish to have a ND constraint measurement with as little variance as possible, which is achieved by introducing one or more constraints, also called “penalty” terms, to the test statistic Eqn. (2.9). These penalty terms will introduce the T2K experiment’s model on the flux, cross section, and detector inefficiencies into the fit.

The new test statistic that includes the constraints,  $\chi_{\text{ND280}}^2$ , is given by

$$\begin{aligned}\chi_{\text{ND280}}^2 &= \chi_{\text{LLR}}^2 + \underbrace{\chi_{\text{xsec}}^2 + \chi_{\text{Flux}}^2 + \chi_{\text{Det}}^2}_{\text{Penalty terms}} \\ &= \chi_{\text{LLR}}^2 - 2 \left( \underbrace{\log \pi(\vec{x})}_{\text{xsec}} + \underbrace{\log \pi(\vec{b})}_{\text{Flux}} + \underbrace{\log \pi(\vec{d})}_{\text{Det}} \right),\end{aligned}\tag{2.10}$$

where each of the PDFs  $\pi(\vec{y} = \{\vec{x}, \vec{b}, \vec{d}\})$  is an assumed multivariate normal distribution

$$\pi(\vec{y}) = C_y \exp \left( -\frac{1}{2} (\vec{y} - \vec{y}_0)^T V_y^{-1} (\vec{y} - \vec{y}_0) \right),\tag{2.11}$$

$\vec{y}_0$  is a vector of the initial parameter values,  $T$  corresponds to the transpose operator,  $C_y$  is the normalization, and  $V_y$  is the covariance matrix for vector  $\vec{y}$ . The full form of the test statistic  $\chi^2_{\text{ND280}}$  is given by

$$\chi^2_{\text{ND280}} = 2 \sum_{i=1}^M \left[ \vec{N}_i^p - \vec{N}_i^d + \vec{N}_i^d \log \left( \frac{\vec{N}_i^d}{\vec{N}_i^p} \right) \right] + (\Delta \vec{y})^T (V_y^{-1}) (\Delta \vec{y}) \quad (2.12)$$

where  $\Delta \vec{y} = \vec{y} - \vec{y}_0$ . It must be stated that the test statistic Eqn. (2.12) purposefully excludes normalization terms since they are constants that do not affect the minimization. Further details on the penalty terms and covariance matrix in Eqn. (2.12) will be discussed in Chapter 4.

The best fit parameters,  $\hat{\vec{y}}$ , are those that minimizes the chi-squared statistic

$$\hat{\vec{y}} = \underset{\vec{y} \in \mathbb{R}^d}{\operatorname{argmin}} \left\{ \chi^2_{\text{LLR}} \left( \vec{N}^d, \vec{N}^p(\vec{y}) \right) + \chi^2_{\text{Penalty}}(\vec{y}) \right\} \quad (2.13)$$

where

$$\chi^2_{\text{Penalty}}(\vec{y}) = (\Delta \vec{y})^T (V_y^{-1}) (\Delta \vec{y})$$

and we recall that  $\vec{N}^p$  is a function of  $\vec{y} = \{\vec{x}, \vec{b}, \vec{d}\}$  as well.

### 2.2.3 Postfit Covariance

Once the global minimum is found, the postfit covariance matrix needs to be calculated. Consider how the chi-squared varies around the global minimum, or also called the maximum likelihood estimate,  $\hat{\vec{y}}$ . The test statistic is given analytically by a Taylor series

$$\chi^2(\vec{y}) = \sum_{n=0}^{\infty} \frac{1}{n!} \left[ (\vec{y} - \hat{\vec{y}})^T \nabla_{\vec{y}} \chi^2 \Big|_{\vec{y}=\hat{\vec{y}}} \right]^n.$$

Since the gradient at  $\hat{\vec{y}}$  is zero, the first non-zero  $\vec{y}$ -dependent term is quadratic in  $\vec{y}$

$$\begin{aligned}\chi^2(\vec{y}) &\approx \chi^2(\hat{\vec{y}}) + \frac{1}{2} (\vec{y} - \hat{\vec{y}})^T \left( \nabla_{\vec{y}} \nabla_{\vec{y}}^T \chi^2(\vec{y}) \Big|_{\vec{y}=\hat{\vec{y}}} \right) (\vec{y} - \hat{\vec{y}}) \\ &\approx \chi^2(\hat{\vec{y}}) + \frac{1}{2} (\vec{y} - \hat{\vec{y}})^T \mathcal{H}(\vec{y} - \hat{\vec{y}}).\end{aligned}$$

where  $\mathcal{H}$  is a square matrix called the Hessian matrix

$$\mathcal{H}_{i,j} = \frac{\partial^2 \chi^2}{\partial y_i \partial y_j} \Big|_{\vec{y}=\hat{\vec{y}}}, \quad (2.14)$$

and  $y_i, y_j \in \vec{y}$ . Assuming that our test statistic is distributed according to a multivariate normal distribution of the form Eqn. (2.11), we find that the inverse of the Hessian matrix is the covariance matrix.

## 2.3 Summary

This chapter describes the mathematical preliminaries of the BANFF fit analysis. We first saw the role of the likelihood function to express the plausibility of data samples given a set of model parameters. We then define a binned likelihood function to estimate model parameters in the oscillation analysis using the ND280 data. Using Wilks' theorem, the likelihood maximization problem is converted to a chi-squared test statistic minimization that is iteratively maximized. Finally, penalty terms are included in the test statistic in order to assert parameter estimates that are consistent with prior systematic uncertainty measurements in T2K.

# Chapter 3

## The PØD Selections and Samples

This chapter describes the development of PØD  $\nu_\mu$  and  $\bar{\nu}_\mu$  charged current (CC) inclusive<sup>13</sup> selections in both FHC and RHC beam configurations for the BANFF fit. These selections are in continuation of previous works that developed  $\nu_\mu$  CC-inclusive selections between the PØD and the TPC. The first such analysis was the  $\nu_\mu$  CC-inclusive cross section using the previous ND280 simulation and reconstruction software release called “Production 5”<sup>14</sup> [36]. That analysis relied on each subdetector’s reconstruction software and developed a track matching algorithm since the ND280 “Global” reconstruction matching was not available in that software production. Another cross section analysis measuring the cross section ratio of  $\bar{\nu}_\mu/\nu_\mu$  also used this “pre-Global” technique with the modern ND280 “Production 6” software<sup>15</sup> [7]. As the inter-detector matching reconstruction became available in Global, two cross section analyzes,  $\nu_\mu$  CC-0 $\pi$  [8] and  $\bar{\nu}_\mu$  CC-0 $\pi$  [11,27], were developed that also used the CC-inclusive selection as pre-selection cuts. A “cut” refers to one or more criteria to

---

<sup>13</sup>A CC-inclusive selection is a set of criteria that select all CC neutrino interaction events as opposed to an CC-exclusive selection like CC-0 $\pi$ .

<sup>14</sup>The ND280 detector reconstruction and Monte Carlo official software updates are given a “Production” designation. The Production 5 software was actively used between 2012 and early 2014 until it was replaced by Production 6. However, physics analyzers are not as rapid to adopt the software updates.

<sup>15</sup>The ND280 “Production 6” software was released in 2014 and is still in active use.

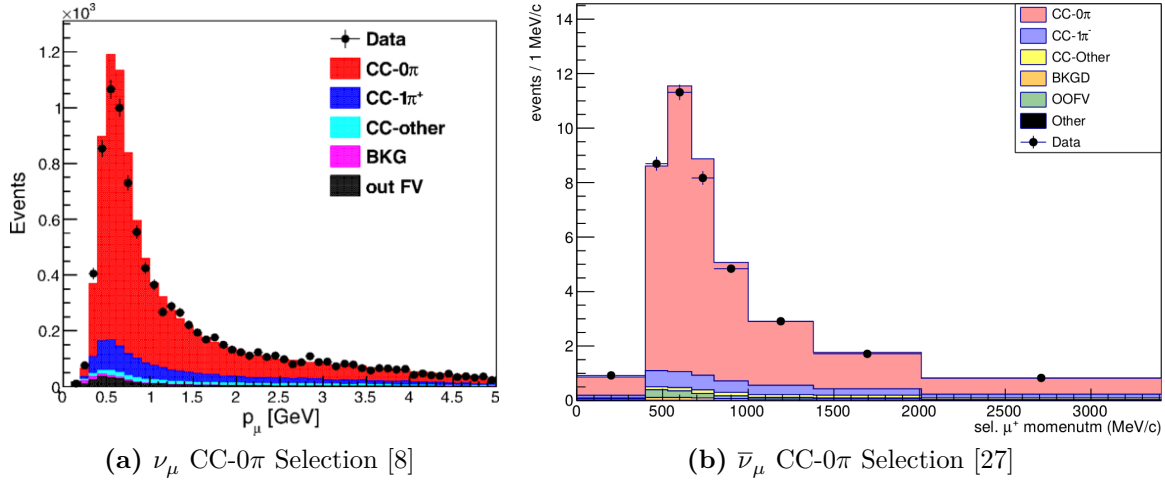


**Figure 3.1:** The PØD  $\nu_\mu$  and  $\bar{\nu}_\mu$  CC-0 $\pi$  selection kinematics. They importantly share the same pre-selection cuts as this analysis. The error bars are statistical only with the prediction sorted into various truth topologies.

select reconstructed events that have desired properties. The pre-selection cuts are designed in particular to filter out poor data quality events. They are well validated with results using these cuts are published as shown in Figure 3.1 on page 64. The selections described in this thesis also employ the same pre-selection cuts with the latest stable Global reconstruction software, Production 6.

This paragraph is a layout of the topics in the chapter. First discussed is the event reconstruction using the “Global” reconstruction software in Section 3.1. The next discussion is on the sample selections in Section 3.2. With the selections established, three CC-inclusive selection are described in the following order: the  $\nu_\mu$  in foreword horn current (FHC) mode selection, the  $\bar{\nu}_\mu$  in reverse horn current (RHC) mode selection, and the  $\nu_\mu$  background in RHC mode selection. The penultimate topic is an examination of the collected samples and their kinematic properties in Section 3.3. Finally, the chapter summary is provided in Section 3.4.

## 3.1 The ND280 Global Reconstruction

The task of the Global reconstruction is to combine all of the ND280 information into a combined reconstructed object. It was originally designed to identify CC- $0\pi$  events in the Tracker, FGD+TPC, region and has been extended to operate with all of ND280.

The Global reconstruction is a software package that attempts to recognize patterns of deposited energy in ND280 and categorize it accordingly. Particles that deposit energy in long, linear segments are categorized as tracks. If multiple tracks originate from a common origin (vertex), it is likely that a true neutrino interaction event occurred near the reconstructed vertex. Particle cascade or shower reconstruction in Global will not be discussed since they are not selected in this thesis.

Each subdetector reconstruction algorithm is run separately as the seed to Global’s track matching algorithms. This includes the PØD’s track-finding algorithm, which defines a PØD track as a linear sequence of “nodes” with one node at each bar layer. Each node represents the approximate position where the particle intersected the bar layer. To facilitate inter-detector matching, Global attempts to “re-fit” the PØD track using a Kalman filter [84]. The re-fit procedure also corrects for particle energy loss as a function of length and multiple scattering processes. A PØD vertex, which is the assumed location of the neutrino interaction, is then associated with the re-fit track using another Kalman filter algorithm. Matching tracks between the PØD and the TPC is done automatically in the ND280 Global fit.

## 3.2 The PØD Selection Cuts

The selection of CC-inclusive events uses a series of cuts to select the muon track. Prior to any cuts and after the reconstruction, corrections are applied first to both data and MC events to correct for well known residual differences between them. This includes correcting the MC flux prediction using the secondary beamline data and reconstruction efficiency

corrections. A complete list of the corrections applied are given in the following reference [4]. The pre-selection cuts (“precuts”) are then applied to extract events that start in the PØD water target (WT) fiducial volume (FV).

The following sections will describe the precuts common to all CC-inclusive selections. The next section describes the specific selections and their cuts to select the main track associated as the lepton candidate. Finally the lepton candidate and event kinematics for all the samples are described.

### 3.2.1 Precuts

The precuts were initially developed to select  $\nu_\mu$  CC-inclusive events using the PØD and TPC subdetector reconstruction algorithms separately [7,36]. They were then used with the Global reconstruction software for the  $\nu_\mu$  CC-0 $\pi$  selection in the FHC beam configuration [8]. All cuts were implemented in psyche [80] which is the software interface that BANFF uses to select events.

Prior to the precuts, neutrino interaction data event must be collected and reconstructed for each T2K beam spill. Each T2K beam spill has eight bunches that are 58 ns long and temporally separated by 581 ns. When the beam spill occurs, the PØD’s Trip-T electronics are triggered to collect data in preset integration cycles aligned with the bunches. Each integration cycle is 480 ns long and is followed by a 100 ns dead-time to prepare for the next cycle [36]. The data collected in each cycle is used to reconstruct neutrino interaction events using the ND280 subdetector and Global software packages.

Each reconstructed event must pass the following cuts before being assigned to a selection:

1. The event has a “good” data quality flag.
  - An event is rejected if any electronics element or subdetector in ND280 is reported as “bad” during the corresponding bunch.
2. There is at least one (1) track reconstructed in the TPC.

- There are no restrictions on the number of tracks fully contained in the PØD or exiting into other subdetectors.
3. The track in the TPC must have more than 18 nodes.
- The TPC reconstruction gathers the vertical and horizontal micromegas that registered collected charge into clusters of “hits”. Each cluster’s charge distribution is used to get a vertical (horizontal) position that is more accurate than the individual readout micromegas. A node is constructed out of each cluster with associated track state information. The set of nodes are used to fit a helix shaped track.
4. The reconstructed vertex is within the PØD WT FV.
- The PØD FV is defined to include as much of the WT regions as possible. Its X and Y borders are 25 cm away from the PØDule edges while the Z borders intersect the last and first half downstream PØDule in the upstream ECal and central ECal, respectively. The FV edges are listed in Table 3.1 on page 68. This volume, while used for track-based analyzes in the past, was optimized for  $\pi^0$  and  $\nu_e$  analyses.
5. All tracks that enter the TPC pass the veto cut
- An event is rejected if any PØD track enters the TPC from outside the “corridor” volume. This cut was designed to eliminate broken tracks when the pre-Global separate subdetector reconstruction was used [28]. In practice, this cut ensures that Global tracks entering the TPC are away from its X and Y edges. The corridor definition is the same as defined in the  $\bar{\nu}_\mu/\nu_\mu$  cross section ratio analysis technical note [29] and shown in Table 3.1 on page 68.

**Table 3.1:** The PØD WT FV (left) and veto corridor volume (right) in the ND280 coordinate system. The corridor spans from the 5th (8th) to 40th (80th) PØDule (scintillator layer). All the units are given in millimeters.

PØD WT FV	Corridor Volume
$-836 < X < 764$	$-988 < X < 910$
$-871 < Y < 869$	$-1020 < Y < 1010$
$-2969 < Z < -1264$	$-3139 < Z < -900$

After passing of all the precuts, a single, global track, which is observed in the TPC, is assigned as the lepton candidate or “main track” of a selected event. While the main track is different for each selected event, the momentum reconstruction is the same. The momentum of the main track,  $P$ , is sum of its measured momentum in the TPC,  $P_{\text{TPC}}$ , with the estimate momentum lost in the PØD,  $\Delta P_{\text{PØD}}$

$$P = P_{\text{TPC}} + \Delta P_{\text{PØD}}. \quad (3.1)$$

The momentum lost in the PØD is estimated by summing the total momentum loss along the track path  $\mathcal{C}$

$$\Delta P = \int_{\mathcal{C}} \left( \frac{dP}{dx} \right) dx, \quad (3.2)$$

where  $dP/dx$  is the momentum loss function. The momentum loss function is related to the energy loss function,  $dE/dx$  via the chain rule

$$\begin{aligned}
\frac{dE}{dx} &= \left( \frac{dE}{dP} \right) \left( \frac{dP}{dx} \right) \\
&= \frac{d}{dP} \left( \sqrt{P^2 c^2 + m^2 c^4} \right) \left( \frac{dP}{dx} \right) \\
&= \left( \frac{P c^2}{E} \right) \left( \frac{dP}{dx} \right) \\
&= \beta c \left( \frac{dP}{dx} \right),
\end{aligned} \tag{3.3}$$

where  $\beta$  is the particle velocity as a ratio of the speed of light  $c$ . Since the reconstructed track's path  $\mathcal{C}$  is not infinitesimally precise due to inherent detector resolution, we must replace the integral with a sum and differential  $dx \rightarrow \Delta x$ . We then arrive at the expression of the momentum loss estimate in the PØD as

$$\Delta P_{\text{PØD}} = \frac{1}{c} \sum_t \left[ \left( \frac{dE}{dx} \right) \left( \frac{\Delta x}{\beta} \right) \right]_t, \tag{3.4}$$

where  $t$  is a discrete step in  $x$  connecting the track nodes. For most tracks entering the TPC, they will be highly relativistic in the PØD ( $\beta \approx 1$ ), and Eqn. (3.4) simplifies to

$$\Delta P_{\text{PØD}} = \frac{1}{c} \sum_t \left[ \left( \frac{dE}{dx} \right) \Delta x \right]_t. \tag{3.5}$$

The next sections describe the selection cuts, first in FHC mode and then RHC mode.

### 3.2.2 The $\nu_\mu$ in FHC Mode CC-Inclusive Selection

As discussed in Section 3.2.1, this selection is the basis for the PØD  $\nu_\mu$  CC-0 $\pi$  analysis [8]. In FHC mode, the vast majority of neutrino interactions are  $\nu_\mu$  CC events that produce an outgoing, negatively charged muon. If there is no negatively charged track in the TPC, the event is likely not a  $\nu_\mu$ -induced interaction. Therefore, the  $\nu_\mu$  in FHC mode CC-inclusive selection in FHC mode has one final cut after the precuts:

1. At least one negatively charged track is reconstructed in the TPC.

- An event is rejected if none of the TPC tracks have a reported negative curvature.

If the event passes this cut, the highest momentum negative (curvature) track, or HMNT, is selected as the lepton candidate. This selection and all subsequent selections are branched into two categories based on the number of tracks counted in the PØD. If there is only one PØD track, and hence only one track in the TPC as required by the precuts, the event is categorized as a “ $\nu_\mu$  in FHC Mode CC 1-Track” event. Otherwise, the event is categorized as a “ $\nu_\mu$  in FHC Mode CC N-Tracks” event.

### 3.2.3 The $\bar{\nu}_\mu$ in RHC Mode CC-Inclusive Selection

In RHC mode, the majority of the beam neutrinos are  $\bar{\nu}_\mu$  since the horn focuses negatively charged pions and deflects positively charged pions. However, the  $\nu_\mu$  background interaction rate in RHC mode is larger than the  $\bar{\nu}_\mu$  background in FHC mode. The reason for this is two fold. Firstly, the antineutrino-nuclear scattering cross section is suppressed by  $\sim 1/3$  compared to the neutrino-nuclear scattering cross section as explained in Section 1.1.1.3. Secondly, the  $\nu_\mu$  flux in RHC is relatively large due to the excess of positively charged pions generated at the target. Therefore there is a non-negligible “wrong-sign” background in RHC mode that we need to reject.

Prior to this analysis, a  $\bar{\nu}_\mu$  CC-0 $\pi$  selection was developed for the PØD [27]. The  $\bar{\nu}_\mu$  CC-0 $\pi$  selection is quite similar to the  $\nu_\mu$  CC-inclusive selection in FHC mode, but relied on the PØD local reconstruction for a particle identification cut. The PØD local reconstruction is, however, unavailable in the event selection software used in the BANFF fit called psyche. So a new selection was developed specifically for this analysis to select  $\bar{\nu}_\mu$  interactions in RHC mode.

The  $\bar{\nu}_\mu$  in RHC mode CC-inclusive selection uses the precuts described in Section 3.2.1 and the has two cuts:

1. At least one positively charged track is reconstructed in the TPC.

- An event is rejected if none of the TPC tracks have a reported positive curvature.
2. The highest momentum positive (curvature) track, or HMPT, must be the highest momentum track.
    - If the highest momentum track has negative curvature, then the event is rejected.

If the event passes these two cuts, the HMPT is the lepton candidate. If there is only one PØD track, the event is categorized as a “ $\bar{\nu}_\mu$  in RHC Mode CC 1-Track” event. Otherwise, the event is categorized as a “ $\bar{\nu}_\mu$  in RHC Mode CC N-Tracks” event.

### 3.2.4 The $\nu_\mu$ in RHC Mode CC-Inclusive Selection

As explained in the previous subsection, the  $\nu_\mu$  background interaction rate in RHC mode is relatively large compared to the  $\bar{\nu}_\mu$  interaction rate. Having a measurement of this background is critical for the oscillation analysis due to the small number of expected  $\bar{\nu}_\mu \rightarrow \bar{\nu}_e$  counts. To date, there is no PØD measurement of  $\nu_\mu$  background in RHC mode, nor any PØD selection to do so. So like the  $\bar{\nu}_\mu$  CC-inclusive selection, a new PØD selection was developed exclusively for this analysis to select  $\nu_\mu$  background events in RHC mode.

The  $\nu_\mu$  background in RHC mode CC-inclusive selection uses the precuts described in Subsection 3.2.1 and has two cuts:

1. At least one negatively charged track is reconstructed in the TPC.
  - An event is rejected if none of the TPC tracks have a reported negative curvature.
2. The HMNT must be the highest momentum track.
  - If the highest momentum track has positive curvature, then the event is rejected.

If the event passes these two cuts, the HMNT is the lepton candidate. If there is only one PØD track, the event is categorized as a “ $\nu_\mu$  Background in RHC Mode CC 1-Track” event. Otherwise, the event is categorized as a “ $\nu_\mu$  Background in RHC Mode CC N-Tracks” event.

**Table 3.2:** T2K data-taking periods and collected POT used in the analysis. The bottom four rows are the aggregated periods grouped by horn current and PØD status, which is how the data analysis is performed. Note that the horns were run briefly at +205 kA for Run 3b when operations resumed after 2011 Tōhoku earthquake.

Run period	Horn current [kA]	PØD status	Data POT ( $\times 10^{20}$ )	MC POT ( $\times 10^{20}$ )
2	+250	Water	0.433934	12.0341
		Air	0.359149	9.23937
3b	+205		0.217273	4.47864
3c	+250		1.36447	26.3227
4			1.78271	34.996
		Water	1.64277	34.9712
5c	-250		0.43468	22.7766
6b		Air	1.28838	14.174
6c			0.505895	5.27562
6d			0.775302	6.884
6e			0.847902	8.59439
7b		Water	2.43682	33.7046
8	+250		1.58053	26.4664
		Air	4.14897	36.0694
Sand	+250		-	11.1988
Sand	-250		-	12.9201
2, 3b, 3c, 4, 8		FHC	Air	7.872757
2, 4, 8			Water	3.656589
6b, 6c, 6d, 6e		RHC	Air	3.382490
5c, 7b			Water	2.852340
				54.53

### 3.3 Selection Kinematics

This section examines the kinematics for each of selections and their respective branches while differentiating between water-in and water-out mode. The data sets used in this analysis are runs 2-8 in both PØD water-in and water-out (air) modes as shown in Table 3.2 on page 72. There will be no data events shown to prevent any potential analysis biases. Simulated events will be arranged into various true categories to study selection kinematics, efficiencies, and purities.

True interactions for these selections are generally divided into four classes:

- A neutrino-induced CCQE interaction ( $\nu$  CCQE):
  - Only NEUT generated neutrino-induced CCQE event at the interaction vertex.
- A neutrino-induced non-CCQE interaction ( $\nu$  non-CCQE):
  - Any NEUT generated neutrino-induced CC and NC event *except* neutrino-induced CCQE at the interaction vertex.
- An antineutrino-induced CCQE interaction ( $\bar{\nu}$  CCQE):
  - Only NEUT generated antineutrino-induced CCQE event at the interaction vertex.
- An antineutrino-induced non-CCQE interaction ( $\bar{\nu}$  non-CCQE):
  - Any NEUT generated antineutrino-induced CC and NC event *except* antineutrino-induced CCQE at the interaction vertex.

These signal classes must occur in the PØD WT FV in order to be selected. The non-CCQE category can be further divided among the dominant T2K CC and all NC interactions modes as enumerated in Table 3.3 on page 74. An out of FV (OOFV) event is any true event that occurs in ND280, but is falsely reconstructed in the PØD FV. Another important ND280 background are true neutrino and antineutrino CC interactions occurring in the sand surrounding the ND280 pit with the muon track falsely reconstructed in the FV. These events are referred to as “sand muon” events and are accounted for accordingly. Since these categories are used frequently in this chapter, the legends used in the histograms are enlarged for the reader’s convenience in Figure 3.2 on page 74.

The ND280 MC uses the GEANT4 software toolkit [15] to simulate the passage of particles through matter. A GEANT4 particle is assigned to a reconstructed track if it contributed the most to the track’s reconstructed hits. The most likely truth matched particles include protons ( $p$ ), both negatively and positively charged muons ( $\mu^\pm$ ), pions ( $\pi^\pm$ ), and

**Table 3.3:** Enumeration of the NEUT interaction modes which are also used in Figure 3.2 on page 74. An arrow indicates a sequence of integer steps from left to right of the arrow.

Interaction mode	$\nu$ ( $\bar{\nu}$ ) NEUT enumeration
CCQE	1 (-1)
2p2h	2 (-2)
CC-1 $\pi$	$11 \rightarrow 16$ ( $-11 \rightarrow -16$ )
non-CCQE	CC-N $\pi$ 21 (-21)
	CC-DIS      26 (-26)
	CC-Other      17, 22, 23 (-17, -22, -23)
	NC      31 $\rightarrow$ 100 (-31 $\rightarrow$ -100)

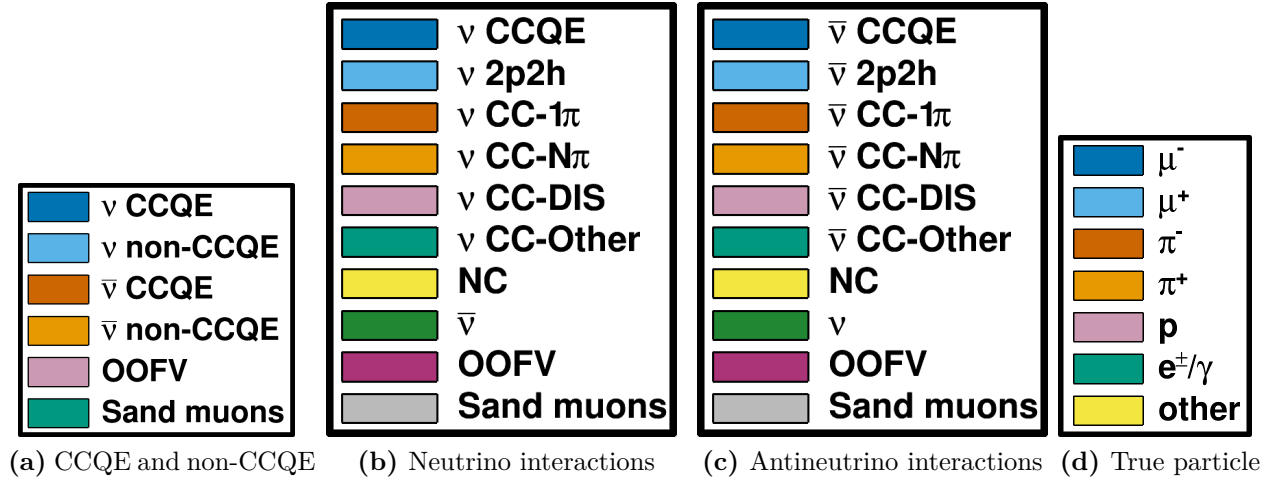


**Figure 3.2:** Frequently used legends that are enlarged for the reader’s convenience.

electrons/positrons ( $e^\pm$ ). In addition, any electron and positron generated from pair production are grouped together as “ $e^\pm/\gamma$ ”. Particles that do not match any of these categories is labeled as “other”.

### 3.3.1 The $\nu_\mu$ in FHC Mode CC 1-Track Sample

This selection provides the CCQE-like samples in FHC mode. Figure 3.3 on page 76 and Figure 3.4 on page 77 displays the momentum and angular distributions that are inputs to BANFF. Comparing between water-in and water-out modes, we see that the reconstructed

kinematics are nearly identical. In the majority of cases, the lepton candidate is the true muon, making this a very pure  $\nu_\mu$  sample. We also see that there are non-CCQE events, which without a particle identification cut, are a irreducible background. Following this paragraph and the following sections, only the PØD water-in mode kinematics will be shown.

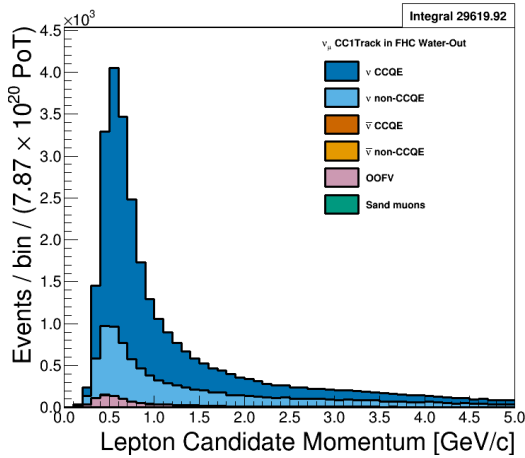
The target nuclei between water-in and water-out modes is shown in Figure 3.5 on page 78. Scattering on the carbon nucleus is the dominant interaction in both modes since the scintillating bars are constructed of polyethylene  $[(\text{CH}_2\text{CH}_2)_n]$  plastic. In water-in mode, the oxygen nucleus is a significant target with hydrogen having a small contribution as well. The brass layers between the PØDules and the water bags introduce copper and zinc nuclei scattering events too. The events on lead nuclei are true OOFV and primarily occur in the last PØDule.

We can examine the efficiencies and purities differentially for true  $\nu_\mu$  CCQE interactions in Figure 3.6 on page 78. The efficiency,  $\epsilon$ , and purity,  $\rho$ , are defined as

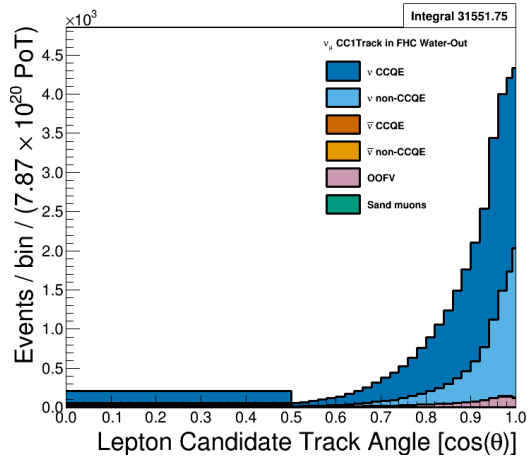
$$\epsilon = \frac{N_{\text{Selected}}^{\text{True}}}{N^{\text{True}}} \quad \rho = \frac{N_{\text{Selected}}^{\text{True}}}{N_{\text{Selected}}}, \quad (3.6)$$

where  $N_{\text{Selected}}^{\text{True}}$  is the number of true, selected events,  $N^{\text{True}}$  is the number of true events, and  $N_{\text{Selected}}$  is the number of selected events. They demonstrate that the purity is highest near 0.5 GeV/c with the efficiency highly dependent on the track angle.

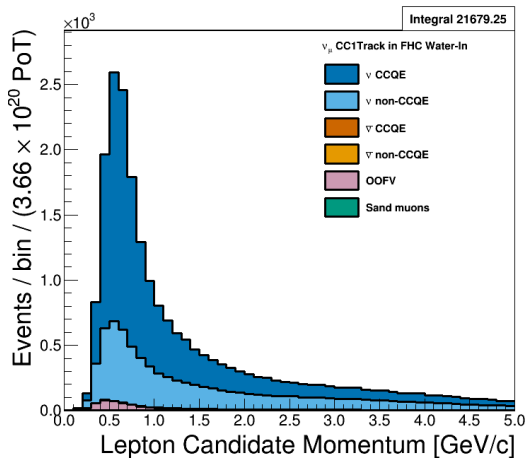
The underlying true kinematics of the interactions are shown in Figure 3.7 on page 79. Using Figure 1.5 on page 14 as reference, the kinematics shown are the true neutrino energy  $E_\nu = k_0$  and 4-momentum transfer  $Q^2 = -q^2$ . These two variables are of theoretical importance since they are used to generate events using NEUT and are used in the BANFF fit. An interesting CCQE-like final state in this selection are correlated nucleon pair scattering



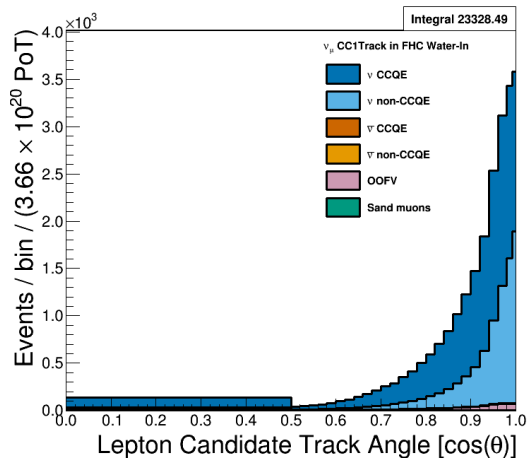
(a) Water-out Momentum



(b) Water-out  $\cos \theta$

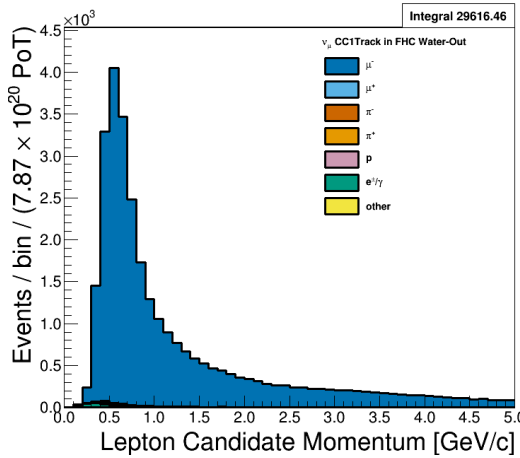


(c) Water-in Momentum

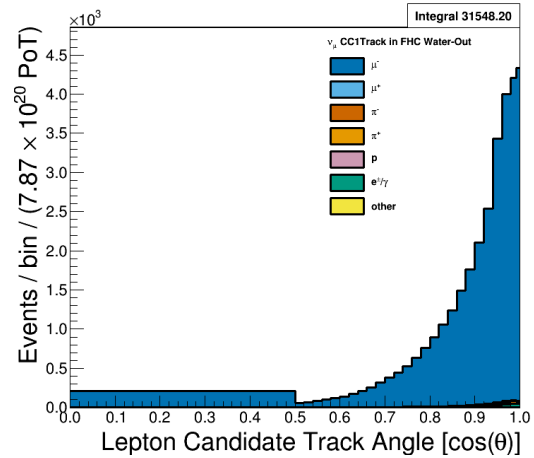


(d) Water-in  $\cos \theta$

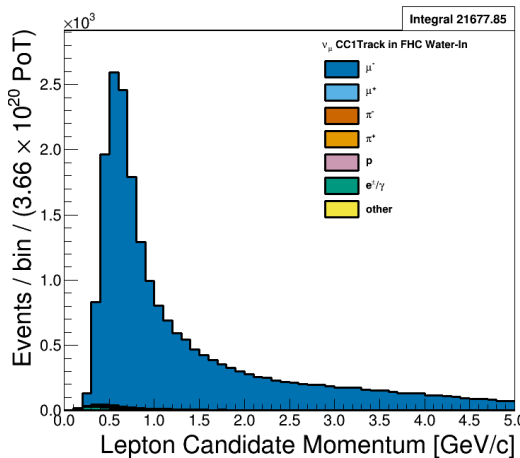
**Figure 3.3:** Reconstructed kinematics of the  $\nu_\mu$  in FHC Mode CC 1-Track selection categorized by CCQE and non-CCQE interactions. The top figures, (a) and (b), use the PØD water-out MC and are normalized to the FHC water-out mode POT. The bottom figures, (c) and (d), use the PØD water-in MC and are normalized to the FHC water-in mode POT. Also a single bin is used in the range of  $0 \leq \cos \theta < 0.5$  in figures (b) and (d).



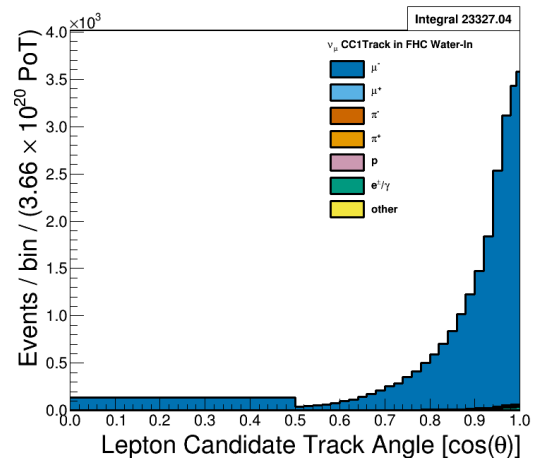
(a) Water-out Momentum



(b) Water-out  $\cos \theta$



(c) Water-in Momentum



(d) Water-in  $\cos \theta$

**Figure 3.4:** Reconstructed kinematics of the  $\nu_\mu$  in FHC Mode CC 1-Track selection categorized by the true particle matched to the main track. The top figures, (a) and (b), use the PØD water-out MC and are normalized to the FHC water-out mode POT. The bottom figures, (c) and (d), use the PØD water-in MC and are normalized to the FHC water-in mode POT. Also a single bin is used in the range of  $0 \leq \cos \theta < 0.5$  in figures (b) and (d).

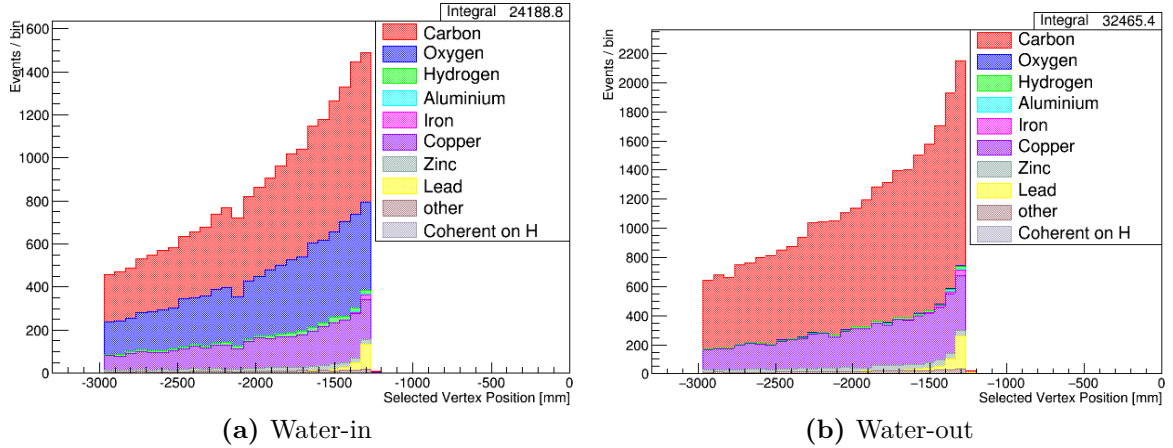


**Figure 3.5:** Reconstructed vertex Z position of the  $\nu_\mu$  in FHC Mode CC 1-Track selection. The events are categorized by the true target nucleus. The number of selected events increases with increasing Z since the probability of an interaction increases as the neutrino crosses more media in the PØD. Due to a software bug in the MC, coherent events on hydrogen (Coherent on H) are a unique category.

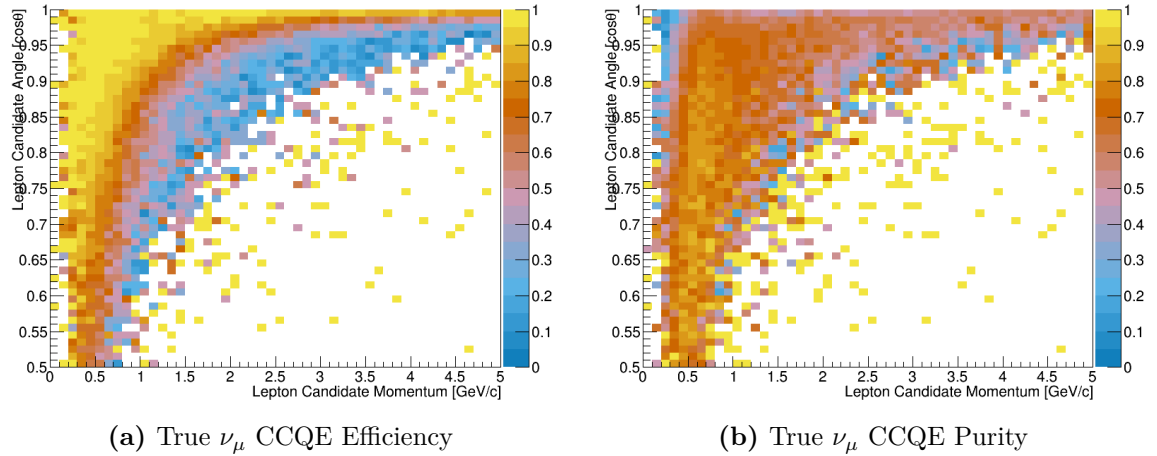


**Figure 3.6:** Efficiency and purity of the  $\nu_\mu$  in FHC Mode CC 1-Track selection. True events are defined as correctly matched  $\mu^-$  tracks from  $\nu_\mu$ -induced CCQE interactions at the vertex.

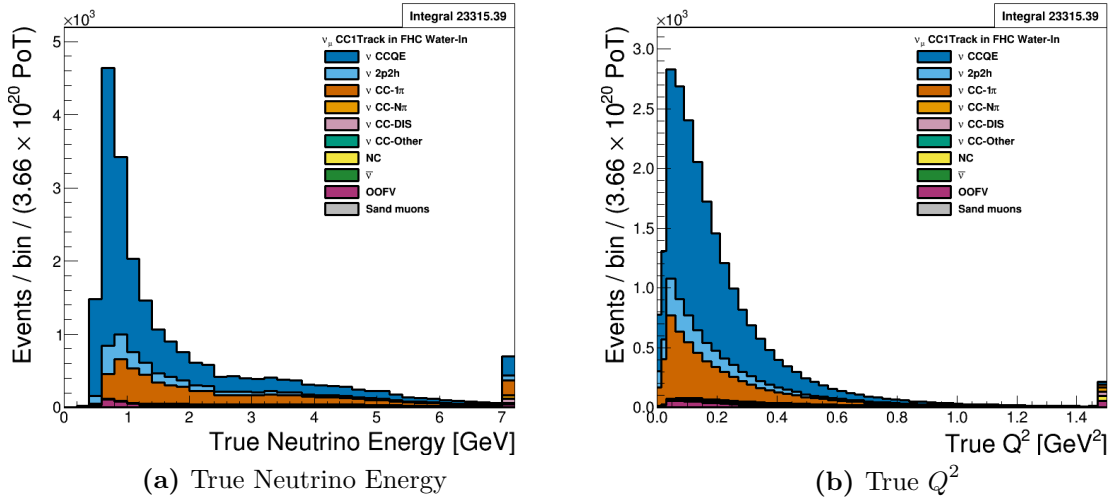


**Figure 3.7:** True kinematics of the  $\nu_\mu$  in FHC Mode CC 1-Track selection. Water-in mode is displayed here only with the last bin shown is used as overflow. The figures use the PØD water-in MC and are normalized to the FHC water-in mode POT.

called “2 particle, 2 hole” (2p2h)<sup>16</sup> events [61]. Interaction model parameters for 2p2h have large systematic uncertainties in T2K and are included the BANFF fit. Therefore these events could help reduce the 2p2h model uncertainties.

This selection contains a modest fraction of non-CCQE interactions. The largest contamination is  $1\pi$  interactions, which can happen primarily for a couple of reasons. Firstly, when the final state pion is produced, it is subject to final state interactions (FSI) where a pion can be absorbed or scattered in the nucleus. Secondly, and more importantly, a pion might not be reconstructed as a track in the PØD if its energy is below reconstruction threshold. Together, the large  $1\pi$  background affects the sensitivity to CC- $0\pi$  and CC- $1\pi$  model parameters in the BANFF fit.

---

<sup>16</sup>The name 2p2h originates from Condensed Matter Physics which motivated the model. In solid state matter, a “hole” refers to the absence of an electron in a valence band. In the High Energy Physics context, 2p2h considers neighboring and interacting nucleon pairs (2p) scattering from an incoming neutrino. The imparted energy on the pair excites them to higher energy states leaving two “hole” states (2h) behind.

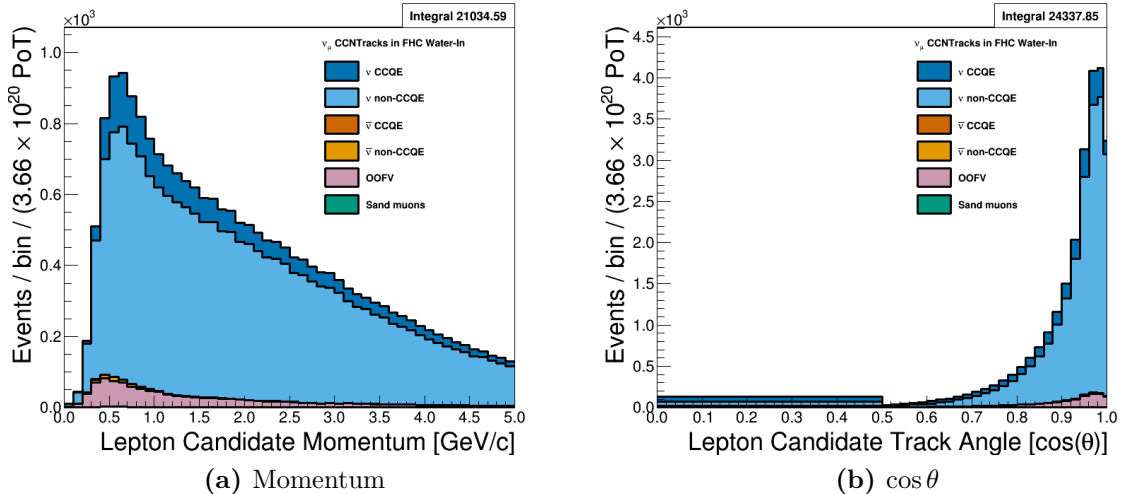


**Figure 3.8:** Reconstructed kinematics of the  $\nu_\mu$  in FHC Mode CC N-Tracks selection categorized by CCQE and non-CCQE interactions. The figures use the PØD water-in MC and are normalized to the FHC water-in mode POT. Also a single bin is used in the range of  $0 \leq \cos \theta < 0.5$  in figure (b).

### 3.3.2 The $\nu_\mu$ in FHC Mode CC N-Tracks Sample

This selection provides non-CCQE-like samples in FHC mode inputs to the BANFF fit. The reconstructed momentum and angular distributions are shown in Figure 3.8 on page 80 and Figure 3.9 on page 81. Since this selection is not optimized for any particular CC topology, there are a variety of interaction modes present including  $1\pi$ , multiple pion ( $N\pi$ ) and deep inelastic scattering (DIS). There are a number of events with a mis-identified main track that are matched to electrons and pions. There is also a relatively larger OOFV contamination compared with the 1-Track selection with some events originating in the upstream ECal as seen in Figure 3.10 on page 81. The vertex position and target materials are quite similar between the 1-Track and N-Tracks selections.

We can examine the efficiencies and purities differentially for the selection in Figure 3.11 on page 82. For the efficiency and purity only, the true signal is any  $\nu_\mu$  CC interaction except  $\nu_\mu$  CCQE (CC non-QE), which the CC 1-Track topology selection is designed to select. The efficiency is high for the higher momenta and higher angle tracks suggesting this is a high  $Q^2$  selection. In addition, the purity is around ~70% in this region.

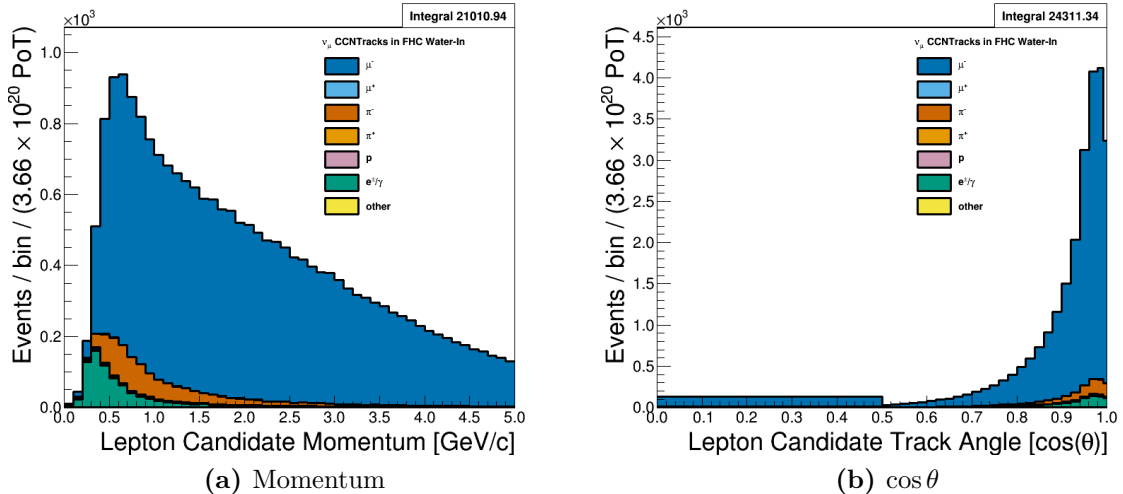


**Figure 3.9:** Reconstructed kinematics of the  $\nu_\mu$  in FHC Mode CC N-Tracks selection categorized by the true particle matched to the main track. The figures use the PØD water-in MC and are normalized to the FHC water-in mode POT. Also a single bin is used in the range of  $0 \leq \cos \theta < 0.5$  in figures (b) and (d).

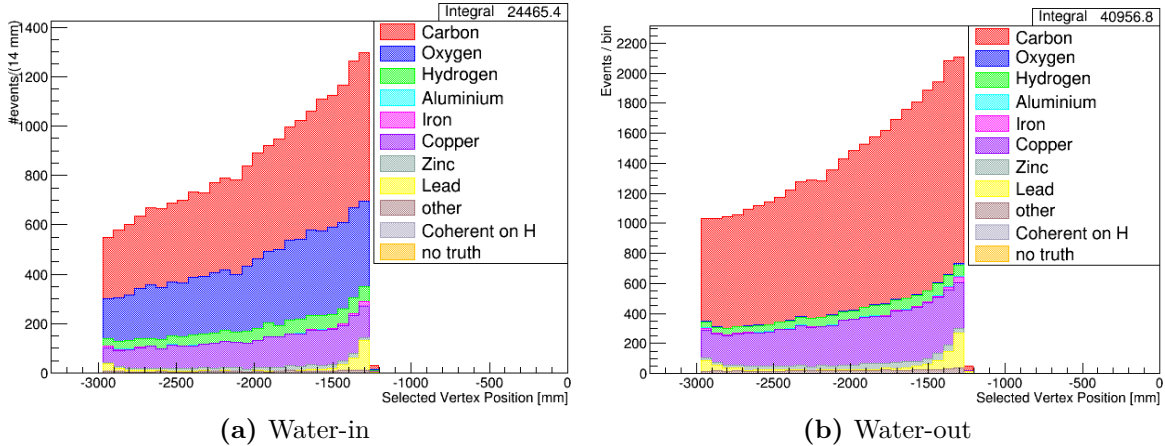


**Figure 3.10:** Reconstructed vertex Z position of the  $\nu_\mu$  in FHC Mode CC N-Tracks selection categorized by the true target nucleus. The number of events increases with increasing Z since the probability of an interaction increases as the neutrino crosses more media in the PØD. Due to a software bug in the MC, coherent events on hydrogen (Coherent on H) are a unique category.

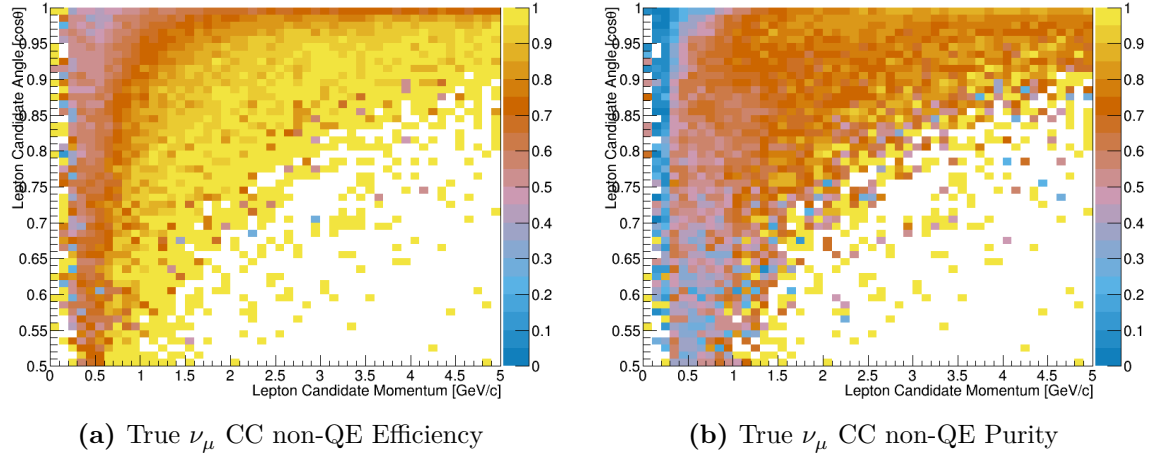


**Figure 3.11:** Efficiency and purity of the  $\nu_\mu$  in FHC Mode CC N-Tracks selection. True events are defined as correctly matched  $\mu^-$  tracks from  $\nu_\mu$ -induced CC non-QE interactions at the vertex.

The fundamental kinematics of the selection are shown in Figure 3.12 on page 83. The selection is relatively  $\nu_\mu$ -pure and captures the high energy tail of the neutrino flux. True kinematics that describe the  $1\pi$ ,  $N\pi$ , and DIS models are parameterized in  $Q^2$  and the hadronic system mass  $W$ . Using Figure 1.5 on page 14, we can define the invariant mass of hadronic system as

$$\begin{aligned} W^2 c^4 &= (p + q)^2 = p^2 + 2p \cdot q + q^2 \\ &= M_N^2 c^4 + 2M_N c^2 (k_0 - k'_0) - Q^2, \end{aligned} \tag{3.7}$$

where  $M_N$  is the mass of the struck nucleon and  $k_0/k'_0$  is the energy of the neutrino/outgoing lepton. A dominant mode in the selection is from the  $1\pi$  interaction from a  $\Delta$  resonance. A resonance is clearly seen in the  $W$  distribution in Figure 3.12 on page 83, which comes from the  $\Delta$  baryon which has a rest mass of  $1.232 \text{ GeV}/c^2$ .

The origin of the mis-identified tracks, in particular the pion matched tracks, becomes more clear since this is a high  $Q^2$  selection. The  $N\pi$  and DIS events, which are high  $Q^2$  events, can yield a post-FSI charged pion track. These pions could have more energy than the outgoing muon or could be the only particle observed in the TPC.

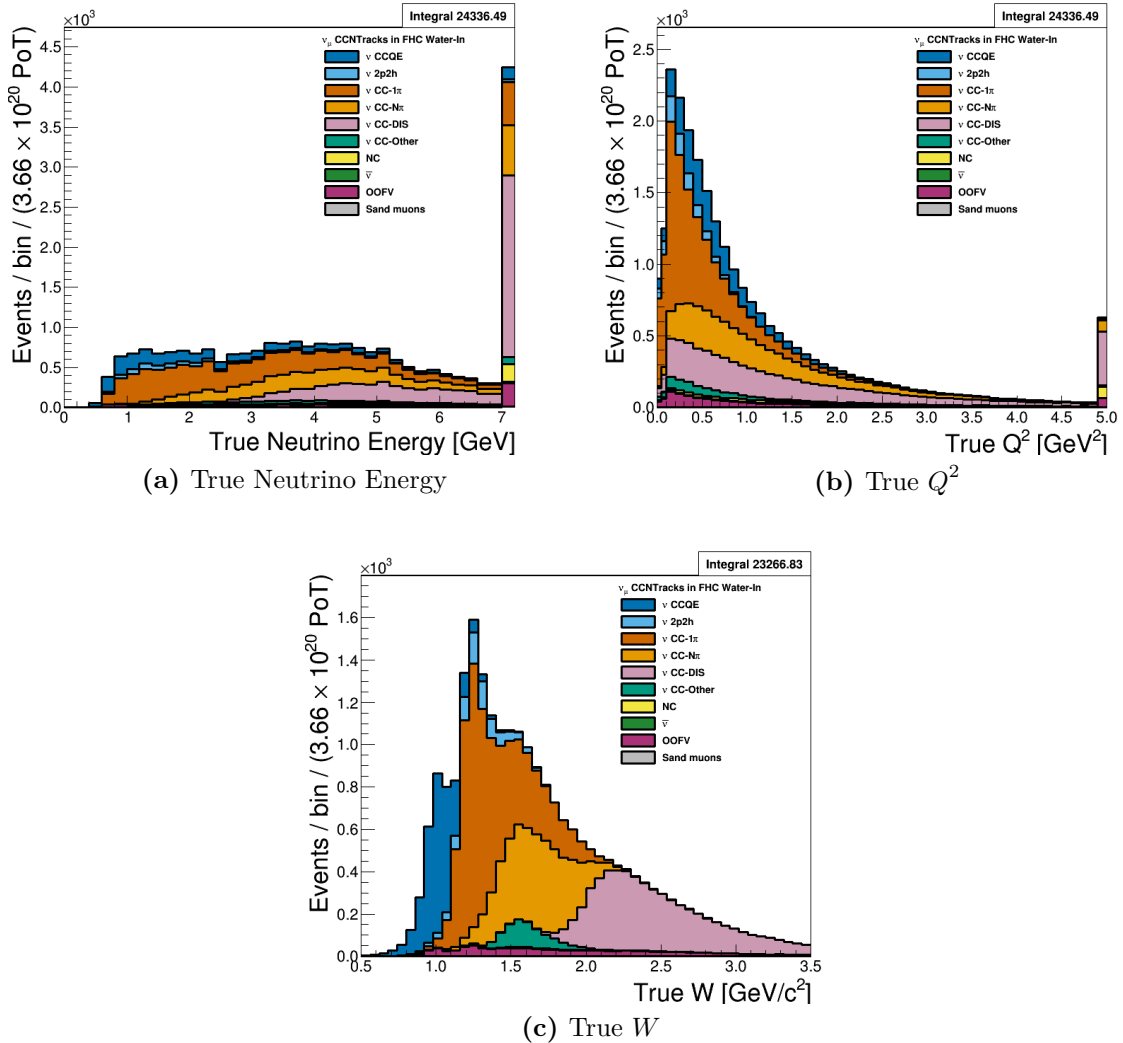


**Figure 3.12:** True kinematics of the  $\nu_\mu$  in FHC Mode CC N-Tracks selection. The last bin shown in (a) and (b) is used as overflow. The figures use the PØD water-in MC and are normalized to the FHC water-in mode POT. In figure (c), the largest resonance comes from the  $\Delta$  baryon. There are higher order resonances in (c) as well.

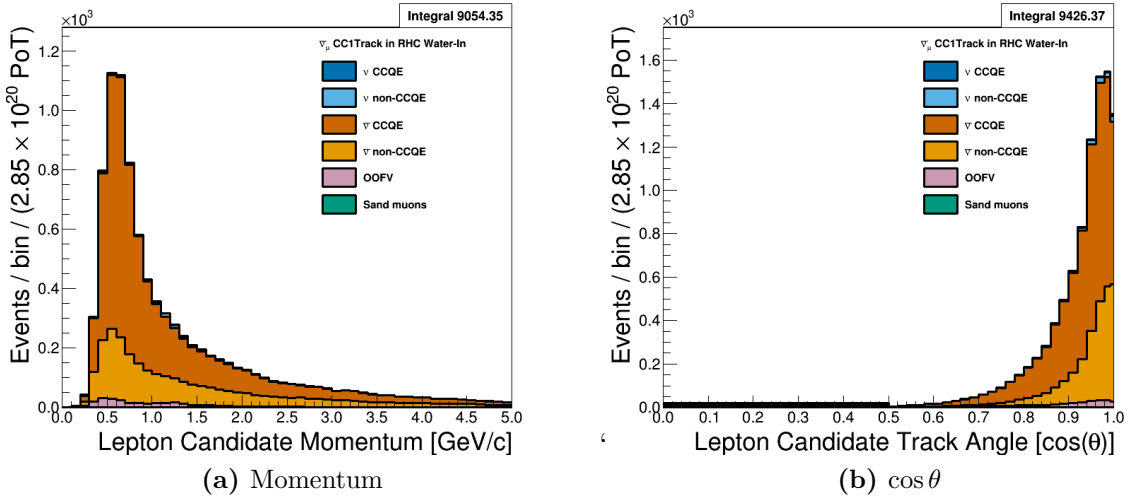


**Figure 3.13:** Reconstructed kinematics of the  $\bar{\nu}_\mu$  in RHC Mode CC 1-Track selection categorized by CCQE and non-CCQE interactions. The figures use the PØD water-in MC and are normalized to the RHC water-in mode POT. Also a single bin is used in the range of  $0 \leq \cos \theta < 0.5$  in figure (b).

### 3.3.3 The $\bar{\nu}_\mu$ in RHC Mode CC 1-Track Sample

This selection provides the  $\bar{\nu}_\mu$  CCQE-like samples in RHC mode that are inputs to the BANFF fit. In Figure 3.13 on page 84 and Figure 3.14 on page 85 display the momentum and angular distributions for this selection. The selection is highly  $\bar{\nu}_\mu$ -pure with the selected lepton candidate being positively charged muons. There is a large OOFV background from proton tracks. They are high momentum ( $> 1$  GeV/c) tracks which, at these energies, are minimum ionizing and can reach into the TPC.

We can examine the efficiencies and purities differentially for the selection in Figure 3.15 on page 85. For the efficiency and purity only, the true signal is a true  $\bar{\nu}_\mu$  CCQE interaction. The two distributions are very similar to the efficiency and purity observed in the  $\nu_\mu$  in FHC Mode CC 1-Track sample, with the efficiency being relatively high (90%) for high statistics regions.

The underlying true kinematics,  $E_\nu$  and  $Q^2$ , of the interactions are shown in Figure 3.16 on page 86. We see a similar true reaction composition with that of the  $\nu_\mu$  in FHC Mode sample in Section 3.3.1. Most reactions are true CCQE with a mixture of 2p2h and 1π

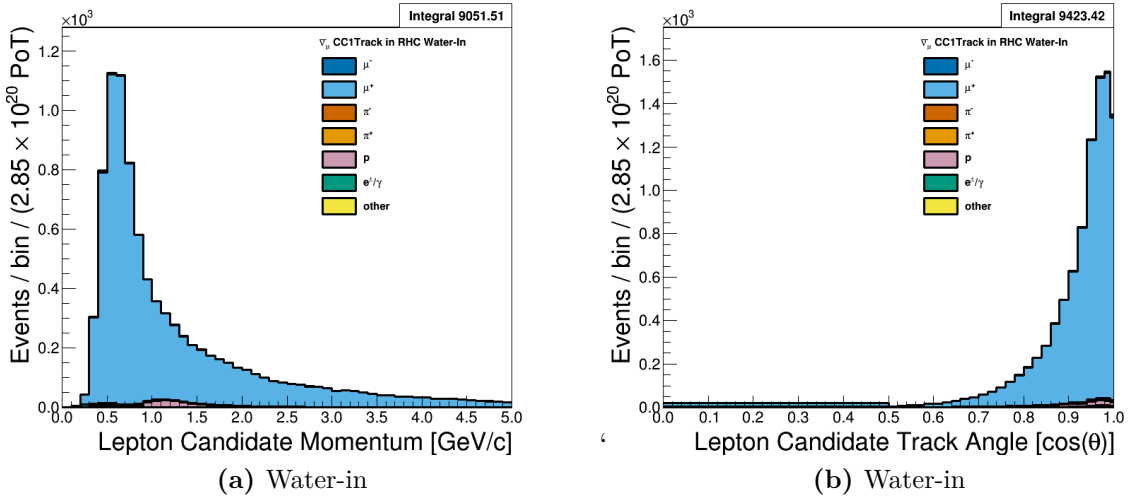


**Figure 3.14:** Reconstructed kinematics of the  $\bar{\nu}_\mu$  in RHC Mode CC 1-Track selection categorized by the true particle matched to the main track. The figures use the PØD water-in MC and are normalized to the RHC water-in mode POT. Also a single bin is used in the range of  $0 \leq \cos \theta < 0.5$  in figure (b).

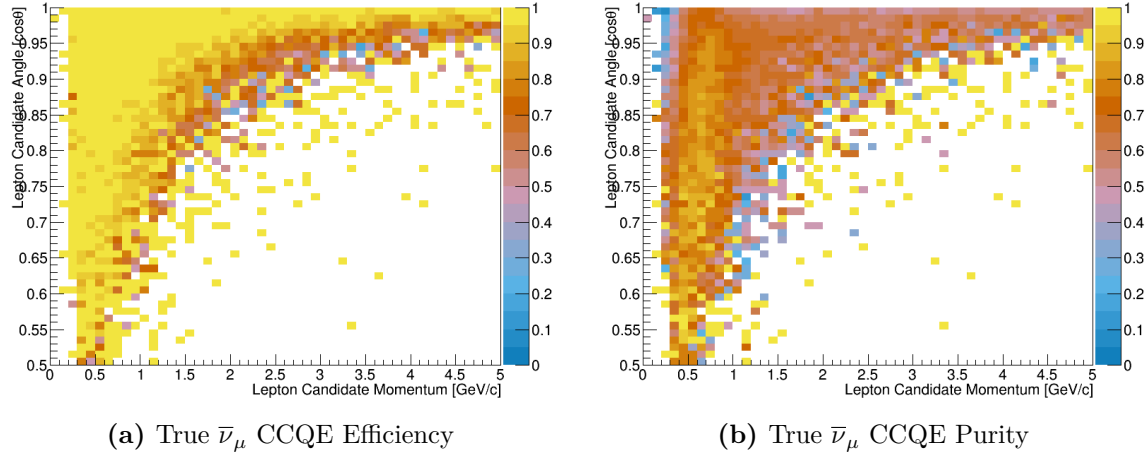


**Figure 3.15:** Efficiency and purity of the  $\bar{\nu}_\mu$  in RHC Mode CC 1-Track selection. The true events are  $\bar{\nu}_\mu$  CCQE at the vertex and the selected lepton candidate is the true  $\mu^+$ .

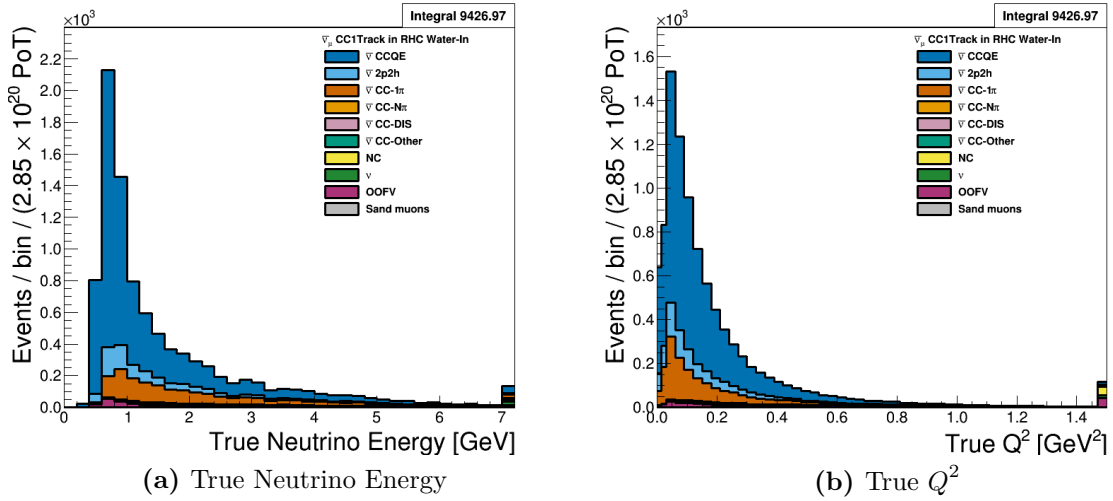


**Figure 3.16:** True kinematics of the  $\bar{\nu}_\mu$  in RHC Mode CC 1-Track selection. Water-in mode is displayed here only with the last bin shown is used as overflow. The figures use the PØD water-in MC and are normalized to the RHC water-in mode POT.

events. As previously seen in Section 3.3.1, the significant  $1\pi$  contamination may reduce the sensitivity to both CC- $0\pi$  and CC- $1\pi$  model parameters in the BANFF fit.

### 3.3.4 The $\bar{\nu}_\mu$ in RHC Mode CC N-Tracks Sample

This selection provides the  $\bar{\nu}_\mu$  non-CCQE-like samples in RHC mode. Figure 3.17 on page 87 and Figure 3.18 on page 87 display the momentum and angular distributions that are inputs to BANFF. The most striking feature of this selection is the number of mis-identified events. In particular tracks matched to protons are selected as the HMPT when the protons are minimum ionizing particles themselves, which is about 1.3 GeV/c. In addition, the intrinsic  $\nu_\mu$  background contribution is comparable to the desired  $\bar{\nu}_\mu$  flavor. These two features should be addressed to increase the utility of the selection for the next iteration of the analysis.

We can examine the efficiencies and purities differentially for the selection in Figure 3.11 on page 82. For the efficiency and purity only, the true signal is any  $\bar{\nu}_\mu$  CC interaction

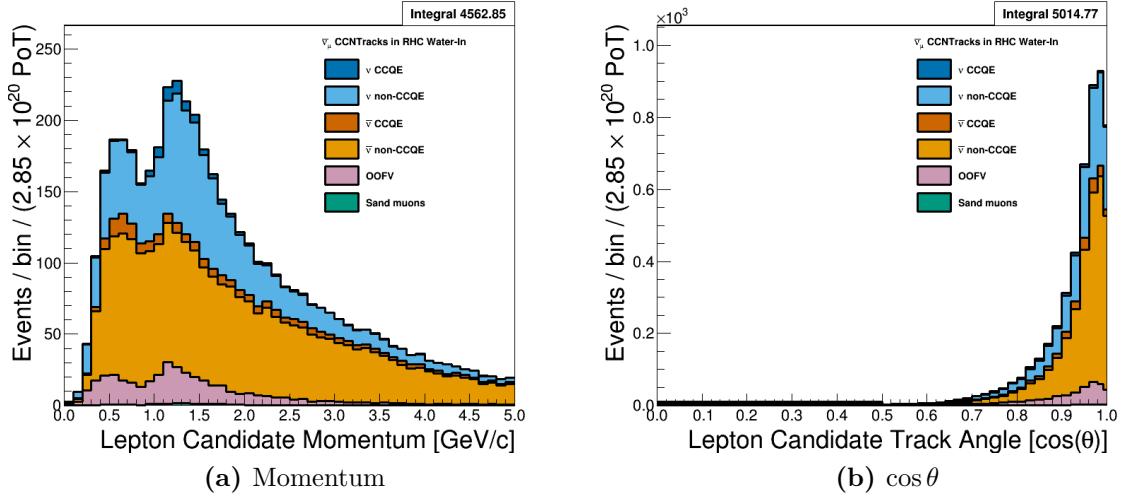


**Figure 3.17:** Reconstructed kinematics of the  $\bar{\nu}_\mu$  in RHC Mode CC N-Tracks selection categorized by CCQE and non-CCQE interactions. The figures use the PØD water-in MC and are normalized to the RHC water-in mode POT. Also a single bin is used in the range of  $0 \leq \cos \theta < 0.5$  in figure (b).

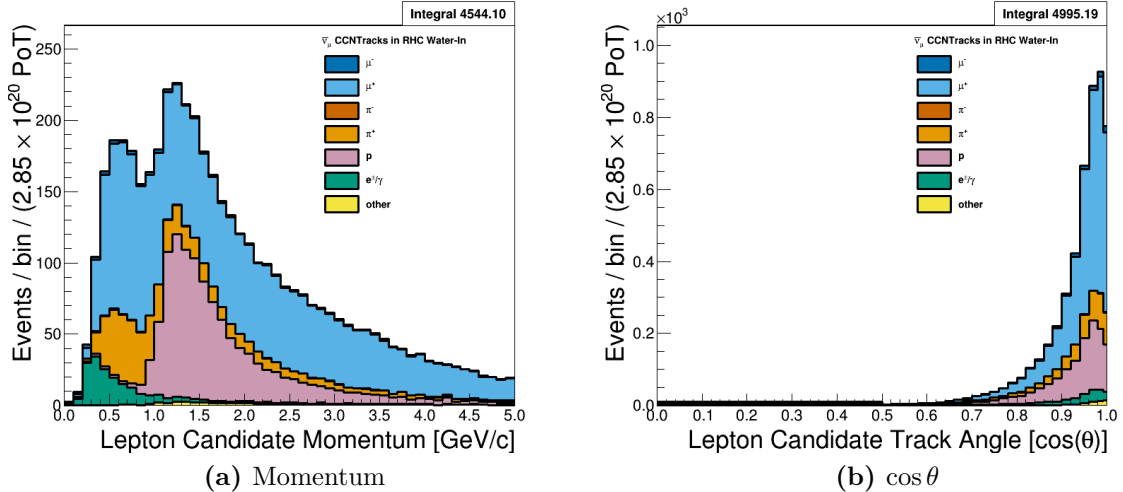


**Figure 3.18:** Reconstructed kinematics of the  $\bar{\nu}_\mu$  in RHC Mode CC N-Tracks selection categorized by the true particle matched to the main track. The figures use the PØD water-in MC and are normalized to the RHC water-in mode POT. Also a single bin is used in the range of  $0 \leq \cos \theta < 0.5$  in figure (b).

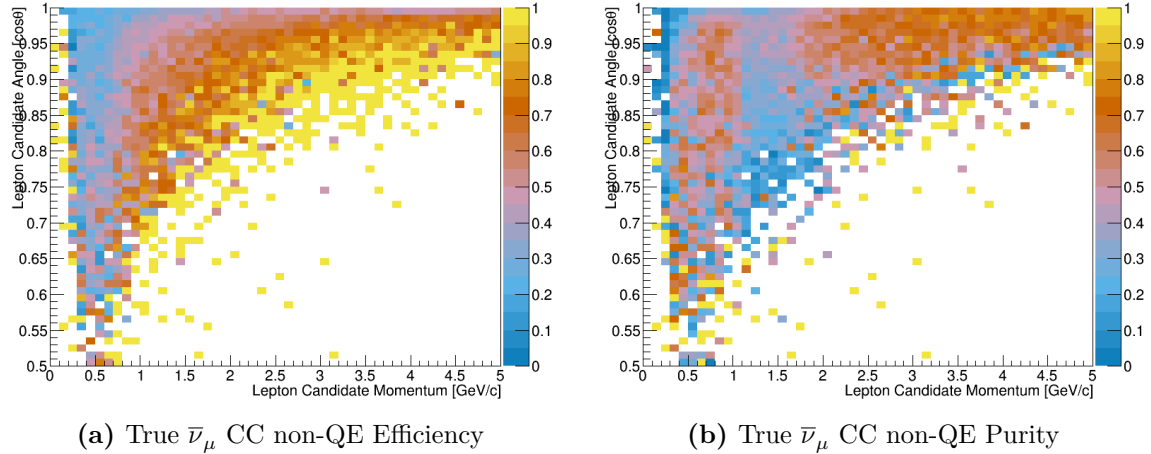


**Figure 3.19:** Efficiency and purity of the  $\bar{\nu}_\mu$  in RHC Mode CC N-Tracks selection. True events are defined as correctly matched  $\mu^+$  tracks from  $\bar{\nu}_\mu$ -induced CC non-QE interactions at the vertex.

except  $\bar{\nu}_\mu$  CCQE which the CC 1-Track selection is designed to select. Both the efficiency and purity are low where statistics are high due to the wrong sign background.

The underlying true kinematics,  $E_\nu$ ,  $Q^2$ , and  $W$ , of the interactions are shown in Figure 3.20 on page 89. Here we see in better detail the origin of the  $\nu_\mu$  contamination. As a function of increasing energy, the  $\bar{\nu}_\mu$  content is decreasing while the relative  $\nu_\mu$  contribution is increasing. The  $\nu_\mu$  events also have high  $Q^2$  which explains the significant number of misidentified proton main track events. For the hadronic final states, the shape of the  $\bar{\nu}_\mu$ -induced resonances is similar to what we saw in Figure 3.12 on page 83. Interestingly, the  $\nu_\mu$  background hadronic mass distribution does not peak in any one region.

### 3.3.5 The $\nu_\mu$ Background in RHC Mode CC 1-Track Sample

This selection provides the  $\nu_\mu$  in RHC, also called wrong-sign background, CCQE-like samples . Figure 3.21 on page 90 and Figure 3.22 on page 91 display the momentum and angular distributions inputs to the BANFF fit. We can see this is a relatively low-angle selection compared to previous selections. Importantly the selection is relatively  $\nu_\mu$ -pure which should help constrain the wrong-sign background in the fit. However, the CCQE

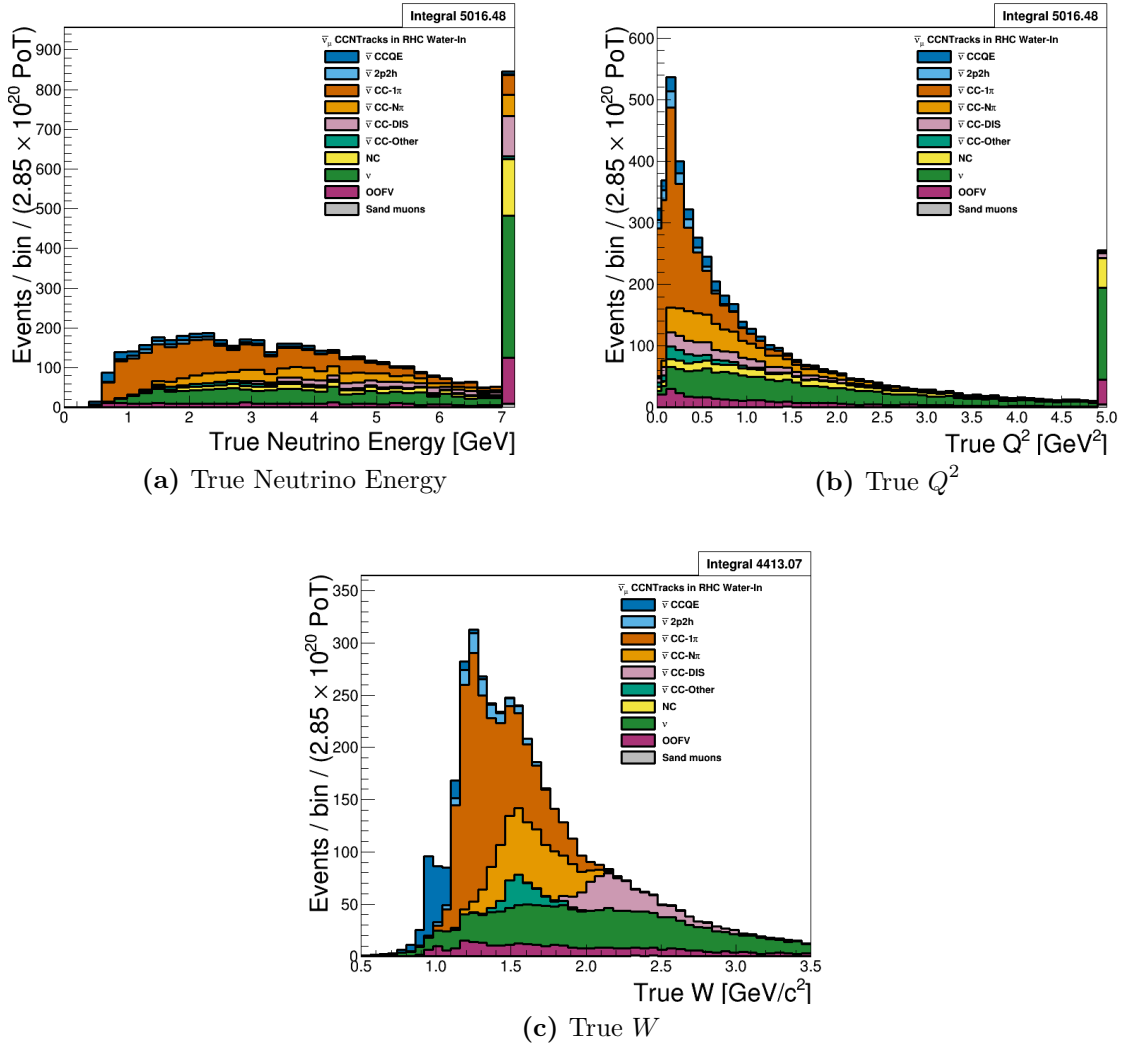


**Figure 3.20:** True kinematics of the  $\bar{\nu}_\mu$  in RHC Mode CC N-Tracks selection. The last bin shown in (a) and (b) is used as overflow. The figures use the PØD water-in MC and are normalized to the RHC water-in mode POT.

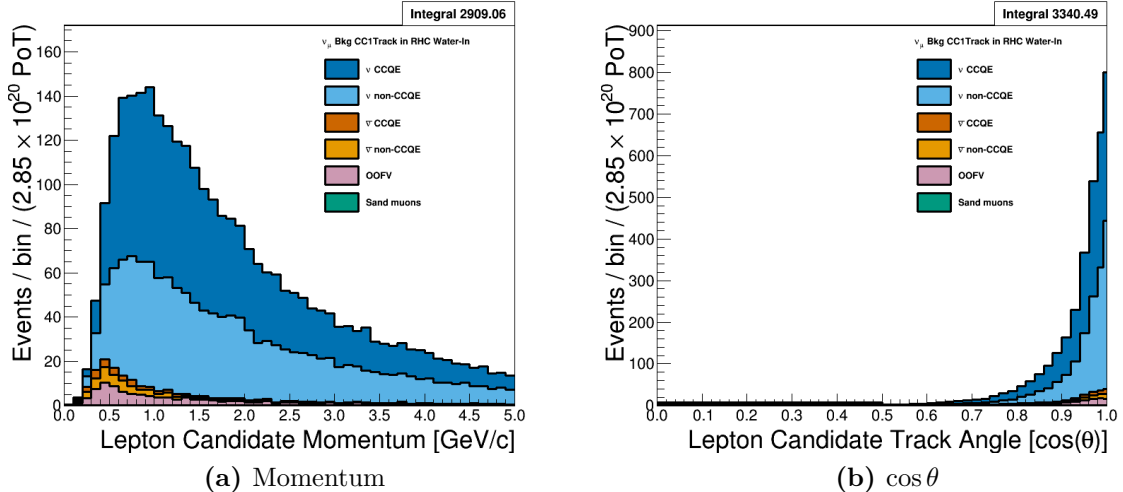


**Figure 3.21:** Reconstructed kinematics of the  $\nu_\mu$  Background in RHC Mode CC 1-Track selection categorized by CCQE and non-CCQE interactions. The figures use the PØD water-in MC and are normalized to the RHC water-in mode POT. Also a single bin is used in the range of  $0 \leq \cos \theta < 0.5$  in figure (b).

purity is modest given number of correctly identified lepton candidates. This feature needs to be addressed in the next iteration of the analysis.

We can examine the efficiencies and purities differentially for the selection in Figure 3.23 on page 91. For the efficiency and purity only, the true signal is a true  $\nu_\mu$  CCQE interaction. The efficiency is similar to the  $\nu_\mu$  in FHC Mode CC 1-Track topology efficiency with banded  $p - \theta$  regions. As for the purity, it is roughly 70% in a banded region between low momenta, low angle and high momenta, high angle tracks.

The underlying true kinematics,  $E_\nu$  and  $Q^2$ , of the selection are shown in Figure 3.24 on page 92. The number of the wrong-sign background events peaks at 1 GeV and is a broad peak compared to the designed sharp  $\bar{\nu}_\mu$  peak at 0.6 GeV as shown in Figure 3.16 on page 86. Since these are higher energy events, there is more available energy to produce resonance states that produce  $1\pi$  topologies. This explains the significant non-CCQE event contamination.

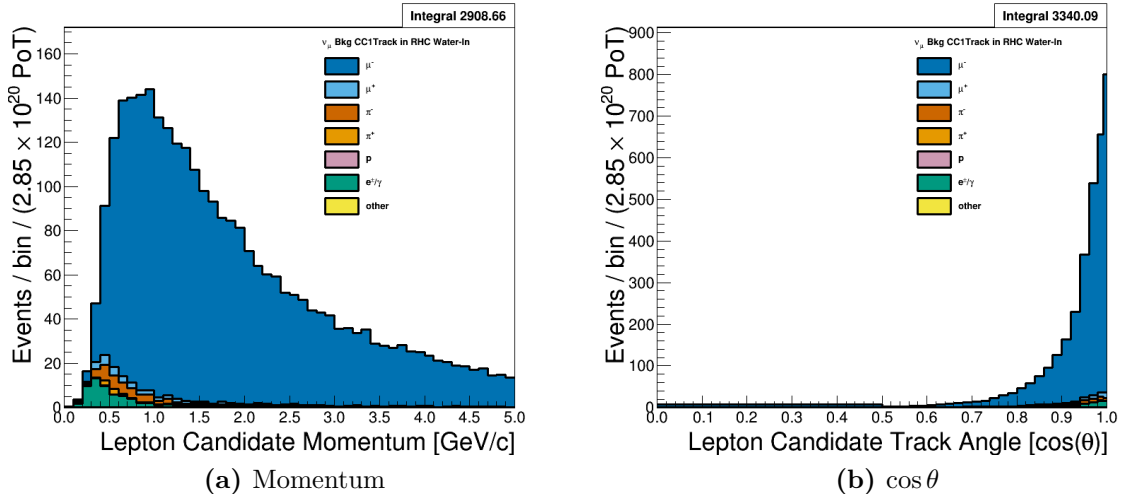


**Figure 3.22:** Reconstructed kinematics of the  $\nu_\mu$  Background in RHC Mode CC 1-Track selection categorized by the true particle matched to the main track. The figures use the PØD water-in MC and are normalized to the RHC water-in mode POT. Also a single bin is used in the range of  $0 \leq \cos \theta < 0.5$  in figure (b).

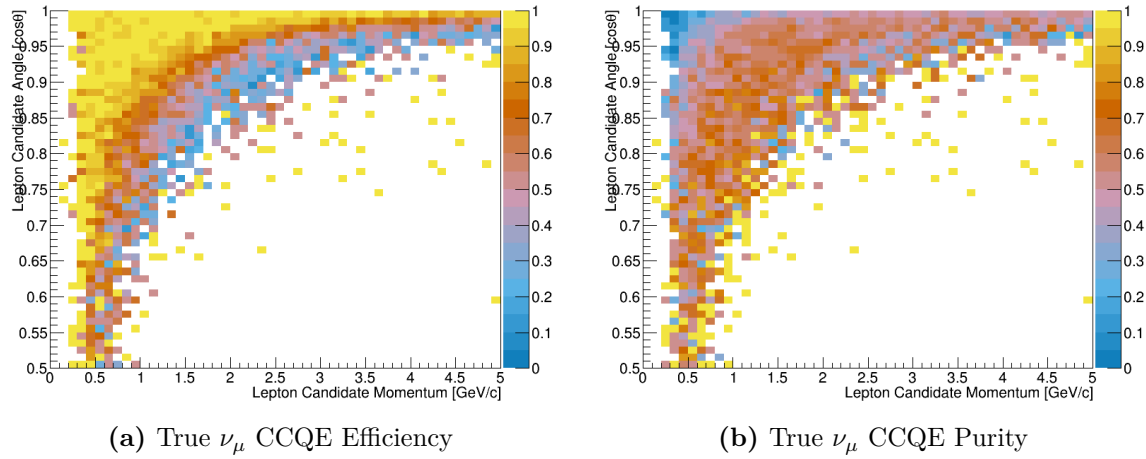


**Figure 3.23:** Efficiency and purity of the  $\nu_\mu$  Background in RHC Mode CC 1-Track selection. The true events are  $\nu_\mu$  CCQE at the vertex and the selected lepton candidate is the true  $\mu^-$ .

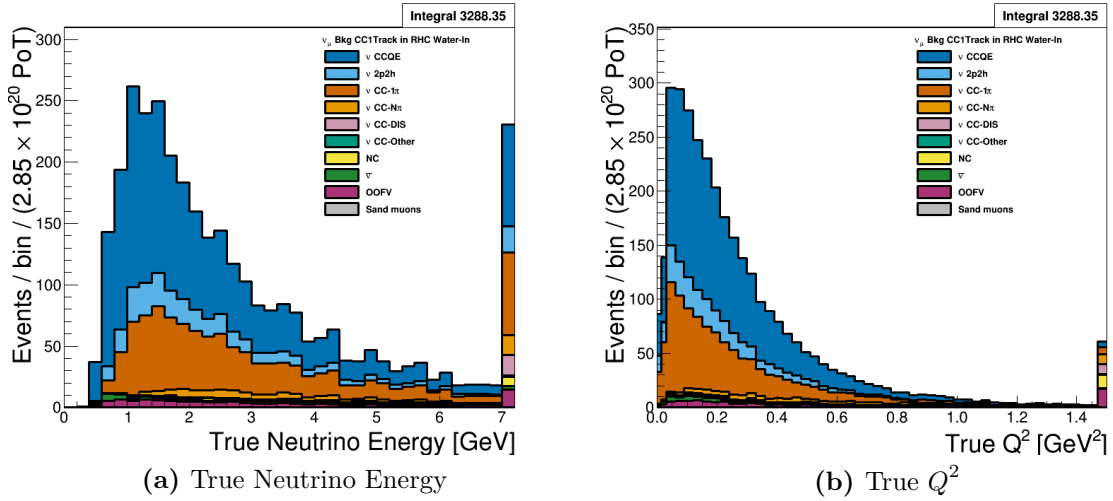


**Figure 3.24:** True kinematics of the  $\nu_\mu$  Background in RHC Mode CC 1-Track selection. Water-in mode is displayed here only with the last bin shown is used as overflow. The figures use the PØD water-in MC and are normalized to the RHC water-in mode POT.

### 3.3.6 The $\nu_\mu$ Background in RHC Mode CC N-Tracks Sample

This selection provides the non-CCQE-like samples for the  $\nu_\mu$  background in RHC mode. Figure 3.25 on page 93 and Figure 3.26 on page 93 show the momentum and angular distributions that are inputs to the BANFF fit. We can see the selection is relatively  $\nu_\mu$ -pure with a significant mis-identified track rate. Interestingly, the misidentified pion main tracks have a high momentum tail.

We can examine the  $\nu_\mu$  CC non-QE efficiency and purity of the selection in Figure 3.27 on page 94. There is a reduction in the purity below 1.5 GeV/c due to the the  $\bar{\nu}_\mu$  selections occupying the same phase space. Fortunately, the efficiency and purity are relatively high above 1.5 GeV/c.

The underlying true kinematics,  $E_\nu$ ,  $Q^2$ , and  $W$ , of the interactions are shown in Figure 3.28 on page 95. As we have seen before with the CC N-Tracks samples, these are high  $E_\nu$  events with large  $Q^2$  exchanges. The invariant hadronic system displays the previously seen resonances, with the largest still being from the  $\Delta$  baryon.

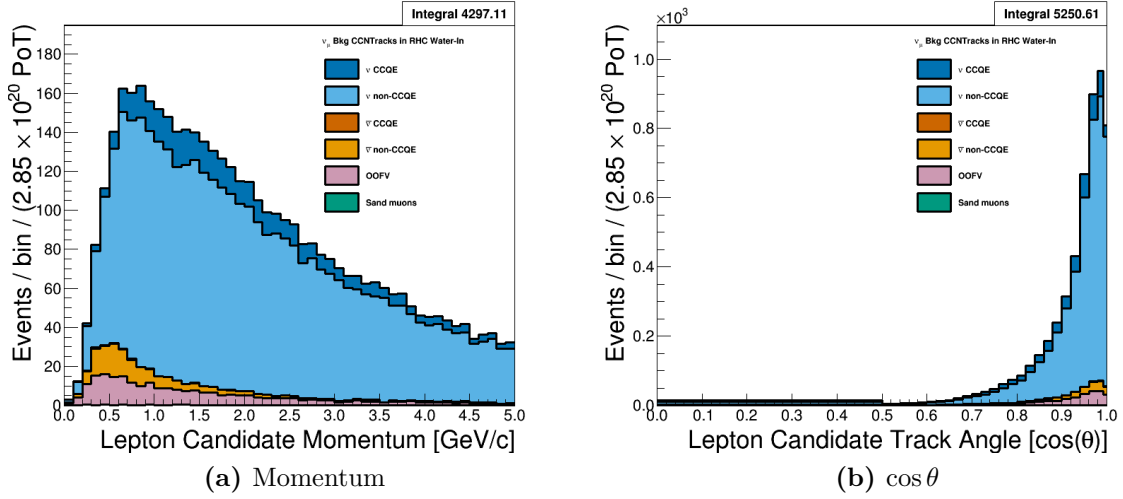


**Figure 3.25:** Reconstructed kinematics of the  $\nu_\mu$  Background in RHC Mode CC 1-Track selection categorized by CCQE and non-CCQE interactions. The figures use the PØD water-in MC and are normalized to the RHC water-in mode POT. Also a single bin is used in the range of  $0 \leq \cos \theta < 0.5$  in figure (b).

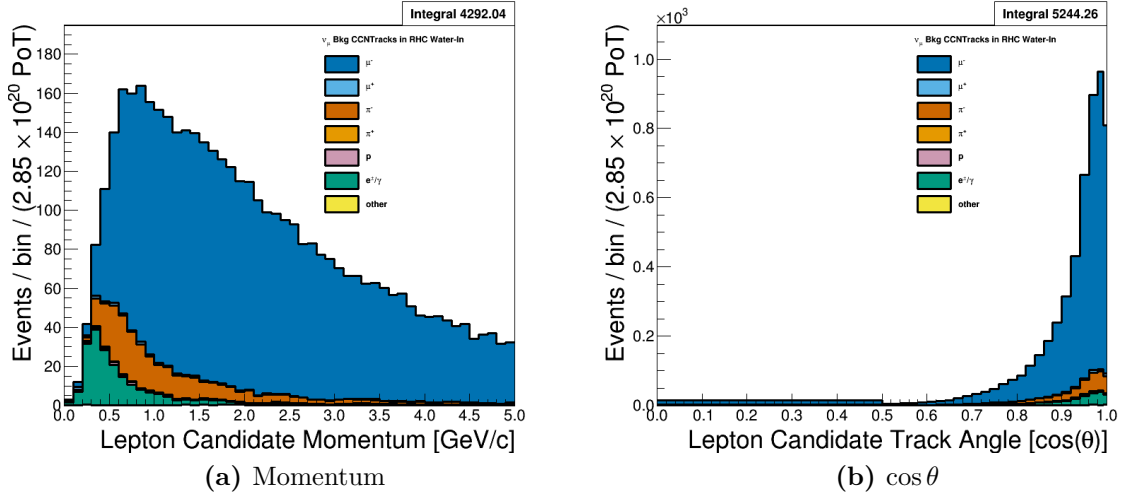


**Figure 3.26:** Reconstructed kinematics of the  $\nu_\mu$  Background in RHC Mode CC 1-Track selection categorized by the true particle matched to the main track. The figures use the PØD water-in MC and are normalized to the RHC water-in mode POT. Also a single bin is used in the range of  $0 \leq \cos \theta < 0.5$  in figure (b).

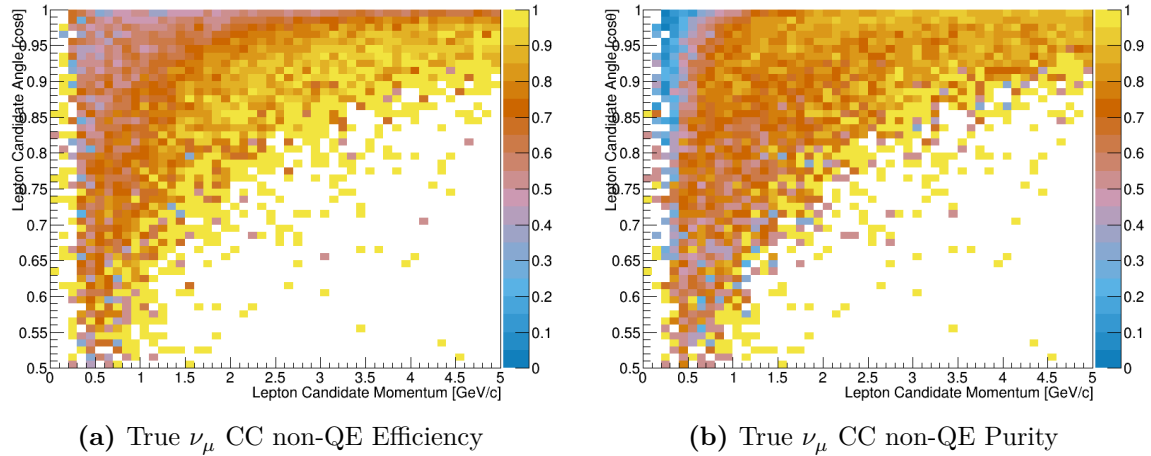


**Figure 3.27:** Efficiency and purity of the  $\nu_\mu$  Background in RHC Mode CC N-Tracks selection. True events are defined as correctly matched  $\mu^-$  tracks from  $\nu_\mu$ -induced CC non-QE interactions at the vertex.

### 3.4 Summary

In this chapter we have examined the selection true and reconstruction kinematics that will be used in the BANFF fit. We see the 1-Track selections yield some reasonably pure CCQE samples. By inverting that cut, we obtain some information on the rate of other topologies like CC- $1\pi$  and high  $Q^2$  CCDIS events. Importantly is the ability of these samples to constrain the correct sign ( $\bar{\nu}_\mu$ ) and wrong sign ( $\nu_\mu$ ) backgrounds in RHC mode, which are very important in the oscillation analysis. We can now move forward to the next chapter to describe the fit parameters and the systematic uncertainties present in the analysis.

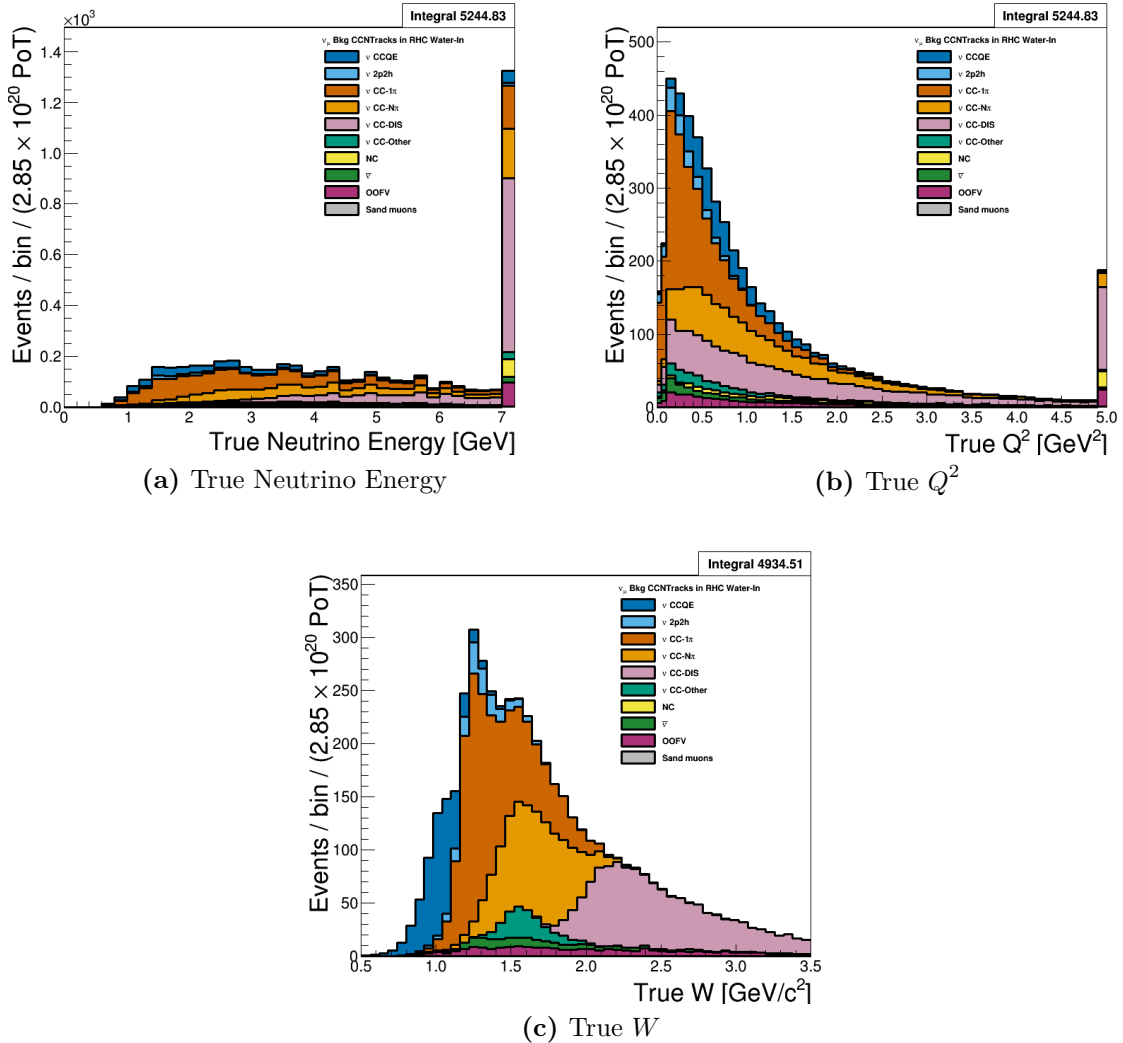


**Figure 3.28:** True kinematics of the  $\nu_\mu$  Background in RHC Mode CC N-Tracks selection. The last bin shown in (a) and (b) is used as overflow. The figures use the PØD water-in MC and are normalized to the RHC water-in mode POT.

# Chapter 4

## The BANFF Fit Parameters

This chapter explores the fit binning and penalty terms in the test statistic used for this analysis. The BANFF fit includes three sources of systematic uncertainties: neutrino flux, cross section model, and detector inefficiencies. The sources of systematic uncertainty, also referred to just as systematics, will be defined and their effects on the analysis will be examined. These three terms directly affect the flux of neutrinos, efficiency of reconstruction, and the cross section for  $\nu_\alpha$  terms, respectively, in the predicted rate equation given in Eqn. (1.56).

This chapter is presented in the following order. The method to define histogram fit bins in the likelihood ratio is discussed in Section 4.1. The parameterization of each penalty term in the test statistic is described in Section 4.2 in the following order: the neutrino flux model, the detector inefficiencies, and the cross section model. The chapter summary is provided in Section 4.3.

### 4.1 Fit Binning

The PØD-only BANFF fit uses the samples described in Chapter 3 to evaluate the log-likelihood ratio term,  $\chi^2_{\text{LLR}}$ . Since this is a binned likelihood in  $(p, \cos \theta)$ , the bin edges need to be defined first.

The BANFF fit binning is optimized to ensure at least 1 predicted Monte Carlo (MC) event in each bin for every PØD sample when scaled to the collected data POT. The fit bins must also account for detector smearing effects. In order to mitigate smearing and event migration, the reconstructed muon track kinematics were examined against correctly identified tracks in one-dimensional kinematic slices. The kinematics are scanned across their full phase spaces in order to understand the required width for a fit bin. The first fit bin is always defined starting from the kinematic maximum.

To determine the optimal momentum fit bins, the momentum resolution with the MC truth matched muon is analyzed. The momentum resolution is defined as

$$R(r, t) = \frac{r - t}{t},$$

where  $r$  is the reconstructed momentum and  $t$  is the true muon momentum. The mean (bias) and standard deviation (stddev) of  $R$  are used as proxies for the true bias and resolution for the prediction. Both quantities and prediction errors were extracted using a bootstrapping algorithm [50] in very fine bins of reconstructed momentum. The bootstrapping algorithm works by random sampling with replacement of the true muon momentum. For each bias and stddev prediction, at least 1000 bootstrapping samples were generated. Each bootstrap bias and stddev value were saved to calculate a prediction mean and error. In the case of relatively “large” prediction errors, additional 10000 bootstrapping samples were generated. The main track momentum resolution for the  $\nu_\mu$  in FHC Mode CC 1-Track sample is shown in Figure 4.1 on page 98 to illustrate the results.

The optimal  $\cos \theta$  fit bins were determined in a very similar manner with the momentum fit bins. While the fit bins and physics are dictated in  $\cos \theta$  space, the detector smearing is a function  $\theta$ . In addition, since the angle can be nearly zero for the most forward-going tracks, the resolution was not used to characterize the angular uncertainties. Instead, the difference (“residual”) between the true and reconstructed angle  $\theta$  with respect to (wrt) the ND280 Z-axis was analyzed. The same bootstrapping algorithm described above was used

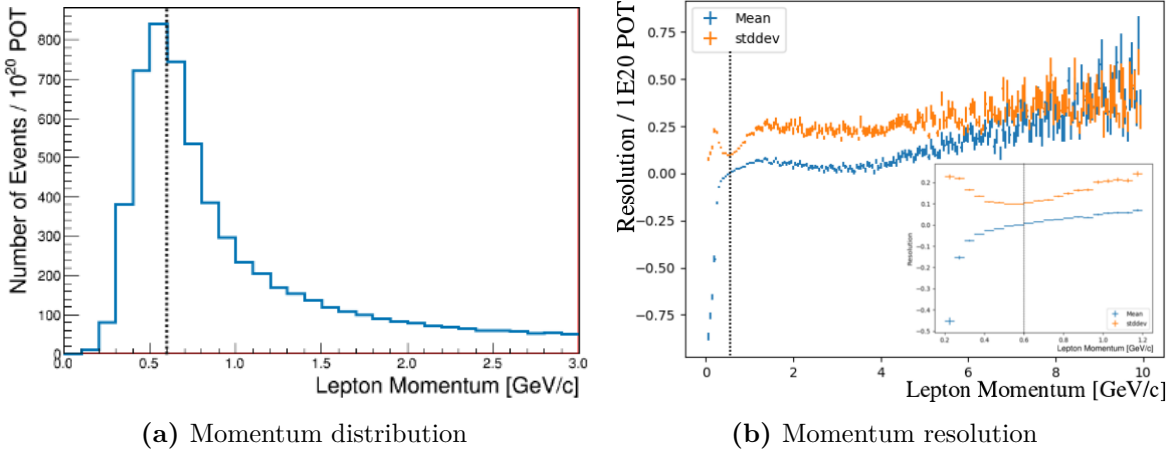


**Figure 4.1:** Main track momentum resolution for the  $\nu_\mu$  in FHC Mode CC 1-Track sample. Only correctly identified muons are used. The number of events is scaled to  $10^{20}$  POT, which is the approximate scale for all the samples in this analysis. A dashed line indicates the maximum of the distribution peak from figure (a). The resolution of the momentum measurement is shown in figure (b) whose error bars are estimated using bootstrapping. In the inset is the momentum resolution zoomed near the momentum distribution maximum.

to determine the mean and std dev of the  $\theta$  residuals. The main track angular residuals for the  $\nu_\mu$  in FHC Mode CC 1-Track sample are shown in Figure 4.2 on page 99 to illustrate the results.

This procedure to define fit bin edges emphasizes regions of high statistics and mitigates regions with low statistics. Since the MC provides about  $10 \times$  the data statistics, the statistical uncertainty for each bin should be negligible in high statistics regions. However, this does not account for the low statistics regions predicted by the nominal MC. We tackle this problem and other systematic uncertainties for the fit bins using bin normalizations as explained in Chapter 2.

#### 4.1.1 Fit Bin Edges

There are a total 988 fit bins with water-in and water-out modes sharing the same bin edges. The finalized fit bins are tabulated below.

- The  $\nu_\mu$  in FHC Mode CC 1-Track water-in and water-out samples:

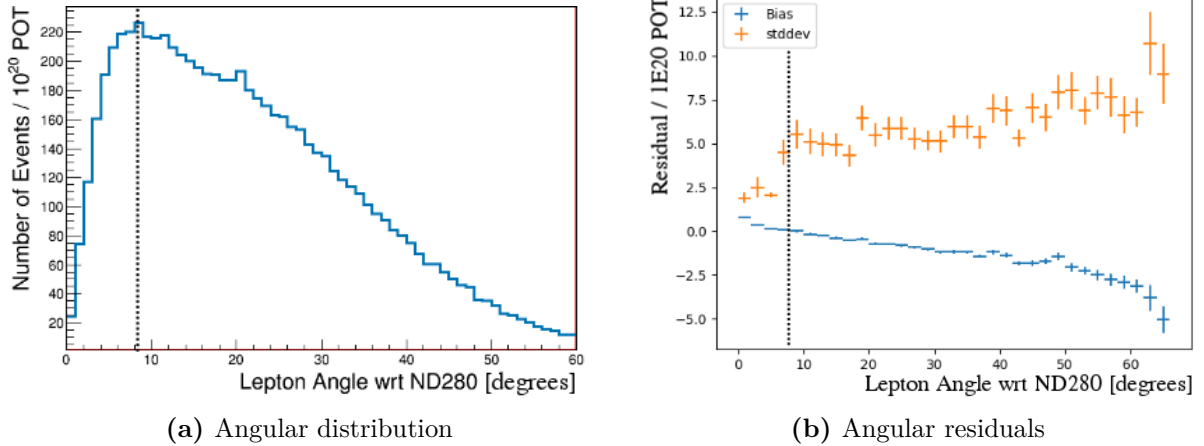


**Figure 4.2:** Main track angular residuals for the  $\nu_\mu$  in FHC Mode CC 1-Track sample. Only correctly identified muons are used. The number of events is scaled to  $10^{20}$  POT, which is the approximate scale for all the samples in this analysis. A dashed line indicates the maximum of the distribution peak from figure (a). The residual of the angular measurement is shown in figure (b) whose error bars are estimated using bootstrapping.

- $p$  [GeV/c]: 0, 0.3, 0.4, 0.5, 0.6, 0.7, 0.8, 1, 1.25, 1.5, 2, 3, 4, 5.5, 30
- $\cos \theta$  : -1, 0.7, 0.8 , 0.88, 0.94, 0.96, 0.975, 0.99, 1
- The  $\nu_\mu$  in FHC Mode CC N-Tracks water-in and water-out samples:
  - $p$  [GeV/c]: 0, 0.4, 0.5, 0.6, 0.7, 0.8, 1, 1.2, 1.5, 1.8, 2.2, 2.7, 3.5, 5, 10, 30
  - $\cos \theta$  : -1, 0.65, 0.77, 0.85, 0.9, 0.94, 0.97, 0.99, 1
- The  $\bar{\nu}_\mu$  in RHC Mode CC 1-Track water-in and water-out samples:
  - $p$  [GeV/c]: 0, 0.4, 0.5, 0.6, 0.7, 0.8, 1, 1.25, 1.5, 2, 3, 30
  - $\cos \theta$  : -1, 0.82, 0.87, 0.9, 0.93, 0.95, 0.97, 0.99, 1
- The  $\bar{\nu}_\mu$  in RHC Mode CC N-Tracks water-in and water-out samples:
  - $p$  [GeV/c]: 0, 0.5, 0.9, 1.25, 1.6, 2, 3, 8, 30
  - $\cos \theta$  : -1, 0.8, 0.89, 0.95, 0.97, 0.99, 1
- The  $\nu_\mu$  in RHC CC 1-Track water-in and water-out samples:

- $p$  [GeV/c]: 0, 0.4, 0.6, 0.8, 1.1, 2, 10
- $\cos \theta$  : -1, 0.78, 0.84, 0.89, 0.92, 0.95, 0.97, 0.98, 0.99, 1
- The  $\nu_\mu$  in RHC CC N-Tracks water-in and water-out samples:
  - $p$  [GeV/c]: 0, 0.4, 0.6, 0.8, 1, 1.5, 2, 3, 10
  - $\cos \theta$  : -1, 0.7, 0.8, 0.85, 0.9, 0.94, 0.965, 0.98, 0.99, 1

## 4.2 Systematic Uncertainties and Penalty Terms

This section provides details on the penalty terms, and hence fit parameters, in the BANFF fit. The cross section and flux penalty terms in this analysis are identical to the previous near detector constraint studies [24, 86]. This provides a one-to-one comparison between the PØD-only and FGD-only flux and cross section predictions. However, due to the different detector technologies between the PØD and FGD, different bin normalization parameters are necessary.

The fit parameters are described in the following order. The first set of parameters are the flux terms. This is followed by a description of the fit bin normalization parameters. The final topic is a description of the cross section parameters.

### 4.2.1 Flux Model Parameters

The T2K neutrino flux model is a description of the neutrino beam energy spectrum for each run period and flavor. This model includes simulations of the proton beam interactions and subsequent hadron production at the target. The predicted hadron production rate, including inside and outside the graphite target, is tuned to the results from the replica target<sup>17</sup> experiment NA61/SHINE [12] and other hadron production experiments. The uncertainties

---

<sup>17</sup>The NA61/SHINE experiment has two graphite targets. A thin 2 cm target and a thick 90 cm target. The thick target is a replica of the T2K graphite target.

in the unoscillated flux tuning are dominated by hadron production. Smaller effects on the unoscillated flux uncertainty include the proton beam profile, off-axis angle, horn current, and horn alignment. Further details about the flux model and uncertainties can be found in the following reference [6]. The flux parameters are especially important since they are used as inputs to the oscillation analysis.

The flux penalty term in the BANFF fit is defined as

$$\chi_{\text{Flux}}^2 = (\vec{b} - \vec{b}_0)^T (V^{\text{Flux}})^{-1} (\vec{b} - \vec{b}_0), \quad (4.1)$$

where  $\vec{b}$  is the vector of flux parameter values,  $\vec{b}_0$  is the vector of the initial parameter values, and  $V^{\text{Flux}}$  is the flux covariance matrix. As a remainder, all penalty terms in this analysis have the form of Eqn. (4.1). Each flux parameter is a neutrino energy bin normalization starting at one (1). Formally, a flux bin is defined as

$$b_i = \frac{N'_{\nu_\alpha,i}}{N_{\nu_\alpha,i}}, \quad (4.2)$$

where  $N_{\nu_\alpha,i}$  and  $N'_{\nu_\alpha,i}$  are the predicted and ND constrained  $\nu_\alpha$  event rates, respectively, in the  $i$ th energy bin. In other words, *each flux term is a ratio of rates. Further, all penalty terms and covariance terms are dimensionless.* A postfit value of 1.1 indicates that all events in that energy bin have an additional weight of 1.1, signaling that the postfit prefers to increase that neutrino flux by 10%. Equivalently, this means  $N'_{\nu_\alpha,i}$  is 10% greater than  $N_{\nu_\alpha,i}$ .

In the BANFF fit, both ND280 and SK flux parameters are estimated simultaneously. This is achieved using correlations between ND280 and SK flux parameters in the covariance matrix. The covariance matrix is provided by the T2K flux group and is shown in Figure 4.3 on page 102. Also shown in Figure 4.3 on page 102 is the Pearson linear correlation coefficient matrix which is defined as

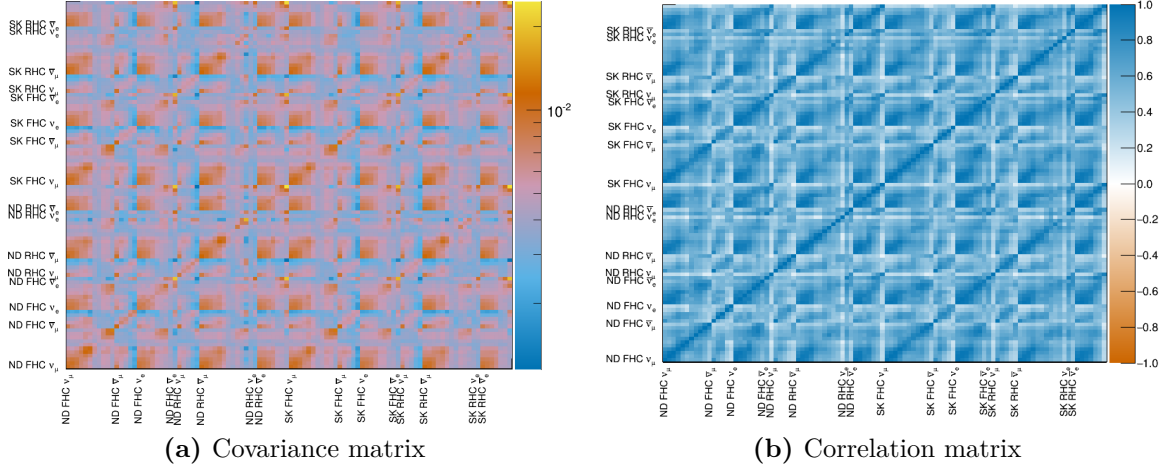


**Figure 4.3:** The BANFF prefit flux covariance matrix. Figure (a) shows the covariance matrix which is the uncertainty of the normalization for the neutrino flux at both ND280 and SK. The covariance matrix is divided into submatrices in groups by detector, beam mode, and neutrino flavor. Figure (b) is the linear correlation coefficient for each covariance term.

$$\rho_{i,j} = \frac{V_{i,j}}{\sqrt{V_{i,i} V_{j,j}}}, \quad (4.3)$$

where  $i$  and  $j$  are bins in  $V$ .

The tabulated flux parameters/bins and uncertainties in this analysis are given in Table 4.1 on page 104. These are the first set of parameters in the fit. The flux parameters are differentiated by neutrino energy, horn current/polarity (FHC mode and RHC mode), neutrino flavor ( $\nu_\mu$ ,  $\bar{\nu}_\mu$ ,  $\nu_e$ , and  $\bar{\nu}_e$ ), and detector (ND280 and SK). There are 50 ND280 and 50 SK flux parameters to yield a total of 100 flux normalizations. In addition, the bin edges are shared between the ND280 and SK. The SK neutrino flux and the flux bin edges are shown in Figure 4.4 on page 103.

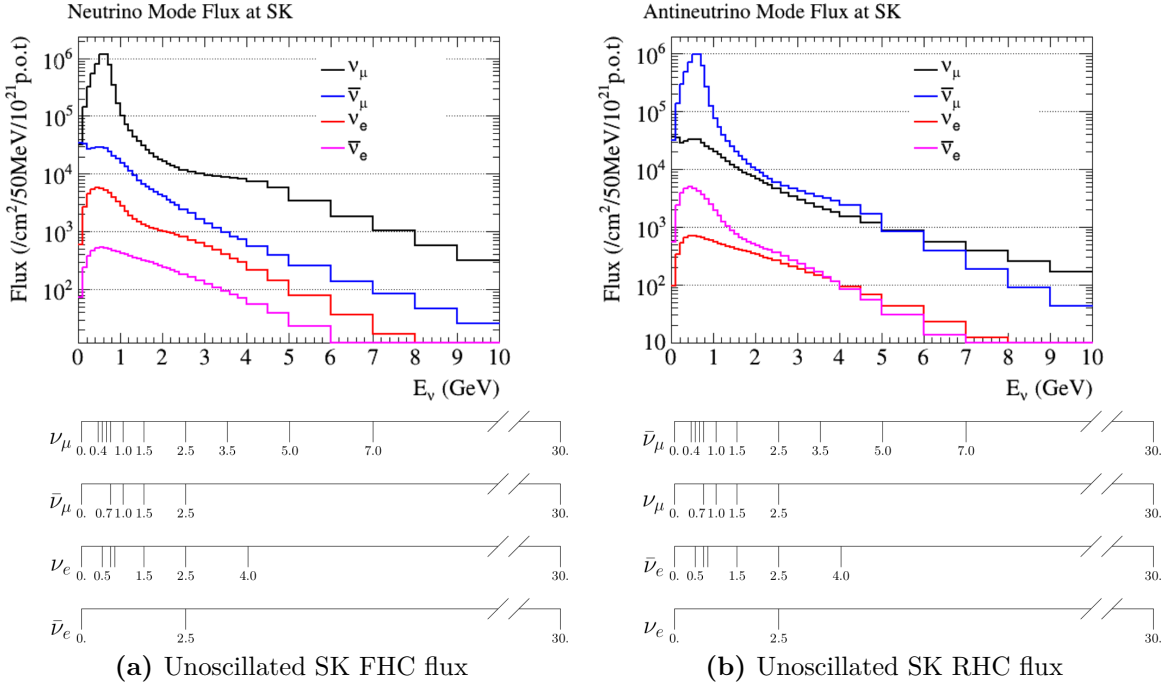


**Figure 4.4:** Neutrino flux prediction at SK and flux bin edges. The flux prediction for FHC (RHC) mode is shown in figure on the left (right). The flux normalization parameters have an assigned energy range and are the same for both the SK and ND280 detectors. The energy binning used is shown below the plots.

---

**Table 4.1:** Flux binning and uncertainties used in the BANFF fit.

<b>Fit index</b>	<b>Beam mode</b>	<b>Bin edges [GeV]</b>	<b>Prefit</b>
0	ND280 $\nu_\mu$ FHC	0.0 - 0.4	$1 \pm 0.100909$
1		0.4 - 0.5	$1 \pm 0.099431$
2		0.5 - 0.6	$1 \pm 0.092025$
3		0.6 - 0.7	$1 \pm 0.085239$
4		0.7 - 1.0	$1 \pm 0.105356$
5		1.0 - 1.5	$1 \pm 0.104375$
6		1.5 - 2.5	$1 \pm 0.073612$
7		2.5 - 3.5	$1 \pm 0.068993$
8		3.5 - 5.0	$1 \pm 0.082334$
9		5.0 - 7.0	$1 \pm 0.097308$
10		7.0 - 30	$1 \pm 0.114706$
11	ND280 $\bar{\nu}_\mu$ FHC	0.0 - 0.7	$1 \pm 0.103804$
12		0.7 - 1.0	$1 \pm 0.084158$
13		1.0 - 1.5	$1 \pm 0.081349$
14		1.5 - 2.5	$1 \pm 0.085208$
15		2.5 - 30	$1 \pm 0.087735$
16	ND280 $\nu_e$ FHC	0.0 - 0.5	$1 \pm 0.091336$
17		0.5 - 0.7	$1 \pm 0.089699$
18		0.7 - 0.8	$1 \pm 0.084648$
19		0.8 - 1.5	$1 \pm 0.079722$
20		1.5 - 2.5	$1 \pm 0.079766$
21		2.5 - 4.0	$1 \pm 0.081399$
22		4.0 - 30	$1 \pm 0.095795$
23	ND280 $\bar{\nu}_e$ FHC	0.0 - 2.5	$1 \pm 0.072069$
24		2.5 - 30	$1 \pm 0.142921$

---

<b>Fit index</b>	<b>Beam mode</b>	<b>Bin edges [GeV]</b>	<b>Prefit</b>
25	ND280 $\nu_\mu$ RHC	0.0 - 0.7	$1 \pm 0.094066$
26		0.7 - 1.0	$1 \pm 0.079866$
27		1.0 - 1.5	$1 \pm 0.080948$
28		1.5 - 2.5	$1 \pm 0.083251$
29		2.5 - 30	$1 \pm 0.082653$
30	ND280 $\bar{\nu}_\mu$ RHC	0.0 - 0.4	$1 \pm 0.107277$
31		0.4 - 0.5	$1 \pm 0.098851$
32		0.5 - 0.6	$1 \pm 0.089710$
33		0.6 - 0.7	$1 \pm 0.084692$
34		0.7 - 1.0	$1 \pm 0.106871$
35		1.0 - 1.5	$1 \pm 0.098711$
36		1.5 - 2.5	$1 \pm 0.073350$
37		2.5 - 3.5	$1 \pm 0.070520$
38		3.5 - 5.0	$1 \pm 0.092905$
39		5.0 - 7.0	$1 \pm 0.089083$
40		7.0 - 30	$1 \pm 0.134911$
41	ND280 $\nu_e$ RHC	0.0 - 2.5	$1 \pm 0.066214$
42		2.5 - 30	$1 \pm 0.086977$
43	ND280 $\bar{\nu}_e$ RHC	0.0 - 0.5	$1 \pm 0.095575$
44		0.5 - 0.7	$1 \pm 0.089033$
45		0.7 - 0.8	$1 \pm 0.088406$
46		0.8 - 1.5	$1 \pm 0.081472$
47		1.5 - 2.5	$1 \pm 0.078353$
48		2.5 - 4.0	$1 \pm 0.089427$
49		4.0 - 30	$1 \pm 0.156972$

---

<b>Fit index</b>	<b>Beam mode</b>	<b>Bin edges [GeV]</b>	<b>Prefit</b>
50	SK $\nu_\mu$ FHC	0.0 - 0.4	$1 \pm 0.102555$
51		0.4 - 0.5	$1 \pm 0.101771$
52		0.5 - 0.6	$1 \pm 0.092573$
53		0.6 - 0.7	$1 \pm 0.084265$
54		0.7 - 1.0	$1 \pm 0.102271$
55		1.0 - 1.5	$1 \pm 0.084528$
56		1.5 - 2.5	$1 \pm 0.066909$
57		2.5 - 3.5	$1 \pm 0.072355$
58		3.5 - 5.0	$1 \pm 0.085299$
59		5.0 - 7.0	$1 \pm 0.096725$
60		7.0 - 30	$1 \pm 0.114112$
61	SK $\bar{\nu}_\mu$ FHC	0.0 - 0.7	$1 \pm 0.103129$
62		0.7 - 1.0	$1 \pm 0.078327$
63		1.0 - 1.5	$1 \pm 0.082367$
64		1.5 - 2.5	$1 \pm 0.082121$
65		2.5 - 30	$1 \pm 0.085123$
66	SK $\nu_e$ FHC	0.0 - 0.5	$1 \pm 0.090918$
67		0.5 - 0.7	$1 \pm 0.087065$
68		0.7 - 0.8	$1 \pm 0.082527$
69		0.8 - 1.5	$1 \pm 0.076514$
70		1.5 - 2.5	$1 \pm 0.075773$
71		2.5 - 4.0	$1 \pm 0.082078$
72		4.0 - 30	$1 \pm 0.092882$
73	SK $\bar{\nu}_e$ FHC	0.0 - 2.5	$1 \pm 0.071921$
74		2.5 - 30	$1 \pm 0.128982$

Fit index	Beam mode	Bin edges [GeV]	Prefit
75	SK $\nu_\mu$ RHC	0.0 - 0.7	$1 \pm 0.093954$
76		0.7 - 1.0	$1 \pm 0.076369$
77		1.0 - 1.5	$1 \pm 0.074900$
78		1.5 - 2.5	$1 \pm 0.078108$
79		2.5 - 30	$1 \pm 0.077505$
80	SK $\bar{\nu}_\mu$ RHC	0.0 - 0.4	$1 \pm 0.108593$
81		0.4 - 0.5	$1 \pm 0.101912$
82		0.5 - 0.6	$1 \pm 0.092787$
83		0.6 - 0.7	$1 \pm 0.082669$
84		0.7 - 1.0	$1 \pm 0.102090$
85		1.0 - 1.5	$1 \pm 0.087732$
86		1.5 - 2.5	$1 \pm 0.068117$
87		2.5 - 3.5	$1 \pm 0.069902$
88		3.5 - 5.0	$1 \pm 0.091711$
89		5.0 - 7.0	$1 \pm 0.084736$
90		7.0 - 30	$1 \pm 0.115488$
91	SK $\nu_e$ RHC	0.0 - 2.5	$1 \pm 0.066204$
92		2.5 - 30	$1 \pm 0.082645$
93	SK $\bar{\nu}_e$ RHC	0.0 - 0.5	$1 \pm 0.095453$
94		0.5 - 0.7	$1 \pm 0.088889$
95		0.7 - 0.8	$1 \pm 0.085644$
96		0.8 - 1.5	$1 \pm 0.078536$
97		1.5 - 2.5	$1 \pm 0.075246$
98		2.5 - 4.0	$1 \pm 0.086384$
99		4.0 - 30	$1 \pm 0.152507$

### 4.2.2 Detector Inefficiencies And Bins Normalization Parameters

In the BANFF fit, fit bin normalization parameters are used to penalize variations in the fit bins. Varying fit bins without constraint is nonphysical due to known detector inefficiencies and their systematic uncertainties. This information is incorporated into the penalty term,  $\chi^2_{\text{Det}}$ . Since improperly modeled inefficiencies can cause events to migrate from bin-to-bin, numerous fake “toy experiments” are performed to evaluate the systematic uncertainties in detector inefficiencies. When all toy experiments are analyzed together, correlated variations among fit bins become apparent. These correlations provide the constraints on freely changing bin normalizations. We will see the result of running such toy experiment variations in the coming pages. Hitherto in this thesis, detector inefficiency uncertainties will be referred to as detector systematics.

All the detector systematics are evaluated either as observable variations or weights. An observable variation affects the physical observables of selected events like the calculated energy loss of a track in the PØD. A weight is a multiplicative factor that alters the normalization of a single event in a bin. There are detector systematics that affect the PØD-only, TPC-only, or both.

This section is organized as follows. The systematics treatment model for the detector systematics developed to evaluate their effects on the analysis is described in Section 4.2.2.1. The specific systematic uncertainties relevant to this analysis are described in Section 4.2.2.2. The detector systematics penalty term used in the BANFF fit is described in Section 4.2.2.3. Finally, the procedure to determine the initial bin normalization is presented in Section 4.2.2.4.

#### 4.2.2.1 Systematic Treatment Models

The BANFF fit analysis uses toy experiment variations to evaluate the effect of detector systematics on the analysis samples. Each toy experiment loops over all the predicted events

and varies the known detector systematic effects. Each systematic effect either varies the event's efficiency weight or event observables. Both the observable variation and efficiency-like weight treatments rely on data-driven studies by comparing data and MC predictions in a control sample<sup>18</sup> (CS). By using a large ensemble of toy experiments, the effect of the detector systematics on the samples is evaluated.

Efficiency-like corrections alter the number of predicted events in a fit bin. The model used to evaluate efficiency-like systematics is given by

$$\epsilon_{\text{Data}}(o) = \left( \frac{\epsilon_{\text{Data}}(o)}{\epsilon_{\text{MC}}(o)} \right)_{\text{CS}} \epsilon_{\text{MC}}(o), \quad (4.4)$$

where  $\epsilon_{\text{MC}}/\epsilon_{\text{Data}}$  denotes the mean selection efficiency of the MC/data as a function of some observable kinematic  $o$ , and  $( )_{\text{CS}}$  refers to the selection efficiency measured in a CS. We need to update this model to account for statistical uncertainties in the CS. The updated model, with  $o$  dependence assumed, is now

$$\epsilon'_{\text{Data}} = \left( \frac{\epsilon_{\text{Data}} + x_{\text{Data}} \cdot \sigma_{\epsilon_{\text{Data}}}}{\epsilon_{\text{MC}} + x_{\text{MC}} \cdot \sigma_{\epsilon_{\text{MC}}}} \right)_{\text{CS}} \epsilon_{\text{MC}} \quad (4.5)$$

where  $\sigma_{\epsilon_{\text{MC}}}/\sigma_{\epsilon_{\text{Data}}}$  is the standard deviation of the efficiency of the MC/Data and  $x_{\text{Data}}$  and  $x_{\text{MC}}$  are uncorrelated, random normally distributed numbers from  $\mathcal{N}(\mu = 0, \sigma^2 = 1)$ . All the variations are applied to the event, simultaneously affecting all observables, and the event selection is rerun. A weight is derived depending if the event is selected,  $w_{\text{eff}}$ , or not selected,  $w_{\text{ineff}}$ . These weights are given below

$$w_{\text{eff}} = \frac{\epsilon'_{\text{Data}}}{\epsilon_{\text{MC}}} \quad (4.6)$$

$$w_{\text{ineff}} = \frac{1 - \epsilon'_{\text{Data}}}{1 - \epsilon_{\text{MC}}}.$$

---

<sup>18</sup>Each control sample is validated in T2K prior to introduction to the BANFF analysis.

Observable variation systematics are evaluated as shifts to physically measured quantities like particle track momentum and track length. The systematic can be evaluated in two different ways:

1. If the reconstructed observable,  $o_{\text{reco}}$ , has a known true value,  $o_{\text{true}}$ , then the difference between those two is used as scaling. The varied observable is given by

$$o' = o_{\text{true}} + (o_{\text{reco}} - o_{\text{true}}) (s + x\sigma_s), \quad (4.7)$$

where  $s$  is the mean scaling parameter used to match the true value,  $\sigma_s$  is the uncertainty on  $s$ , and  $x$  is a random number from  $\mathcal{N}(\mu = 0, \sigma^2 = 1)$ . The mean scaling parameter and its uncertainty are determined from the standard deviations observed in the data and MC by

$$s = \frac{\delta^{\text{data}}}{\delta^{\text{MC}}} \quad \sigma_s = s \left| \frac{\sigma_{\delta^{\text{data}}}}{\delta^{\text{data}}} - \frac{\sigma_{\delta^{\text{MC}}}}{\delta^{\text{MC}}} \right|. \quad (4.8)$$

2. If the MC reconstructed observable is corrected to match the mean from some CS reconstructed observable. The varied observable in this case is given by

$$o' = o_{\text{Nom}} + \Delta o + x\sigma_{\Delta o}, \quad (4.9)$$

where  $o'$  is the varied observable value,  $o_{\text{Nom}}$  is the nominal MC value,  $\Delta o$  is the average correction to the observable,  $\sigma_{\Delta o}$  is the uncertainty on the correction, and  $x$  is a random, normal number from  $\mathcal{N}(\mu = 0, \sigma^2 = 1)$ .

Additional uncertainties from the magnetic field are also special cases of the 2nd observable variation method specifically for the TPC momentum [86]. They are:

- The TPC laser calibration corrections are applied after the magnetic field (B-field) mapping corrections. The B-field corrections are applied at event reconstruction while

the calibration corrections are treated as a systematic uncertainty. The varied momentum is given by

$$p' = p_{\text{Nom}} + x(p_{\text{Map}} - p_{\text{Nom}}), \quad (4.10)$$

where  $p_{\text{Nom}}$  is the nominal MC prediction using the B-field corrections and  $p_{\text{Map}}$  is the updated momentum using the additional laser calibration mapping.

- The momentum depends on some scale parameter  $s$ . The varied momentum due to the scale uncertainty is given by

$$p' = p_{\text{Nom}}(1 + x\sigma_s), \quad (4.11)$$

where  $\sigma_s$  is the uncertainty on the scale. In this parameterization,  $s$  is the scale of the ND280 solenoid current.

After all observables are varied and applied to the event, the event selection cuts are applied again. By doing so after all variations are applied, the full impact of the systematic on the sample and analysis bins can be evaluated.

#### 4.2.2.2 Detector Systematics

Since this analysis uses the PØD and TPC detectors, systematics that affect both must be included in the toy experiments. The complete set of detector systematics and their treatment in the analysis are listed in Table 4.2 on page 112. The TPC-only systematics that have been used in previous BANFF fit analysis are included in this analysis. Details on the TPC-only systematics are discussed in the following references [6, 86]. There are four PØD-only detector systematics that are considered for this BANFF fit analysis:

- The PØD detector energy loss scale,
- The PØD detector energy loss resolution,

**Table 4.2:** List of detector systematics in the analysis. The TPC-only systematics are discussed in the following reference [6]. The PØD mass and track matching systematics were not available in the BANFF framework and treated as uncorrelated additions to the covariance matrix.

Systematic effect	Affected detectors	Treatment
PØD energy loss scale	PØD	observable variation
PØD energy loss resolution	PØD	observable variation
PØD mass	PØD	(see text)
PØD-TPC matching eff.	PØD, TPC	(see text)
Pion secondary interactions	PØD, TPC	efficiency
Proton secondary interactions	PØD, TPC	efficiency
Magnetic field distortion	TPC	observable variation
TPC charge misassignment	TPC	efficiency
TPC cluster efficiency	TPC	efficiency
TPC momentum resolution	TPC	observable variation
TPC momentum scale	TPC	observable variation
TPC particle identification	TPC	observable variation
TPC track quality efficiency	TPC	efficiency
TPC tracking efficiency	TPC	efficiency

- The PØD-TPC inter-detector matching efficiency, and
- The PØD detector fiducial mass.

The PØD energy loss scale and resolution affect the measured momentum in the PØD and are very significant sources of uncertainty. In the  $\nu_\mu$  CC-0 $\pi$  cross section analysis [8], the same selection as the  $\nu_\mu$  in FHC Mode CC 1-Track selection, the scale and resolution contributed 1.3% and 6.7%, respectively, to the cross section uncertainty. Those large uncertainties can be attributed to the design of the PØD. It is optimized for  $\pi^0$  detection as opposed to a dedicated tracking detector like the FGD. Slight variations in the track reconstruction can significantly alter the energy loss as measured in Eqn. (3.4).

The remaining systematics, the PØD mass and the PØD-TPC matching efficiency, were not available to analyze in toy experiments variations. They were not implemented in the BANFF framework and unavailable to implement due to time constraints on this author. Instead, they were treated as additional uncorrelated systematics on each bin normalization

uncertainty with the normalization value remaining fixed.

The PØD mass uncertainty is a normalization systematic which affects the event rate. This is a challenging systematic for analyses of recent T2K data due to increasingly faulty sensors to measure the water content. The procedure to fill the water bags required filling them in unison to prevent uneven bulging. However, faulty sensors would provide poor quality data, hence bags were under and overfilled. This effect alters the expected event rate as a function of position.

Another problem with the mass uncertainty is due to structure deformations in the PØD. To understand how the PØD has deformed, it is important to understand how the PØD is mounted in the ND280 detector. Each corner of the PØD is mounted to the ND280 basket leaving the those corners spatially fixed. When the water bags are filled, the WT volume expands or “bulges” from the middle. The upstream end of the PØD, the Upstream ECal, resists deformations since it is physically against the ND280 support structure and magnet yoke. The downstream end of the PØD, or the Central ECal (CECal), is free to deform, however, since there is a few centimeters air gap between it and the TPC. The CECal, which has a design thickness of 304 mm [19], was observed to bulge about 7-8 mm from its center due to WT bulging as well [83].

This left more water volume, and importantly more mass, in the most downstream water bags compared to the upstream bags. This additional mass or bulging effect is evident in the vertex distribution as a function of the Z-position as shown in Figure 4.5 on page 114.

Prior PØD analyses have estimated the mass uncertainty using similar toy experiment techniques, but did not integrate them into the BANFF framework. In particular in the  $\nu_\mu$  in CC-0 $\pi$  analysis [8], the PØD mass had an 1.5% systematic effect on the cross section. Since the PØD mass uncertainty estimate was determined using the same toy experiment variation method, a conservative estimate of 2% on the mass uncertainty is included in this analysis.

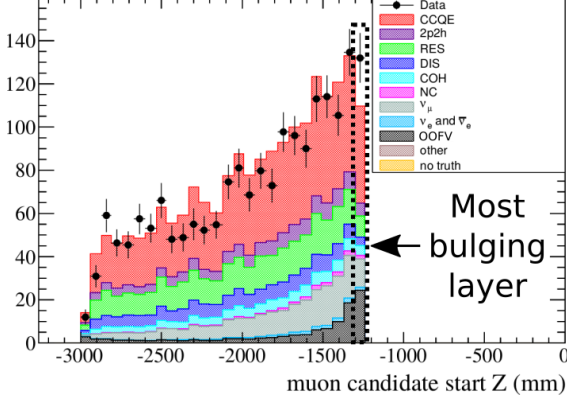


**Figure 4.5:** Vertex distribution showing evidence of bulging. In the  $\bar{\nu}_\mu/\nu_\mu$  cross section ratio analysis, a significant excess of events in the most downstream layer of the PØD (black, dashed line box) was observed. Initially thought to be OOFV events, the analyzers removed the most downstream and upstream layers in their analysis. This distribution was produced using the run 5, RHC period using selection precuts 1 through 4 and a having a positive track in the TPC. Each event is categorized by true interaction mode according to NEUT. This figure was altered for clarity from the following reference [29].

The PØD and TPC (PØD-TPC) inter-detector track matching efficiency is estimated to have a small systematic effect on the analysis. It was analyzed to have over a 99.8% data and MC efficiency in the single track  $\nu_\mu$  CC- $0\pi$  analysis and thus was neglected. However, since this analysis includes  $> 1$  track samples, the matching efficiency for non-single track samples is unknown. The best constraint on multiple track inter-detector matching is from the private T2K technical note on the single bin  $\bar{\nu}_\mu/\nu_\mu$  cross section analysis [29]. The analysis estimated the uncertainty at less than 0.14%, albeit using the “pre-Global” technique mentioned in Chapter 3. Because their track matching algorithm is different than Global’s algorithm, the uncertainty is not guaranteed to remain constant across the fit bins. A conservative estimate of 1% for the PØD-TPC matching efficiency was chosen in order to account for the inherent uncertainty in this systematic.

Now that we know the systematics that affect the analysis, we can now begin to understand how the detector systematic penalty term  $\chi^2_{\text{Det}}$  is modeled in the BANFF fit.

#### 4.2.2.3 Toy Experiments and the Detector Systematics Penalty

The bin normalization penalty parameters are restrictions on freely varying fit bins. To determine the correlations between bins, a large ensemble of toy experiments is generated. As described in Section 4.2.2.1, each toy experiment varies event observables, the momentum and angle of the main track, and number of events in a fit bin. The bin normalization parameter for the  $i$ th bin, or  $d_i$ , is defined as

$$d_i = \frac{\langle N_i \rangle_{\text{toys}}}{N_i}, \quad (4.12)$$

where  $N_i$  predicted number of events in fit bin  $i$  and  $\langle N_i \rangle_{\text{toys}}$  is the average number of events in fit bin  $i$  evaluated over all toy experiments (toys). The predicted event rate for bin  $i$  is given by

$$N_i = \sum_k^{N_{\text{MC}}} \delta_{i,k}^{\text{bin}} w_k, \quad (4.13)$$

where  $N_{\text{MC}}$  being the number of unweighted MC events,  $\delta_{i,k}^{\text{bin}}$  determines if the  $k$ th event goes into analysis bin  $i$  as a function of  $(p, \cos \theta)$ , and  $w_k$  is the product of all of the weights applied to the  $k$ th event. The weights used in Eqn. (4.13) are

$$w_k = w_k^{\text{POT}} \times w_k^{\text{Flux}} \times w_k^{\text{xsec}} \times w_k^{\text{Det}}, \quad (4.14)$$

(see Eqn. (2.8) for all possible weights). The number of events in fit bin  $i$ , averaged over all toy experiments (toys), is given by

$$\begin{aligned} \langle N_i \rangle_{\text{toys}} &= \frac{1}{N_{\text{toys}}} \sum_{t=1}^{N_{\text{toys}}} (N_i)_t \\ &= \frac{1}{N_{\text{toys}}} \sum_{t=1}^{N_{\text{toys}}} \left( \sum_k^{N_{\text{MC}}} [\delta_{i,k}^{\text{bin}} w_k] \right)_t, \end{aligned} \quad (4.15)$$

where now each MC event has a toy variation out of  $N_{\text{toys}}$  total toys. We average the results of the toys to smooth out variations among all toy experiments. In this analysis, and in

previous BANFF analyses as well,  $N_{\text{toys}} = 2000$  toys were generated as to have a small sample size uncertainty.

As stated before, all the penalty parameters are dimensionless and the detector systematics covariance matrix must be constructed carefully. The bin-to-bin event rate covariance,  $V_{i,j}^{\text{Cov}}$ , between bins  $i$  and  $j$  is

$$V_{i,j}^{\text{Cov}} = \frac{1}{N_{\text{toys}}} \sum_{t=1}^{N_{\text{toys}}} \left( (N_i)_t - \langle N_i \rangle_{\text{toys}} \right) \left( (N_j)_t - \langle N_j \rangle_{\text{toys}} \right), \quad (4.16)$$

where  $(N_i)_t$  is defined in Eqn. (4.15). We also need to account for statistical uncertainties in the fit bins, and so let us define  $V_{i,j}^{\text{Stat}}$  as

$$V_{i,j}^{\text{Stat}} = \delta_{i,j} \sum_k^{N^{\text{MC}}} \delta_{i,k}^{\text{bin}} w_k^2, \quad (4.17)$$

where  $\delta_{i,j}$  is the Kronecker delta function. In order to incorporate  $V_{i,j}^{\text{Cov}}$  and  $V_{i,j}^{\text{Stat}}$  uncertainties, the total detector covariance matrix,  $V_{i,j}^{\text{Det}}$ , in the BANFF fit is defined as

$$V_{i,j}^{\text{Det}} = \frac{V_{i,j}^{\text{Cov}} + V_{i,j}^{\text{Stat}}}{N_i N_j}, \quad (4.18)$$

which is indeed dimensionless as required by Eqn. (4.12) since we divided out the predicted event rate in bins  $i$  and  $j$ .

As stated before, the PØD mass and track matching efficiency systematics are treated as uncorrelated systematics. In order to propagate their systematic uncertainties into the analysis, the detector covariance matrix given in Eqn. (4.18) needs to be updated. The updated covariance matrix is given by

$$V_{i,j}^{\text{Det}} \leftarrow \left( \tilde{V}_{i,j}^{\text{Det}} + \tilde{\sigma}_{\text{Mass}}^2 + \tilde{\sigma}_{\text{Match}}^2 \right) d_i d_j, \quad (4.19)$$

where  $\tilde{V}_{i,j}^{\text{Det}}$  is the fractional covariance

$$\tilde{V}_{i,j}^{\text{Det}} = \frac{V_{i,j}^{\text{Det}}}{d_i d_j}, \quad (4.20)$$

$d_i/d_j$  are the bin normalization parameters, and  $\sigma_{\text{Mass}}^2 = 2\%$  and  $\sigma_{\text{Match}}^2 = 1\%$  are the PØD mass and PØD-TPC matching efficiency systematic uncertainties, respectively, estimated in Section 4.2.2.2. Together, the two additional sources of uncertainty increase each term in the covariance matrix by  $0.0005d_i d_j$ . Specifically, the uncertainty in all the bin normalization parameters (square-root of the diagonal terms in the covariance matrix) increases by about 2.23%. The updated detector covariance matrix now accounts for the PØD mass and TPC matching inefficiency systematics.

The penalty term,  $\chi_{\text{Det}}^2$ , in the fit is given by

$$\chi_{\text{Det}}^2 = (\vec{d} - \vec{d}_0)^T (V^{\text{Det}})^{-1} (\vec{d} - \vec{d}_0)^T, \quad (4.21)$$

where  $\vec{d}_0$  is the initial values of the parameters, and  $V^{\text{Det}}$  is given by Eqn. (4.19).

#### 4.2.2.4 Bin Normalization Parameters

While there could be one observable normalization for each analysis bin, a single normalization can be assigned to multiple analysis bins. The purpose is to reduce the number of fit parameters since the time to fit increases non-linearly with the number of fit parameters and events. Previously, the observable normalization edges were determined by combining fit bins with “similar” covariance. This method proved problematic since the fit bins with relatively higher statistics were shared with the same observable normalization parameter. This left the remaining low statistics regions of  $(p, \cos \theta)$  phase space more susceptible to systematic variations in the toy experiments.

A new procedure was developed to improve the shortcomings of old procedure which required careful consideration of the statistical uncertainties and variations between observable normalization prefit values. This procedure can be imagined as reducing the number

of contours in a topographic map while considering external constraints from other sensing data. The first step in the procedure is to initialize all of the observable normalization bin edges to be the same as the fit bin edges. All steps after this are performed iteratively.

Starting with observable normalization bin with the highest statistics, a decision is made to merge it with all immediate adjacent bins. If the individual fractional errors differ significantly before the merge, do not merge them. In this analysis, a factor of 10 in fractional uncertainty was determined to sufficiently describe bin similarity by using values larger and smaller than 10 and observing no significant differences in the end result. Additionally if the two unmerged bin normalizations differ by more than 10%, perform the bin merging. This step serves to smooth out the observable normalization prefit space. The procedure is also written in pseudocode in Algorithm 1.

The results of the procedure are shown visually in Figure 4.6 on page 120, Figure 4.7 on page 121, and Figure 4.8 on page 122. While the problem of the highest statistics bins being assigned to a single observable normalization parameter is still present, fluctuations between adjacent observable normalization parameters is iteratively minimized.

A considerable drawback to using toy experiments to estimate the bin normalization values and covariance matrix is that not all detector systematics affect the fit observables ( $p, \cos \theta$ ) in the same way. There are non-symmetric systematics and they are especially non-Gaussian in their effects. Therefore, the covariance matrix from Eqn. (4.18) is not an exact representation of the detector systematics. To demonstrate this, results of varied number of events are shown in Figure 4.9 on page 123. However, the bin normalization standard deviations are very wide and able to effectively cover the range of possible bin normalizations, which minimizes the non-Gaussian effects of the systematic. All the varied toy experiment results are provided in Appendix D.

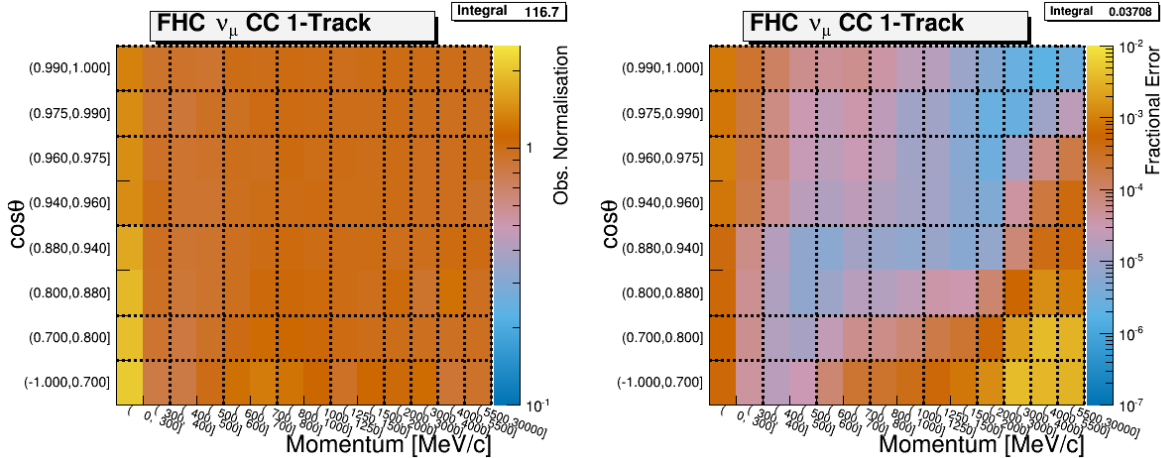
The detector systematic that had the largest effect on the observable normalization prediction was the PØD energy loss resolution (ELossRes) which alters the amount of particle energy deposited in the PØD. This systematic was developed for the  $\nu_\mu$  CC-0 $\pi$  cross section

```

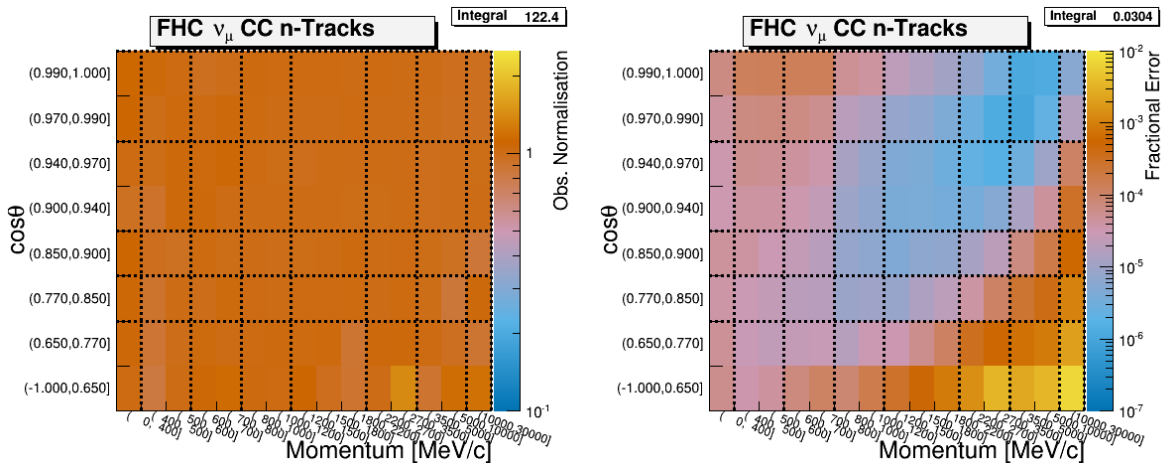
repeat
    redo  $\leftarrow$  False;
    for each normalization bin d do //sorted from min to max  $\delta\%$ 
        for each neighboring analysis bin f do
            d'  $\leftarrow$  normalization bin assigned to f;
            if d' is same as d then
                Continue to next analysis bin;
            end
            if  $\delta\%(d) \geq 10 \times \delta\%(d')$  then
                d is assigned as normalization bin for f;
                redo  $\leftarrow$  True;
                Continue to next analysis bin;
            end
            max_norm  $\leftarrow$  max(norm(d), norm(d'));
            min_norm  $\leftarrow$  min(norm(d), norm(d'));
            if max_norm  $\geq 1.1 \times$  min_norm then
                d is assigned as normalization bin for f;
                redo  $\leftarrow$  True;
            end
        end
    end
    Recalculate bin normalizations;
    until redo is False;

```

**Algorithm 1:** Algorithm to merge normalization bins. The “ $\delta\%$ ” operator returns the fractional statistical uncertainty for the bin. Since multiple fit bins can be assigned to a single normalization bin, the statistics of all fits bins are included. The “norm” operator returns the normalization value for a normalization bin determined by Eqn. (4.13). Finally, the min/max functions return the minimum/maximum element in a tuple, respectively.

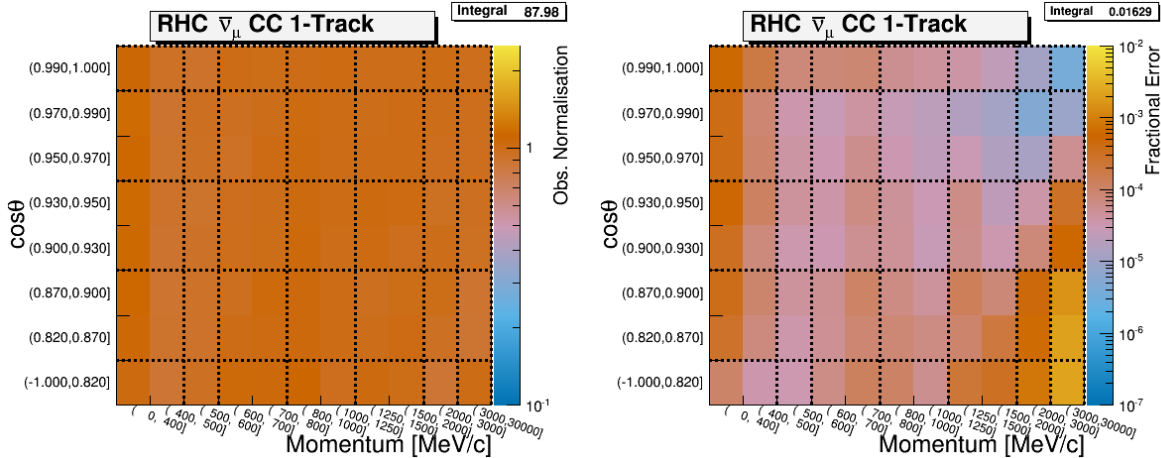


(a) The  $\nu_\mu$  in FHC Mode CC 1-Track sample

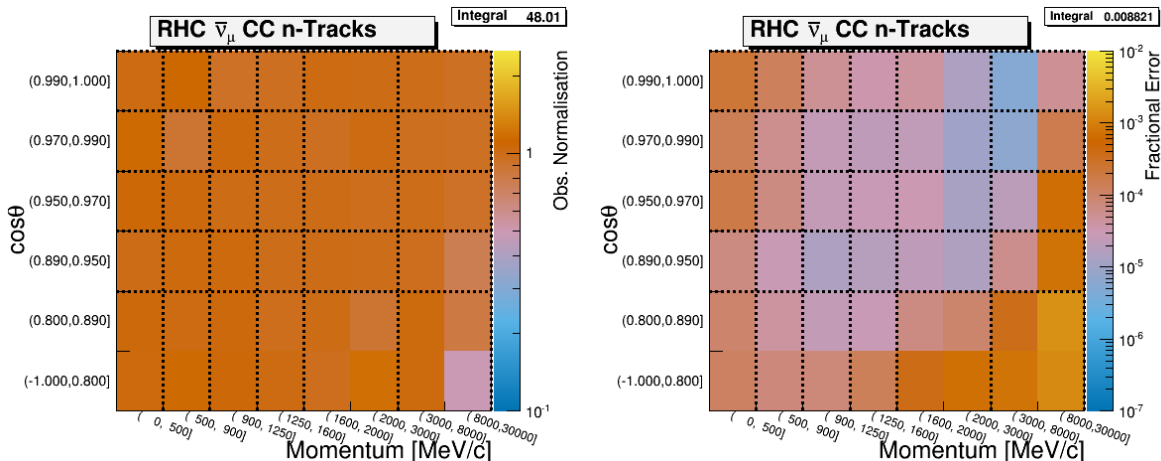


(b) The  $\nu_\mu$  in FHC Mode CC N-Tracks sample

**Figure 4.6:** Bin normalization edges for the  $\nu_\mu$  in FHC Mode samples. The left and right plots show the bin normalization and the bin statistical fractional error, respectively, if each fit bin had a single bin normalization. The dashed lines indicate the edges of the bin normalization parameters finalized for this analysis. Water-in and water-out modes are qualitatively the same.

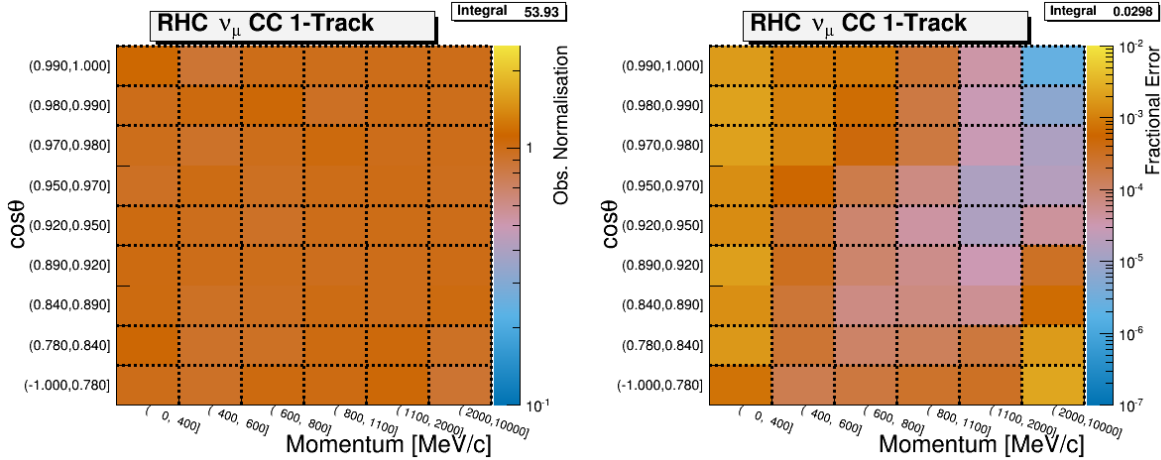


(a) The  $\bar{\nu}_\mu$  in RHC Mode CC 1-Track sample

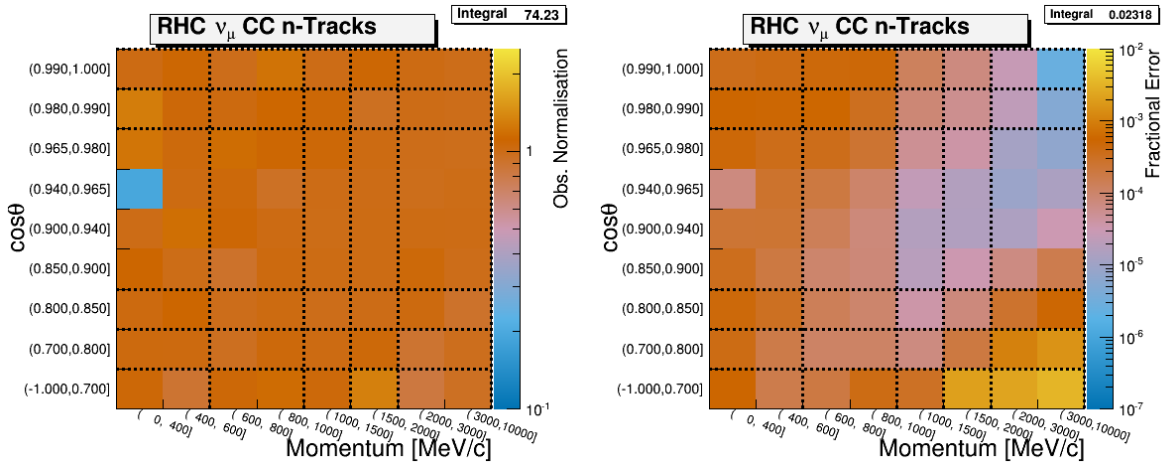


(b) The  $\bar{\nu}_\mu$  in RHC Mode CC N-Tracks sample

**Figure 4.7:** Bin normalization edges for the  $\bar{\nu}_\mu$  in RHC Mode samples. The left and right plots show the bin normalization and the bin statistical fractional error, respectively, if each fit bin had a single bin normalization. The dashed lines indicate the edges of the bin normalization parameters finalized for this analysis. Water-in and water-out modes are qualitatively the same.



(a) The  $\nu_\mu$  in RHC CC 1-Track sample



(b) The  $\nu_\mu$  in RHC CC N-Tracks sample

**Figure 4.8:** Bin normalization edges for the  $\nu_\mu$  Background in RHC Mode samples. The left and right plots show the bin normalization and the bin statistical fractional error, respectively, if each fit bin had a single bin normalization. The dashed lines indicate the edges of the bin normalization parameters finalized for this analysis. Water-in and water-out modes are qualitatively the same.

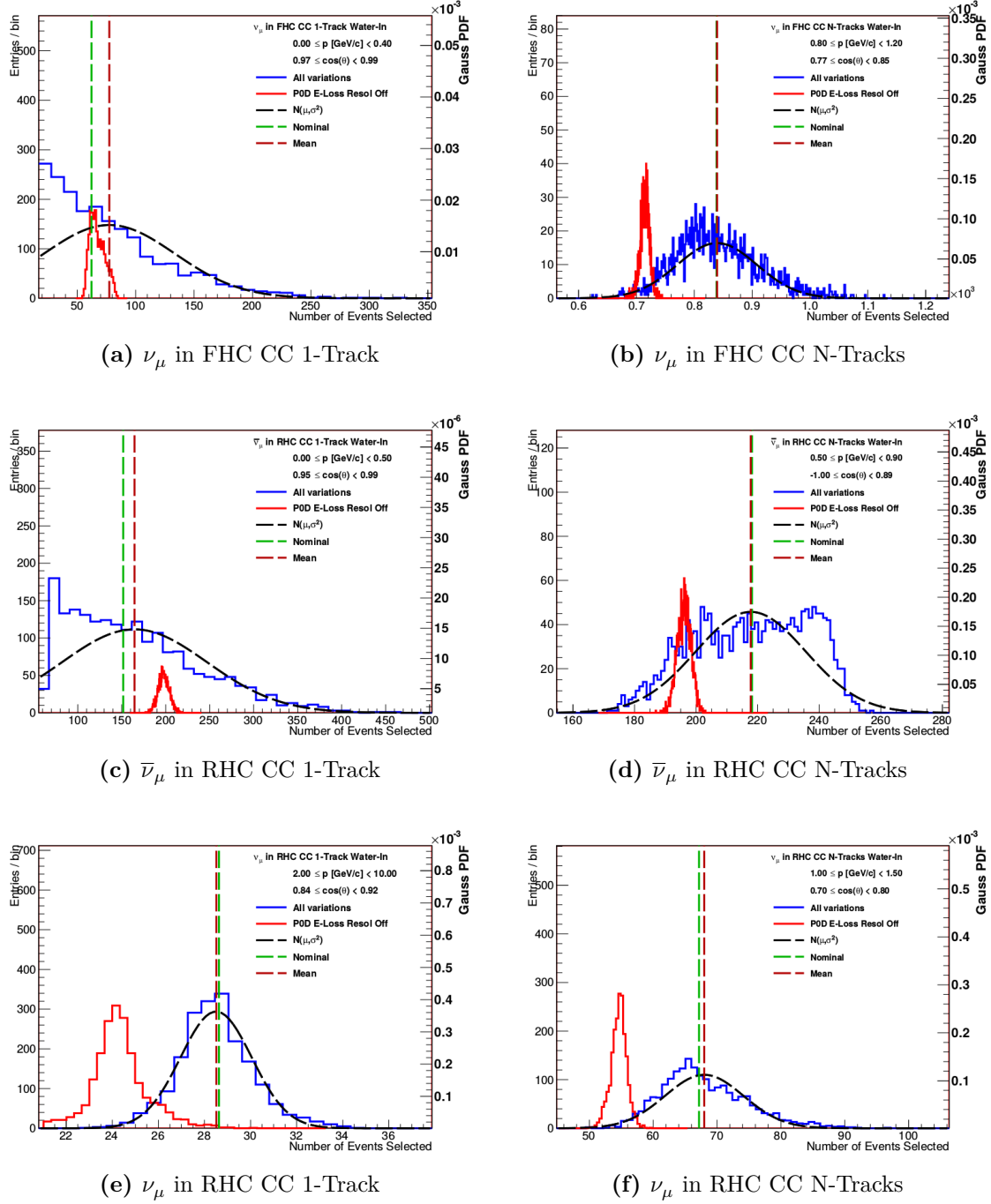


**Figure 4.9:** Event variations in representative observable normalization bins. Shown in each sub-figure the varied event rate from all toy experiments in a particular observable normalization bin. The blue curve has all the systematics enabled while the red curve has the ELossRes systematic disabled. Vertical dashed lines show the unvaried, weighted MC prediction and varied mean of all toy experiments. The ratio of the horizontal positions of each vertical line is the prefit normalization value for that bin. A Gaussian with variance extracted from the covariance matrix is shown to illustrate the bin's estimate on the normalization uncertainty.

analysis, it was identified as the largest detector systematic uncertainty in the cross section measurement [89]. When the deposited energy in the PØD is varied, it also changes the distance the truth matched particle travels in the PØD. Hence, this systematic changes the likelihood of a particle being reconstructed as a track. The observed effect is that for bins with relatively low muon momentum, the number of predicted events can vary in a non-Gaussian manner as shown in Figure 4.9 on page 123.

An unexpected phenomenon was observed when comparing the toy experiments with and without the ELossRes variation applied. With the ELossRes variation disabled in the toy experiments, a relatively large shift in the bin prediction was observed compared to the nominal prediction. This shift was expected, but what was not expected was the direction of the shift as shown in Figure 4.9 on page 123. In most cases, the shift is below the nominal MC value. However, in many of the bins, that the shape location of the prediction is above the expectation. This behavior was unexpected prior to running the toy experiment variations.

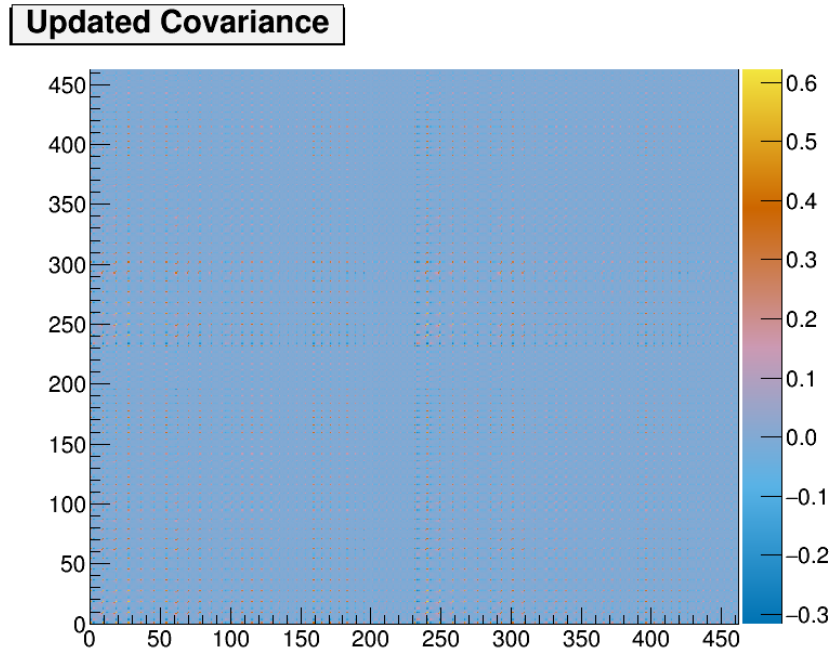
A relationship between the prediction shape location and selection purity as a function of  $(p, \cos \theta)$  was discovered. In high purity  $(p, \cos \theta)$ -regions of the 1-Track samples, the shape location of the prediction in the disabled ELossRes toy experiments was below the nominal MC prediction. When the 1-Track sample purity was lower, however, the shape location was above it. This effect is likely due to events migrating from the 1-Track samples into the N-Tracks samples due to multiple particles in the event.

The finalized observable normalization bins are listed below. There are in total  $N_d = 461$  bin normalization parameters. The covariance matrix used in the BANFF fit is shown in Figure 4.10 on page 126. Their respective fit indices, prefit values, and prefit standard deviations are tabulated in Appendix B.

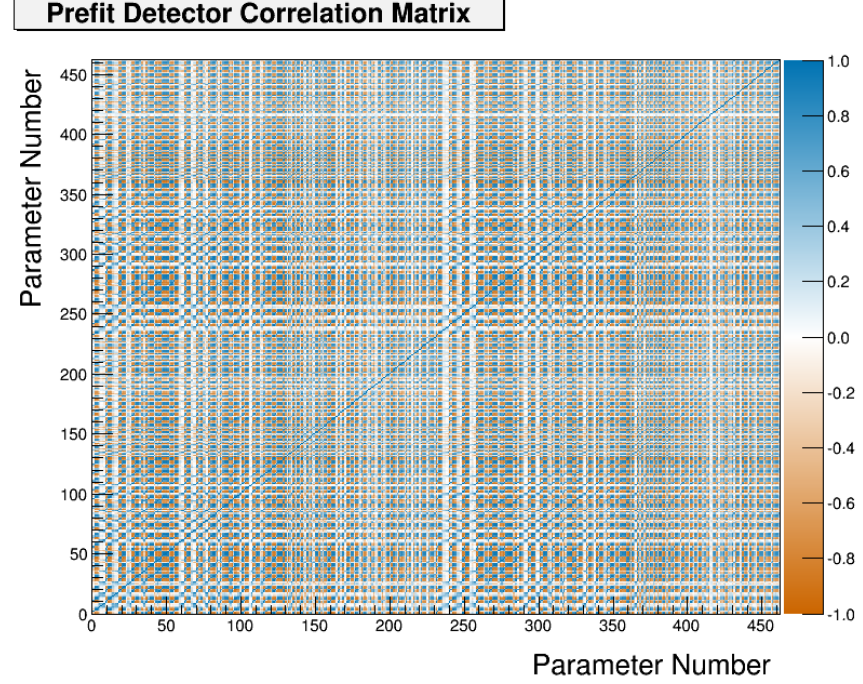
- The  $\nu_\mu$  in FHC Mode CC 1-Track samples bin normalization edges:
  - $p$  [GeV/c]: 0, 0.4, 0.6, 0.8, 1.25, 2, 3, 4, 5.5, 30
  - $\cos \theta$ : -1, 0.7, 0.8, 0.94, 0.975, 0.99, 1

- The  $\nu_\mu$  in FHC Mode CC N-Tracks samples bin normalization edges:
  - $p$  [GeV/c]: 0, 0.4, 0.6, 0.8, 1.2, 2.2, 3.5, 10, 30
  - $\cos \theta$  : -1, 0.77, 0.85, 0.9, 0.97, 1
- The  $\bar{\nu}_\mu$  in RHC Mode CC 1-Track samples bin normalization edges:
  - $p$  [GeV/c]: 0, 0.5, 0.6, 0.8, 1.25, 2, 3, 30
  - $\cos \theta$  : -1, 0.82, 0.9, 0.95, 0.99, 1
- The  $\bar{\nu}_\mu$  in RHC Mode CC N-Tracks samples bin normalization edges:
  - $p$  [GeV/c]: 0, 0.5, 0.9, 1.25, 1.6, 3, 30
  - $\cos \theta$  : -1, 0.89, 0.95, 0.97, 0.99, 1
- The  $\nu_\mu$  in RHC Mode CC 1-Track samples bin normalization edges:
  - $p$  [GeV/c]: 0, 0.4, 0.6, 0.8, 1.1, 2, 10
  - $\cos \theta$  : -1, 0.78, 0.84, 0.92, 0.95, 0.98, 0.99, 1
- The  $\nu_\mu$  in RHC Mode CC N-Tracks samples bin normalization edges:
  - $p$  [GeV/c]: 0, 0.6, 1, 1.5, 2, 10
  - $\cos \theta$  : -1, 0.7, 0.8, 0.85, 0.98, 0.99, 1

To better understand how effective the choice of bin normalizations parameters are at characterizing the data variance, principal component analysis was performed using all the available toy experiments. Principal component analysis is the process of a eigenvalue decomposition of a square matrix,  $M$ . The principal components of  $M$ , which describe the data variance, are the eigenvectors. The relative importance of each eigenvector is set by the magnitude of the associated eigenvalue.



(a) Covariance matrix



(b) Correlation matrix

**Figure 4.10:** Detector penalty covariance matrix. Shown in figure (a) is covariance matrix and (b) is the correlation matrix. Note that the parameter indices, which represent the bin normalization indices, are offset from their fit indices value by 99.

Using this prescription, we define the sample variance,  $S$ , as

$$S = \frac{1}{N_{\text{toys}}} X^T X,$$

where  $X$  is a  $N_{\text{toys}} \times N_d$  matrix of the predicted number of events (not the normalization!) in each normalization bin. The eigenvalue decomposition of  $S$  is given by

$$S = U^T \Lambda U,$$

where  $U$  is the eigenvector matrix of  $S$  and  $\Lambda$  is a diagonal matrix of the  $S$  matrix eigenvalues. What is useful using principal component analysis is that the eigenvalues and eigenvectors are sorted from largest to smallest magnitude. The sample variance eigenvalues are shown in Table 4.3 on page 128. The first, and hence largest, eigenvalue is two orders of magnitude larger than the next largest eigenvalue, which means that the majority of the bin-to-bin variance can be explained by the first eigenvector. The first eigenvector's coefficients are shown in Figure 4.11 on page 128. We see that all the components are negative and clustered.

**Table 4.3:** Eigenvalues of the sample covariance. The values are sorted from largest to smallest in magnitude. Note that the parameter indices, which represent the bin normalization indices, are offset from their fit indices value by 99.

Index	0	1	2	3	...	458	459	460	461
Eigenvalue	2029	16.45	12.87	11.10	...	0.05325	0.05129	0.04955	0.03992

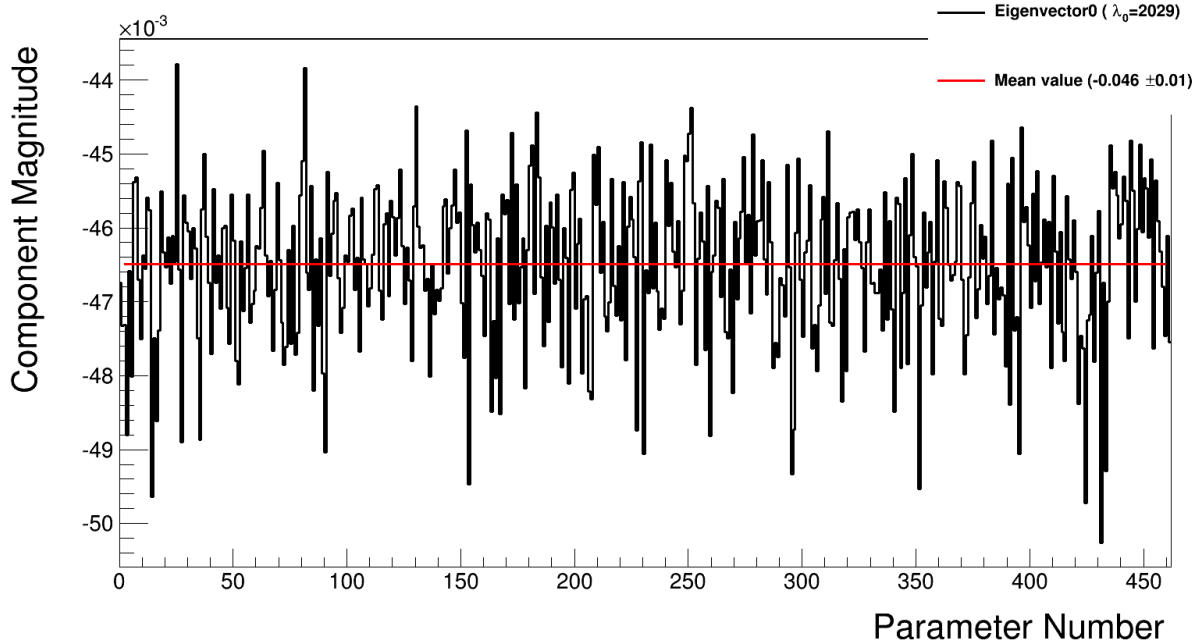


**Figure 4.11:** Principal component for the sample variance. This is the eigenvector associated with the largest eigenvalue of magnitude. Each parameter coefficient refers to the slope of the axis that describes most of the variance in the sample. The coefficients are all negative and are of similar magnitude. Together, they suggest all the normalization parameters respond linearly and uniformly. Note that the parameter indices, which represent the bin normalization indices, are offset from their fit indices value by 99.

This result is interpreted to mean we can expect the bins normalizations postfit values to shift all together uniformly.

Additionally, we can estimate the effective degrees of freedom for the bin normalization parameters. The effective degrees of freedom is given by

$$df(r) = \sum_{i=0}^{N_d} \frac{\lambda_i}{\lambda_i + r}, \quad (4.22)$$

where  $\lambda_i$  are the eigenvalues of  $\Lambda$  and  $r$  is a tunable parameter [50]. The idea behind Eqn. (4.22) is that although all  $N_d$  coefficients will be non-zero, they are restricted to vary by the magnitude of  $r$ . In particular,  $r$  represents the regularization strength for the detector systematics penalty, which is set to one ( $r = 1$ ) in the BANFF fit. If there was no (regularization) penalty, or  $r = 0$ , then the number of degrees of freedom is  $df(0)=N_d$ . It is found that there are about 137 effective degrees of freedom for the bin normalization parameters, or 29% of  $N_d$ . This suggests that a much smaller number bin normalization parameters can effectively describe the sample variance. This is particularly important to consider for a future BANFF fit analysis since this can provide a computational performance while maintaining predictability power in the ND constraint measurement. No further reduction in the number of bin normalization parameters were pursued due to time constraints.

### 4.2.3 Cross Section Model

There are a number of neutrino-nucleus interaction model parameters implemented in the BANFF fit to account for the uncertainties in cross section measurements. They are frequently updated to account for new models and constraints from external data. The cross section models used in this analysis use the T2K 2017 parameterization, which is a canonical set of parameters shared among all analyses in T2K. A gross description of the cross section model is provided here with a full description in the following reference [9].

There are three types of cross section parameters: shape, normalization, and functional. A cross section shape parameter,  $x^{\text{Shape}}$ , is defined as a shift in the location of a certain feature in the cross section. The shape parameters are stored in one dimensional splines

$$w(x^{\text{Shape}}) = \frac{d^n \sigma(x^{\text{Shape}})}{dz^n} / \frac{d^n \sigma(x_0^{\text{Shape}})}{dz^n},$$

where  $d^n \sigma/dz^n$  is a  $n$  dimensional cross section of  $z$  dependent parameters, and  $x_0^{\text{Shape}}$  is the nominal value of the shape parameter. As a design choice, the shape location parameters

all start with a prefit value of zero (0). A cross section normalization parameter,  $x_i^{\text{Norm}}$ , is defined as

$$x^{\text{Norm}} = \frac{p'}{p}, \quad (4.23)$$

where  $p$  and  $p'$  are NEUT nominal and ND constrained parameters, respectively. And finally functional parameters are scalars to model a cross section function of a true kinematic. For example, if a cross section is given by  $\sigma(x) = mx + b$ ,  $m$  and  $b$  are the functional parameters in the model. Combining these parameters into a single vector  $\vec{x}$ , the cross section penalty term,  $\chi_{\text{Det}}^2$ , is given by

$$\chi_{\text{Det}}^2 = (\vec{x} - \vec{x}_0)^T (V^{\text{xsec}})^{-1} (\vec{x} - \vec{x}_0),$$

where  $\vec{x}_0$  is the initial values of the cross section parameters, and  $V^{\text{xsec}}$  is the cross section model covariance matrix.

The next sections deal with the model parameterizations and systematic uncertainties in the NEUT version 5.3.3 [86] interaction library which is used in T2K MC and oscillation analysis.

#### 4.2.3.1 The CC-0 $\pi$ Model

The cross section models with the largest impact on T2K’s oscillation sensitivity are CCQE and CCQE-like interactions, collectively called CC-0 $\pi$ . At energies near the  $\nu_e$  appearance maximum,  $E_\nu = 0.6$  GeV, the CCQE interaction is the largest contributor to the neutrino cross section as shown in Figure 1.30 on page 52. The nominal CCQE model in NEUT is a Spectral Function (SF) from Benhar *et al* [22]. An alternative CCQE model incorporates the Llewellyn-Smith dipole axial form factor<sup>19</sup> [31, 57] and BBBA05 vector form factors coupled to a Smith-Moniz Relativistic Fermi Gas [25, 64, 79] (RFG). A CCQE-like excitation mode involves correlated nucleon pair scattering called “2 particle, 2 hole” [61] (2p2h).

---

<sup>19</sup>A form factor is a measure of scattering amplitude in the form of the Fourier transform of some charge distribution.

An additional nuclear model called the “Random Phase Approximation” (RPA) [34, 63] is used to modify single nucleon scattering by accounting for nucleon correlations inside the nucleus. The default CC- $0\pi$  model for T2K analyses is the combination of the Llewellyn-Smith+RFG model, 2p2h excitation, and RPA nuclear model. This combination was selected due to poor data matching with the SF model [86].

The CC- $0\pi$  model has three CCQE parameters: the dipole axial form factor mass  $M_A^{\text{QE}}$  from the Llewellyn-Smith model, and two Fermi momentum parameters  $p_F$ , one for  $^{12}\text{C}$  and one for  $^{16}\text{O}$  that describe the momentum of nucleons on the surface of a RFG. In the past, using these parameters has been shown to work as effective parameters in T2K when unconstrained. In this analysis, these three parameter are unconstrained. In other words, a flat prior is used for  $M_A^{\text{QE}}$ ,  $p_F^C$ , and  $p_F^O$ .

For the 2p2h excitation, there are a total of five parameters to describe the model. Three are normalization terms: the  $\nu$  interaction on  $^{12}\text{C}$ , the  $\bar{\nu}$  interaction on  $^{12}\text{C}$ , and the scaling for  $^{12}\text{C} \rightarrow ^{16}\text{O}$ . The remaining two systematic parameters in the 2p2h excitation are shape parameters, one for  $^{12}\text{C}$  and one for  $^{16}\text{O}$ . They are used constrain the interplay of the contributing modes in 2p2h. One contributing mode is the Meson Exchange Current (MEC) which involves a virtual meson exchange between the nucleons. The other mode is nucleon-nucleon (NN) correlations which involves virtual particle exchange. A shape value of -1 determines 2p2h is completely due to MEC, 0 is the nominal MC 2p2h model, and +1 determines 2p2h is completely due to NN. Any differences in the event rate in the region between  $\pm 1$  is absorbed by a interference term. However, since no existing T2K nor external neutrino data can constrain the neutrino-induced 2p2h interaction, a flat prior is set for all 2p2h parameters.

The other nuclear interaction in the CC- $0\pi$  model uses the Nieves RPA model [63] to describe nucleon correlations. The RPA model primarily alters the single nucleon cross section and has dependence on both  $E_\nu$  and  $Q^2$ . A functional weighting scheme called “BeRPA” having only  $Q^2$  dependence was found to work well to mimic the inherent uncertainties in

the Nieves RPA model. The BeRPA functional is given by

$$w(Q^2) = \begin{cases} A\beta_0^3(x) + B\beta_1^3(x) + p_1\beta_2^3(x) + D\beta_3^3(x) & Q^2 \leq U \\ 1 + p_2 \exp(-E[Q^2 - U]), & Q^2 > U \end{cases} \quad (4.24)$$

where  $x = Q^2/U$ ,  $\beta_i^n(x)$  are the Bernstein polynomials [39]

$$\beta_i^n(x) = \binom{n}{i} x^i (1-x)^{n-i} \quad x \in [0, 1], \quad (4.25)$$

$p_1$  and  $p_2$  absorb the continuity conditions,

$$p_1 = D + \frac{UE(D-1)}{3}, \quad p_2 = D-1, \quad (4.26)$$

and  $A$ ,  $B$ ,  $D$ ,  $E$ , and  $U$  are the functional parameters. The parameter  $U$  is fixed to prevent unwieldy correlations from appearing.

#### 4.2.3.2 The CC-1 $\pi$ Model

Another important exclusive channel in NEUT is resonance states that produce a single pion or CC-1 $\pi$ . The CC-1 $\pi$  model incorporates the Rein-Seghal model of neutrino-induced  $\Delta$  resonance decay [45–47, 68] with lepton mass corrections [23, 48]. There are just three tunable parameters in the model. They are resonant axial mass  $M_A^{\text{Res}}$ , the axial form factor normalization  $C_A^5$ , and the isospin=1/2 ( $I_{1/2}$ ) background normalization. These three parameters are known to effectively describe neutrino-induced single pion production data from Brookhaven National Laboratory [55] and Argonne National Laboratory [67]. It is important to know that  $M_A^{\text{Res}}$  and  $C_A^5$  are strongly anticorrelated due to the parameterization of the form factor

$$f(Q^2) = C_A^5 \left( 1 + \frac{Q^2}{(M_A^{\text{Res}} c^2)^2} \right)^{-2}. \quad (4.27)$$

#### 4.2.3.3 Coherent Pion Production

Coherent scattering refers to scattering where the wavelength of the incoming particle is larger than the target. In the case of coherent neutrino-nucleus scattering, the neutrino's de Broglie wavelength is larger than the size of the nucleus. In the scattering, no quantum numbers are exchanged, but the nucleus experiences a momentum boost. In coherent pion production, the in-flight virtual boson is converted into a pion with that pion exchanging a Pomeron [5] with the nucleus. The coherent scattering model is described by Rein-Sehgal [69]. Lookup tables are used to scale the cross section to external data [86] and the Berger-Sehgal model [23]. Three tunable normalization parameters are used describe the coherent production model: CC on  $^{12}\text{C}$ , CC on  $^{16}\text{O}$ , and NC on all nuclei. As a design choice, both CC parameters are 100% correlated with one another, meaning that any change in one parameter changes the other identically.

#### 4.2.3.4 High Energy Scattering Model

There are two parameters that describe high energy neutrino scattering. One is a CC deep inelastic scattering (DIS) interaction shape parameter called “CC DIS”. The other is a normalization for NC interactions called “NC Other”. The CC DIS parameter, which also includes multiple pion production, is modeled as a function of  $E_\nu$  with a simple uncertainty relation of

$$\frac{0.4}{E_\nu \text{ [GeV]}} (\%),$$

where the uncertainty at 4.0 GeV is 10%. The NC Other parameter is a normalization on NC DIS, single kaon production, single  $\eta$ -meson production, and NC elastic processes with a flat 30% fractional uncertainty [86].

#### 4.2.3.5 Final State Interactions

Final state interactions [44] (FSI) are effects that alter final state pions from neutrino-nucleus events before the pion exits the nucleus. The microscopic model in NEUT is a cascade implementation of the Salcedo-Oset model [73] which describes interactions in the nucleus as probabilities of position and momentum tuned to the world data [70]. These processes are divided into six classes with one parameter for each. These classes are the low energy inelastic scattering (INEL), high energy INEL, pion absorption (ABS), pion production (PROD), low energy charge exchange (CEX), and high energy CEX. The low and high energy transition for both the inelastic scattering and charge exchange processes occurs at  $p_\pi = 500$  MeV/c.

#### 4.2.3.6 Fixed Parameters

As mentioned in the CC- $0\pi$  model, the BeRPA  $U$  parameter is fixed to minimize correlations with the other BeRPA scale parameters. However, there are four other fixed normalization parameters in the BANFF fit since they correspond to SK only parameters. They are included in the fit in order to maintain consistency between the ND280 constraint and oscillation analysis parameterizations. In other words, they are spectators in the BANFF fit. These parameters are the CC  $\nu_e/\nu_\mu$  event rate ratio, CC  $\bar{\nu}_e/\bar{\nu}_\mu$  event rate ratio, NC- $1\gamma$  event rate, and NC other far detector event rate.

#### 4.2.3.7 Prefit Values and Covariance Matrix

There are a total of 31 cross section parameters in the BANFF fit, five of which are fixed. The fit parameters are listed in Table 4.4 on page 135 with the associated covariance matrix shown in Figure 4.12 on page 137. Following the definition of the flux and bin normalization parameters, cross section parameters are defined as fractional differences either in shape, scale, or normalization. If no prefit uncertainty is shown in Table 4.4 on page 135, and emphasized using red font, then the parameter had a flat prior assigned. A model parameter with an asterisk (\*) next to it is fixed in the fit. Abbreviations used in this table are “dim.-

“less” for dimensionless, “norm.” for normalization, “Near” for ND280, “Far” for Super-Kamiokande, and “bkg” for background. Parameters with physical units are shown in both dimensionless and dimensional values for comparison. Prefit values are relative to the NEUT nominal value.

**Table 4.4:** Cross section model parameters in the fit. See the text for a full description.

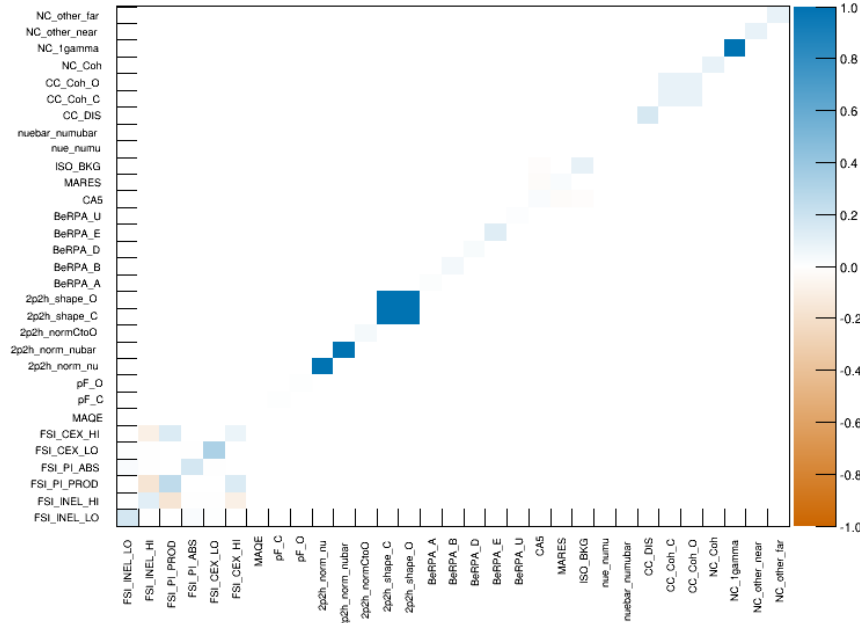
Fit index	Topology	Model	Parameter	Prefit
562	All	FSI	Low energy INEL	$0 \pm 0.41$
563			High energy INEL	$0 \pm 0.34$
564			PROD	$0 \pm 0.41$
565			ABS	$0 \pm 0.5$
566			Low energy CEX	$0 \pm 0.57$
567			High energy CEX	$0 \pm 0.28$
568	CC-0 $\pi$	Llewellyn-Smith	$M_A^{\text{QE}}$ (dim.-less)	1
			$M_A^{\text{QE}}$ (GeV/c $^2$ )	1.20
569		RFG	$p_F^C$ (dim.-less)	1
			$p_F^C$ (MeV/c)	217
570			$p_F^O$ (dim.-less)	1
			$p_F^O$ (MeV/c)	225
571		Nieves 2p2h	$\nu$ norm. on $^{12}\text{C}$	1
572			$\bar{\nu}$ norm. on $^{12}\text{C}$	1
573			$^{12}\text{C} \rightarrow ^{16}\text{O}$ norm.	1
574			$^{16}\text{C}$ shape location	0
575			$^{12}\text{O}$ shape location	0
576	BeRPA	BeRPA	$A$	$0.59 \pm 0.118$
577			$B$	$1.05 \pm 0.21$
578			$D$	$1.13 \pm 0.1695$

Fit index	Topology	Model	Parameter	Prefit
579			$E$	$0.88 \pm 0.352$
580			$U^*$	$1.2 \pm 0.1$
581	CC-1 $\pi$	Rein-Seghal resonant 1 $\pi$ prodction	$C_A^5$	$0.96 \pm 0.148$
582			$M_A^{\text{Res}}$ (dim.-less)	$1.1263 \pm 0.157$
			$M_A^{\text{Res}}$ (GeV/c <sup>2</sup> )	$1.07 \pm 0.15$
583			$I_{1/2}$ bkg. norm.	$0.74 \pm 0.307$
584	Other	Event rate at SK	CC- $\nu_e/\nu_\mu$ *	$1 \pm 0.0282$
585			CC- $\bar{\nu}_e/\bar{\nu}_\mu$ *	$1 \pm 0.0282$
586		Coherent pion production	CC DIS shape location	$0 \pm 0.4$
587			CC norm. on <sup>12</sup> C	$1 \pm 0.3$
588			CC norm. on <sup>16</sup> O	$1 \pm 0.3$
589			NC norm.	$1 \pm 0.3$
590		Event rate	NC-1 $\gamma$ *	$1 \pm 1$
591			NC Other Near	$1 \pm 0.3$
592			NC Other Far*	$1 \pm 0.3$

### 4.3 Summary

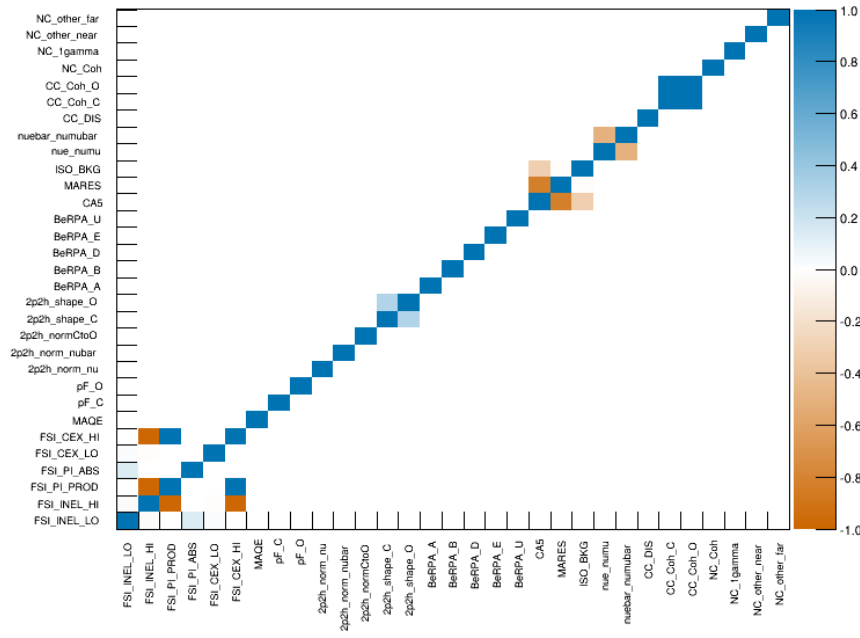
This chapter has described all the fit bins and parameters that go into the BANFF fit. For the fit bins, they are used in the LLR term to model the best possible fit between data and MC without any constraints. However, since there are known systematic uncertainties in the flux, detector inefficiencies, and cross sections, we have described their parameterizations to force the fit work within those constraints. The flux model is constrained by T2K primary and secondary beamline data while the cross sections are constrained by external data.

**Prefit XSec Covariance Matrix**



(a) Covariance matrix

**Prefit XSec Correlation Matrix**



(b) Correlation matrix

**Figure 4.12:** Cross section parameters prefit covariance and correlation matrices.

Finally, the detector systematics are determined via an ensemble of toy experiments based on well established control samples in the ND280 detector.

The next chapter describe the set of validation studies used to examine how the BANFF fit performs.

# Chapter 5

## Validation of the BANFF Fit Procedure

This chapter will present the checks, tests and validations of the BANFF fit using the MC simulation as input. The test using the weighted MC as the data is referred as an Asimov<sup>20</sup> data fit [35]. There next are two other validation tests that use two different data sets that have altered events weights (reweighted) compared to the MC. These are referred to as fake data sets.

The chapter is presented in the following order. The first topic is the Asimov data fit discussed in Section 5.1. The following section explores the results of the two fake data fits in Section 5.2. A chapter summary is provided in Section 5.3.

### 5.1 Asimov Data Fit

Asimov data refers to replacing the ensemble of simulated data sets by a single representative one [35]. In this analysis, this involves fitting the MC data set to itself for the primary purpose of checking the closure of the fitting framework. The Asimov set is produced with

---

<sup>20</sup>An Asimov data refers replacing the ensemble of simulated data sets by a single representative one.

## Prefit Correlation Matrix

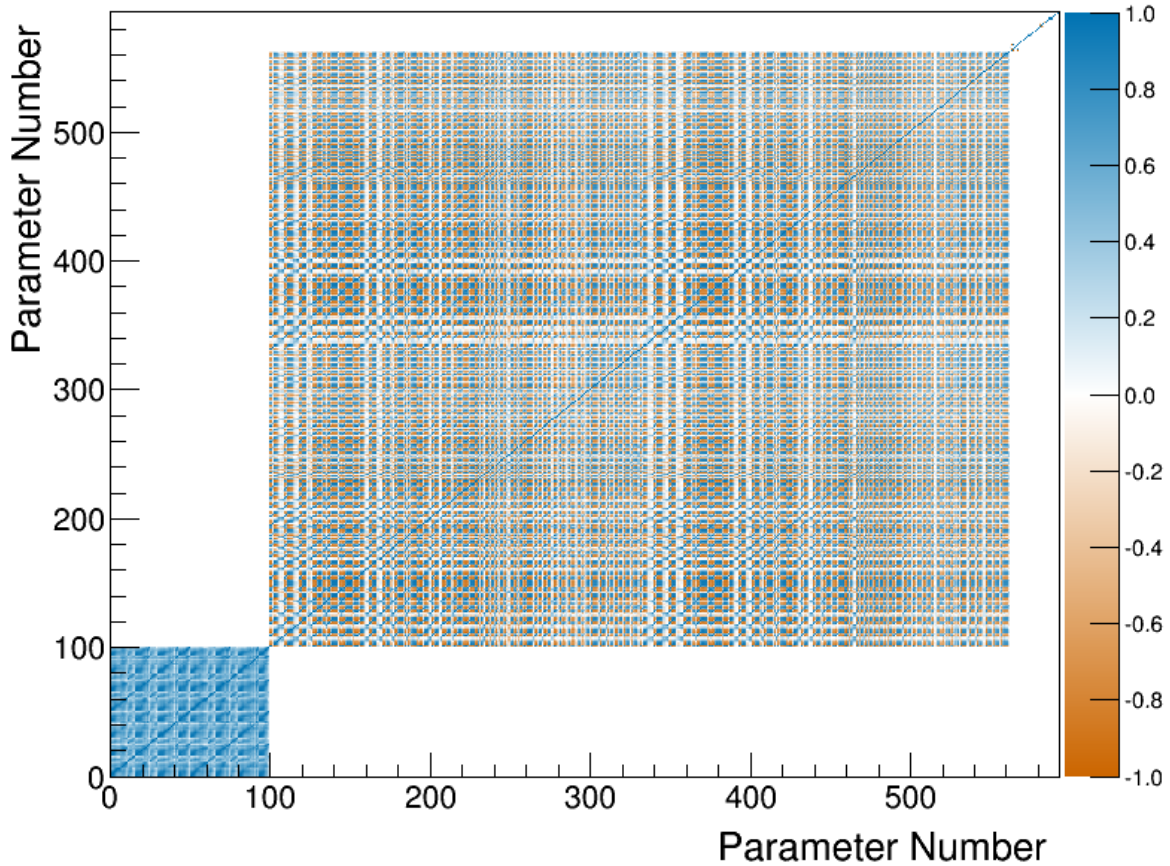


**Figure 5.1:** Complete prefit correlation matrix for the BANFF fit. The first 100 parameters are the flux bins. Between 100 and 561 are the bin normalization parameters. Finally 562 through 592 are the cross section parameters.

the same models as is implemented in the fitter and has all parameters set to their prior central values as defined in Chapter 4. Instead of statistically sampling from the MC, which can insert statistical variations into the fit, the Asimov data set is created by scaling the set down to the full T2K POT with additional finer corrections like flux and cross section weights. The prefit correlation matrix is shown in Figure 5.1 on page 140.

In addition to running an Asimov fit, other metrics were examined in the Asimov set. Shown first is a comparison of the event rates before and after applying weights to the MC. Next is an examination of the cross section weight functions. Finally is a set of scans of the

test statistic space to check that the sample and penalty terms are behaving as expected. Then the Asimov data set fit is examined.

### 5.1.1 Event Rate

Shown in Table 5.1 on page 142 are the event rates for the various samples for the Asimov fit. The data events column refers to real T2K data collected in ND280. The proceeding columns refer to MC events only after applying different weights. The POT weight is a gross normalization that scales the MC event rate to the data rate. The other weights, which were discussed in Chapter 2, are the flux, cross section, and detector corrections. As expected, we see that applying the POT weight scales the MC event rate close to that of the data. The other weights are fine tuning corrections to the rate from known systematics like flux and cross sections. The set of samples after applying all the weights is referred to as Asimov data set.

**Table 5.1:** Event rate table for Asimov set. The “Raw MC” column refers the number of events in the sample from the nominal MC prediction without any weights applied. From left to right, applications of weights are applied to understand their affect on the samples. The “POT only” column refers to applying the POT weight to all events. Columns with “POT+Flux”, “POT+xsec”, and “POT+Det” refer to applying the POT weight together with the flux, cross section, and detector weights, respectively. The “Prefit” column has the POT, flux, cross section, and detector (POT+Flux+xsec+Det) weights all multiplied together.

Sample name	Data events	Raw MC events	Application of weights				Prefit
			POT only	POT+Flux	POT+xsec	POT+Det	POT+flux+xsec+Det
$\nu_\mu$ 1-Trk Wtr	27151.00	526226.00	26270.98	28766.86	24222.45	26286.14	27327.94
$\nu_\mu$ N-Trks	31013.00	529538.00	26708.61	31464.27	26267.19	26708.74	31098.20
$\bar{\nu}_\mu$ RHC 1-Trk	8779.00	176007.00	9152.04	9365.78	8321.76	9161.91	8461.37
$\bar{\nu}_\mu$ RHC N-Trks	4613.00	93132.00	4876.93	5014.74	4652.01	4876.81	4802.12
$\nu_\mu$ RHC 1-Trk	3502.00	56861.00	2933.20	3182.20	2747.29	2938.29	3025.76
$\nu_\mu$ RHC N-Trks	5424.00	85599.00	4460.10	4988.89	4413.01	4464.45	4956.19
$\nu_\mu$ 1-Trk Air	23504.00	309373.00	23383.39	25319.17	21594.49	23402.63	23603.03
$\nu_\mu$ N-Trks	32736.00	371986.00	28495.10	33255.58	27822.42	28505.66	32302.08
$\bar{\nu}_\mu$ RHC 1-Trk	6681.00	75374.00	7374.13	7512.47	6732.25	7381.37	6767.79
$\bar{\nu}_\mu$ RHC N-Trks	4437.00	47951.00	4689.16	4820.43	4446.52	4690.57	4544.72
$\nu_\mu$ RHC 1-Trk	2324.00	20943.00	2049.01	2198.46	1916.33	2052.56	2067.12
$\nu_\mu$ RHC N-Trks	4801.00	42098.00	4119.63	4586.22	4050.71	4122.39	4567.72
Total	154965.00	2335088.00	144512.28	160475.06	137186.41	144591.53	153524.03

### 5.1.2 One Sigma Variation of Cross Section Parameters

It is difficult to predict the impact of cross section parameters variations in the BANFF fit since the fit samples contain many interaction modes themselves. In particular, a single parameter variation can also be explained by many parameters individually varied. To understand the effect of the cross section parameter variations on the fit samples, each cross section parameter was varied by  $\pm 1$  standard deviation. This also ensures the spline weight functions, which are generated for each event prior to the BANFF fit, are functioning properly. The results of the variations are shown in Appendix D.

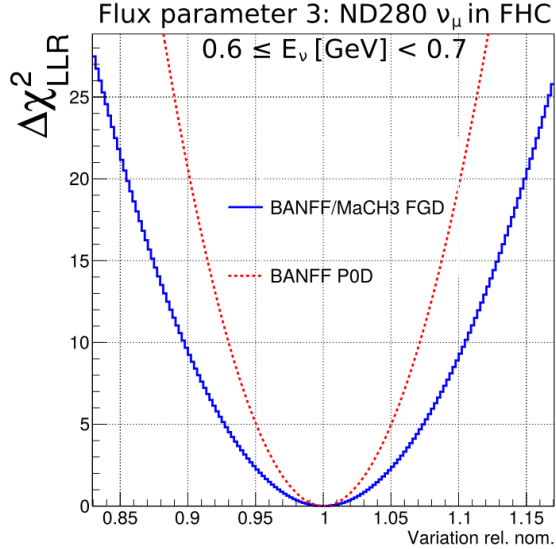
### 5.1.3 Log-Likelihood Scans

Log-likelihood scans of the sample and penalty terms were examined in the Asimov data set. The results of the scans are shown in Figure 5.2 on page 144 with comparisons between the PØD-only samples and FGD-only samples shown. It can be seen that the PØD-only data has similar sensitivity and shape dependence on the flux parameters to that of the FGD-only data. Also observed is that the penalties are the identical for both PØD- and FGD-only sets and parabolic in shape as expected since the penalties are modeled using a Gaussian. The complete set of scans is contained in Appendix E and Appendix F.

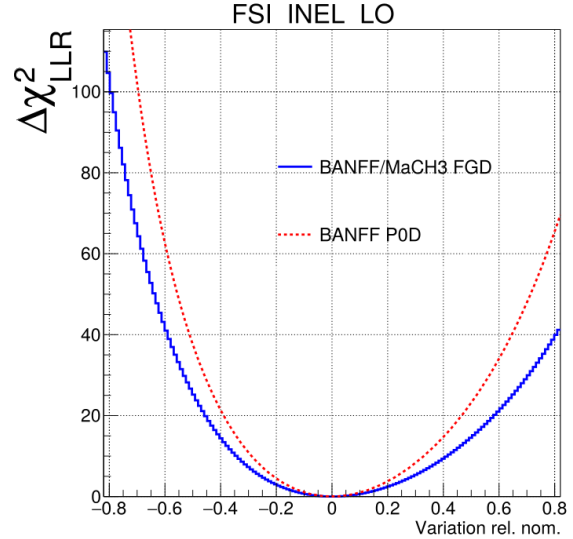
### 5.1.4 Fit Results

The postfit results of the Asimov data fit are shown from Figure 5.3 on page 145 to Figure 5.6 on page 148. In order to provide a unified graphical representation for all the parameters, the prefit and postfit cross section shape parameters are adjusted to be relative to one (1).

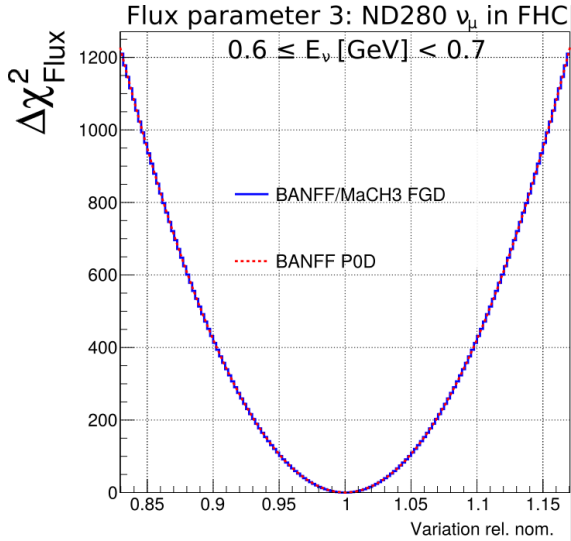
We see that the postfit parameters have uncertainties that are different compared to their prefit values. This is expected since correlations between the sub-matrices in the covariance matrix, which were assumed uncorrelated to start, have been calculated. The complete



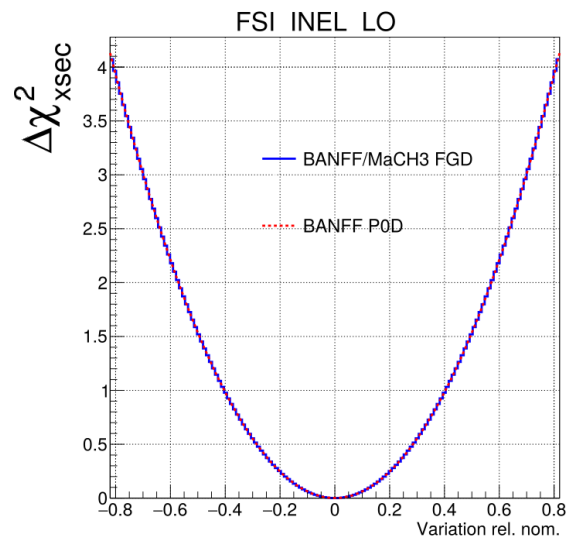
(a) Flux normalization  $b_3$   $\Delta\chi^2_{\text{LLR}}$  scan



(b) FSI low energy inelastic shape location  $\Delta\chi^2_{\text{LLR}}$  scan



(c) Flux normalization  $b_3$   $\Delta\chi^2_{\text{Flux}}$  scan



(d) FSI low energy inelastic shape location  $\Delta\chi^2_{\text{xsec}}$  scan

**Figure 5.2:** Comparison of  $\Delta\chi^2$  scans for variations in fit parameters in the Asimov set. Two parameters are varied: parameter 3 (left) corresponding to a flux bin normalization and 562 (right) corresponding to a FSI shape location parameter. The top panel shows the change in the LLR test statistic  $\Delta\chi^2_{\text{LLR}}$  while the bottom panel shows the penalty terms. In all sub-figures are comparisons between the BANFF/MaCH3 FGD 2017 results [6] against the BANFF P0D-only results. Special thanks goes to Clarence Wret (c.wret@rochester.edu) of the University of Rochester for generating the plots.

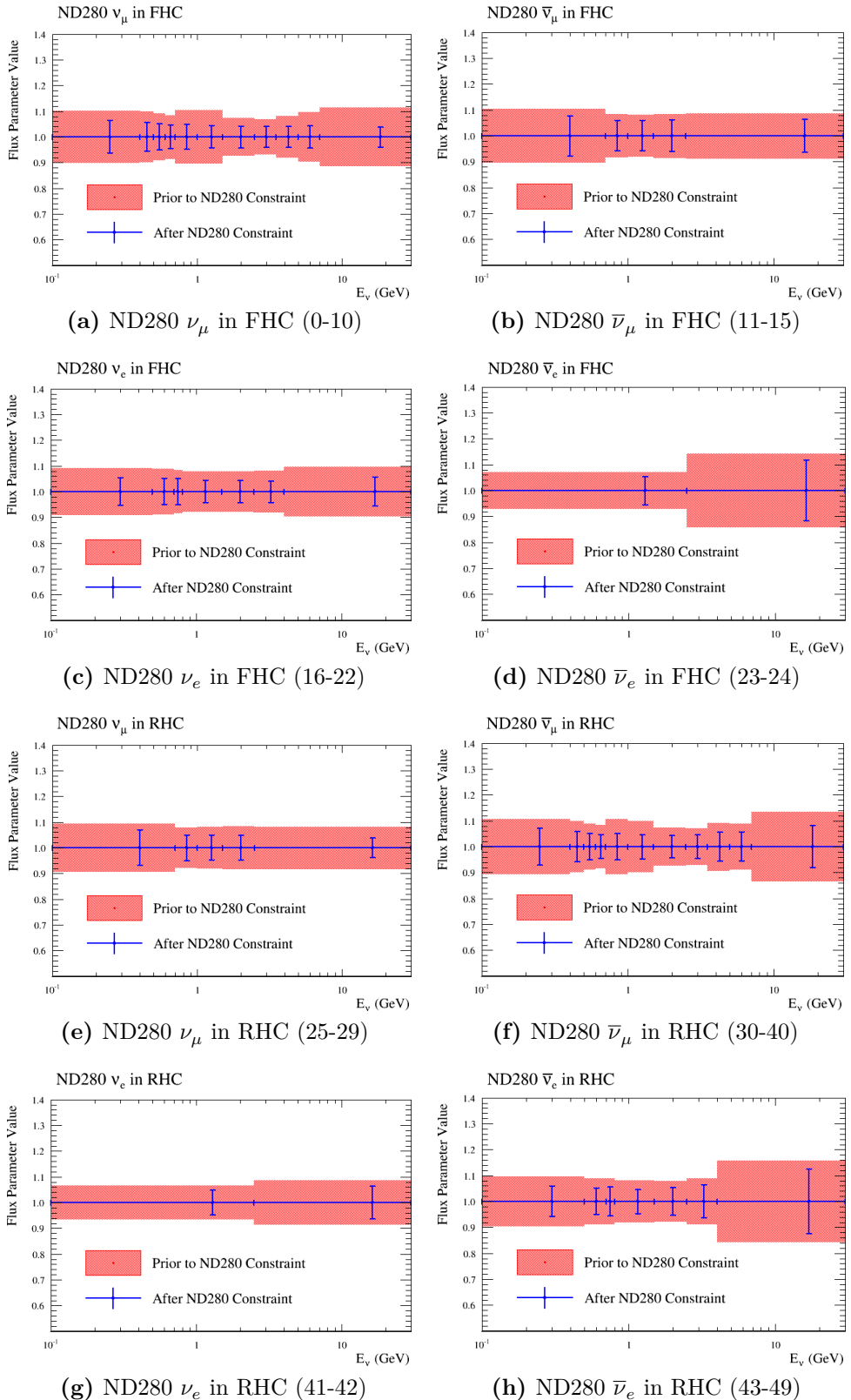


**Figure 5.3:** Asimov fit results for the Flux at ND280. The numbers in parentheses indicate the fit indices.

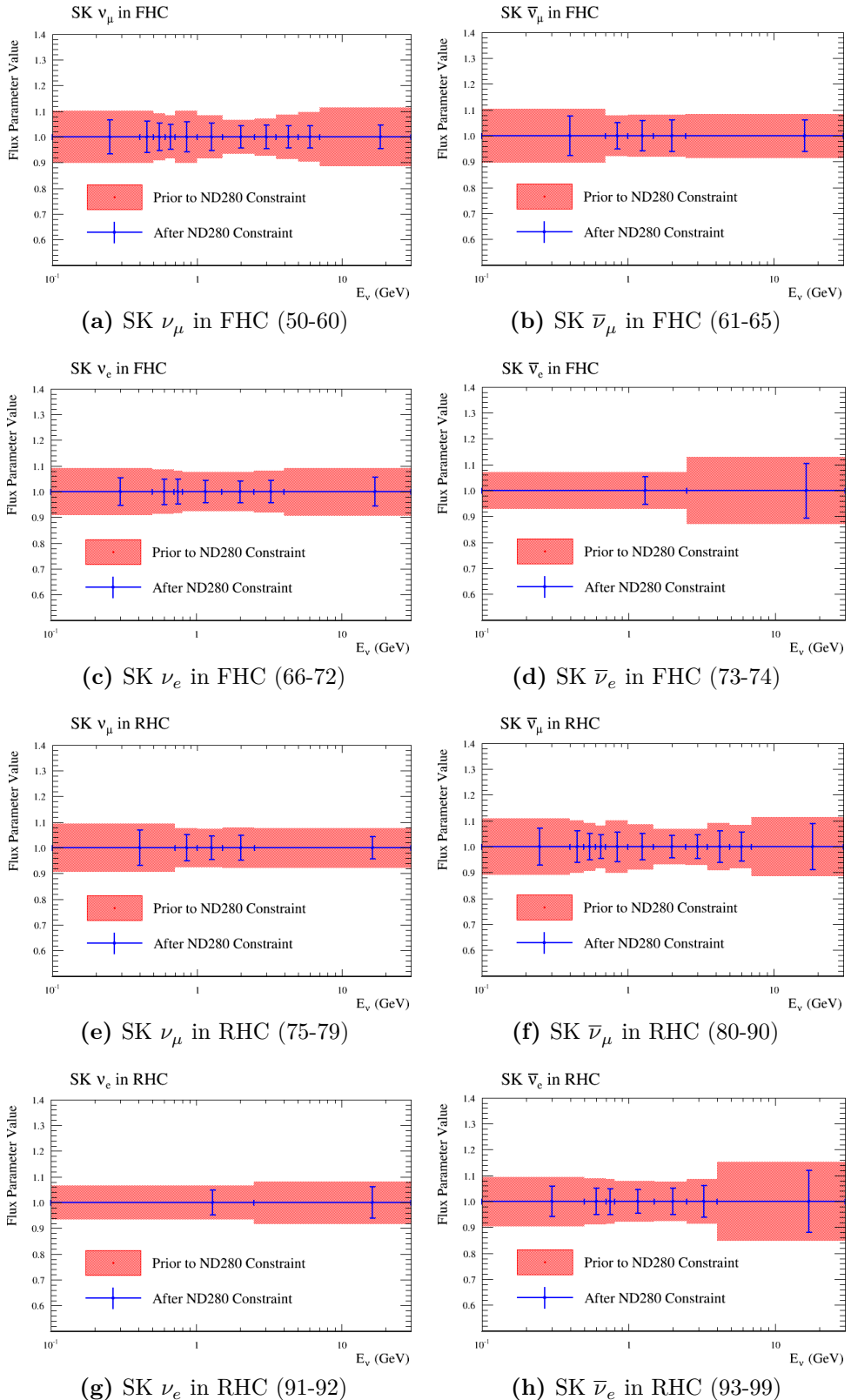


**Figure 5.4:** Asimov fit results for the Flux at Super-K. The numbers in parentheses indicate the fit indices .

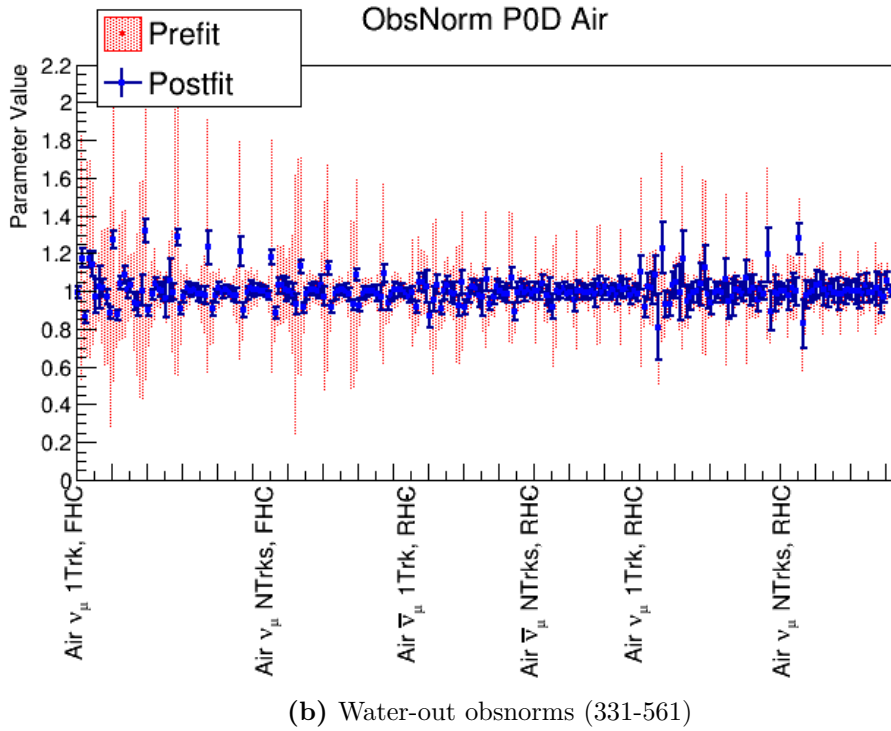
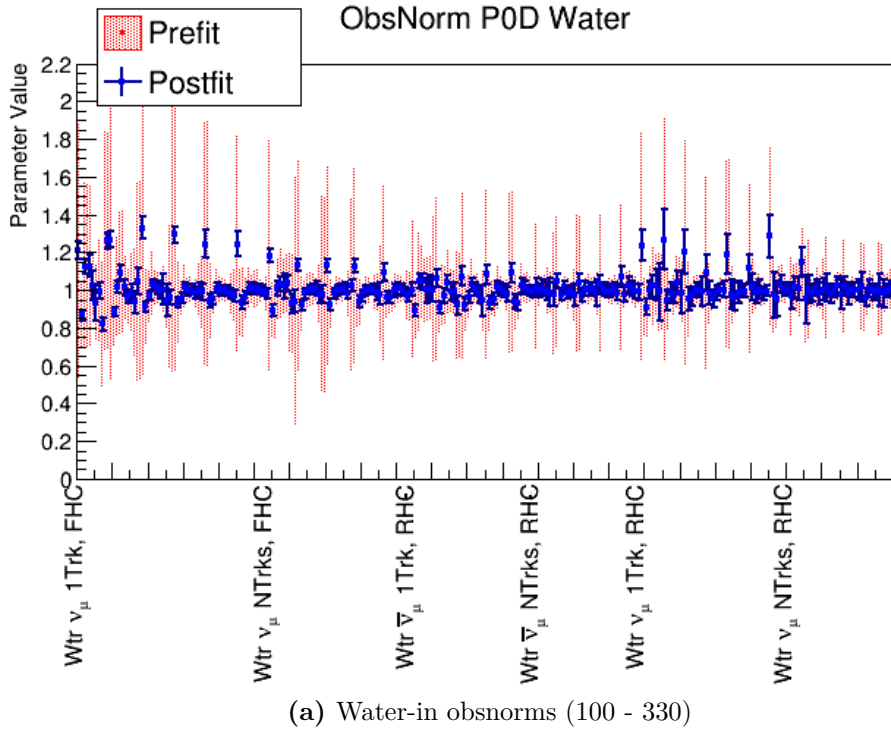
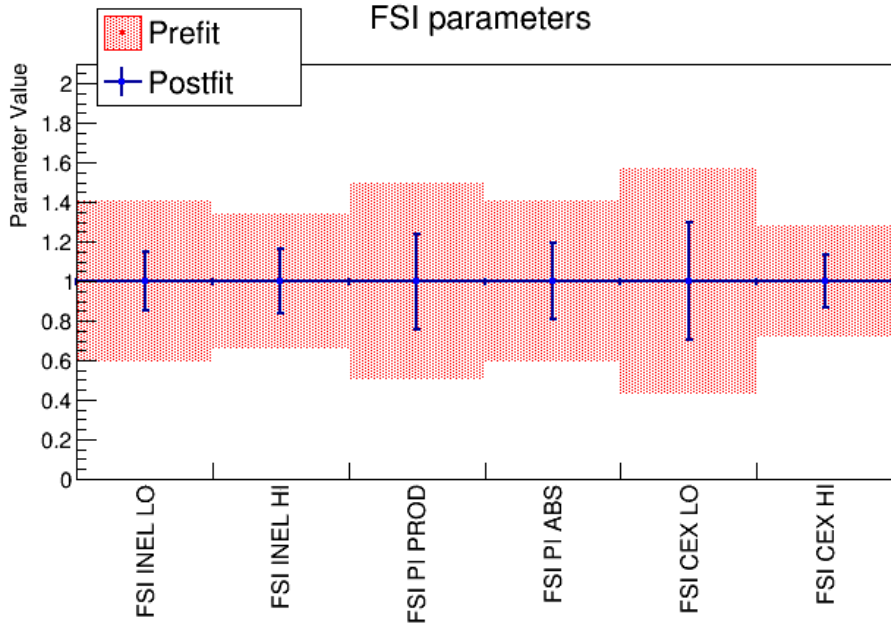
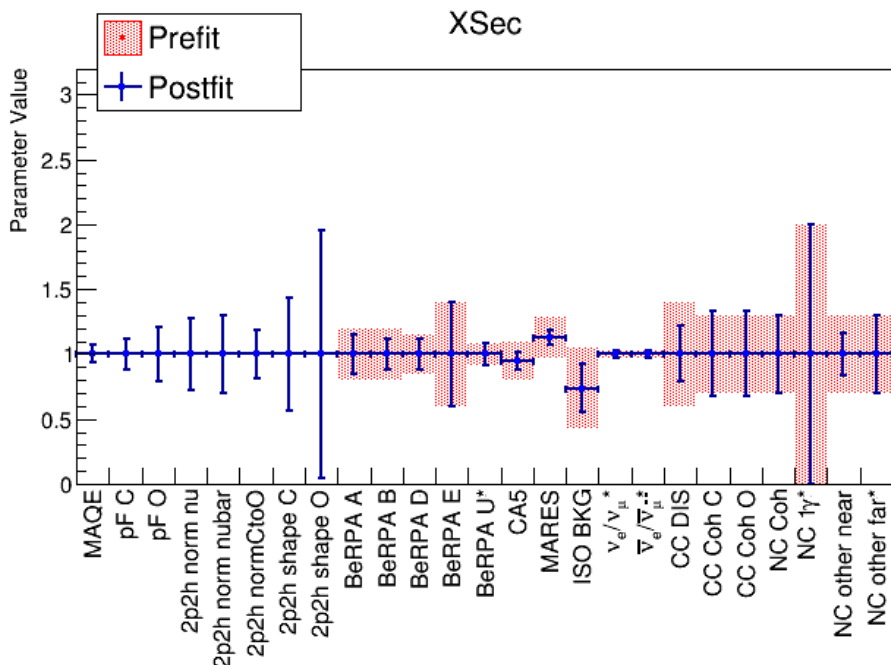


**Figure 5.5:** Asimov fit results for the obsnorm parameters. The numbers in parentheses indicate the fit indices. The large jumps in the bin normalization parameters is an artifact of the indexing choice with the indices increasing in increasing momentum in constant angular slices. Compare the changes in the bin normalizations in the  $\nu_\mu$  in FHC Mode CC 1-Track in Figure 4.6 on page 120.



(a) FSI (562-567)



(b) Cross Section (568-592)

**Figure 5.6:** Asimov fit results for the FSI and cross section parameters. The numbers in parentheses indicate the fit indices. In order to provide a consistent presentation of parameter changes between prefit and postfit among all parameters, shape location and scale parameters are adjusted to prefits of one (1). In effect, the value and uncertainties for all parameters are fractional changes.

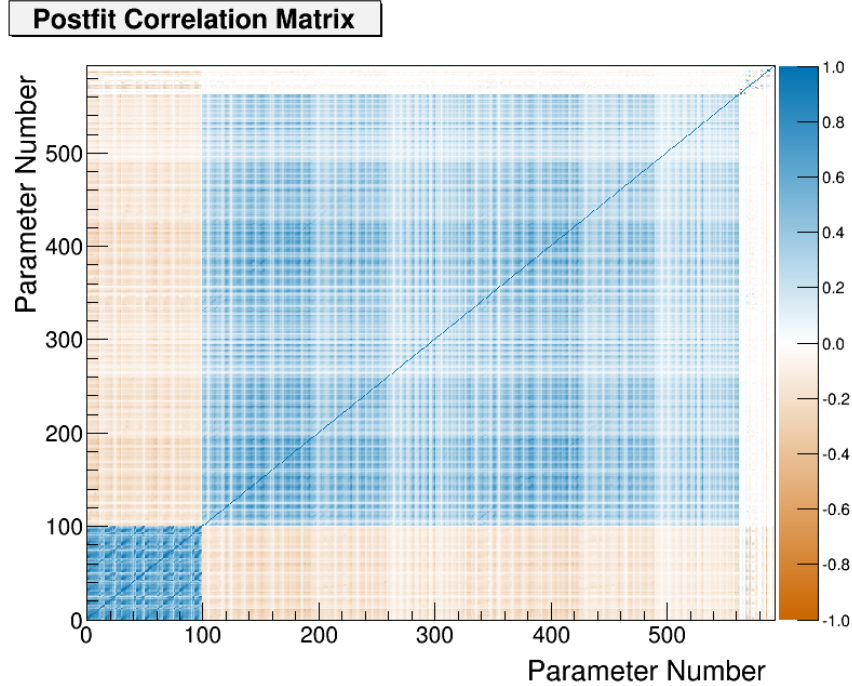


**Figure 5.7:** Complete postfit correlation matrix for the Asimov data fit.

postfit correlation matrix is shown in Figure 5.7 on page 149 and the flux and cross section only correlation matrix is shown in Figure 5.8 on page 150. We observe significant anti-correlations between each of the sub-matrices, which is predicted from Eqn. (2.7) since any increase in one parameter weight forces a decrease in the others.

## 5.2 Fake Data Fits

In this section, we examine the results of BANFF fits when given data sets with non-physical alterations. As stated earlier, these are called fake data sets since we are treating these as data in the fit. The fake data sets initially start as the Asimov data set and have variations applied to them. Here we are only interested in varying the flux and cross section parameters since they are the parameters that are propagated to the oscillation analysis. There were two fake data sets generated for the tests. One data set varies the neutrino flux in a single flux bin and the other varies the single pion production rate.

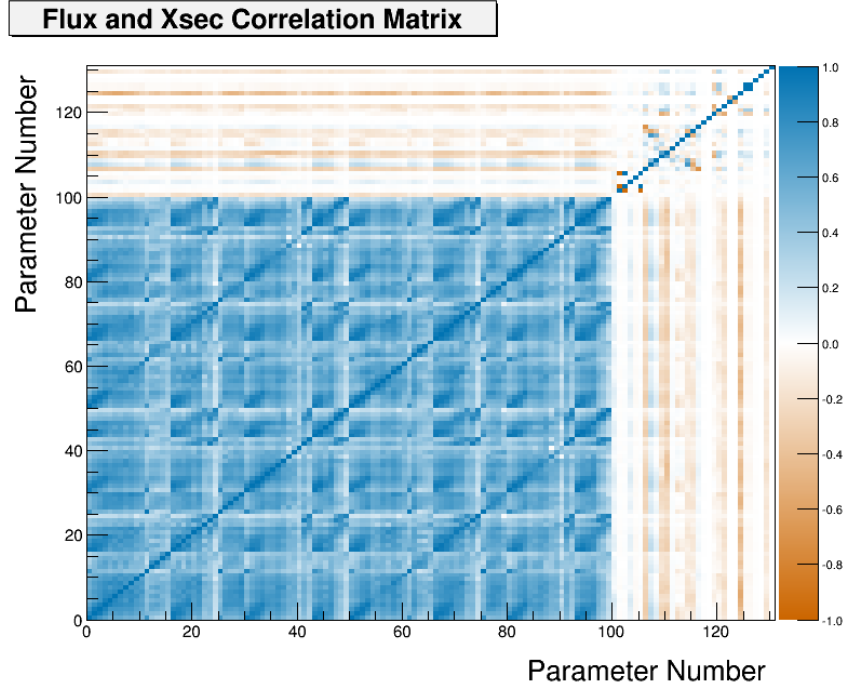


**Figure 5.8:** Flux and cross section postfit correlation matrix for the Asimov data fit. The parameters from 1-100 are the flux parameters and all parameters after are the cross section.

While other fake data sets could be generated that are more or less similar to the Asimov data set, that is not the purpose of fitting to fake data sets. *The purpose of these tests is to show the fit can converge when provided with non-Asimov data sets and we can understand the results.* It is known in the BANFF group that the BANFF fitting software is not guaranteed to converge on a global minimum when using altered Asimov data. In particular, fitting FGD-only data generated from random and uncorrelated variations of all fit flux, cross section, and bin normalization parameters, 127 out of 500 fits ( $\sim 25\%$ ) reported fit convergence problems. So convergence is not assured in all situations, but is possible. We can establish that a credible PØD-only real data fit result is possible by demonstrating 1) the BANFF fit converges with PØD-only fake data and 2) that we can sensibly understand those fit results.

The information provided from fake data tests is also useful to understand possible biases in the fit results. For instance, since the PØD samples have a relatively low sensitivity to CC- $1\pi$  interactions, real differences between data and MC could be explained by variations in non CC- $1\pi$  model parameters. We will get a sense of the biases in the following two fake

data tests. The first fake data test analyzed is referred to as the “High Energy Neutrino Flux Variation” which varies the high energy  $\nu_\mu$  flux in FHC mode. The following fake data test is referred to as the “Single Pion Event Rate Variation” which alters the single pion production event rate uniformly.

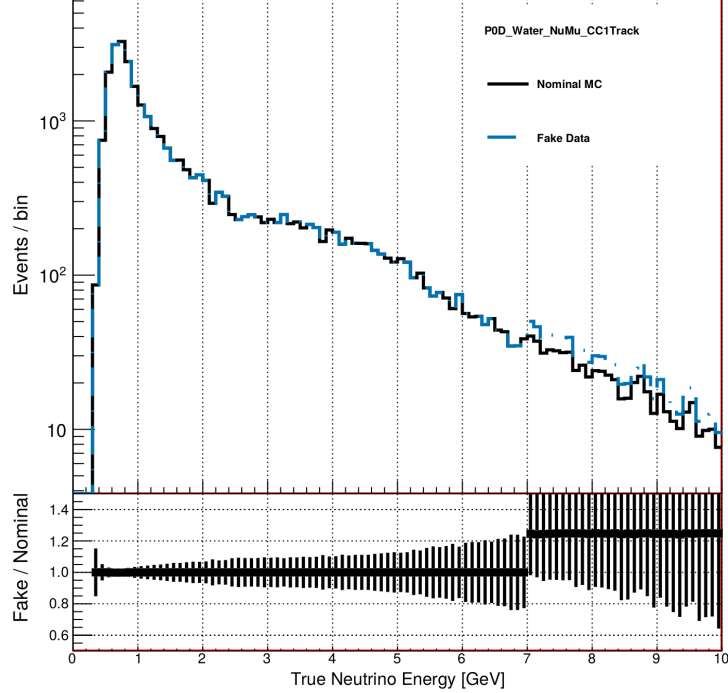
### 5.2.1 High Energy Neutrino Flux Variation

This fake data set is almost identical to the Asimov data set except an arbitrarily large increase in the  $\nu_\mu$  flux between 7 and 30 GeV by +25% in FHC mode only. This variation was chosen since this energy range corresponds precisely to flux parameter  $b_{10}$  and it could affect all analysis bins. The true neutrino energy distribution of the fake data used in this study is shown in Figure 5.9 on page 152 and Figure 5.10 on page 153.

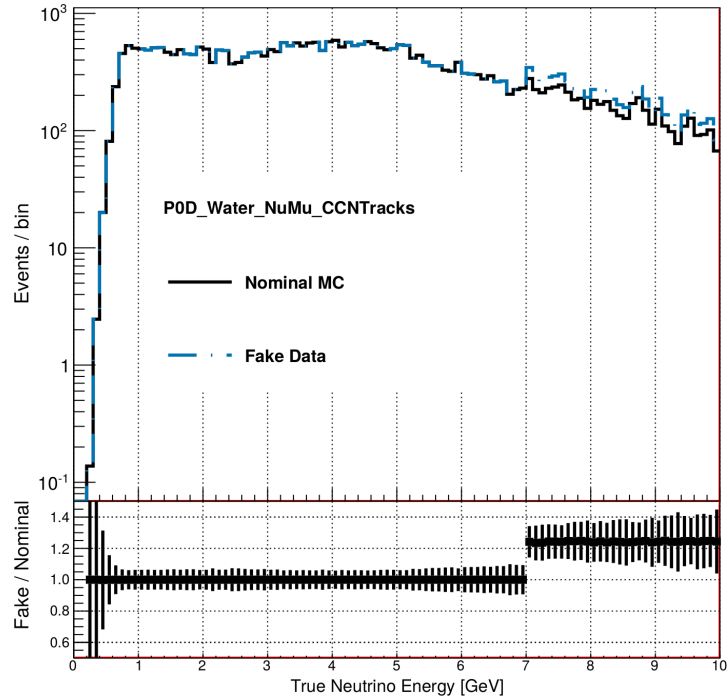
The postfit parameter plots are shown in Figure 5.11 on page 154. We see that the target flux parameter  $b_{10}$  has significantly increased from its prefit value by almost +20%. However, due to correlations in the flux covariance matrix, other flux parameters have also changed. The BANFF fit prefers to increase the previous energy flux parameter and the high energy  $\nu_e$  flux parameters as well. While we saw that the flux and hence event rate was not changed in the RHC samples, the RHC flux parameters are also slightly affected. However, the RHC flux parameters are still well within prefit uncertainties. The statement is true for the cross section and FSI parameters. We can conclude from this study that the fit will resolve large, nonphysical differences between the Asimov prediction and the data with many correlated parameter variations.

### 5.2.2 Single Pion Event Rate Variation

This fake data set is very similar to the Asimov set except for a +25% increase in the number of resonant single pion events in all analysis samples. This was implemented by taking all true NEUT CC- $1\pi$  events, extracting the event weight, and increasing it by



(a) The  $\nu_\mu$  in FHC Mode CC 1-Track sample



(b) The  $\nu_\mu$  in FHC Mode CC N-Tracks sample

**Figure 5.9:** Neutrino energy distributions in the High Energy Neutrino Flux variation fake data set. The fake data (dashed-blue) is nearly identical to the Asimov set (black) except the +25% increase in the  $\nu_\mu$  in FHC mode rate at energies greater than 7 GeV. In the figures, “Nominal MC” refers to the Asimov prediction and “Fake Data” is the altered data set. The ratio of the fake data to the nominal MC is shown below each histogram with the errors being statistical only.

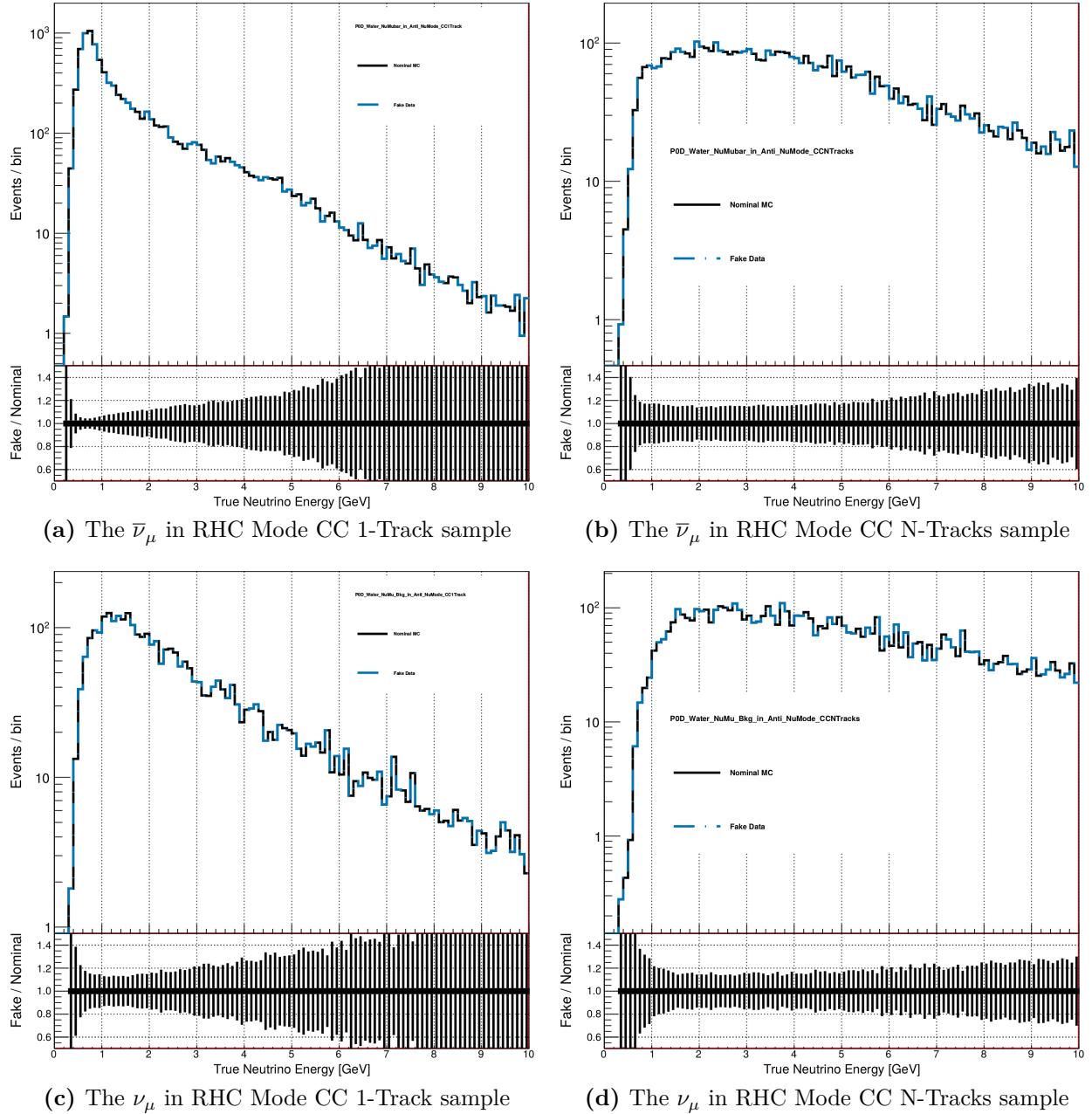
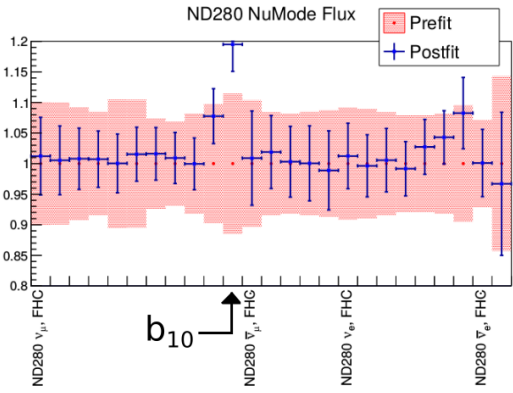
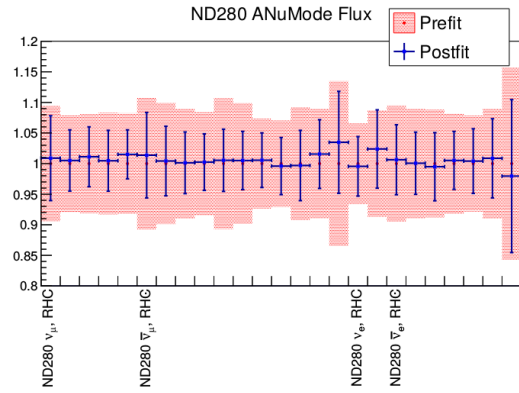


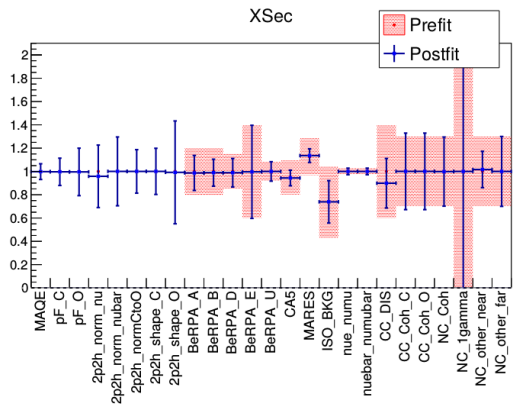
**Figure 5.10:** Neutrino energy distributions in the High Energy Neutrino Flux variation fake data set (continued). The fake data (dashed-blue) is nearly identical to the Asimov set (black) except the +25% increase in the  $\nu_\mu$  in FHC mode rate at energies greater than 7 GeV. In the figures, “Nominal MC” refers to the Asimov prediction and “Fake Data” is the altered data set. The ratio of the fake data to the nominal MC is shown below each histogram with the errors being statistical only.



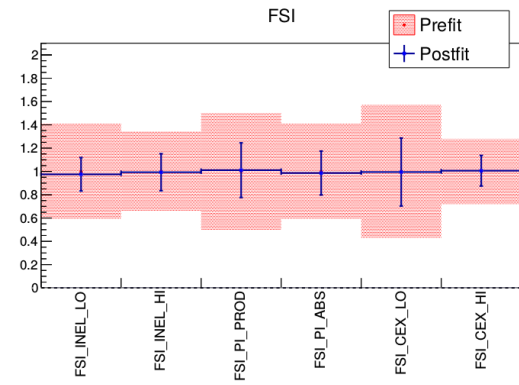
(a) The ND280 FHC mode flux parameters



(b) The ND280 RHC mode flux parameters



(c) Cross section parameters



(d) The FSI parameters

**Figure 5.11:** Postfit parameters for the high energy  $\nu_\mu$  in FHC flux variation fake data fit. All the flux parameters in FHC are shown together and ordered sequentially from left to right. The same is true the RHC flux.

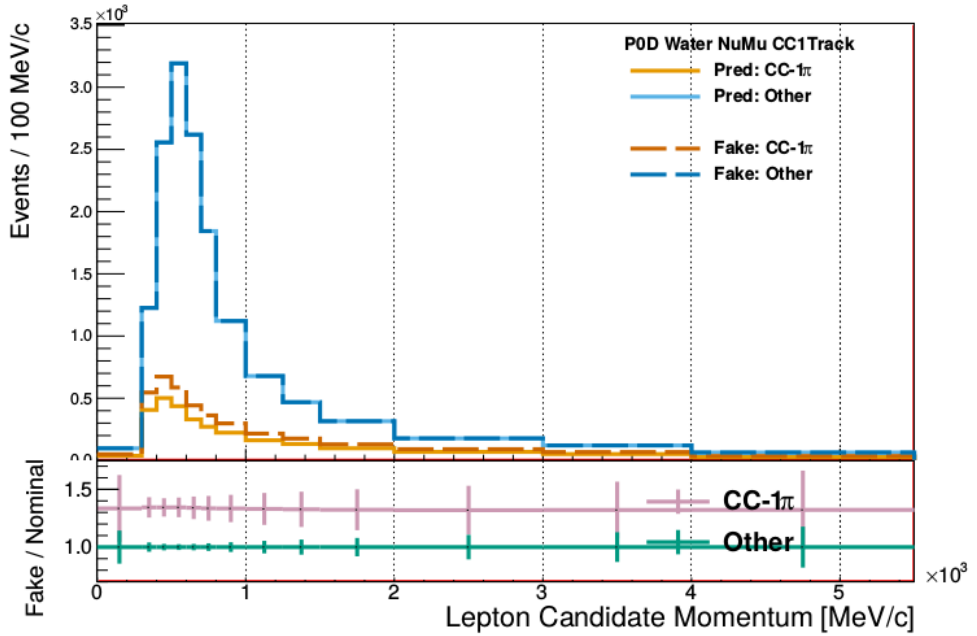
+25%. This is what is observed in the lepton candidate momentum distributions as shown in Figure 5.12 on page 156 and Figure 5.13 on page 157.

This fake data test will help us understand the BANFF fit response due to poor data matching with a cross section model. The ideal result of this test is that the postfit value of  $C_A^5$  is increased by +25% and all other parameters are unchanged like the results seen in Appendix D. However, this is not a realistic expectation given that there are no dedicated CC- $1\pi$  samples, thus the sensitivity to CC- $1\pi$  parameters is expected to be small. In particular, the  $C_A^5$  and  $M_A^{\text{Res}}$  parameters are strongly anticorrelated with one another, meaning that these parameters will be forced to shift in opposite directions. From our intuition gained in the first fake data fit, we can expect non-CC- $1\pi$  parameters to vary especially groups of flux parameters together.

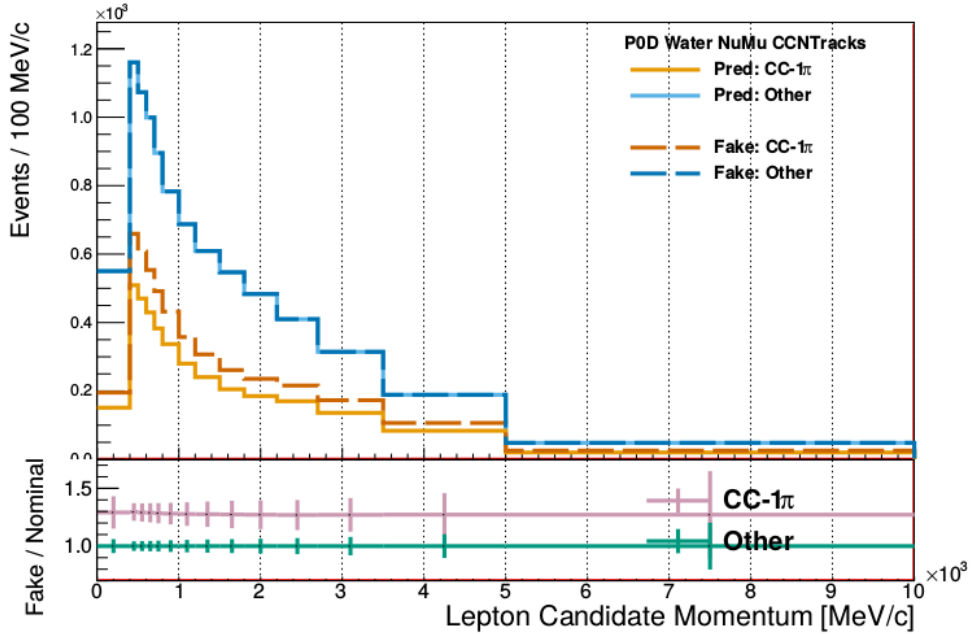
The postfit results for this fake data set are shown in Figure 5.14 on page 158. We observe that the CC- $1\pi$  parameter  $C_A^5$  increased by  $\sim 10\%$ , but this is not enough to account for the input fake data shift. We also notice that due to anticorrelations,  $M_A^{\text{Res}}$  was decreased by several percent. What the fit prefers is to increase the isospin= $1/2$  background, 2p2h normalization, and all the flux parameters. As seen in the first fake data set, we see that in the presence of nonphysical variations to the physics, the fit prefers to spread out variations among the other parameters. However, this time the variations are shared among both the flux and cross section parameters.

## 5.3 Summary

We have validated that the BANFF fit works and tested its robustness in a variety of scenarios. We learned from the Asimov data set, which is the T2K nominal MC corrected to data POT with fine tuning corrections, in particular how the flux and cross section parameters affect the samples. In the fake data sets, we saw the effect of the penalty terms and how their correlations influence the fit. While more rigorous tests could establish where



(a) The  $\nu_\mu$  in FHC Mode CC 1-Track sample



(b)  $\nu_\mu$  in FHC Mode CC N-Tracks

**Figure 5.12:** Lepton candidate momentum distributions in the Single Pion Event Rate Variation fake data set. The nominal MC and fake data predictions are shown as solid and dashed lines, respectively. True CC-1 $\pi$  events are differentiated from all other interactions to illustrate the event scaling applied. A ratio plot of CC-1 $\pi$  events to all other interaction events shown beneath each main histogram.

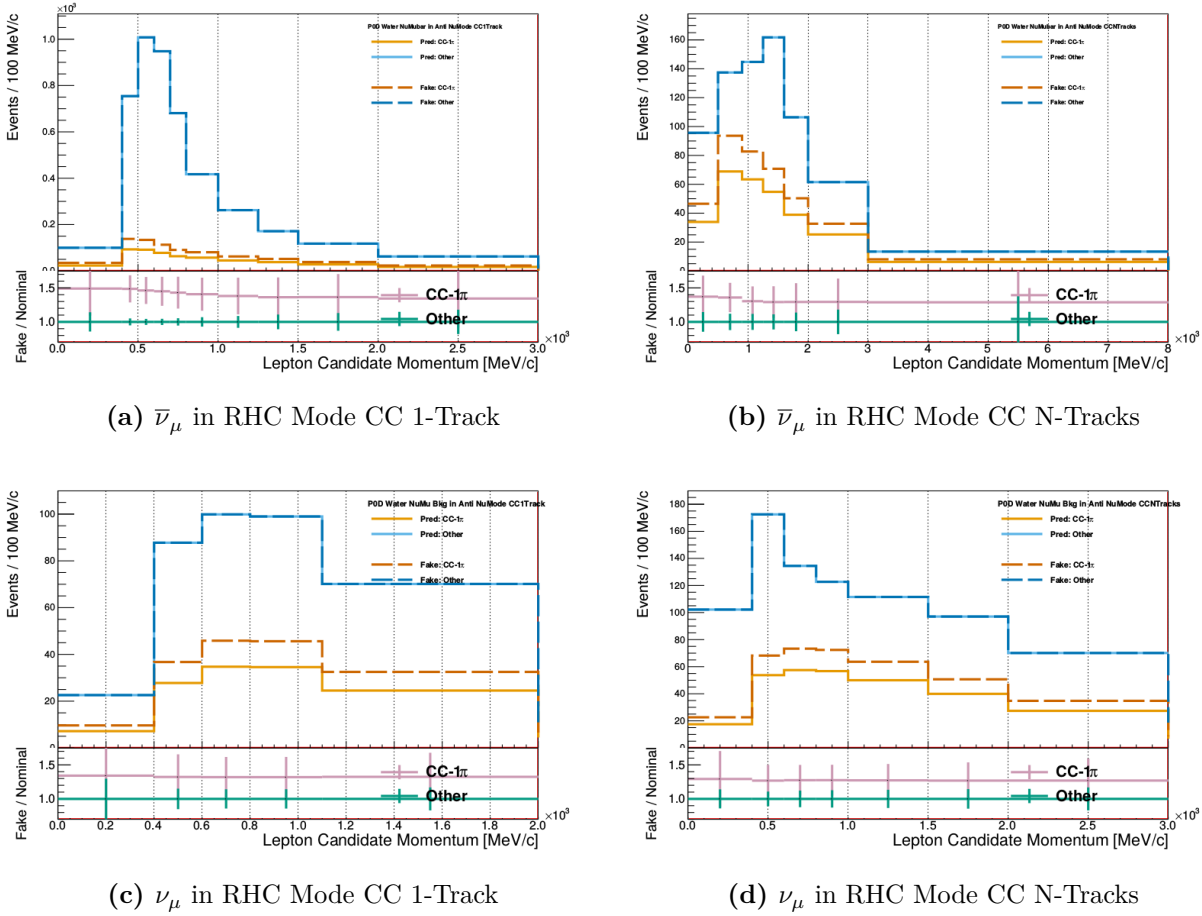


**Figure 5.13:** Lepton candidate momentum distributions in the Single Pion Event Rate Variation fake data set (continued). The nominal MC and fake data predictions are shown as solid and dashed lines, respectively. True CC-1 $\pi$  events are differentiated from all other interactions to illustrate the event scaling applied. A ratio plot of CC-1 $\pi$  events to all other interaction events shown beneath each main histogram.

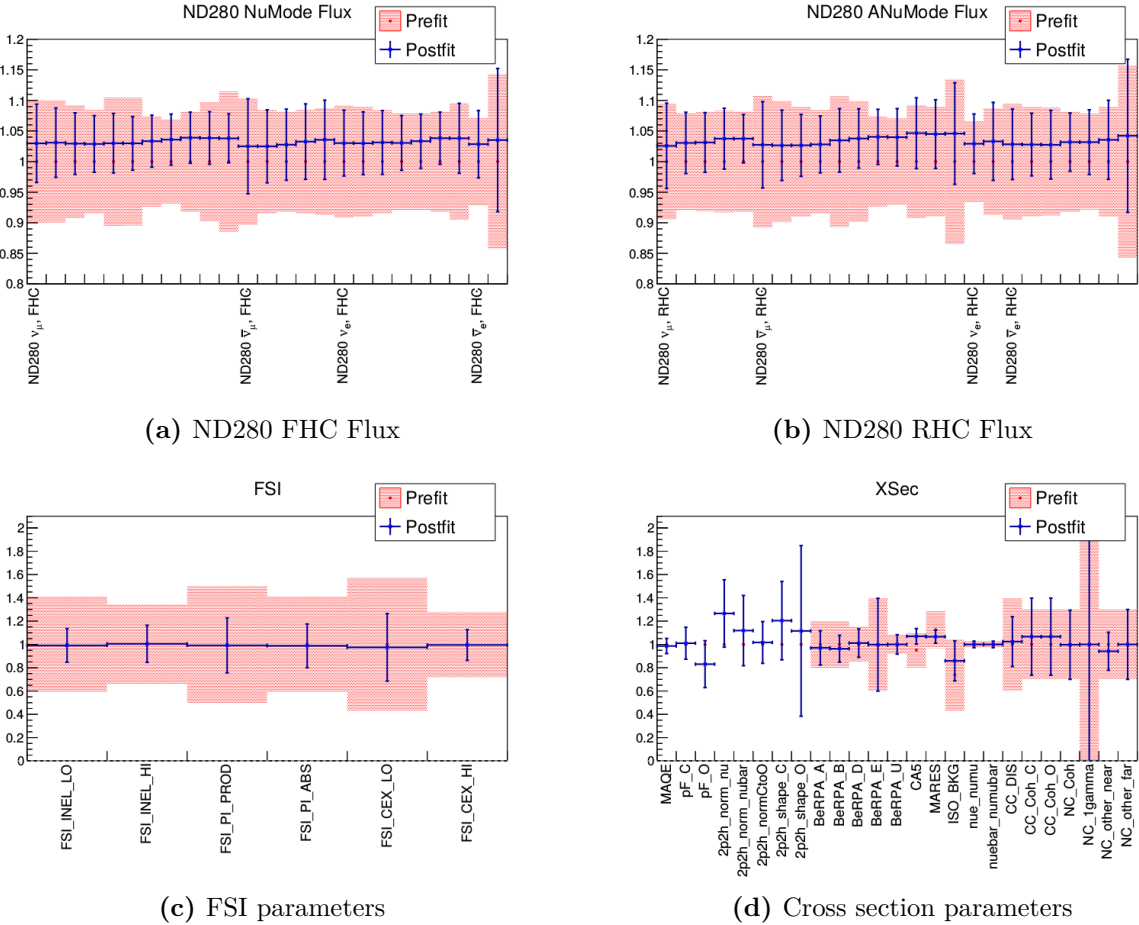


**Figure 5.14:** Postfit parameters for the Single Pion Event Rate Variation fake data fit. All the flux parameters in FHC are shown together and ordered sequentially from left to right. The same is true the RHC flux.

biases exist, these limitations are beyond the scope of this thesis. What has been established is that sensible fit results using the PØD selections are possible. We will now use the real PØD data in the BANFF fit.

# Chapter 6

## Results of the BANFF Fit Using the PØD Samples

This chapter explores the results of performing the BANFF fit using the PØD-only samples. We have confirmed that the fit machinery is working and that the samples demonstrate sensitivity to flux and cross section parameters. The focus in this chapter is to examine the results of the PØD-only data fit and compare it against the FGD-only result.

The chapter will proceed in the following order. First, since we have remained purposefully blind up to this state in the analysis, the data will be examined in Section 6.1. Next the postfit results will be carefully examined and compared with that of the FGD-only fit in Section 6.2. A hypothesis test is performed to qualify the level of agreement between the two fits in Section 6.3. Finally, a chapter summary is provided in Section 6.4.

### 6.1 Prefit Sample Distributions

This section presents the first look at the data for the 12 samples according to the fit bins set in Chapter 4. The samples are categorized into four true interaction modes as described earlier:  $\nu$  CCQE,  $\nu$  non-CCQE,  $\bar{\nu}$  CCQE, and  $\bar{\nu}$  non-CCQE. However, true fiducial volume (FV) and out of FV events are not differentiated in this case. The prefit samples with the

data shown are presented between Figure 6.1 on page 162 and Figure 6.12 on page 173. First the water-in samples are displayed, and then the water-out samples are shown. As we saw before, the water-in and water-out samples are qualitatively the same.

In general, we notice good agreement between the data and prefit distributions. Their agreement is represented in one-dimensional profiles with the data to prefit ratio shown below the histograms. Evidence of the PØD bulging effect in the most downstream layers can be seen in all water-in samples. In particular, since there is more true mass in the most downstream layers, particles with lower momenta are more likely to enter the TPC than predicted by the MC using the as-built mass. Better agreement is observed in the water-out periods, but there is some data tension.

## 6.2 Postfit Results

The results of the PØD-only BANFF fit are presented here. Starting with an initial test statistic of  $\chi^2_{\text{ND}280} = 3022.2$ , the MINUIT optimization routine required 149661 iterations to find the global minimum at  $\hat{\chi}^2_{\text{ND}280} = 1412.28$ . An additional 176000 iterations were required to calculate the Hessian matrix. The computing resources used for the fit are presented in Appendix Chapter G.

Specific topics on the postfit results are presented in the following order. First is an examination of the postfit samples in one-dimensional profiles and two-dimensional spaces. Next is a comparison of the parameter values among the prefit, PØD-only, and FGD-only results. And the final topic is a hypothesis test on the level of agreement between the PØD-only and FGD-only BANFF fit results.

### 6.2.1 Postfit Sample Distributions

Presented below are the 12 samples again, but with the parameters extracted from the fit applied to the fit bins. This ensures that we have a) not altered the data, and b) that the

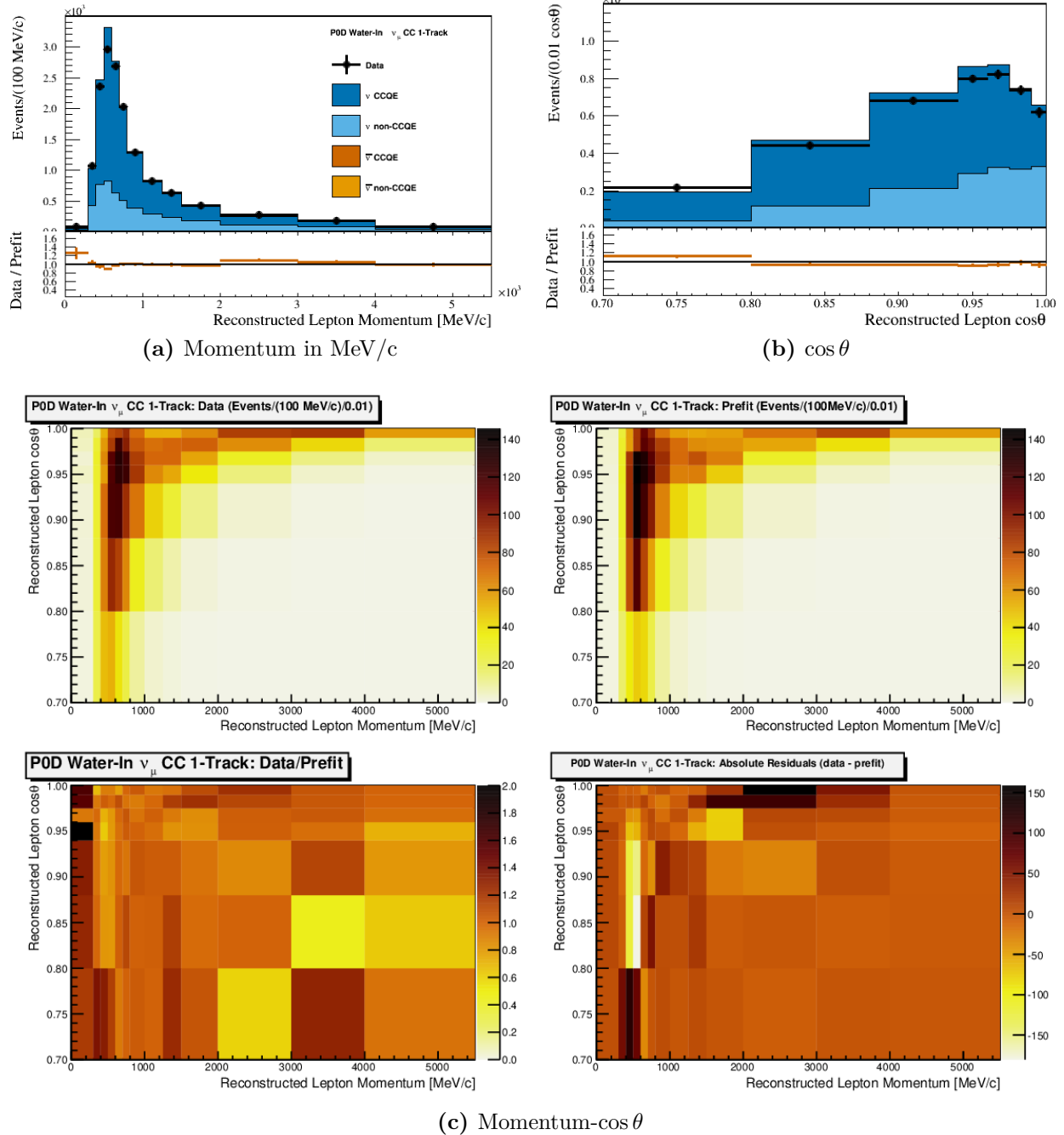


**Figure 6.1:** Data and prefit expectation for the PØD Water-In  $\nu_\mu$  in FHC Mode CC 1-Track sample. Sub-figure (a) shows the momentum one-dimensional profile in all but the highest momentum fit bin. Sub-figure (b) shows the  $\cos \theta$  one-dimensional profile in all but the highest angle fit bin. Shown in both (a) and (b) is the ratio between data and the prefit value. Sub-figure (c) shows a grid of two-dimensional data and prefit distributions in the same phase space as (a) and (b). Moving from top-left to bottom-right in (c) is the data, prefit, data to prefit ratio, and data to prefit difference.

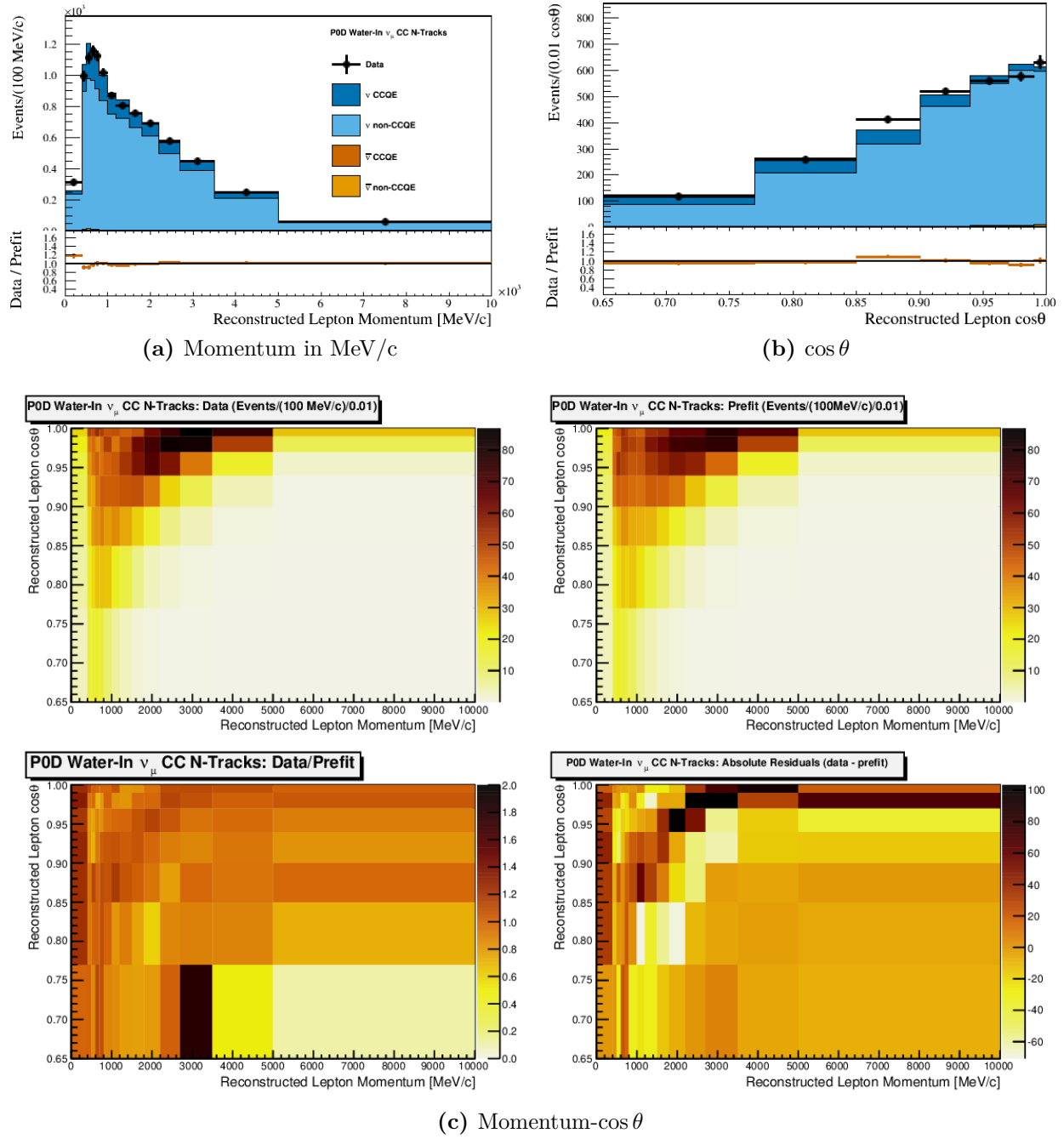


**Figure 6.2:** Data and prefit expectation for the PØD Water-In  $\nu_\mu$  in FHC Mode CC N-Tracks sample. Sub-figure (a) shows the momentum one-dimensional profile in all but the highest momentum fit bin. Sub-figure (b) shows the  $\cos\theta$  one-dimensional profile in all but the highest angle fit bin. Shown in both (a) and (b) is the ratio between data and the prefit value. Sub-figure (c) shows a grid of two-dimensional data and prefit distributions in the same phase space as (a) and (b). Moving from top-left to bottom-right in (c) is the data, prefit, data to prefit ratio, and data to prefit difference.

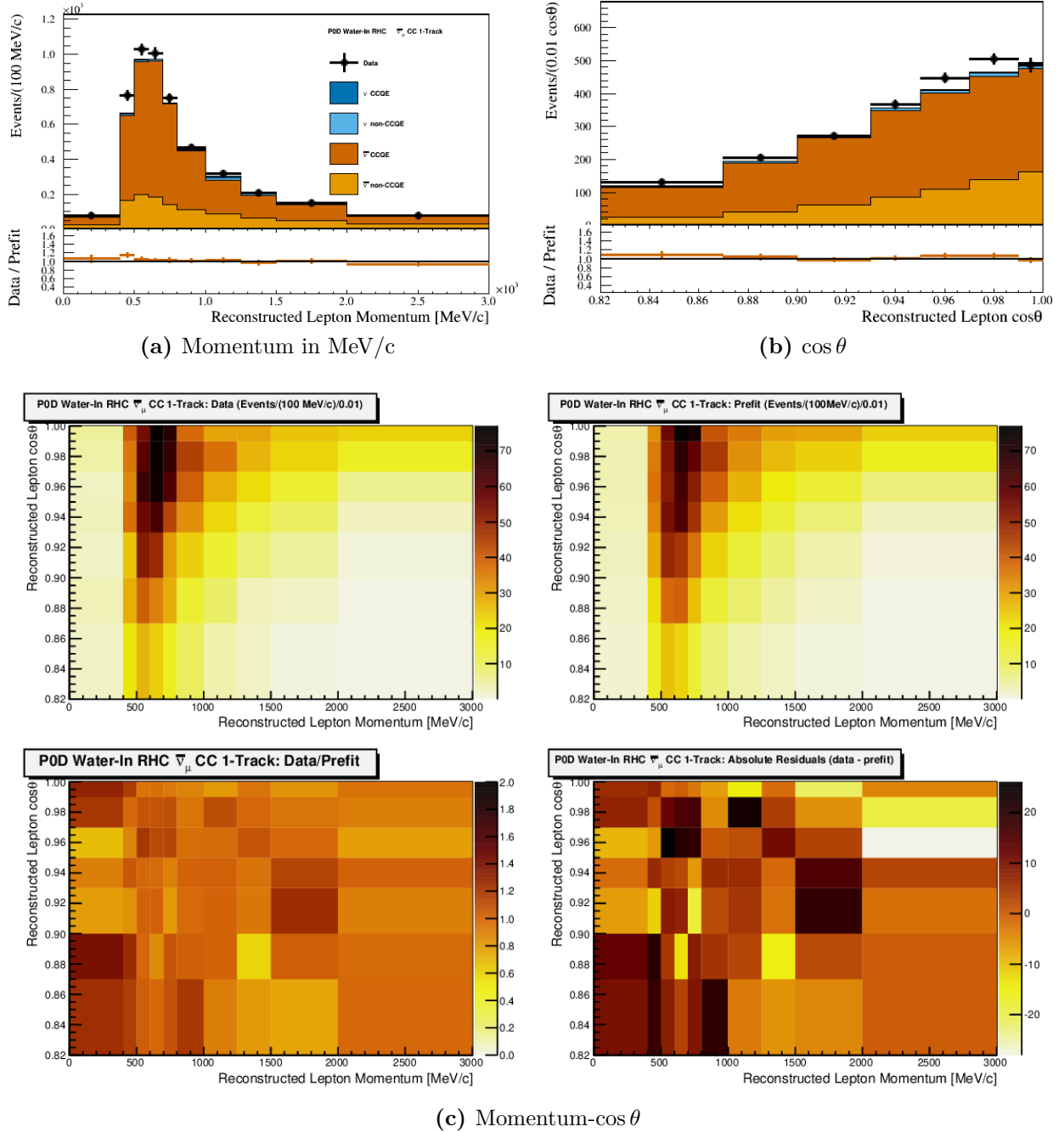


**Figure 6.3:** Data and prefit expectation for the PØD Water-In  $\bar{\nu}_\mu$  in RHC Mode CC 1-Track sample. Sub-figure (a) shows the momentum one-dimensional profile in all but the highest momentum fit bin. Sub-figure (b) shows the  $\cos\theta$  one-dimensional profile in all but the highest angle fit bin. Shown in both (a) and (b) is the ratio between data and the prefit value. Sub-figure (c) shows a grid of two-dimensional data and prefit distributions in the same phase space as (a) and (b). Moving from top-left to bottom-right in (c) is the data, prefit, data to prefit ratio, and data to prefit difference.

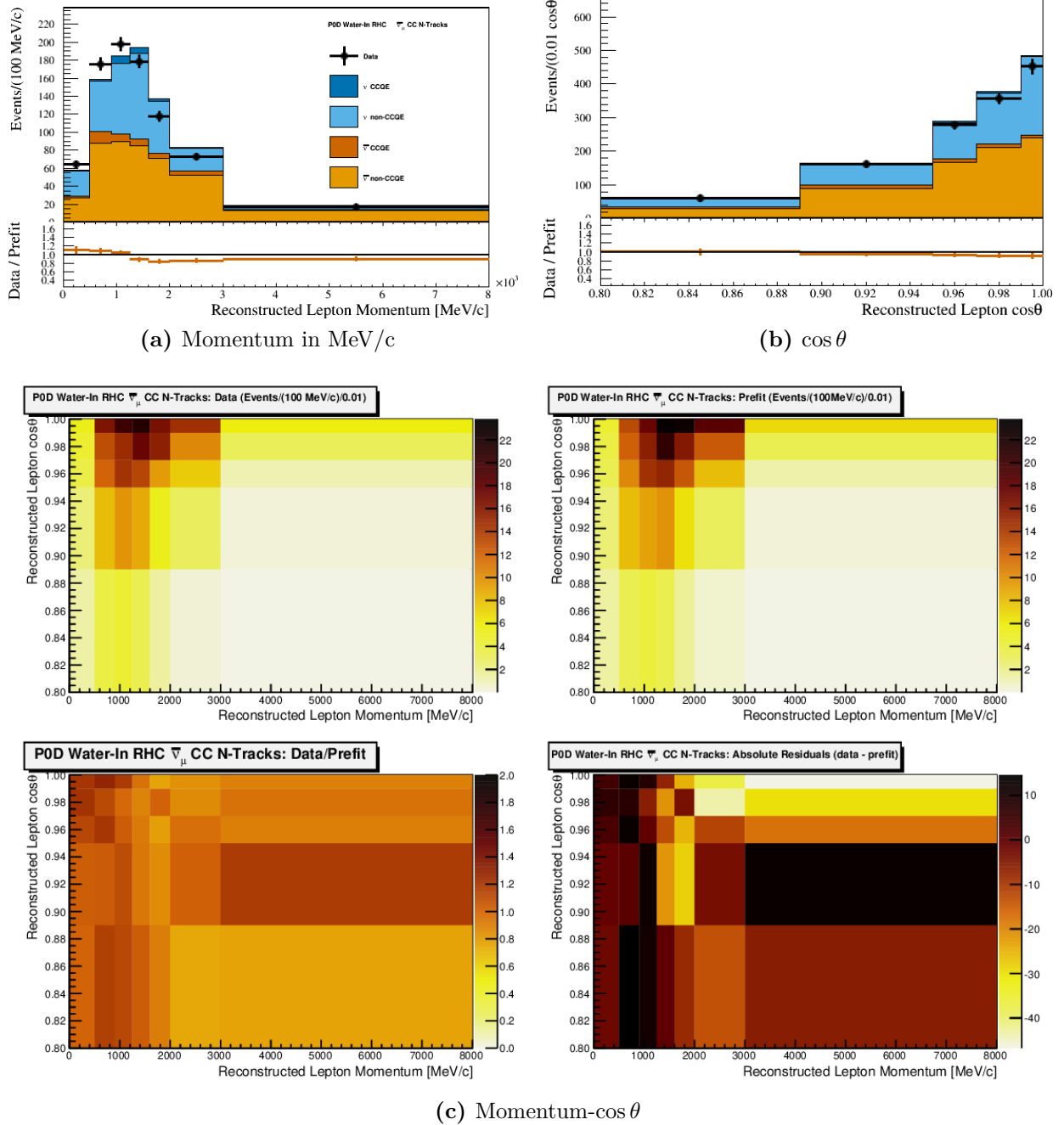


**Figure 6.4:** Data and prefit expectation for the PØD Water-In  $\bar{\nu}_\mu$  in RHC Mode CC N-Tracks sample. Sub-figure (a) shows the momentum one-dimensional profile in all but the highest momentum fit bin. Sub-figure (b) shows the  $\cos\theta$  one-dimensional profile in all but the highest angle fit bin. Shown in both (a) and (b) is the ratio between data and the prefit value. Sub-figure (c) shows a grid of two-dimensional data and prefit distributions in the same phase space as (a) and (b). Moving from top-left to bottom-right in (c) is the data, prefit, data to prefit ratio, and data to prefit difference.

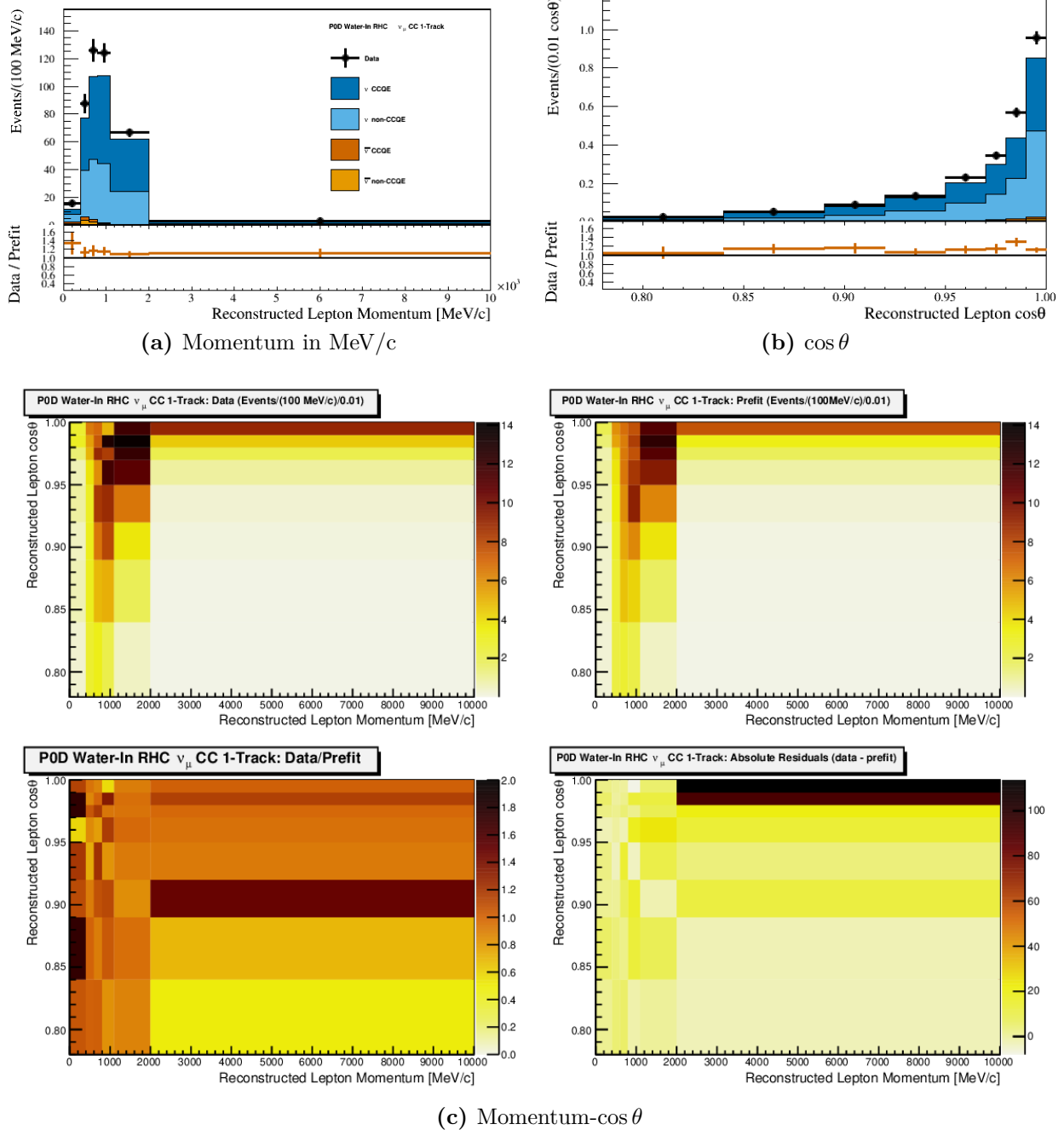


**Figure 6.5:** Data and prefit expectation for the PØD Water-In  $\nu_\mu$  in RHC Mode CC 1-Track sample. Sub-figure (a) shows the momentum one-dimensional profile in all but the highest momentum fit bin. Sub-figure (b) shows the  $\cos\theta$  one-dimensional profile in all but the highest angle fit bin. Shown in both (a) and (b) is the ratio between data and the prefit value. Sub-figure (c) shows a grid of two-dimensional data and prefit distributions in the same phase space as (a) and (b). Moving from top-left to bottom-right in (c) is the data, prefit, data to prefit ratio, and data to prefit difference.

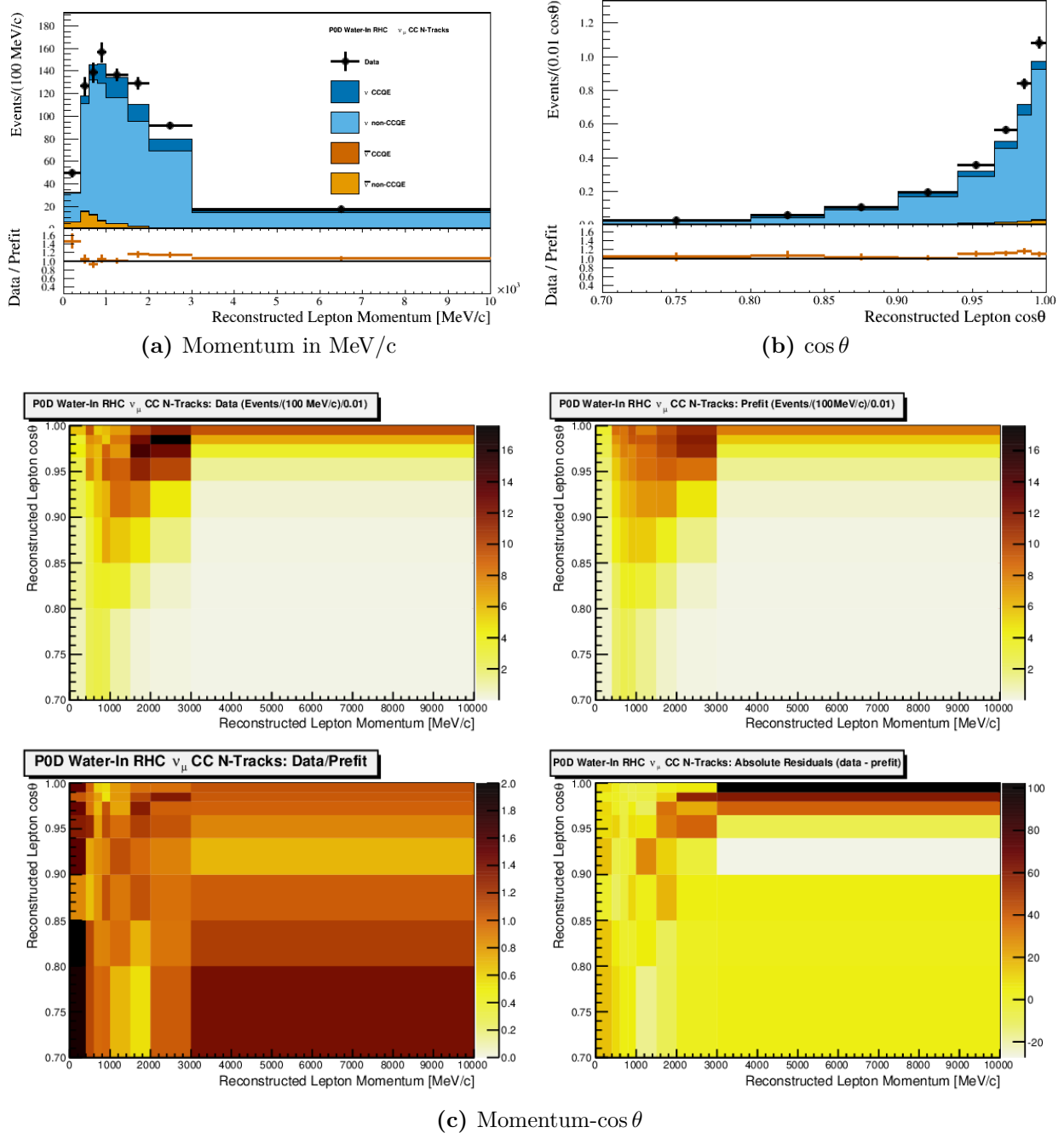


**Figure 6.6:** Data and prefit expectation for the PØD Water-In  $\nu_\mu$  in RHC Mode CC N-Tracks sample. Sub-figure (a) shows the momentum one-dimensional profile in all but the highest momentum fit bin. Sub-figure (b) shows the  $\cos \theta$  one-dimensional profile in all but the highest angle fit bin. Shown in both (a) and (b) is the ratio between data and the prefit value. Sub-figure (c) shows a grid of two-dimensional data and prefit distributions in the same phase space as (a) and (b). Moving from top-left to bottom-right in (c) is the data, prefit, data to prefit ratio, and data to prefit difference.

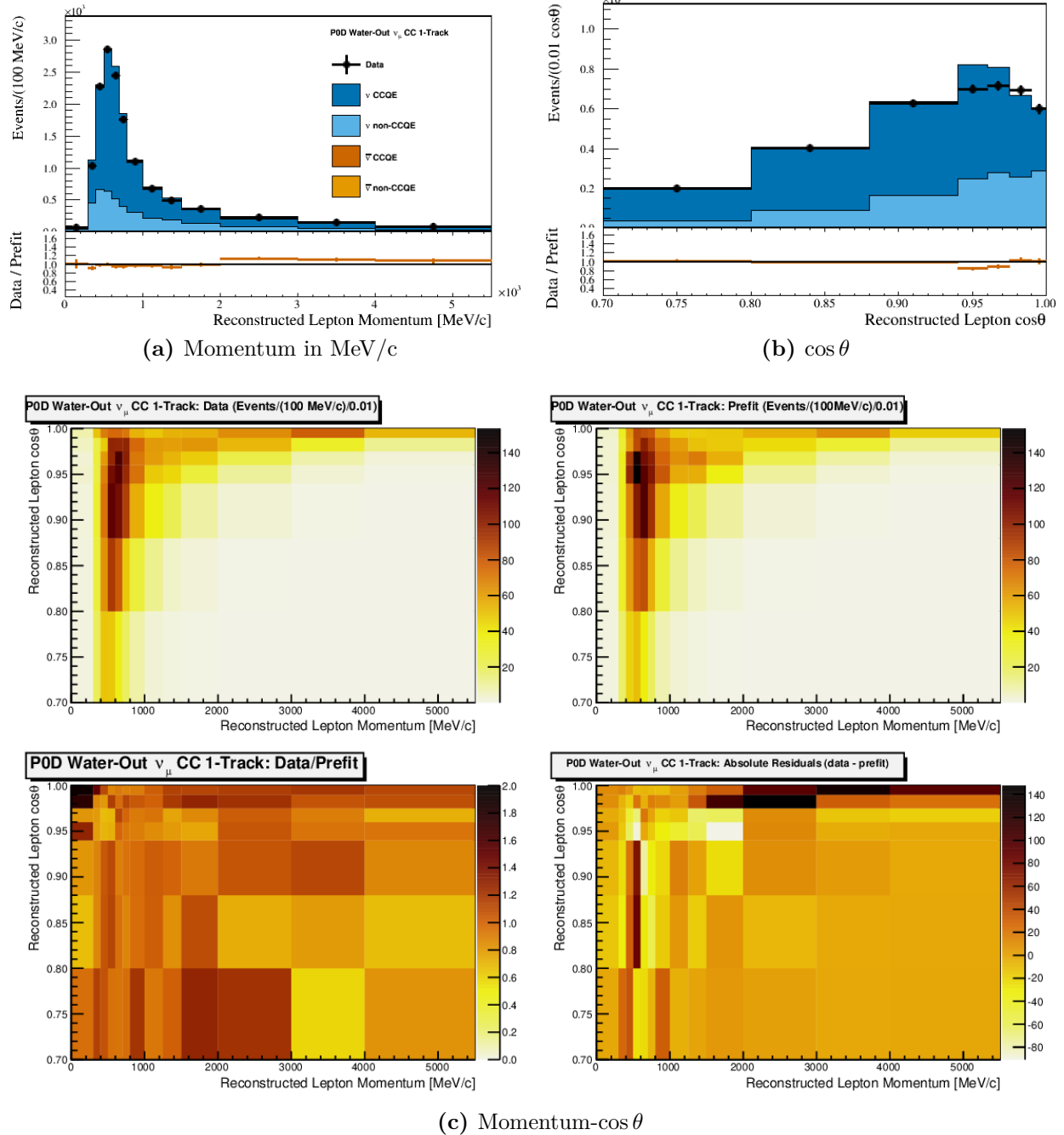


**Figure 6.7:** Data and prefit expectation for the PØD Water-Out  $\nu_\mu$  in FHC Mode CC 1-Track sample. Sub-figure (a) shows the momentum one-dimensional profile in all but the highest momentum fit bin. Sub-figure (b) shows the  $\cos\theta$  one-dimensional profile in all but the highest angle fit bin. Shown in both (a) and (b) is the ratio between data and the prefit value. Sub-figure (c) shows a grid of two-dimensional data and prefit distributions in the same phase space as (a) and (b). Moving from top-left to bottom-right in (c) is the data, prefit, data to prefit ratio, and data to prefit difference.

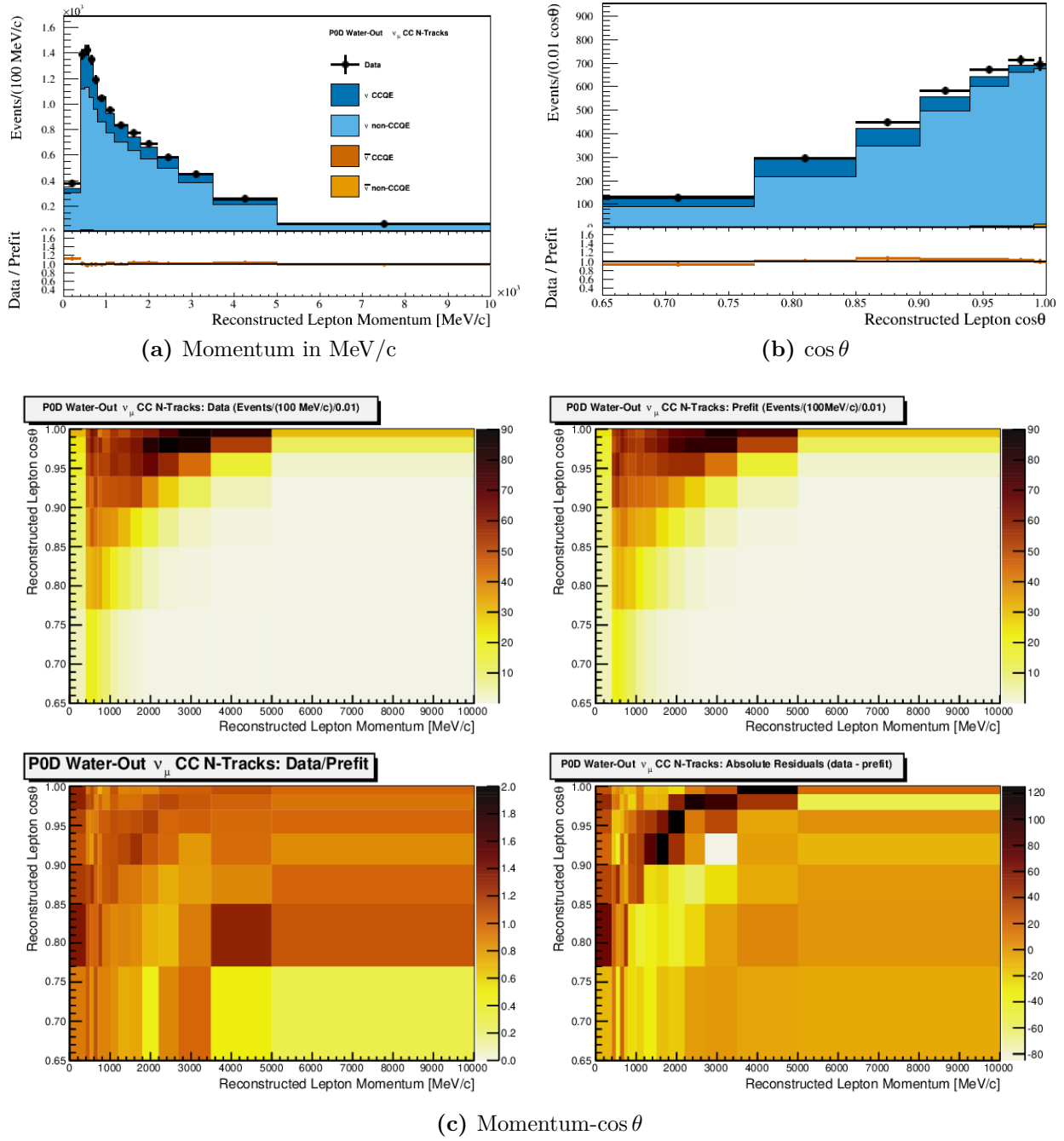


**Figure 6.8:** Data and prefit expectation for the PØD Water-Out  $\nu_\mu$  in FHC Mode CC N-Tracks sample. Sub-figure (a) shows the momentum one-dimensional profile in all but the highest momentum fit bin. Sub-figure (b) shows the  $\cos\theta$  one-dimensional profile in all but the highest angle fit bin. Shown in both (a) and (b) is the ratio between data and the prefit value. Sub-figure (c) shows a grid of two-dimensional data and prefit distributions in the same phase space as (a) and (b). Moving from top-left to bottom-right in (c) is the data, prefit, data to prefit ratio, and data to prefit difference.

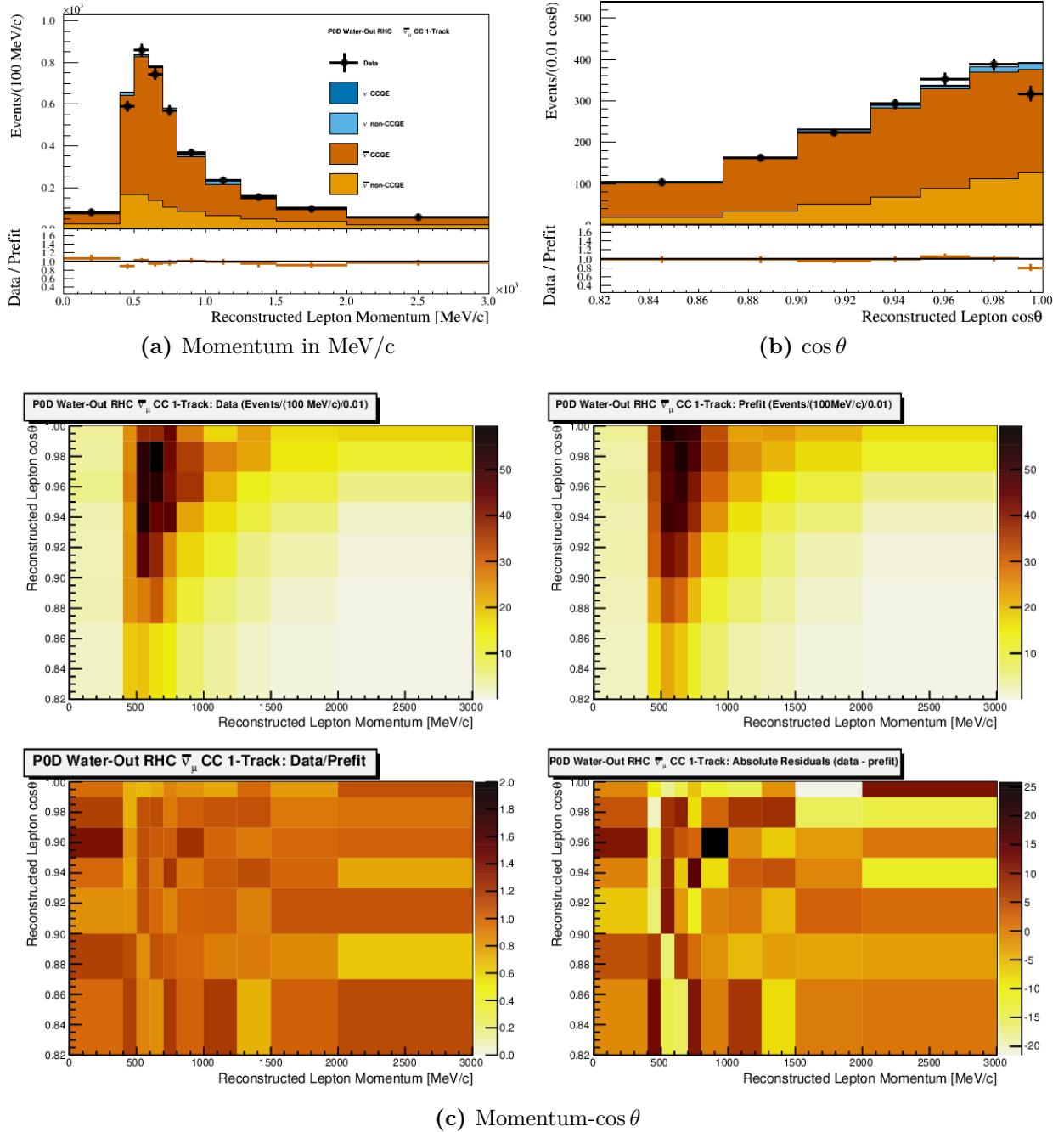


**Figure 6.9:** Data and prefit expectation for the PØD Water-Out  $\bar{\nu}_\mu$  in RHC Mode CC 1-Track sample. Sub-figure (a) shows the momentum one-dimensional profile in all but the highest momentum fit bin. Sub-figure (b) shows the  $\cos \theta$  one-dimensional profile in all but the highest angle fit bin. Shown in both (a) and (b) is the ratio between data and the prefit value. Sub-figure (c) shows a grid of two-dimensional data and prefit distributions in the same phase space as (a) and (b). Moving from top-left to bottom-right in (c) is the data, prefit, data to prefit ratio, and data to prefit difference.

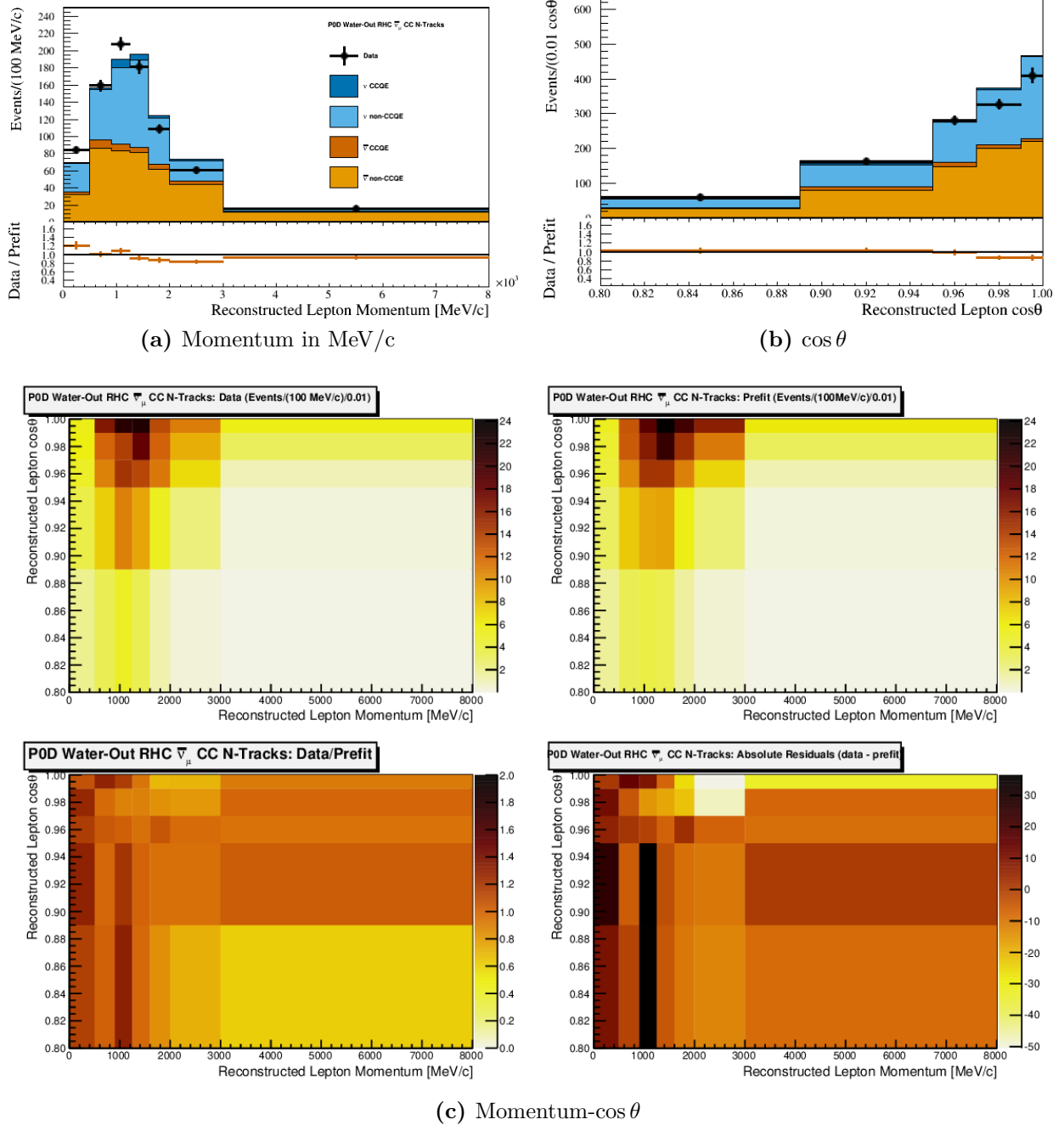


**Figure 6.10:** Data and prefit expectation for the P0D Water-Out  $\bar{\nu}_\mu$  in RHC Mode CC N-Tracks sample. Sub-figure (a) shows the momentum one-dimensional profile in all but the highest momentum fit bin. Sub-figure (b) shows the  $\cos\theta$  one-dimensional profile in all but the highest angle fit bin. Shown in both (a) and (b) is the ratio between data and the prefit value. Sub-figure (c) shows a grid of two-dimensional data and prefit distributions in the same phase space as (a) and (b). Moving from top-left to bottom-right in (c) is the data, prefit, data to prefit ratio, and data to prefit difference.

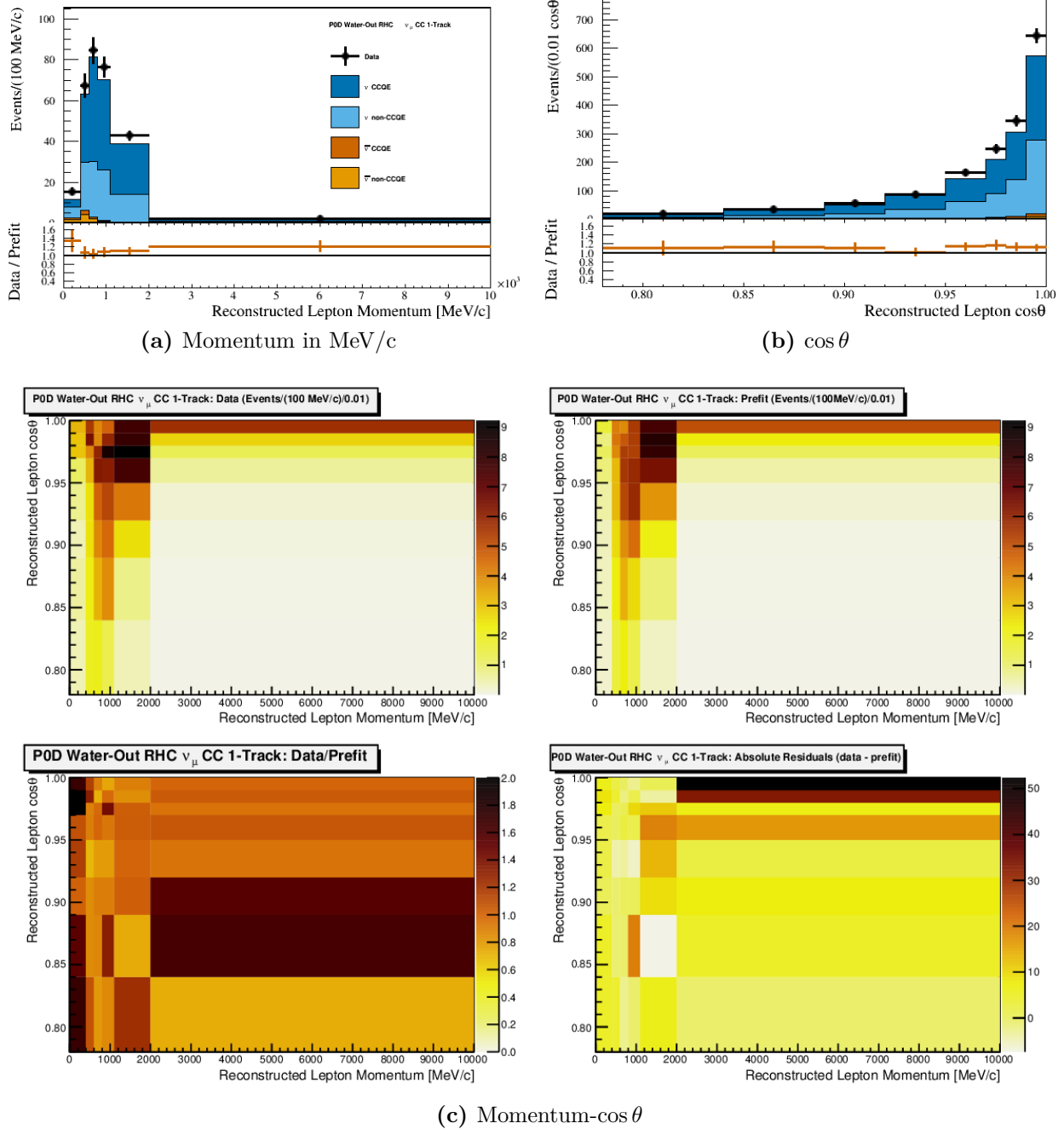


**Figure 6.11:** Data and prefit expectation for the PØD Water-Out  $\nu_\mu$  in RHC Mode CC 1-Track sample. Sub-figure (a) shows the momentum one-dimensional profile in all but the highest momentum fit bin. Sub-figure (b) shows the  $\cos \theta$  one-dimensional profile in all but the highest angle fit bin. Shown in both (a) and (b) is the ratio between data and the prefit value. Sub-figure (c) shows a grid of two-dimensional data and prefit distributions in the same phase space as (a) and (b). Moving from top-left to bottom-right in (c) is the data, prefit, data to prefit ratio, and data to prefit difference.

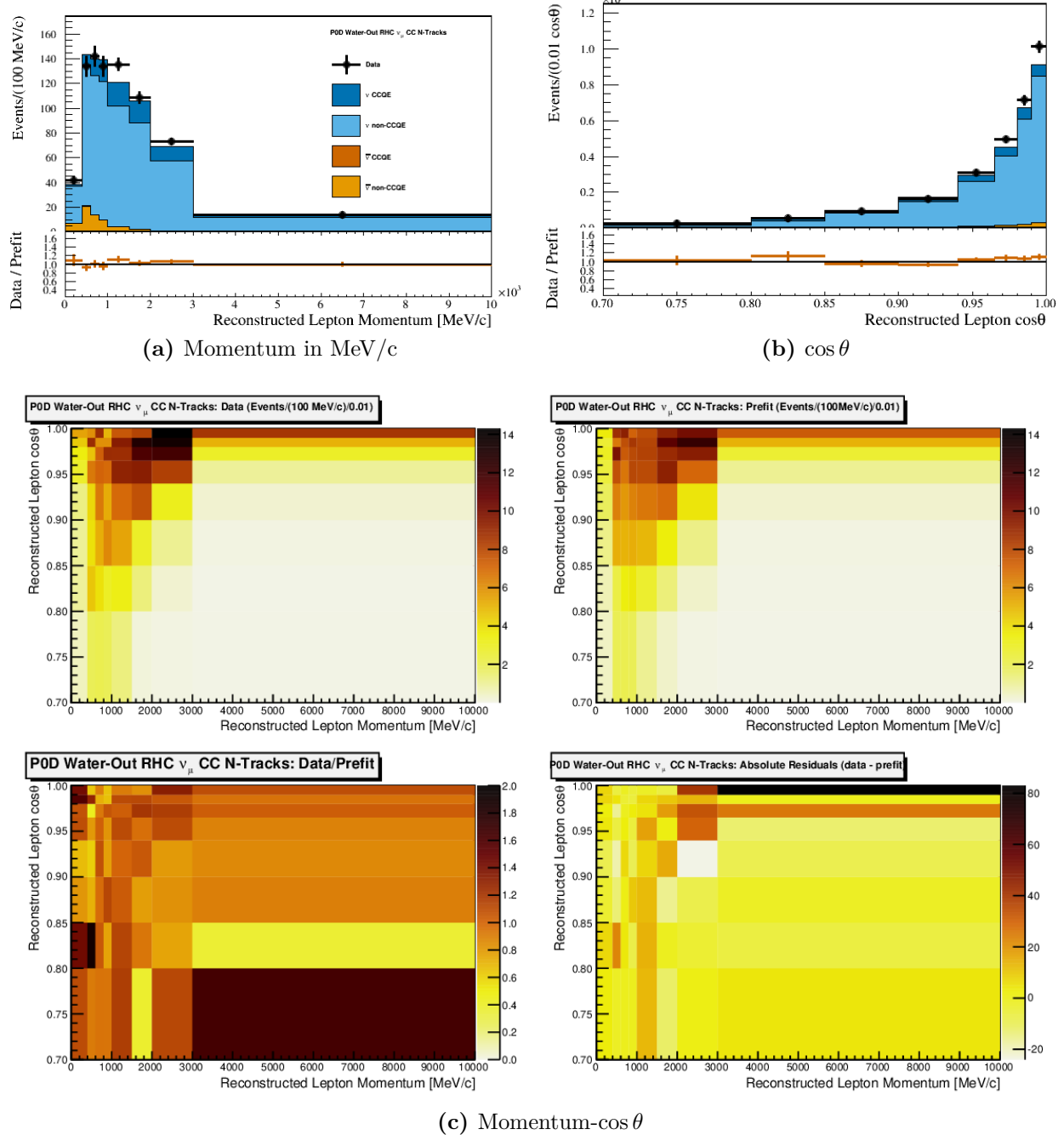


**Figure 6.12:** Data and prefit expectation for the PØD Water-Out  $\nu_\mu$  in RHC Mode CC N-Tracks sample. Sub-figure (a) shows the momentum one-dimensional profile in all but the highest momentum fit bin. Sub-figure (b) shows the  $\cos \theta$  one-dimensional profile in all but the highest angle fit bin. Shown in both (a) and (b) is the ratio between data and the prefit value. Sub-figure (c) shows a grid of two-dimensional data and prefit distributions in the same phase space as (a) and (b). Moving from top-left to bottom-right in (c) is the data, prefit, data to prefit ratio, and data to prefit difference.

fitted parameters (postfit) have improved the data matching as a result. The samples are shown in Figure 6.13 on page 175 to Figure 6.24 on page 186 in the same order as presented in the previous section.

We see an improved agreement between the postfit prediction and the data. Still, there is some poor data matching, in particular, in the lowest momentum bins. This seems to be balanced between the water-in and water-out modes since the flux parameters affect the samples the same way. Given there still is tension in those lowest momentum bins, perhaps the water mass systematic uncertainty was under estimated in this analysis.

It is hypothesized that if the mass systematic was indeed underestimated, the data to postfit ratio would converge towards 1 with decreasing  $\cos\theta$  in the water-in sample's lowest momentum bins. If better agreement is observed in those higher angle bins compared to the lower angle bins, this would support the idea that the mass systematic uncertainty is underestimated. However, there was a weak trend observed in the water-in samples, and such a weak one could be coincidental given the number of bins. Therefore, it is difficult to draw any conclusions if the mass systematic uncertainty was underestimated until other constraints are provided.

Now that we have examined the postfit samples and seen that the prediction has indeed changed, we can proceed to look at the parameter values.

### 6.2.2 Parameter Value and Correlation Comparisons

The postfit parameters from the PØD-only BANFF fit are shown in Figure 6.25 on page 191 through Figure 6.28 on page 194. A complete listing of the prefit and postfit values is given in Appendix H. Additionally, a comparison is made between the PØD-only results with that of the FGD-only results. It must be stated that while the PØD-only and FGD-only fits are using the same 2017 canonical cross section parameterization, the analyses had different POT exposures. This PØD-only analysis fit uses run periods 2 – 8, or about  $11.5 \times 10^{20}$  ( $6.23 \times 10^{20}$ ) POT in FHC (RHC) mode. The FGD-only fit uses runs 2 – 6, or

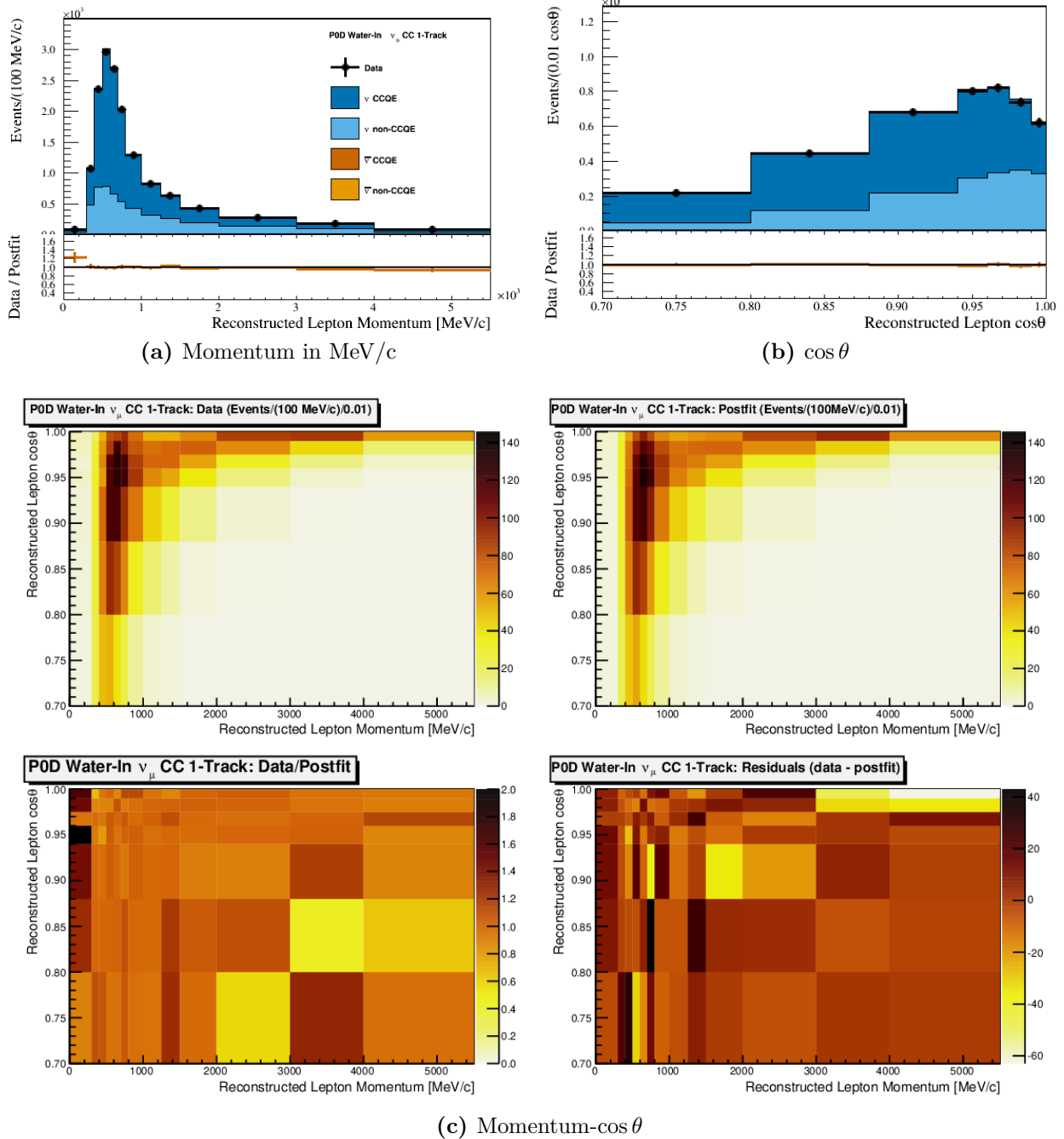


**Figure 6.13:** Data and postfit for the PØD Water-In  $\nu_\mu$  in FHC Mode CC 1-Track sample. Sub-figure (a) shows the momentum one-dimensional profile in all but the highest momentum fit bin. Sub-figure (b) shows the  $\cos \theta$  one-dimensional profile in all but the highest angle fit bin. Shown in both (a) and (b) is the ratio between data and the postfit value. Sub-figure (c) shows a grid of two-dimensional data and postfit distributions in the same phase space as (a) and (b). Moving from top-left to bottom-right in (c) is the data, postfit, data to postfit ratio, and data to postfit difference.

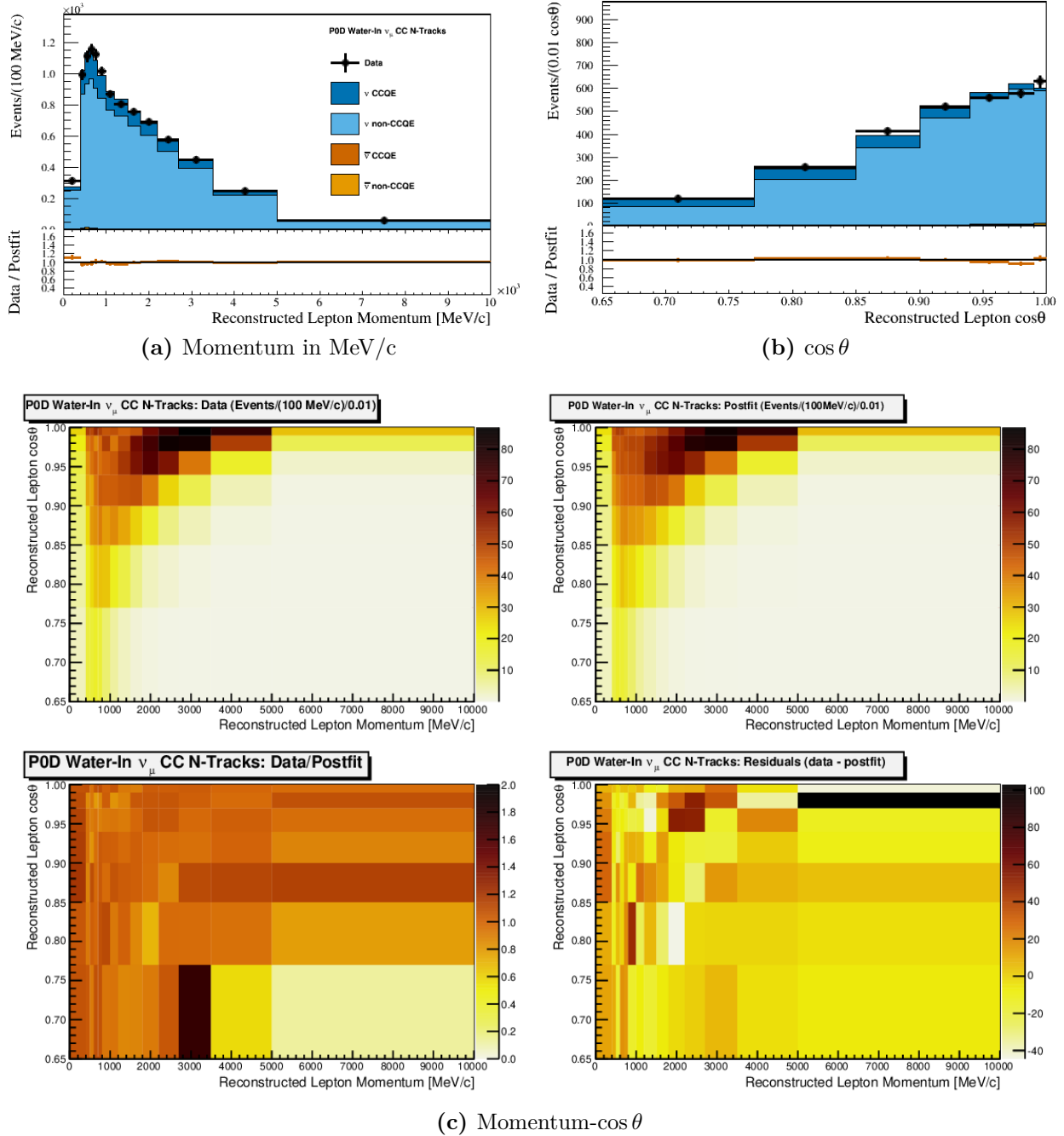


**Figure 6.14:** Data and postfit for the PØD Water-In  $\nu_\mu$  in FHC Mode CC 1-Track sample. Sub-figure (a) shows the momentum one-dimensional profile in all but the highest momentum fit bin. Sub-figure (b) shows the  $\cos \theta$  one-dimensional profile in all but the highest angle fit bin. Shown in both (a) and (b) is the ratio between data and the postfit value. Sub-figure (c) shows a grid of two-dimensional data and postfit distributions in the same phase space as (a) and (b). Moving from top-left to bottom-right in (c) is the data, postfit, data to postfit ratio, and data to postfit difference.

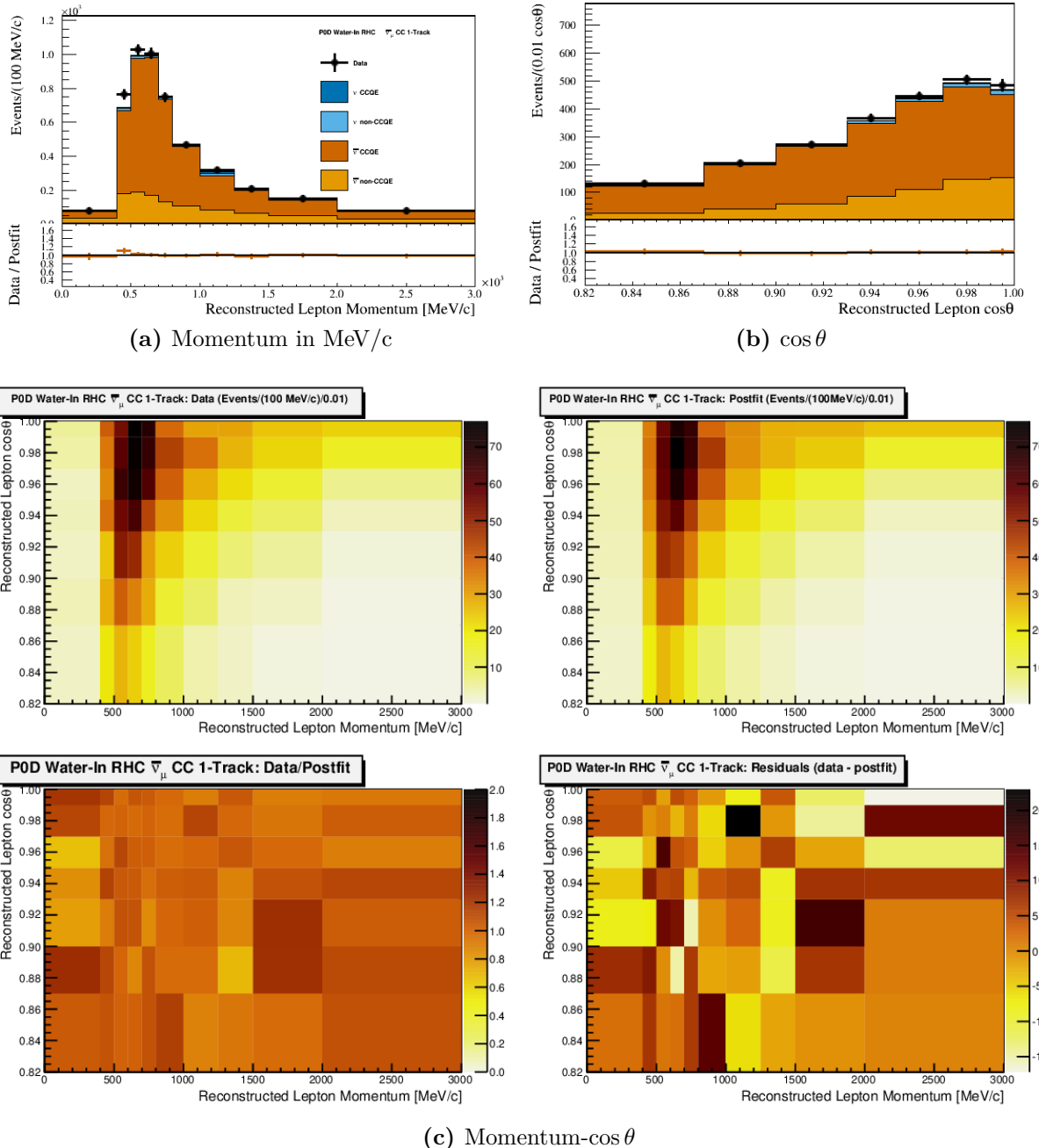


**Figure 6.15:** Data and postfit for the PØD Water-In  $\bar{\nu}_\mu$  in RHC Mode CC 1-Track sample. Sub-figure (a) shows the momentum one-dimensional profile in all but the highest momentum fit bin. Sub-figure (b) shows the  $\cos \theta$  one-dimensional profile in all but the highest angle fit bin. Shown in both (a) and (b) is the ratio between data and the postfit value. Sub-figure (c) shows a grid of two-dimensional data and postfit distributions in the same phase space as (a) and (b). Moving from top-left to bottom-right in (c) is the data, postfit, data to postfit ratio, and data to postfit difference.

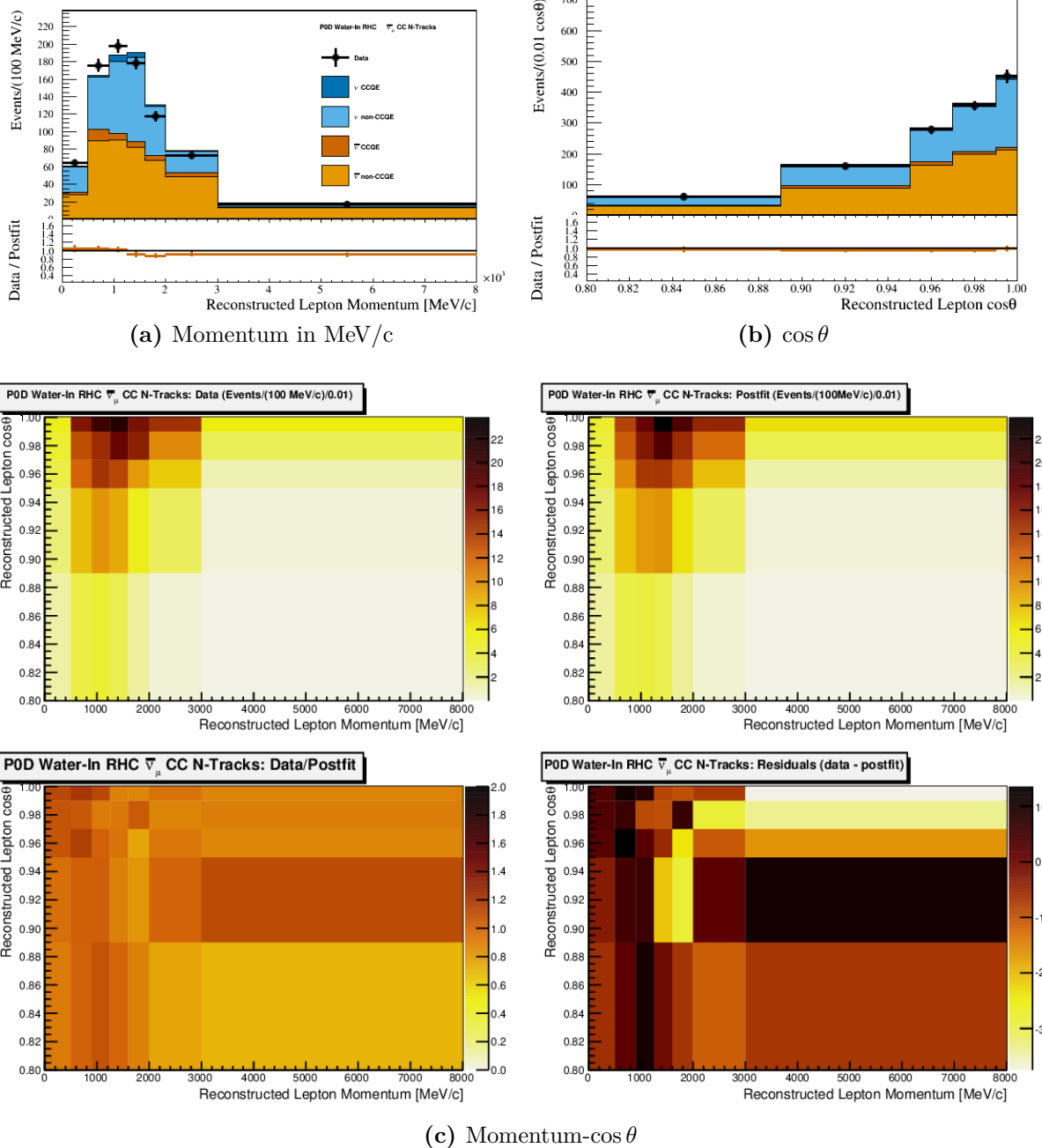


**Figure 6.16:** Data and postfit for the PØD Water-In  $\bar{\nu}_\mu$  in RHC Mode CC N-Tracks sample. Sub-figure (a) shows the momentum one-dimensional profile in all but the highest momentum fit bin. Sub-figure (b) shows the  $\cos \theta$  one-dimensional profile in all but the highest angle fit bin. Shown in both (a) and (b) is the ratio between data and the postfit value. Sub-figure (c) shows a grid of two-dimensional data and postfit distributions in the same phase space as (a) and (b). Moving from top-left to bottom-right in (c) is the data, postfit, data to postfit ratio, and data to postfit difference.

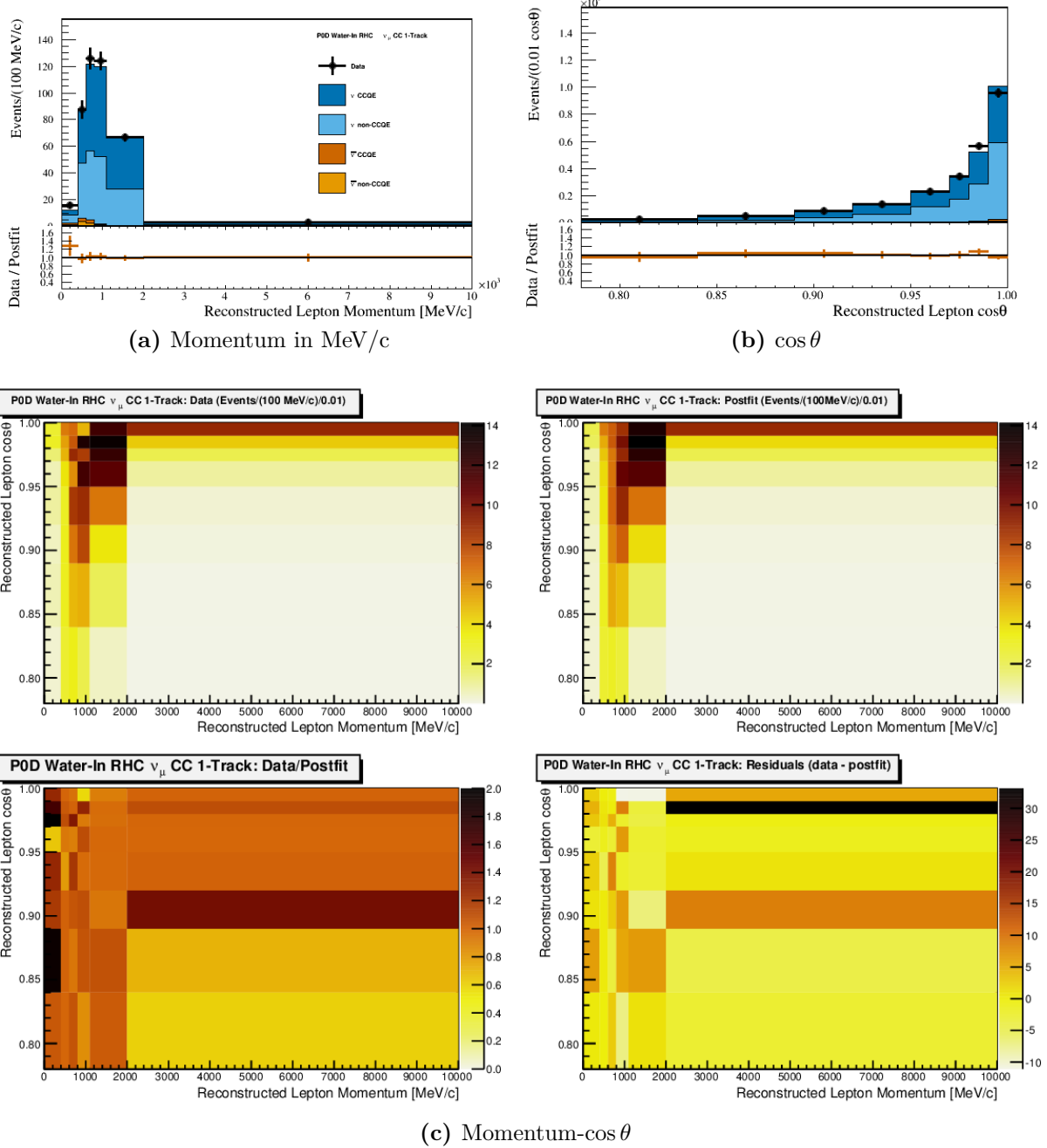


**Figure 6.17:** Data and postfit for the PØD Water-In  $\nu_\mu$  in RHC Mode CC 1-Track sample. Sub-figure (a) shows the momentum one-dimensional profile in all but the highest momentum fit bin. Sub-figure (b) shows the  $\cos \theta$  one-dimensional profile in all but the highest angle fit bin. Shown in both (a) and (b) is the ratio between data and the postfit value. Sub-figure (c) shows a grid of two-dimensional data and postfit distributions in the same phase space as (a) and (b). Moving from top-left to bottom-right in (c) is the data, postfit, data to postfit ratio, and data to postfit difference.

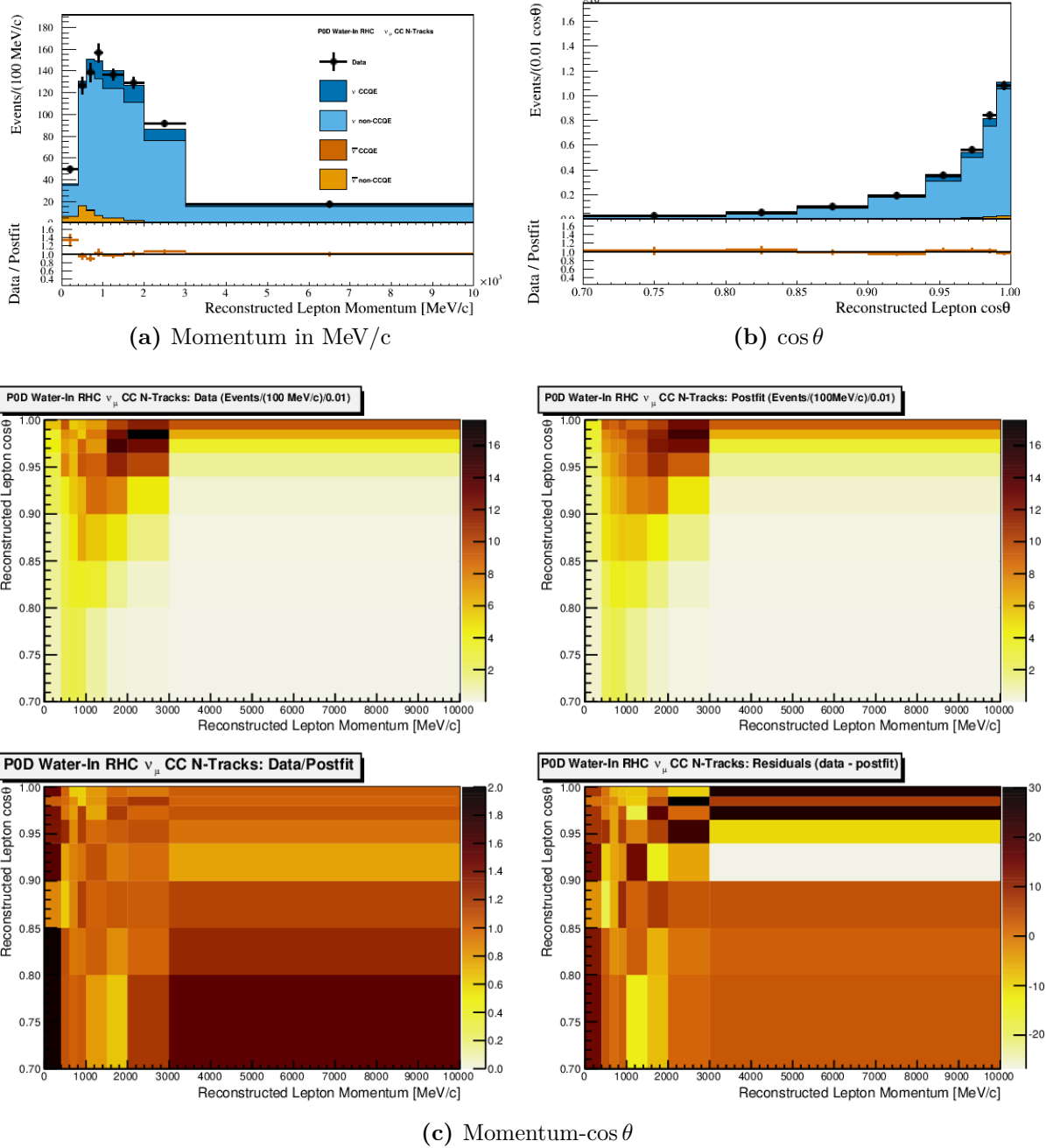


**Figure 6.18:** Data and postfit for the PØD Water-In  $\nu_\mu$  in RHC Mode CC N-Tracks sample. Sub-figure (a) shows the momentum one-dimensional profile in all but the highest momentum fit bin. Sub-figure (b) shows the  $\cos\theta$  one-dimensional profile in all but the highest angle fit bin. Shown in both (a) and (b) is the ratio between data and the postfit value. Sub-figure (c) shows a grid of two-dimensional data and postfit distributions in the same phase space as (a) and (b). Moving from top-left to bottom-right in (c) is the data, postfit, data to postfit ratio, and data to postfit difference.

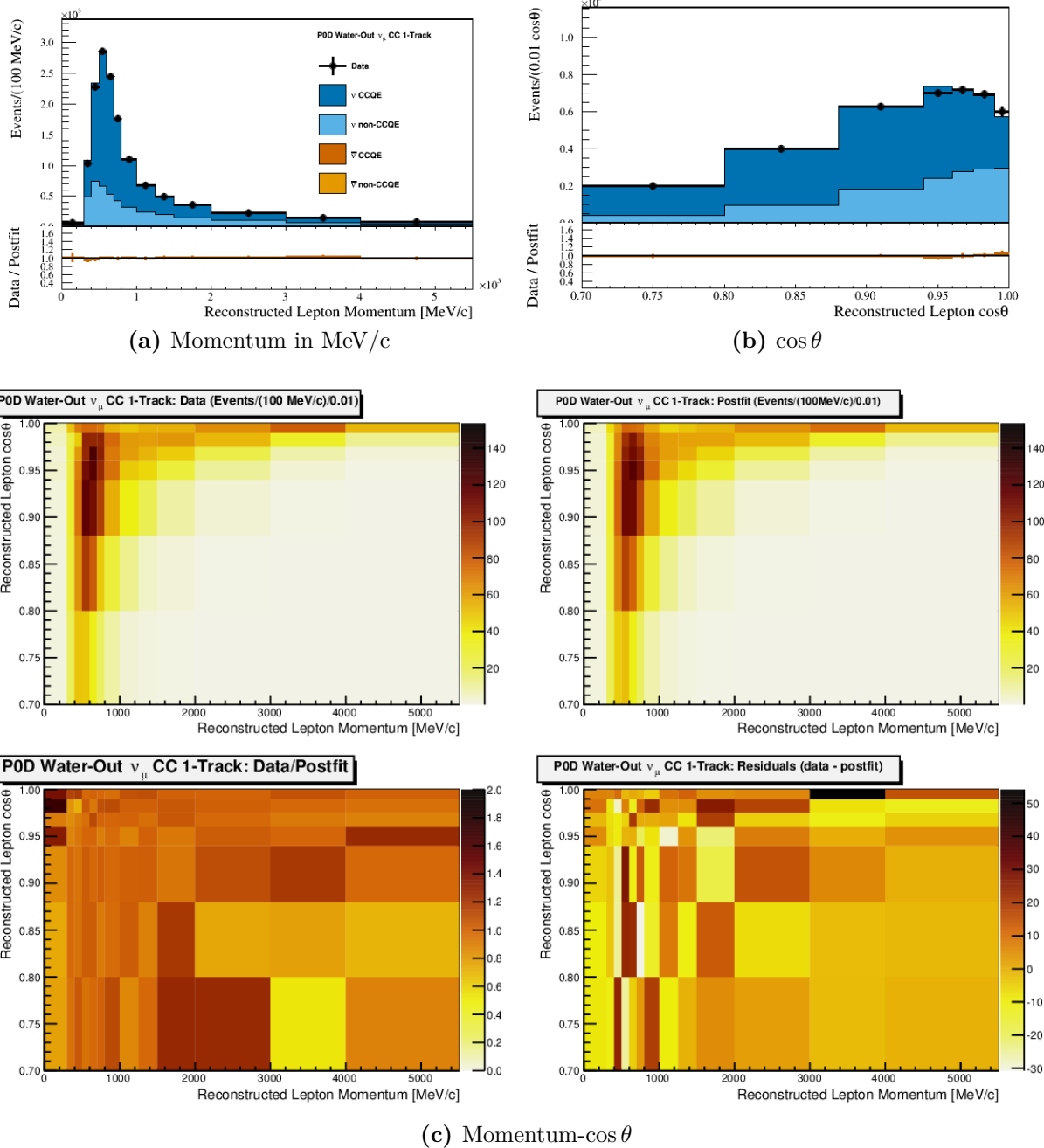


**Figure 6.19:** Data and postfit for the PØD Water-Out  $\nu_\mu$  in FHC Mode CC 1-Track sample. Sub-figure (a) shows the momentum one-dimensional profile in all but the highest momentum fit bin. Sub-figure (b) shows the  $\cos\theta$  one-dimensional profile in all but the highest angle fit bin. Shown in both (a) and (b) is the ratio between data and the postfit value. Sub-figure (c) shows a grid of two-dimensional data and postfit distributions in the same phase space as (a) and (b). Moving from top-left to bottom-right in (c) is the data, postfit, data to postfit ratio, and data to postfit difference.

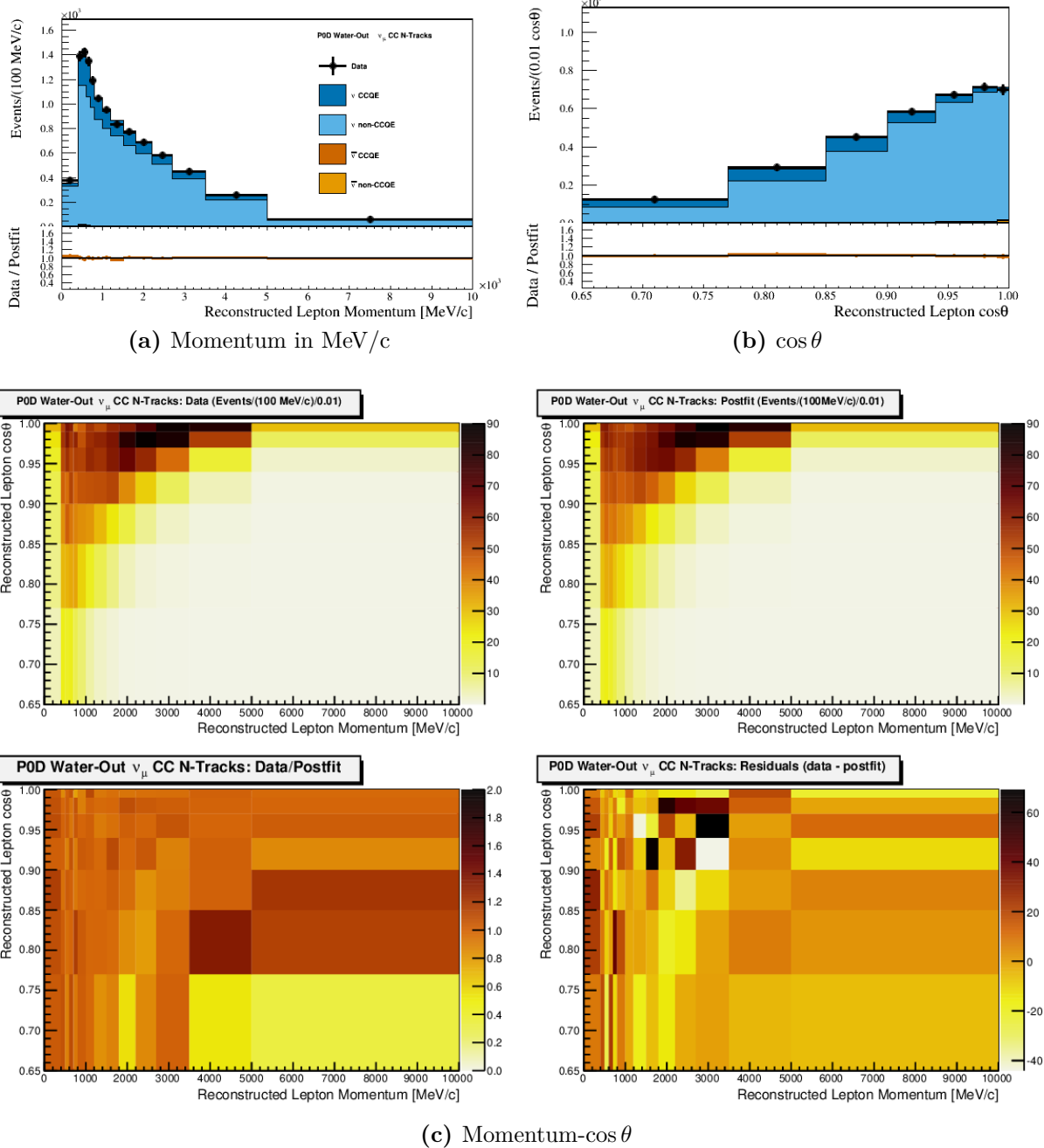


**Figure 6.20:** Data and postfit for the PØD Water-Out  $\nu_\mu$  in FHC Mode CC N-Tracks sample. Sub-figure (a) shows the momentum one-dimensional profile in all but the highest momentum fit bin. Sub-figure (b) shows the  $\cos\theta$  one-dimensional profile in all but the highest angle fit bin. Shown in both (a) and (b) is the ratio between data and the postfit value. Sub-figure (c) shows a grid of two-dimensional data and postfit distributions in the same phase space as (a) and (b). Moving from top-left to bottom-right in (c) is the data, postfit, data to postfit ratio, and data to postfit difference.

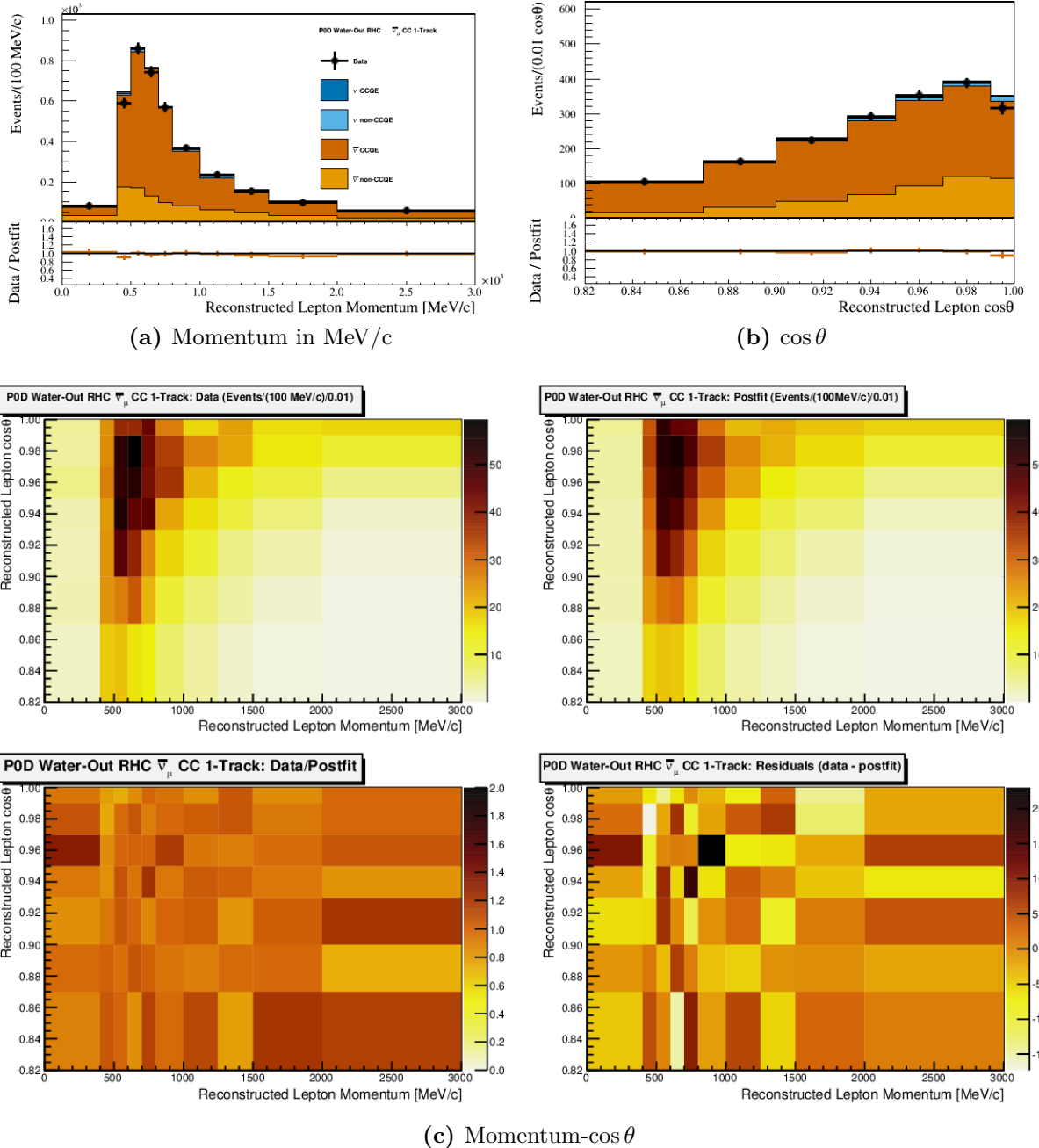


**Figure 6.21:** Data and postfit for the PØD Water-Out  $\bar{\nu}_\mu$  in RHC Mode CC 1-Track sample. Sub-figure (a) shows the momentum one-dimensional profile in all but the highest momentum fit bin. Sub-figure (b) shows the  $\cos\theta$  one-dimensional profile in all but the highest angle fit bin. Shown in both (a) and (b) is the ratio between data and the postfit value. Sub-figure (c) shows a grid of two-dimensional data and postfit distributions in the same phase space as (a) and (b). Moving from top-left to bottom-right in (c) is the data, postfit, data to postfit ratio, and data to postfit difference.

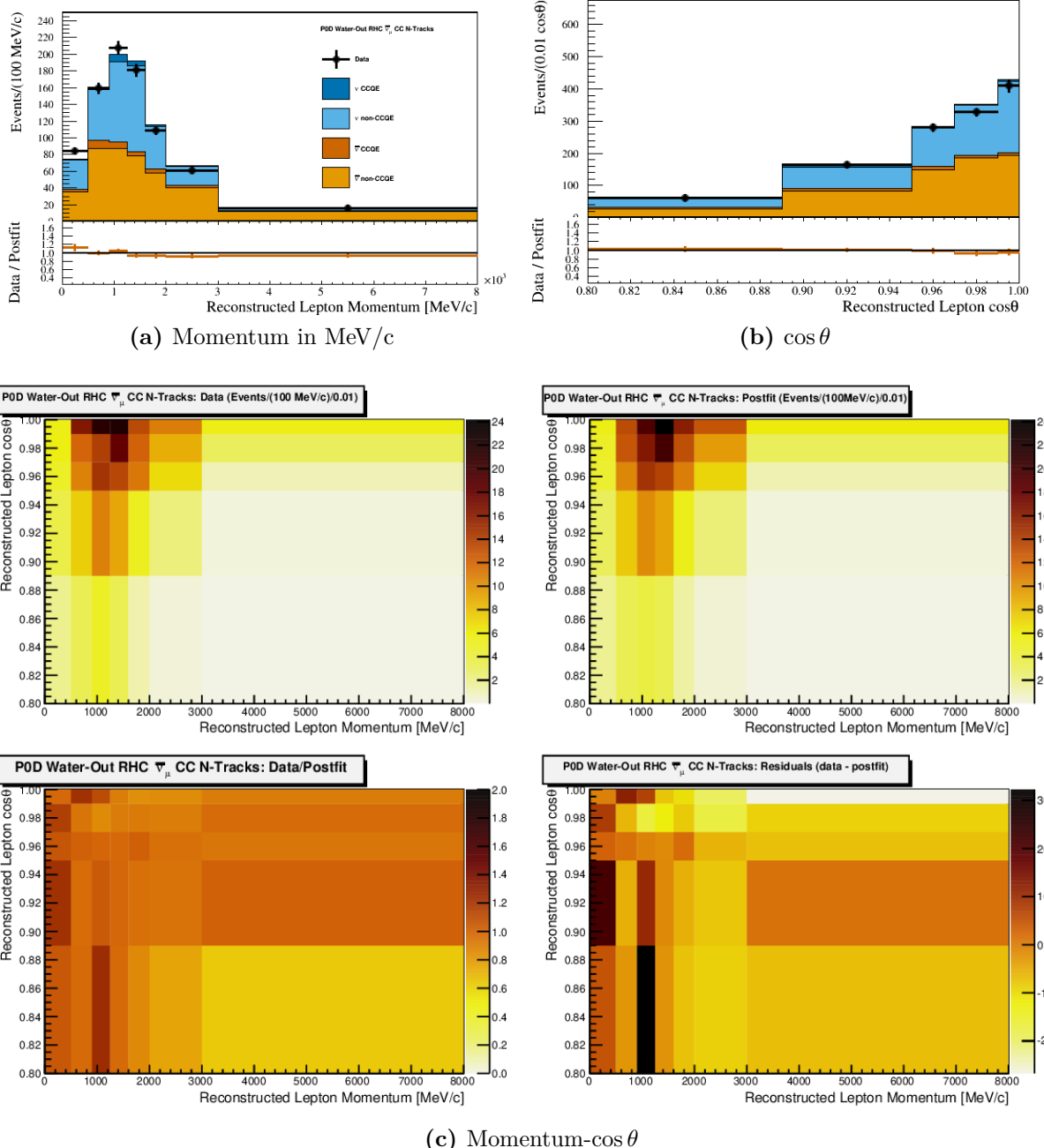


**Figure 6.22:** Data and postfit for the PØD Water-Out  $\bar{\nu}_\mu$  in RHC Mode CC N-Tracks sample. Sub-figure (a) shows the momentum one-dimensional profile in all but the highest momentum fit bin. Sub-figure (b) shows the  $\cos\theta$  one-dimensional profile in all but the highest angle fit bin. Shown in both (a) and (b) is the ratio between data and the postfit value. Sub-figure (c) shows a grid of two-dimensional data and postfit distributions in the same phase space as (a) and (b). Moving from top-left to bottom-right in (c) is the data, postfit, data to postfit ratio, and data to postfit difference.

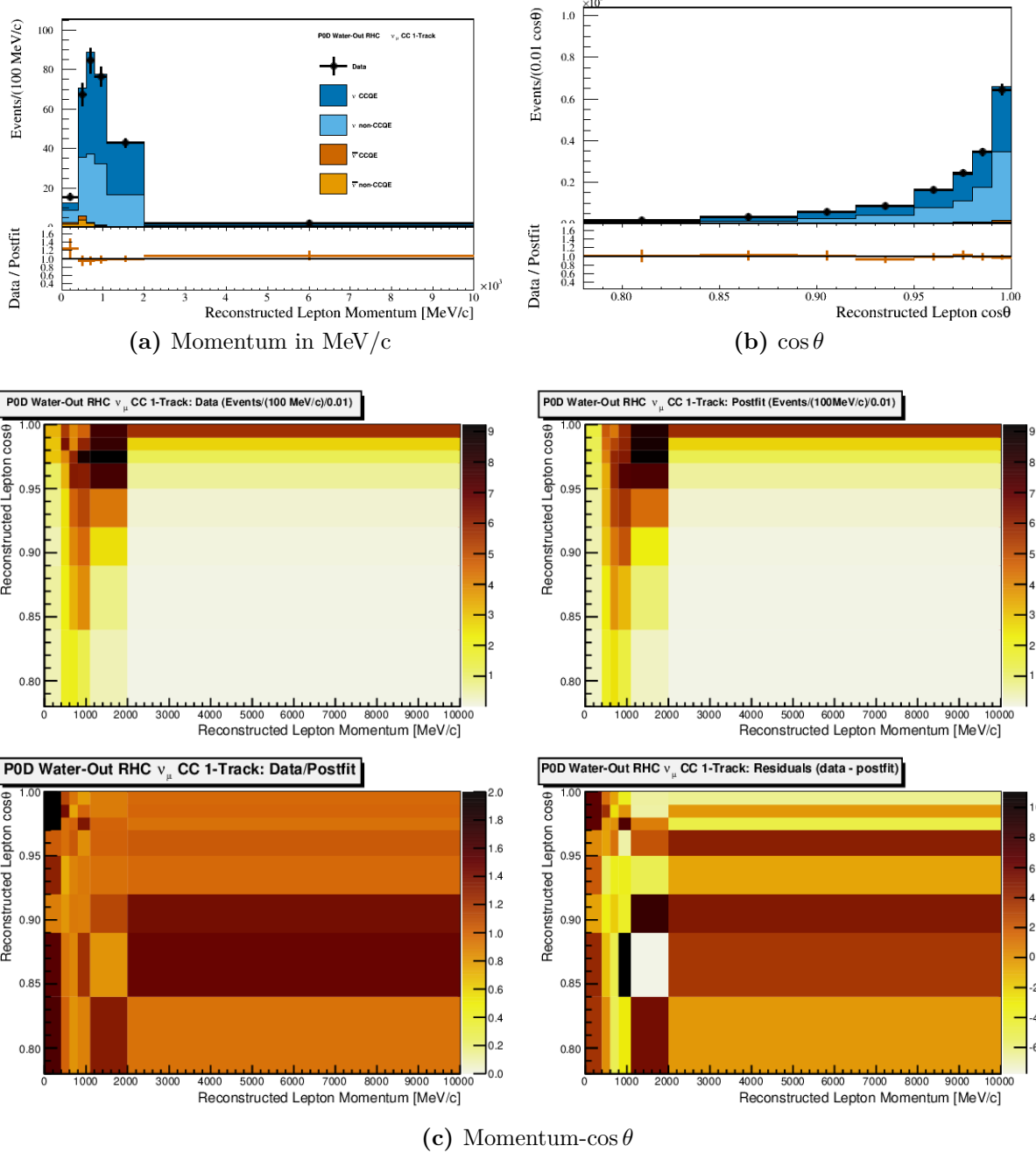


**Figure 6.23:** Data and postfit for the PØD Water-Out  $\nu_\mu$  in RHC Mode CC 1-Track sample. Sub-figure (a) shows the momentum one-dimensional profile in all but the highest momentum fit bin. Sub-figure (b) shows the  $\cos\theta$  one-dimensional profile in all but the highest angle fit bin. Shown in both (a) and (b) is the ratio between data and the postfit value. Sub-figure (c) shows a grid of two-dimensional data and postfit distributions in the same phase space as (a) and (b). Moving from top-left to bottom-right in (c) is the data, postfit, data to postfit ratio, and data to postfit difference.

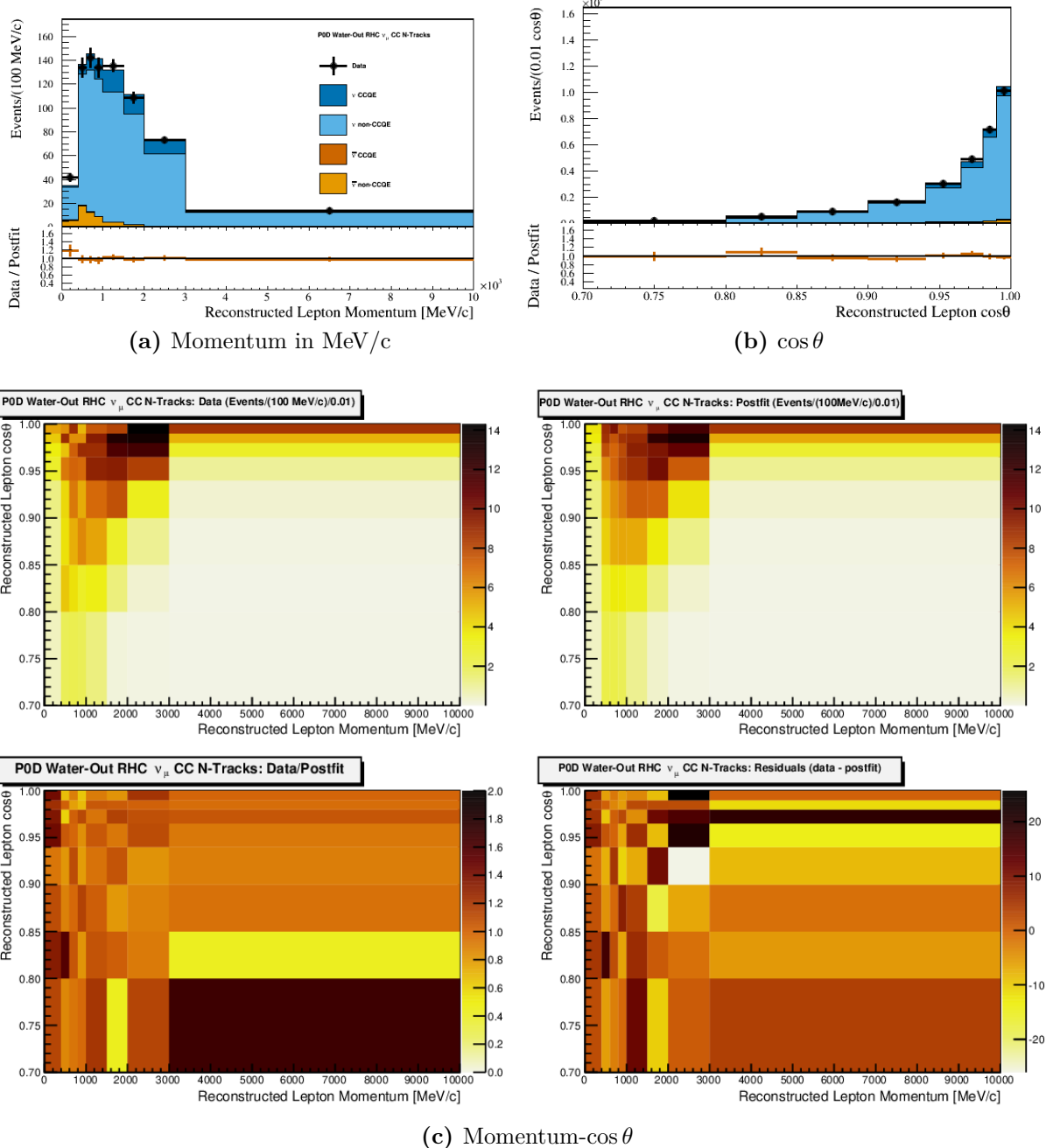


**Figure 6.24:** Data and postfit for the PØD Water-Out  $\nu_\mu$  in RHC Mode CC N-Tracks sample. Sub-figure (a) shows the momentum one-dimensional profile in all but the highest momentum fit bin. Sub-figure (b) shows the  $\cos\theta$  one-dimensional profile in all but the highest angle fit bin. Shown in both (a) and (b) is the ratio between data and the postfit value. Sub-figure (c) shows a grid of two-dimensional data and postfit distributions in the same phase space as (a) and (b). Moving from top-left to bottom-right in (c) is the data, postfit, data to postfit ratio, and data to postfit difference.

about  $5.81 \times 10^{20}$  ( $2.84 \times 10^{20}$ ) POT in FHC (RHC) modes. So the PØD-only fit has an additional statistical advantage. This does not affect the actual fitting procedure since the POT weights scale the MC prediction to the data.

In order to understand how the two analyses compare to each other in terms of sensitivity to the flux and cross section parameters, we need to examine each detector's integrated mass-luminosity. The number of incident neutrinos crossing either the FGD or PØD detector is the product of its respective fiducial mass and POT exposure. While the PØD has much more mass, the water-in and water-out modes are mutually exclusive, resulting in a reduced aggregate POT exposure as compared to each static FGD for each water-in and water-out running periods. Also since the FGD2 has a larger water mass fraction compared to the PØD water-in mode, the expected number of neutrino-oxygen interaction events are very similar. The comparative advantage of the PØD-only data lies in the number of neutrino-carbon events, which is about 10 times greater than the FGD. These numbers and more are tabulated in Table 6.1 on page 188.

**Table 6.1:** Neutrino-nucleon exposure on target elements in the PØD-only and FGD-only analyses. The FGD1 and FGD2 masses were calculated using the following sources [16, 58, 59]. The PØD mass was taken from the following source [77]. The other mass elements include hydrogen, copper, and heavier elements.

Detector	(kg)	Fiducial volume mass			POT ( $10^{20}$ )		kg POT ( $10^{24}$ )	PØD-to-FGD (kg POT)		
		$^{12}\text{C}$ (%)	$^{16}\text{O}$ (%)	other (%)	FHC	RHC		$^{12}\text{C}$	$^{16}\text{O}$	other
PØD Water-out	3570	70	0.67	19.33	7.872	-	2.81	3.99	-	9.21
	985	86	3.7	10.3	5.81	-	0.572			
PØD Water-In	5470	45	30	25	3.657	-	2.00	10.63	1.43	8.05
	972	15	74	11	5.81	-	0.565			
PØD Water-out	3570	70	0.67	19.33	-	3.382	1.207	3.513	-	8.10
	985	86	3.7	10.3	-	2.84	0.280			
PØD Water-In	5470	45	30	25	-	2.852	1.56	16.9	2.29	12.8
	972	15	74	11	-	2.84	0.276			

There is good agreement between the PØD-only and FGD-only BANFF flux parameter values. The flux parameters in both fits follow the same shape trends, but with the PØD-only fit parameters having a higher expectation comparatively. Also, the magnitude of the flux uncertainties is similar between the two, which suggests that the two configurations are statistically similar.

If we examine the bin normalization parameters for the PØD-only fit in Figure 6.28 on page 194, they are suggesting a reduction in the event rate across most bins. This high flux, low bin normalization result is likely due to the anticorrelated relationship between them as indicated in the correlation matrix shown in Figure 6.30 on page 196. This has been observed in previous BANFF analyses. Interestingly, the results of the principal components analysis on the bin normalizations in Section 4.2.2.4 are observed here as well. The analysis predicted most of the parameters would shift in unison, and we see that trend largely replicated in the postfit values. This indicates that we can possibly reduce the number of bin normalizations and still obtain a similar postfit result.

The cross section parameters are also quite similar between the two fits, with some larger uncertainties in the PØD-only result. The CCQE and BeRPA parameters are in very good agreement with both preferring a significant increase in the BeRPA  $B$  scale parameter. There is tension in the fits with the  $M_A^{\text{Res}}$  parameter which is not currently understood. However, if the difference in the postfit parameters is distributed according to a chi-squared distribution, then this deviation is not unexpected. We will explore this idea further with a hypothesis test in the next section.

A couple of interesting features are observed in the 2p2h parameters. Firstly is the 2p2h  $\nu$  normalization on carbon which is about two-times larger in the PØD-only fit than the FGD-only fit. This normalization result is currently an unknown phenomenon. It could be explained by the fact that the PØD has nearly twice as much non-carbon and non-oxygen elements, which is mostly brass, by mass fraction as in the FGD (see Table 6.1 on page 188). The second feature involves the 2p2h shape parameters, *both of which have postfit values at*

*the physical limit of +1, or +2 as shown graphically in Figure 6.27 on page 193.* This predicts that the 2p2h interaction has no nucleon-nucleon correlation mode and is only due to the pionless-Delta-decay mode. This result is an artifact of the cross section parameterization that is also shared with the FGD result. This issue has been addressed in the latest cross section parameterization and BANFF analysis [62].

To provide an uncertainty on those shape parameters, even though they are situated at a discontinuity in the derivative, a “mirrored” spline was implemented as shown in Figure 6.29 on page 195. The mirrored spline was shown by the BANFF group to not affect the postfit results while providing a calculable uncertainty in MINUIT for the Hessian matrix [24]. To further investigate the impact of a mirrored spline, the oscillation analysis group used the same splines in the Bayesian analysis, which uses a Markov chain Monte Carlo method to explore the parameter space. The Bayesian analysis observed some small relative changes in the 2p2h and  $I_{1/2}$  background normalizations and BeRPA  $E$  root-mean-square using the mirrored spline. However, the parameters that received the largest shifts are already poorly constrained by the ND280 data, and so they have a minuscule effect on the fit.

The postfit correlations are shown in Figure 6.30 on page 196. The full matrix shows large anticorrelations between the systematic parameters sets. Largest in magnitude are the flux and cross section parameters. To better see the correlations for those sets, they are zoomed into on Figure 6.31 on page 197. For only the cross section parameters, the correlations are shown in Figure 6.32 on page 198.

## 6.3 Statistical Significance of Parameter Agreement Between the PØD and FGD BANFF Fits

We can now quantify of the agreement between the PØD-only BANFF fit and that of the FGD-only BANFF fit. As a starting assumption, let the FGD-only result be the expectation of the result. We wish to test the hypothesis,  $H_1$ , that the PØD-only data and FGD-only

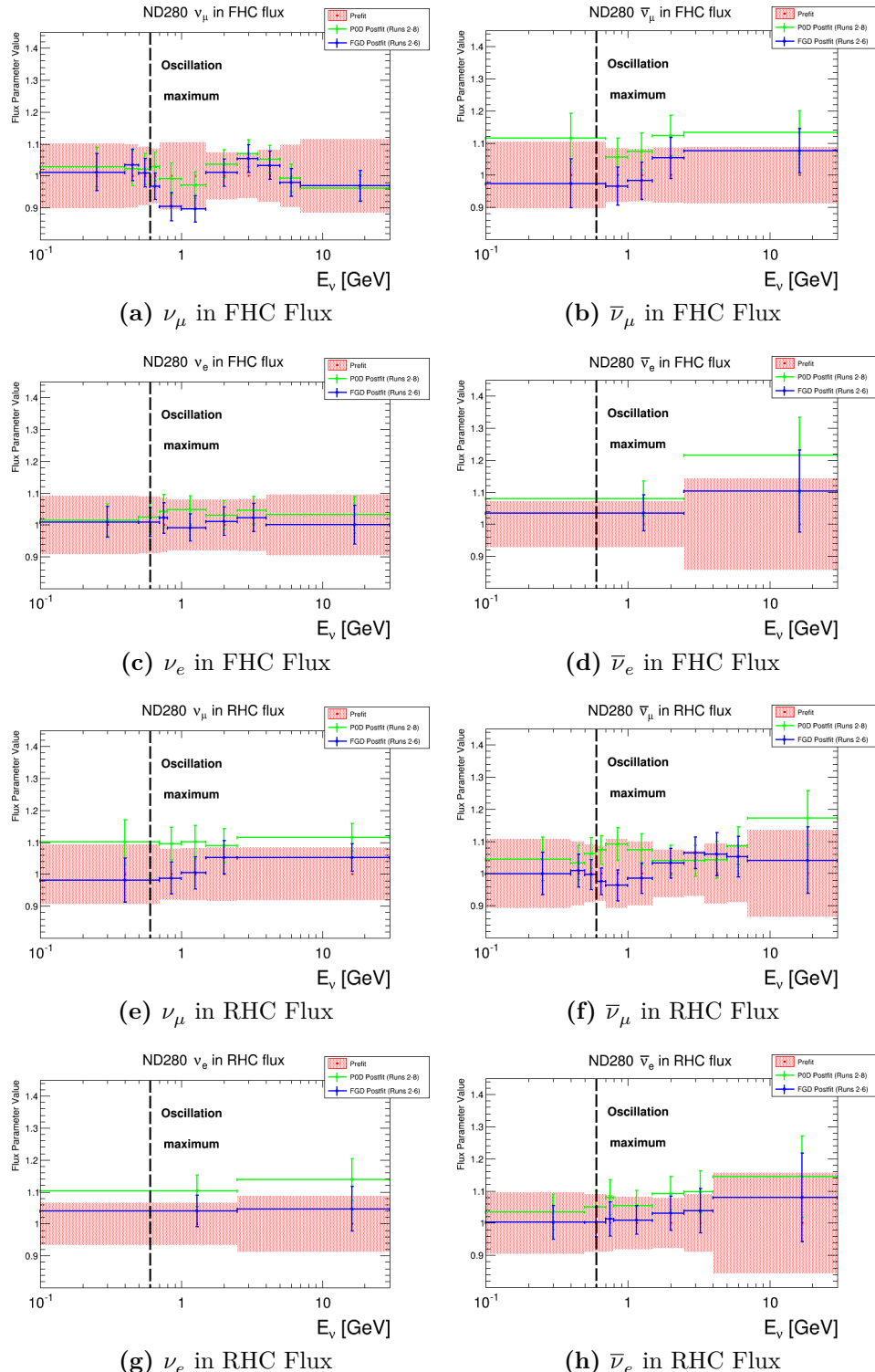


**Figure 6.25:** Postfit ND280 flux parameters for the PØD-only (green) and FGD-only (blue) BANFF fit as functions of neutrino energy. The energy that maximizes the  $\nu_\mu \rightarrow \nu_e$  oscillation (0.6 GeV) is shown with a dashed, black line.

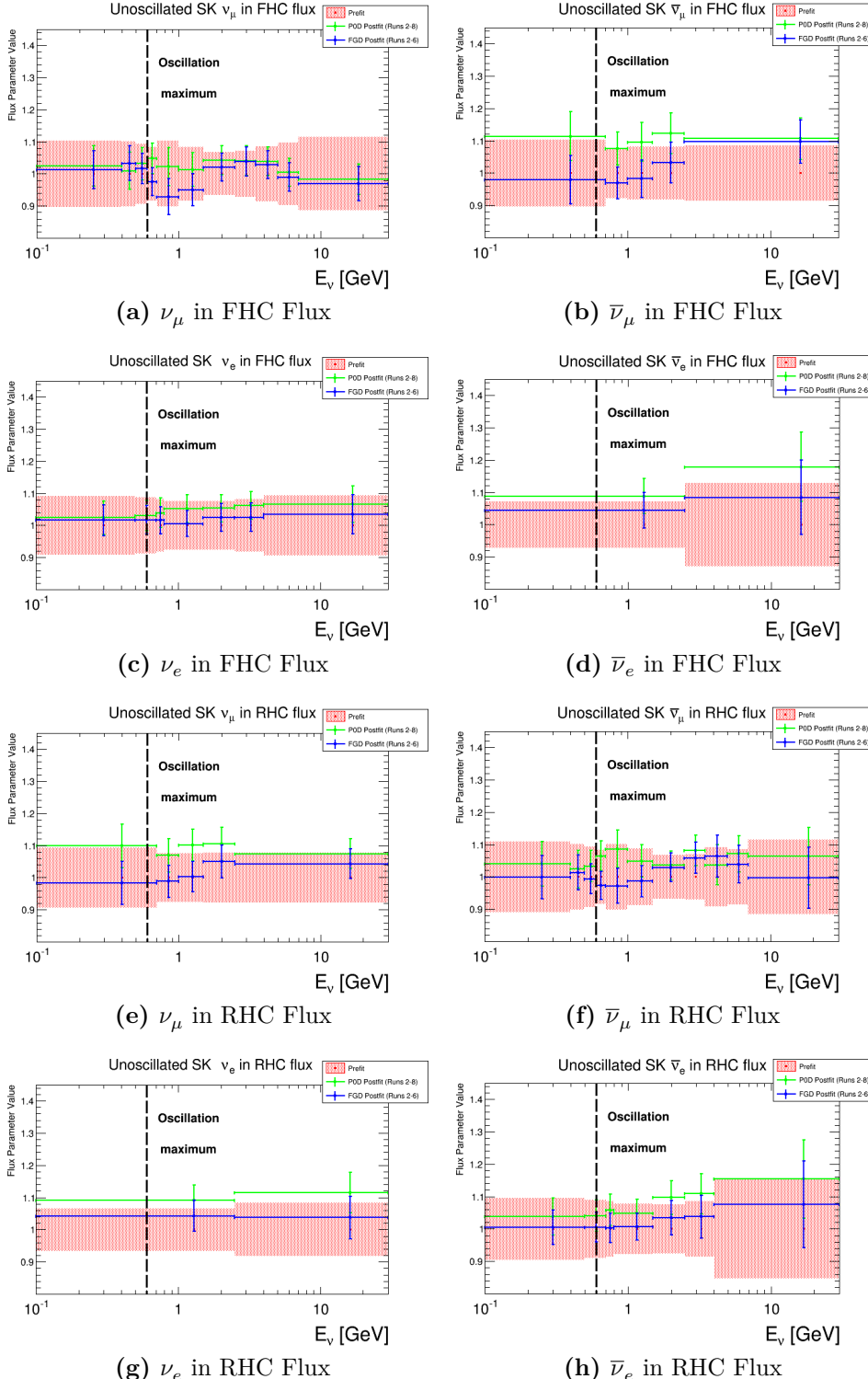
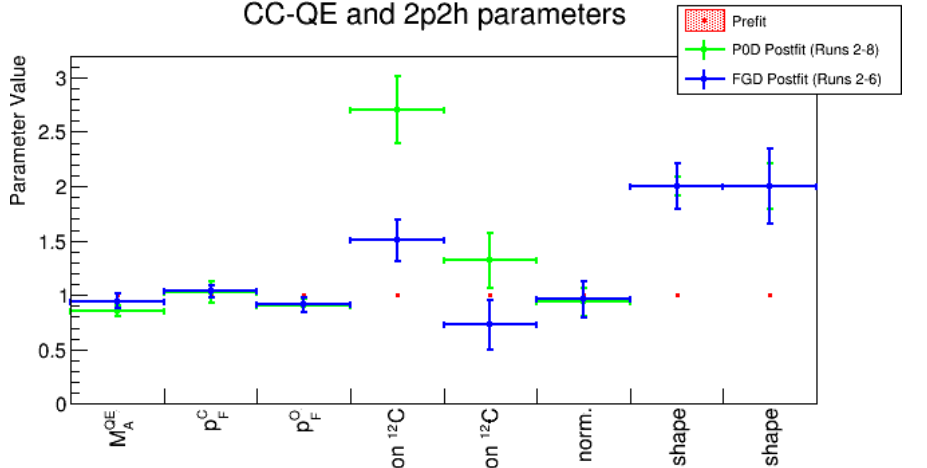
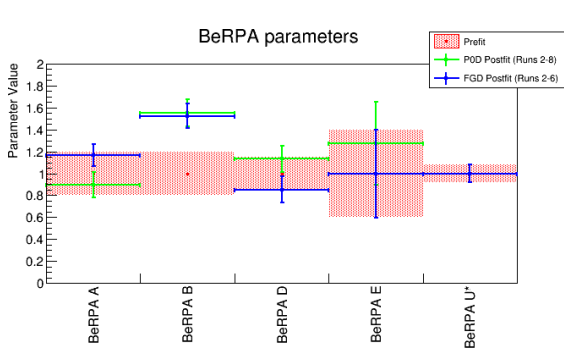


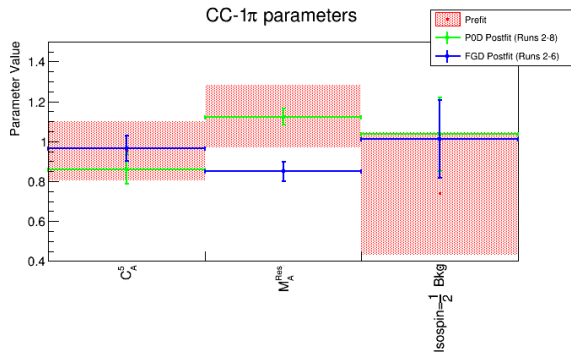
**Figure 6.26:** Postfit SK flux parameters for the PØD-only (green) and FGD-only (blue) BANFF fit as functions of neutrino energy. The energy that maximizes the  $\nu_\mu \rightarrow \nu_e$  oscillation (0.6 GeV) is shown with a dashed, black line.



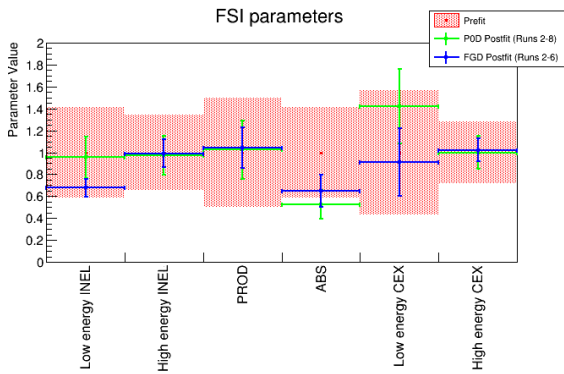
(a) CC- $0\pi$  Parameters



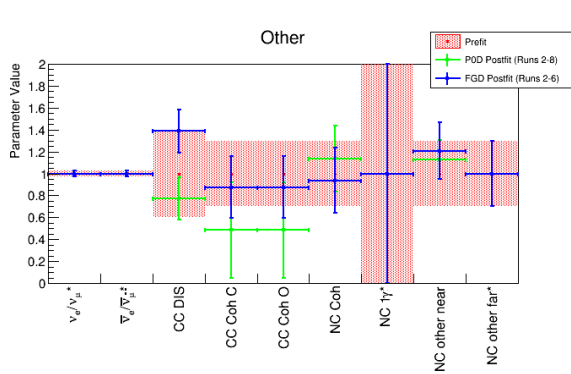
(b) BeRPA Parameters



(c) CC- $1\pi$  Parameters

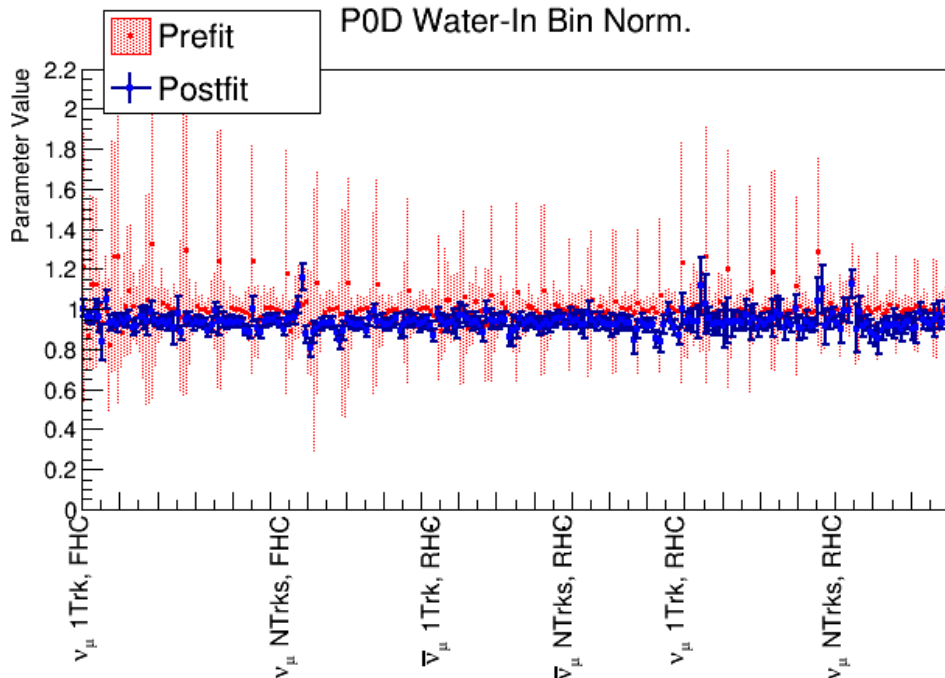


(d) FSI Parameters

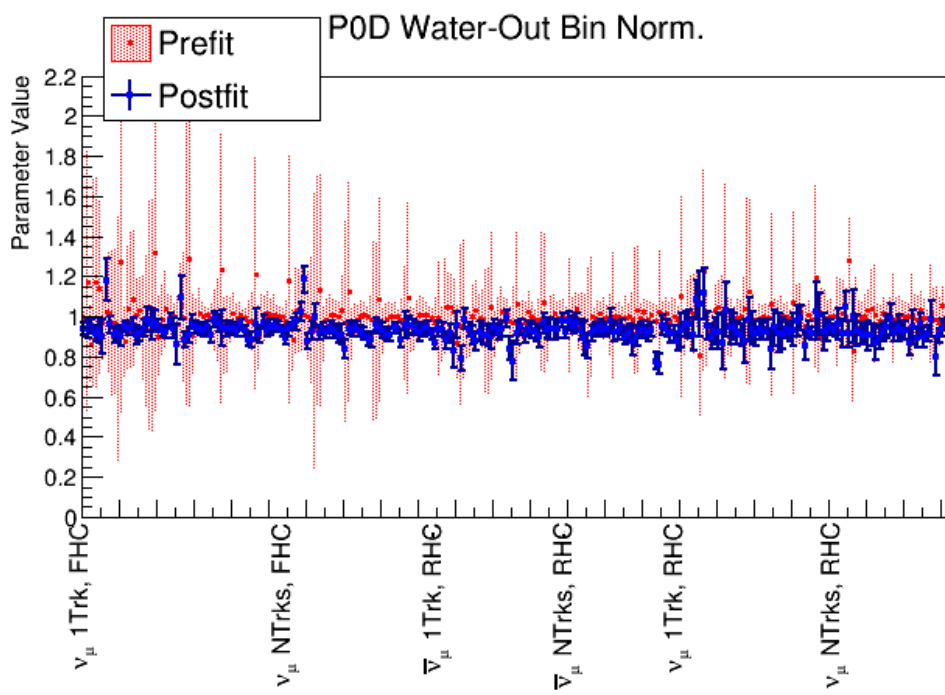


(e) CC-Other and NC-Other Parameters

**Figure 6.27:** Postfit cross section parameters for the PØD-only (green) and FGD-only (blue) BANFF fit. In these figures, all shape and scale factor parameters are adjusted to 1 to provide a consistent graphical representation of all fit parameters. Shape parameters always have a prefit value of 0. Parameters without prefit uncertainties had a flat prior applied to them and an asterisk (\*) represents a fixed parameter.



(a) Water-In



(b) Water-Out

**Figure 6.28:** Prefit and postfit PØD bin normalization parameters.

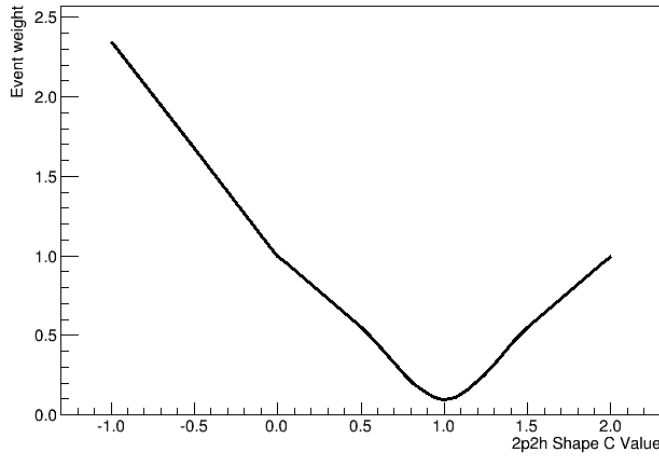


**Figure 6.29:** The “mirrored” spline for a single event. The spline represents an event weight and variations from the prefit value of 0 alters the event weight. The 2p2h shape splines are mirrored about the value of +1 to provide an uncertainty in the postfit result.

data are sampling from two different neutrino interaction populations. We can also call this the alternative hypothesis. The null hypothesis,  $H_0$ , is that PØD-only and FGD-only data are sampled from the same interaction population. For each measurement  $X_i$  that is independently and identically distributed from a standard normal  $\mathcal{N}(\mu = 0, \sigma^2 = 1)$ , then the following function

$$\chi^2 = \sum_i X_i^2, \quad (6.1)$$

is distributed according to a chi-square distribution

$$F(\chi^2, r) = \frac{1}{2^{r/2}\Gamma(r/2)} (\chi^2)^{(r/2-1)} e^{(-\chi^2/2)}, \quad (6.2)$$

where  $r$  is the number of degrees of freedom (NDOF) and  $\Gamma(x)$  is the Gamma function. We can calculate a p-value to reject the null hypothesis at the  $\alpha$ -level.

If we let  $p_i^{\text{PØD}} (p_i^{\text{FGD}})$  represent the measurement of the  $i$ th parameter for the PØD-only (FGD-only) BANFF fit, then our test statistic can be formally defined as

$$\chi_{\text{PØDvsFGD}}^2 = \sum_i \sum_j \frac{(p_i^{\text{PØD}} - p_i^{\text{FGD}})(p_j^{\text{PØD}} - p_j^{\text{FGD}})}{V_{i,j}^{\text{PØDvsFGD}}} \quad (6.3)$$

### Postfit Correlation Matrix

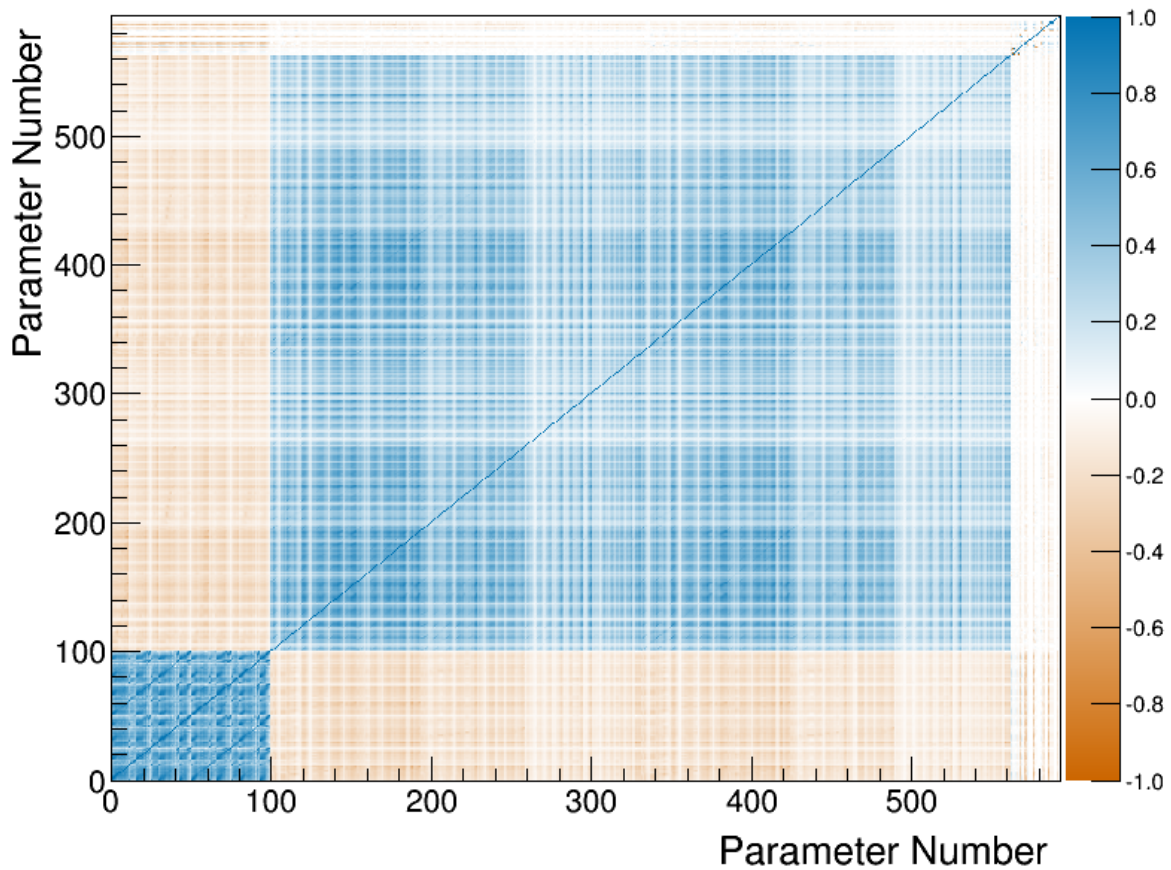
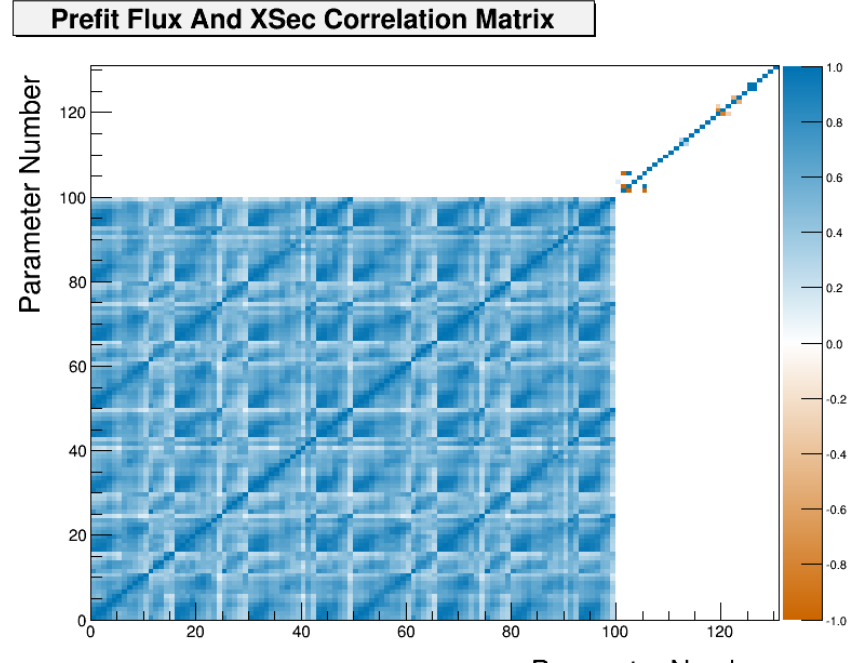
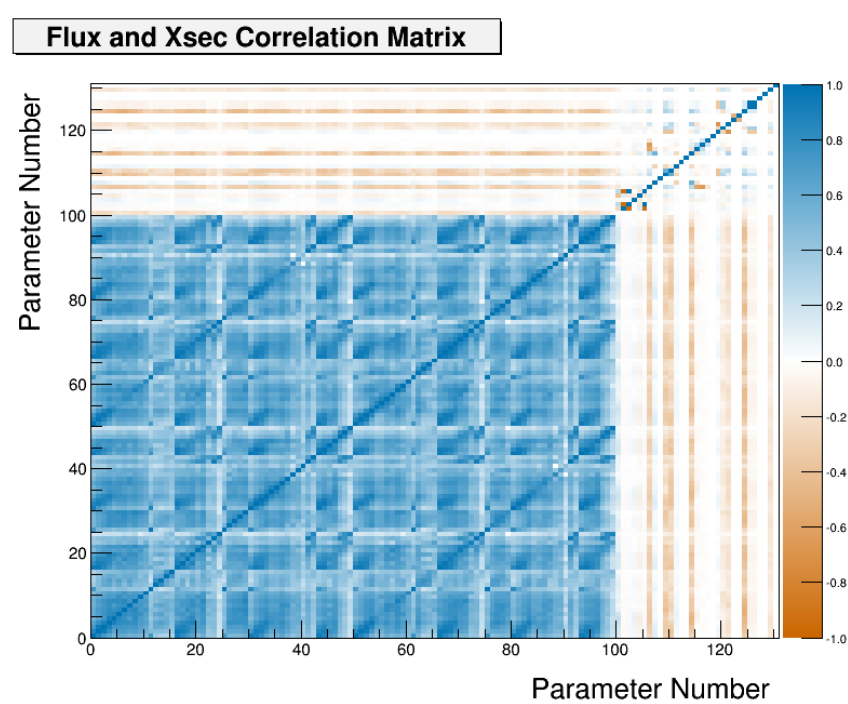


**Figure 6.30:** Postfit correlation matrix. The first 100 parameters are the flux parameters with the first 50 corresponding to ND280 and the last 50 with Super-K. Between 100 and 561 are the bin normalization parameters. The last 31 are the cross section parameters.



(a) Prefit flux and cross sections correlations



(b) Postfit flux and cross section correlations

**Figure 6.31:** Prefit and post fit flux and cross section parameter correlations. In (a) and (b), the prefit and postfit, respectively, correlation matrices for the flux and cross section parameters are shown. The first 50 parameters correspond to the ND280 flux with the last 50 with the SK flux. The final 31 parameters are for the cross section.

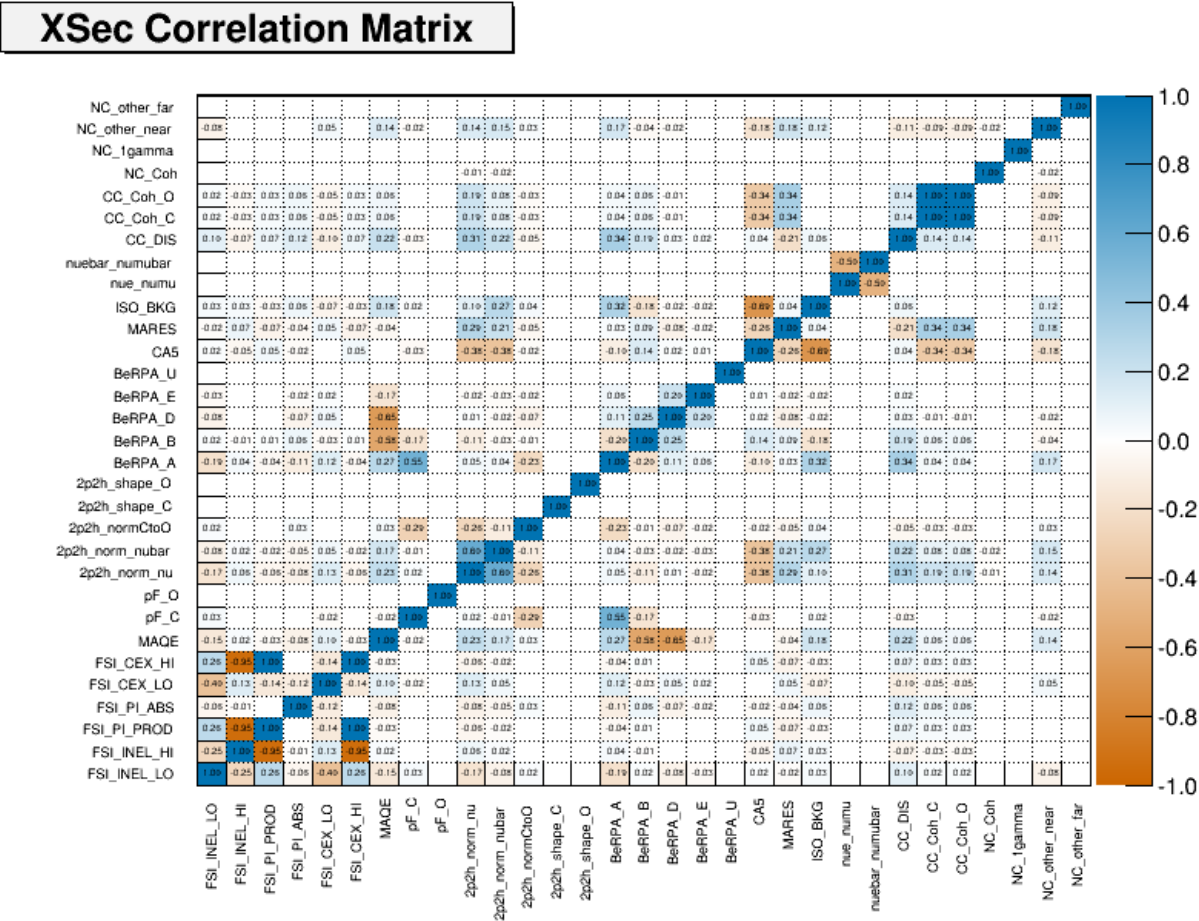


**Figure 6.32:** Postfit cross section correlation matrix

where  $V_{i,j}^{\text{P}\emptyset\text{DvsFGD}}$  is the covariance of measurement  $i, j$ . Since the purpose of the BANFF fit is to provide a constraint on the SK flux and cross section models, we will ignore the ND flux bins and  $(p, \cos \theta)$  bin normalization parameters. Also we assume for simplicity that the P $\emptyset$ D and FGD data are completely uncorrelated. This simplifies the test statistic to

$$\begin{aligned}\chi_{\text{PvF}}^2 &= \sum_i \frac{(p_i^{\text{P}\emptyset\text{D}} - p_i^{\text{FGD}})^2}{V_{i,i}^{\text{P}\emptyset\text{D}} + V_{i,i}^{\text{FGD}}} , \\ &= (\chi_{\text{PvF}}^2)^{\text{Flux}} + (\chi_{\text{PvF}}^2)^{\text{xsec}}\end{aligned}\quad (6.4)$$

where  $V_{i,i}^{\text{P}\emptyset\text{D}}/V_{i,i}^{\text{FGD}}$  is the variance of the  $i$ th parameter in the P $\emptyset$ D versus FGD-only (PvF) BANFF fit measurements. We have divided the test statistic into two terms: the flux and the cross section (xsec) contributions.

We can calculate a p-value,  $p$ , of observing a test statistic at least as extreme in a chi-square distribution by integrating the right-hand tail of the chi-square distribution using the inverse cumulative distribution function (ICDF)

$$p(\chi^2, r) = \int_{\chi^2}^{\infty} F(x', r) dx', \quad (6.5)$$

where  $\chi^2$  is the test-statistic from 6.4.

Now let us count the NDOF for the p-value calculation. There are 50 SK flux parameters and 31 cross section parameters. However, five of cross section parameters are fixed. Additionally, we have assumed the FGD-only result is our expectation, and so we have one less NDOF. This leaves us with

$$r = \underbrace{50}_{\text{Flux}} + \underbrace{(31 - 5)}_{\text{xsec}} - 1 = 75 \text{ NDOF.}$$

If we wish to reject the null hypothesis at the 5% level, a chi-squared value of 96.21 or greater is required.

We must qualify the assumptions about the above null hypothesis test. Assuming the two data fits are completely uncorrelated is not fully justified, and the correct method would be to run a joint FGD-PØD fit to extract the correlations. *By assuming that the fits are uncorrelated, this provides an upper limit on rejecting the null hypothesis.* The reasoning for this is that the well constrained parameters in both fits should be positively correlated since the same neutrino beam is being observed, and this reduces the magnitude of the chi-squared test statistic. We observe that the PØD-only flux parameters are skewed above the FGD-only flux parameters, and, therefore, their difference is not normally distributed about zero. This indicates a large, positive correlation between the two measurements, and this would decrease the magnitude of the  $(\chi^2_{\text{PvF}})^{\text{Flux}}$  contribution in the test statistic as anticipated. Since the ND280 data is most sensitive to the CC-0 $\pi$  parameters, we observe most of the CC-0 $\pi$  parameters in both fits are positively correlated. Hence, the magnitude of the  $(\chi^2_{\text{PvF}})^{\text{xsec}}$  term is decreased as well. Since we now understand the limitations of the test statistic and its purpose, we can proceed to calculate the p-value.

We find that the reduced test statistic is

$$\tilde{\chi}^2_{\text{PvF}} = \frac{\chi^2_{\text{PvF}}}{r} = \frac{81.41}{75} \approx 1.085,$$

of which indicates good agreement between the two measurements for the ND constraint. This corresponds to a p-value of  $p = 0.2865$  or a 28.65% probability of obtaining a larger test statistic. This result is shown in Figure 6.33 on page 201. Since this is not sufficiently close to the 5% level, we fail to reject the null hypothesis. *We can conclude that the PØD-only fit, FGD-only fit, and subsequent fits describe the same data in T2K.*

### 6.3.1 Receiver Operating Characteristic

To demonstrate the differences between the PØD and FGD parameter estimates, receiver operating characteristic (ROC) curves are provided in Appendix I. The advantage of ROC

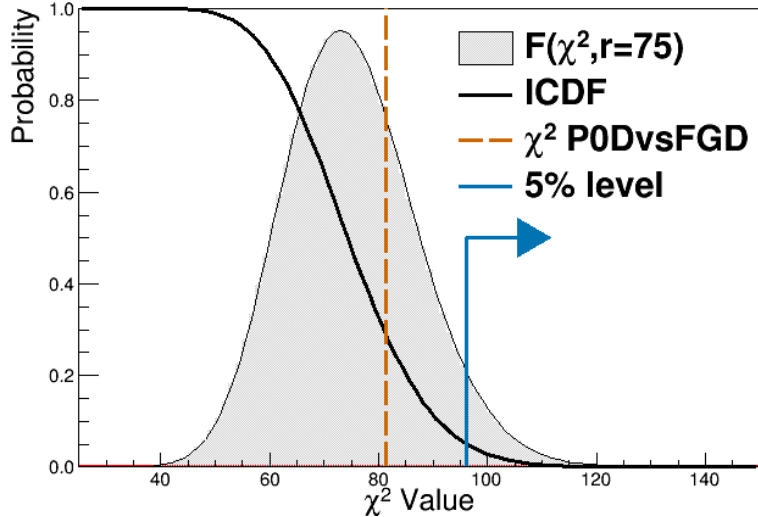


**Figure 6.33:** P-value for the PØD vs FGD ND constraint. Shown in solid black is the inverse cumulative distribution function (ICDF) with 75 NDOF. The chi-squared PDF is shown in gray with arbitrary normalization. The obtained value of the test statistic, shown as a dashed, red line, is 81.41 which is below the 5% level, shown as a solid, blue arrow.

curves over a p-value calculation is that the differences between the two fits can be statistically quantified for all parameters. These curves provide an indication of which fit has better constraints in parameter space, suggest the limitation of each fit, and provide guidance for future researchers.

## 6.4 Summary

In this chapter, we have explored the postfit results for the PØD-only data set and compared it against the FGD-only fit. While the FGD-only data samples have about twice as many more neutrino-oxygen events than the PØD-only data, which helps with sensitivity of the oxygen cross section parameters, the accumulated neutrino exposures are similar. Moreover, we observe a good level of agreement between the two fits with the largest differences observed with less constrained parameters like those that characterize the 2p2h interaction. A hypothesis test was performed to quantify if the PØD-only and FGD-only data are similar or not. In order to reject the null hypothesis, which is that the two sets are similar, at the 5% level, a  $\chi^2$  of 96.21 or greater was needed. A chi-squared of 81.41 was obtained, correspond-

ing to a p-value of 28.65, which is insufficient to reject the null hypothesis. Therefore, using the BANFF fit method with the current PØD samples and cross section parameterization, the ND280 constraint is expected to be largely similar if propagated to the next stage in the oscillation analysis. We will examine this in the final chapter.

# Chapter 7

## Discussion

This chapter serves to summarize the methods and results shown in this thesis. The Tokai to Kamioka (T2K) experiment is a long baseline, neutrino oscillation experiment designed to observe a  $\nu_\mu$  beam oscillate into  $\nu_e$ . With the aid of the Japan Proton Accelerator Research Complex (J-PARC), a dedicated near detector called ND280 is located downstream of the neutrino production source to observe the beam before oscillations occur. Since the start of data collection, the fine grain detector (FGD) in ND280 has provided constraints on the neutrino flux and neutrino-water interaction modes important to the oscillation analysis. This thesis is an analysis of an independent measurement of the ND280 constraint using a maximum likelihood estimate in the Beam and Near Detector Flux Task Force (BANFF) framework with samples from the pi-zero detector (PØD).

Analysis samples have been developed with the PØD to capture a wide variety of interaction modes in T2K, importantly interactions classified as charged current quasi-elastic (CCQE) which constitute the highest cross section in the T2K neutrino energy spectrum. While the PØD has a larger volume compared to the FGD, which means it has more neutrino interactions to select, the PØD is less sensitive to non-CCQE interactions like CC single pion production. This limitation is largely due to the design of the detector and sample selection which reduce its  $(p, \cos \theta)$  sensitivity to the lower energy outgoing muons. The systematic

uncertainties inherent in the samples were controlled for in a similar manner with previous BANFF analyses.

The PØD-only data fit shows very good agreement with the FGD-only result using the same flux and cross section parameters. Trends in the postfit parameters like the flux shape and the quantum mechanical correlation affects on the observable cross section were observed in both sets of fits. A hypothesis test was conducted to test if the PØD-only and FGD-only data fits are consistent with one another. The test produced

$$\tilde{\chi}^2 = \frac{\chi^2}{\text{NDOF}} = \frac{81.41}{75}, \quad p = 0.2865,$$

which indicates the test failed to reject the null hypothesis. *This is another way of saying the PØD provides a similar ND280 constraint compared to the FGD.*

Other topics discussed in this chapter are presented in the following order. First shown is a prediction of the oscillated samples at SK using the ND constraint in Section 7.1. Possible analysis improvements are discussed in Section 7.2. Finally, the prospect of a joint PØD and FGD fit are discussed in Section ??-Joint:.

## 7.1 Prediction of the T2K Oscillation Analysis Samples

In this section, we analyze the BANFF fit as the input for the oscillation analysis. We are explicitly NOT performing the oscillation analysis, but we are building a prediction of the oscillated neutrino samples using the frequentist framework described in the 2017 oscillation analysis publication [6]. We then compare the prediction with the observed neutrino energy spectra of the four CCQE-enriched samples at Super-Kamiokande (SK). These samples are the FHC mode ( $\nu$ -mode)  $\nu_\mu$  sample, the RHC mode ( $\bar{\nu}$ -mode)  $\bar{\nu}_\mu$  sample, the  $\nu$ -mode  $\nu_e$  sample, and the  $\bar{\nu}$ -mode  $\bar{\nu}_e$  sample.

**Table 7.1:** Oscillation parameters used as inputs for studies of simulated data.

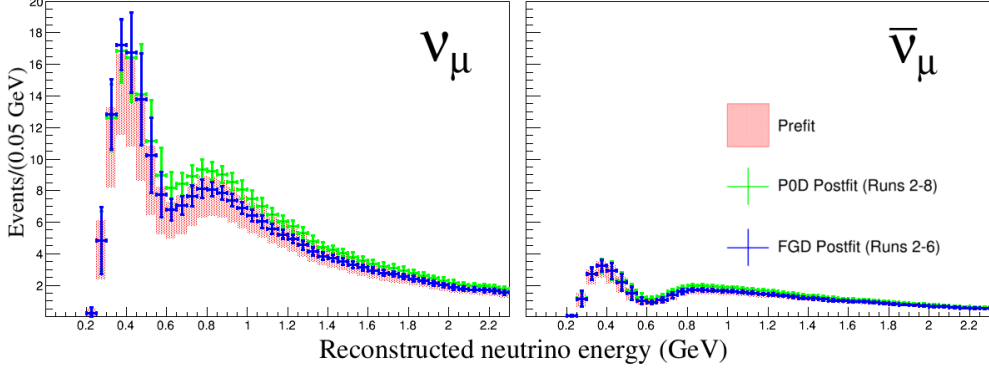
Parameter	Value	Units
Mass hierarchy	Normal	
$\Delta m_{21}^2$	7.53	$10^{-5}$ eV $^2/c^4$
$ \Delta m_{32}^2 $	2.509	$10^{-3}$ eV $^2/c^4$
$\sin^2 \theta_{23}$	0.528	1
$\sin^2 2\theta_{12}$	0.846	1
$\sin^2 2\theta_{13}$	0.0857	1
$\delta_{\text{CP}}$	-1.601	rad
$e^-$ density	2.6	g/cm $^3$
Baseline length	295	km
$\nu$ -mode luminosity	14.7	$10^{20}$ POT
$\bar{\nu}$ -mode luminosity	7.6	$10^{20}$ POT

**Table 7.2:** Number of events expected in the SK CCQE-enriched samples.

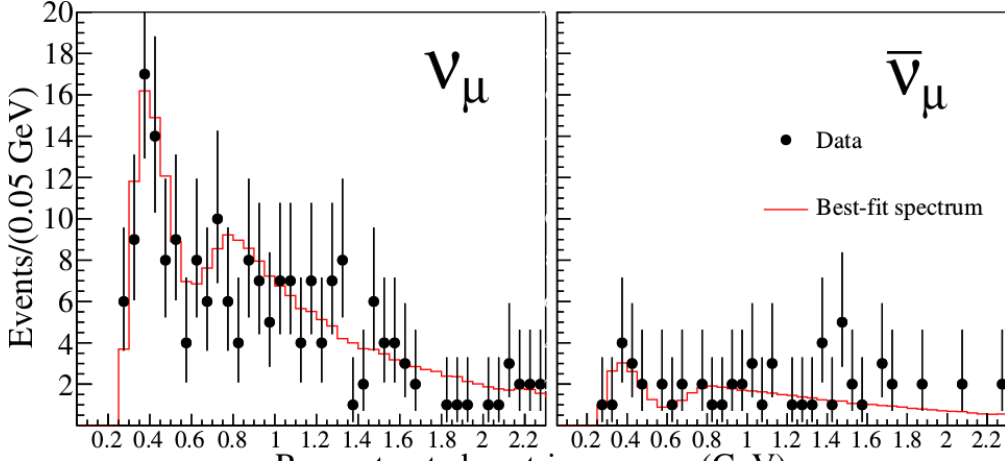
	Prefit	PØD-only	FGD-only	Observed
$\nu_\mu$ CCQE ( $< 2.3$ GeV)	207.34	252.41	228.07	201
$\bar{\nu}_\mu$ CCQE ( $< 2.3$ GeV)	49.67	58.14	52.47	57
$\nu_e$ CCQE ( $< 1.3$ GeV)	65.61	83.01	74.71	74
$\bar{\nu}_e$ CCQE ( $< 1.3$ GeV)	7.74	9.03	8.15	7

The SK prediction is built with the following ingredients: the flux and cross section parameter estimates from the BANFF fit parameter estimates and covariance matrix, the nominal set of SK detector systematics in the frequentist analysis software, and the full three-flavor oscillation probabilities. The full three-flavor oscillation parameters used are the same as listed in TABLE II in the 2018 CP violation search paper [10], which are shown in Table 7.1 on page 205 for convenience. The observed spectra are also taken from the 2018 CP violation search paper, which had a integrated luminosity of  $2.2 \times 10^{21}$  POT.

The spectra are shown in the following order. First are the of the  $\nu_\mu$  CCQE and  $\bar{\nu}_\mu$  CCQE-enriched samples together shown in Figure 7.1 on page 206. Next is the  $\nu_e$  CCQE-enriched sample shown in Figure 7.2 on page 206. Finally is the  $\bar{\nu}_e$  CCQE-enriched sample shown in Figure 7.3 on page 207. The integrated spectra are tabulated in Table 7.2 on page 205.

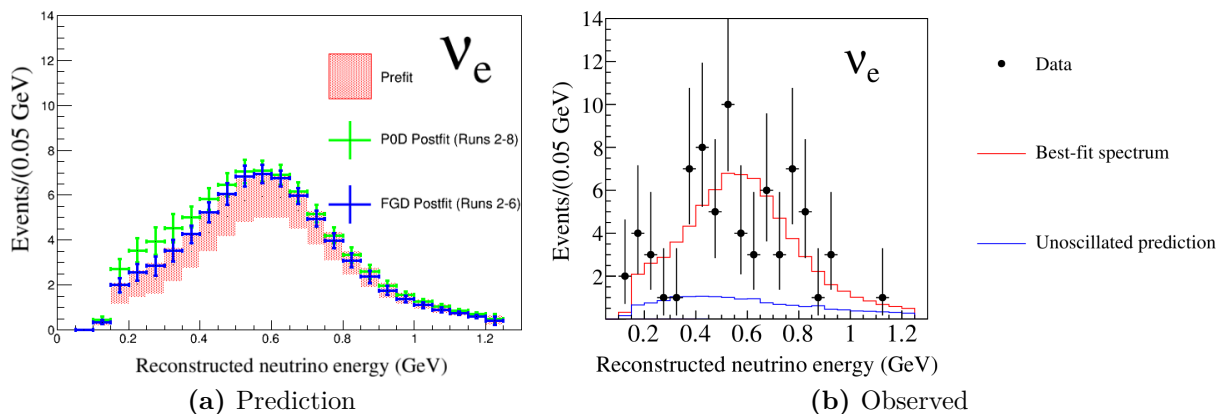


(a) Prediction

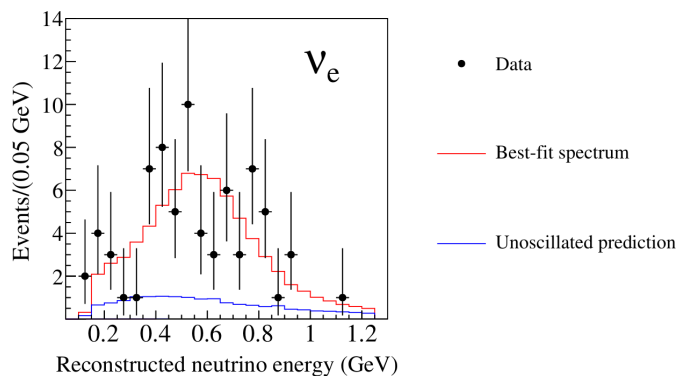


(b) Observed

**Figure 7.1:** Reconstructed  $\nu_\mu$  (left) and  $\bar{\nu}_\mu$  (right) CCQE-enriched energy distributions at SK. The top figure is the predicted spectra while the bottom is the observed spectra. The observed spectra is taken from the 2018 CP violation search publication [10].



(a) Prediction



(b) Observed

**Figure 7.2:** Reconstructed  $\nu_e$  CCQE-enriched energy distribution at SK. The observed spectra is taken from the 2018 CP violation search publication [10].

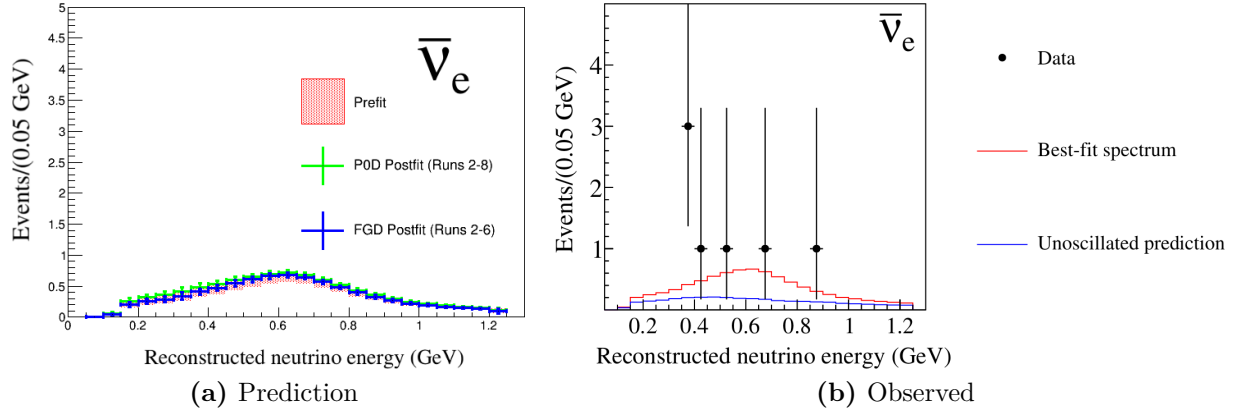


**Figure 7.3:** Reconstructed  $\bar{\nu}_e$  CCQE-enriched energy distribution at SK. The observed spectra is taken from the 2018 CP violation search publication [10].

We observe that each PØD-only predicted spectrum is systematically higher than each FGD-only predicted spectrum. However, the more interesting differences are the integrated prediction. While the FGD-only prediction has better agreement with both the  $\nu_e$  and  $\nu_\mu$  CCQE samples, the PØD-only prediction is agrees well with the  $\bar{\nu}_\mu$  CCQE sample. It is difficult to judge the agreement of the  $\bar{\nu}_e$  CCQE sample due to small statistics. However, this all suggests that including the PØD data samples can improve the ND constraint in RHC mode.

## 7.2 Analysis Improvements

Looking forward, the PØD-only analysis can be improved significantly. The PØD selections in this thesis are simplistic compared to the recent developments in the T2K experiment. The author was a part of the second generation cross section analysis of single pion production in the PØD, which utilized deep learning techniques, to select a relatively pure CC-1 $\pi$  sample. These details are provided in Appendix A. Additionally, the PØD  $\bar{\nu}_\mu$  CC-0 $\pi$  analysis [27] was able to achieve a high-purity CCQE-like sample using almost identical cuts as presented in this thesis. However, both the CC-1 $\pi$  and CC-0 $\pi$  analyses use cuts that are

not yet available in the BANFF framework due to technical difficulties and lack of expertise in the collaboration.

Also more validation studies could be done to understand the sensitivity of the PØD samples. A test of the biases of the fit parameters requires fitting an ensemble of “fake data” sets, which are variations of the Asimov set. This all requires significant amount of computational time to complete<sup>21</sup>.

There are other possible improvements to the ND constraint analysis using the methods developed for machine learning applications. The following two sections are on topics to improve the BANFF fit analysis in its current state. These methods are quite general and rely on the fundamentals of parameter estimation techniques in statistics. A section summary is provided to summarize their details.

First is a discussion on applying a different regularization strength. Second is a method to reduce the number of effective bin normalization parameters using a different penalty function called the Lasso.

### 7.2.1 Regularization Strength

Recall that the BANFF ND constraint test statistic is defined as

$$\chi_{\text{ND280}}^2 = \chi_{\text{LLR}}^2(\vec{N}^d, \vec{N}^p) + \chi_{\text{Penalty}}^2(\Delta \vec{y})$$

where  $\vec{N}^d$  and  $\vec{N}^p$  are the binned data and prediction measurements, respectively, and  $\Delta \vec{y}$  is the difference between postfit and prefit parameter values in the fit. This equation is similar to the general class of parameter regression using regularization [50]

$$\hat{\beta} = \underset{f \in \mathcal{F}, \beta \in \mathbb{R}^d}{\operatorname{argmin}} \left\{ L(\eta, f(\vec{\beta})) + \lambda J(f) \right\} , \quad (7.1)$$

---

<sup>21</sup>Also not to mention the carbon footprint left afterwards.

where  $L$  is a loss function<sup>22</sup> of measurements  $\eta$ ,  $J(f)$  is a penalty function,  $f(\vec{\beta})$  is a  $d$ -dimensional function of  $\vec{\beta}$ ,  $\lambda$  is the regularization parameter, and  $\mathcal{F}$  is a space of function on which  $J(f)$  is defined. In regularized regression problems, the penalty term serves to solve an ill posed problem by adding external information. Similarly, the regularization parameter controls the importance of the penalty. We recognize that the loss function  $L$  is the log-likelihood ratio term  $\chi_{\text{LLR}}^2$ , and penalty term is  $J = \chi_{\text{Penalty}}^2$  with regularization strength  $\lambda = 1$ .

In defining the BANFF test statistic in Chapter 2, the regularization term  $\lambda$  was set to 1 without justification. We can test the effectiveness of this choice using cross-validation. Cross-Validation provides an estimate on the prediction error as well as determines the “optimal” choice of regularization. In cross-validation, the input data is randomly split into  $K$  equal sized partitions. For the  $k \in K$  data partition, we fit the model to the other  $K - 1$  parts of the data and calculate a prediction error  $P$ .

In this verification of the regularization strength, the test statistic is altered to include a regularization term

$$\begin{aligned}\chi_{\text{ND280}}^2 &= \chi_{\text{LLR}}^2 + \lambda \chi_{\text{Penalty}}^2(\vec{y}) \\ &= \chi_{\text{LLR}}^2 + \lambda (\vec{y} - \vec{y}_0)^T V^{-1} (\vec{y} - \vec{y}_0),\end{aligned}\tag{7.2}$$

and the data is split into  $K = 5$  partitions. The prediction error,  $P$ , in this analysis is defined as

$$P_k \left( \left( \chi_{\text{train}}^2 \right)^{-k}, \left( \chi_{\text{test}}^2 \right)^k \right) = \left| \left( \chi_{\text{train}}^2 \right)^{-k} - \left( \chi_{\text{test}}^2 \right)^k \right| \tag{7.3}$$

where  $\left( \chi_{\text{train}}^2 \right)^{-k}$  is the fitted model statistic on all but the  $k$ th partition, and  $\left( \chi_{\text{test}}^2 \right)^k$  is prediction from the fitted model on the  $k$ th partition. This definition of  $P$  is useful since the penalty terms cancel, leaving only the difference in log-likelihood terms. The optimal regularization strength is determined by minimizing the cross-validation error,

---

<sup>22</sup> $L$  is also called an objective function.

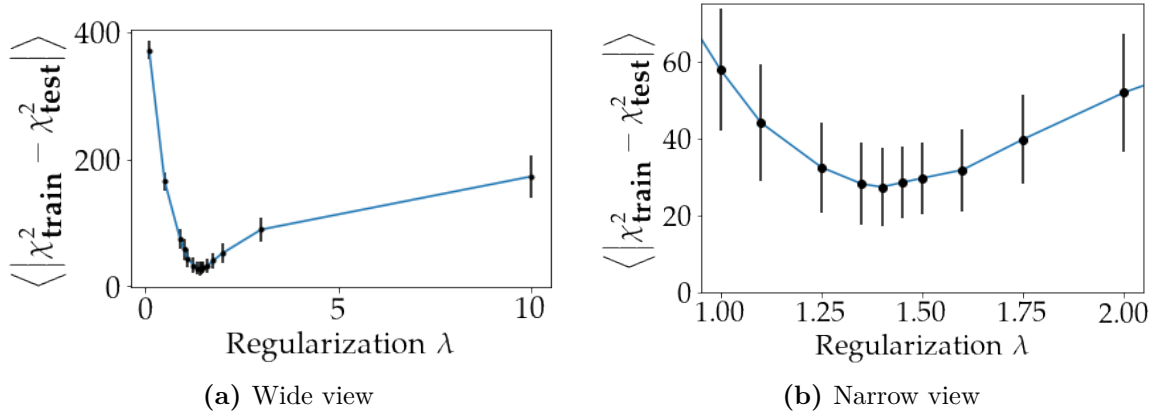


**Figure 7.4:** Cross-validation curve for the BANFF fit regularization strength. Figure (a) examines the cross-validation error for a wide range of regularization strengths. Figure (b) zooms in on the minimized error. The error bars shown are statistical only.

$$\begin{aligned} \text{CV}(\lambda) &= \langle |\chi^2_{\text{train}} - \chi^2_{\text{test}}| \rangle \\ &= \frac{1}{5} \sum_{k=1}^5 P_k \left( (\chi^2_{\text{train}})^{-k}, (\chi^2_{\text{test}})^k \right), \end{aligned} \quad (7.4)$$

which is the average prediction error.

Results of the cross-validation are shown in Figure 7.4 on page 210. We see that while the penalty strength of  $\lambda = 1$  nearly minimizes the cross-validation error, slightly larger penalties are preferred. The cross-validation error curve is minimized roughly at  $\lambda = 1.4$ , and it is roughly quadratic in the neighborhood around the minimum. Therefore, a more regularized solution is preferred with the data sample.

Another data fit with  $\lambda = 1.4$  was performed with the following results. The MINUIT optimization routine required 175602 (149661) iterations to find the global minimum at  $\hat{\chi}^2_{\text{ND}280} = 1344.89$  (1412.28) with the regularized (non-regularized) penalty term. The flux parameters have significantly reduced uncertainties compared to the  $\lambda = 1$  result. The cross section parameters are relatively the same as before except for the CC coherent uncertainties which are much smaller. There was no observed changes in the bin normalization parameters as well. This suggests that the flux covariance matrix input needs to reexamined for future BANFF fit analyses. The postfit parameters are presented in Appendix J.

## 7.2.2 Alternative Penalty

Consider solving the linear regression problem

$$\vec{\eta} = X\vec{\beta} \quad (7.5)$$

where  $X$  is a  $p \times d$  matrix of  $d$  model features from  $p$  measurements,  $\vec{\beta}$  is a vector of regression weights with  $p$  rows, and  $\vec{\eta}$  is a response vector. There are many approaches to solving Eqn. (7.5) using Eqn. (7.1). A popular solution is the  $l_2$ -regularization constraint [50]

$$\operatorname{argmin}_{\vec{\beta} \in \mathbb{R}^d} \left\{ L(\vec{\eta}, \vec{\beta}) + \lambda \sum_i |\beta_i|^2 \right\} \quad (7.6)$$

where the sum of squares of the weights  $\beta_i$  sets the constraint and  $L$  is the loss function. A popular choice of  $L$  is using ordinary least squares

$$L(\vec{\eta}, \vec{\beta}) = \sum_j |\vec{\eta} - X\vec{\beta}|^2,$$

which provides the lowest variance in parameter weights.

With some algebra, we can rewrite the BANFF test statistic Eqn. (2.13) into the form of Eqn. (7.6). We again recognize  $\chi_{\text{LLR}}^2$  is the loss function  $L$  which leaves the penalty term to be tackled. The (inverse) covariance matrix is symmetric and real and can be decomposed as

$$V^{-1} = U^T \Lambda U$$

where  $U$  and  $\Lambda$  are the matrix of the eigenvectors and eigenvalues, respectively, of  $V^{-1}$ . Since the eigenvalues are real and positive, the matrix  $\Lambda$  can be expressed as the square of a diagonal matrix  $\Gamma$

$$\Lambda = \Gamma^2.$$

We can now rewrite the penalty term as an inner product of two vectors.

$$\begin{aligned}\chi_{\text{Penalty}}^2 &= (\Delta \vec{y})^T V^{-1} (\Delta \vec{y}) \\ &= (\Delta \vec{y})^T U^T \Gamma^2 U (\Delta \vec{y}) \\ &= (\Gamma U \Delta \vec{y})^T (\Gamma U \Delta \vec{y}).\end{aligned}$$

If we let  $\vec{\psi} = \Gamma U \Delta \vec{y}$ , then the penalty term becomes

$$\chi_{\text{Penalty}}^2 = (\vec{\psi})^T \vec{\psi} = \sum_j |\psi_j|^2$$

and test statistic is now

$$\chi_{\text{ND280}}^2 = \chi_{\text{LLR}}^2(N^d, N^p) + \|\psi\|_2^2 , \quad (7.7)$$

where  $\|\cdot\|_2^2$  is shorthand for the  $l_2$ -regularization constraint sum of squares. We see that the BANFF test statistic is indeed a  $l_2$ -regularized solution with  $\Delta \vec{y}$ , recast as  $\vec{\psi}$ , acting as the parameter weight vector and has the regularization strength  $\lambda = 1$ .

Consider now another solution to Eqn. (7.5) using the  $l_1$ -regularization constraint or least absolute shrinkage and selection operator (Lasso)<sup>23</sup>

$$\underset{\vec{\beta} \in \mathbb{R}^d}{\operatorname{argmin}} \left\{ L(\vec{\eta}, \vec{\beta}) + \lambda \|\beta\|_1 \right\}, \quad (7.8)$$

where  $\|\cdot\|_1$  indicates the sum of absolute values of the parameter weight terms. What is unique about the Lasso is its ability to promote model solutions with few nonzero coefficient weights, sometimes called sparse solutions. In other words, predictor parameters with no model impact are excluded in the solution using the  $l_1$ -regularized constraint. Thus the Lasso has the advantage of providing an interpretable model in situations with very high

<sup>23</sup>The Lasso or  $l_1$ -regularization constraint is commonly employed in parameter estimation problems in linear systems. For example, the method has been used in cancer class prediction with gene expression profiling in the “PAM” package [82]. The Lasso has also been shown to work with generalized linear models [42].

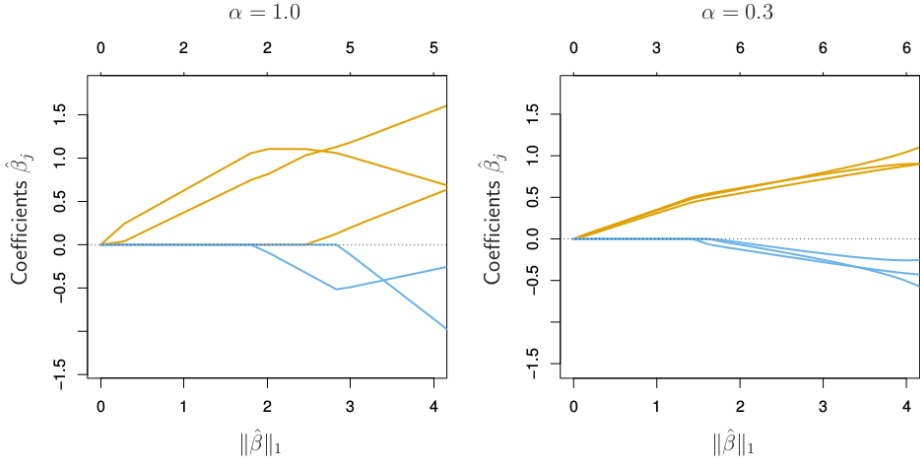


**Figure 7.5:** The Lasso vs elastic net constraint. Six variables are shown and the highly correlated variables are in groups of three. The Lasso estimate, left, estimate exhibits erratic behavior as the regularization strength  $\lambda$  is varied. The elastic net, right, pulls highly correlated variables together. In both panels, the vertical axis is the magnitude of the parameter weights (coefficients), the bottom horizontal axis is the regularization strength as measured by the estimate  $\|\hat{\beta}\|_1$ , and top horizontal axis is the count of non-zero parameter weights. This figure was taken directly from the following reference [51].

parameter spaces. However, the Lasso does not handle highly correlated variables very well. This is overcome by combining the Lasso with  $l_2$ -regularization which is called the elastic net constraint

$$\operatorname{argmin}_{\vec{\beta} \in \mathbb{R}^d} \left\{ L(\vec{\eta}, \vec{\beta}) + \lambda \left( \frac{1}{2} (1 - \alpha) \|\beta_i\|_2^2 + \alpha \|\beta_i\|_1 \right) \right\},$$

where  $\alpha$  is the “budget” between the Lasso and  $l_2$ -regularization. The results of using the Lasso and elastic net with highly correlated variables is shown in Figure 7.5 on page 213. The elastic net controls for strong within-group correlations and has a unique solution. Further details about the Lasso and elastic net can be found in the following reference [51].

We can potentially reduce the dimensionality of the ND constraint by utilizing the elastic net. Using the elastic net constraint provides a data-driven method to determine the number of important bin normalizations in the analysis. The method to define the fit binning described in Chapter 4 would be unchanged. What changes is that instead of merging fit bins prior to the fit, the elastic net determines which bin normalizations are important or not important. Along with cross-validation, fit bins with minimal to no impact on the fit can be

excluded or combined with important fit bins. Then the best fit parameters and covariance matrix using the current BANFF machinery can still be found.

Another possibility in the future is for the BANFF fit to use the elastic net to directly estimate the flux and cross section parameters. The challenge with this approach is that using non-Gaussian priors, the covariance matrix is no longer calculable using the Hess matrix. This is a general critique of the BANFF fit postfit error estimates since there are non-Gaussian priors for many of the cross section parameters. Instead, bootstrap methods could be employed to infer the parameter covariances. This is further discussed in the following reference [50].

### 7.2.3 Analysis Improvement Summary

We have explored topics that can potentially improve the BANFF fit analysis. Improved sensitivity to CC- $0\pi$  and CC- $1\pi$  model parameters using already developed PØD selections is possible if the BANFF software is updated. We also examined two topics developed in machine learning practices to improve parameter estimation. The first was a study on the strength of the penalty term. It was shown that we can find a tuning, or regularization, parameter for the penalty term that reduces the parameter variance but at cost of some parameter bias. The second topic was a general discussion on using a different BANFF fit test statistic called the Lasso. The Lasso has the attractive feature, without user input, of determining which parameters are unimportant in a model fit. The implication here is that the number bin normalization parameters in the BANFF fit can be effectively shrunk using the data itself.

## 7.3 Future Prospects: Joint PØD+FGD Fit

There are potential improvements in a “joint” PØD+FGD BANFF fit for the T2K experiment. As shown in the previous chapter, the number of neutrino-carbon and neutrino-oxygen

events can be significantly increased by including the PØD data. This will enhance the fit's sensitivity, and possibly improve constraints on poorly constrained parameters like that of the 2p2h interaction. There is an additional observed tension in each of the predicted SK sample spectrum between the PØD-only and FGD-only fits, which needs to be resolved.

However, since the fits were performed on different T2K run periods, an equal POT exposure comparison is useful here. Proposing to run a “joint” PØD+FGD ND constraint using T2K runs 2 - 8, the updated neutrino-nucleus exposures are given in Table 7.3 on page 216. We see that while the number of neutrino-carbon events is still larger in the PØD. However, the PØD has 25% fewer neutrino-oxygen events in FHC mode and 9% more in RHC mode. We can estimate the fractional statistical error ( $\delta N$ ) reduction in a joint fit using the data from Table 7.3 on page 216 assuming the FGD fit is the nominal ND constraint. The fractional errors decrease approximately by

$$\begin{aligned}\delta N_{^{12}C}^{\text{FGD1-FHC}} &= \frac{1}{\sqrt{N_{^{12}C}^{\text{FGD1-FHC}}}} \xrightarrow{+\text{PØD Air}} \frac{1}{\sqrt{(1 + 2.01)N_{^{12}C}^{\text{FGD1-FHC}}}} \sim \frac{1}{\sqrt{3.01}} \approx 0.576 \\ \delta N_{^{16}O}^{\text{FGD2-FHC}} &= \frac{1}{\sqrt{N_{^{16}O}^{\text{FGD2-FHC}}}} \xrightarrow{+\text{PØD Water}} \frac{1}{\sqrt{(1 + 0.72)N_{^{12}C}^{\text{FGD1-FHC}}}} \sim \frac{1}{\sqrt{1.72}} \approx 0.762 \\ \delta N_{^{12}C}^{\text{FGD1-RHC}} &= \frac{1}{\sqrt{N_{^{12}C}^{\text{FGD1-RHC}}}} \xrightarrow{+\text{PØD Air}} \frac{1}{\sqrt{(1 + 1.60)N_{^{12}C}^{\text{FGD1-RHC}}}} \sim \frac{1}{\sqrt{2.60}} \approx 0.620 \\ \delta N_{^{16}O}^{\text{FGD2-RHC}} &= \frac{1}{\sqrt{N_{^{16}O}^{\text{FGD2-RHC}}}} \xrightarrow{+\text{PØD Water}} \frac{1}{\sqrt{(1 + 1.04)N_{^{12}C}^{\text{FGD2-RHC}}}} \sim \frac{1}{\sqrt{2.04}} \approx 0.700,\end{aligned}$$

where combinations of FGD1/2 and FHC/RHC represent the FGD in the different beam modes, and a right-pointing arrow indicates adding the PØD data. These results indicate a fractional statistical error reductions around  $1/\sqrt{2}$  for both neutrino-oxygen events and also potentially stronger flux constraint from higher statistics.

**Table 7.3:** Neutrino-nucleon exposure on target elements in a joint PØD and FGD analysis using T2K runs 2 - 8.

Detector	POT ( $10^{20}$ )		kg POT ( $10^{24}$ )	PØD-to-FGD (kg POT)		
	FHC	RHC		$^{12}\text{C}$	$^{16}\text{O}$	other
PØD Water-out FGD1	7.872	-	2.81	2.01	-	4.64
	11.529	-	1.14			
PØD Water-In FGD2	3.657	-	2.00	5.36	0.724	4.06
	11.529	-	1.12			
PØD Water-out FGD1	-	3.382	1.207	1.60	-	3.69
	-	6.234	0.614			
PØD Water-In FGD2	-	2.852	1.56	7.72	1.04	5.85
	-	6.234	0.606			

Employing both the FGD and PØD in a joint BANFF fit was attempted, but the fit failed to converge due to machine precision limits. Including both detectors with the FGD parameterization described in reference [24] more than doubles the number of parameters and events than a single detector-only fit. This not only requires more iterations to ensure the test statistic global minimum is found, but also requires more calculations per iteration as well. For instance, the required time to ensure the joint PØD+FGD Asimov fit started at the global minimum took 10 times larger than the PØD-only Asimov fit. So parameter shrinkage must be performed on both analyses if reasonable computational speed and maximum statistical power are desired in the BANFF fit. This is further discussed in Appendix Chapter G.

# Bibliography

- [1] K. Abe et al., The T2K Experiment, *Nucl. Instrum. Meth.*, A659:106–135, 2011. 28, 31, 33, 36, 39, 43, 47, 48
- [2] K. Abe et al., Measurements of the T2K neutrino beam properties using the INGRID on-axis near detector, *Nucl. Instrum. Meth.*, A694:211–223, 2012. 38, 39
- [3] K. Abe et al., Observation of Electron Neutrino Appearance in a Muon Neutrino Beam, *Phys. Rev. Lett.*, 112:061802, 2014. 29
- [4] K. Abe et al., Measurements of neutrino oscillation in appearance and disappearance channels by the T2K experiment with  $6.6 \times 10^{20}$  protons on target, *Phys. Rev. D*, 91:072010, April 2015. 55, 66
- [5] K. Abe et al., Measurement of Coherent pi(+) Production in Low Energy Neutrino-Carbon Scattering, *Phys. Rev. Lett.*, 117(19), NOV 4 2016. 133
- [6] K. Abe et al., Measurement of neutrino and antineutrino oscillations by the T2K experiment including a new additional sample of  $\nu_e$  interactions at the far detector, *Phys. Rev. D*, 96(9), NOV 21 2017. 51, 56, 101, 111, 112, 144, 204
- [7] K. Abe et al., Measurement of  $\nu_\mu$  and  $\bar{\nu}_\mu$  charged current inclusive cross sections and their ratio with the T2K off-axis near detector, *Phys. Rev. D*, 96(5), September 2017. 46, 63, 66

- [8] K. Abe et al., First measurement of the  $\nu_\mu$  charged-current cross section on a water target without pions in the final state, *Phys. Rev. D*, 97:012001, January 2018. 63, 64, 66, 69, 112, 113
- [9] K. Abe et al., Search for  $CP$  Violation in Neutrino and Antineutrino Oscillations by the T2K Experiment with  $2.2 \times 10^{21}$  Protons on Target, *Phys. Rev. Lett.*, 121:171802, October 2018. 29, 129
- [10] K. Abe et al., Search for CP Violation in Neutrino and Antineutrino Oscillations by the T2K Experiment with  $2.2 \times 10^{21}$  Protons on Target, *Phys. Rev. Lett.*, 121(17):171802, 2018. 205, 206, 207
- [11] K. Abe et al., First Measurement of the Anti-NuMu Charge Current Double Differential Cross Section on Water without Pions in the Final State, *Phys. Rev. D.*, Forthcoming. 63
- [12] N. Abgrall et al., Measurements of  $\pi^\pm$ ,  $K^\pm$ ,  $K_S^0$ ,  $\Lambda$  and proton production in proton-carbon interactions at 31 GeV/c with the NA61/SHINE spectrometer at the CERN SPS, *Eur. Phys. J. C*, 76:84, 2016. 52, 100
- [13] M. A. Acero et al., New constraints on oscillation parameters from  $\nu_e$  appearance and  $\nu_\mu$  disappearance in the NOvA experiment, *Phys. Rev. D*, 98:032012, Aug 2018. 28
- [14] C. Adams et al., The Long-Baseline Neutrino Experiment: Exploring Fundamental Symmetries of the Universe, 2013, arXiv:1307.7335. 5, 24, 27
- [15] S. Agostinelli et al., GEANT4: A Simulation toolkit, *Nucl. Instrum. Meth.*, A506:250–303, 2003. 73
- [16] P. A. Amaudruz et al., The T2K Fine-Grained Detectors, *Nucl. Instrum. Meth. A*, A696:1–31, 2012. 188

- [17] J. Arafune et al., CP violation and matter effect in long baseline neutrino oscillation experiments, *Phys. Rev. D*, 56:3093–3099, September 1997. 26
- [18] S. Assylbekov, *Measurement of  $\nu_\mu$ -induced charged-current single  $\pi^+$  production on H20*, PhD thesis, Colorado State University, Fort Collins, 2014. 228, 232
- [19] S. Assylbekov et al., The T2K ND280 Off-Axis Pi-Zero Detector, *Nucl. Instrum. Meth.*, A686:48–63, 2012. 113
- [20] S. Baker et al., Clarification of the use of Chi-Square and Likelihood Functions in Fits to Histograms, *Nucl. Instrum. Meth.*, A221:437–442, 1983. 57
- [21] P. Ballmoos, Antimatter in the Universe: Constraints from Gamma-Ray Astronomy, *Hyperfine Interact.*, 228(1):91–100, October 2014. 26
- [22] O. Benhar et al., Spectral function of finite nuclei and scattering of GeV electrons, *Nucl. Phys.*, A579:193–517, 1994. 130
- [23] Ch. Berger and L. M. Seghal, Lepton mass effects in single pion production by neutrinos, *Phys. Rev. D*, 76:113004, December 2007. 132, 133
- [24] S. Bienstock et al., Constraining the Flux and Cross Section Models with Data from the ND280 Detector using FGD1 and FGD2 for the 2017 Joint Oscillation Analysis, 2017, T2K-TN-324. 100, 190, 217, 303
- [25] R. Bradford et al., A new parameterization of the nucleon elastic form factors, *Nucl. Phys.*, B159(127), 2006. 130
- [26] R. Brun and F. Rademakers, ROOT - An object oriented data analysis framework, *Nucl. Instrum. Meth. A*, 389(1):81 – 86, 1997, See also <http://root.cern.ch/>. 229, 329
- [27] T. Campbell, *Measurement of the muon anti-neutrino charged current double differential cross section with no pions in the final state on water using the pi-zero detector at T2K*,

PhD thesis, Colorado State University, Fort Collins, Colorado, USA, 2018, Available at  
<https://hdl.handle.net/10217/189329>. 63, 64, 70, 207

- [28] T. Campbell et al., Analysis of  $\nu_\mu$  Charged Current Inclusive Events in the PØD in Runs 1+2+3+4, March 2014, T2K-TN-80 v4. 67
- [29] T. Campbell et al., The ANuMu/NuMu Cross Sections Ratio With the P0D+TPC Samples, 2017. 67, 114
- [30] J-PARC Center, What is J-PARC?, January 2019, <https://j-parc.jp/researcher/en/about/what/index.html>, Accessed on 26 January 2019. 31
- [31] L. H. Chan et al., Nucleon Form Factors and Their Interpretation, *Phys. Rev.*, 141:1298–1307, January 1966. 130
- [32] A. Chulliat et al., The US/UK World Magnetic Model for 2015-2020, Technical report, National Geophysical Data Center, NOAA, 2015. 41
- [33] B. T. Cleveland et al., Measurement of the Solar Electron Neutrino Flux with the Homestake Chlorine Detector, *Astronomical Journal*, 496:505–526, March 1998. 15
- [34] G. Co', Random phase approximation and neutrino-nucleus cross sections, *Acta Phys. Polon.*, B37:2235–2242, 2006. 131
- [35] G. Cowan et al., Asymptotic formulae for likelihood-based tests of new physics, *Eur. Phys. J.*, C71:1554, 2011, [Erratum: Eur. Phys. J.C73,2501(2013)]. 139
- [36] R. Das, *Measurement of NuMu induced charged current inclusive cross section on water using the near detector of the T2K experiment*, PhD thesis, Colorado State University, Fort Collins, Colorado, USA, 2016, Available at <https://hdl.handle.net/10217/189398>. 63, 66

- [37] A. de Gouvea et al., Working Group Report: Neutrinos, In *Proceedings, 2013 Community Summer Study on the Future of U.S. Particle Physics: Snowmass on the Mississippi*, 2013, arXiv:1310.4340. 24
- [38] I. Esteban et al., Global analysis of three-flavour neutrino oscillations: synergies and tensions in the determination of  $\theta_{23}$ ,  $\delta_{\text{CP}}$ , and the mass ordering, 2018, arXiv:1811.05487. 25
- [39] R. T. Farouki, The Bernstein polynomial basis: A centennial retrospective, *Computer Aided Geometric Design*, 29(6):379–419, 2012. 132
- [40] A. Ferrero, The ND280 Near Detector of the T2K Experiment, *AIP Conference Proceedings*, 1189(1):77–82, 2009. 28
- [41] J. A. Formaggio and G. P. Zeller, From eV to EeV: Neutrino Cross Sections Across Energy Scales, *Rev. Mod. Phys.*, 84:1307–1341, 2012. 52, 53
- [42] J. Friedman et al., Regularization Paths for Generalized Linear Models via Coordinate Descent, *Journal of Statistical Software, Articles*, 33(1):1–22, 2010. 212
- [43] S. Fukuda et al., The Super-Kamiokande detector, *Nucl. Instrum. Meth. A*, 501(2):418–462, 2003. 28
- [44] T. Golan et al., Final State Interactions Effects in Neutrino-Nucleus Interactions, *Phys. Rev. C*, 86:015505, 2012. 134
- [45] K. M. Graczyk et al.,  $C_A^5$  axial form factor from bubble chamber experiments, *Phys. Rev.*, D80:093001, 2009. 132
- [46] K. M. Graczyk et al., Electroweak form factors of the  $\Delta(1232)$  resonance, *Phys. Rev. D*, 90:093001, November 2014. 132
- [47] K. M. Graczyk and J. T. Sobczyk, Form factors in the quark resonance model, *Phys.*

*Rev. D*, 77:053001, March 2008. 132

- [48] K. M. Graczyk and J.T. Sobczyk, Lepton mass effects in weak charged current single pion production, *Phys. Rev. D*, 77:053003, March 2008. 132
- [49] M. Hartz et al., Constraining the Flux and Cross Section Models with Data from the ND280 Detector for the 2014/15 Oscillation Analysis, Technical report, T2K Collaboration, May 2015, T2K-TN-220 v4. 58
- [50] T. Hastie et al., *The Elements of Statistical Learning: Data Mining, Inference, and Prediction*, Springer Series in Statistics, Springer New York, New York, NY, 2009. 97, 129, 208, 211, 214
- [51] T. Hastie et al., *Statistical Learning with Sparsity: The Lasso and Generalizations*, Chapman and Hall/CRC monographs on statistics and applied probability, CRC Press, Taylor and Francis Group, Boca Raton, 2015. 213
- [52] Y. Hayato, A neutrino interaction simulation program library NEUT, *Acta Phys. Polon.*, B40:2477–2489, 2009. 52
- [53] A. Hoecker et al., TMVA: Toolkit for Multivariate Data Analysis, *PoS*, ACAT:040, 2007. 229
- [54] C. Jarlskog, A Basis Independent Formulation of the Connection Between Quark Mass Matrices, CP Violation and Experiment,, *Z. Phys.*, C29:491–497, 1985. 25
- [55] T. Kitagaki et al., Charged-current exclusive pion production in neutrino-deuterium interactions, *Phys. Rev. D*, 34:2554–2565, November 1986. 132
- [56] E. Komatsu et al., Seven-year Wilkinson Microwave Anisotropy Probe (WMAP) Observations: Cosmological Interpretation, *Astrophys. J.*, 192:18, February 2011. 27
- [57] C. H. Llewellyn Smith, Neutrino Reactions at Accelerator Energies, *Phys. Rept.*, 3:261–

- [58] F. Lodovico and P. Martins, Measurement of the Charged Current Coherent Pion Production Cross-Section on Carbon and Oxygen using the ND280 tracker, Technical report, T2K Collaboration, 2017, T2K-TN-290. 188
- [59] A. Longhin et al., Measurement of the inclusive charged-current numu cross section in plastic using the ND280 tracker Run 5c data, Technical report, T2K Collaboration, 2016, T2K-TN-249v8. 188
- [60] Z Maki et al., Remarks on the Unified Model of Elementary Particles, *Progr. Theor. Exp. Phys.*, 28(5), 1962. 20
- [61] M. Martini et al., A Unified approach for nucleon knock-out, coherent and incoherent pion production in neutrino interactions with nuclei, *Phys. Rev.*, C80:065501, 2009. 79, 130
- [62] Jacob Alexander Morrison, *Effect of New Samples in the T2K Off-Axis Near Detector for the T2K Oscillation Analysis*, PhD thesis, Michigan State University, East Lansing, Michigan, 2019, Available at <https://doi.org/10.25335/hy4e-wy68>. 190
- [63] J. Nieves et al., Inclusive Charged–Current Neutrino–Nucleus Reactions, *Phys. Rev.*, C83:045501, 2011. 131
- [64] K. Niewczas and J.T. Sobczyk, Search for nucleon-nucleon correlations in neutrino-argon scattering, *Phys. Rev.*, C93(3):035502, 2016. 130
- [65] B. Pontecorvo, Inverse Beta Processes and Nonconservation of Lepton Charge, *J. Exp. Theor. Phys.*, 28(5), 1957. 20
- [66] B. Pontecorvo, Mesonium and Anti-Mesonium, *Sov. Phys. JETP*, 6:429, 1957. 16
- [67] G. M. Radecky and others, Study of single-pion production by weak charged currents

- in low-energy  $\nu d$  interactions, *Phys. Rev. D*, 25:1161–1173, March 1982. 132
- [68] D. Rein and L. M. Sehgal, Neutrino-excitation of baryon resonances and single pion production, *Ann. Phys.*, 133(1):79–153, 1981. 132
- [69] D. Rein and L. M. Sehgal, Coherent  $\pi^0$  production in neutrino reactions, *Nucl. Phys. B*, 223(1):29–44, 1983. 133
- [70] G. Rowe et al., Energy-dependent phase shift analysis of pion-nucleon scattering below 400 MeV, *Phys. Rev. C*, 18:584–589, July 1978. 134
- [71] P. K. Saha et al., Simulation, measurement, and mitigation of beam instability caused by the kicker impedance in the 3-GeV rapid cycling synchrotron at the Japan Proton Accelerator Research Complex, *Phys. Rev. Accel. Beams*, 21:024203, February 2018. 32
- [72] A. D. Sakharov, Violation of CP invariance, C asymmetry, and baryon asymmetry of the universe, *Soviet Physics Uspekhi*, 34(5):392, 1991. 27
- [73] L.L. Salcedo et al., Computer simulation of inclusive pion nuclear reactions, *Nucl. Phys. A*, 484(3):557–592, 1988. 134
- [74] J. Schechter and J. W. F. Valle, Neutrinoless double- $\beta$  decay in  $SU(2) \times U(1)$  theories, *Phys. Rev. D*, 25:2951–2954, 1982. 22
- [75] N. Schmitz, *Neutrinophysik*, Teubner, Stuttgart, 1997. 21
- [76] J. Schwehr et al., Measurement of the  $\nu_\mu$  CC1 $\pi^+$  Differential Cross Sections in  $\mu$  Momentum and Angle in the P0D, Ocotober 2018, T2K-TN-333v2. 53
- [77] Jaclyn Schwehr, *Measurement of the Differential Charged Current Single Pion Cross Section Using Muon Momentum and Muon Angle In the Pi Zero Detector of the T2K Experiment*, PhD thesis, Colorado State University, Fort Collins, Colorado, 2018, Available at <https://hdl.handle.net/10217/189398>. 188, 228, 229, 232

- [78] T. Sekiguchi et al., Development and operational experience of magnetic horn system for T2K experiment, *Nucl. Instrum. Meth. A*, 789:57–80, 2015. 33
- [79] R.A. Smith and E.J. Moniz, Neutrino reactions on nuclear targets, *Nucl. Phys. B*, 43:605–622, 1972. 130
- [80] Alfonso Andrés García Soto, *Study of the  $\nu_\mu$  interactions via charged current in the T2K near detector*, PhD thesis, Universitat Autònoma de Barcelona, 2017, Available at <http://hdl.handle.net/10803/405705>. 66
- [81] M. Tanabashi et al., The Review of Particle Physics, *Phys. Rev. D*, 98(030001), 2018. 22, 25
- [82] R. Tibshirani et al., Diagnosis of multiple cancer types by shrunken centroids of gene expression, *Proceedings of the National Academy of Sciences of the United States of America*, 99(10):6567–6572, MAY 14 2002. 212
- [83] W. Toki, Update of P0D Inspection, Private communication, June 2016. 113
- [84] G. Welch and G. Bishop, An Introduction to the Kalman Filter, Technical Report 95041, University of North Carolina at Chapel Hill, Chapel Hill, NC 27599-3175, July 2006. 65
- [85] L. Wolfenstein, Neutrino oscillations in matter, *Phys. Rev. D*, 17:2369–2374, May 1978. 25
- [86] Carl Vincent Clarence Wret, *Minimising Systematic Uncertainties in the T2K Experiment Using Near-Detector and External Data*, PhD thesis, Imperial College London, 2019, Available at <https://t2k.org/docs/thesis/097/clarencewretthesis>. 100, 110, 111, 130, 131, 133
- [87] Y. Yamazaki, Accelerator technical design report for high-intensity proton accelerator

facility project, J-PARC, Report 2002-013, KEK, 2003. 32

- [88] T. Yang, *A Study of Muon Neutrino to Electron Neutrino Oscillations in the MINOS Experiment*, PhD thesis, Stanford University, 2009, Available at <https://searchworks.stanford.edu/view/7945131>. 230
- [89] T. Yuan et al., Double Differential Measurement of the Flux Averaged  $\nu_\mu$  CC0Pi Cross Section on Water, August 2016, T2K-TN-258 v4.6.1. 124
- [90] K. Zuber, *Neutrino Physics*, CRC Press, Boca Raton, FL., 2nd edition, 2012. 3, 16, 20, 28

## Appendix A

# Contributions to the PØD CC-1 $\pi$ Analysis

Prior to the work on the near detector constraint, I participated in the PØD  $\nu_\mu$  CC-1 $\pi$  cross section on water analysis. This was a second generation analysis designed to make significant improvements to the first generation analysis, which was a single bin measurement [18]. The primary goal of the analysis was to provide a differential measurement in muon kinematics. The challenges were to identify the muon and pion while measuring their respective momenta. The results of the analysis are given in the following thesis [77] and a publication is in preparation.

My primary contributions to the analysis included developing the particle identification (PID) tools and momentum calibration for muon and pion tracks. Machine learning based selection cuts were added in the analysis chain that were exclusively designed to exploit the PØD local reconstruction since the ND280 global reconstruction was not available during development. These selection cuts provided the means to make PID cuts to select only one muon and one pion in a two track event. To provide a differential cross section measurement in the muon kinematics, a momentum measurement was developed and calibrated for the analysis.

The first section describes my contributions to the development of the machine learning PID tools. The second section includes the description of the momentum measurement and calibration method.

## A.1 Particle Identification Tools

Since there are no particle identification (PID) tools in the local PØD reconstruction, the PØD CC- $1\pi$  analysis developed a unique set of tools were designed specifically to select muon and pion tracks. These details are explained in further detail in the following thesis [77]. The approach taken by this analysis was to use machine learning techniques for event selection and PID for each track. Only reconstructed topological information were used to minimize interaction vertex model and detector model dependencies.

Machine learning is a rapidly developing field of study in which a computer system can perform a certain task without explicit instructions. For classification based problems, the goal is to assign two or more labels to a set of input vectors. Training a classifier requires a sample of pre-classified data to determine which attributes of each datum can be used to best separate data of unknown classification. Unclassified data are then assigned a classification based on their position in attribute space.

The specific machine learning technique used in this analysis is a random forest method called Boosted Decision Tree (BDT) implemented in the ROOT [26] Toolkit for Multivariate Analysis (TMVA) package [53]. A decision tree is a binary tree classifier that applies rectangular cuts on inputs features until a stop condition is reached. In order to prevent model overfitting to the training set, a set of decision trees (forest) are generated by scaling misclassified events by a “boost” weight. By averaging the results over the forest, an enhancement of the model performance is achieved.

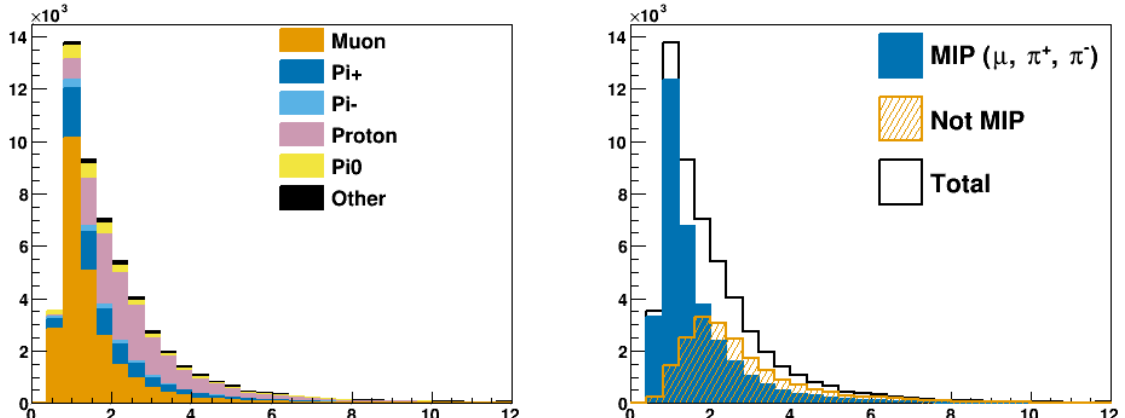
The inputs for the BDTs were developed from topological track information in both the longitudinal and transverse directions of PØD tracks. A traditional longitudinal track mea-

surement is the mean energy deposition in a tracking calorimeter or TPC, or the “ $dE/dx$ ” of the track. The idea behind using topological information is that they reduce neutrino interaction model dependence. This should also minimize the detector model dependence assuming the detector systematics have been studied sufficiently with control samples. The inputs I developed for the BDTs were motivated from the work done at MINOS to select tracks using machine learning classifiers [88]. Many of the input features provided discriminating power for minimizing ionizing particle (MIP) tracks from other non-MIP particle tracks like protons. Examples of the longitudinal and transverse topological features I developed are shown in Figure A.1.

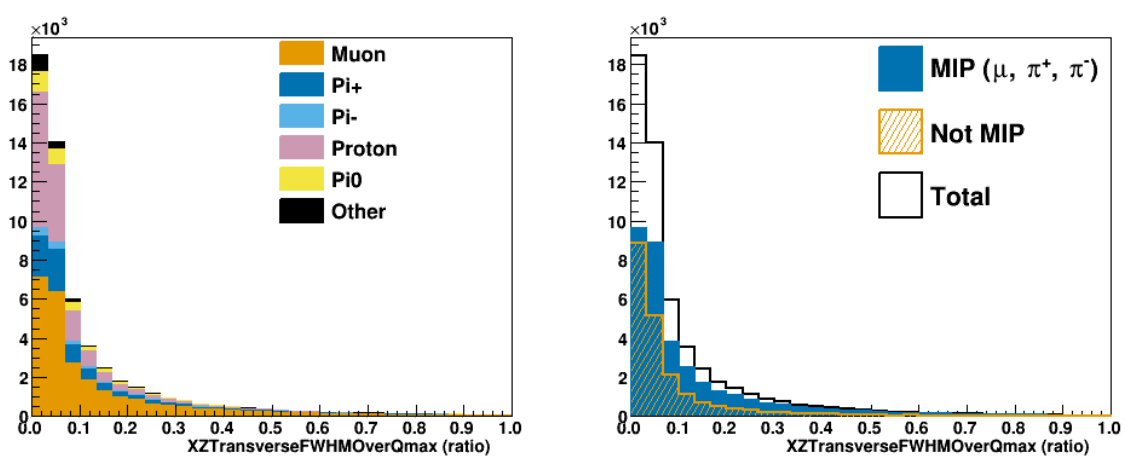
The CC-1 $\pi$  analysis used two BDTs classifiers to make event selections. The first classifier provided a continuous discriminator to classify tracks as MIP-like or not. Selected events are those that have two MIP tracks. The second BDT classifier helps assign which track is the muon and pion using a likelihood cut describe.

In developing the BDT classifiers, cross validation studies were performed to identify the best input features. Cross validation is a model validation technique that assess how the model generalizes to independent data sets. In particular, the model is trained on a “training” set and it evaluated on a “testing” set to ensure the results are similar between them. The training and testing sets were equally populated using random sampling of the input data. This is especially important since I needed to perform data imputation for any missing information in the training, which can affect the results of the model. The chosen method of data imputation was to assign a handpicked default value based on feature distribution.

Also in the cross validation procedure, variable selection was determined by training models with and without the variable to assess the variable’s importance. A variable was removed from the final BDT model if removing it had minimal impact on the receiver operating characteristic curve, which is a diagnostic on the performance of a binary classifier.



(a) Longitudinal feature



(b) Transverse feature

**Figure A.1:** Topological track features developed for the machine learning classifier cuts. The top figure shows a longitudinal feature and the bottom shows a transverse feature. The left figures categorize tracks by their particle species while the right figures consider MIP and not-MIP distinctions.

**Table A.1:** Selection statistics for the CC-1 $\pi$  analysis. For each event passing the pre-selection cuts, to select  $\nu_\mu$  events, there must be one muon-like track passing the MIP BDT. The result of the second track MIP BDT determined if it was selected as a CC-1 $\pi$  event or a sideband event. Two sidebands, labeled “near” and “far”, were used to help constrain backgrounds in the analysis [77].

Selection	Total events	Signal events	Purity	Efficiency
After pre-selection	6258.6	1278.2	0.204	0.269
One MIP-like track	3533.3	998.4	0.283	0.210
Selected signal	970.2	598.7	0.617	0.126
“Near” sideband	757.3	255.7	0.338	0.0538
“Far” sideband	1805.8	144.0	0.0798	0.0303

This procedure dramatically reduced the number of input features selected in the BDT models.

The selection purity and efficiency for the analysis are shown in Table A.1 on page 232. Compared to the first generation analysis, the selected signal efficiency increased by a factor of two from around 6% to 12%, and the its purity also increased from 50% to 61% [18].

## A.2 Momentum Reconstruction

The algorithm to reconstruct particle momentum in CC-1 $\pi$  analysis integrates the average energy deposition per unit of areal density along the track through the PØD. The path of the track is determined by the energy depositions in each scintillator plane of the PØD associated with the reconstructed track object. The integration for contained tracks is done starting at the end of the reconstructed track, where the momentum is assumed to be close to zero to the start position of the reconstructed track. In cases where the track exits the PØD into TPC1, the momentum calculated by TPC1 is used as the starting momentum and the integration begins at the point where the track exited the PØD. (For this discussion the downstream ECal is considered to be part of the PØD, and the difference in areal density is taken into consideration.) Events with tracks that exit the PØD but do not enter TPC1 (do not have a matched track in TPC1) are excluded from the analysis.

Relativistic particles will generally deposit energy as Minimum Ionizing Particles (MIPs) as characterized by the Bethe-Bloch curve in (A.1)

$$-\frac{dT}{dx} = K z^2 \frac{Z}{A} \frac{1}{\beta^2} \left[ \frac{1}{2} \ln \left( \frac{2m_e c^2 (\beta \gamma)^2 T_{\max}}{I^2} \right) - \beta^2 - \frac{\delta(\beta \gamma)}{2} \right] \quad (\text{A.1})$$

with

$$T_{\max} = \frac{2m_e c^2 (\beta \gamma)^2}{1 + 2\gamma \frac{m_e}{M} + \left( \frac{m_e}{M} \right)^2}$$

where  $T$  is the kinetic energy,  $x$  is the distance traveled,  $K$  is proportional to the material density,  $I$  is the mean excitation potential in eV,  $z$  is the charge,  $c$  is the speed of light,  $M$  is the rest mass of the particle,  $m_e$  is the rest mass of the electron,  $\beta$  is the velocity as a fraction of  $c$ , and  $\gamma$  is the Lorentz relativistic factor  $(1 - \beta^2)^{-0.5}$ . Both muons ( $m_\mu = 105.6 \text{ MeV}/c^2$ ) and pions ( $m_\pi = 139.5 \text{ MeV}/c^2$ ) are relativistic at the energies required to be detected and reconstructed by the PØD.

### A.2.1 Momentum Tool

The Momentum Tool (MT), the collection of functions that estimate a particle's momentum in the PØD, was initially developed to estimate the kinetic energy of protons fully contained in the PØD. The MT estimated the proton's momentum by summing up the assumed ionization energy loss in each material traversed over the range of the track in the PØD. Stopping power data for different materials came from the NIST PSTAR catalog as a function of kinetic energy. The MT was extended to measurements of muon and pion momenta for tracks originating in the PØD and entering TPC1. The extension involved converting kinetic energy to  $\beta \gamma = p/(Mc)$ , the dimensionless quantity of a particle's momentum divided by its mass.

The starting kinetic energy for the MT is given by (A.2),

$$T_{i,\alpha} = \begin{cases} \sqrt{(p_{\text{TPC1}}c)^2 + (m_\alpha c^2)^2} - m_\alpha c^2 & \text{if } p_{\text{TPC1}} \neq 0 \\ \epsilon_\alpha & \text{otherwise} \end{cases} \quad (\text{A.2})$$

where the index  $\alpha$  denotes either a muon, proton, or pion. The starting kinetic energy  $\epsilon$  for muons and pions is 30 MeV and for protons is 50 MeV. A study showed that the resulting momentum distributions for the muon and pion did not change when using a starting point smaller than 30 MeV.

The MT steps through the PØD along the path defined by a collection of track-nodes. A track-node is a collection of time-correlated hits inside active material with charged-weighted position and direction. The direction vector points to the next node except in the case of the last track-node, in which case, it uses the previous node's direction. The positions of two successive nodes and the associated direction vector determine the angle,  $\theta$ , of the track w.r.t. the PØD z-axis. The MT numerically integrates the energy loss for each material traversed in the following manner,

$$\Delta T = \left( \frac{dT}{d\rho_A} \right)_{\text{mat}} (\Delta\rho_A)$$

$$T \rightarrow T + \Delta T$$

where the index “mat” represents each material in the path,  $\rho_A$  is the areal density, and  $\Delta\rho_A$  is a small step of 0.05 gram/cm<sup>2</sup> in areal density. Each  $\Delta\rho_A$  step in  $dT/d\rho_A$  is evaluated at the point  $\beta\gamma = (\beta\gamma)_0 + \Delta(\beta\gamma)/2$  where  $(\beta\gamma)_0$  is the value of  $\beta\gamma$  for a single particle of kinetic energy  $T$  and  $\Delta(\beta\gamma)$  is the density correction term from (A.1).

### A.2.2 Momentum Calibration

The muon and pion track momenta were calibrated for all the track topologies in the analysis. To avoid biasing the calibration to the NEUT generator kinematics, the muon and

pion tracks were selected from true events passing the particle identification cuts. Additionally, calibration training samples were extracted using subsets of the monte carlo (MC). Specifically, about  $1.16 \times 10^{21}$  POT from both water-in and water-out MC were used. This is about  $5\times$  and  $3\times$  the data statistics for water-in and water-out modes, respectively, in the measurement.

A bias subtraction method is applied on each track to calibrate to the true momentum. To characterize the momentum bias, a two-dimensional histogram of the true-vs-reconstructed momenta over the full particle's phase-space is created and used to generate a profile histogram of the momentum bias as a function of the reconstructed momentum. This profile histogram is also constructed with each bin to have approximately equal statistics so as to minimize the impact of statistical fluctuations. The profile is then carefully examined for features, such as tails, maxima, or minima, in order to characterize the shape with a function. Next a closed form function that reasonably describes the shape of the bias is identified. The metric for determining if the chosen function is "adequate" is to require at least four bins in the profile and that a chi-squared fit value is similar to the number of degrees of freedom. Once the suitable functional form,  $R$ , is fitted to the profile histogram, the calibrated momentum,  $p_c$  is calculated using (A.3)

$$p_c = [1 - R(p_r)] \times p_r \quad (\text{A.3})$$

where  $p_r$  is the uncalibrated, raw momentum.

To illustrate the method of calibration, the calibration method for true CC-1 $\pi$  muon tracks fully contained in the PØD is shown in Figure A.2. There is better agreement between the true and reconstructed momenta, but additional variance is introduced. The increase in the variance is expected since a bias correction will introduce a larger spread to the momentum distribution. The calibration function for this set is given by

$$R(p_r [\text{GeV}/c]) = 0.02955 + \frac{0.045662}{1 + \exp [-24.61 (p_r - 0.4415)]}$$

and is shown in Figure A.3.

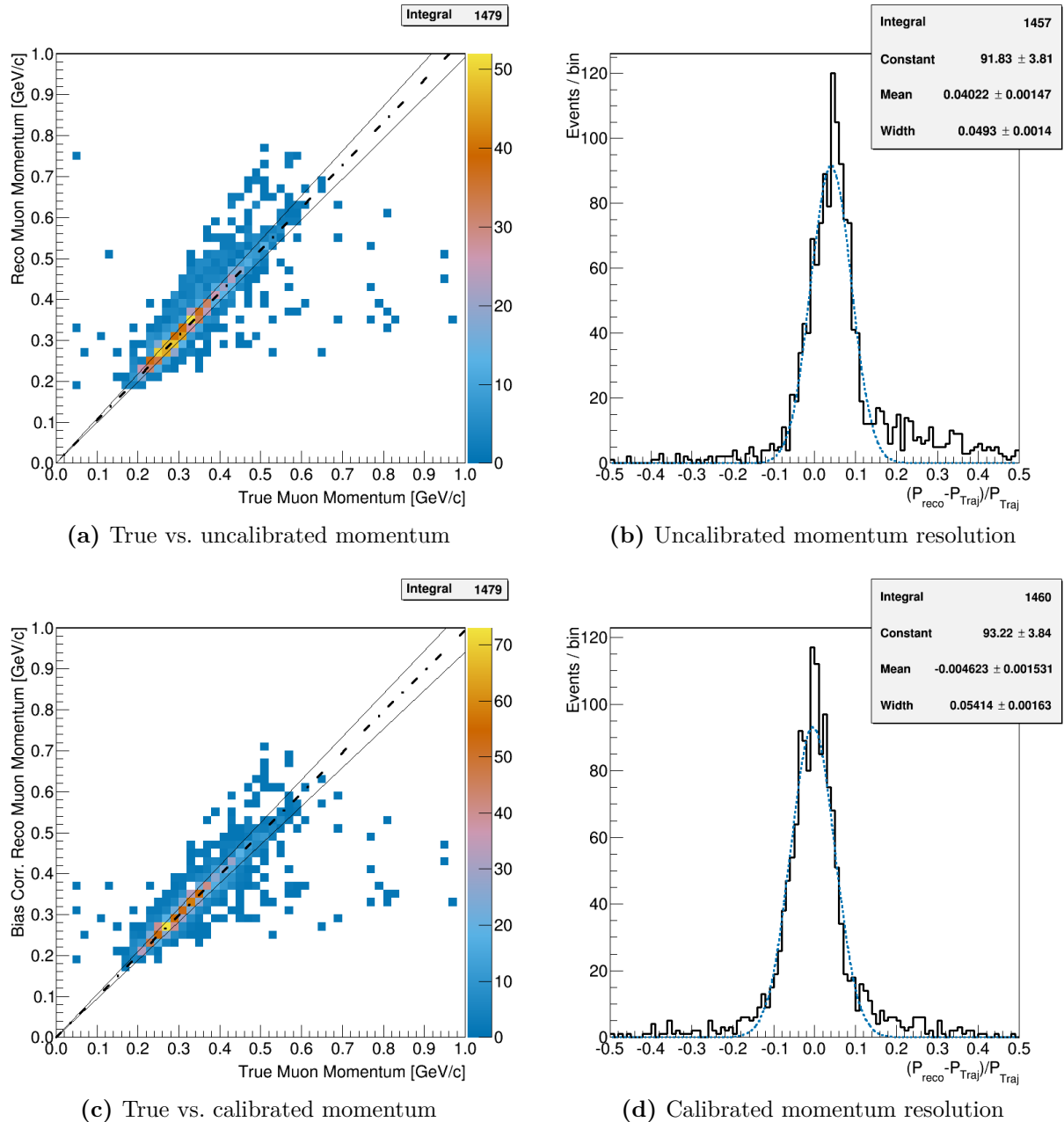


**Figure A.2:** The momentum for true muon tracks events before (top) and after (bottom) the calibration. These muon tracks are fully contained in the PØD and are fitted using an algorithm aided by a Kalman filter in the PØD reconstruction. The plots on the left are scatter plots of the true vs. reconstructed momentum while the right plots show the resolution of the momentum. After the calibration, the muon tracks have nearly no bias, but at the cost of some additional variance as indicated by the Gaussian fits in (b) and (d). The extracted Gaussian fit mean and standard deviation are shown as dashed-dot and solid lines, respectively, in (a) and (c).

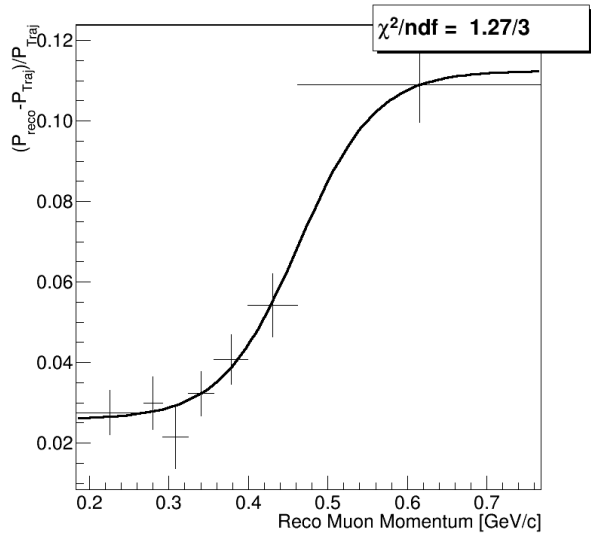


**Figure A.3:** The profile histogram for the momentum resolution as function of the reconstructed momentum for PØD water-in contained muons. The smooth black curve is a characterization using a logistic function. Each bin in the profile has equal statistics to minimize statistical fluctuations.

# Appendix B

## The PØD-Only Bin Normalization Parameters

The observable normalizations used in the PØD-only BANFF fit are tabulated here. In Table B.1 on page 239, FHC mode is assumed unless RHC mode is specified and the initialisms “1-Trk”, “N-Trks”, “Wtr”, and “Air” represent the 1-Track selection, N-Tracks selection, PØD water-in mode, and PØD water-out mode, respectively.

**Table B.1:** Observable normalization fit bins.

Fit Index	Sample	p [GeV/c]	$\cos\theta$	Prefit
100	$\nu_\mu$ 1-Trk Wtr	$0 \leq p < 0.40$	$-1 \leq \cos\theta < 0.70$	$1.21 \pm 0.67$
101		$0.40 \leq p < 0.60$	$-1 \leq \cos\theta < 0.70$	$0.87 \pm 0.18$
102		$0.60 \leq p < 0.80$	$-1 \leq \cos\theta < 0.70$	$1.12 \pm 0.44$
103		$0.80 \leq p < 1.25$	$-1 \leq \cos\theta < 0.70$	$1.13 \pm 0.43$
104		$1.25 \leq p < 2.00$	$-1 \leq \cos\theta < 0.70$	$1.02 \pm 0.17$
105		$2.00 \leq p < 3.00$	$-1 \leq \cos\theta < 0.70$	$0.93 \pm 0.20$
106		$3.00 \leq p < 4.00$	$-1 \leq \cos\theta < 0.70$	$1.00 \pm 0.28$
107		$4.00 \leq p < 5.50$	$-1 \leq \cos\theta < 0.70$	$0.82 \pm 0.33$
108		$5.50 \leq p < 30$	$-1 \leq \cos\theta < 0.70$	$1.26 \pm 0.58$

Fit Index	Sample	p [GeV/c]	$\cos\theta$	Prefit
109		$0 \leq p < 0.40$	$0.70 \leq \cos\theta < 0.80$	$1.27 \pm 0.74$
110	$\nu_\mu$ 1-Trk Wtr	$0.40 \leq p < 0.60$	$0.70 \leq \cos\theta < 0.80$	$0.89 \pm 0.18$
111		$0.60 \leq p < 0.80$	$0.70 \leq \cos\theta < 0.80$	$1.02 \pm 0.27$
112		$0.80 \leq p < 1.25$	$0.70 \leq \cos\theta < 0.80$	$1.09 \pm 0.33$
113		$1.25 \leq p < 2.00$	$0.70 \leq \cos\theta < 0.80$	$1.02 \pm 0.17$
114		$2.00 \leq p < 3.00$	$0.70 \leq \cos\theta < 0.80$	$0.96 \pm 0.15$
115		$3.00 \leq p < 4.00$	$0.70 \leq \cos\theta < 0.80$	$0.99 \pm 0.21$
116		$4.00 \leq p < 5.50$	$0.70 \leq \cos\theta < 0.80$	$0.94 \pm 0.29$
117		$5.50 \leq p < 30$	$0.70 \leq \cos\theta < 0.80$	$1.05 \pm 0.53$
118		$0 \leq p < 0.40$	$0.80 \leq \cos\theta < 0.94$	$1.33 \pm 0.78$
119		$0.40 \leq p < 0.60$	$0.80 \leq \cos\theta < 0.94$	$0.91 \pm 0.21$
120	$\nu_\mu$ 1-Trk Wtr	$0.60 \leq p < 0.80$	$0.80 \leq \cos\theta < 0.94$	$0.97 \pm 0.14$
121		$0.80 \leq p < 1.25$	$0.80 \leq \cos\theta < 0.94$	$1.03 \pm 0.17$
122		$1.25 \leq p < 2.00$	$0.80 \leq \cos\theta < 0.94$	$1.01 \pm 0.09$
123		$2.00 \leq p < 3.00$	$0.80 \leq \cos\theta < 0.94$	$1.00 \pm 0.05$
124		$3.00 \leq p < 4.00$	$0.80 \leq \cos\theta < 0.94$	$1.00 \pm 0.12$
125		$4.00 \leq p < 5.50$	$0.80 \leq \cos\theta < 0.94$	$0.95 \pm 0.15$
126		$5.50 \leq p < 30$	$0.80 \leq \cos\theta < 0.94$	$0.96 \pm 0.38$
127		$0 \leq p < 0.40$	$0.94 \leq \cos\theta < 0.97$	$1.29 \pm 0.73$
128		$0.40 \leq p < 0.60$	$0.94 \leq \cos\theta < 0.97$	$0.93 \pm 0.22$
129		$0.60 \leq p < 0.80$	$0.94 \leq \cos\theta < 0.97$	$0.96 \pm 0.09$
130	$\nu_\mu$ 1-Trk Wtr	$0.80 \leq p < 1.25$	$0.94 \leq \cos\theta < 0.97$	$1.02 \pm 0.11$
131		$1.25 \leq p < 2.00$	$0.94 \leq \cos\theta < 0.97$	$1.00 \pm 0.07$
132		$2.00 \leq p < 3.00$	$0.94 \leq \cos\theta < 0.97$	$1.00 \pm 0.03$
133		$3.00 \leq p < 4.00$	$0.94 \leq \cos\theta < 0.97$	$0.99 \pm 0.08$
134		$4.00 \leq p < 5.50$	$0.94 \leq \cos\theta < 0.97$	$1.00 \pm 0.14$

Fit Index	Sample	$p$ [GeV/c]	$\cos\theta$	Prefit
135		$5.50 \leq p < 30$	$0.94 \leq \cos\theta < 0.97$	$0.99 \pm 0.20$
136		$0 \leq p < 0.40$	$0.97 \leq \cos\theta < 0.99$	$1.25 \pm 0.65$
137		$0.40 \leq p < 0.60$	$0.97 \leq \cos\theta < 0.99$	$0.94 \pm 0.20$
138		$0.60 \leq p < 0.80$	$0.97 \leq \cos\theta < 0.99$	$0.95 \pm 0.08$
139		$0.80 \leq p < 1.25$	$0.97 \leq \cos\theta < 0.99$	$1.01 \pm 0.11$
140	$\nu_\mu$ 1-Trk Wtr	$1.25 \leq p < 2.00$	$0.97 \leq \cos\theta < 0.99$	$1.00 \pm 0.07$
141		$2.00 \leq p < 3.00$	$0.97 \leq \cos\theta < 0.99$	$1.00 \pm 0.06$
142		$3.00 \leq p < 4.00$	$0.97 \leq \cos\theta < 0.99$	$1.00 \pm 0.03$
143		$4.00 \leq p < 5.50$	$0.97 \leq \cos\theta < 0.99$	$0.98 \pm 0.10$
144		$5.50 \leq p < 30$	$0.97 \leq \cos\theta < 0.99$	$0.97 \pm 0.14$
145		$0 \leq p < 0.40$	$0.99 \leq \cos\theta < 1$	$1.25 \pm 0.58$
146		$0.40 \leq p < 0.60$	$0.99 \leq \cos\theta < 1$	$0.93 \pm 0.18$
147		$0.60 \leq p < 0.80$	$0.99 \leq \cos\theta < 1$	$0.96 \pm 0.11$
148		$0.80 \leq p < 1.25$	$0.99 \leq \cos\theta < 1$	$1.01 \pm 0.11$
149		$1.25 \leq p < 2.00$	$0.99 \leq \cos\theta < 1$	$1.01 \pm 0.08$
150	$\nu_\mu$ 1-Trk Wtr	$2.00 \leq p < 3.00$	$0.99 \leq \cos\theta < 1$	$1.01 \pm 0.10$
151		$3.00 \leq p < 4.00$	$0.99 \leq \cos\theta < 1$	$1.00 \pm 0.06$
152		$4.00 \leq p < 5.50$	$0.99 \leq \cos\theta < 1$	$1.00 \pm 0.05$
153		$5.50 \leq p < 30$	$0.99 \leq \cos\theta < 1$	$0.98 \pm 0.10$
154	$\nu_\mu$ N-Trks Wtr	$0 \leq p < 0.40$	$-1 \leq \cos\theta < 0.77$	$1.18 \pm 0.61$
155		$0.40 \leq p < 0.60$	$-1 \leq \cos\theta < 0.77$	$0.89 \pm 0.15$
156		$0.60 \leq p < 0.80$	$-1 \leq \cos\theta < 0.77$	$1.01 \pm 0.16$
157		$0.80 \leq p < 1.20$	$-1 \leq \cos\theta < 0.77$	$1.03 \pm 0.19$
158		$1.20 \leq p < 2.20$	$-1 \leq \cos\theta < 0.77$	$1.02 \pm 0.15$
159		$2.20 \leq p < 3.50$	$-1 \leq \cos\theta < 0.77$	$1.04 \pm 0.16$
160	$\nu_\mu$ N-Trks Wtr	$3.50 \leq p < 10.0$	$-1 \leq \cos\theta < 0.77$	$0.93 \pm 0.26$

Fit Index	Sample	p [GeV/c]	$\cos\theta$	Prefit
161		$10.0 \leq p < 30$	$-1 \leq \cos\theta < 0.77$	$0.94 \pm 0.67$
162		$0 \leq p < 0.40$	$0.77 \leq \cos\theta < 0.85$	$1.13 \pm 0.56$
163		$0.40 \leq p < 0.60$	$0.77 \leq \cos\theta < 0.85$	$0.92 \pm 0.15$
164		$0.60 \leq p < 0.80$	$0.77 \leq \cos\theta < 0.85$	$0.98 \pm 0.07$
165		$0.80 \leq p < 1.20$	$0.77 \leq \cos\theta < 0.85$	$1.00 \pm 0.09$
166		$1.20 \leq p < 2.20$	$0.77 \leq \cos\theta < 0.85$	$1.01 \pm 0.08$
167		$2.20 \leq p < 3.50$	$0.77 \leq \cos\theta < 0.85$	$1.01 \pm 0.06$
168		$3.50 \leq p < 10.0$	$0.77 \leq \cos\theta < 0.85$	$0.98 \pm 0.16$
169		$10.0 \leq p < 30$	$0.77 \leq \cos\theta < 0.85$	$0.98 \pm 0.52$
170	$\nu_\mu$ N-Trks Wtr	$0 \leq p < 0.40$	$0.85 \leq \cos\theta < 0.90$	$1.13 \pm 0.53$
171		$0.40 \leq p < 0.60$	$0.85 \leq \cos\theta < 0.90$	$0.92 \pm 0.14$
172		$0.60 \leq p < 0.80$	$0.85 \leq \cos\theta < 0.90$	$0.98 \pm 0.05$
173		$0.80 \leq p < 1.20$	$0.85 \leq \cos\theta < 0.90$	$1.00 \pm 0.07$
174		$1.20 \leq p < 2.20$	$0.85 \leq \cos\theta < 0.90$	$1.00 \pm 0.06$
175		$2.20 \leq p < 3.50$	$0.85 \leq \cos\theta < 0.90$	$1.01 \pm 0.05$
176		$3.50 \leq p < 10.0$	$0.85 \leq \cos\theta < 0.90$	$0.99 \pm 0.12$
177		$10.0 \leq p < 30$	$0.85 \leq \cos\theta < 0.90$	$1.03 \pm 0.46$
178		$0 \leq p < 0.40$	$0.90 \leq \cos\theta < 0.97$	$1.13 \pm 0.52$
179		$0.40 \leq p < 0.60$	$0.90 \leq \cos\theta < 0.97$	$0.94 \pm 0.13$
180	$\nu_\mu$ N-Trks Wtr	$0.60 \leq p < 0.80$	$0.90 \leq \cos\theta < 0.97$	$0.97 \pm 0.06$
181		$0.80 \leq p < 1.20$	$0.90 \leq \cos\theta < 0.97$	$0.99 \pm 0.08$
182		$1.20 \leq p < 2.20$	$0.90 \leq \cos\theta < 0.97$	$1.00 \pm 0.07$
183		$2.20 \leq p < 3.50$	$0.90 \leq \cos\theta < 0.97$	$1.00 \pm 0.03$
184		$3.50 \leq p < 10.0$	$0.90 \leq \cos\theta < 0.97$	$0.99 \pm 0.10$
185		$10.0 \leq p < 30$	$0.90 \leq \cos\theta < 0.97$	$0.98 \pm 0.25$
186		$0 \leq p < 0.40$	$0.97 \leq \cos\theta < 1$	$1.09 \pm 0.47$

Fit Index	Sample	p [GeV/c]	$\cos\theta$	Prefit
187		$0.40 \leq p < 0.60$	$0.97 \leq \cos\theta < 1$	$0.96 \pm 0.11$
188		$0.60 \leq p < 0.80$	$0.97 \leq \cos\theta < 1$	$0.96 \pm 0.09$
189		$0.80 \leq p < 1.20$	$0.97 \leq \cos\theta < 1$	$1.00 \pm 0.09$
190	$\nu_\mu$ N-Trks Wtr	$1.20 \leq p < 2.20$	$0.97 \leq \cos\theta < 1$	$1.01 \pm 0.09$
191		$2.20 \leq p < 3.50$	$0.97 \leq \cos\theta < 1$	$1.01 \pm 0.08$
192		$3.50 \leq p < 10.0$	$0.97 \leq \cos\theta < 1$	$0.99 \pm 0.05$
193		$10.0 \leq p < 30$	$0.97 \leq \cos\theta < 1$	$0.97 \pm 0.13$
194	$\bar{\nu}_\mu$ RHC 1-Trk Wtr	$0 \leq p < 0.50$	$-1 \leq \cos\theta < 0.82$	$1.00 \pm 0.36$
195		$0.50 \leq p < 0.60$	$-1 \leq \cos\theta < 0.82$	$0.90 \pm 0.15$
196		$0.60 \leq p < 0.80$	$-1 \leq \cos\theta < 0.82$	$1.05 \pm 0.26$
197		$0.80 \leq p < 1.25$	$-1 \leq \cos\theta < 0.82$	$1.04 \pm 0.20$
198		$1.25 \leq p < 2.00$	$-1 \leq \cos\theta < 0.82$	$1.00 \pm 0.17$
199		$2.00 \leq p < 3.00$	$-1 \leq \cos\theta < 0.82$	$1.01 \pm 0.17$
200	$\bar{\nu}_\mu$ RHC 1-Trk Wtr	$3.00 \leq p < 30$	$-1 \leq \cos\theta < 0.82$	$1.00 \pm 0.39$
201		$0 \leq p < 0.50$	$0.82 \leq \cos\theta < 0.90$	$1.06 \pm 0.43$
202		$0.50 \leq p < 0.60$	$0.82 \leq \cos\theta < 0.90$	$0.91 \pm 0.13$
203		$0.60 \leq p < 0.80$	$0.82 \leq \cos\theta < 0.90$	$0.97 \pm 0.16$
204		$0.80 \leq p < 1.25$	$0.82 \leq \cos\theta < 0.90$	$1.04 \pm 0.17$
205		$1.25 \leq p < 2.00$	$0.82 \leq \cos\theta < 0.90$	$1.00 \pm 0.11$
206		$2.00 \leq p < 3.00$	$0.82 \leq \cos\theta < 0.90$	$0.99 \pm 0.11$
207		$3.00 \leq p < 30$	$0.82 \leq \cos\theta < 0.90$	$0.92 \pm 0.28$
208		$0 \leq p < 0.50$	$0.90 \leq \cos\theta < 0.95$	$1.07 \pm 0.44$
209		$0.50 \leq p < 0.60$	$0.90 \leq \cos\theta < 0.95$	$0.93 \pm 0.14$
210	$\bar{\nu}_\mu$ RHC 1-Trk Wtr	$0.60 \leq p < 0.80$	$0.90 \leq \cos\theta < 0.95$	$0.96 \pm 0.11$
211		$0.80 \leq p < 1.25$	$0.90 \leq \cos\theta < 0.95$	$1.03 \pm 0.14$
212		$1.25 \leq p < 2.00$	$0.90 \leq \cos\theta < 0.95$	$1.01 \pm 0.08$

Fit Index	Sample	p [GeV/c]	$\cos\theta$	Prefit
213		$2.00 \leq p < 3.00$	$0.90 \leq \cos\theta < 0.95$	$0.98 \pm 0.06$
214		$3.00 \leq p < 30$	$0.90 \leq \cos\theta < 0.95$	$0.95 \pm 0.17$
215		$0 \leq p < 0.50$	$0.95 \leq \cos\theta < 0.99$	$1.08 \pm 0.45$
216		$0.50 \leq p < 0.60$	$0.95 \leq \cos\theta < 0.99$	$0.93 \pm 0.16$
217		$0.60 \leq p < 0.80$	$0.95 \leq \cos\theta < 0.99$	$0.96 \pm 0.09$
218		$0.80 \leq p < 1.25$	$0.95 \leq \cos\theta < 0.99$	$1.02 \pm 0.12$
219		$1.25 \leq p < 2.00$	$0.95 \leq \cos\theta < 0.99$	$1.01 \pm 0.07$
220	$\bar{\nu}_\mu$ RHC 1-Trk Wtr	$2.00 \leq p < 3.00$	$0.95 \leq \cos\theta < 0.99$	$1.00 \pm 0.04$
221		$3.00 \leq p < 30$	$0.95 \leq \cos\theta < 0.99$	$0.98 \pm 0.09$
222		$0 \leq p < 0.50$	$0.99 \leq \cos\theta < 1$	$1.09 \pm 0.43$
223		$0.50 \leq p < 0.60$	$0.99 \leq \cos\theta < 1$	$0.94 \pm 0.15$
224		$0.60 \leq p < 0.80$	$0.99 \leq \cos\theta < 1$	$0.93 \pm 0.10$
225		$0.80 \leq p < 1.25$	$0.99 \leq \cos\theta < 1$	$1.02 \pm 0.12$
226		$1.25 \leq p < 2.00$	$0.99 \leq \cos\theta < 1$	$1.01 \pm 0.08$
227		$2.00 \leq p < 3.00$	$0.99 \leq \cos\theta < 1$	$1.00 \pm 0.07$
228		$3.00 \leq p < 30$	$0.99 \leq \cos\theta < 1$	$0.99 \pm 0.05$
229	$\bar{\nu}_\mu$ RHC N-Trks Wtr	$0 \leq p < 0.50$	$-1 \leq \cos\theta < 0.89$	$1.02 \pm 0.34$
230		$0.50 \leq p < 0.90$	$-1 \leq \cos\theta < 0.89$	$1.00 \pm 0.09$
231		$0.90 \leq p < 1.25$	$-1 \leq \cos\theta < 0.89$	$1.01 \pm 0.07$
232		$1.25 \leq p < 1.60$	$-1 \leq \cos\theta < 0.89$	$0.99 \pm 0.13$
233		$1.60 \leq p < 3.00$	$-1 \leq \cos\theta < 0.89$	$0.99 \pm 0.11$
234		$3.00 \leq p < 30$	$-1 \leq \cos\theta < 0.89$	$0.98 \pm 0.33$
235		$0 \leq p < 0.50$	$0.89 \leq \cos\theta < 0.95$	$1.05 \pm 0.34$
236		$0.50 \leq p < 0.90$	$0.89 \leq \cos\theta < 0.95$	$0.97 \pm 0.05$
237		$0.90 \leq p < 1.25$	$0.89 \leq \cos\theta < 0.95$	$1.02 \pm 0.06$
238		$1.25 \leq p < 1.60$	$0.89 \leq \cos\theta < 0.95$	$0.98 \pm 0.09$

Fit Index	Sample	p [GeV/c]	$\cos\theta$	Prefit
239		$1.60 \leq p < 3.00$	$0.89 \leq \cos\theta < 0.95$	$0.99 \pm 0.06$
240	$\bar{\nu}_\mu$ RHC N-Trks Wtr	$3.00 \leq p < 30$	$0.89 \leq \cos\theta < 0.95$	$0.98 \pm 0.14$
241		$0 \leq p < 0.50$	$0.95 \leq \cos\theta < 0.97$	$1.04 \pm 0.36$
242		$0.50 \leq p < 0.90$	$0.95 \leq \cos\theta < 0.97$	$0.97 \pm 0.05$
243		$0.90 \leq p < 1.25$	$0.95 \leq \cos\theta < 0.97$	$1.01 \pm 0.05$
244		$1.25 \leq p < 1.60$	$0.95 \leq \cos\theta < 0.97$	$1.00 \pm 0.09$
245		$1.60 \leq p < 3.00$	$0.95 \leq \cos\theta < 0.97$	$1.01 \pm 0.06$
246		$3.00 \leq p < 30$	$0.95 \leq \cos\theta < 0.97$	$0.98 \pm 0.12$
247		$0 \leq p < 0.50$	$0.97 \leq \cos\theta < 0.99$	$1.03 \pm 0.37$
248		$0.50 \leq p < 0.90$	$0.97 \leq \cos\theta < 0.99$	$1.01 \pm 0.05$
249		$0.90 \leq p < 1.25$	$0.97 \leq \cos\theta < 0.99$	$1.00 \pm 0.05$
250	$\bar{\nu}_\mu$ RHC N-Trks Wtr	$1.25 \leq p < 1.60$	$0.97 \leq \cos\theta < 0.99$	$0.99 \pm 0.07$
251		$1.60 \leq p < 3.00$	$0.97 \leq \cos\theta < 0.99$	$1.01 \pm 0.07$
252		$3.00 \leq p < 30$	$0.97 \leq \cos\theta < 0.99$	$0.99 \pm 0.07$
253		$0 \leq p < 0.50$	$0.99 \leq \cos\theta < 1$	$1.07 \pm 0.39$
254		$0.50 \leq p < 0.90$	$0.99 \leq \cos\theta < 1$	$0.98 \pm 0.07$
255		$0.90 \leq p < 1.25$	$0.99 \leq \cos\theta < 1$	$1.02 \pm 0.08$
256		$1.25 \leq p < 1.60$	$0.99 \leq \cos\theta < 1$	$1.01 \pm 0.08$
257		$1.60 \leq p < 3.00$	$0.99 \leq \cos\theta < 1$	$0.99 \pm 0.09$
258		$3.00 \leq p < 30$	$0.99 \leq \cos\theta < 1$	$0.99 \pm 0.06$
259	$\nu_\mu$ RHC 1-Trk Wtr	$0 \leq p < 0.40$	$-1 \leq \cos\theta < 0.78$	$1.24 \pm 0.60$
260		$0.40 \leq p < 0.60$	$-1 \leq \cos\theta < 0.78$	$0.91 \pm 0.16$
261		$0.60 \leq p < 0.80$	$-1 \leq \cos\theta < 0.78$	$1.00 \pm 0.13$
262		$0.80 \leq p < 1.10$	$-1 \leq \cos\theta < 0.78$	$1.02 \pm 0.21$
263		$1.10 \leq p < 2.00$	$-1 \leq \cos\theta < 0.78$	$1.03 \pm 0.17$
264		$2.00 \leq p < 10.0$	$-1 \leq \cos\theta < 0.78$	$0.99 \pm 0.21$

Fit Index	Sample	p [GeV/c]	$\cos\theta$	Prefit
265		$0 \leq p < 0.40$	$0.78 \leq \cos\theta < 0.84$	$1.27 \pm 0.64$
266		$0.40 \leq p < 0.60$	$0.78 \leq \cos\theta < 0.84$	$0.95 \pm 0.16$
267		$0.60 \leq p < 0.80$	$0.78 \leq \cos\theta < 0.84$	$0.99 \pm 0.06$
268		$0.80 \leq p < 1.10$	$0.78 \leq \cos\theta < 0.84$	$0.98 \pm 0.11$
269		$1.10 \leq p < 2.00$	$0.78 \leq \cos\theta < 0.84$	$1.04 \pm 0.14$
270	$\nu_\mu$ RHC 1-Trk Wtr	$2.00 \leq p < 10.0$	$0.78 \leq \cos\theta < 0.84$	$0.99 \pm 0.16$
271		$0 \leq p < 0.40$	$0.84 \leq \cos\theta < 0.92$	$1.20 \pm 0.60$
272		$0.40 \leq p < 0.60$	$0.84 \leq \cos\theta < 0.92$	$0.95 \pm 0.20$
273		$0.60 \leq p < 0.80$	$0.84 \leq \cos\theta < 0.92$	$0.97 \pm 0.07$
274		$0.80 \leq p < 1.10$	$0.84 \leq \cos\theta < 0.92$	$1.00 \pm 0.08$
275		$1.10 \leq p < 2.00$	$0.84 \leq \cos\theta < 0.92$	$1.00 \pm 0.08$
276		$2.00 \leq p < 10.0$	$0.84 \leq \cos\theta < 0.92$	$1.00 \pm 0.10$
277		$0 \leq p < 0.40$	$0.92 \leq \cos\theta < 0.95$	$1.10 \pm 0.52$
278		$0.40 \leq p < 0.60$	$0.92 \leq \cos\theta < 0.95$	$0.99 \pm 0.16$
279		$0.60 \leq p < 0.80$	$0.92 \leq \cos\theta < 0.95$	$0.95 \pm 0.06$
280	$\nu_\mu$ RHC 1-Trk Wtr	$0.80 \leq p < 1.10$	$0.92 \leq \cos\theta < 0.95$	$0.99 \pm 0.04$
281		$1.10 \leq p < 2.00$	$0.92 \leq \cos\theta < 0.95$	$1.00 \pm 0.07$
282		$2.00 \leq p < 10.0$	$0.92 \leq \cos\theta < 0.95$	$1.00 \pm 0.06$
283		$0 \leq p < 0.40$	$0.95 \leq \cos\theta < 0.98$	$1.19 \pm 0.50$
284		$0.40 \leq p < 0.60$	$0.95 \leq \cos\theta < 0.98$	$0.98 \pm 0.15$
285		$0.60 \leq p < 0.80$	$0.95 \leq \cos\theta < 0.98$	$0.96 \pm 0.09$
286		$0.80 \leq p < 1.10$	$0.95 \leq \cos\theta < 0.98$	$0.99 \pm 0.07$
287		$1.10 \leq p < 2.00$	$0.95 \leq \cos\theta < 0.98$	$1.00 \pm 0.06$
288		$2.00 \leq p < 10.0$	$0.95 \leq \cos\theta < 0.98$	$1.00 \pm 0.04$
289		$0 \leq p < 0.40$	$0.98 \leq \cos\theta < 0.99$	$1.12 \pm 0.46$
290	$\nu_\mu$ RHC 1-Trk Wtr	$0.40 \leq p < 0.60$	$0.98 \leq \cos\theta < 0.99$	$1.01 \pm 0.15$

Fit Index	Sample	p [GeV/c]	$\cos\theta$	Prefit
291		$0.60 \leq p < 0.80$	$0.98 \leq \cos\theta < 0.99$	$0.98 \pm 0.09$
292		$0.80 \leq p < 1.10$	$0.98 \leq \cos\theta < 0.99$	$1.00 \pm 0.09$
293		$1.10 \leq p < 2.00$	$0.98 \leq \cos\theta < 0.99$	$0.98 \pm 0.07$
294		$2.00 \leq p < 10.0$	$0.98 \leq \cos\theta < 0.99$	$1.00 \pm 0.03$
295		$0 \leq p < 0.40$	$0.99 \leq \cos\theta < 1$	$1.29 \pm 0.47$
296		$0.40 \leq p < 0.60$	$0.99 \leq \cos\theta < 1$	$0.98 \pm 0.20$
297		$0.60 \leq p < 0.80$	$0.99 \leq \cos\theta < 1$	$0.95 \pm 0.16$
298		$0.80 \leq p < 1.10$	$0.99 \leq \cos\theta < 1$	$1.03 \pm 0.10$
299		$1.10 \leq p < 2.00$	$0.99 \leq \cos\theta < 1$	$1.01 \pm 0.08$
300	$\nu_\mu$ RHC 1-Trk Wtr	$2.00 \leq p < 10.0$	$0.99 \leq \cos\theta < 1$	$1.00 \pm 0.03$
301	$\nu_\mu$ RHC N-Trks Wtr	$0 \leq p < 0.60$	$-1 \leq \cos\theta < 0.70$	$0.97 \pm 0.21$
302		$0.60 \leq p < 1.00$	$-1 \leq \cos\theta < 0.70$	$1.01 \pm 0.13$
303		$1.00 \leq p < 1.50$	$-1 \leq \cos\theta < 0.70$	$1.01 \pm 0.15$
304		$1.50 \leq p < 2.00$	$-1 \leq \cos\theta < 0.70$	$1.15 \pm 0.19$
305		$2.00 \leq p < 10.0$	$-1 \leq \cos\theta < 0.70$	$0.95 \pm 0.23$
306		$0 \leq p < 0.60$	$0.70 \leq \cos\theta < 0.80$	$1.00 \pm 0.26$
307		$0.60 \leq p < 1.00$	$0.70 \leq \cos\theta < 0.80$	$0.99 \pm 0.08$
308		$1.00 \leq p < 1.50$	$0.70 \leq \cos\theta < 0.80$	$1.01 \pm 0.11$
309		$1.50 \leq p < 2.00$	$0.70 \leq \cos\theta < 0.80$	$0.98 \pm 0.09$
310	$\nu_\mu$ RHC N-Trks Wtr	$2.00 \leq p < 10.0$	$0.70 \leq \cos\theta < 0.80$	$1.00 \pm 0.16$
311		$0 \leq p < 0.60$	$0.80 \leq \cos\theta < 0.85$	$1.01 \pm 0.28$
312		$0.60 \leq p < 1.00$	$0.80 \leq \cos\theta < 0.85$	$0.98 \pm 0.06$
313		$1.00 \leq p < 1.50$	$0.80 \leq \cos\theta < 0.85$	$1.00 \pm 0.08$
314		$1.50 \leq p < 2.00$	$0.80 \leq \cos\theta < 0.85$	$1.02 \pm 0.08$
315		$2.00 \leq p < 10.0$	$0.80 \leq \cos\theta < 0.85$	$0.98 \pm 0.11$
316		$0 \leq p < 0.60$	$0.85 \leq \cos\theta < 0.98$	$1.02 \pm 0.25$

Fit Index	Sample	p [GeV/c]	$\cos\theta$	Prefit
317		$0.60 \leq p < 1.00$	$0.85 \leq \cos\theta < 0.98$	$0.98 \pm 0.07$
318		$1.00 \leq p < 1.50$	$0.85 \leq \cos\theta < 0.98$	$1.00 \pm 0.07$
319		$1.50 \leq p < 2.00$	$0.85 \leq \cos\theta < 0.98$	$1.00 \pm 0.07$
320	$\nu_\mu$ RHC N-Trks Wtr	$2.00 \leq p < 10.0$	$0.85 \leq \cos\theta < 0.98$	$1.00 \pm 0.06$
321		$0 \leq p < 0.60$	$0.98 \leq \cos\theta < 0.99$	$1.02 \pm 0.24$
322		$0.60 \leq p < 1.00$	$0.98 \leq \cos\theta < 0.99$	$0.96 \pm 0.10$
323		$1.00 \leq p < 1.50$	$0.98 \leq \cos\theta < 0.99$	$1.01 \pm 0.09$
324		$1.50 \leq p < 2.00$	$0.98 \leq \cos\theta < 0.99$	$0.99 \pm 0.09$
325		$2.00 \leq p < 10.0$	$0.98 \leq \cos\theta < 0.99$	$0.99 \pm 0.04$
326		$0 \leq p < 0.60$	$0.99 \leq \cos\theta < 1$	$1.00 \pm 0.25$
327		$0.60 \leq p < 1.00$	$0.99 \leq \cos\theta < 1$	$0.98 \pm 0.11$
328		$1.00 \leq p < 1.50$	$0.99 \leq \cos\theta < 1$	$1.00 \pm 0.09$
329		$1.50 \leq p < 2.00$	$0.99 \leq \cos\theta < 1$	$1.01 \pm 0.10$
330	$\nu_\mu$ RHC N-Trks Wtr	$2.00 \leq p < 10.0$	$0.99 \leq \cos\theta < 1$	$1.00 \pm 0.04$
331	$\nu_\mu$ 1-Trk Air	$0 \leq p < 0.40$	$-1 \leq \cos\theta < 0.70$	$1.17 \pm 0.66$
332		$0.40 \leq p < 0.60$	$-1 \leq \cos\theta < 0.70$	$0.86 \pm 0.19$
333		$0.60 \leq p < 0.80$	$-1 \leq \cos\theta < 0.70$	$1.17 \pm 0.53$
334		$0.80 \leq p < 1.25$	$-1 \leq \cos\theta < 0.70$	$1.15 \pm 0.44$
335		$1.25 \leq p < 2.00$	$-1 \leq \cos\theta < 0.70$	$0.97 \pm 0.19$
336		$2.00 \leq p < 3.00$	$-1 \leq \cos\theta < 0.70$	$1.02 \pm 0.19$
337		$3.00 \leq p < 4.00$	$-1 \leq \cos\theta < 0.70$	$1.02 \pm 0.31$
338		$4.00 \leq p < 5.50$	$-1 \leq \cos\theta < 0.70$	$0.97 \pm 0.37$
339		$5.50 \leq p < 30$	$-1 \leq \cos\theta < 0.70$	$0.88 \pm 0.62$
340	$\nu_\mu$ 1-Trk Air	$0 \leq p < 0.40$	$0.70 \leq \cos\theta < 0.80$	$1.27 \pm 0.75$
341		$0.40 \leq p < 0.60$	$0.70 \leq \cos\theta < 0.80$	$0.87 \pm 0.17$
342		$0.60 \leq p < 0.80$	$0.70 \leq \cos\theta < 0.80$	$1.04 \pm 0.31$

Fit Index	Sample	p [GeV/c]	$\cos\theta$	Prefit
343		$0.80 \leq p < 1.25$	$0.70 \leq \cos\theta < 0.80$	$1.09 \pm 0.34$
344		$1.25 \leq p < 2.00$	$0.70 \leq \cos\theta < 0.80$	$1.01 \pm 0.18$
345		$2.00 \leq p < 3.00$	$0.70 \leq \cos\theta < 0.80$	$1.03 \pm 0.17$
346		$3.00 \leq p < 4.00$	$0.70 \leq \cos\theta < 0.80$	$0.94 \pm 0.27$
347		$4.00 \leq p < 5.50$	$0.70 \leq \cos\theta < 0.80$	$0.93 \pm 0.38$
348		$5.50 \leq p < 30$	$0.70 \leq \cos\theta < 0.80$	$1.00 \pm 0.58$
349		$0 \leq p < 0.40$	$0.80 \leq \cos\theta < 0.94$	$1.32 \pm 0.79$
350	$\nu_\mu$ 1-Trk Air	$0.40 \leq p < 0.60$	$0.80 \leq \cos\theta < 0.94$	$0.90 \pm 0.20$
351		$0.60 \leq p < 0.80$	$0.80 \leq \cos\theta < 0.94$	$0.98 \pm 0.17$
352		$0.80 \leq p < 1.25$	$0.80 \leq \cos\theta < 0.94$	$1.04 \pm 0.19$
353		$1.25 \leq p < 2.00$	$0.80 \leq \cos\theta < 0.94$	$1.01 \pm 0.10$
354		$2.00 \leq p < 3.00$	$0.80 \leq \cos\theta < 0.94$	$1.00 \pm 0.07$
355		$3.00 \leq p < 4.00$	$0.80 \leq \cos\theta < 0.94$	$0.97 \pm 0.14$
356		$4.00 \leq p < 5.50$	$0.80 \leq \cos\theta < 0.94$	$1.06 \pm 0.22$
357		$5.50 \leq p < 30$	$0.80 \leq \cos\theta < 0.94$	$1.00 \pm 0.33$
358		$0 \leq p < 0.40$	$0.94 \leq \cos\theta < 0.97$	$1.29 \pm 0.73$
359		$0.40 \leq p < 0.60$	$0.94 \leq \cos\theta < 0.97$	$0.91 \pm 0.20$
360	$\nu_\mu$ 1-Trk Air	$0.60 \leq p < 0.80$	$0.94 \leq \cos\theta < 0.97$	$0.97 \pm 0.11$
361		$0.80 \leq p < 1.25$	$0.94 \leq \cos\theta < 0.97$	$1.02 \pm 0.12$
362		$1.25 \leq p < 2.00$	$0.94 \leq \cos\theta < 0.97$	$1.00 \pm 0.07$
363		$2.00 \leq p < 3.00$	$0.94 \leq \cos\theta < 0.97$	$1.01 \pm 0.04$
364		$3.00 \leq p < 4.00$	$0.94 \leq \cos\theta < 0.97$	$0.98 \pm 0.09$
365		$4.00 \leq p < 5.50$	$0.94 \leq \cos\theta < 0.97$	$0.98 \pm 0.15$
366		$5.50 \leq p < 30$	$0.94 \leq \cos\theta < 0.97$	$0.98 \pm 0.21$
367		$0 \leq p < 0.40$	$0.97 \leq \cos\theta < 0.99$	$1.23 \pm 0.68$
368		$0.40 \leq p < 0.60$	$0.97 \leq \cos\theta < 0.99$	$0.91 \pm 0.20$

Fit Index	Sample	p [GeV/c]	$\cos\theta$	Prefit
369		$0.60 \leq p < 0.80$	$0.97 \leq \cos\theta < 0.99$	$0.98 \pm 0.12$
370	$\nu_\mu$ 1-Trk Air	$0.80 \leq p < 1.25$	$0.97 \leq \cos\theta < 0.99$	$1.02 \pm 0.11$
371		$1.25 \leq p < 2.00$	$0.97 \leq \cos\theta < 0.99$	$0.99 \pm 0.08$
372		$2.00 \leq p < 3.00$	$0.97 \leq \cos\theta < 0.99$	$1.01 \pm 0.06$
373		$3.00 \leq p < 4.00$	$0.97 \leq \cos\theta < 0.99$	$1.00 \pm 0.04$
374		$4.00 \leq p < 5.50$	$0.97 \leq \cos\theta < 0.99$	$0.98 \pm 0.11$
375		$5.50 \leq p < 30$	$0.97 \leq \cos\theta < 0.99$	$0.98 \pm 0.15$
376		$0 \leq p < 0.40$	$0.99 \leq \cos\theta < 1$	$1.21 \pm 0.58$
377		$0.40 \leq p < 0.60$	$0.99 \leq \cos\theta < 1$	$0.90 \pm 0.16$
378		$0.60 \leq p < 0.80$	$0.99 \leq \cos\theta < 1$	$0.99 \pm 0.12$
379		$0.80 \leq p < 1.25$	$0.99 \leq \cos\theta < 1$	$1.02 \pm 0.12$
380	$\nu_\mu$ 1-Trk Air	$1.25 \leq p < 2.00$	$0.99 \leq \cos\theta < 1$	$1.01 \pm 0.09$
381		$2.00 \leq p < 3.00$	$0.99 \leq \cos\theta < 1$	$1.01 \pm 0.10$
382		$3.00 \leq p < 4.00$	$0.99 \leq \cos\theta < 1$	$1.00 \pm 0.06$
383		$4.00 \leq p < 5.50$	$0.99 \leq \cos\theta < 1$	$1.00 \pm 0.05$
384		$5.50 \leq p < 30$	$0.99 \leq \cos\theta < 1$	$0.98 \pm 0.10$
385	$\nu_\mu$ N-Trks Air	$0 \leq p < 0.40$	$-1 \leq \cos\theta < 0.77$	$1.18 \pm 0.62$
386		$0.40 \leq p < 0.60$	$-1 \leq \cos\theta < 0.77$	$0.88 \pm 0.15$
387		$0.60 \leq p < 0.80$	$-1 \leq \cos\theta < 0.77$	$1.03 \pm 0.21$
388		$0.80 \leq p < 1.20$	$-1 \leq \cos\theta < 0.77$	$1.03 \pm 0.21$
389		$1.20 \leq p < 2.20$	$-1 \leq \cos\theta < 0.77$	$1.01 \pm 0.16$
390	$\nu_\mu$ N-Trks Air	$2.20 \leq p < 3.50$	$-1 \leq \cos\theta < 0.77$	$1.00 \pm 0.22$
391		$3.50 \leq p < 10.0$	$-1 \leq \cos\theta < 0.77$	$0.99 \pm 0.32$
392		$10.0 \leq p < 30$	$-1 \leq \cos\theta < 0.77$	$0.93 \pm 0.69$
393		$0 \leq p < 0.40$	$0.77 \leq \cos\theta < 0.85$	$1.13 \pm 0.58$
394		$0.40 \leq p < 0.60$	$0.77 \leq \cos\theta < 0.85$	$0.91 \pm 0.14$

Fit Index	Sample	p [GeV/c]	$\cos\theta$	Prefit
395		$0.60 \leq p < 0.80$	$0.77 \leq \cos\theta < 0.85$	$0.99 \pm 0.10$
396		$0.80 \leq p < 1.20$	$0.77 \leq \cos\theta < 0.85$	$1.01 \pm 0.11$
397		$1.20 \leq p < 2.20$	$0.77 \leq \cos\theta < 0.85$	$1.01 \pm 0.08$
398		$2.20 \leq p < 3.50$	$0.77 \leq \cos\theta < 0.85$	$1.00 \pm 0.08$
399		$3.50 \leq p < 10.0$	$0.77 \leq \cos\theta < 0.85$	$1.03 \pm 0.18$
400	$\nu_\mu$ N-Trks Air	$10.0 \leq p < 30$	$0.77 \leq \cos\theta < 0.85$	$0.97 \pm 0.51$
401		$0 \leq p < 0.40$	$0.85 \leq \cos\theta < 0.90$	$1.12 \pm 0.55$
402		$0.40 \leq p < 0.60$	$0.85 \leq \cos\theta < 0.90$	$0.92 \pm 0.13$
403		$0.60 \leq p < 0.80$	$0.85 \leq \cos\theta < 0.90$	$0.99 \pm 0.08$
404		$0.80 \leq p < 1.20$	$0.85 \leq \cos\theta < 0.90$	$1.00 \pm 0.08$
405		$1.20 \leq p < 2.20$	$0.85 \leq \cos\theta < 0.90$	$1.01 \pm 0.07$
406		$2.20 \leq p < 3.50$	$0.85 \leq \cos\theta < 0.90$	$1.00 \pm 0.06$
407		$3.50 \leq p < 10.0$	$0.85 \leq \cos\theta < 0.90$	$0.98 \pm 0.13$
408		$10.0 \leq p < 30$	$0.85 \leq \cos\theta < 0.90$	$0.93 \pm 0.45$
409		$0 \leq p < 0.40$	$0.90 \leq \cos\theta < 0.97$	$1.09 \pm 0.51$
410	$\nu_\mu$ N-Trks Air	$0.40 \leq p < 0.60$	$0.90 \leq \cos\theta < 0.97$	$0.93 \pm 0.11$
411		$0.60 \leq p < 0.80$	$0.90 \leq \cos\theta < 0.97$	$0.99 \pm 0.08$
412		$0.80 \leq p < 1.20$	$0.90 \leq \cos\theta < 0.97$	$1.00 \pm 0.08$
413		$1.20 \leq p < 2.20$	$0.90 \leq \cos\theta < 0.97$	$1.00 \pm 0.07$
414		$2.20 \leq p < 3.50$	$0.90 \leq \cos\theta < 0.97$	$1.00 \pm 0.03$
415		$3.50 \leq p < 10.0$	$0.90 \leq \cos\theta < 0.97$	$0.99 \pm 0.10$
416		$10.0 \leq p < 30$	$0.90 \leq \cos\theta < 0.97$	$0.97 \pm 0.28$
417		$0 \leq p < 0.40$	$0.97 \leq \cos\theta < 1$	$1.09 \pm 0.48$
418		$0.40 \leq p < 0.60$	$0.97 \leq \cos\theta < 1$	$0.94 \pm 0.12$
419		$0.60 \leq p < 0.80$	$0.97 \leq \cos\theta < 1$	$0.98 \pm 0.11$
420	$\nu_\mu$ N-Trks Air	$0.80 \leq p < 1.20$	$0.97 \leq \cos\theta < 1$	$1.01 \pm 0.10$

Fit Index	Sample	p [GeV/c]	$\cos\theta$	Prefit
421		$1.20 \leq p < 2.20$	$0.97 \leq \cos\theta < 1$	$1.01 \pm 0.09$
422		$2.20 \leq p < 3.50$	$0.97 \leq \cos\theta < 1$	$1.01 \pm 0.07$
423		$3.50 \leq p < 10.0$	$0.97 \leq \cos\theta < 1$	$0.99 \pm 0.06$
424		$10.0 \leq p < 30$	$0.97 \leq \cos\theta < 1$	$0.97 \pm 0.13$
425	$\bar{\nu}_\mu$ RHC 1-Trk Air	$0 \leq p < 0.50$	$-1 \leq \cos\theta < 0.82$	$0.99 \pm 0.29$
426		$0.50 \leq p < 0.60$	$-1 \leq \cos\theta < 0.82$	$0.92 \pm 0.14$
427		$0.60 \leq p < 0.80$	$-1 \leq \cos\theta < 0.82$	$1.05 \pm 0.24$
428		$0.80 \leq p < 1.25$	$-1 \leq \cos\theta < 0.82$	$1.05 \pm 0.18$
429		$1.25 \leq p < 2.00$	$-1 \leq \cos\theta < 0.82$	$1.02 \pm 0.17$
430	$\bar{\nu}_\mu$ RHC 1-Trk Air	$2.00 \leq p < 3.00$	$-1 \leq \cos\theta < 0.82$	$0.87 \pm 0.19$
431		$3.00 \leq p < 30$	$-1 \leq \cos\theta < 0.82$	$0.96 \pm 0.41$
432		$0 \leq p < 0.50$	$0.82 \leq \cos\theta < 0.90$	$1.03 \pm 0.35$
433		$0.50 \leq p < 0.60$	$0.82 \leq \cos\theta < 0.90$	$0.91 \pm 0.12$
434		$0.60 \leq p < 0.80$	$0.82 \leq \cos\theta < 0.90$	$1.00 \pm 0.16$
435		$0.80 \leq p < 1.25$	$0.82 \leq \cos\theta < 0.90$	$1.03 \pm 0.15$
436		$1.25 \leq p < 2.00$	$0.82 \leq \cos\theta < 0.90$	$0.99 \pm 0.12$
437		$2.00 \leq p < 3.00$	$0.82 \leq \cos\theta < 0.90$	$0.99 \pm 0.15$
438		$3.00 \leq p < 30$	$0.82 \leq \cos\theta < 0.90$	$0.93 \pm 0.31$
439		$0 \leq p < 0.50$	$0.90 \leq \cos\theta < 0.95$	$1.05 \pm 0.37$
440	$\bar{\nu}_\mu$ RHC 1-Trk Air	$0.50 \leq p < 0.60$	$0.90 \leq \cos\theta < 0.95$	$0.92 \pm 0.11$
441		$0.60 \leq p < 0.80$	$0.90 \leq \cos\theta < 0.95$	$0.98 \pm 0.12$
442		$0.80 \leq p < 1.25$	$0.90 \leq \cos\theta < 0.95$	$1.03 \pm 0.12$
443		$1.25 \leq p < 2.00$	$0.90 \leq \cos\theta < 0.95$	$1.02 \pm 0.08$
444		$2.00 \leq p < 3.00$	$0.90 \leq \cos\theta < 0.95$	$0.97 \pm 0.08$
445		$3.00 \leq p < 30$	$0.90 \leq \cos\theta < 0.95$	$0.97 \pm 0.19$
446		$0 \leq p < 0.50$	$0.95 \leq \cos\theta < 0.99$	$1.06 \pm 0.37$

<b>Fit Index</b>	<b>Sample</b>	<b>p [GeV/c]</b>	<b>cosθ</b>	<b>Prefit</b>
447		$0.50 \leq p < 0.60$	$0.95 \leq \cos \theta < 0.99$	$0.93 \pm 0.12$
448		$0.60 \leq p < 0.80$	$0.95 \leq \cos \theta < 0.99$	$0.97 \pm 0.11$
449		$0.80 \leq p < 1.25$	$0.95 \leq \cos \theta < 0.99$	$1.02 \pm 0.10$
450	$\bar{\nu}_\mu$ RHC 1-Trk Air	$1.25 \leq p < 2.00$	$0.95 \leq \cos \theta < 0.99$	$1.00 \pm 0.07$
451		$2.00 \leq p < 3.00$	$0.95 \leq \cos \theta < 0.99$	$0.99 \pm 0.04$
452		$3.00 \leq p < 30$	$0.95 \leq \cos \theta < 0.99$	$0.99 \pm 0.10$
453		$0 \leq p < 0.50$	$0.99 \leq \cos \theta < 1$	$1.07 \pm 0.35$
454		$0.50 \leq p < 0.60$	$0.99 \leq \cos \theta < 1$	$0.89 \pm 0.12$
455		$0.60 \leq p < 0.80$	$0.99 \leq \cos \theta < 1$	$0.99 \pm 0.11$
456		$0.80 \leq p < 1.25$	$0.99 \leq \cos \theta < 1$	$1.02 \pm 0.11$
457		$1.25 \leq p < 2.00$	$0.99 \leq \cos \theta < 1$	$0.99 \pm 0.09$
458		$2.00 \leq p < 3.00$	$0.99 \leq \cos \theta < 1$	$1.01 \pm 0.07$
459		$3.00 \leq p < 30$	$0.99 \leq \cos \theta < 1$	$0.99 \pm 0.06$
460	$\bar{\nu}_\mu$ RHC N-Trks Air	$0 \leq p < 0.50$	$-1 \leq \cos \theta < 0.89$	$1.00 \pm 0.29$
461		$0.50 \leq p < 0.90$	$-1 \leq \cos \theta < 0.89$	$1.00 \pm 0.10$
462		$0.90 \leq p < 1.25$	$-1 \leq \cos \theta < 0.89$	$1.04 \pm 0.09$
463		$1.25 \leq p < 1.60$	$-1 \leq \cos \theta < 0.89$	$0.98 \pm 0.14$
464		$1.60 \leq p < 3.00$	$-1 \leq \cos \theta < 0.89$	$0.98 \pm 0.13$
465		$3.00 \leq p < 30$	$-1 \leq \cos \theta < 0.89$	$0.92 \pm 0.33$
466		$0 \leq p < 0.50$	$0.89 \leq \cos \theta < 0.95$	$1.00 \pm 0.31$
467		$0.50 \leq p < 0.90$	$0.89 \leq \cos \theta < 0.95$	$0.99 \pm 0.06$
468		$0.90 \leq p < 1.25$	$0.89 \leq \cos \theta < 0.95$	$1.02 \pm 0.06$
469		$1.25 \leq p < 1.60$	$0.89 \leq \cos \theta < 0.95$	$0.99 \pm 0.11$
470	$\bar{\nu}_\mu$ RHC N-Trks Air	$1.60 \leq p < 3.00$	$0.89 \leq \cos \theta < 0.95$	$0.99 \pm 0.06$
471		$3.00 \leq p < 30$	$0.89 \leq \cos \theta < 0.95$	$0.96 \pm 0.16$
472		$0 \leq p < 0.50$	$0.95 \leq \cos \theta < 0.97$	$1.00 \pm 0.32$

Fit Index	Sample	p [GeV/c]	$\cos\theta$	Prefit
473		$0.50 \leq p < 0.90$	$0.95 \leq \cos\theta < 0.97$	$1.00 \pm 0.07$
474		$0.90 \leq p < 1.25$	$0.95 \leq \cos\theta < 0.97$	$1.00 \pm 0.06$
475		$1.25 \leq p < 1.60$	$0.95 \leq \cos\theta < 0.97$	$1.00 \pm 0.11$
476		$1.60 \leq p < 3.00$	$0.95 \leq \cos\theta < 0.97$	$1.00 \pm 0.06$
477		$3.00 \leq p < 30$	$0.95 \leq \cos\theta < 0.97$	$0.99 \pm 0.13$
478		$0 \leq p < 0.50$	$0.97 \leq \cos\theta < 0.99$	$1.03 \pm 0.32$
479		$0.50 \leq p < 0.90$	$0.97 \leq \cos\theta < 0.99$	$0.99 \pm 0.07$
480	$\bar{\nu}_\mu$ RHC N-Trks Air	$0.90 \leq p < 1.25$	$0.97 \leq \cos\theta < 0.99$	$1.02 \pm 0.07$
481		$1.25 \leq p < 1.60$	$0.97 \leq \cos\theta < 0.99$	$0.99 \pm 0.10$
482		$1.60 \leq p < 3.00$	$0.97 \leq \cos\theta < 0.99$	$1.01 \pm 0.08$
483		$3.00 \leq p < 30$	$0.97 \leq \cos\theta < 0.99$	$0.98 \pm 0.09$
484		$0 \leq p < 0.50$	$0.99 \leq \cos\theta < 1$	$1.02 \pm 0.31$
485		$0.50 \leq p < 0.90$	$0.99 \leq \cos\theta < 1$	$1.01 \pm 0.07$
486		$0.90 \leq p < 1.25$	$0.99 \leq \cos\theta < 1$	$1.02 \pm 0.08$
487		$1.25 \leq p < 1.60$	$0.99 \leq \cos\theta < 1$	$0.98 \pm 0.10$
488		$1.60 \leq p < 3.00$	$0.99 \leq \cos\theta < 1$	$1.00 \pm 0.09$
489		$3.00 \leq p < 30$	$0.99 \leq \cos\theta < 1$	$0.99 \pm 0.07$
490	$\nu_\mu$ RHC 1-Trk Air	$0 \leq p < 0.40$	$-1 \leq \cos\theta < 0.78$	$1.10 \pm 0.50$
491		$0.40 \leq p < 0.60$	$-1 \leq \cos\theta < 0.78$	$0.92 \pm 0.12$
492		$0.60 \leq p < 0.80$	$-1 \leq \cos\theta < 0.78$	$1.03 \pm 0.16$
493		$0.80 \leq p < 1.10$	$-1 \leq \cos\theta < 0.78$	$1.02 \pm 0.20$
494		$1.10 \leq p < 2.00$	$-1 \leq \cos\theta < 0.78$	$1.08 \pm 0.14$
495		$2.00 \leq p < 10.0$	$-1 \leq \cos\theta < 0.78$	$0.81 \pm 0.31$
496		$0 \leq p < 0.40$	$0.78 \leq \cos\theta < 0.84$	$1.23 \pm 0.50$
497		$0.40 \leq p < 0.60$	$0.78 \leq \cos\theta < 0.84$	$0.93 \pm 0.18$
498		$0.60 \leq p < 0.80$	$0.78 \leq \cos\theta < 0.84$	$0.93 \pm 0.09$

<b>Fit Index</b>	<b>Sample</b>	<b>p [GeV/c]</b>	<b>cosθ</b>	<b>Prefit</b>
499		$0.80 \leq p < 1.10$	$0.78 \leq \cos \theta < 0.84$	$1.03 \pm 0.12$
500	$\nu_\mu$ RHC 1-Trk Air	$1.10 \leq p < 2.00$	$0.78 \leq \cos \theta < 0.84$	$1.05 \pm 0.14$
501		$2.00 \leq p < 10.0$	$0.78 \leq \cos \theta < 0.84$	$1.00 \pm 0.21$
502		$0 \leq p < 0.40$	$0.84 \leq \cos \theta < 0.92$	$1.17 \pm 0.49$
503		$0.40 \leq p < 0.60$	$0.84 \leq \cos \theta < 0.92$	$0.95 \pm 0.15$
504		$0.60 \leq p < 0.80$	$0.84 \leq \cos \theta < 0.92$	$0.97 \pm 0.08$
505		$0.80 \leq p < 1.10$	$0.84 \leq \cos \theta < 0.92$	$1.00 \pm 0.10$
506		$1.10 \leq p < 2.00$	$0.84 \leq \cos \theta < 0.92$	$1.00 \pm 0.08$
507		$2.00 \leq p < 10.0$	$0.84 \leq \cos \theta < 0.92$	$1.04 \pm 0.16$
508		$0 \leq p < 0.40$	$0.92 \leq \cos \theta < 0.95$	$1.13 \pm 0.47$
509		$0.40 \leq p < 0.60$	$0.92 \leq \cos \theta < 0.95$	$0.99 \pm 0.13$
510	$\nu_\mu$ RHC 1-Trk Air	$0.60 \leq p < 0.80$	$0.92 \leq \cos \theta < 0.95$	$0.94 \pm 0.09$
511		$0.80 \leq p < 1.10$	$0.92 \leq \cos \theta < 0.95$	$0.99 \pm 0.07$
512		$1.10 \leq p < 2.00$	$0.92 \leq \cos \theta < 0.95$	$1.00 \pm 0.06$
513		$2.00 \leq p < 10.0$	$0.92 \leq \cos \theta < 0.95$	$0.99 \pm 0.08$
514		$0 \leq p < 0.40$	$0.95 \leq \cos \theta < 0.98$	$1.06 \pm 0.46$
515		$0.40 \leq p < 0.60$	$0.95 \leq \cos \theta < 0.98$	$0.95 \pm 0.14$
516		$0.60 \leq p < 0.80$	$0.95 \leq \cos \theta < 0.98$	$0.97 \pm 0.11$
517		$0.80 \leq p < 1.10$	$0.95 \leq \cos \theta < 0.98$	$1.01 \pm 0.10$
518		$1.10 \leq p < 2.00$	$0.95 \leq \cos \theta < 0.98$	$1.00 \pm 0.07$
519		$2.00 \leq p < 10.0$	$0.95 \leq \cos \theta < 0.98$	$0.99 \pm 0.06$
520	$\nu_\mu$ RHC 1-Trk Air	$0 \leq p < 0.40$	$0.98 \leq \cos \theta < 0.99$	$1.07 \pm 0.46$
521		$0.40 \leq p < 0.60$	$0.98 \leq \cos \theta < 0.99$	$1.00 \pm 0.15$
522		$0.60 \leq p < 0.80$	$0.98 \leq \cos \theta < 0.99$	$1.02 \pm 0.16$
523		$0.80 \leq p < 1.10$	$0.98 \leq \cos \theta < 0.99$	$0.96 \pm 0.10$
524		$1.10 \leq p < 2.00$	$0.98 \leq \cos \theta < 0.99$	$1.01 \pm 0.08$

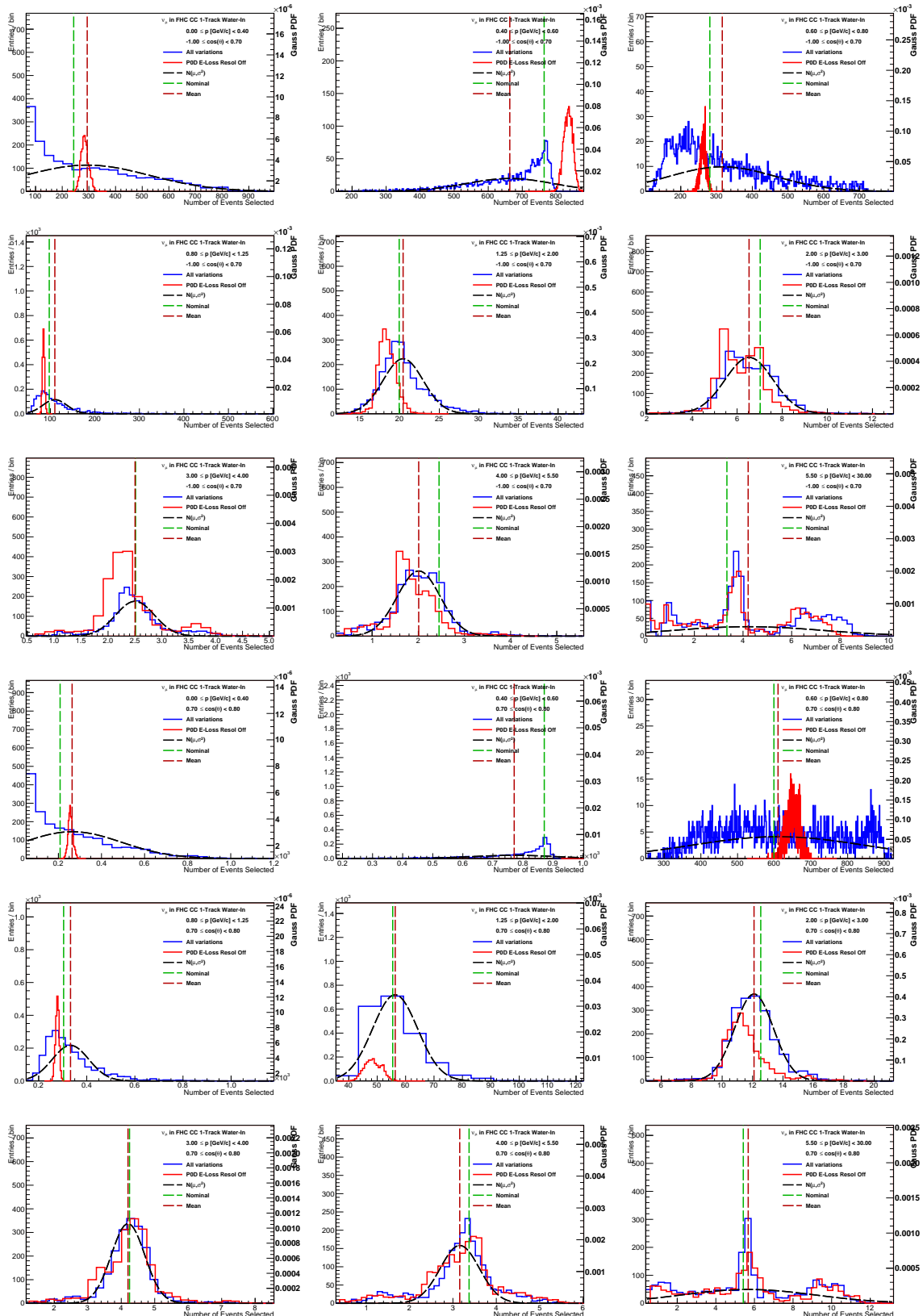
Fit Index	Sample	p [GeV/c]	$\cos\theta$	Prefit
525		$2.00 \leq p < 10.0$	$0.98 \leq \cos\theta < 0.99$	$0.99 \pm 0.04$
526		$0 \leq p < 0.40$	$0.99 \leq \cos\theta < 1$	$1.19 \pm 0.46$
527		$0.40 \leq p < 0.60$	$0.99 \leq \cos\theta < 1$	$0.89 \pm 0.17$
528		$0.60 \leq p < 0.80$	$0.99 \leq \cos\theta < 1$	$0.99 \pm 0.15$
529		$0.80 \leq p < 1.10$	$0.99 \leq \cos\theta < 1$	$0.99 \pm 0.10$
530	$\nu_\mu$ RHC 1-Trk Air	$1.10 \leq p < 2.00$	$0.99 \leq \cos\theta < 1$	$1.00 \pm 0.09$
531		$2.00 \leq p < 10.0$	$0.99 \leq \cos\theta < 1$	$1.00 \pm 0.03$
532	$\nu_\mu$ RHC N-Trks Air	$0 \leq p < 0.60$	$-1 \leq \cos\theta < 0.70$	$0.97 \pm 0.22$
533		$0.60 \leq p < 1.00$	$-1 \leq \cos\theta < 0.70$	$1.02 \pm 0.17$
534		$1.00 \leq p < 1.50$	$-1 \leq \cos\theta < 0.70$	$1.00 \pm 0.14$
535		$1.50 \leq p < 2.00$	$-1 \leq \cos\theta < 0.70$	$1.28 \pm 0.22$
536		$2.00 \leq p < 10.0$	$-1 \leq \cos\theta < 0.70$	$0.83 \pm 0.25$
537		$0 \leq p < 0.60$	$0.70 \leq \cos\theta < 0.80$	$0.98 \pm 0.22$
538		$0.60 \leq p < 1.00$	$0.70 \leq \cos\theta < 0.80$	$0.99 \pm 0.09$
539		$1.00 \leq p < 1.50$	$0.70 \leq \cos\theta < 0.80$	$1.00 \pm 0.11$
540	$\nu_\mu$ RHC N-Trks Air	$1.50 \leq p < 2.00$	$0.70 \leq \cos\theta < 0.80$	$1.03 \pm 0.11$
541		$2.00 \leq p < 10.0$	$0.70 \leq \cos\theta < 0.80$	$1.04 \pm 0.20$
542		$0 \leq p < 0.60$	$0.80 \leq \cos\theta < 0.85$	$1.01 \pm 0.25$
543		$0.60 \leq p < 1.00$	$0.80 \leq \cos\theta < 0.85$	$0.98 \pm 0.08$
544		$1.00 \leq p < 1.50$	$0.80 \leq \cos\theta < 0.85$	$1.01 \pm 0.08$
545		$1.50 \leq p < 2.00$	$0.80 \leq \cos\theta < 0.85$	$1.00 \pm 0.08$
546		$2.00 \leq p < 10.0$	$0.80 \leq \cos\theta < 0.85$	$0.99 \pm 0.12$
547		$0 \leq p < 0.60$	$0.85 \leq \cos\theta < 0.98$	$0.99 \pm 0.22$
548		$0.60 \leq p < 1.00$	$0.85 \leq \cos\theta < 0.98$	$1.00 \pm 0.10$
549		$1.00 \leq p < 1.50$	$0.85 \leq \cos\theta < 0.98$	$1.01 \pm 0.07$
550	$\nu_\mu$ RHC N-Trks Air	$1.50 \leq p < 2.00$	$0.85 \leq \cos\theta < 0.98$	$1.00 \pm 0.07$

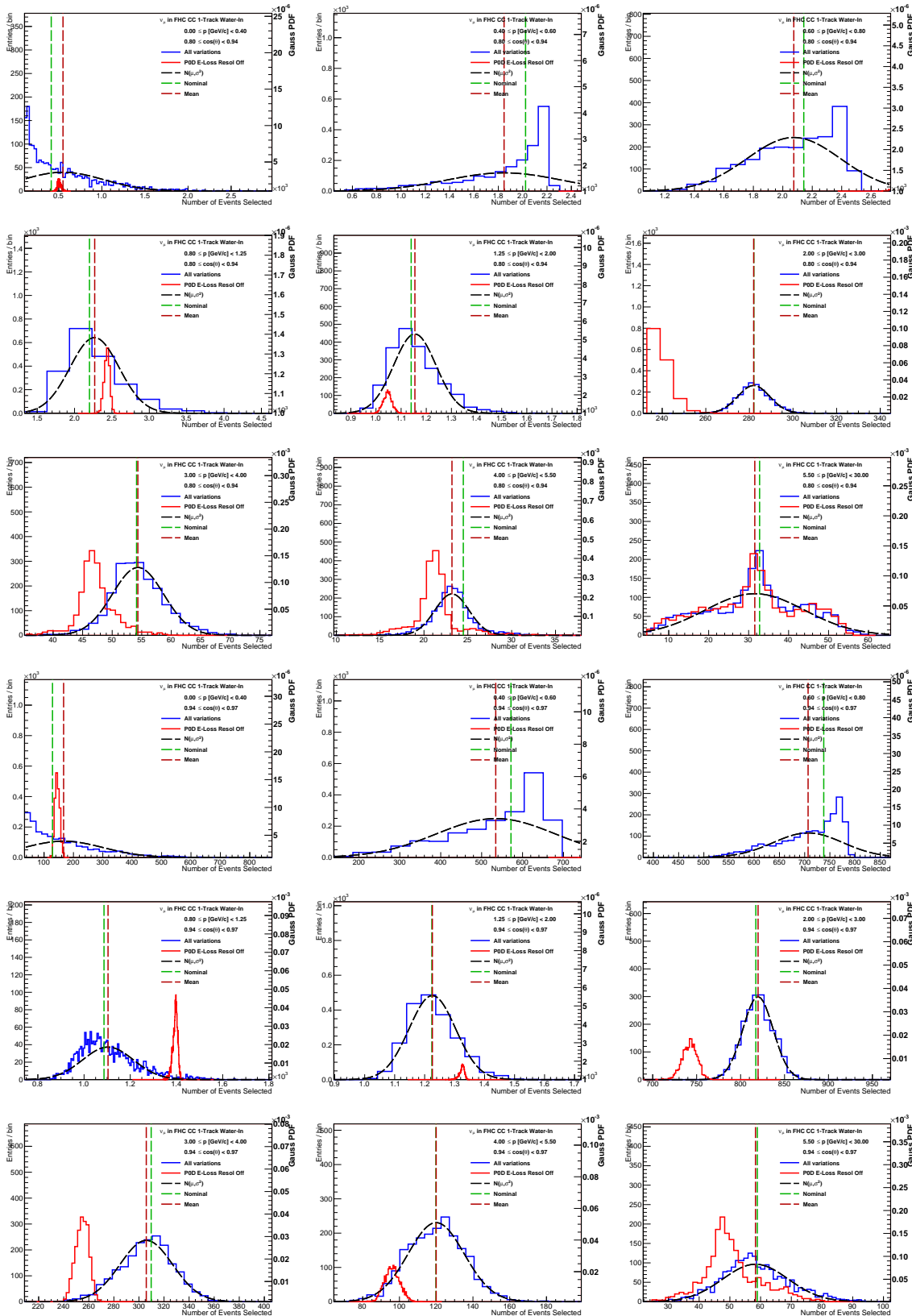
<b>Fit Index</b>	<b>Sample</b>	<b>p [GeV/c]</b>	<b>cosθ</b>	<b>Prefit</b>
551		$2.00 \leq p < 10.0$	$0.85 \leq \cos \theta < 0.98$	$1.00 \pm 0.07$
552		$0 \leq p < 0.60$	$0.98 \leq \cos \theta < 0.99$	$1.00 \pm 0.22$
553		$0.60 \leq p < 1.00$	$0.98 \leq \cos \theta < 0.99$	$0.99 \pm 0.12$
554		$1.00 \leq p < 1.50$	$0.98 \leq \cos \theta < 0.99$	$1.04 \pm 0.10$
555		$1.50 \leq p < 2.00$	$0.98 \leq \cos \theta < 0.99$	$0.99 \pm 0.10$
556		$2.00 \leq p < 10.0$	$0.98 \leq \cos \theta < 0.99$	$0.99 \pm 0.04$
557		$0 \leq p < 0.60$	$0.99 \leq \cos \theta < 1$	$1.01 \pm 0.24$
558		$0.60 \leq p < 1.00$	$0.99 \leq \cos \theta < 1$	$0.99 \pm 0.16$
559		$1.00 \leq p < 1.50$	$0.99 \leq \cos \theta < 1$	$0.97 \pm 0.12$
560	$\nu_\mu$ RHC N-Trks Air	$1.50 \leq p < 2.00$	$0.99 \leq \cos \theta < 1$	$1.06 \pm 0.10$
561		$2.00 \leq p < 10.0$	$0.99 \leq \cos \theta < 1$	$1.00 \pm 0.04$

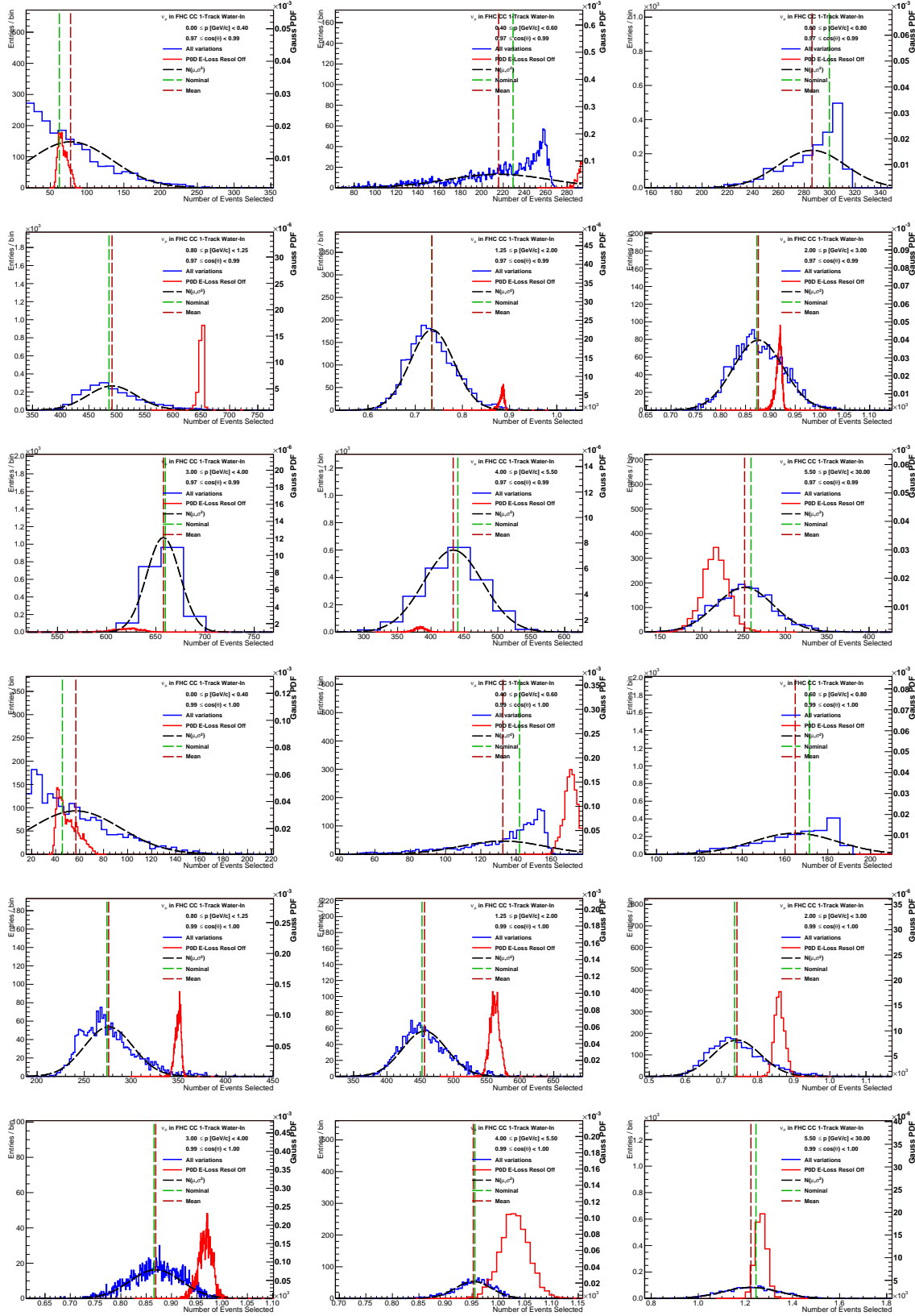
## Appendix C

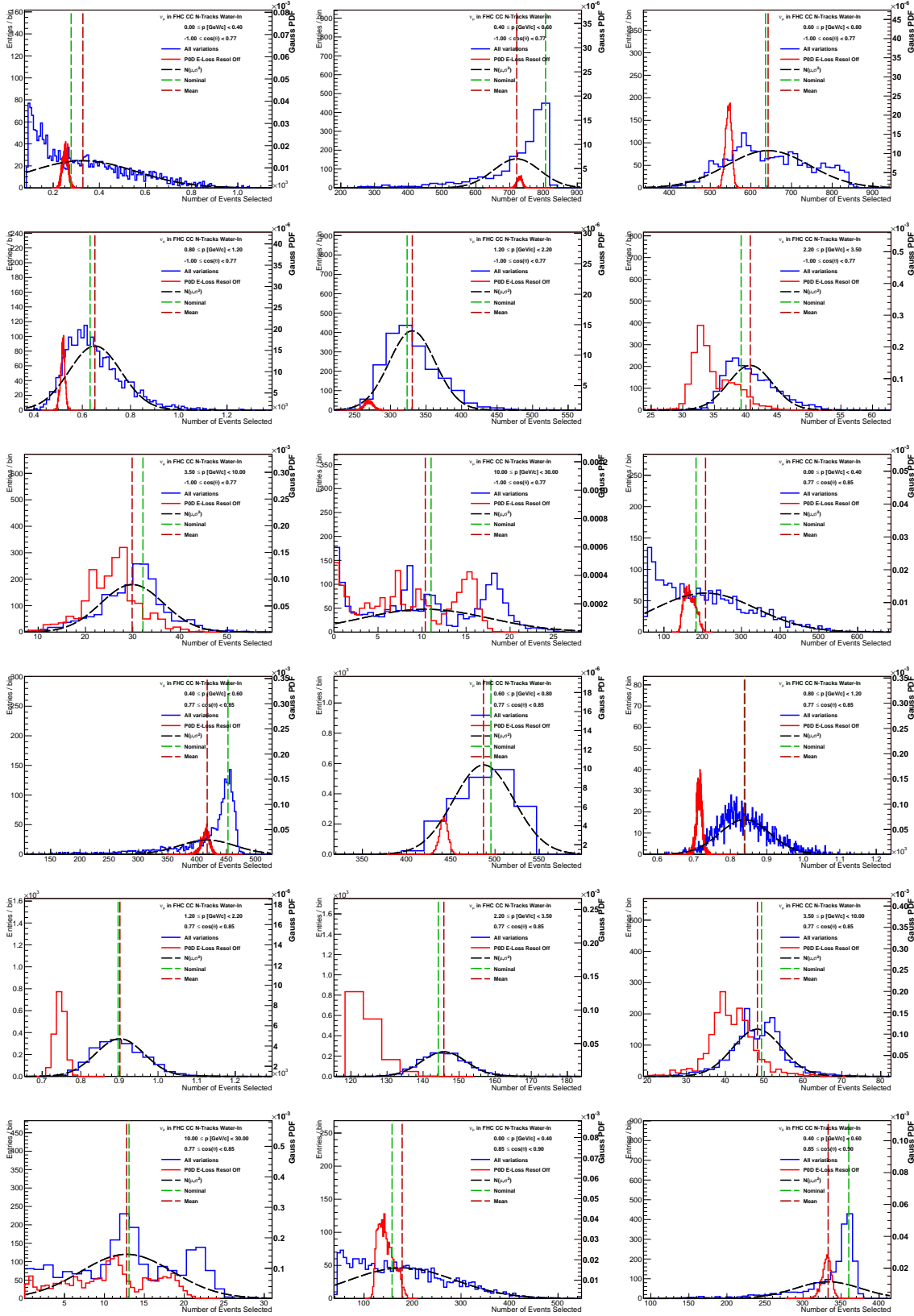
### Toy Experiment Variations

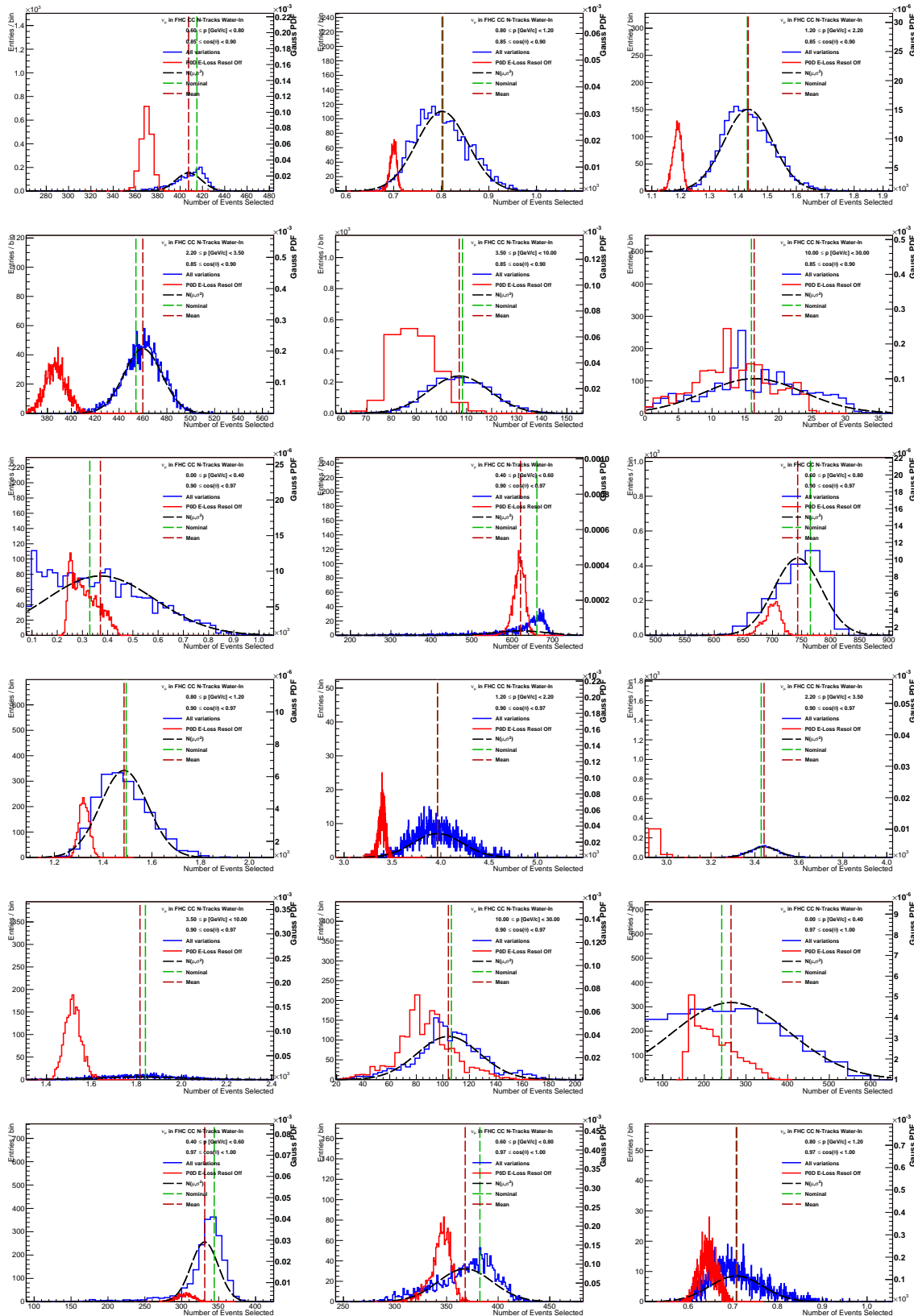
In this appendix is the collection of all toy experiments used to make observable normalization parameters and detector covariance matrix. Each of the observable bin relevant samples and  $(p, \cos \theta)$  edges are listed in the plots. The nominal MC (Nominal) predicted value and varied mean are shown as differently dashed lines. A normal curve, whose variance was extracted from the covariance matrix itself, is shown to illustrate the estimate on the bin normalization uncertainty. In addition, toy experiment variations with the PØD energy loss resolution off (E-Loss Resol Off) is shown to demonstrate the absence of the energy correction and its affect on when not varied.

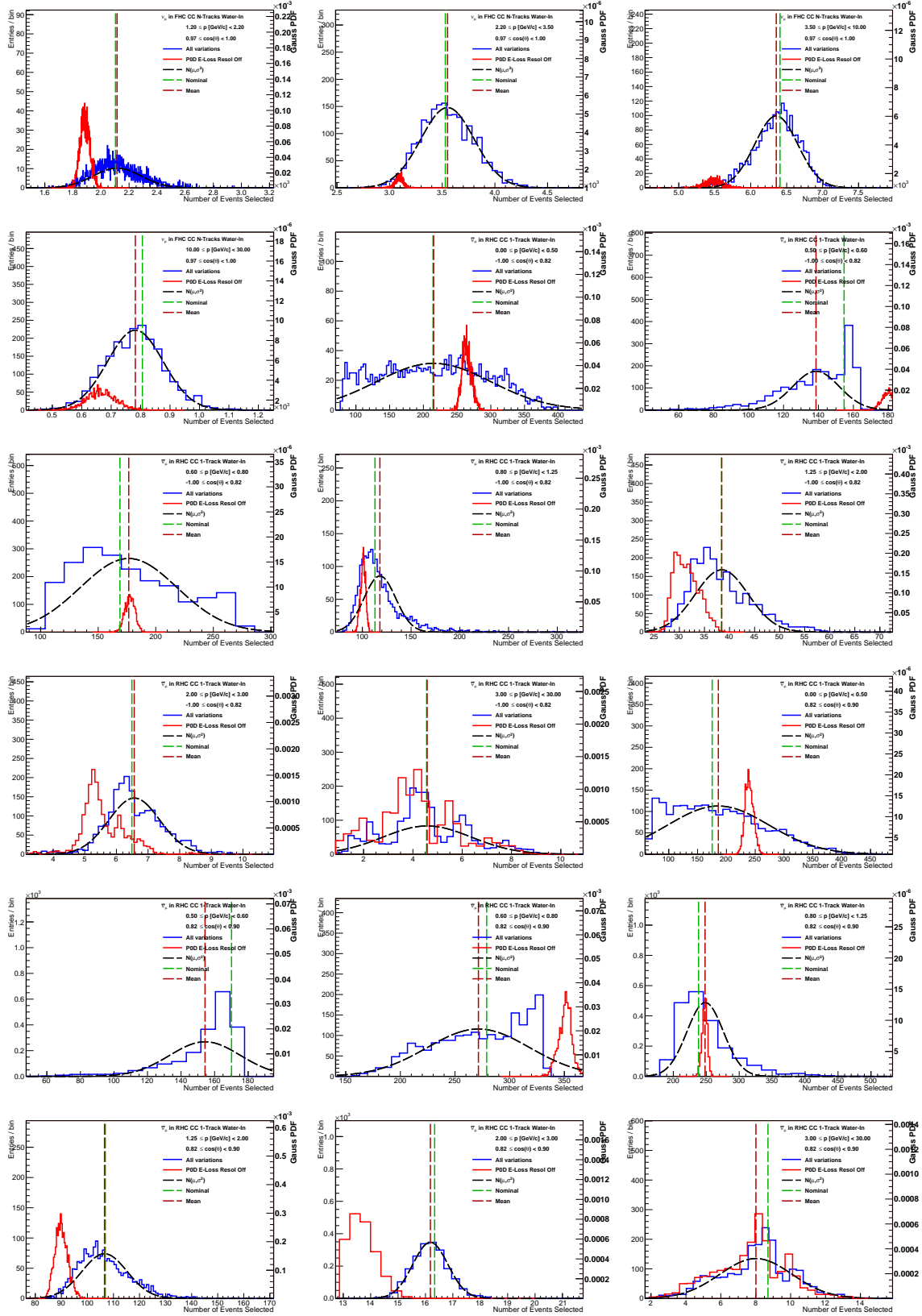


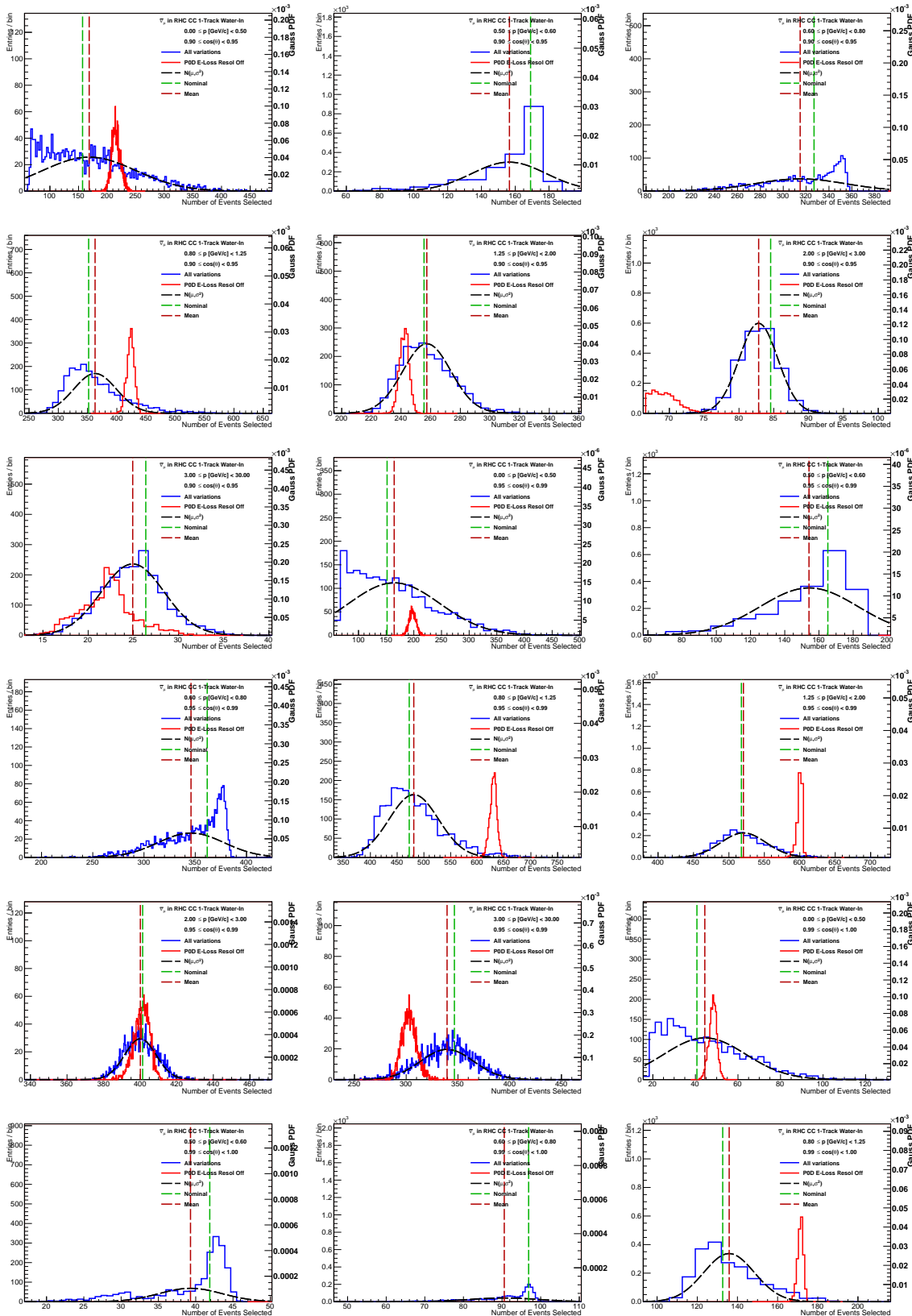


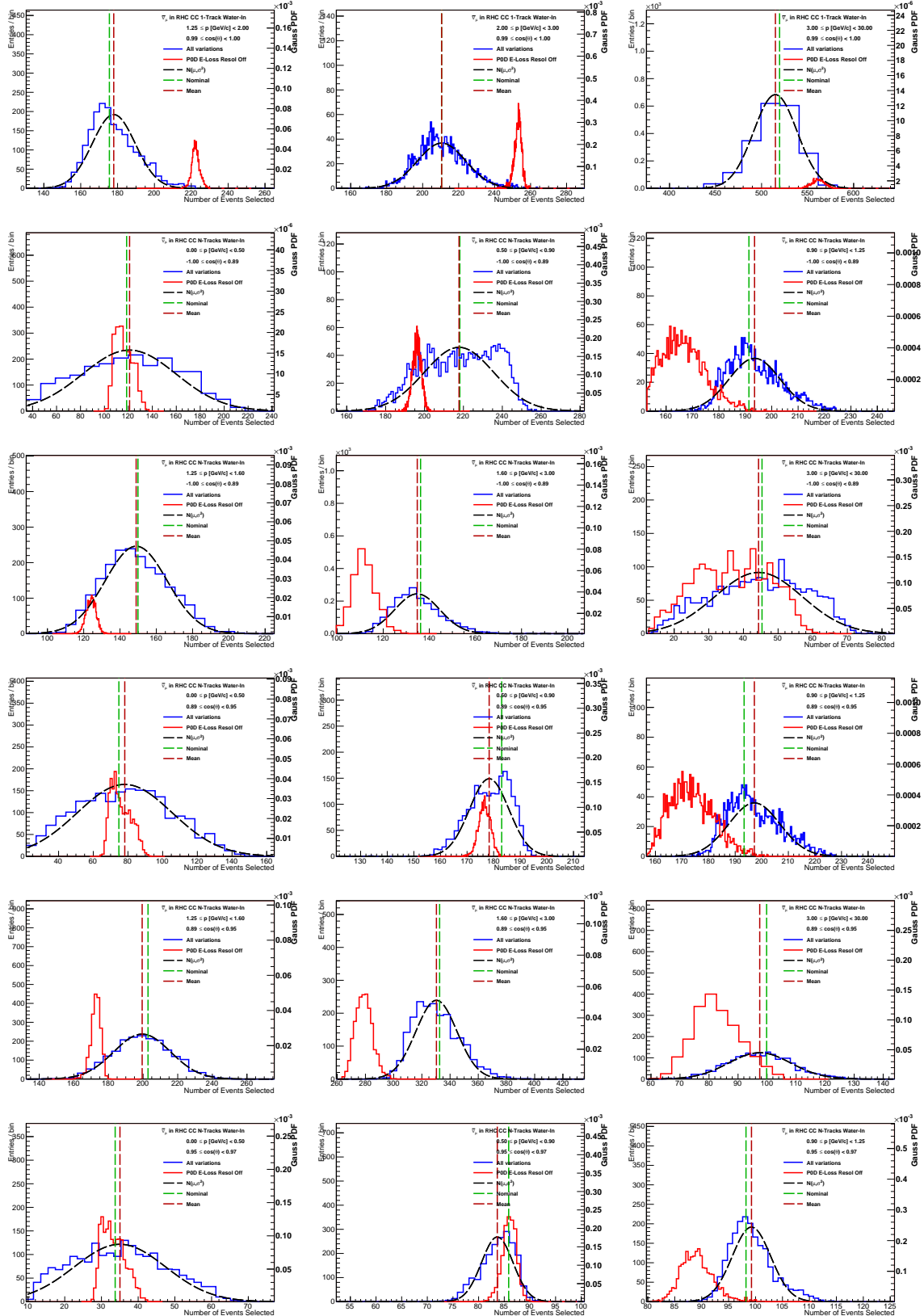


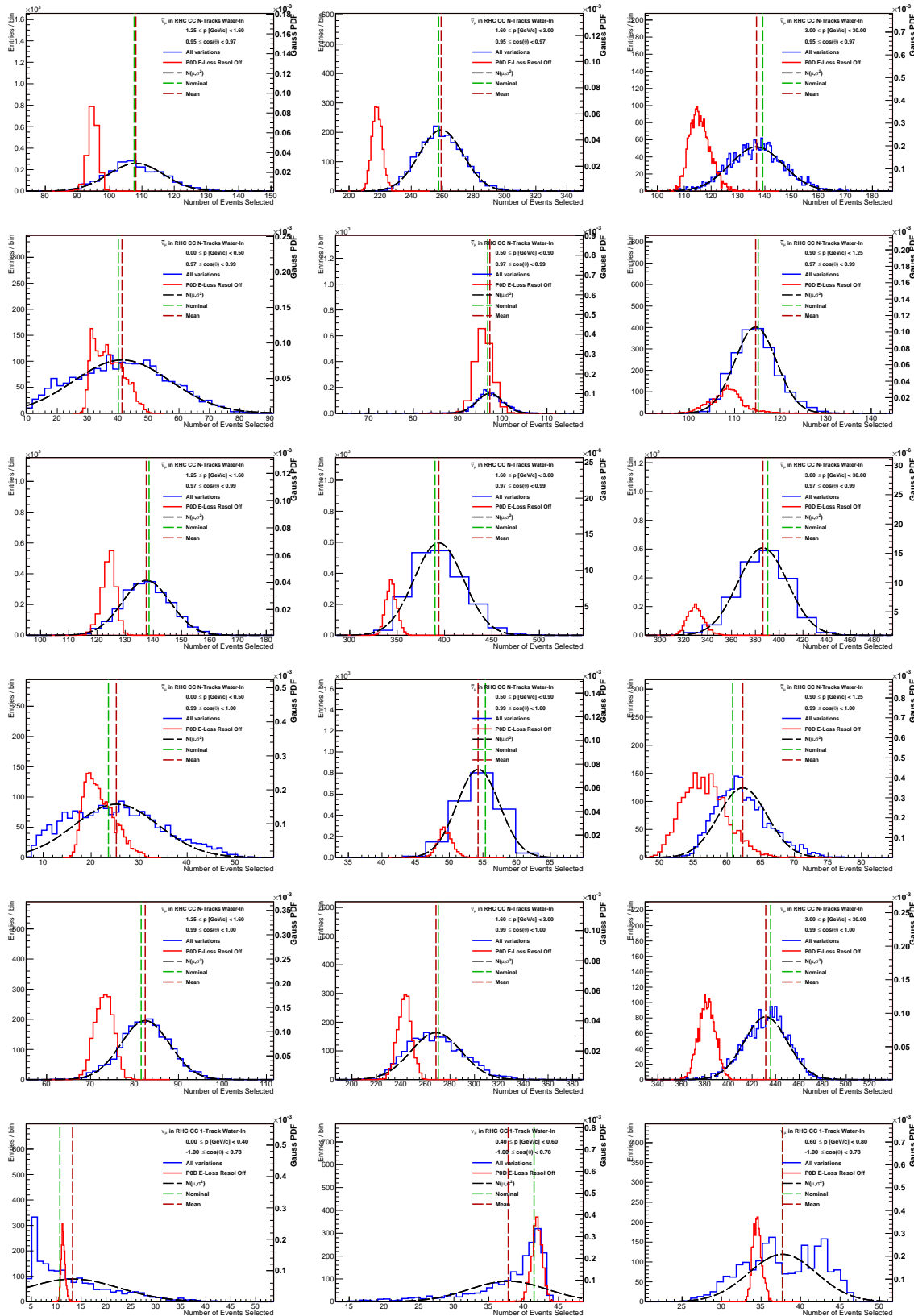


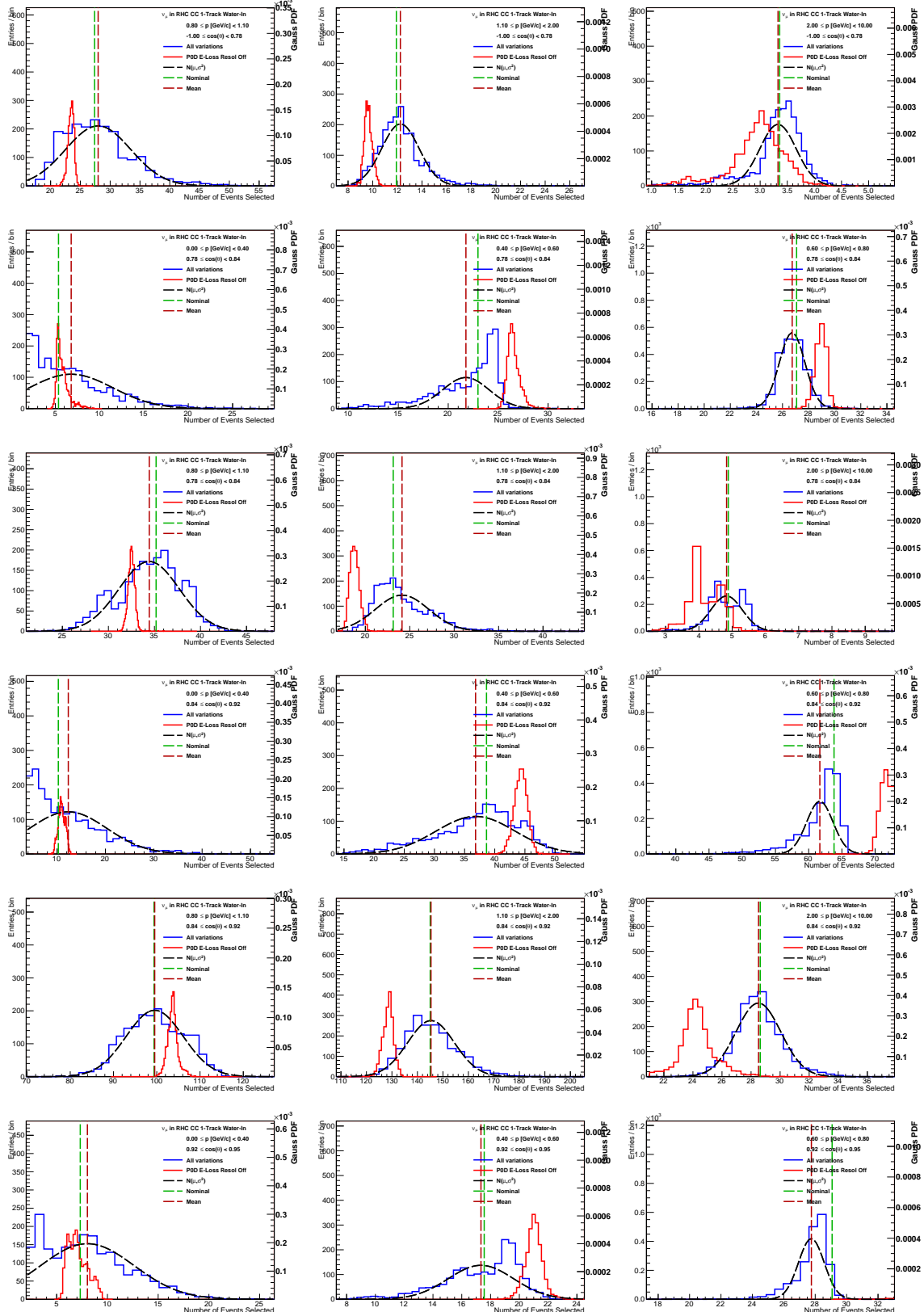


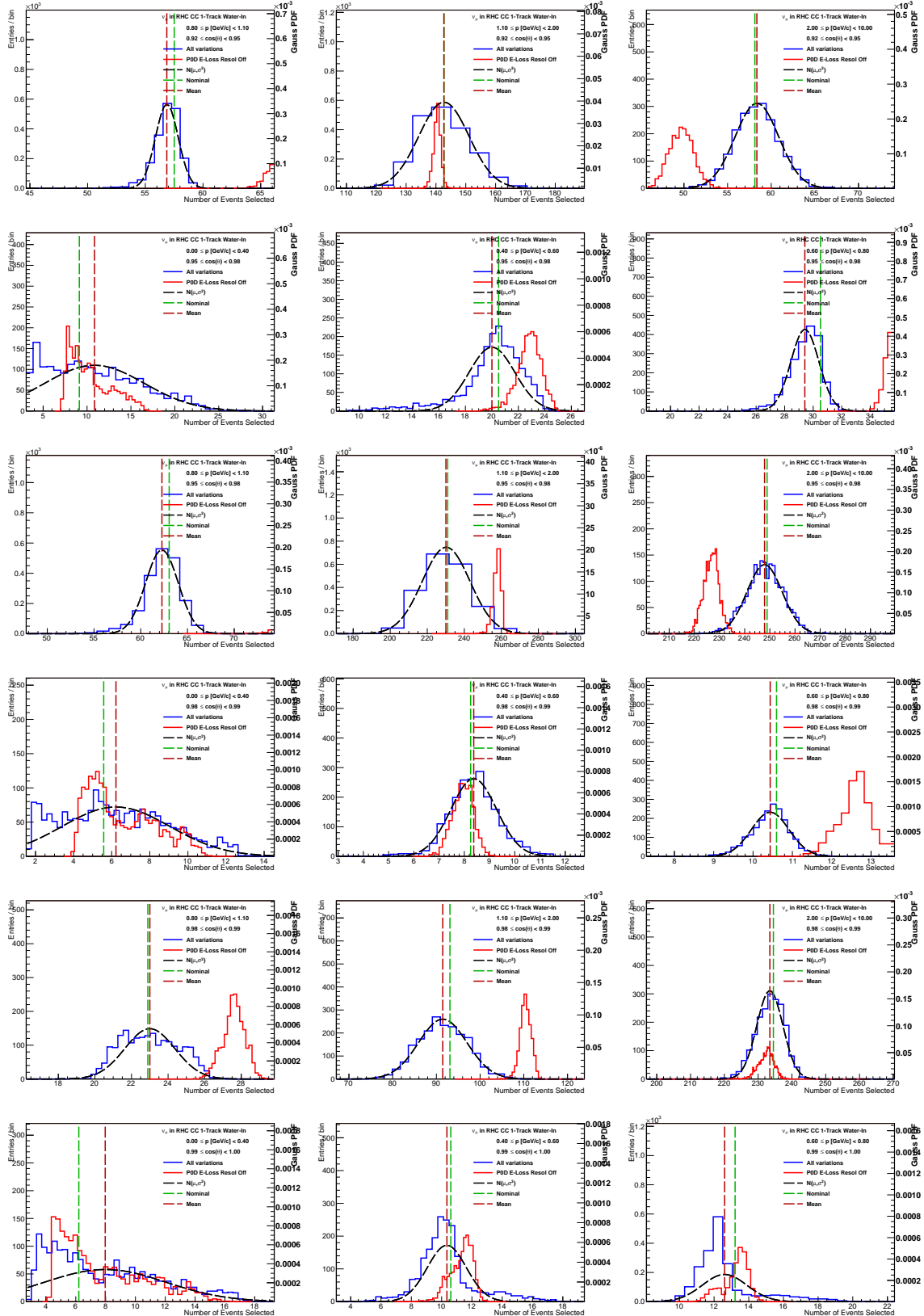


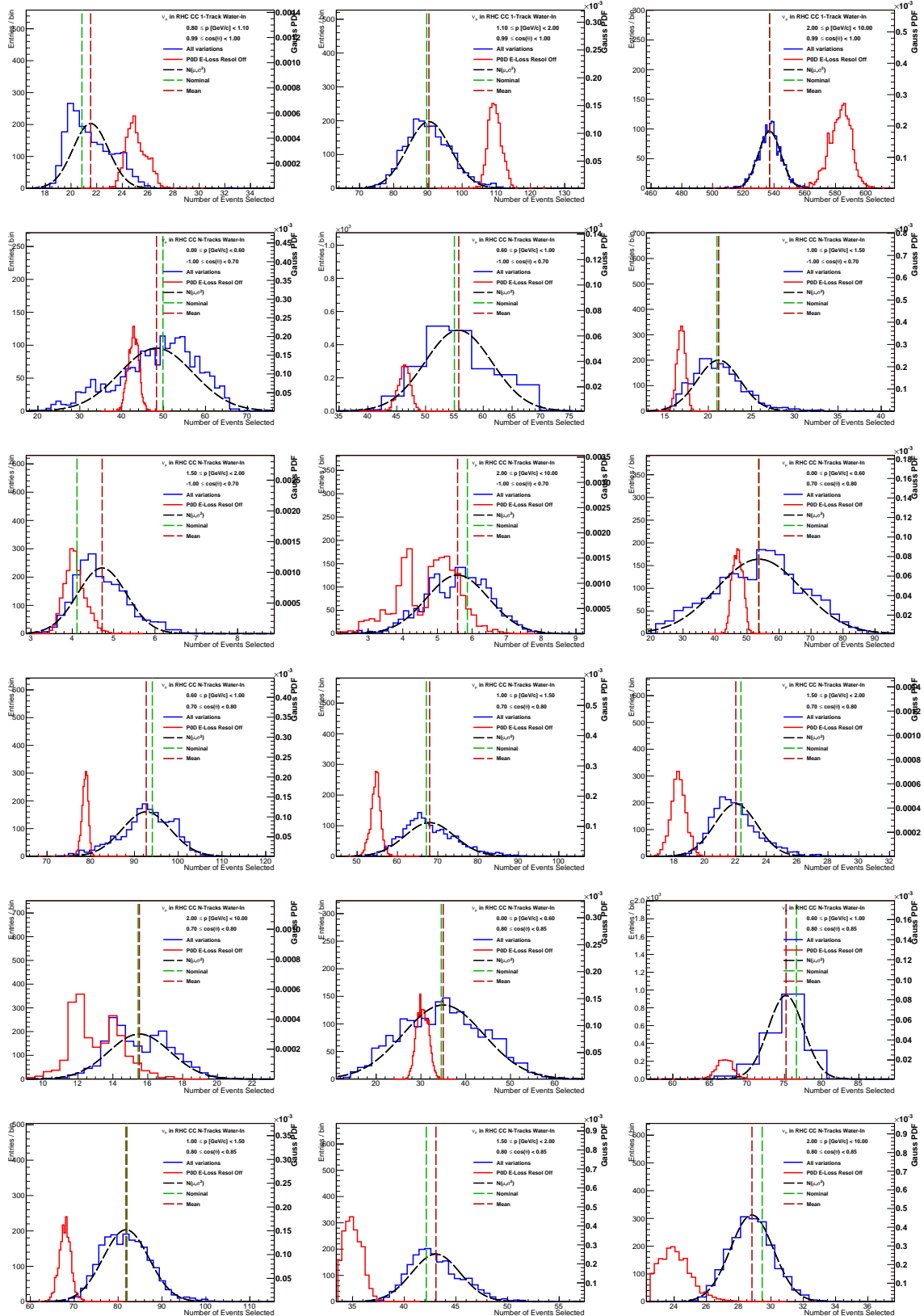


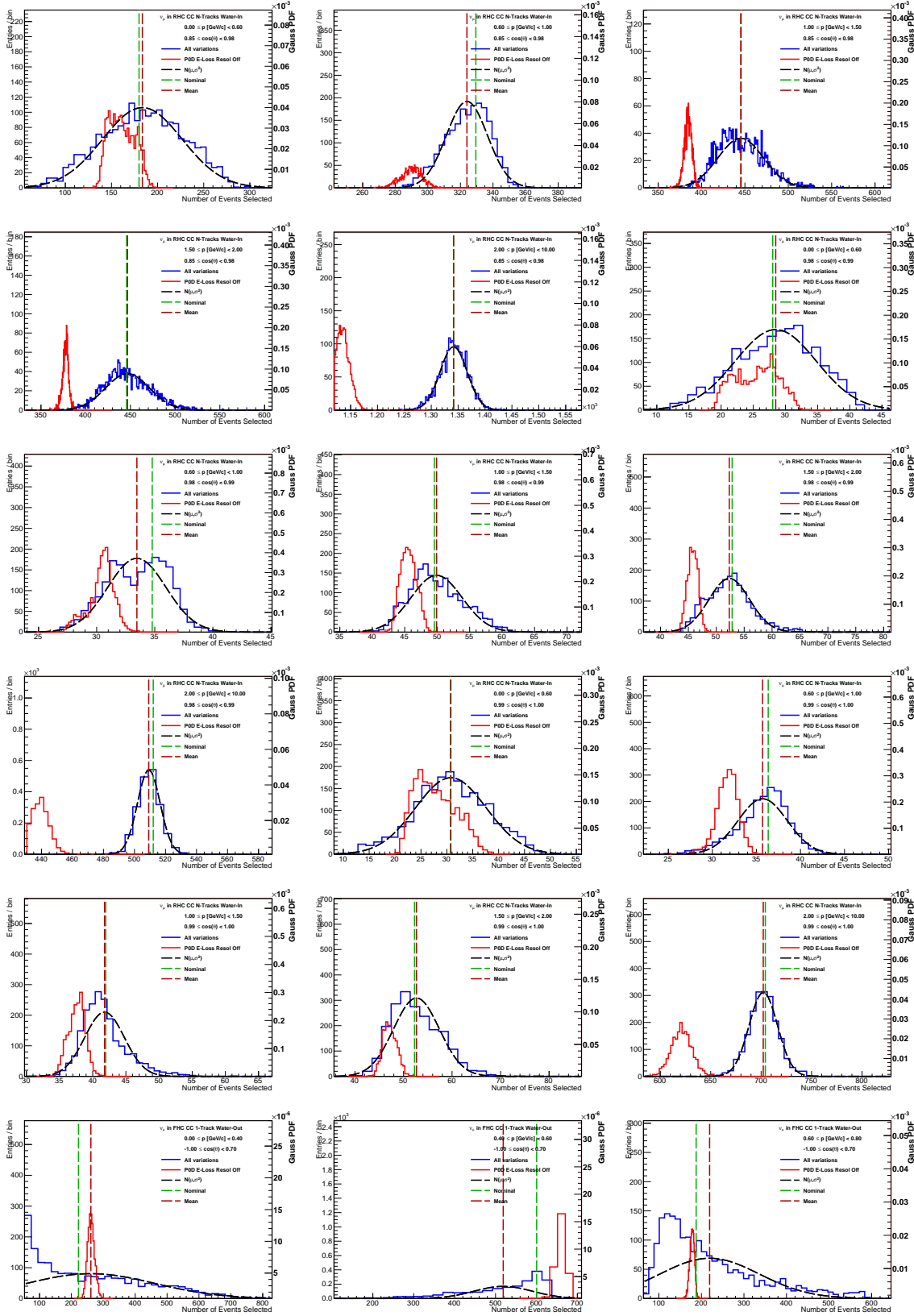


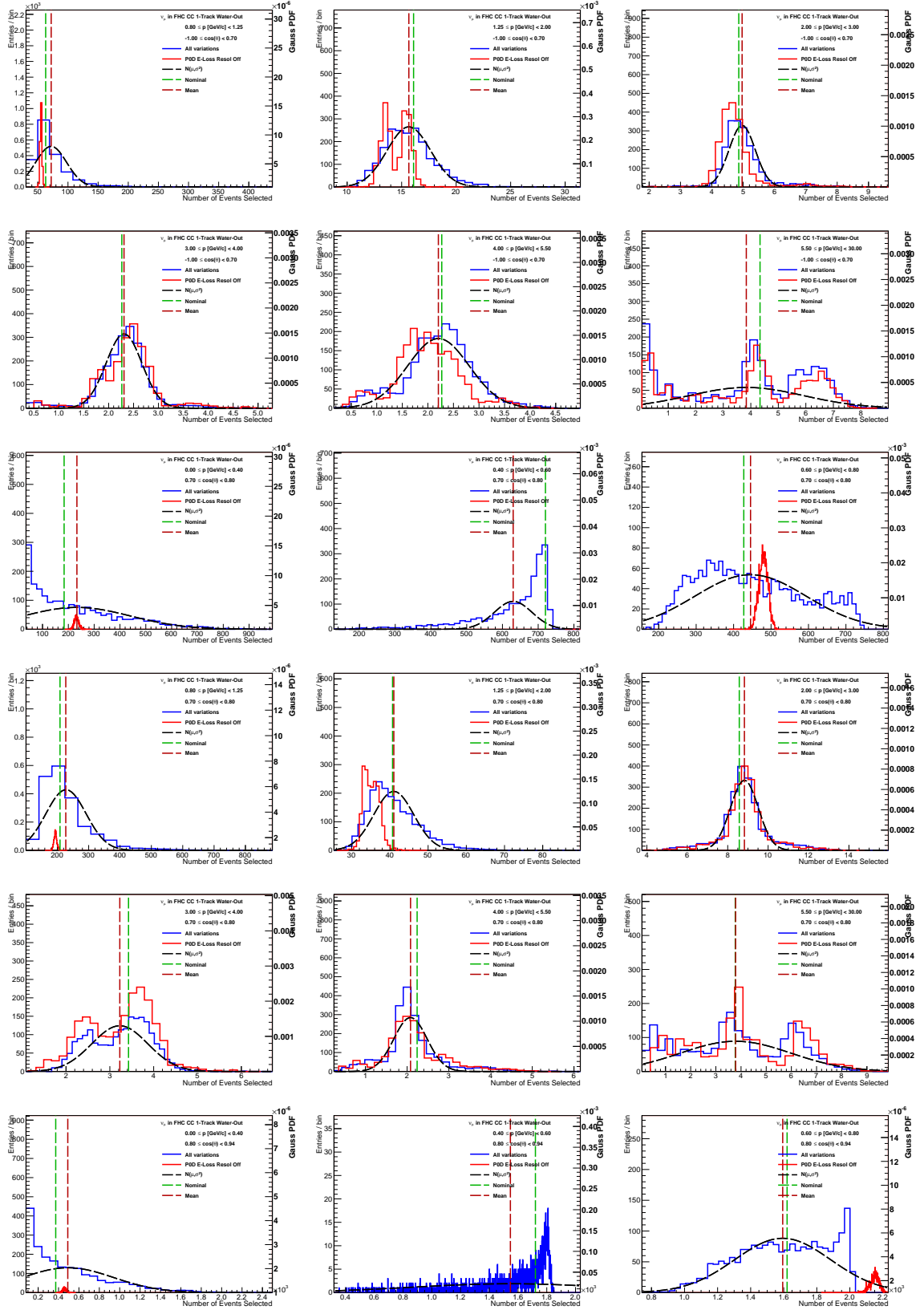


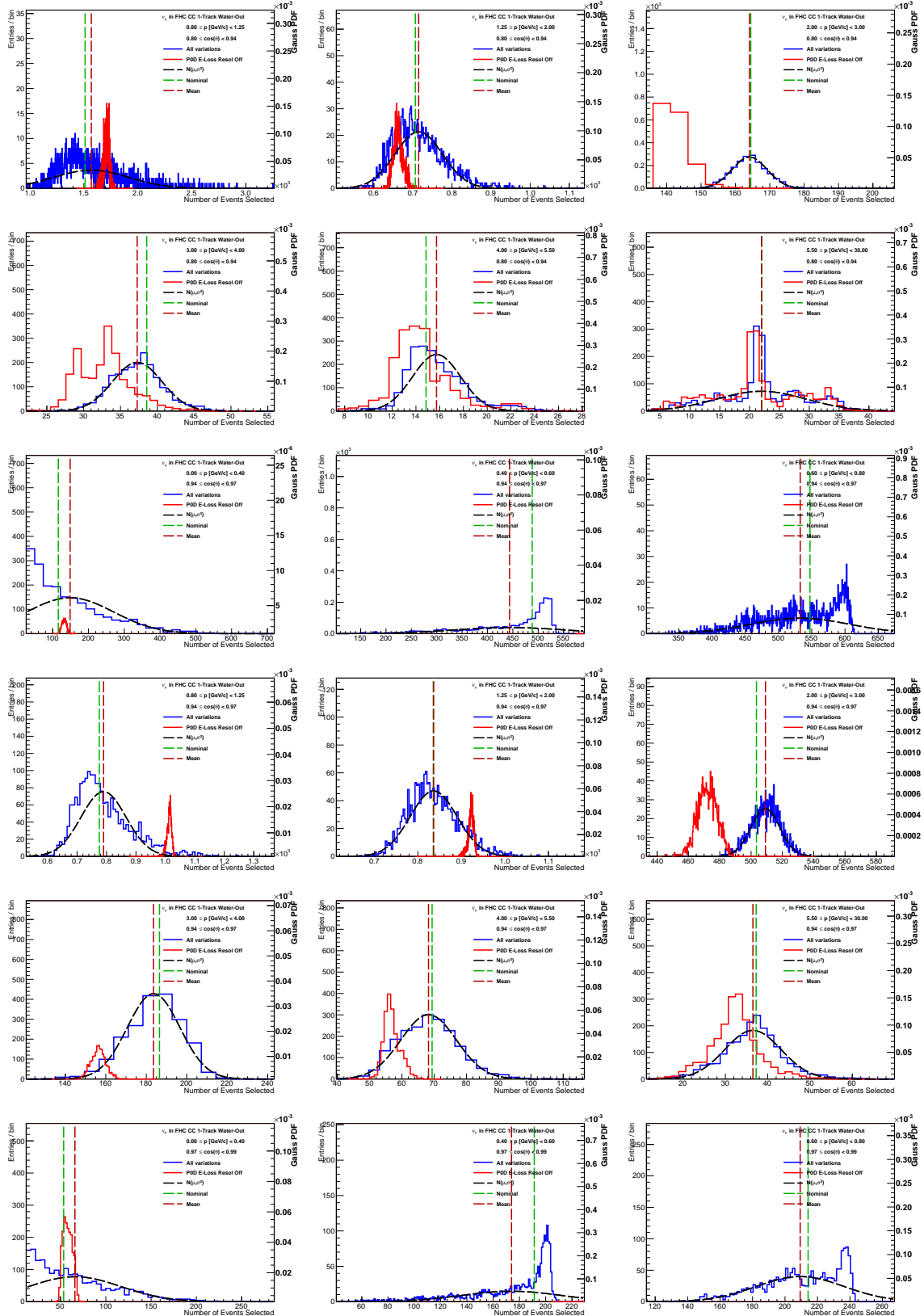


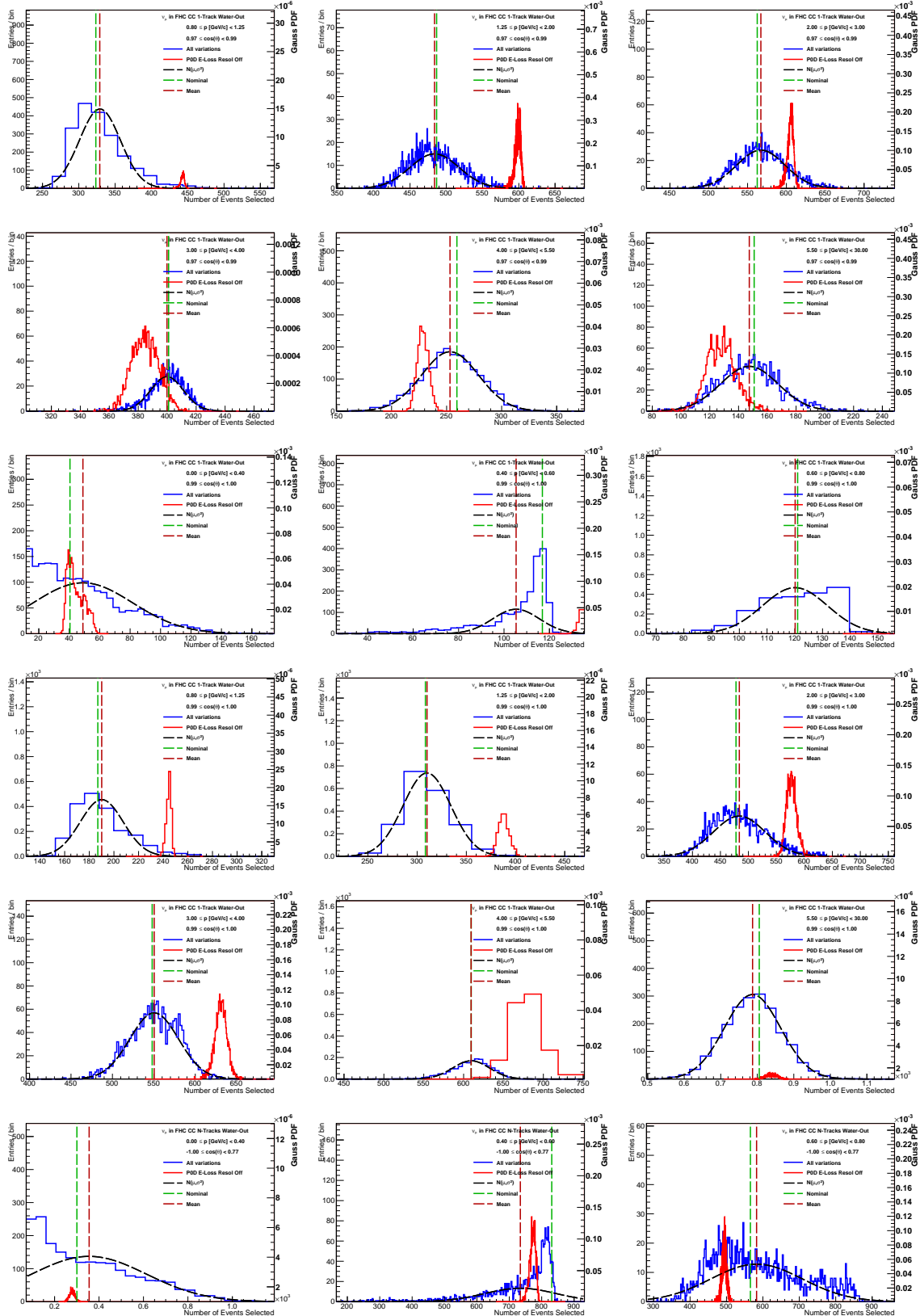


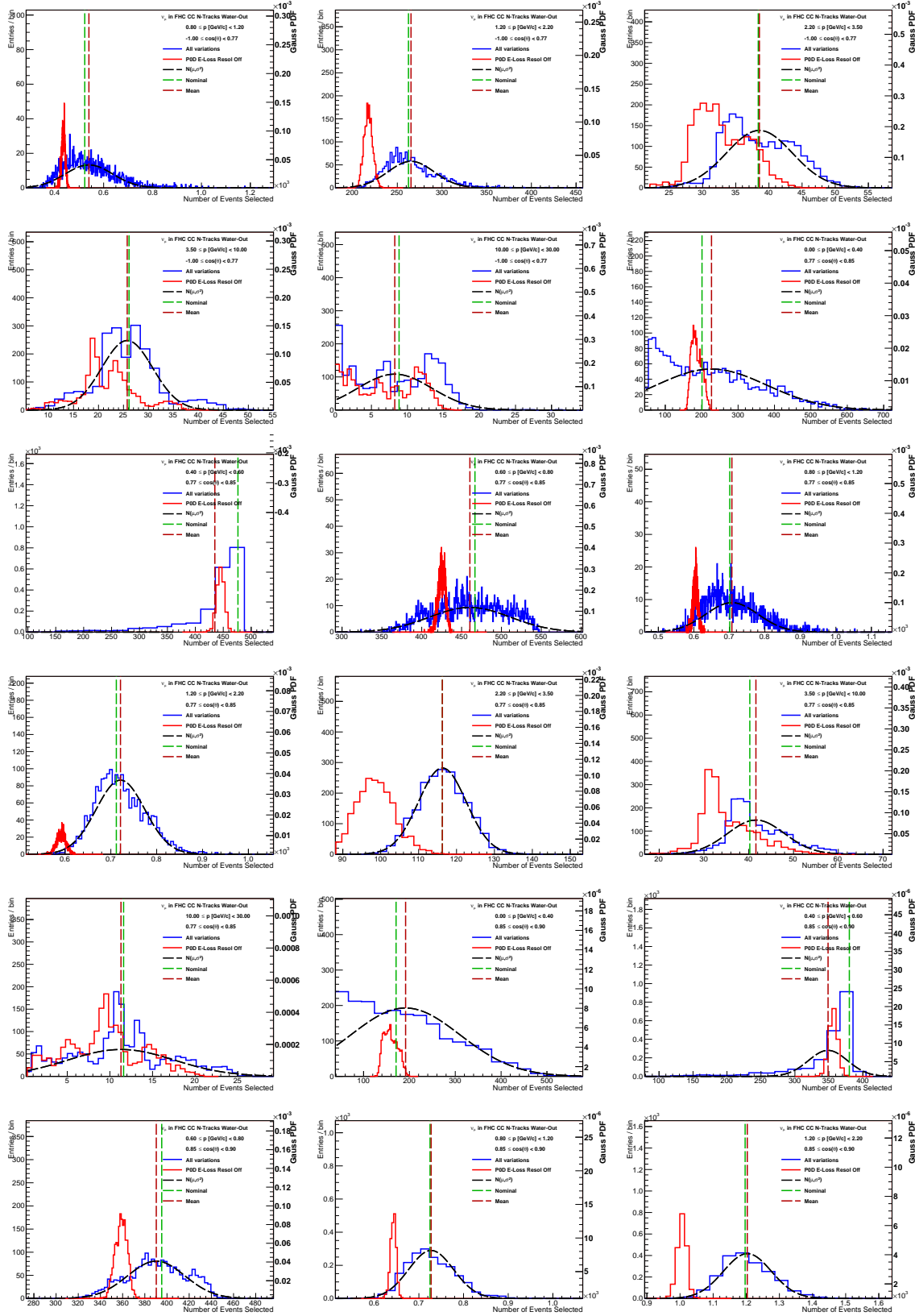


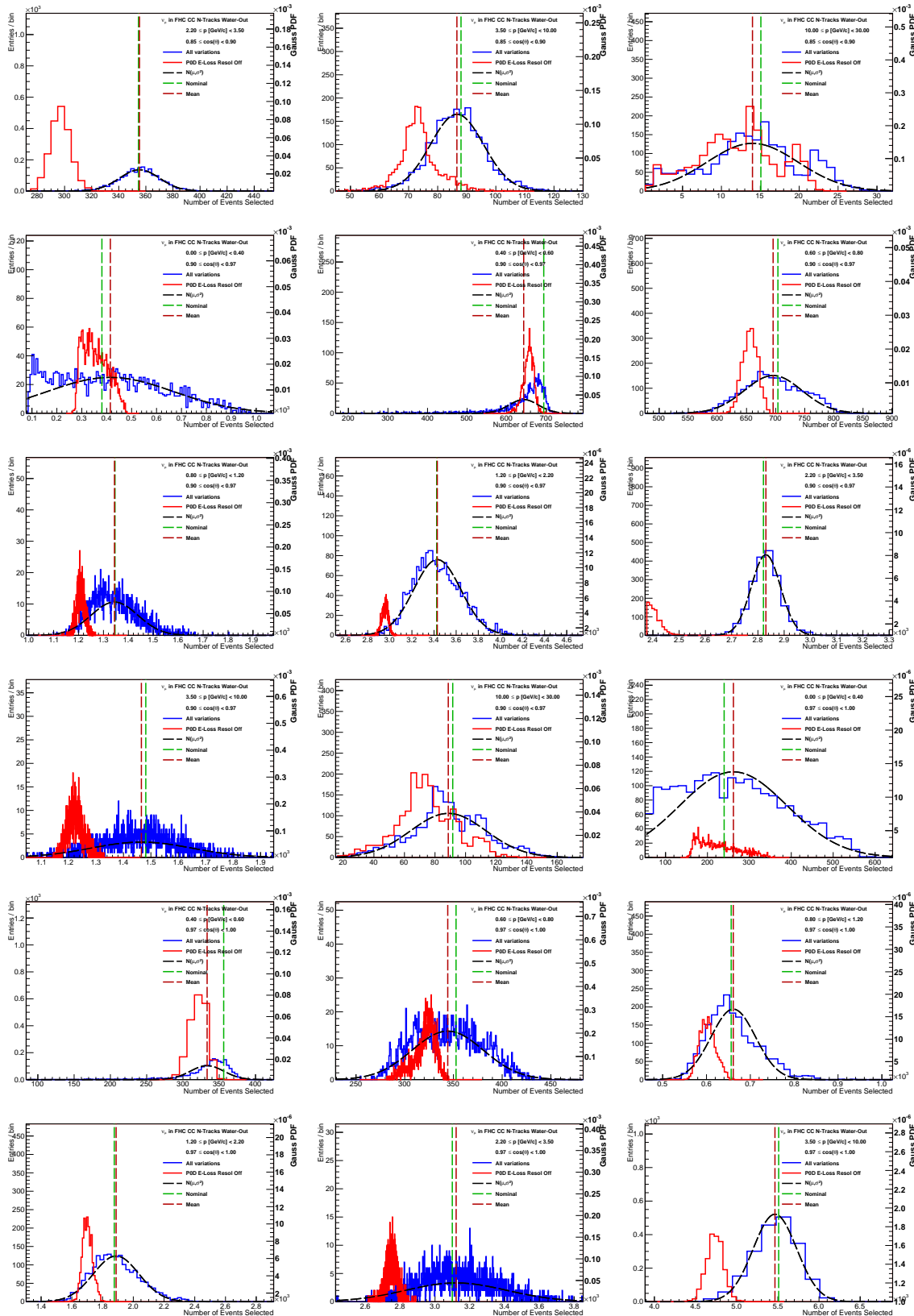


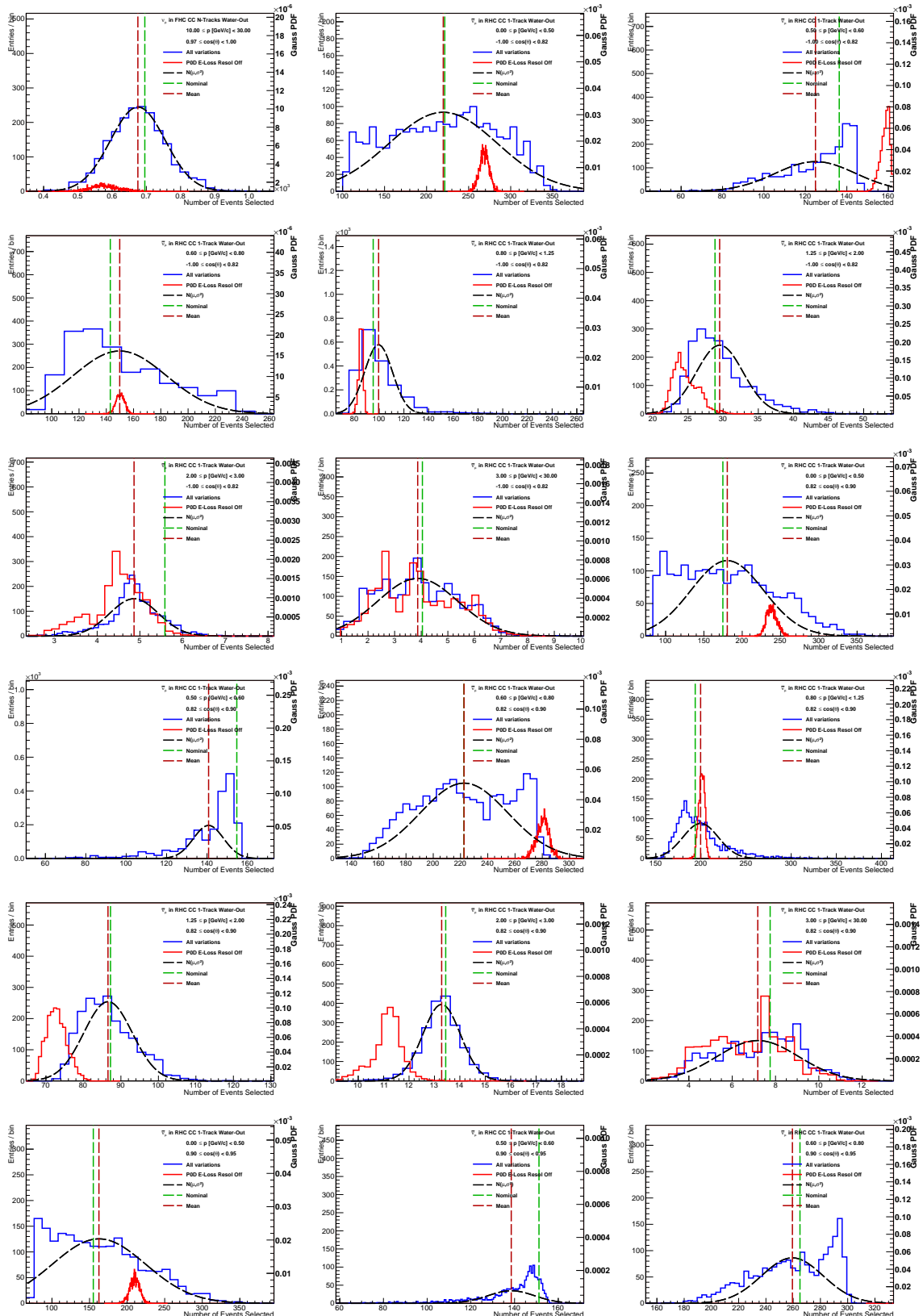


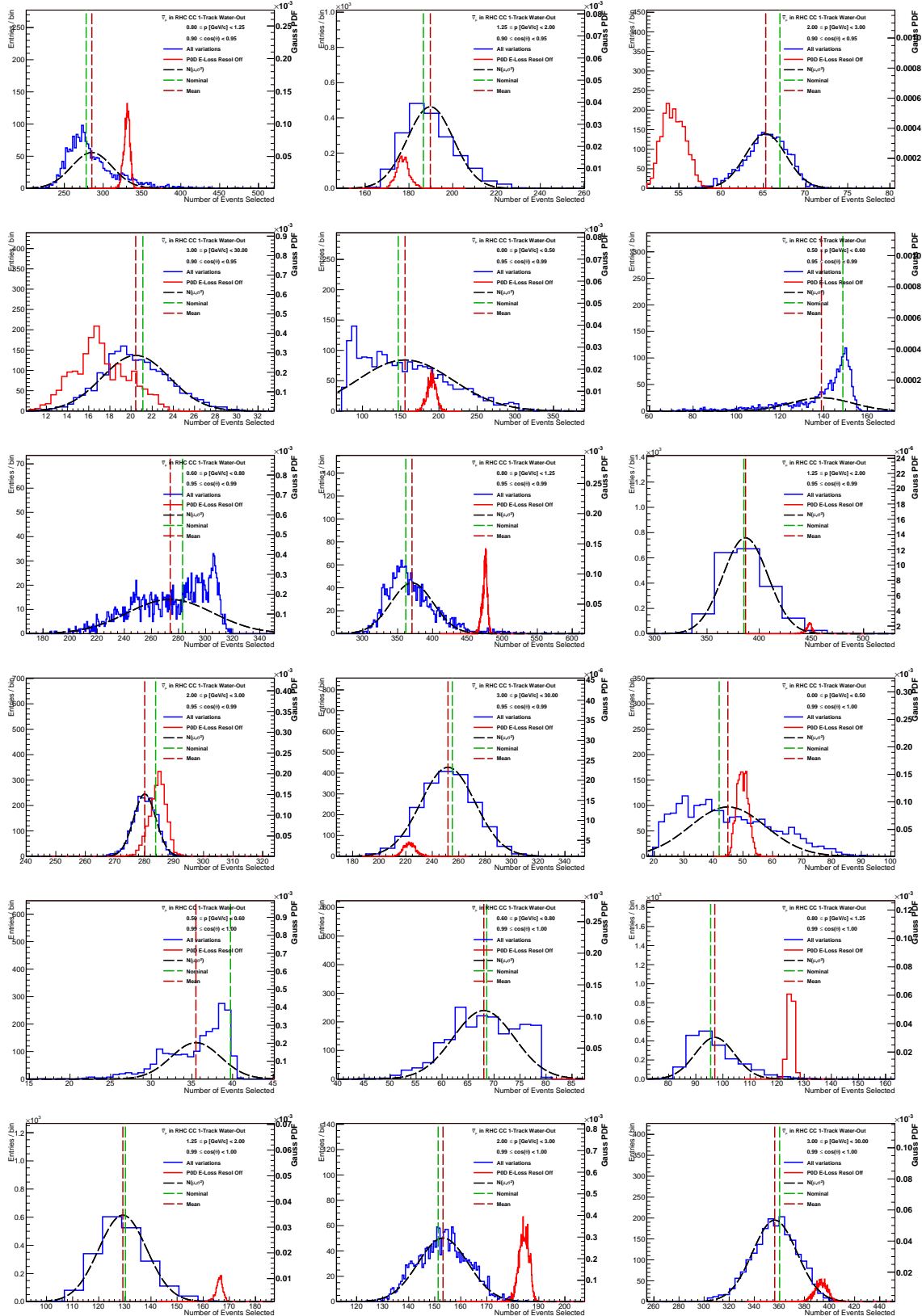


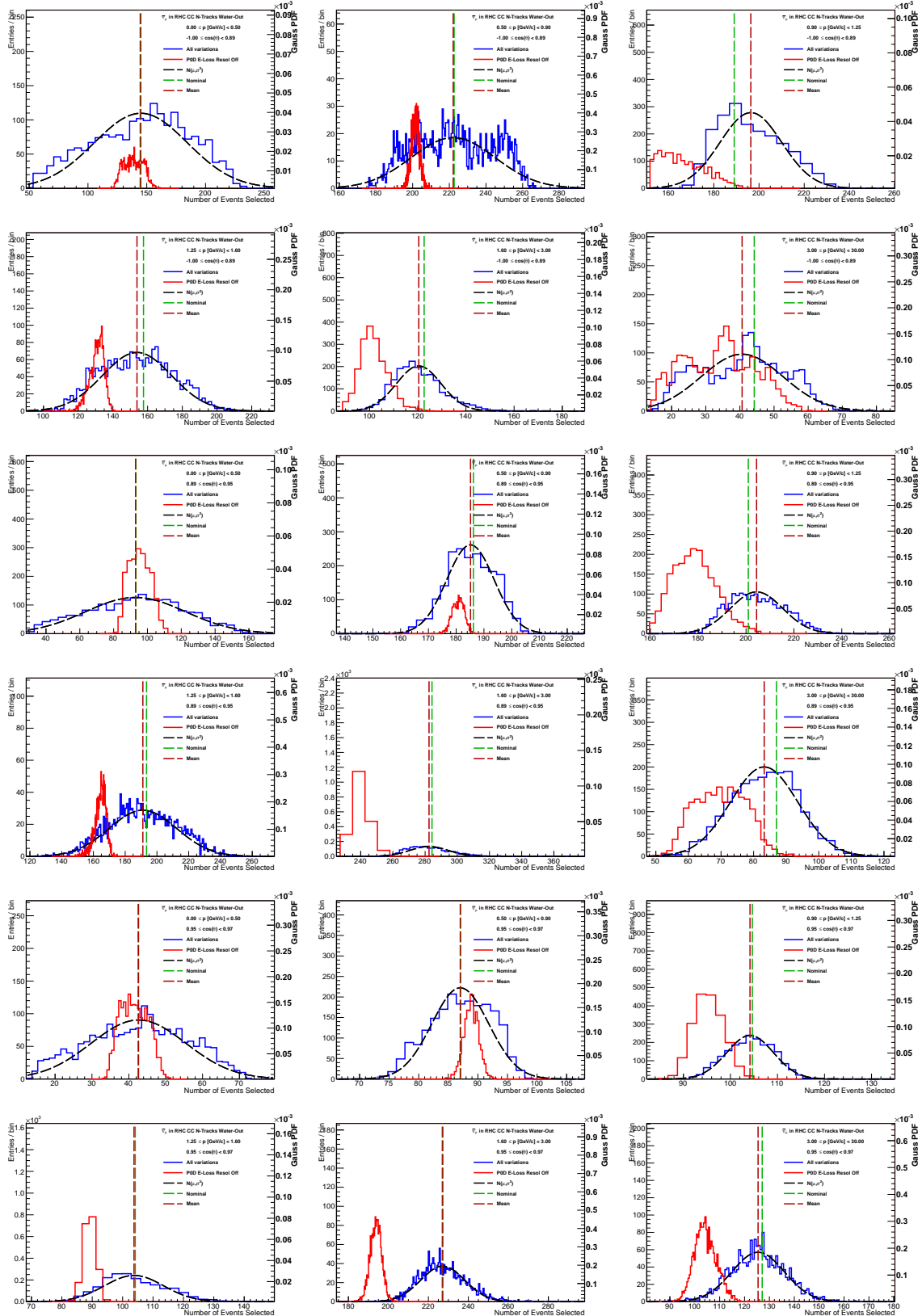


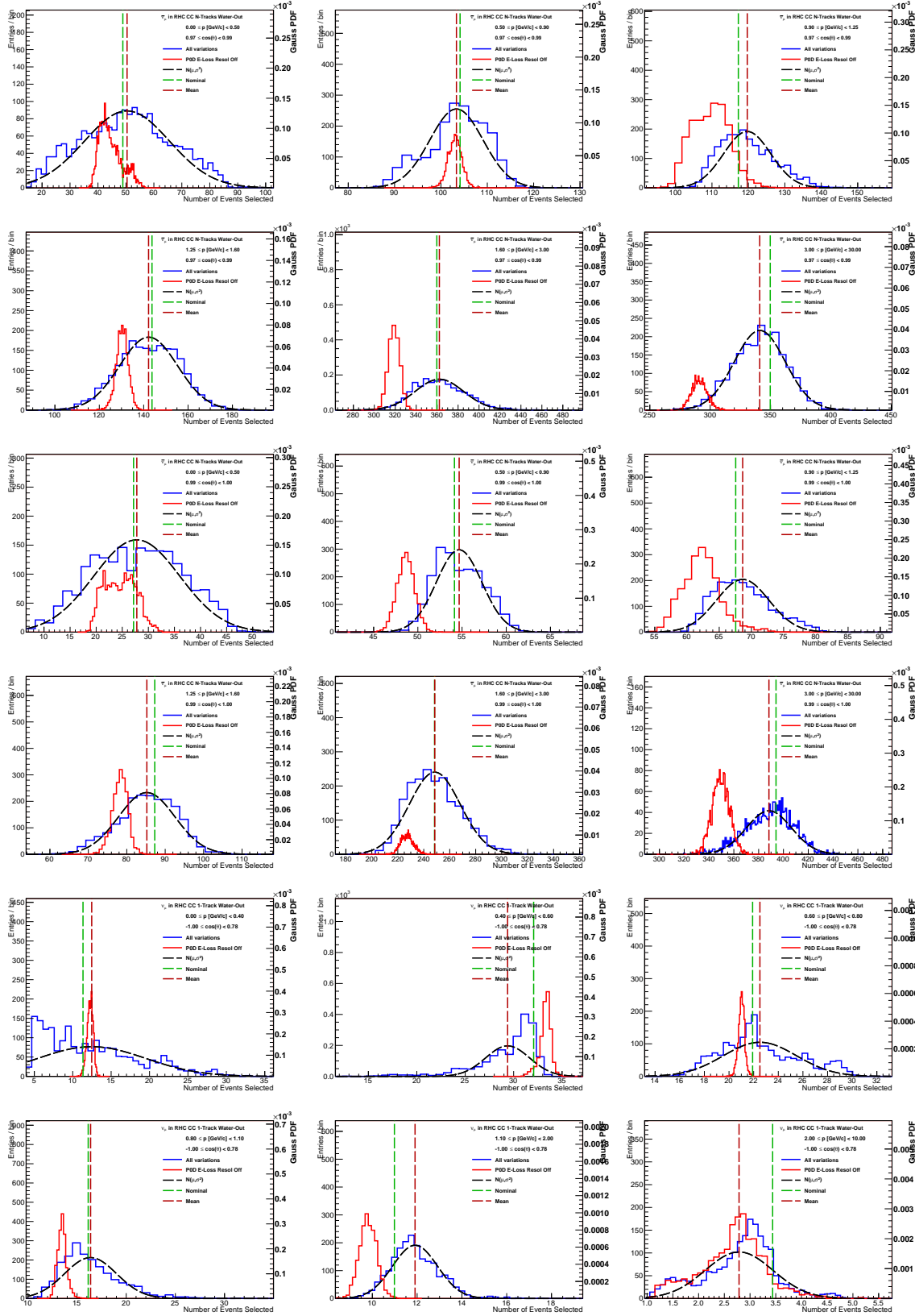


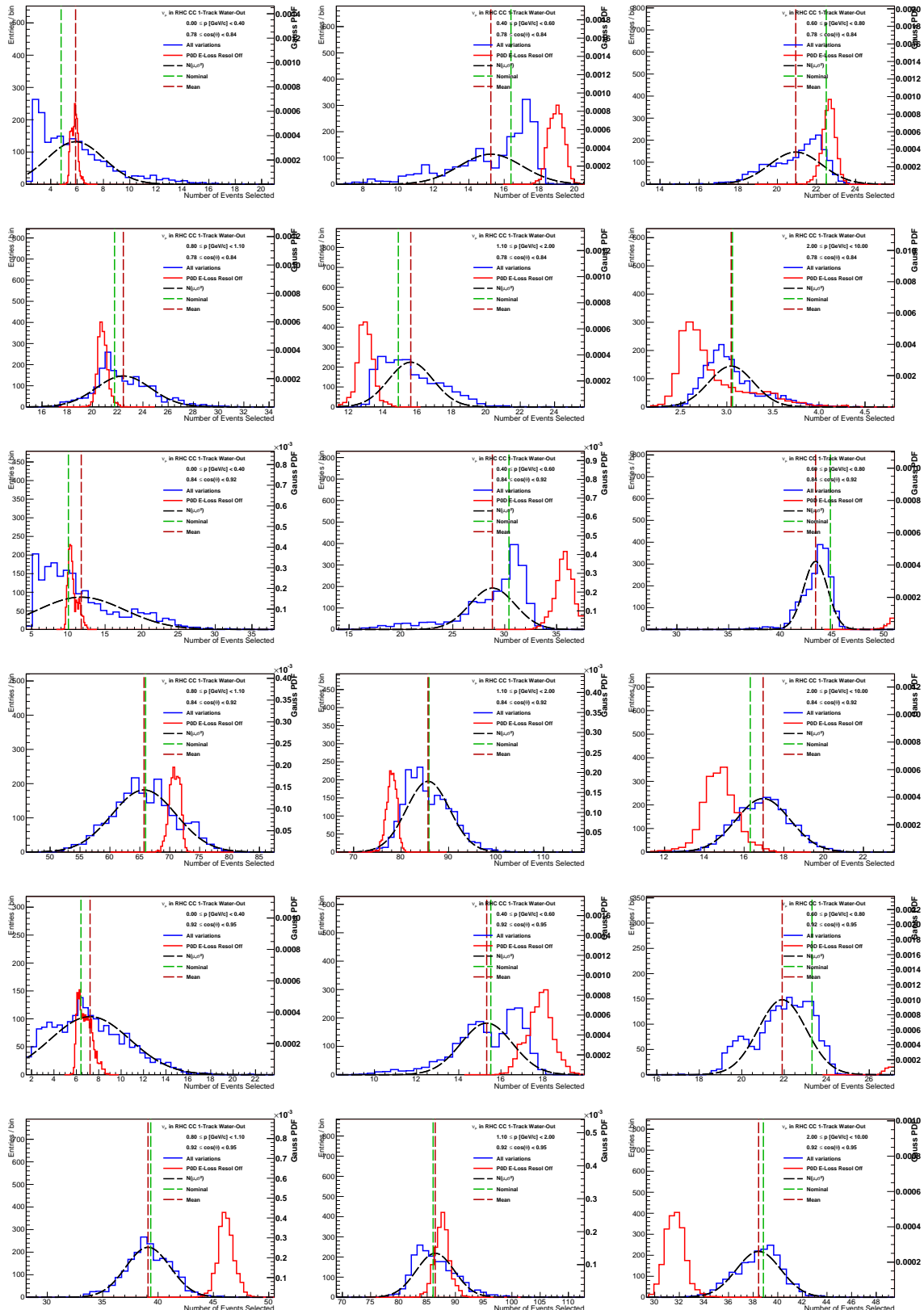


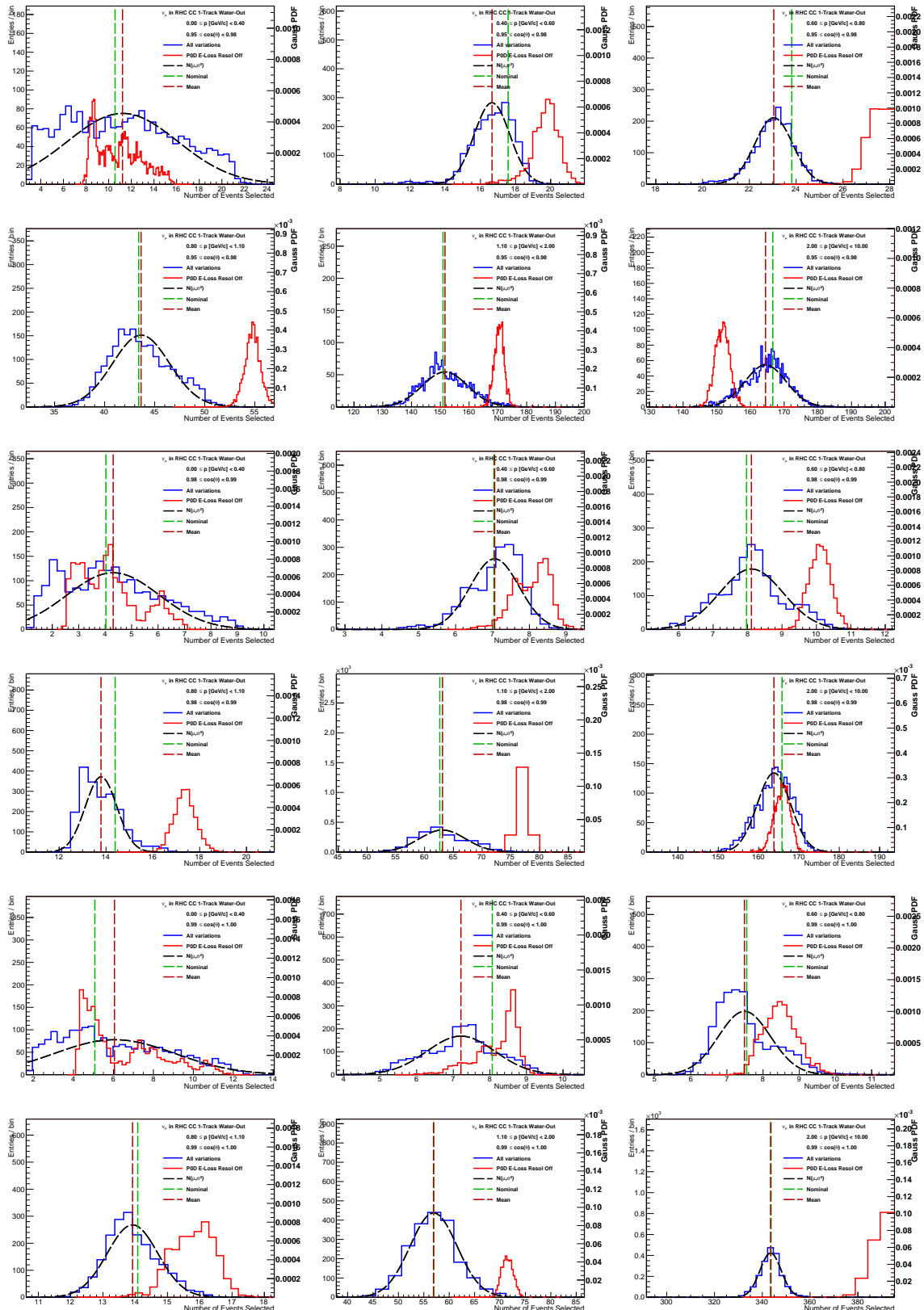


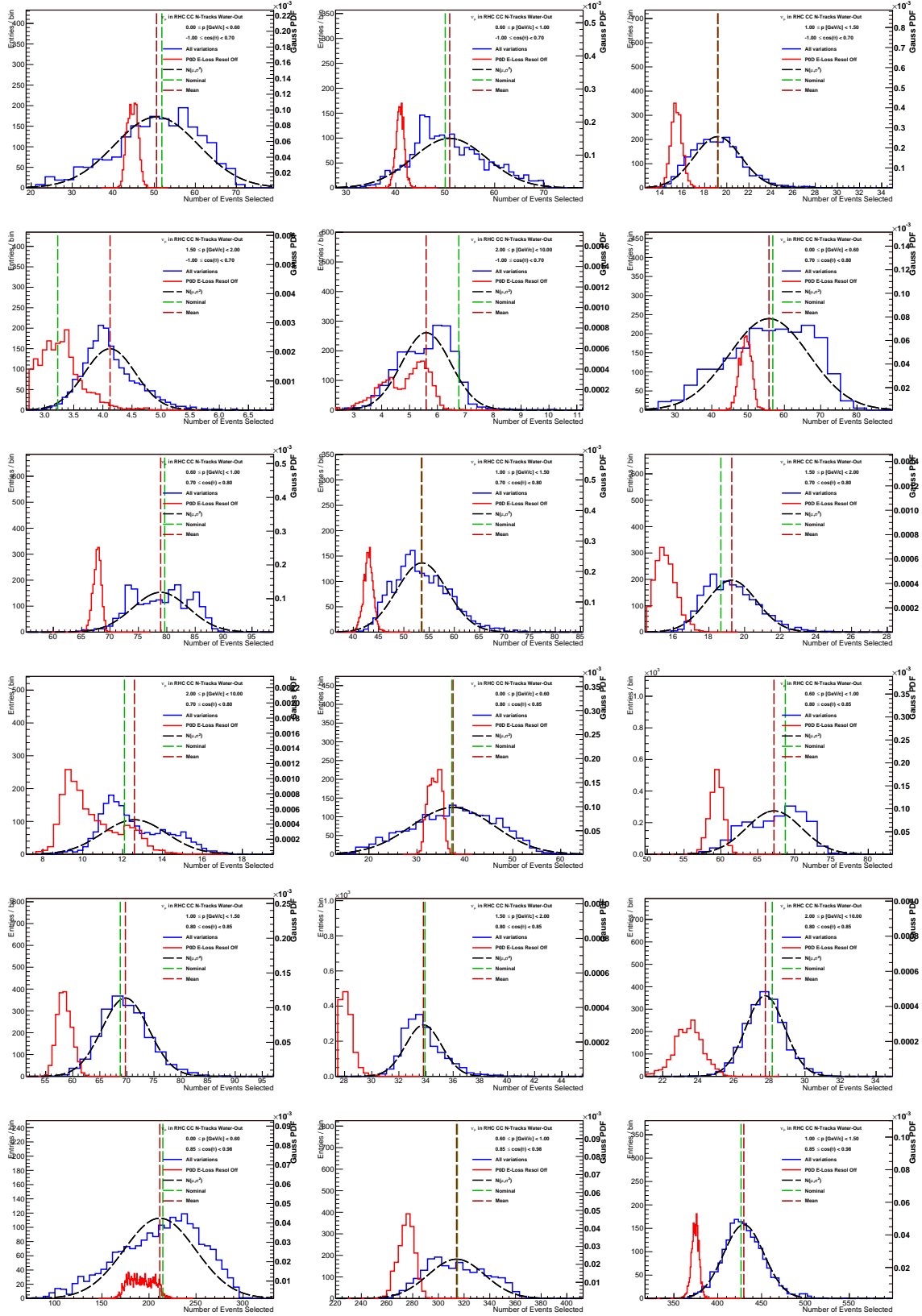


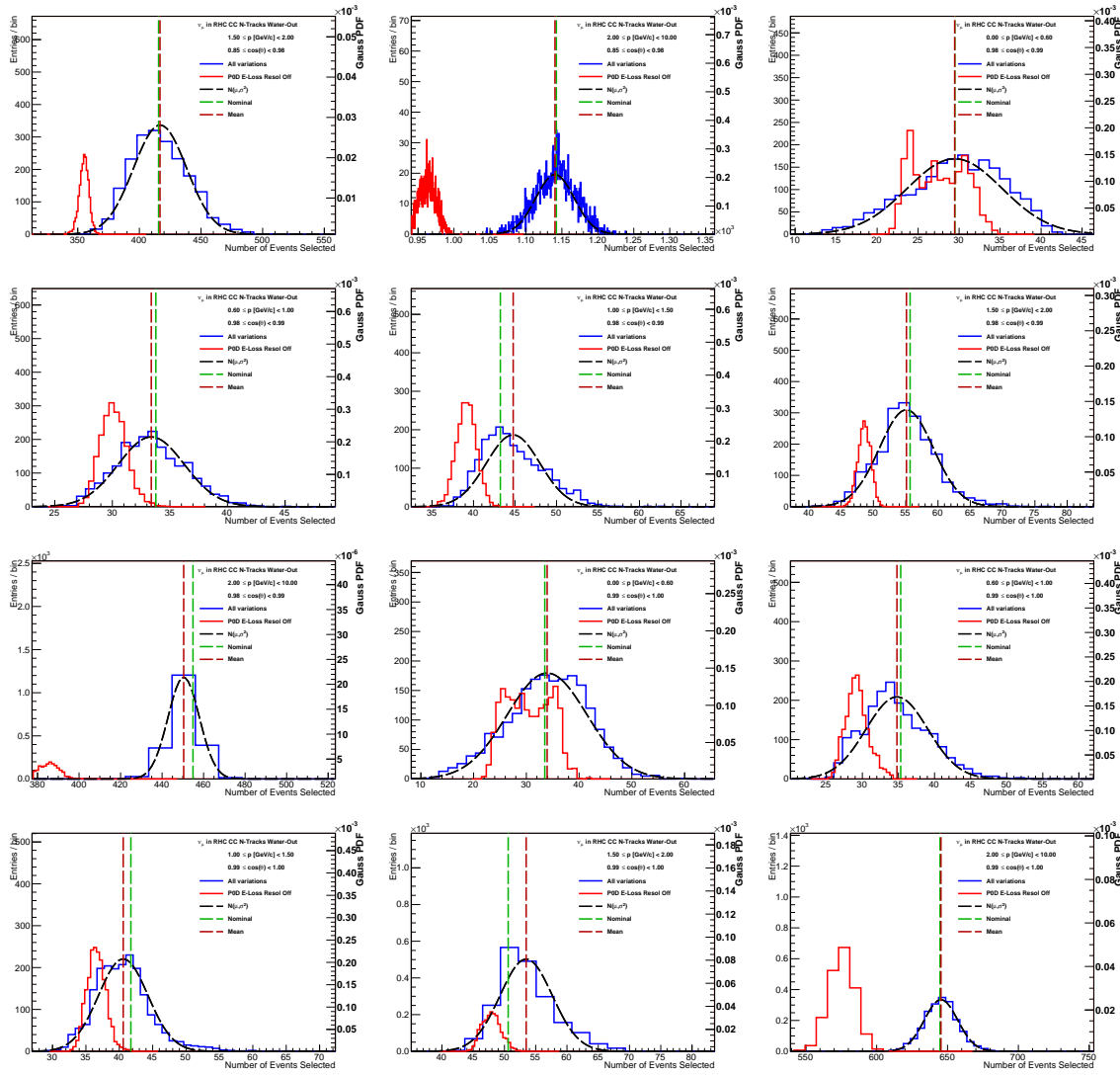












# Appendix D

## Variations of the Cross Section Parameters

This appendix is a tabulation of variations of the cross section parameters and their uncorrelated affect on the analysis samples. The variations are shown in Table D.1. Note that the “nominal” column refers to all weighted events in the sample. When a “ $\pm 1\sigma$ ” variation is applied, the corresponding fractional change is reported.

**Table D.1:** Event rate variations per cross section parameter variation.

Parameter	$1\sigma$ value	Sample	$-1\sigma$ (%)	nominal	$+1\sigma$ (%)
562 : FSI Low energy INEL	0.41	$\nu_\mu$ 1-Trk Wtr	-0.9	27316.74	0.7
		$\nu_\mu$ N-Trks	0.7	30904.32	-0.5
		$\bar{\nu}_\mu$ RHC 1-Trk	-0.5	8414.09	0.4
		$\bar{\nu}_\mu$ RHC N-Trks	1.0	4724.34	-0.7
		$\nu_\mu$ RHC 1-Trk	-1.2	3022.10	0.9
		$\nu_\mu$ RHC N-Trks	0.5	4928.38	-0.4
		$\nu_\mu$ 1-Trk Air	-0.9	23605.76	0.7
		$\nu_\mu$ N-Trks	0.5	32304.13	-0.4
		$\bar{\nu}_\mu$ RHC 1-Trk	-0.6	6767.65	0.5
		$\bar{\nu}_\mu$ RHC N-Trks	0.8	4544.65	-0.6
563 : FSI High energy INEL	0.34	$\nu_\mu$ RHC 1-Trk	-1.5	2067.37	1.4
		$\nu_\mu$ RHC N-Trks	0.6	4568.13	-0.7
		$\nu_\mu$ 1-Trk Wtr	-0.2	27316.74	0.2
		$\nu_\mu$ N-Trks	-0.1	30904.32	0.2
		$\bar{\nu}_\mu$ RHC 1-Trk	-0.1	8414.09	0.1
		$\bar{\nu}_\mu$ RHC N-Trks	-0.0	4724.34	0.1
		$\nu_\mu$ RHC 1-Trk	-0.4	3022.10	0.4
		$\nu_\mu$ RHC N-Trks	-0.1	4928.38	0.1
		$\nu_\mu$ 1-Trk Air	-0.2	23605.76	0.1
		$\nu_\mu$ N-Trks	-0.2	32304.13	0.2

Parameter	$1\sigma$ value	Sample	$-1\sigma$ (%)	nominal	$+1\sigma$ (%)
<b>564 : FSI PROD</b>	<b>0.50</b>	$\nu_\mu$ 1-Trk Wtr	-0.1	27316.74	0.1
		$\nu_\mu$ N-Trks	-0.0	30904.32	0.1
		$\bar{\nu}_\mu$ RHC 1-Trk	-0.0	8414.09	0.0
		$\bar{\nu}_\mu$ RHC N-Trks	0.1	4724.34	-0.0
		$\nu_\mu$ RHC 1-Trk	-0.1	3022.10	0.1
		$\nu_\mu$ RHC N-Trks	-0.1	4928.38	0.1
		$\nu_\mu$ 1-Trk Air	-0.0	23605.76	0.1
		$\nu_\mu$ N-Trks	-0.1	32304.13	0.1
		$\bar{\nu}_\mu$ RHC 1-Trk	-0.0	6767.65	0.0
		$\bar{\nu}_\mu$ RHC N-Trks	0.2	4544.65	-0.1
<b>565 : FSI ABS</b>	<b>0.41</b>	$\nu_\mu$ RHC 1-Trk	-0.1	2067.37	0.1
		$\nu_\mu$ RHC N-Trks	-0.1	4568.13	0.1
		$\nu_\mu$ 1-Trk Wtr	-0.7	27316.74	0.5
		$\nu_\mu$ N-Trks	0.6	30904.32	-0.5
		$\bar{\nu}_\mu$ RHC 1-Trk	-0.6	8414.09	0.5
		$\bar{\nu}_\mu$ RHC N-Trks	1.0	4724.34	-0.8
		$\nu_\mu$ RHC 1-Trk	-1.0	3022.10	0.8
		$\nu_\mu$ RHC N-Trks	0.5	4928.38	-0.4
		$\nu_\mu$ 1-Trk Air	-0.7	23605.76	0.6
		$\nu_\mu$ N-Trks	0.6	32304.13	-0.4

Parameter	$1\sigma$ value	Sample	$-1\sigma$ (%)	nominal	$+1\sigma$ (%)
<b>566 : FSI Low energy CEX</b>	<b>0.57</b>	$\nu_\mu$ 1-Trk Wtr	0.3	27316.74	-0.2
		$\nu_\mu$ N-Trks	-0.3	30904.32	0.2
		$\bar{\nu}_\mu$ RHC 1-Trk	0.2	8414.09	-0.1
		$\bar{\nu}_\mu$ RHC N-Trks	-0.2	4724.34	0.2
		$\nu_\mu$ RHC 1-Trk	0.4	3022.10	-0.3
		$\nu_\mu$ RHC N-Trks	-0.3	4928.38	0.2
		$\nu_\mu$ 1-Trk Air	0.3	23605.76	-0.2
		$\nu_\mu$ N-Trks	-0.3	32304.13	0.2
		$\bar{\nu}_\mu$ RHC 1-Trk	0.2	6767.65	-0.1
		$\bar{\nu}_\mu$ RHC N-Trks	-0.3	4544.65	0.3
<b>567 : FSI High energy CEX</b>	<b>0.28</b>	$\nu_\mu$ RHC 1-Trk	0.2	2067.37	-0.2
		$\nu_\mu$ RHC N-Trks	-0.1	4568.13	0.1
		$\nu_\mu$ 1-Trk Wtr	-0.0	27316.74	0.0
		$\nu_\mu$ N-Trks	-0.0	30904.32	0.0
		$\bar{\nu}_\mu$ RHC 1-Trk	-0.0	8414.09	0.0
		$\bar{\nu}_\mu$ RHC N-Trks	0.0	4724.34	-0.0
		$\nu_\mu$ RHC 1-Trk	-0.1	3022.10	0.1
		$\nu_\mu$ RHC N-Trks	-0.0	4928.38	0.0
		$\nu_\mu$ 1-Trk Air	-0.0	23605.76	0.0
		$\nu_\mu$ N-Trks	-0.1	32304.13	0.1

Parameter	$1\sigma$ value	Sample	$-1\sigma$ (%)	nominal	$+1\sigma$ (%)
<b>568 : <math>M_A^{QE}</math></b>	<b>0.03</b>	$\nu_\mu$ 1-Trk Wtr	-0.8	27316.74	0.8
		$\nu_\mu$ N-Trks	-0.4	30904.32	0.4
		$\bar{\nu}_\mu$ RHC 1-Trk	-0.7	8414.09	0.7
		$\bar{\nu}_\mu$ RHC N-Trks	-0.2	4724.34	0.3
		$\nu_\mu$ RHC 1-Trk	-0.9	3022.10	0.9
		$\nu_\mu$ RHC N-Trks	-0.4	4928.38	0.4
		$\nu_\mu$ 1-Trk Air	-0.8	23605.76	0.8
		$\nu_\mu$ N-Trks	-0.5	32304.13	0.5
		$\bar{\nu}_\mu$ RHC 1-Trk	-0.7	6767.65	0.7
		$\bar{\nu}_\mu$ RHC N-Trks	-0.2	4544.65	0.3
<b>569 : <math>p_F^C</math></b>	<b>0.06</b>	$\nu_\mu$ RHC 1-Trk	-0.9	2067.37	0.9
		$\nu_\mu$ RHC N-Trks	-0.4	4568.13	0.4
		$\nu_\mu$ 1-Trk Wtr	0.8	27316.74	-0.7
		$\nu_\mu$ N-Trks	0.0	30904.32	-0.0
		$\bar{\nu}_\mu$ RHC 1-Trk	0.7	8414.09	-0.7
		$\bar{\nu}_\mu$ RHC N-Trks	0.0	4724.34	-0.0
		$\nu_\mu$ RHC 1-Trk	0.4	3022.10	-0.4
		$\nu_\mu$ RHC N-Trks	0.0	4928.38	-0.0
		$\nu_\mu$ 1-Trk Air	1.1	23605.76	-1.0
		$\nu_\mu$ N-Trks	0.0	32304.13	-0.0

Parameter	$1\sigma$ value	Sample	$-1\sigma$ (%)	nominal	$+1\sigma$ (%)
<b>570 : <math>p_F^O</math></b>	<b>0.06</b>	$\nu_\mu$ 1-Trk Wtr	0.4	27316.74	-0.4
		$\nu_\mu$ N-Trks	0.0	30904.32	-0.0
		$\bar{\nu}_\mu$ RHC 1-Trk	0.5	8414.09	-0.5
		$\bar{\nu}_\mu$ RHC N-Trks	0.0	4724.34	-0.0
		$\nu_\mu$ RHC 1-Trk	0.3	3022.10	-0.3
		$\nu_\mu$ RHC N-Trks	0.0	4928.38	-0.0
		$\nu_\mu$ 1-Trk Air	0.0	23605.76	-0.0
		$\nu_\mu$ N-Trks	0.0	32304.13	-0.0
		$\bar{\nu}_\mu$ RHC 1-Trk	0.0	6767.65	-0.0
		$\bar{\nu}_\mu$ RHC N-Trks	-0.0	4544.65	-0.0
		$\nu_\mu$ RHC 1-Trk	-0.0	2067.37	0.0
		$\nu_\mu$ RHC N-Trks	0.0	4568.13	-0.0
<b>571 : 2p2h <math>\nu</math> norm. on <math>^{12}\text{C}</math></b>	<b>1.00</b>	$\nu_\mu$ 1-Trk Wtr	-8.9	27316.74	8.9
		$\nu_\mu$ N-Trks	-3.0	30904.32	3.0
		$\bar{\nu}_\mu$ RHC 1-Trk	-0.1	8414.09	0.1
		$\bar{\nu}_\mu$ RHC N-Trks	-0.2	4724.34	0.2
		$\nu_\mu$ RHC 1-Trk	-9.0	3022.10	9.0
		$\nu_\mu$ RHC N-Trks	-2.6	4928.38	2.6
		$\nu_\mu$ 1-Trk Air	-8.1	23605.76	8.1
		$\nu_\mu$ N-Trks	-3.3	32304.13	3.3
		$\bar{\nu}_\mu$ RHC 1-Trk	-0.1	6767.65	0.1
		$\bar{\nu}_\mu$ RHC N-Trks	-0.2	4544.65	0.2
		$\nu_\mu$ RHC 1-Trk	-8.6	2067.37	8.6
		$\nu_\mu$ RHC N-Trks	-2.8	4568.13	2.8

Parameter	$1\sigma$ value	Sample	$-1\sigma$ (%)	nominal	$+1\sigma$ (%)
572 : 2p2h $\bar{\nu}$ norm. on $^{12}\text{C}$	1.00	$\nu_\mu$ 1-Trk Wtr	-0.0	27316.74	0.0
		$\nu_\mu$ N-Trks	-0.0	30904.32	0.0
		$\bar{\nu}_\mu$ RHC 1-Trk	-9.3	8414.09	9.3
		$\bar{\nu}_\mu$ RHC N-Trks	-2.1	4724.34	2.1
		$\nu_\mu$ RHC 1-Trk	-0.2	3022.10	0.2
		$\nu_\mu$ RHC N-Trks	-0.0	4928.38	0.0
		$\nu_\mu$ 1-Trk Air	-0.0	23605.76	0.0
		$\nu_\mu$ N-Trks	-0.0	32304.13	0.0
		$\bar{\nu}_\mu$ RHC 1-Trk	-8.9	6767.65	8.9
		$\bar{\nu}_\mu$ RHC N-Trks	-2.2	4544.65	2.2
		$\nu_\mu$ RHC 1-Trk	-0.3	2067.37	0.3
		$\nu_\mu$ RHC N-Trks	-0.0	4568.13	0.0
573 : 2p2h $^{12}\text{C} \rightarrow ^{16}\text{O}$ norm.	0.20	$\nu_\mu$ 1-Trk Wtr	-0.6	27316.74	0.6
		$\nu_\mu$ N-Trks	-0.2	30904.32	0.2
		$\bar{\nu}_\mu$ RHC 1-Trk	-0.8	8414.09	0.8
		$\bar{\nu}_\mu$ RHC N-Trks	-0.2	4724.34	0.2
		$\nu_\mu$ RHC 1-Trk	-0.8	3022.10	0.8
		$\nu_\mu$ RHC N-Trks	-0.2	4928.38	0.2
		$\nu_\mu$ 1-Trk Air	-0.0	23605.76	0.0
		$\nu_\mu$ N-Trks	-0.0	32304.13	0.0
		$\bar{\nu}_\mu$ RHC 1-Trk	-0.0	6767.65	0.0
		$\bar{\nu}_\mu$ RHC N-Trks	-0.0	4544.65	0.0
		$\nu_\mu$ RHC 1-Trk	-0.0	2067.37	0.0
		$\nu_\mu$ RHC N-Trks	-0.0	4568.13	0.0

Parameter	$1\sigma$ value	Sample	$-1\sigma$ (%)	nominal	$+1\sigma$ (%)
574 : 2p2h $^{12}\text{C}$ shape location	2.00	$\nu_\mu$ 1-Trk Wtr	3.8	27316.74	0.0
		$\nu_\mu$ N-Trks	-1.1	30904.32	0.0
		$\bar{\nu}_\mu$ RHC 1-Trk	0.2	8414.09	0.0
		$\bar{\nu}_\mu$ RHC N-Trks	-0.8	4724.34	0.0
		$\nu_\mu$ RHC 1-Trk	4.3	3022.10	0.0
		$\nu_\mu$ RHC N-Trks	-0.8	4928.38	0.0
		$\nu_\mu$ 1-Trk Air	5.7	23605.76	0.0
		$\nu_\mu$ N-Trks	-1.5	32304.13	0.0
		$\bar{\nu}_\mu$ RHC 1-Trk	0.2	6767.65	0.0
		$\bar{\nu}_\mu$ RHC N-Trks	-1.1	4544.65	0.0
575 : 2p2h $^{16}\text{O}$ shape location	2.00	$\nu_\mu$ RHC 1-Trk	8.1	2067.37	0.0
		$\nu_\mu$ RHC N-Trks	-1.4	4568.13	0.0
		$\nu_\mu$ 1-Trk Wtr	2.1	27316.74	0.0
		$\nu_\mu$ N-Trks	-0.5	30904.32	0.0
		$\bar{\nu}_\mu$ RHC 1-Trk	0.1	8414.09	0.0
		$\bar{\nu}_\mu$ RHC N-Trks	-0.5	4724.34	0.0
		$\nu_\mu$ RHC 1-Trk	3.2	3022.10	0.0
		$\nu_\mu$ RHC N-Trks	-0.6	4928.38	0.0
		$\nu_\mu$ 1-Trk Air	0.0	23605.76	0.0
		$\nu_\mu$ N-Trks	-0.0	32304.13	0.0

Parameter	$1\sigma$ value	Sample	$-1\sigma$ (%)	nominal	$+1\sigma$ (%)
576 : BeRPA A scale	0.12	$\nu_\mu$ 1-Trk Wtr	-5.1	27316.74	5.1
		$\nu_\mu$ N-Trks	-0.3	30904.32	0.3
		$\bar{\nu}_\mu$ RHC 1-Trk	-4.7	8414.09	4.7
		$\bar{\nu}_\mu$ RHC N-Trks	-0.2	4724.34	0.2
		$\nu_\mu$ RHC 1-Trk	-3.5	3022.10	3.5
		$\nu_\mu$ RHC N-Trks	-0.1	4928.38	0.1
		$\nu_\mu$ 1-Trk Air	-5.1	23605.76	5.1
		$\nu_\mu$ N-Trks	-0.3	32304.13	0.3
		$\bar{\nu}_\mu$ RHC 1-Trk	-4.6	6767.65	4.6
		$\bar{\nu}_\mu$ RHC N-Trks	-0.1	4544.65	0.1
577 : BeRPA B scale	0.21	$\nu_\mu$ RHC 1-Trk	-3.7	2067.37	3.7
		$\nu_\mu$ RHC N-Trks	-0.2	4568.13	0.2
		$\nu_\mu$ 1-Trk Wtr	-3.4	27316.74	3.4
		$\nu_\mu$ N-Trks	-0.6	30904.32	0.6
		$\bar{\nu}_\mu$ RHC 1-Trk	-2.6	8414.09	2.6
		$\bar{\nu}_\mu$ RHC N-Trks	-0.2	4724.34	0.2
		$\nu_\mu$ RHC 1-Trk	-3.1	3022.10	3.1
		$\nu_\mu$ RHC N-Trks	-0.4	4928.38	0.4
		$\nu_\mu$ 1-Trk Air	-3.3	23605.76	3.3
		$\nu_\mu$ N-Trks	-0.6	32304.13	0.6

Parameter	$1\sigma$ value	Sample	$-1\sigma$ (%)	nominal	$+1\sigma$ (%)
<b>578 : BeRPA D scale</b>	<b>0.17</b>	$\nu_\mu$ 1-Trk Wtr	-1.3	27316.74	1.3
		$\nu_\mu$ N-Trks	-1.0	30904.32	1.0
		$\bar{\nu}_\mu$ RHC 1-Trk	-1.0	8414.09	1.0
		$\bar{\nu}_\mu$ RHC N-Trks	-0.5	4724.34	0.5
		$\nu_\mu$ RHC 1-Trk	-1.7	3022.10	1.7
		$\nu_\mu$ RHC N-Trks	-0.9	4928.38	0.9
		$\nu_\mu$ 1-Trk Air	-1.1	23605.76	1.1
		$\nu_\mu$ N-Trks	-0.9	32304.13	0.9
		$\bar{\nu}_\mu$ RHC 1-Trk	-0.9	6767.65	0.9
		$\bar{\nu}_\mu$ RHC N-Trks	-0.4	4544.65	0.4
<b>579 : BeRPA E scale</b>	<b>0.35</b>	$\nu_\mu$ RHC 1-Trk	-1.4	2067.37	1.4
		$\nu_\mu$ RHC N-Trks	-0.9	4568.13	0.9
		$\nu_\mu$ 1-Trk Wtr	-0.1	27316.74	0.1
		$\nu_\mu$ N-Trks	-0.0	30904.32	0.0
		$\bar{\nu}_\mu$ RHC 1-Trk	-0.1	8414.09	0.1
		$\bar{\nu}_\mu$ RHC N-Trks	0.0	4724.34	-0.0
		$\nu_\mu$ RHC 1-Trk	-0.1	3022.10	0.1
		$\nu_\mu$ RHC N-Trks	-0.0	4928.38	0.0
		$\nu_\mu$ 1-Trk Air	-0.1	23605.76	0.1
		$\nu_\mu$ N-Trks	-0.0	32304.13	0.0

Parameter	$1\sigma$ value	Sample	$-1\sigma$ (%)	nominal	$+1\sigma$ (%)
580 : BeRPA U scale*	0.10	$\nu_\mu$ 1-Trk Wtr	0.7	27316.74	-0.7
		$\nu_\mu$ N-Trks	0.1	30904.32	-0.1
		$\bar{\nu}_\mu$ RHC 1-Trk	0.6	8414.09	-0.5
		$\bar{\nu}_\mu$ RHC N-Trks	0.0	4724.34	-0.0
		$\nu_\mu$ RHC 1-Trk	0.7	3022.10	-0.6
		$\nu_\mu$ RHC N-Trks	0.1	4928.38	-0.1
		$\nu_\mu$ 1-Trk Air	0.7	23605.76	-0.6
		$\nu_\mu$ N-Trks	0.1	32304.13	-0.1
		$\bar{\nu}_\mu$ RHC 1-Trk	0.5	6767.65	-0.5
		$\bar{\nu}_\mu$ RHC N-Trks	0.0	4544.65	-0.0
581 : $C_A^5$	0.15	$\nu_\mu$ RHC 1-Trk	0.7	2067.37	-0.6
		$\nu_\mu$ RHC N-Trks	0.1	4568.13	-0.1
		$\nu_\mu$ 1-Trk Wtr	-3.4	27316.74	3.9
		$\nu_\mu$ N-Trks	-4.4	30904.32	5.0
		$\bar{\nu}_\mu$ RHC 1-Trk	-2.7	8414.09	3.4
		$\bar{\nu}_\mu$ RHC N-Trks	-4.7	4724.34	5.8
		$\nu_\mu$ RHC 1-Trk	-4.5	3022.10	5.2
		$\nu_\mu$ RHC N-Trks	-4.1	4928.38	4.7
		$\nu_\mu$ 1-Trk Air	-2.9	23605.76	3.3
		$\nu_\mu$ N-Trks	-4.6	32304.13	5.2

Parameter	$1\sigma$ value	Sample	$-1\sigma$ (%)	nominal	$+1\sigma$ (%)
<b>582 : <math>M_A^{\text{RES}}</math></b>	<b>0.16</b>	$\nu_\mu$ 1-Trk Wtr	-2.1	27316.74	1.9
		$\nu_\mu$ N-Trks	-4.8	30904.32	5.1
		$\bar{\nu}_\mu$ RHC 1-Trk	-1.6	8414.09	1.6
		$\bar{\nu}_\mu$ RHC N-Trks	-4.8	4724.34	5.8
		$\nu_\mu$ RHC 1-Trk	-3.1	3022.10	2.9
		$\nu_\mu$ RHC N-Trks	-4.8	4928.38	5.3
		$\nu_\mu$ 1-Trk Air	-1.7	23605.76	1.5
		$\nu_\mu$ N-Trks	-4.6	32304.13	4.9
		$\bar{\nu}_\mu$ RHC 1-Trk	-1.4	6767.65	1.5
		$\bar{\nu}_\mu$ RHC N-Trks	-4.8	4544.65	5.9
		$\nu_\mu$ RHC 1-Trk	-2.5	2067.37	2.3
		$\nu_\mu$ RHC N-Trks	-4.7	4568.13	5.2
<b>583 : I=<math>^{1/2}</math> bkg. norm.</b>	<b>0.31</b>	$\nu_\mu$ 1-Trk Wtr	-1.1	27316.74	1.8
		$\nu_\mu$ N-Trks	-2.4	30904.32	3.7
		$\bar{\nu}_\mu$ RHC 1-Trk	-0.8	8414.09	1.3
		$\bar{\nu}_\mu$ RHC N-Trks	-3.1	4724.34	4.8
		$\nu_\mu$ RHC 1-Trk	-1.7	3022.10	2.5
		$\nu_\mu$ RHC N-Trks	-2.5	4928.38	3.8
		$\nu_\mu$ 1-Trk Air	-1.1	23605.76	1.6
		$\nu_\mu$ N-Trks	-2.4	32304.13	3.6
		$\bar{\nu}_\mu$ RHC 1-Trk	-0.7	6767.65	1.1
		$\bar{\nu}_\mu$ RHC N-Trks	-3.0	4544.65	4.5
		$\nu_\mu$ RHC 1-Trk	-1.6	2067.37	2.4
		$\nu_\mu$ RHC N-Trks	-2.4	4568.13	3.7

Parameter	$1\sigma$ value	Sample	$-1\sigma$ (%)	nominal	$+1\sigma$ (%)
<b>584 : CC-<math>\nu_e/\nu_\mu^*</math></b>	<b>0.03</b>	$\nu_\mu$ 1-Trk Wtr	0.0	27316.74	0.0
		$\nu_\mu$ N-Trks	0.0	30904.32	0.0
		$\bar{\nu}_\mu$ RHC 1-Trk	0.0	8414.09	0.0
		$\bar{\nu}_\mu$ RHC N-Trks	0.0	4724.34	0.0
		$\nu_\mu$ RHC 1-Trk	0.0	3022.10	0.0
		$\nu_\mu$ RHC N-Trks	0.0	4928.38	0.0
		$\nu_\mu$ 1-Trk Air	0.0	23605.76	0.0
		$\nu_\mu$ N-Trks	0.0	32304.13	0.0
		$\bar{\nu}_\mu$ RHC 1-Trk	0.0	6767.65	0.0
		$\bar{\nu}_\mu$ RHC N-Trks	0.0	4544.65	0.0
<b>585 : CC-<math>\bar{\nu}_e/\bar{\nu}_\mu^*</math></b>	<b>0.03</b>	$\nu_\mu$ RHC 1-Trk	0.0	2067.37	0.0
		$\nu_\mu$ RHC N-Trks	0.0	4568.13	0.0
		$\nu_\mu$ 1-Trk Wtr	0.0	27316.74	0.0
		$\nu_\mu$ N-Trks	0.0	30904.32	0.0
		$\bar{\nu}_\mu$ RHC 1-Trk	0.0	8414.09	0.0
		$\bar{\nu}_\mu$ RHC N-Trks	0.0	4724.34	0.0
		$\nu_\mu$ RHC 1-Trk	0.0	3022.10	0.0
		$\nu_\mu$ RHC N-Trks	0.0	4928.38	0.0
		$\nu_\mu$ 1-Trk Air	0.0	23605.76	0.0
		$\nu_\mu$ N-Trks	0.0	32304.13	0.0

Parameter	$1\sigma$ value	Sample	$-1\sigma$ (%)	nominal	$+1\sigma$ (%)
586 : CC-DIS shape location	0.40	$\nu_\mu$ 1-Trk Wtr	-0.4	27316.74	0.4
		$\nu_\mu$ N-Trks	-4.2	30904.32	4.2
		$\bar{\nu}_\mu$ RHC 1-Trk	-0.3	8414.09	0.3
		$\bar{\nu}_\mu$ RHC N-Trks	-4.3	4724.34	4.3
		$\nu_\mu$ RHC 1-Trk	-0.7	3022.10	0.7
		$\nu_\mu$ RHC N-Trks	-4.4	4928.38	4.4
		$\nu_\mu$ 1-Trk Air	-0.3	23605.76	0.3
		$\nu_\mu$ N-Trks	-3.9	32304.13	3.9
		$\bar{\nu}_\mu$ RHC 1-Trk	-0.2	6767.65	0.2
		$\bar{\nu}_\mu$ RHC N-Trks	-4.2	4544.65	4.2
587 : CC Coherent on $^{12}\text{C}$ norm.	0.30	$\nu_\mu$ RHC 1-Trk	-0.6	2067.37	0.6
		$\nu_\mu$ RHC N-Trks	-4.1	4568.13	4.1
		$\nu_\mu$ 1-Trk Wtr	-0.1	27316.74	0.1
		$\nu_\mu$ N-Trks	-0.2	30904.32	0.2
		$\bar{\nu}_\mu$ RHC 1-Trk	-0.1	8414.09	0.1
		$\bar{\nu}_\mu$ RHC N-Trks	-0.4	4724.34	0.4
		$\nu_\mu$ RHC 1-Trk	-0.1	3022.10	0.1
		$\nu_\mu$ RHC N-Trks	-0.2	4928.38	0.2
		$\nu_\mu$ 1-Trk Air	-0.1	23605.76	0.1
		$\nu_\mu$ N-Trks	-0.3	32304.13	0.3

Parameter	$1\sigma$ value	Sample	$-1\sigma$ (%)	nominal	$+1\sigma$ (%)
588 : CC Coherent on $^{16}\text{O}$ norm.	0.30	$\nu_\mu$ 1-Trk Wtr	-0.0	27316.74	0.0
		$\nu_\mu$ N-Trks	-0.1	30904.32	0.1
		$\bar{\nu}_\mu$ RHC 1-Trk	-0.1	8414.09	0.1
		$\bar{\nu}_\mu$ RHC N-Trks	-0.2	4724.34	0.2
		$\nu_\mu$ RHC 1-Trk	-0.1	3022.10	0.1
		$\nu_\mu$ RHC N-Trks	-0.1	4928.38	0.1
		$\nu_\mu$ 1-Trk Air	-0.0	23605.76	0.0
		$\nu_\mu$ N-Trks	-0.0	32304.13	0.0
		$\bar{\nu}_\mu$ RHC 1-Trk	-0.0	6767.65	0.0
		$\bar{\nu}_\mu$ RHC N-Trks	-0.0	4544.65	0.0
589 : NC Coherent norm.	0.30	$\nu_\mu$ RHC 1-Trk	-0.0	2067.37	0.0
		$\nu_\mu$ RHC N-Trks	-0.0	4568.13	0.0
		$\nu_\mu$ 1-Trk Wtr	-0.0	27316.74	0.0
		$\nu_\mu$ N-Trks	-0.0	30904.32	0.0
		$\bar{\nu}_\mu$ RHC 1-Trk	-0.0	8414.09	0.0
		$\bar{\nu}_\mu$ RHC N-Trks	-0.0	4724.34	0.0
		$\nu_\mu$ RHC 1-Trk	-0.0	3022.10	0.0
		$\nu_\mu$ RHC N-Trks	-0.0	4928.38	0.0
		$\nu_\mu$ 1-Trk Air	-0.0	23605.76	0.0
		$\nu_\mu$ N-Trks	-0.0	32304.13	0.0

Parameter	$1\sigma$ value	Sample	$-1\sigma$ (%)	nominal	$+1\sigma$ (%)
590 : NC-1 $\gamma^*$	1.00	$\nu_\mu$ 1-Trk Wtr	-0.0	27316.74	0.0
		$\nu_\mu$ N-Trks	-0.0	30904.32	0.0
		$\bar{\nu}_\mu$ RHC 1-Trk	0.0	8414.09	0.0
		$\bar{\nu}_\mu$ RHC N-Trks	-0.0	4724.34	0.0
		$\nu_\mu$ RHC 1-Trk	0.0	3022.10	0.0
		$\nu_\mu$ RHC N-Trks	0.0	4928.38	0.0
		$\nu_\mu$ 1-Trk Air	-0.0	23605.76	0.0
		$\nu_\mu$ N-Trks	0.0	32304.13	0.0
		$\bar{\nu}_\mu$ RHC 1-Trk	0.0	6767.65	0.0
		$\bar{\nu}_\mu$ RHC N-Trks	-0.0	4544.65	0.0
591 : NC Other Near	0.30	$\nu_\mu$ RHC 1-Trk	0.0	2067.37	0.0
		$\nu_\mu$ RHC N-Trks	0.0	4568.13	0.0
		$\nu_\mu$ 1-Trk Wtr	-0.1	27316.74	0.1
		$\nu_\mu$ N-Trks	-0.6	30904.32	0.6
		$\bar{\nu}_\mu$ RHC 1-Trk	-0.2	8414.09	0.2
		$\bar{\nu}_\mu$ RHC N-Trks	-1.9	4724.34	1.9
		$\nu_\mu$ RHC 1-Trk	-0.2	3022.10	0.2
		$\nu_\mu$ RHC N-Trks	-0.8	4928.38	0.8
		$\nu_\mu$ 1-Trk Air	-0.1	23605.76	0.1
		$\nu_\mu$ N-Trks	-0.6	32304.13	0.6

Parameter	$1\sigma$ value	Sample	$-1\sigma$ (%)	nominal	$+1\sigma$ (%)	
<b>591 : NC Other Far*</b>	<b>0.30</b>	$\nu_\mu$ 1-Trk Wtr	-0.1	27316.74	0.1	
		$\nu_\mu$ N-Trks	-0.4	30904.32	0.4	
		$\bar{\nu}_\mu$ RHC 1-Trk	-0.1	8414.09	0.1	
		$\bar{\nu}_\mu$ RHC N-Trks	-1.2	4724.34	1.2	
		$\nu_\mu$ RHC 1-Trk	-0.1	3022.10	0.1	
		$\nu_\mu$ RHC N-Trks	-0.5	4928.38	0.5	
		$\nu_\mu$ 1-Trk Air	-0.1	23605.76	0.1	
		$\nu_\mu$ N-Trks	-0.6	32304.13	0.6	
		$\bar{\nu}_\mu$ RHC 1-Trk	-0.3	6767.65	0.3	
		$\bar{\nu}_\mu$ RHC N-Trks	-1.8	4544.65	1.8	
		$\nu_\mu$ RHC 1-Trk	-0.2	2067.37	0.2	
		$\nu_\mu$ RHC N-Trks	-0.8	4568.13	0.8	

# Appendix E

## Log-Likelihood Sample Scans

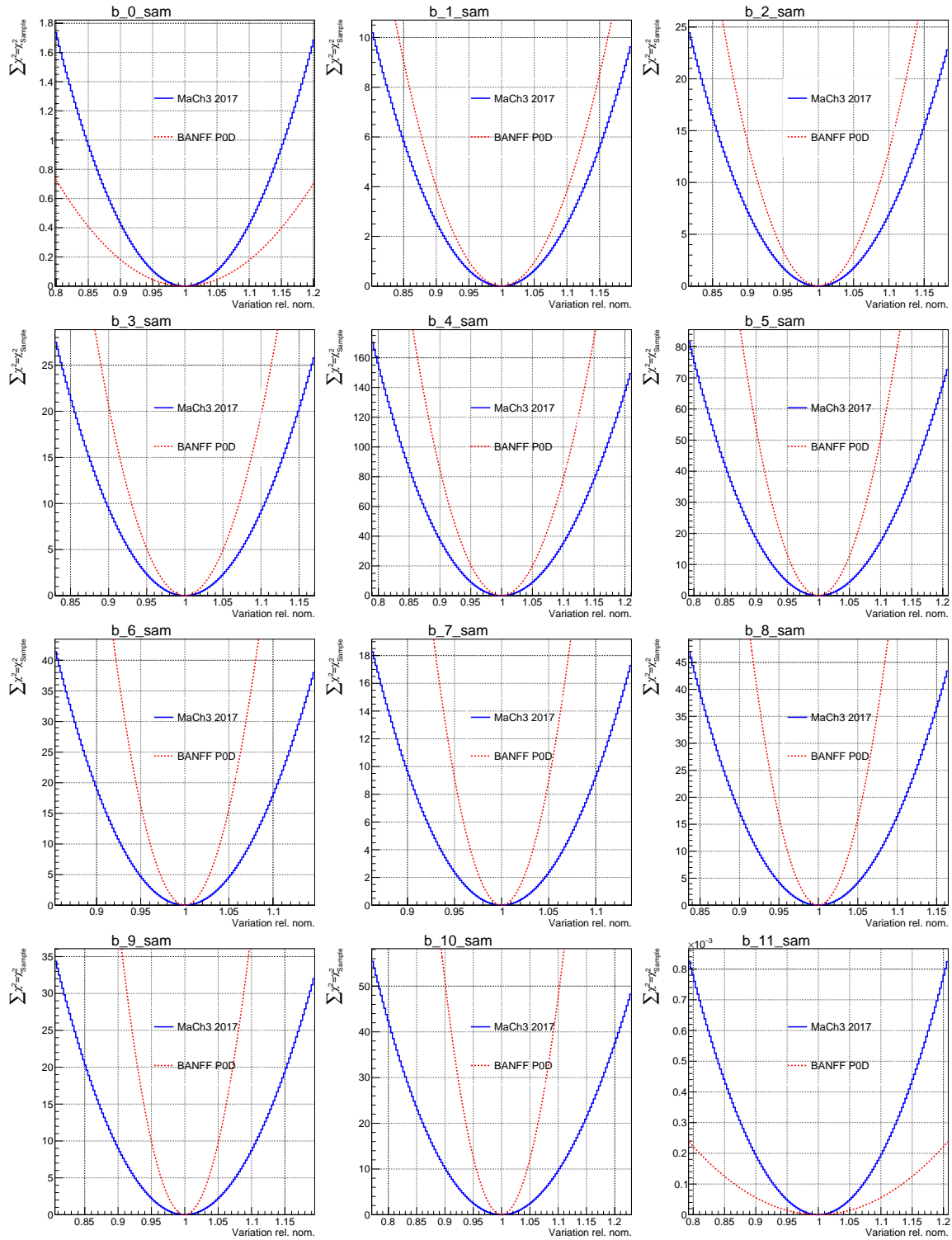
This appendix examines the PØD-only BANFF fit likelihood term  $\Delta\chi^2_{\text{LLR}} = \chi^2_{\text{sample}}$  response (scans) to variations in flux and cross section parameters. For the cross section terms, the scans shapes correspond to the shape of the spline weight. In addition, comparison scans are provided for the FGD MaCh3 2017 analysis. Extensive comparisons were made to ensure that the FGD MaCh3 and FGD BANFF analyses have identical splines. So it is an equal comparison with the FGD BANFF as shown in Chapter 4. In some cases, the PØD-only scans indicate higher sensitivity to parameters than the FGD.

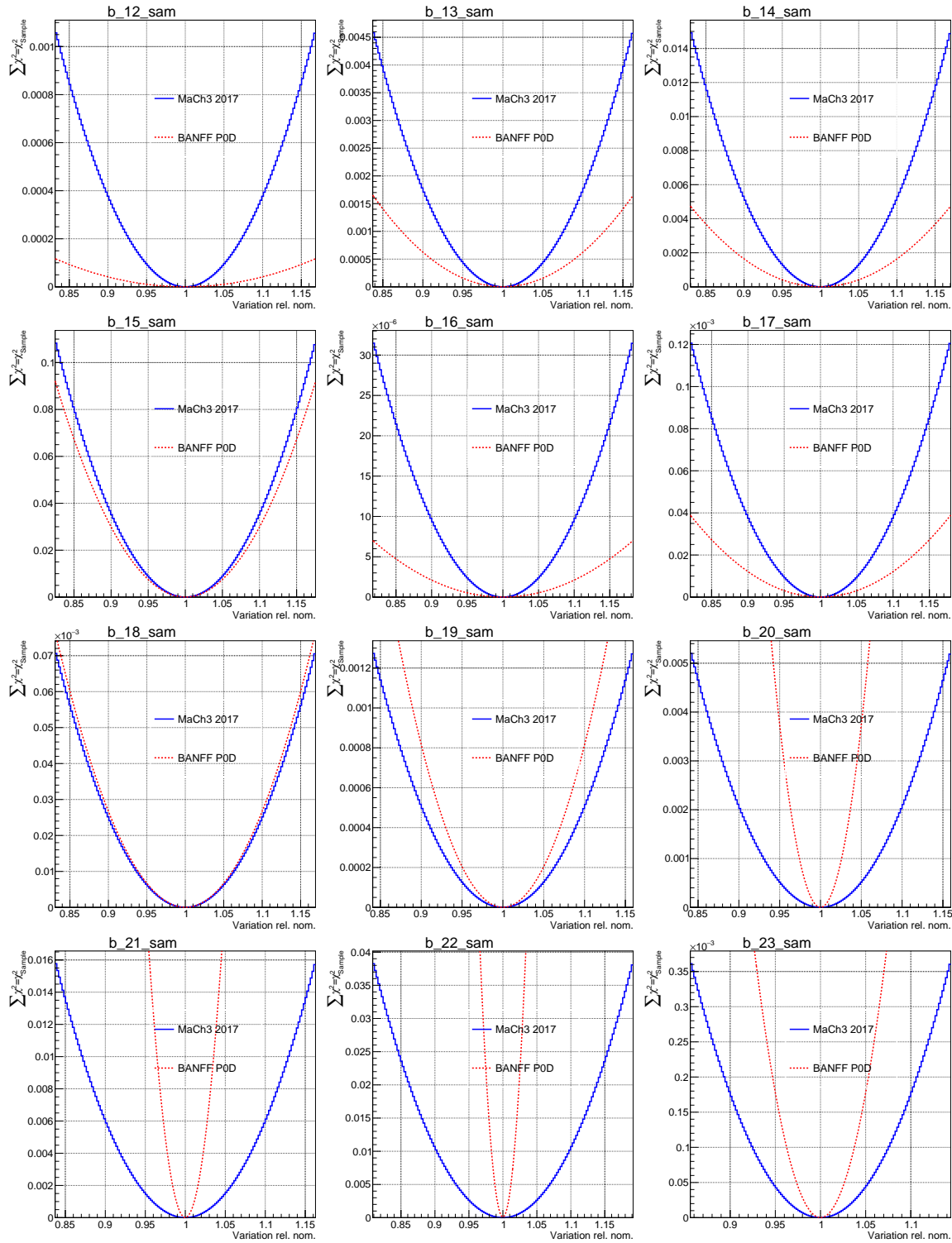
These were generously produced by Clarence Wret ([c.wret@rochester.edu](mailto:c.wret@rochester.edu)) of the University of Rochester. The likelihood scans are ordered as such. The first 50 plots “b\_0\_sam” through “b\_49\_sam” are the ND280 flux sample contributions. The next 50 “b\_50\_sam” through “b\_99\_sam” are the sample contributions that affect the SK flux. The last scans are variations on the cross section parameters. Due to a bug in plotting script, the scans 2p2h shape location for  $^{12}\text{C}$  and  $^{16}\text{O}$  were empty for the PØD. The correct PØD scans are shown in Figure E.1 on page 315 with the MaCH3 inputs reproduced as faithfully as possible.

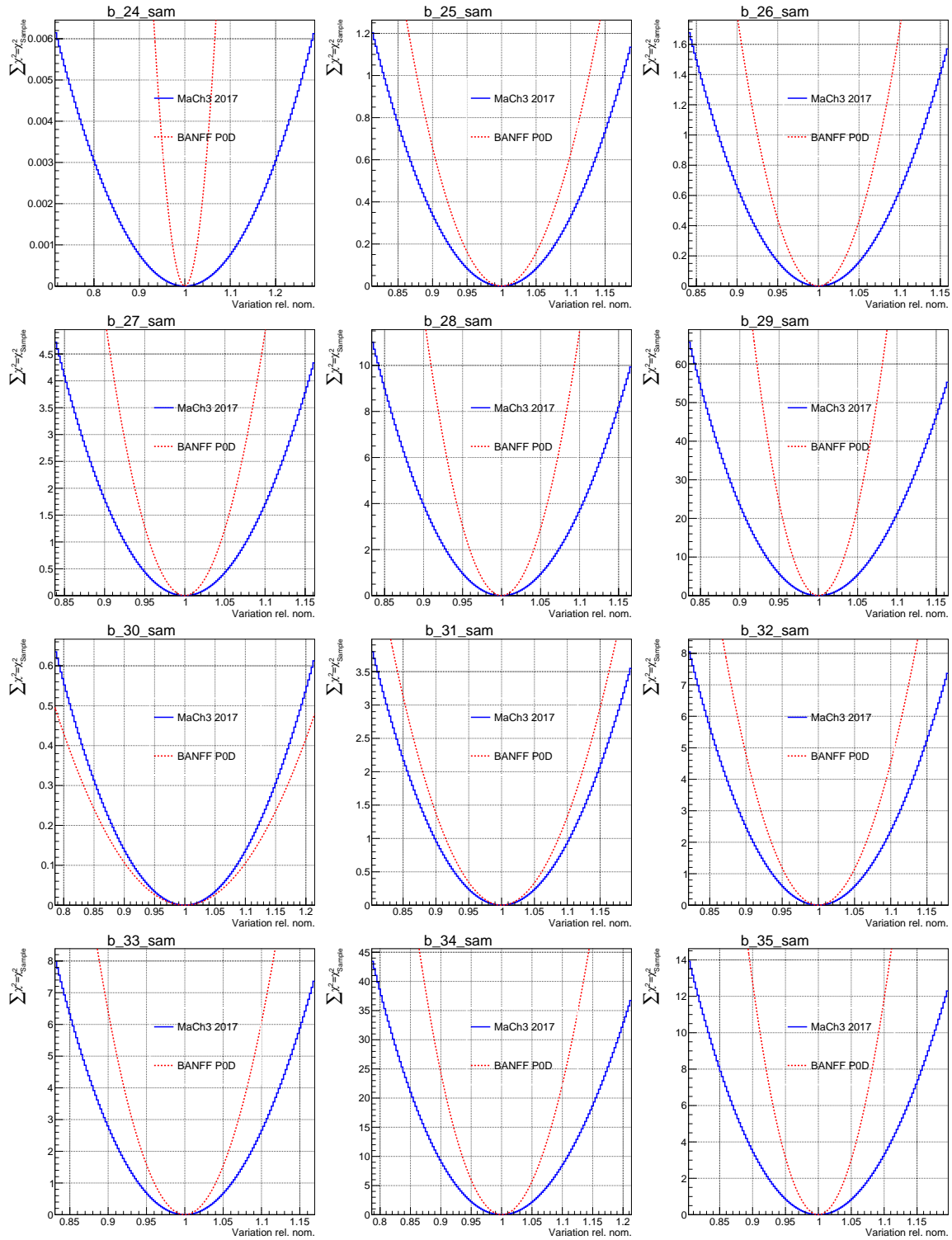
As expected, the SK flux variations are flat with respect to the sample chi-squared. This is due model parameterization in which the ND280 samples only affect the ND280 flux

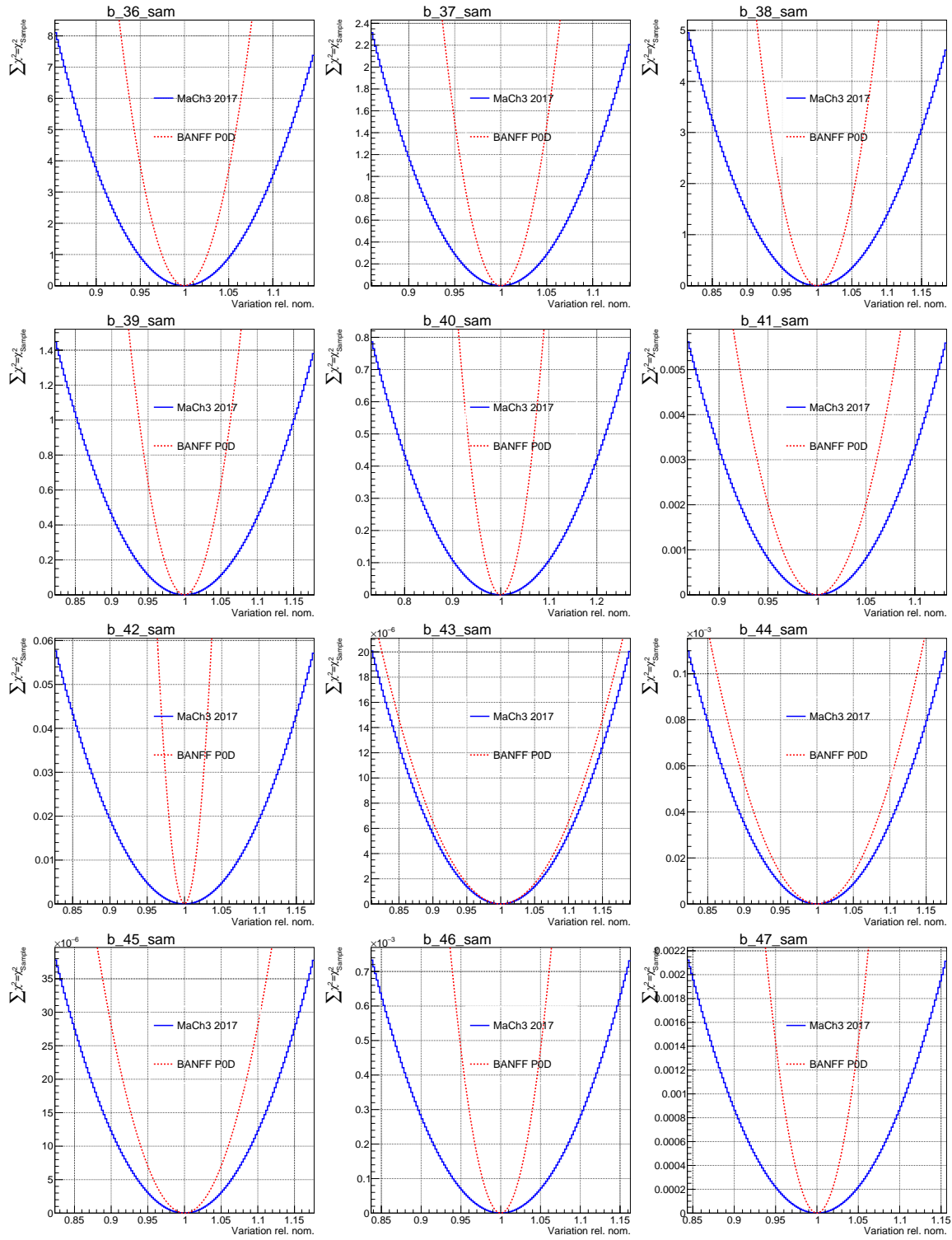
parameters. In other words, the log-likelihood scans for the SK flux parameters have no affect on the ND280 sample events.

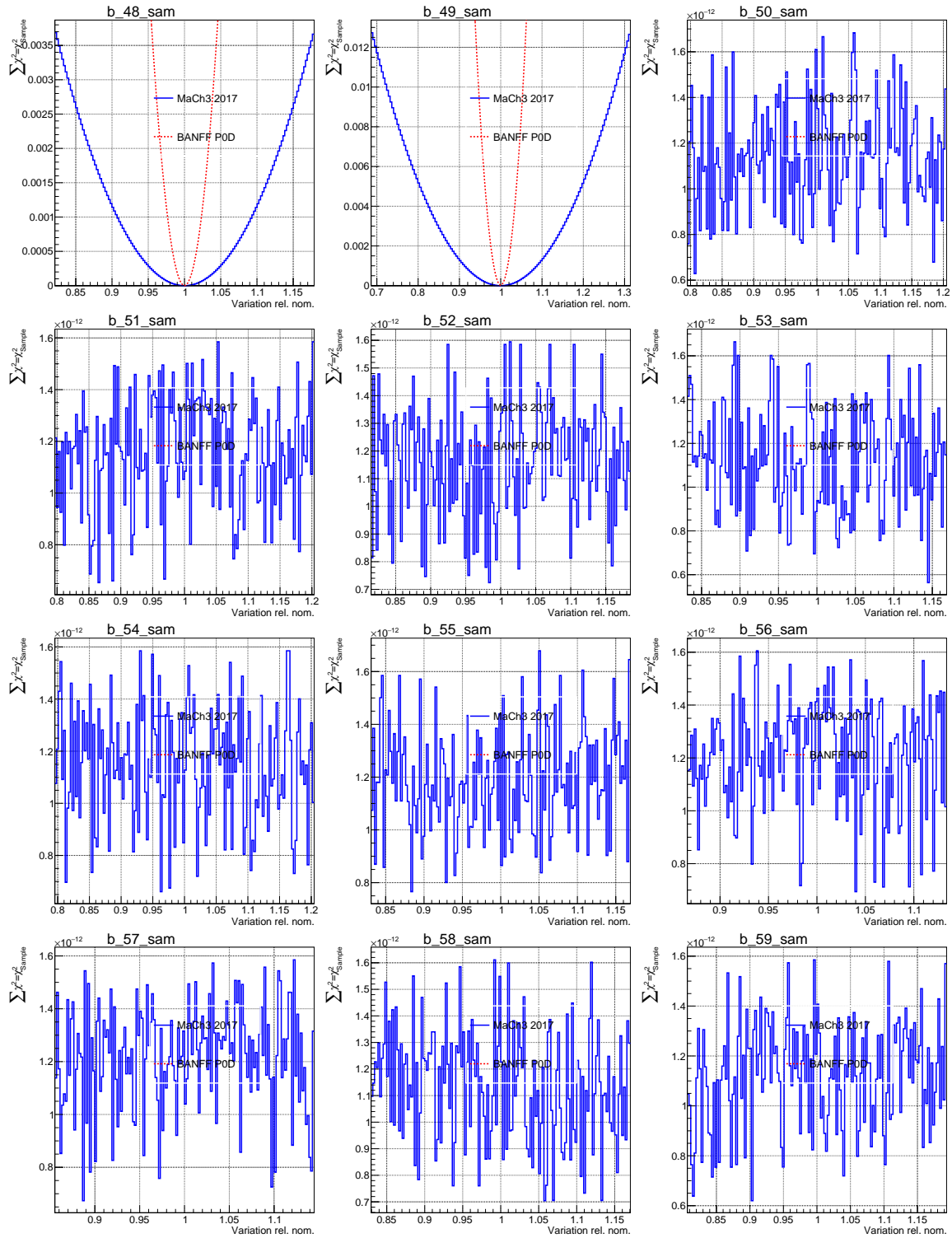
Some of cross section parameter splines are reflected about a point in order to properly calculate correlations between parameters. In previous fits to data, the 2p2h  $^{12}\text{C}$  and  $^{16}\text{O}$  shape location terms hit their physical boundaries at +1. The result was that the fitter MINUIT inaccurately calculated the Hess matrix. The decision was made to reflect, also called “mirroring”, the splines about a certain point to expand the limit. Tests showed that this did not affect the postfit results for any parameters, but the correlations between all other parameters was calculated to less than 1% [24].

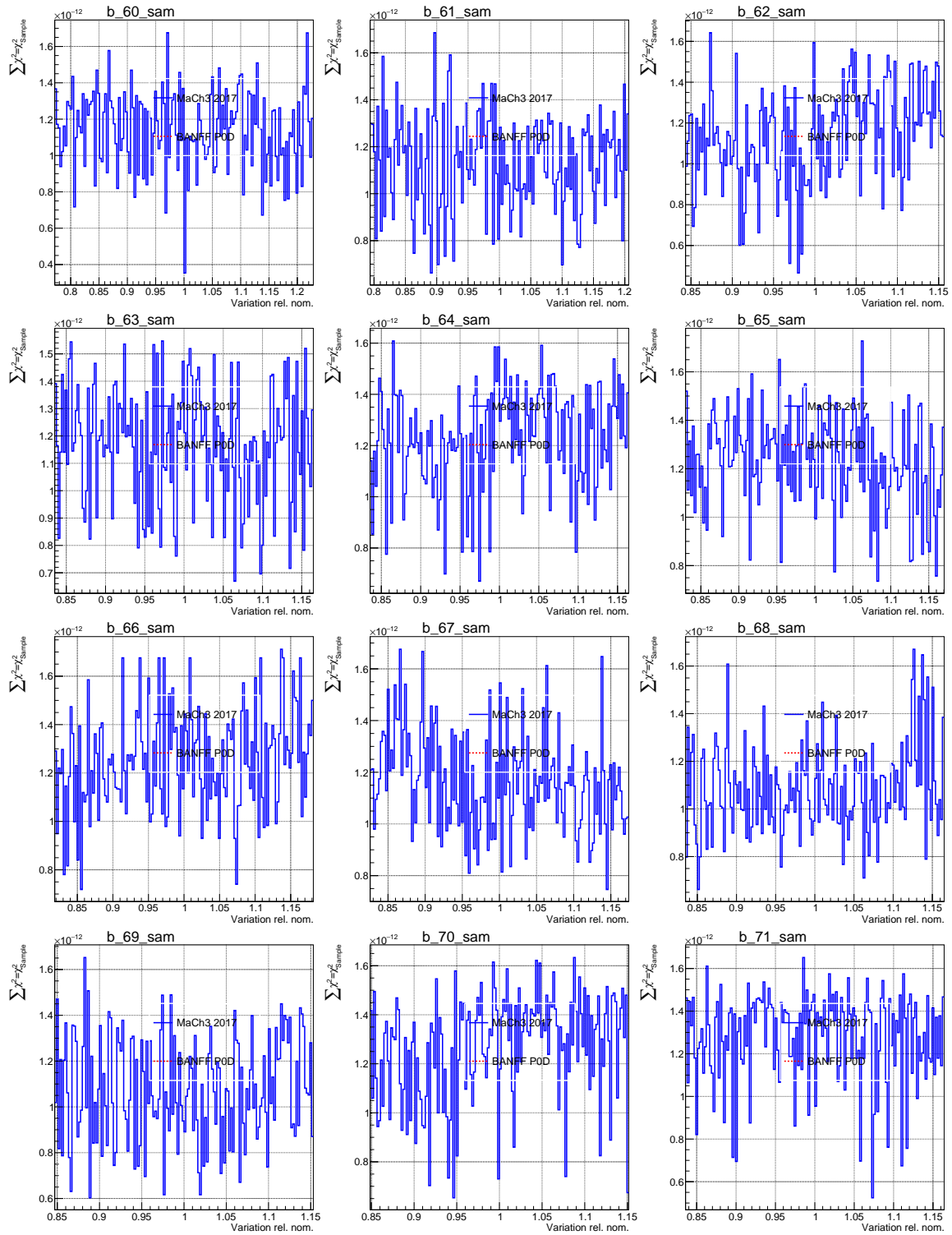


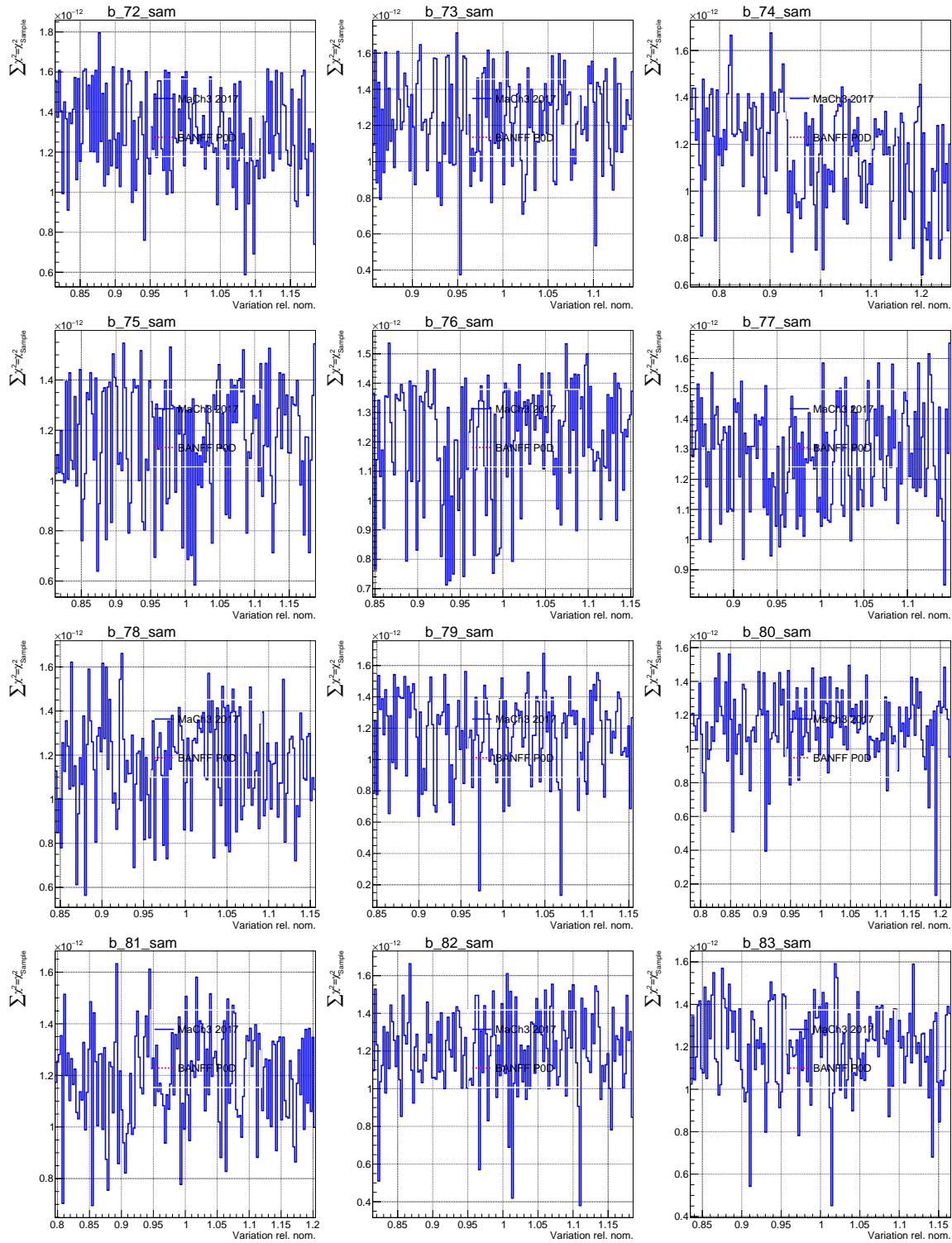


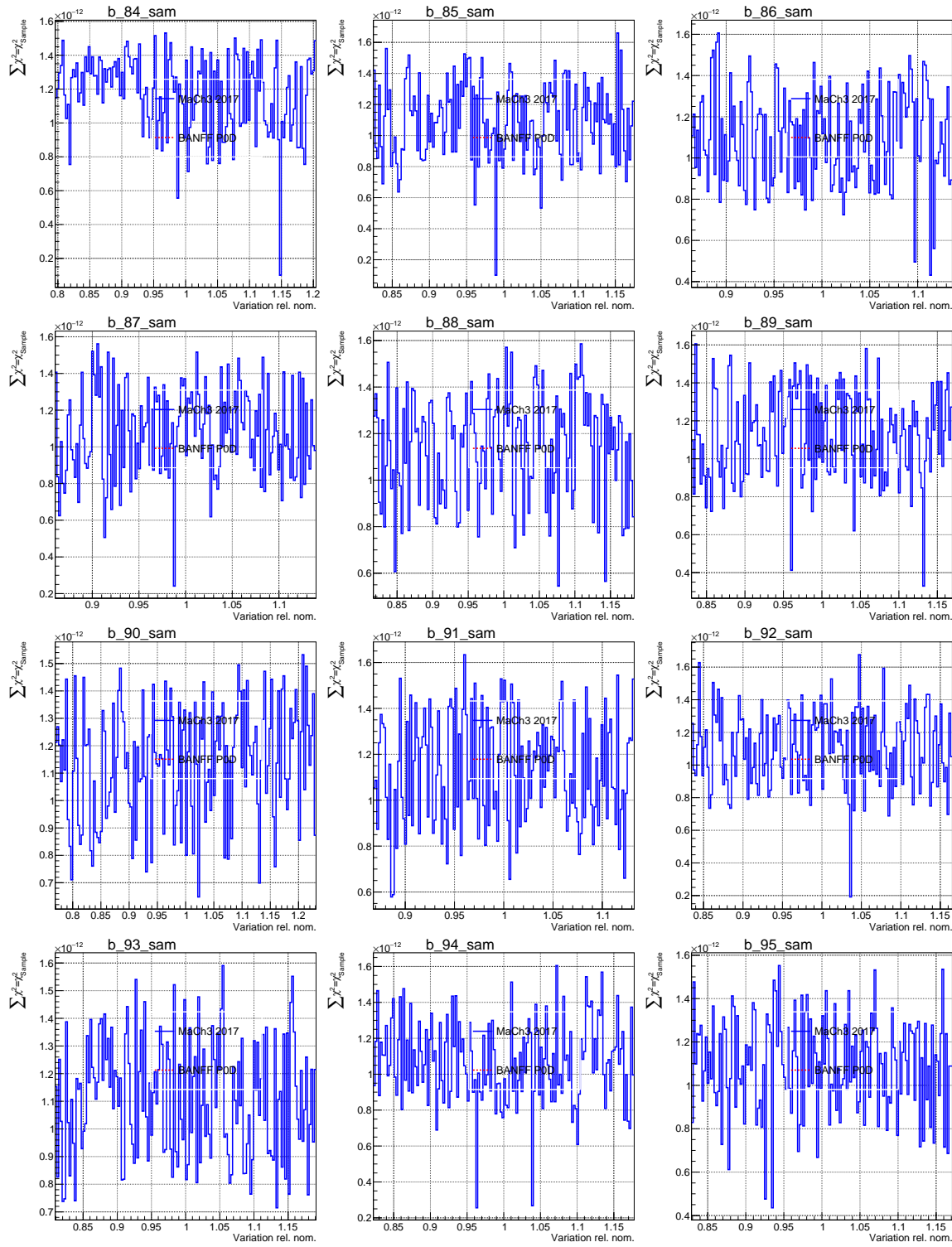


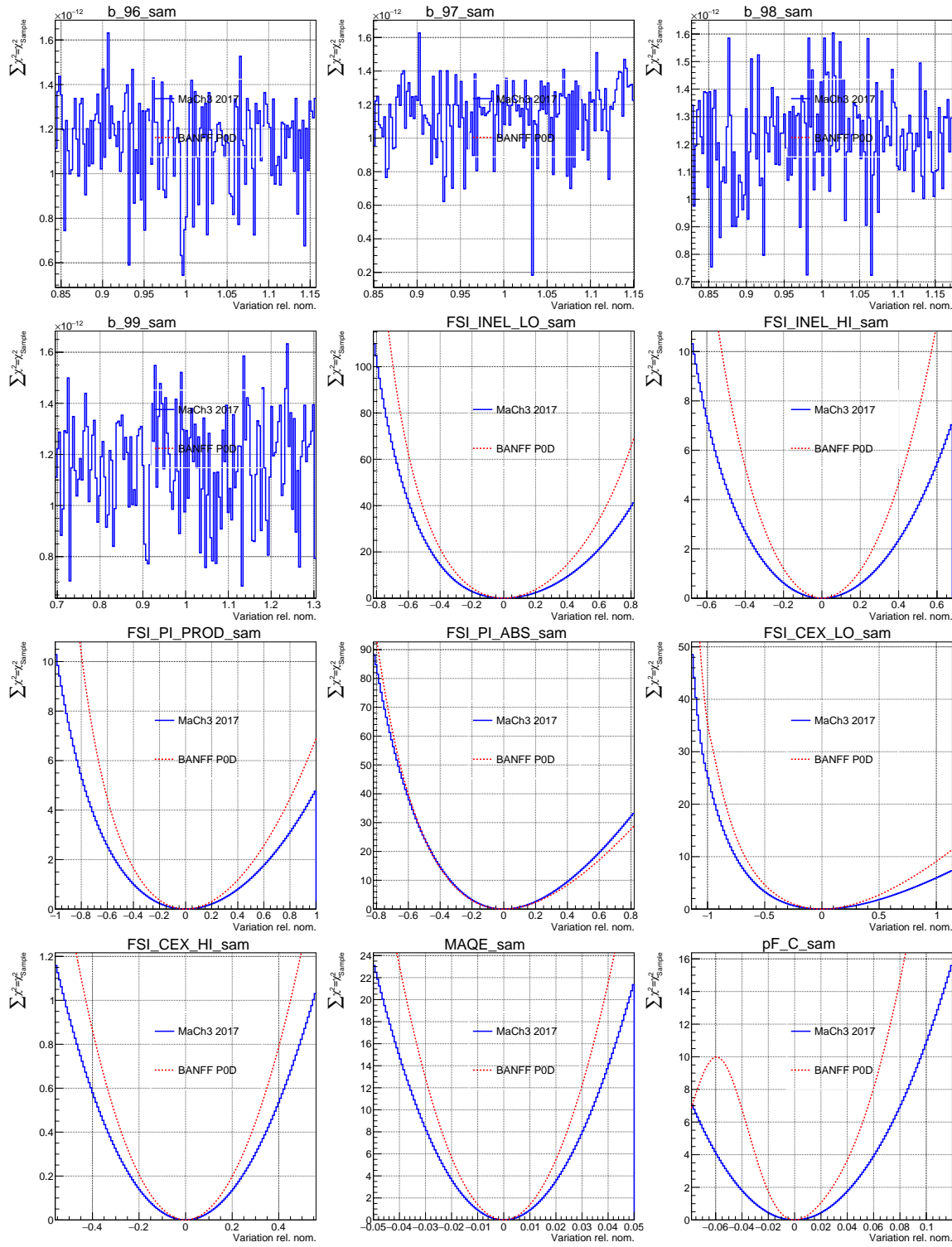


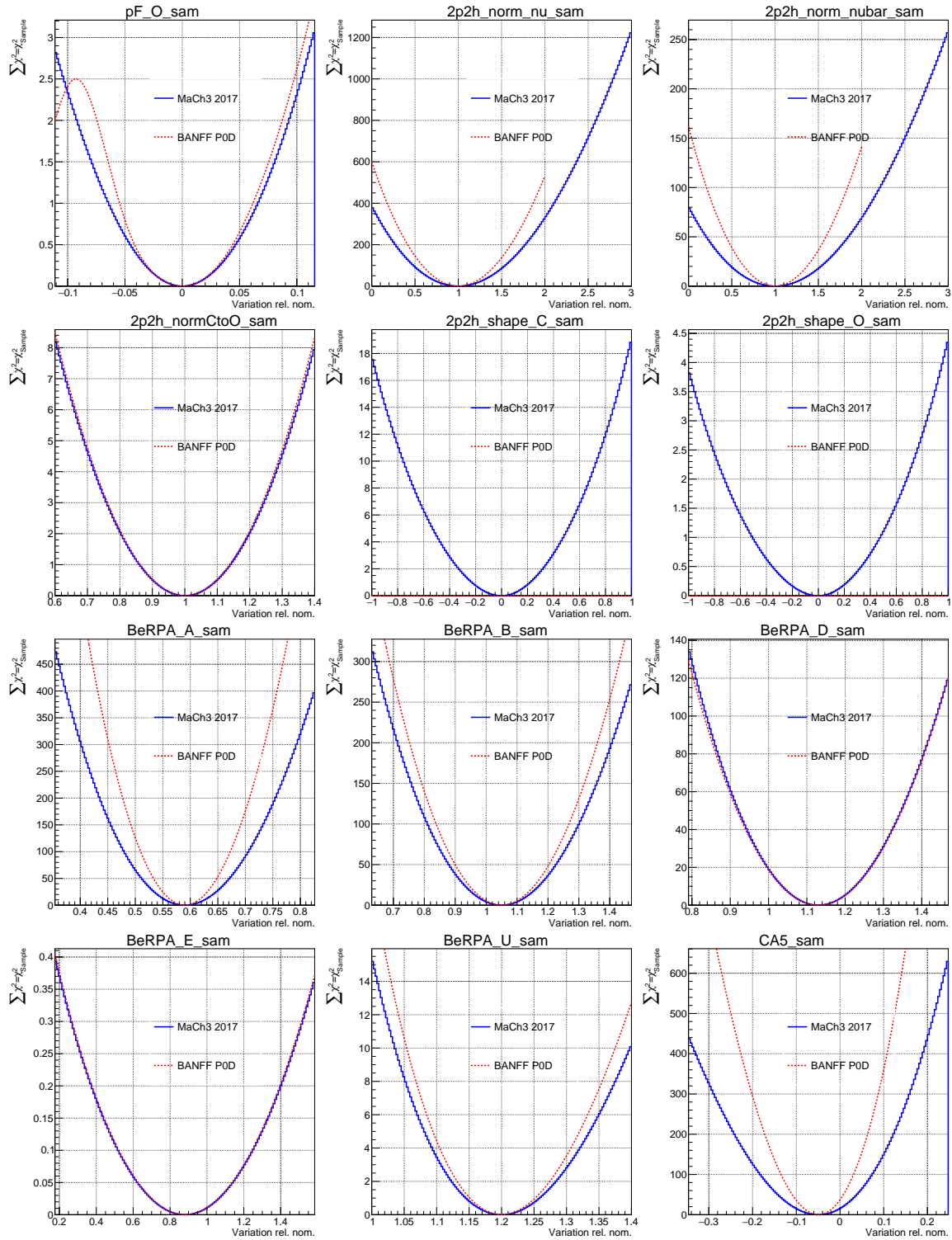


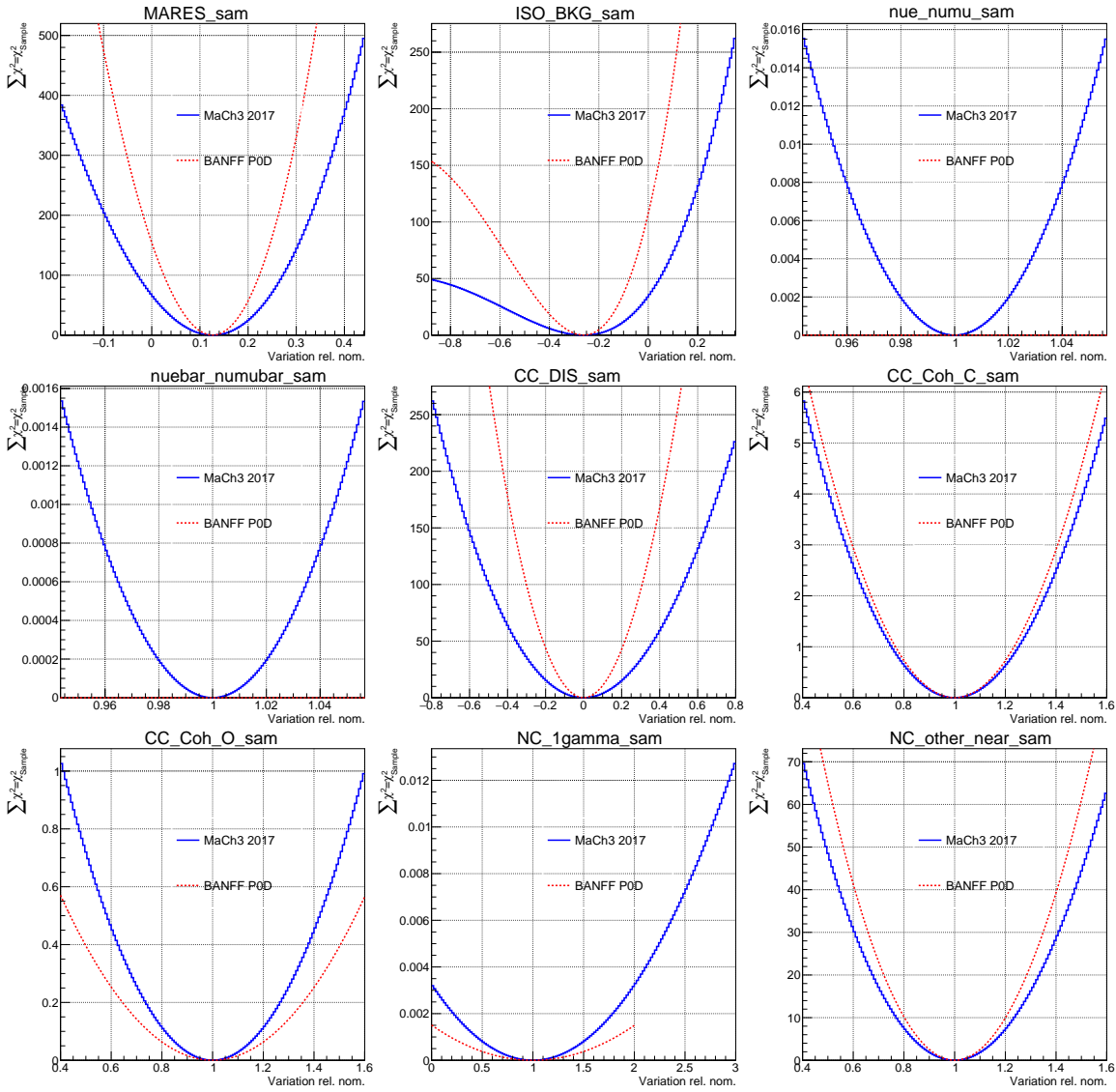












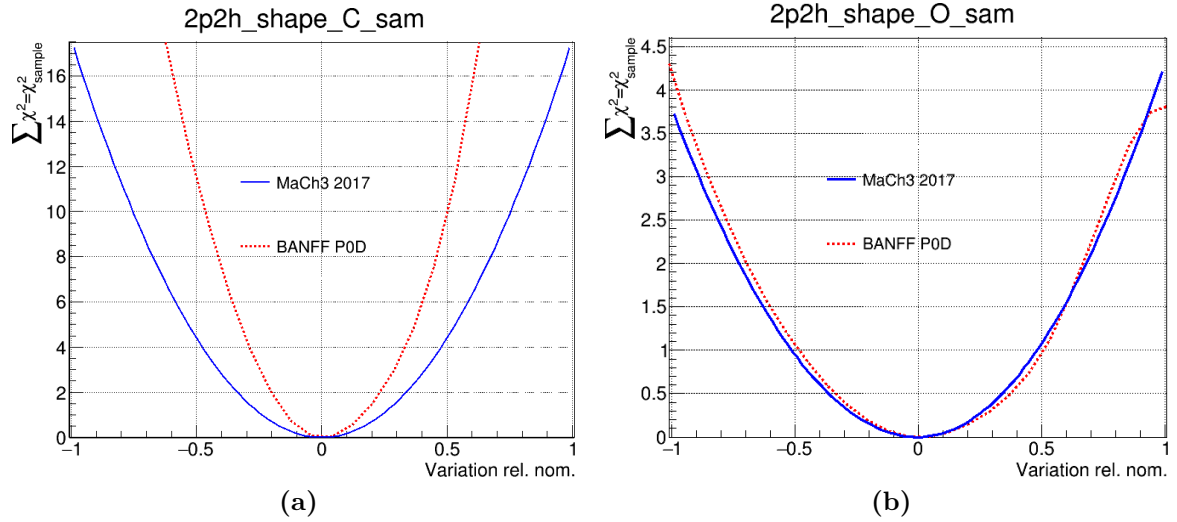
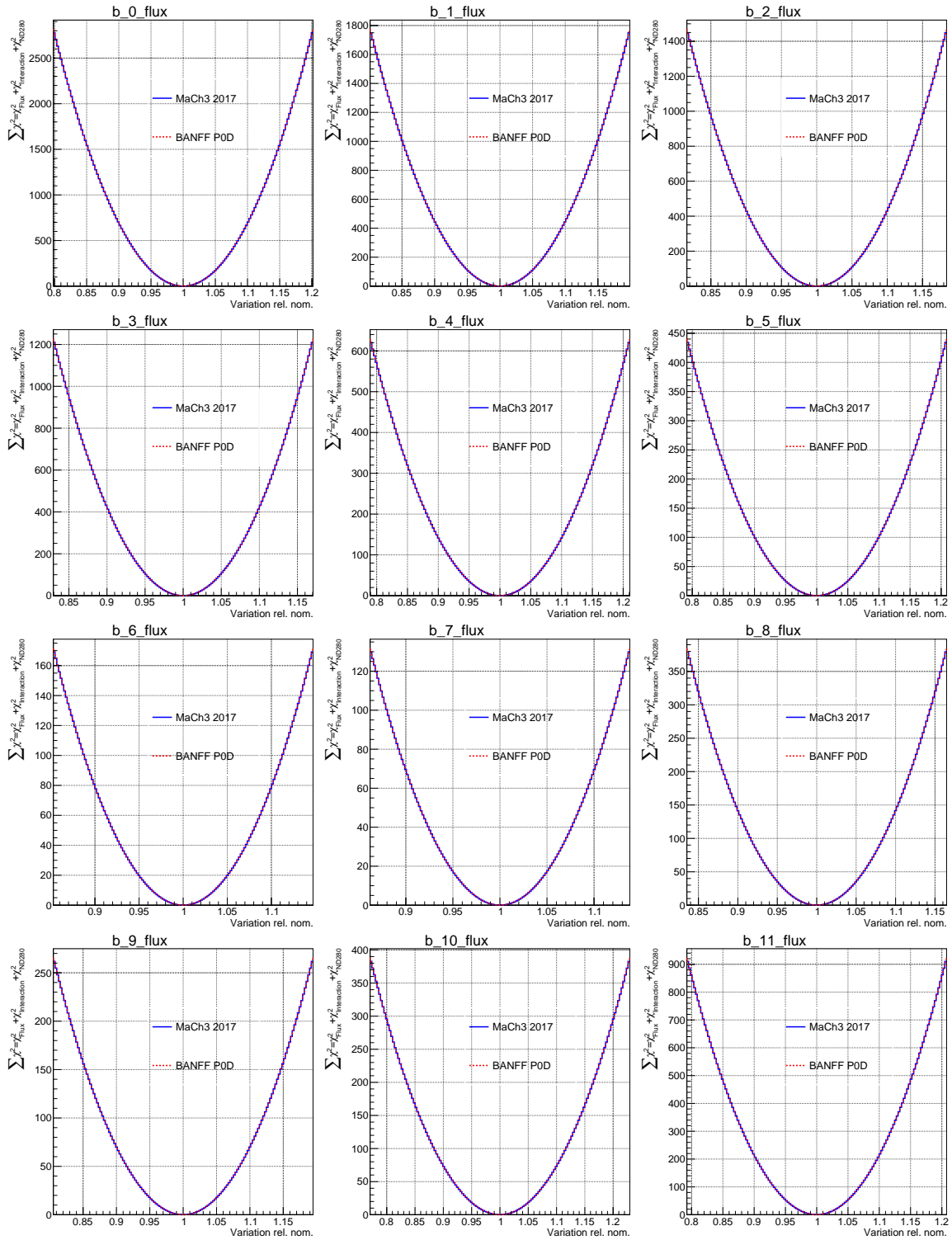


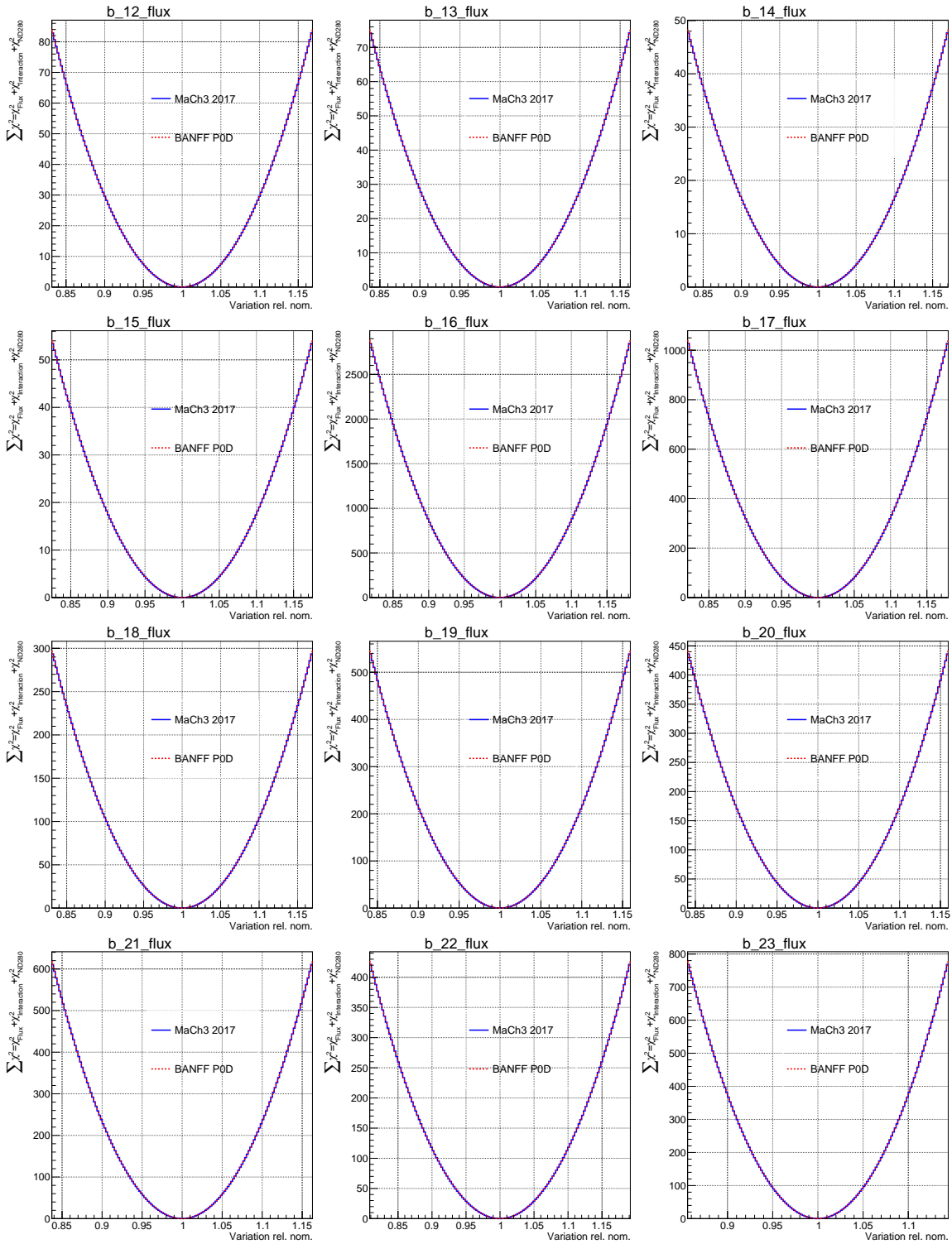
**Figure E.1:** Correct PØD scans with faithful reproductions of the MaCh3 scans for the 2p2h shape location cross section parameters.

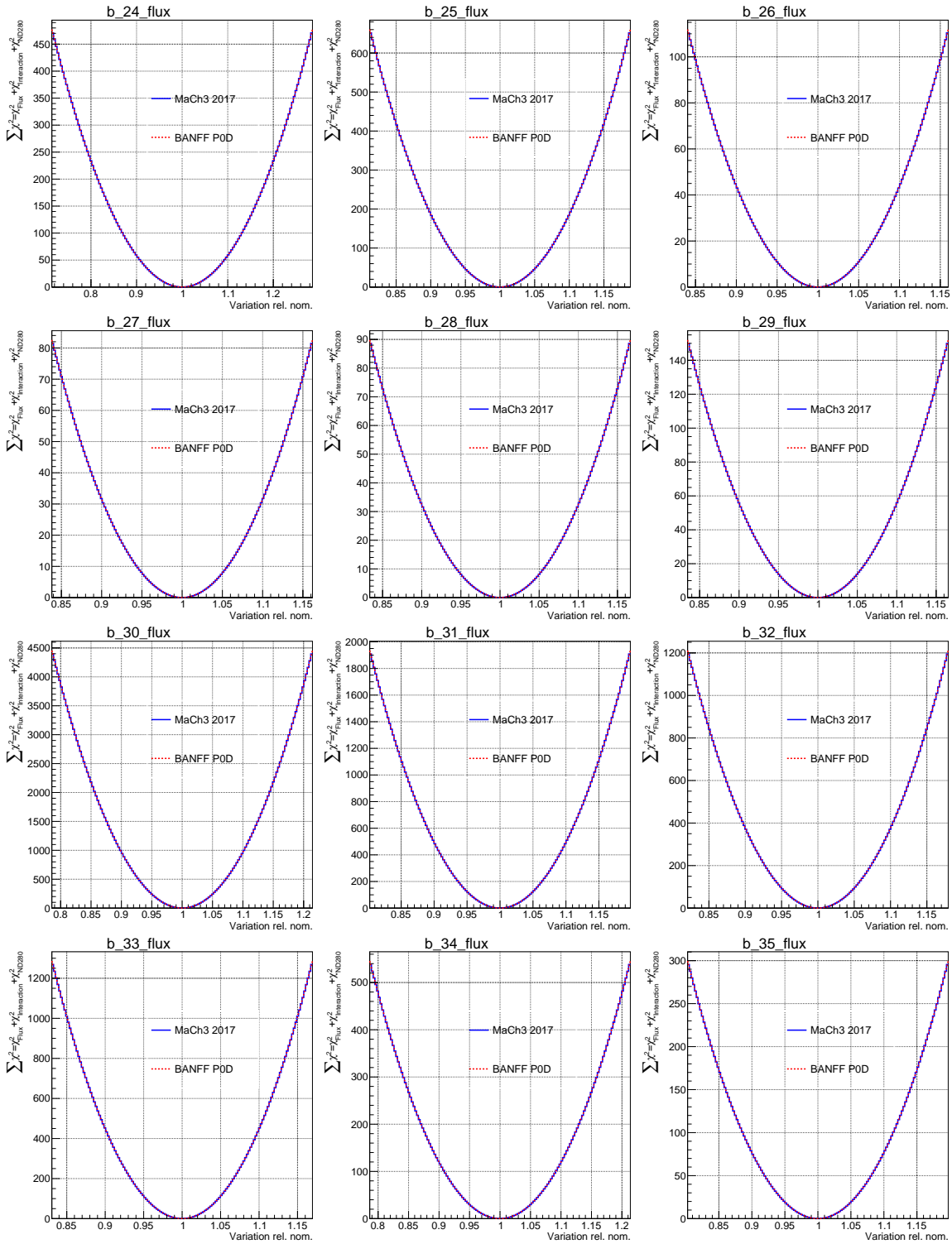
## Appendix F

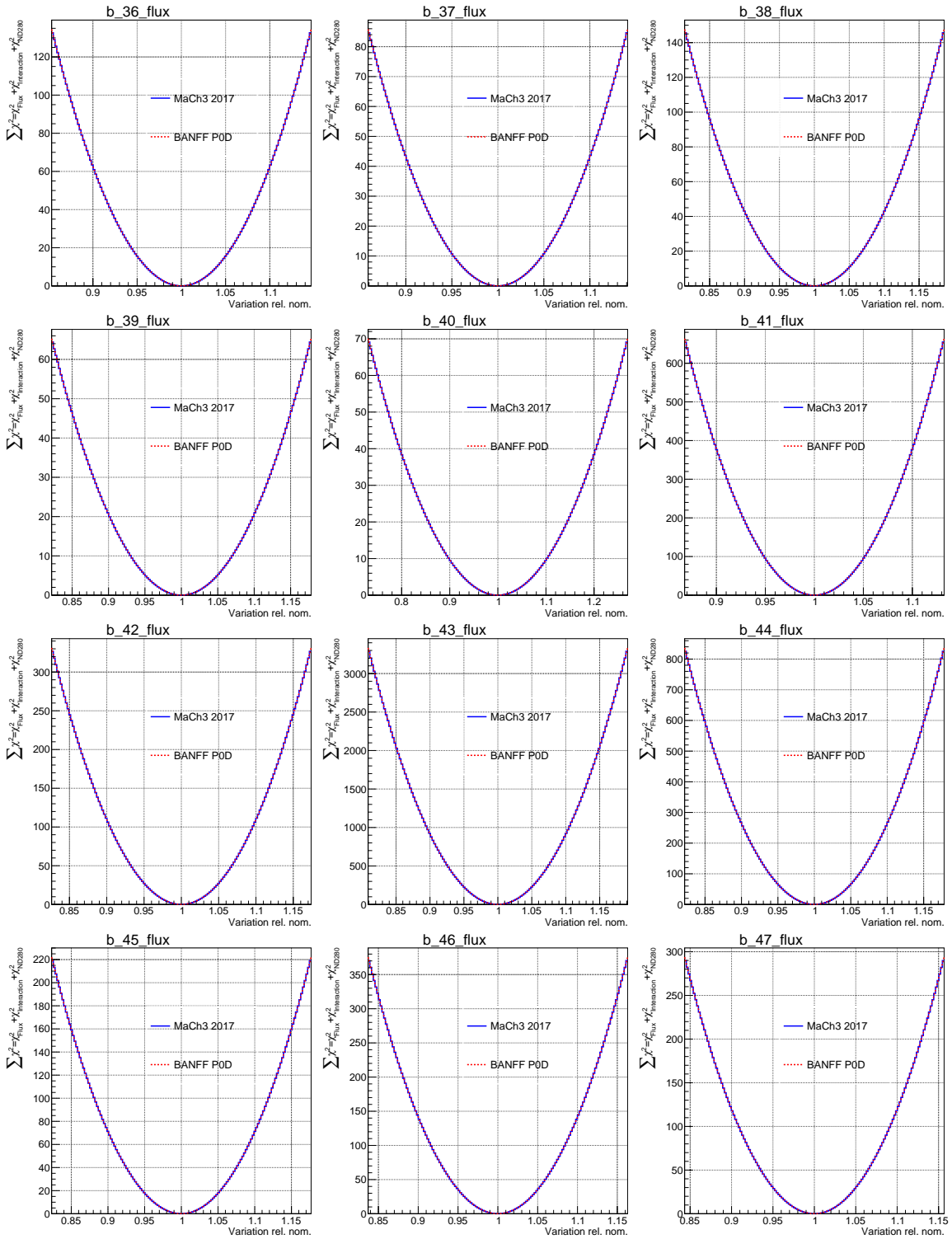
### Log-Likelihood Penalty Scans

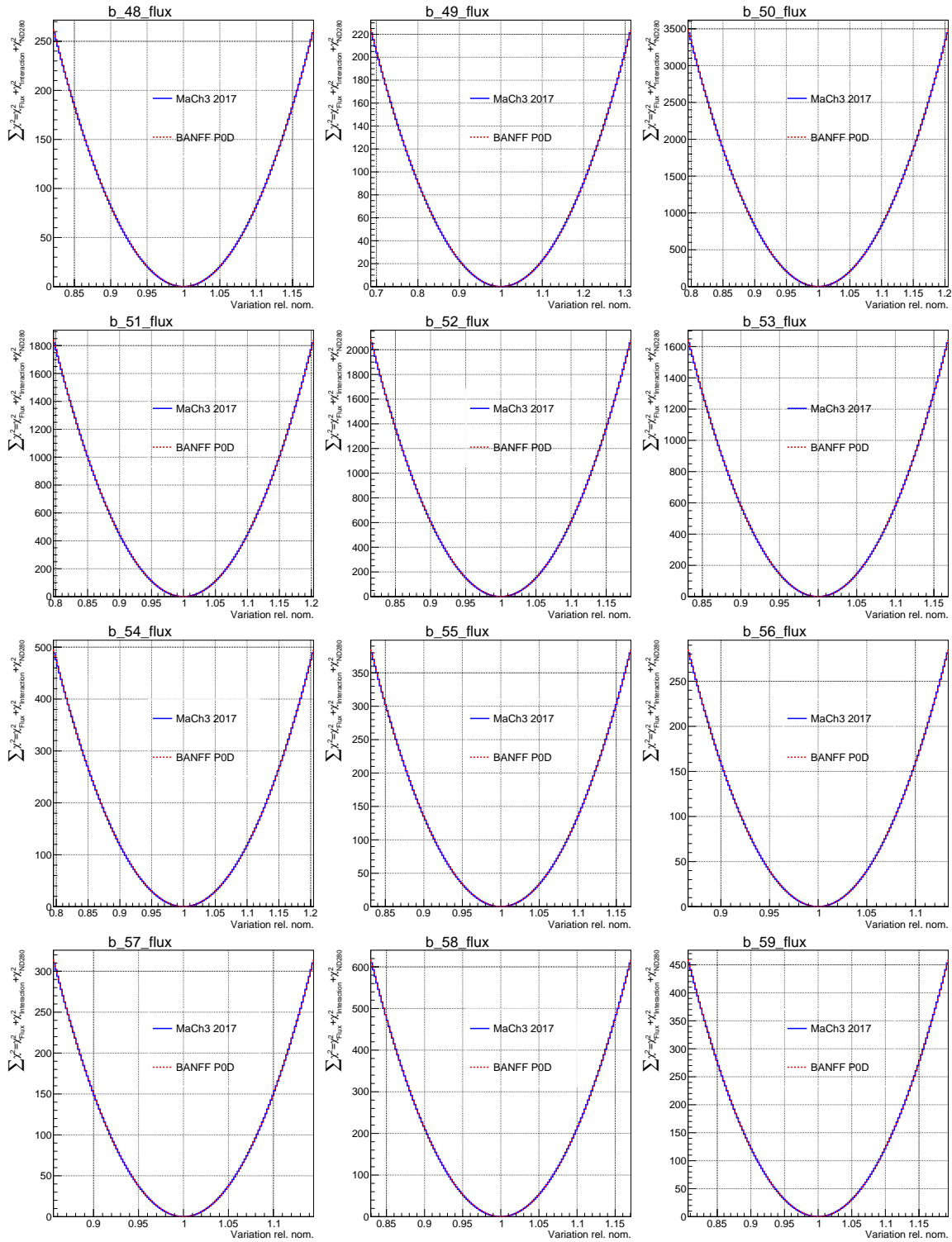
This appendix examines the PØD-only BANFF fit penalty terms  $\chi_{\text{Flux}}^2 + \chi_{\text{xsec}}^2 + \chi_{\text{Det}}^2$  response (scans) to variations in flux and cross section parameters. In addition, comparison scans are provided for the FGD MaCH3/BANFF 2017 analysis. In all cases, the penalty terms overlap indicating the parameters have the same prior constraints between analyses.

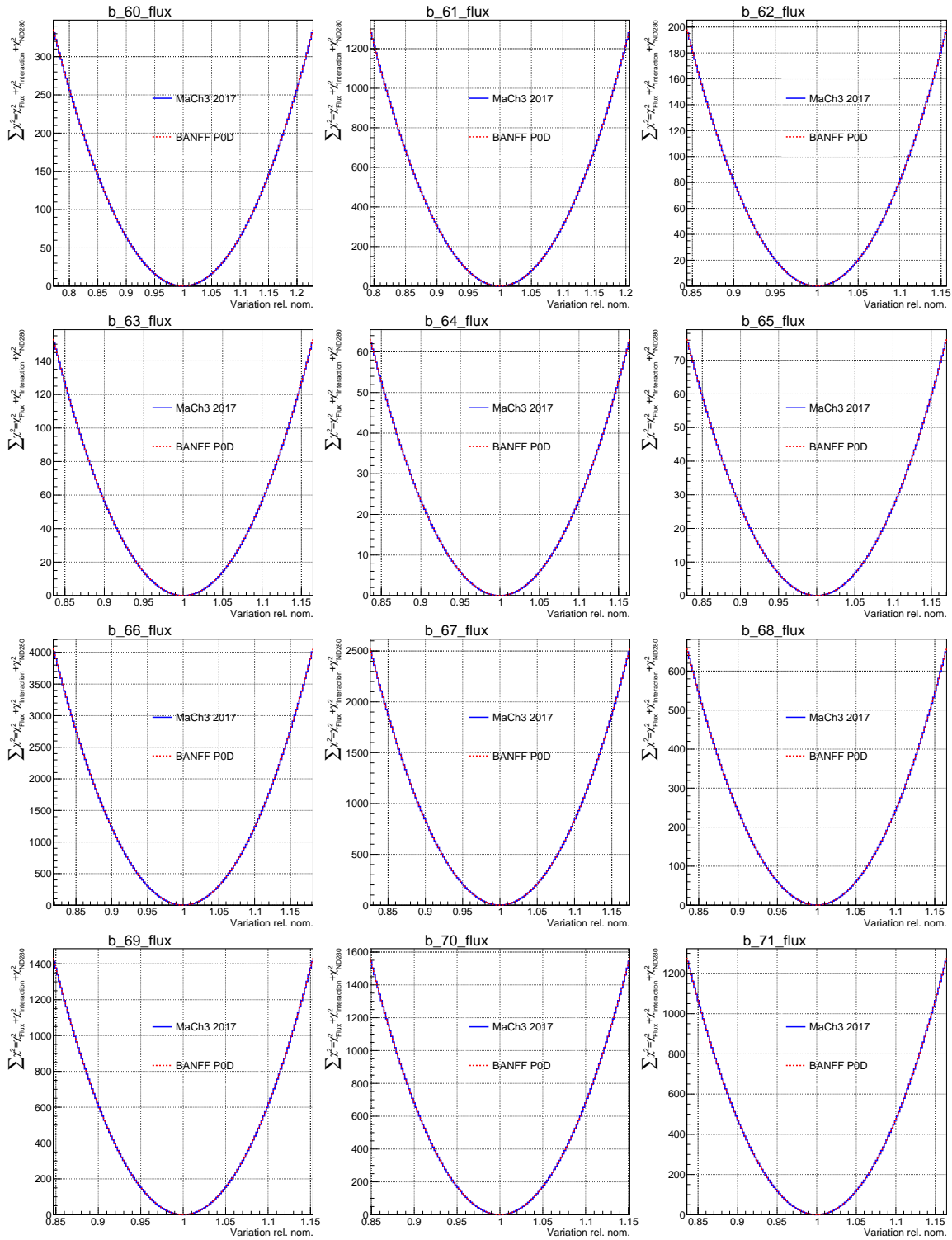


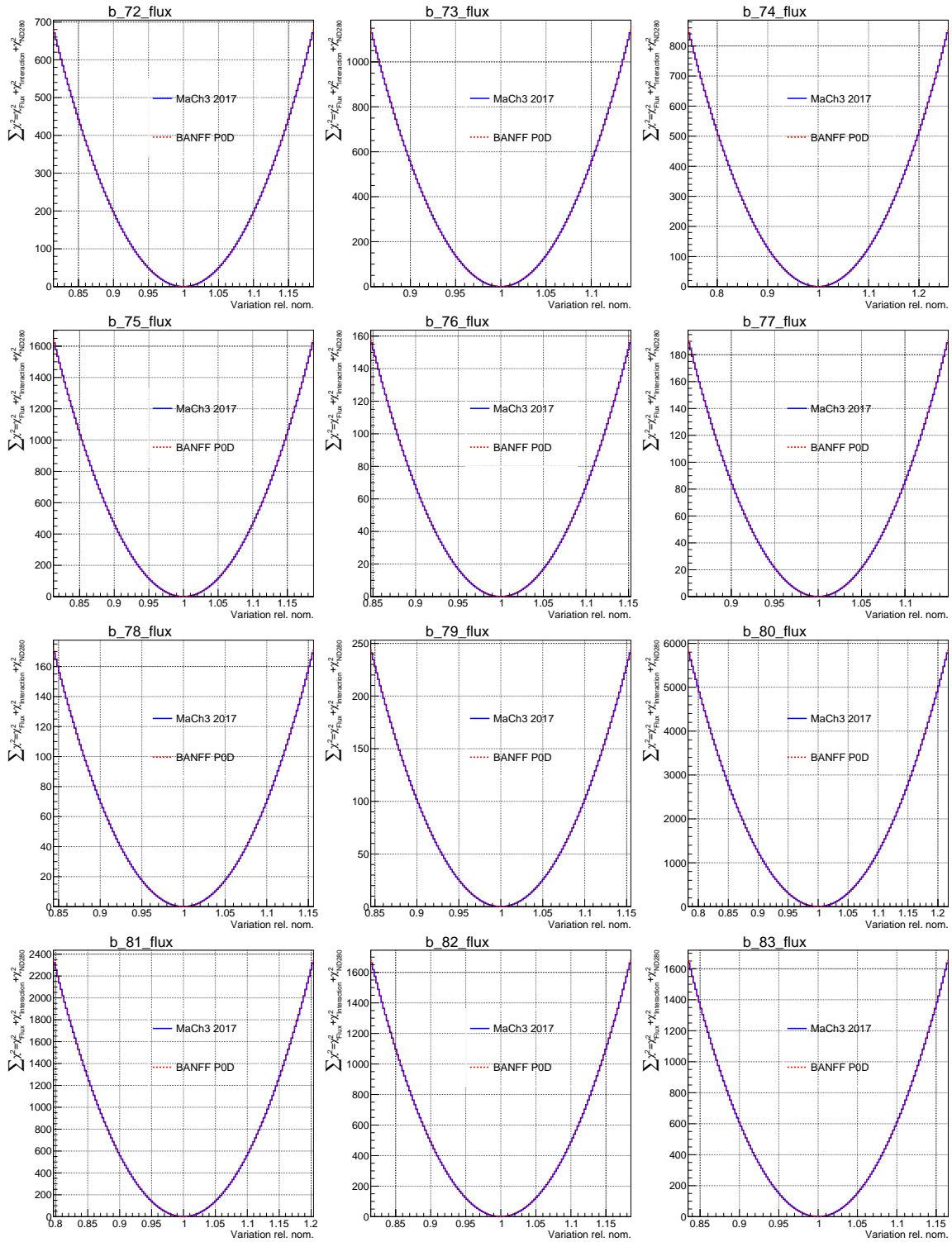


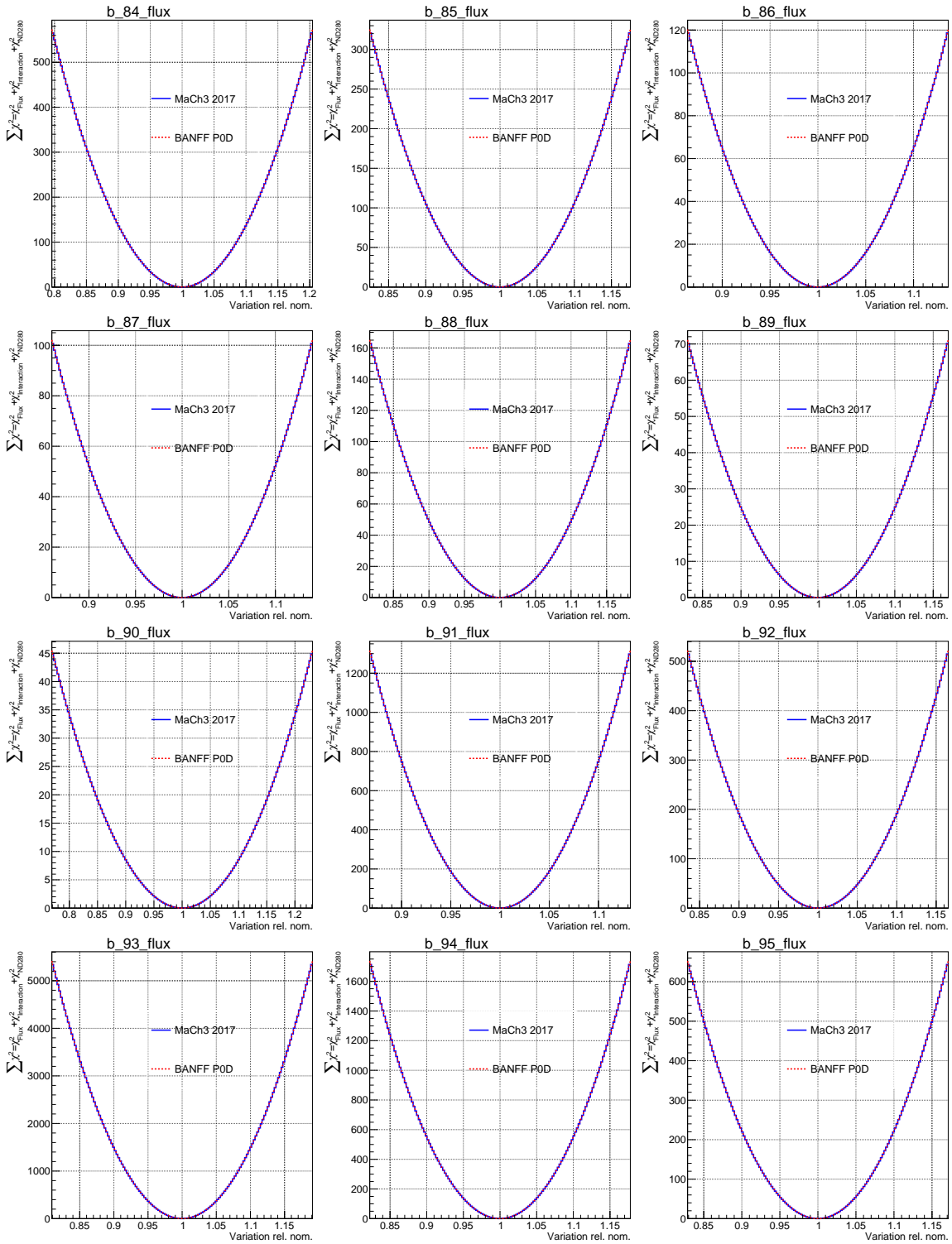


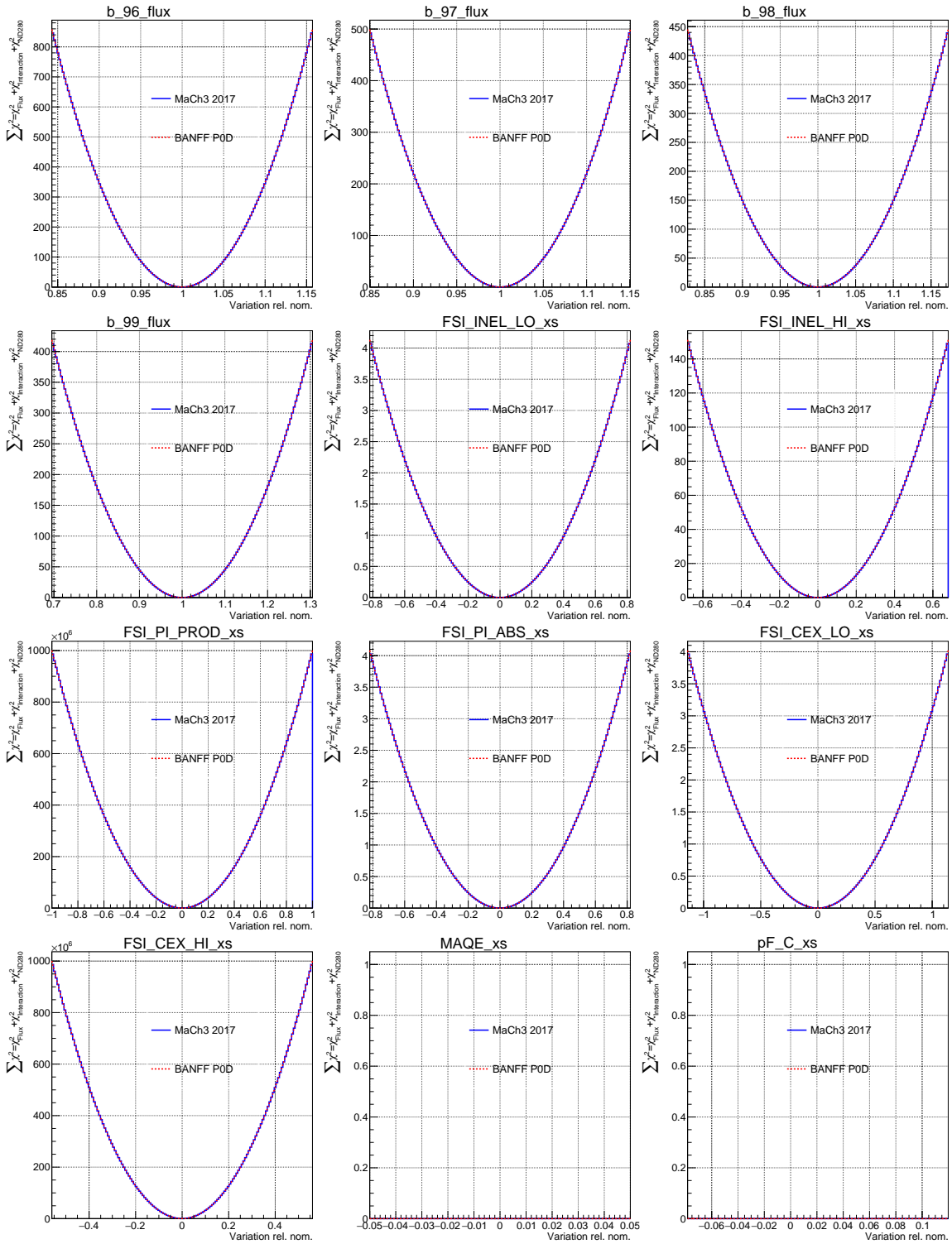


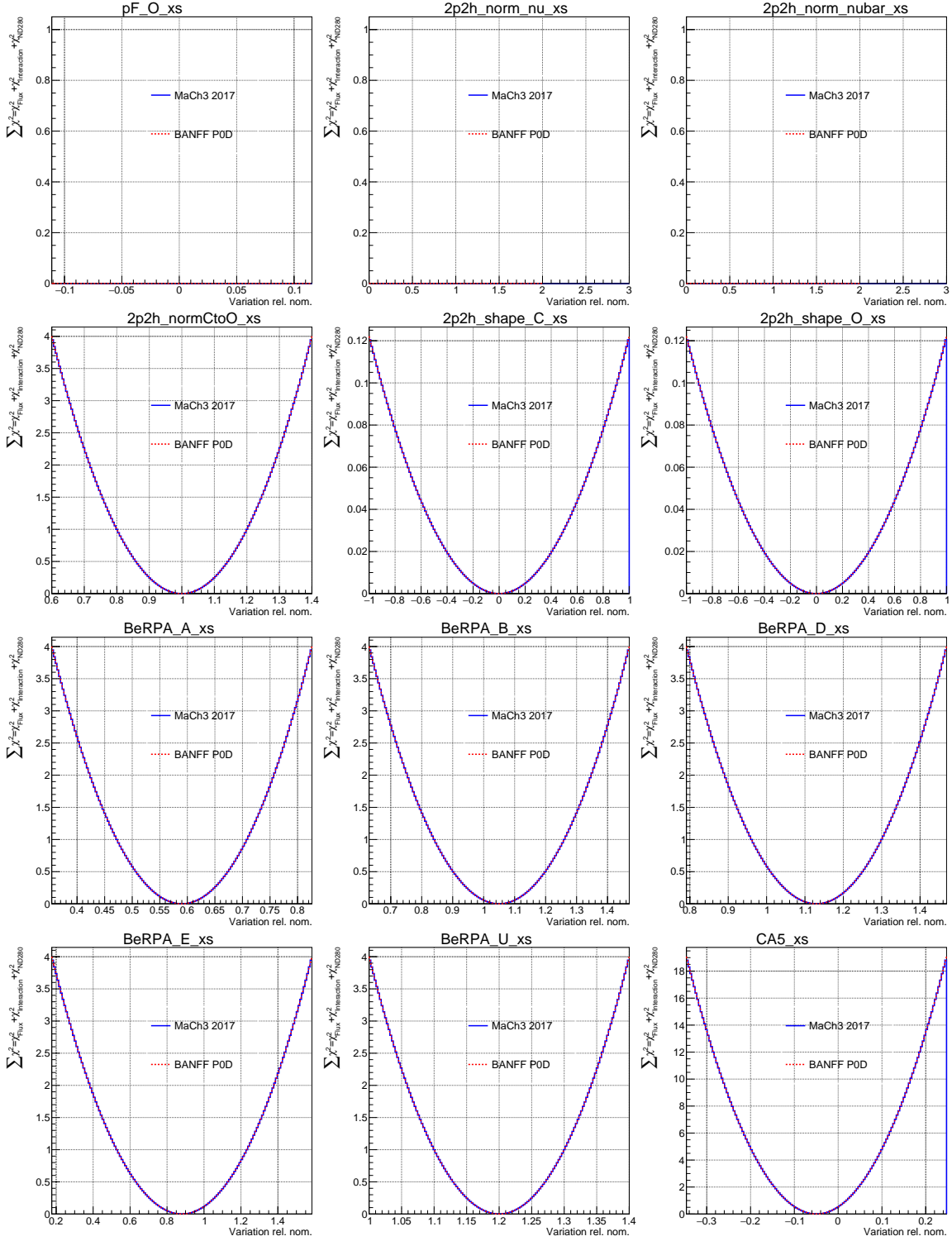


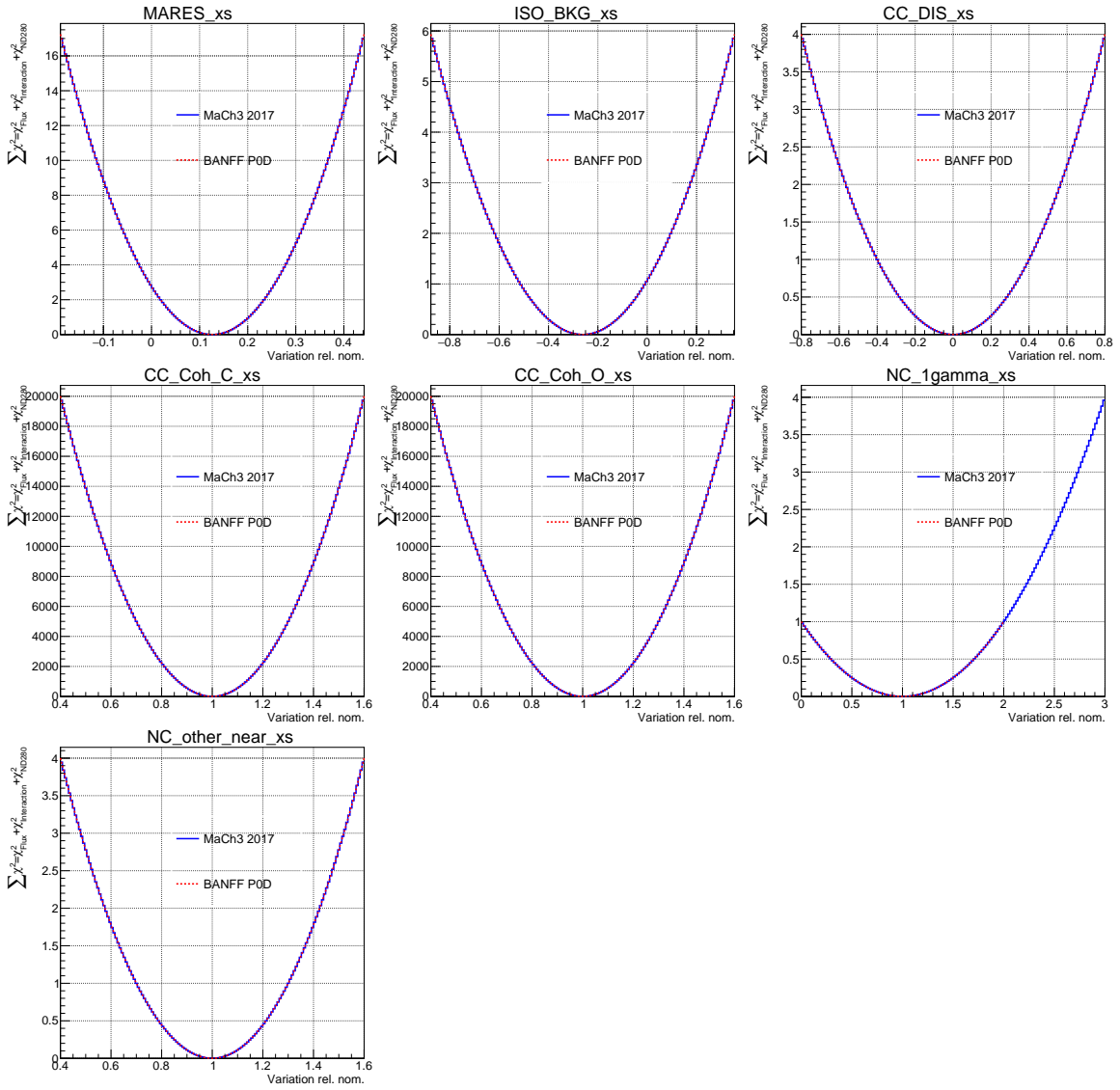












# Appendix G

## Computing Resources

This appendix provides the details on the computing resources used to produce the BANFF fit. All the computing resources were provided by the W. M. Keck high performance computing (HPC) cluster at Colorado State University. The HPC cluster is maintained by the Engineering Technology Services team at the Walter Scott, Jr. College of Engineering. A list of the computing resources used in this thesis is provided in Table G.1 on page 328.

The HPC cluster has a dedicated batch queue scheduler which supports the OpenMP and MPI parallel processing environments. While the user can restrict jobs to specific compute nodes in the batch queue, the scheduler will assign jobs to any available nodes on a first come, first serve basis with some exceptions. The BANFF fit studies in this thesis usually used the default scheduler options except when to prioritize certain jobs over others. The typical resource usage is explained in the next paragraph.

**Table G.1:** Computing resources used in this thesis.

Avail. nodes	Node CPU	#CPUs per node	#cores per CPU	Clock rate [GHz]	Cache [MB]	RAM [GB]
19	Xeon E5-2640	2	6	2.5	15	256
7	Xeon E5-2620 v3			2.4		64
4						256
15	Xeon E5-2620 v4		8	2.1	20	64

The PØD-only data BANFF fit result was calculated using a compute node with two E5-2620 v4 central processing units (CPUs) and 64 GB of random access memory (RAM). The data and Monte Carlo (MC) events are loaded in RAM from binary ROOT [26] files that are stored on the HPC cluster’s hard disk drives. The total job time was 27.5 hours using the OpenMP parallel processing environment with all 16 cores employed, which is reasonable in terms of large scale computational work. This includes loading the data and MC, finding the global minimum, and calculating the Hess matrix. However, a significant fraction of the time, about 6.2 hours, was spent preparing the fit by preloading the data and MC events into RAM. The maximum consumed RAM for the fit was about 40 GB.

In exploring a joint PØD+FGD BANFF fit using the canonical T2K 2018 cross section parameterization, the Asimov fit job required two weeks to complete, or about 10 times longer than the PØD-only Asimov fit. The significant increase in job “walltime” is because the number of fit parameters almost doubled in comparison. This illustrates the nonlinear relationship between the required fit time versus number of fit parameters. Additionally, when using the actual PØD+FGD data, the fit failed to converge on a global minimum due to machine precision limits. So for a future joint analysis, careful consideration on the number of needed fit parameters is necessary.

## Appendix H

### The PØD-Only Postfit Parameters

In this appendix is the complete listing of the fit parameters, both in prefit and postfit values. The parameters are listed in Table H.1 on page 331. The first 50 are ND280 flux parameters then followed by 50 SK flux parameters as defined in Table 4.1 on page 104,. Between 100 and 561 are the bin normalization parameters defined in Appendix B. The last 31 are cross section parameters as defined in Table 4.4 on page 135.

---

**Table H.1:** Prefit and postfit parameters with errors.

Index	Prefit	$\pm$ error	Postfit	$\pm$ error
0	1.00	0.10	1.03	0.06
1	1.00	0.10	1.02	0.05
2	1.00	0.09	1.02	0.05
3	1.00	0.09	1.03	0.05
4	1.00	0.11	0.99	0.05
5	1.00	0.10	0.97	0.04
6	1.00	0.07	1.04	0.04
7	1.00	0.07	1.07	0.04
8	1.00	0.08	1.05	0.04
9	1.00	0.10	0.99	0.04
10	1.00	0.11	0.96	0.04
11	1.00	0.10	1.11	0.08
12	1.00	0.08	1.06	0.06
13	1.00	0.08	1.07	0.06
14	1.00	0.09	1.12	0.06
15	1.00	0.09	1.13	0.07
16	1.00	0.09	1.01	0.05
17	1.00	0.09	1.02	0.05
18	1.00	0.08	1.04	0.05
19	1.00	0.08	1.05	0.04
20	1.00	0.08	1.03	0.04
21	1.00	0.08	1.05	0.04
22	1.00	0.10	1.03	0.06
23	1.00	0.07	1.08	0.06
24	1.00	0.14	1.22	0.12

Index	Prefit	$\pm$ error	Postfit	$\pm$ error
25	1.00	0.09	1.10	0.07
26	1.00	0.08	1.10	0.05
27	1.00	0.08	1.10	0.05
28	1.00	0.08	1.09	0.05
29	1.00	0.08	1.12	0.04
30	1.00	0.11	1.05	0.07
31	1.00	0.10	1.03	0.05
32	1.00	0.09	1.06	0.05
33	1.00	0.08	1.07	0.04
34	1.00	0.11	1.09	0.05
35	1.00	0.10	1.07	0.05
36	1.00	0.07	1.04	0.05
37	1.00	0.07	1.04	0.05
38	1.00	0.09	1.04	0.06
39	1.00	0.09	1.09	0.06
40	1.00	0.13	1.17	0.08
41	1.00	0.07	1.10	0.05
42	1.00	0.09	1.14	0.07
43	1.00	0.10	1.03	0.06
44	1.00	0.09	1.05	0.05
45	1.00	0.09	1.08	0.06
46	1.00	0.08	1.05	0.05
47	1.00	0.08	1.09	0.05
48	1.00	0.09	1.10	0.06
49	1.00	0.16	1.14	0.13
50	1.00	0.10	1.02	0.06

Index	Prefit	$\pm$ error	Postfit	$\pm$ error
51	1.00	0.10	1.01	0.06
52	1.00	0.09	1.03	0.05
53	1.00	0.08	1.05	0.05
54	1.00	0.10	1.02	0.06
55	1.00	0.08	1.01	0.05
56	1.00	0.07	1.04	0.05
57	1.00	0.07	1.04	0.05
58	1.00	0.09	1.04	0.04
59	1.00	0.10	1.00	0.04
60	1.00	0.11	0.98	0.05
61	1.00	0.10	1.11	0.08
62	1.00	0.08	1.08	0.05
63	1.00	0.08	1.10	0.06
64	1.00	0.08	1.12	0.06
65	1.00	0.09	1.11	0.06
66	1.00	0.09	1.02	0.05
67	1.00	0.09	1.03	0.05
68	1.00	0.08	1.04	0.05
69	1.00	0.08	1.05	0.04
70	1.00	0.08	1.05	0.04
71	1.00	0.08	1.06	0.04
72	1.00	0.09	1.07	0.06
73	1.00	0.07	1.09	0.05
74	1.00	0.13	1.18	0.11
75	1.00	0.09	1.10	0.07
76	1.00	0.08	1.07	0.05

Index	Prefit	$\pm$ error	Postfit	$\pm$ error
77	1.00	0.07	1.10	0.05
78	1.00	0.08	1.10	0.05
79	1.00	0.08	1.07	0.05
80	1.00	0.11	1.04	0.07
81	1.00	0.10	1.02	0.06
82	1.00	0.09	1.03	0.05
83	1.00	0.08	1.06	0.05
84	1.00	0.10	1.09	0.06
85	1.00	0.09	1.05	0.05
86	1.00	0.07	1.04	0.05
87	1.00	0.07	1.08	0.05
88	1.00	0.09	1.04	0.06
89	1.00	0.08	1.07	0.06
90	1.00	0.12	1.06	0.09
91	1.00	0.07	1.09	0.05
92	1.00	0.08	1.11	0.06
93	1.00	0.10	1.04	0.06
94	1.00	0.09	1.04	0.05
95	1.00	0.09	1.06	0.05
96	1.00	0.08	1.05	0.04
97	1.00	0.08	1.10	0.05
98	1.00	0.09	1.11	0.06
99	1.00	0.15	1.15	0.12
100	1.21	0.67	1.00	0.04
101	0.87	0.18	0.96	0.03
102	1.12	0.44	0.96	0.04

Index	Prefit	$\pm$ error	Postfit	$\pm$ error
103	1.13	0.43	0.99	0.05
104	1.02	0.17	0.96	0.08
105	0.93	0.20	0.84	0.09
106	1.00	0.28	1.05	0.05
107	0.82	0.33	0.93	0.04
108	1.26	0.58	0.94	0.03
109	1.27	0.74	0.92	0.04
110	0.89	0.18	0.95	0.03
111	1.02	0.27	0.93	0.03
112	1.09	0.33	0.96	0.04
113	1.02	0.17	0.91	0.04
114	0.96	0.15	0.92	0.03
115	0.99	0.21	0.97	0.04
116	0.94	0.29	0.96	0.06
117	1.05	0.53	0.94	0.07
118	1.33	0.78	0.99	0.05
119	0.91	0.21	0.95	0.03
120	0.97	0.14	0.93	0.03
121	1.03	0.17	0.94	0.03
122	1.01	0.09	0.93	0.03
123	1.00	0.05	0.94	0.04
124	1.00	0.12	0.91	0.08
125	0.95	0.15	0.98	0.08
126	0.96	0.38	0.88	0.04
127	1.29	0.73	0.95	0.04
128	0.93	0.22	0.96	0.03

Index	Prefit	$\pm$ error	Postfit	$\pm$ error
129	0.96	0.09	0.92	0.03
130	1.02	0.11	0.94	0.03
131	1.00	0.07	0.93	0.03
132	1.00	0.03	0.93	0.03
133	0.99	0.08	0.89	0.03
134	1.00	0.14	0.92	0.04
135	0.99	0.20	0.99	0.04
136	1.25	0.65	0.94	0.07
137	0.94	0.20	0.95	0.04
138	0.95	0.08	0.93	0.03
139	1.01	0.11	0.94	0.03
140	1.00	0.07	0.93	0.03
141	1.00	0.06	0.94	0.03
142	1.00	0.03	0.93	0.03
143	0.98	0.10	0.90	0.03
144	0.97	0.14	0.88	0.03
145	1.25	0.58	1.00	0.06
146	0.93	0.18	0.91	0.04
147	0.96	0.11	0.89	0.03
148	1.01	0.11	0.94	0.03
149	1.01	0.08	0.95	0.03
150	1.01	0.10	0.95	0.03
151	1.00	0.06	0.95	0.03
152	1.00	0.05	0.93	0.03
153	0.98	0.10	0.90	0.03
154	1.18	0.61	0.95	0.03

Index	Prefit	$\pm$ error	Postfit	$\pm$ error
155	0.89	0.15	0.95	0.03
156	1.01	0.16	0.96	0.04
157	1.03	0.19	1.02	0.04
158	1.02	0.15	1.16	0.07
159	1.04	0.16	0.87	0.04
160	0.93	0.26	0.81	0.05
161	0.94	0.67	0.89	0.06
162	1.13	0.56	0.90	0.03
163	0.92	0.15	0.93	0.03
164	0.98	0.07	0.93	0.03
165	1.00	0.09	0.93	0.03
166	1.01	0.08	0.93	0.03
167	1.01	0.06	0.88	0.04
168	0.98	0.16	0.84	0.05
169	0.98	0.52	0.89	0.05
170	1.13	0.53	0.95	0.03
171	0.92	0.14	0.93	0.03
172	0.98	0.05	0.92	0.03
173	1.00	0.07	0.92	0.03
174	1.00	0.06	0.92	0.03
175	1.01	0.05	0.89	0.03
176	0.99	0.12	0.95	0.03
177	1.03	0.46	0.99	0.03
178	1.13	0.52	0.94	0.03
179	0.94	0.13	0.94	0.04
180	0.97	0.06	0.92	0.03

Index	Prefit	$\pm$ error	Postfit	$\pm$ error
181	0.99	0.08	0.92	0.03
182	1.00	0.07	0.94	0.03
183	1.00	0.03	0.95	0.03
184	0.99	0.10	0.89	0.04
185	0.98	0.25	0.92	0.06
186	1.09	0.47	0.95	0.04
187	0.96	0.11	0.94	0.03
188	0.96	0.09	0.95	0.03
189	1.00	0.09	0.92	0.04
190	1.01	0.09	0.93	0.03
191	1.01	0.08	0.94	0.03
192	0.99	0.05	0.92	0.03
193	0.97	0.13	0.87	0.03
194	1.00	0.36	0.97	0.03
195	0.90	0.15	0.95	0.03
196	1.05	0.26	0.92	0.04
197	1.04	0.20	0.93	0.04
198	1.00	0.17	0.94	0.06
199	1.01	0.17	0.92	0.06
200	1.00	0.39	0.97	0.06
201	1.06	0.43	0.97	0.04
202	0.91	0.13	0.95	0.03
203	0.97	0.16	0.93	0.04
204	1.04	0.17	0.94	0.04
205	1.00	0.11	0.92	0.05
206	0.99	0.11	0.88	0.05

Index	Prefit	$\pm$ error	Postfit	$\pm$ error
207	0.92	0.28	0.99	0.05
208	1.07	0.44	0.95	0.05
209	0.93	0.14	0.94	0.04
210	0.96	0.11	0.94	0.03
211	1.03	0.14	0.95	0.03
212	1.01	0.08	0.95	0.03
213	0.98	0.06	0.87	0.05
214	0.95	0.17	0.89	0.08
215	1.08	0.45	0.91	0.05
216	0.93	0.16	0.95	0.03
217	0.96	0.09	0.93	0.03
218	1.02	0.12	0.94	0.03
219	1.01	0.07	0.94	0.03
220	1.00	0.04	0.93	0.03
221	0.98	0.09	0.91	0.04
222	1.09	0.43	0.92	0.04
223	0.94	0.15	0.94	0.04
224	0.93	0.10	0.93	0.04
225	1.02	0.12	0.94	0.04
226	1.01	0.08	0.96	0.04
227	1.00	0.07	0.95	0.03
228	0.99	0.05	0.92	0.03
229	1.02	0.34	0.96	0.04
230	1.00	0.09	0.94	0.04
231	1.01	0.07	0.95	0.04
232	0.99	0.13	0.93	0.05

Index	Prefit	$\pm$ error	Postfit	$\pm$ error
233	0.99	0.11	0.92	0.07
234	0.98	0.33	0.97	0.06
235	1.05	0.34	0.95	0.04
236	0.97	0.05	0.93	0.03
237	1.02	0.06	0.95	0.03
238	0.98	0.09	0.93	0.03
239	0.99	0.06	0.92	0.03
240	0.98	0.14	0.92	0.06
241	1.04	0.36	0.92	0.05
242	0.97	0.05	0.93	0.04
243	1.01	0.05	0.94	0.04
244	1.00	0.09	0.93	0.04
245	1.01	0.06	0.93	0.04
246	0.98	0.12	0.84	0.07
247	1.03	0.37	0.90	0.05
248	1.01	0.05	0.94	0.04
249	1.00	0.05	0.92	0.04
250	0.99	0.07	0.92	0.03
251	1.01	0.07	0.92	0.03
252	0.99	0.07	0.85	0.04
253	1.07	0.39	0.84	0.05
254	0.98	0.07	0.93	0.04
255	1.02	0.08	0.99	0.04
256	1.01	0.08	0.94	0.04
257	0.99	0.09	0.91	0.04
258	0.99	0.06	0.87	0.04

Index	Prefit	$\pm$ error	Postfit	$\pm$ error
259	1.24	0.60	1.00	0.08
260	0.91	0.16	0.94	0.05
261	1.00	0.13	0.95	0.05
262	1.02	0.21	0.94	0.06
263	1.03	0.17	0.94	0.08
264	0.99	0.21	1.11	0.14
265	1.27	0.64	1.03	0.15
266	0.95	0.16	0.95	0.06
267	0.99	0.06	0.92	0.05
268	0.98	0.11	0.93	0.05
269	1.04	0.14	0.93	0.06
270	0.99	0.16	0.91	0.11
271	1.20	0.60	0.94	0.11
272	0.95	0.20	0.93	0.06
273	0.97	0.07	0.94	0.05
274	1.00	0.08	0.94	0.04
275	1.00	0.08	0.93	0.04
276	1.00	0.10	0.97	0.07
277	1.10	0.52	0.93	0.09
278	0.99	0.16	0.96	0.06
279	0.95	0.06	0.91	0.05
280	0.99	0.04	0.94	0.04
281	1.00	0.07	0.93	0.03
282	1.00	0.06	0.95	0.04
283	1.19	0.50	0.95	0.09
284	0.98	0.15	0.99	0.07

Index	Prefit	$\pm$ error	Postfit	$\pm$ error
285	0.96	0.09	0.97	0.07
286	0.99	0.07	0.91	0.06
287	1.00	0.06	0.94	0.03
288	1.00	0.04	0.92	0.03
289	1.12	0.46	1.00	0.07
290	1.01	0.15	0.91	0.06
291	0.98	0.09	0.90	0.05
292	1.00	0.09	0.94	0.05
293	0.98	0.07	0.92	0.03
294	1.00	0.03	0.92	0.03
295	1.29	0.47	1.04	0.11
296	0.98	0.20	1.10	0.12
297	0.95	0.16	0.92	0.09
298	1.03	0.10	0.95	0.05
299	1.01	0.08	0.98	0.03
300	1.00	0.03	0.93	0.03
301	0.97	0.21	0.90	0.07
302	1.01	0.13	1.00	0.06
303	1.01	0.15	0.99	0.06
304	1.15	0.19	1.12	0.07
305	0.95	0.23	0.90	0.12
306	1.00	0.26	0.99	0.07
307	0.99	0.08	0.91	0.05
308	1.01	0.11	0.93	0.04
309	0.98	0.09	0.89	0.06
310	1.00	0.16	0.87	0.05

Index	Prefit	$\pm$ error	Postfit	$\pm$ error
311	1.01	0.28	0.86	0.08
312	0.98	0.06	0.90	0.05
313	1.00	0.08	0.93	0.04
314	1.02	0.08	0.92	0.05
315	0.98	0.11	0.93	0.07
316	1.02	0.25	0.92	0.05
317	0.98	0.07	0.90	0.06
318	1.00	0.07	0.92	0.04
319	1.00	0.07	0.94	0.04
320	1.00	0.06	0.90	0.06
321	1.02	0.24	0.91	0.08
322	0.96	0.10	0.99	0.05
323	1.01	0.09	0.95	0.05
324	0.99	0.09	0.93	0.04
325	0.99	0.04	0.92	0.03
326	1.00	0.25	0.94	0.08
327	0.98	0.11	0.97	0.07
328	1.00	0.09	0.93	0.03
329	1.01	0.10	1.00	0.04
330	1.00	0.04	0.94	0.03
331	1.17	0.66	0.94	0.05
332	0.86	0.19	0.95	0.03
333	1.17	0.53	0.92	0.04
334	1.15	0.44	0.93	0.06
335	0.97	0.19	0.90	0.09
336	1.02	0.19	1.18	0.11

Index	Prefit	$\pm$ error	Postfit	$\pm$ error
337	1.02	0.31	0.96	0.04
338	0.97	0.37	0.91	0.04
339	0.88	0.62	0.92	0.03
340	1.27	0.75	0.90	0.04
341	0.87	0.17	0.95	0.03
342	1.04	0.31	0.94	0.03
343	1.09	0.34	0.95	0.04
344	1.01	0.18	0.91	0.04
345	1.03	0.17	0.91	0.03
346	0.94	0.27	0.94	0.04
347	0.93	0.38	0.99	0.06
348	1.00	0.58	0.96	0.08
349	1.32	0.79	0.98	0.06
350	0.90	0.20	0.95	0.03
351	0.98	0.17	0.93	0.03
352	1.04	0.19	0.93	0.03
353	1.01	0.10	0.98	0.04
354	1.00	0.07	0.94	0.05
355	0.97	0.14	0.86	0.10
356	1.06	0.22	1.09	0.11
357	1.00	0.33	0.88	0.04
358	1.29	0.73	0.91	0.04
359	0.91	0.20	0.97	0.03
360	0.97	0.11	0.95	0.03
361	1.02	0.12	0.94	0.03
362	1.00	0.07	0.93	0.03

Index	Prefit	$\pm$ error	Postfit	$\pm$ error
363	1.01	0.04	0.95	0.03
364	0.98	0.09	0.91	0.04
365	0.98	0.15	0.99	0.04
366	0.98	0.21	0.97	0.04
367	1.23	0.68	0.94	0.09
368	0.91	0.20	0.94	0.04
369	0.98	0.12	0.94	0.04
370	1.02	0.11	0.94	0.03
371	0.99	0.08	0.93	0.03
372	1.01	0.06	0.96	0.03
373	1.00	0.04	0.93	0.03
374	0.98	0.11	0.89	0.03
375	0.98	0.15	0.89	0.04
376	1.21	0.58	0.96	0.08
377	0.90	0.16	0.91	0.04
378	0.99	0.12	0.97	0.04
379	1.02	0.12	0.93	0.04
380	1.01	0.09	0.95	0.04
381	1.01	0.10	0.95	0.03
382	1.00	0.06	0.95	0.03
383	1.00	0.05	0.93	0.03
384	0.98	0.10	0.89	0.03
385	1.18	0.62	0.94	0.04
386	0.88	0.15	0.96	0.03
387	1.03	0.21	0.98	0.04
388	1.03	0.21	1.02	0.04

Index	Prefit	$\pm$ error	Postfit	$\pm$ error
389	1.01	0.16	1.18	0.07
390	1.00	0.22	0.88	0.04
391	0.99	0.32	0.93	0.05
392	0.93	0.69	1.00	0.06
393	1.13	0.58	0.92	0.03
394	0.91	0.14	0.94	0.03
395	0.99	0.10	0.92	0.03
396	1.01	0.11	0.95	0.03
397	1.01	0.08	0.93	0.03
398	1.00	0.08	0.91	0.04
399	1.03	0.18	0.91	0.05
400	0.97	0.51	0.84	0.05
401	1.12	0.55	0.94	0.03
402	0.92	0.13	0.93	0.03
403	0.99	0.08	0.95	0.03
404	1.00	0.08	0.93	0.03
405	1.01	0.07	0.91	0.03
406	1.00	0.06	0.89	0.03
407	0.98	0.13	0.88	0.03
408	0.93	0.45	0.96	0.03
409	1.09	0.51	0.95	0.03
410	0.93	0.11	0.93	0.04
411	0.99	0.08	0.91	0.04
412	1.00	0.08	0.91	0.03
413	1.00	0.07	0.95	0.03
414	1.00	0.03	0.94	0.03

Index	Preft	$\pm$ error	Postfit	$\pm$ error
415	0.99	0.10	0.89	0.04
416	0.97	0.28	0.96	0.07
417	1.09	0.48	0.95	0.05
418	0.94	0.12	0.95	0.03
419	0.98	0.11	0.94	0.03
420	1.01	0.10	0.92	0.04
421	1.01	0.09	0.94	0.04
422	1.01	0.07	0.94	0.03
423	0.99	0.06	0.91	0.03
424	0.97	0.13	0.87	0.03
425	0.99	0.29	0.94	0.04
426	0.92	0.14	0.93	0.03
427	1.05	0.24	0.88	0.04
428	1.05	0.18	0.92	0.05
429	1.02	0.17	0.83	0.08
430	0.87	0.19	0.96	0.07
431	0.96	0.41	0.79	0.06
432	1.03	0.35	0.99	0.05
433	0.91	0.12	0.94	0.04
434	1.00	0.16	0.91	0.05
435	1.03	0.15	0.87	0.05
436	0.99	0.12	0.93	0.05
437	0.99	0.15	0.91	0.05
438	0.93	0.31	0.90	0.05
439	1.05	0.37	0.90	0.06
440	0.92	0.11	0.95	0.04

Index	Prefit	$\pm$ error	Postfit	$\pm$ error
441	0.98	0.12	0.93	0.04
442	1.03	0.12	0.94	0.04
443	1.02	0.08	0.99	0.04
444	0.97	0.08	0.84	0.06
445	0.97	0.19	0.78	0.10
446	1.06	0.37	0.92	0.06
447	0.93	0.12	0.95	0.04
448	0.97	0.11	0.91	0.04
449	1.02	0.10	0.94	0.04
450	1.00	0.07	0.93	0.04
451	0.99	0.04	0.92	0.04
452	0.99	0.10	0.90	0.05
453	1.07	0.35	0.97	0.05
454	0.89	0.12	0.94	0.05
455	0.99	0.11	0.94	0.05
456	1.02	0.11	0.94	0.05
457	0.99	0.09	0.94	0.05
458	1.01	0.07	0.98	0.03
459	0.99	0.06	0.92	0.03
460	1.00	0.29	0.98	0.04
461	1.00	0.10	0.96	0.04
462	1.04	0.09	0.97	0.05
463	0.98	0.14	0.93	0.05
464	0.98	0.13	0.89	0.09
465	0.92	0.33	0.85	0.06
466	1.00	0.31	0.92	0.04

Index	Prefit	$\pm$ error	Postfit	$\pm$ error
467	0.99	0.06	0.93	0.03
468	1.02	0.06	0.95	0.03
469	0.99	0.11	0.93	0.03
470	0.99	0.06	0.94	0.04
471	0.96	0.16	0.98	0.06
472	1.00	0.32	0.92	0.05
473	1.00	0.07	0.92	0.04
474	1.00	0.06	0.95	0.04
475	1.00	0.11	0.90	0.04
476	1.00	0.06	0.92	0.04
477	0.99	0.13	0.88	0.07
478	1.03	0.32	0.90	0.05
479	0.99	0.07	0.93	0.04
480	1.02	0.07	0.93	0.04
481	0.99	0.10	0.92	0.04
482	1.01	0.08	0.93	0.04
483	0.98	0.09	0.78	0.04
484	1.02	0.31	0.76	0.05
485	1.01	0.07	0.96	0.05
486	1.02	0.08	0.94	0.05
487	0.98	0.10	0.91	0.04
488	1.00	0.09	0.92	0.04
489	0.99	0.07	0.87	0.04
490	1.10	0.50	0.93	0.09
491	0.92	0.12	0.96	0.06
492	1.03	0.16	0.96	0.07

Index	Prefit	$\pm$ error	Postfit	$\pm$ error
493	1.02	0.20	0.91	0.08
494	1.08	0.14	1.08	0.10
495	0.81	0.31	1.06	0.16
496	1.23	0.50	1.11	0.13
497	0.93	0.18	0.96	0.07
498	0.93	0.09	0.90	0.06
499	1.03	0.12	0.92	0.07
500	1.05	0.14	0.93	0.09
501	1.00	0.21	0.87	0.14
502	1.17	0.49	1.04	0.14
503	0.95	0.15	0.95	0.08
504	0.97	0.08	0.95	0.07
505	1.00	0.10	0.92	0.06
506	1.00	0.08	0.91	0.05
507	1.04	0.16	0.88	0.11
508	1.13	0.47	0.98	0.11
509	0.99	0.13	0.94	0.08
510	0.94	0.09	0.92	0.07
511	0.99	0.07	0.94	0.05
512	1.00	0.06	0.93	0.04
513	0.99	0.08	0.94	0.05
514	1.06	0.46	0.83	0.10
515	0.95	0.14	0.95	0.09
516	0.97	0.11	0.92	0.10
517	1.01	0.10	0.92	0.08
518	1.00	0.07	0.94	0.05

Index	Preft	$\pm$ error	Postfit	$\pm$ error
519	0.99	0.06	0.92	0.04
520	1.07	0.46	0.93	0.08
521	1.00	0.15	0.98	0.08
522	1.02	0.16	0.99	0.06
523	0.96	0.10	0.85	0.07
524	1.01	0.08	0.94	0.04
525	0.99	0.04	0.92	0.03
526	1.19	0.46	1.03	0.14
527	0.89	0.17	1.01	0.10
528	0.99	0.15	0.92	0.09
529	0.99	0.10	0.93	0.06
530	1.00	0.09	0.95	0.04
531	1.00	0.03	0.93	0.03
532	0.97	0.22	0.96	0.08
533	1.02	0.17	0.92	0.07
534	1.00	0.14	1.05	0.07
535	1.28	0.22	0.91	0.07
536	0.83	0.25	1.00	0.13
537	0.98	0.22	0.93	0.08
538	0.99	0.09	0.92	0.06
539	1.00	0.11	0.91	0.05
540	1.03	0.11	0.90	0.07
541	1.04	0.20	0.91	0.05
542	1.01	0.25	0.87	0.08
543	0.98	0.08	0.89	0.06
544	1.01	0.08	0.92	0.05

Index	Prefit	$\pm$ error	Postfit	$\pm$ error
545	1.00	0.08	0.95	0.06
546	0.99	0.12	0.99	0.08
547	0.99	0.22	0.92	0.05
548	1.00	0.10	0.95	0.07
549	1.01	0.07	0.93	0.05
550	1.00	0.07	0.93	0.05
551	1.00	0.07	0.87	0.07
552	1.00	0.22	0.95	0.09
553	0.99	0.12	0.90	0.05
554	1.04	0.10	0.96	0.06
555	0.99	0.10	0.90	0.05
556	0.99	0.04	0.91	0.04
557	1.01	0.24	0.99	0.09
558	0.99	0.16	0.80	0.10
559	0.97	0.12	0.91	0.04
560	1.06	0.10	0.94	0.04
561	1.00	0.04	0.96	0.03
562	0.00	0.41	-0.04	0.19
563	0.00	0.34	-0.03	0.18
564	0.00	0.50	0.03	0.26
565	0.00	0.41	-0.47	0.13
566	0.00	0.57	0.42	0.34
567	0.00	0.28	0.01	0.15
568	1.00	0.03	0.85	0.05
569	1.00	0.06	1.03	0.10
570	1.00	0.06	0.91	0.06

Index	Prefit	$\pm$ error	Postfit	$\pm$ error
571	1.00	1.00	2.71	0.31
572	1.00	1.00	1.32	0.25
573	1.00	0.20	0.94	0.13
574	1.00	3.00	2.00	0.09
575	1.00	3.00	2.00	0.21
576	0.59	0.12	0.53	0.07
577	1.05	0.21	1.63	0.13
578	1.13	0.17	1.28	0.13
579	0.88	0.35	1.12	0.33
580	1.20	0.10	1.20	0.10
581	0.95	0.15	0.86	0.07
582	1.13	0.16	1.12	0.04
583	0.74	0.31	1.04	0.18
584	1.00	0.03	1.00	0.03
585	1.00	0.03	1.00	0.03
586	0.00	0.40	-0.23	0.20
587	1.00	0.30	0.48	0.44
588	1.00	0.30	0.48	0.44
589	1.00	0.30	1.13	0.30
590	1.00	1.00	1.00	1.00
591	1.00	0.30	1.13	0.18
592	1.00	0.30	1.00	0.30

# Appendix I

## Postfit Receiver Operating Characteristic Curves

The receiver operating characteristic (ROC) curves for the PØD vs FGD-only fits are provided in this appendix. They provide a graphical diagnostic to interpret each fit's sensitivity in the fit parameter space. The first 50 (0-49) are the ND280 flux parameters. The next 50 (50-99) are the Super-Kamiokande flux parameters. The final set (100 - 131) are the cross section parameters.

The ROC curves are generated in the following manner. Each ROC curve measures the agreement of the PØD-only fit parameter estimate (PØD coverage) as a function of the FGD-only parameter estimate (FGD coverage). Since the postfit parameter uncertainties are assumed to be normally distributed, two normal distributions are used to evaluate the agreement using the respective fit mean and fit standard deviation. Each point on the ROC curve is the integrated overlap of each normal distribution.

The level of agreement is quantified using the Gini coefficient, which measures the inequality of the fit parameter space coverage. A Gini coefficient of 0 indicates maximal agreement of the two parameters mean and standard deviation, while a value of close to 1 indicates estimates are in strong tension. The coefficient is defined as the absolute difference

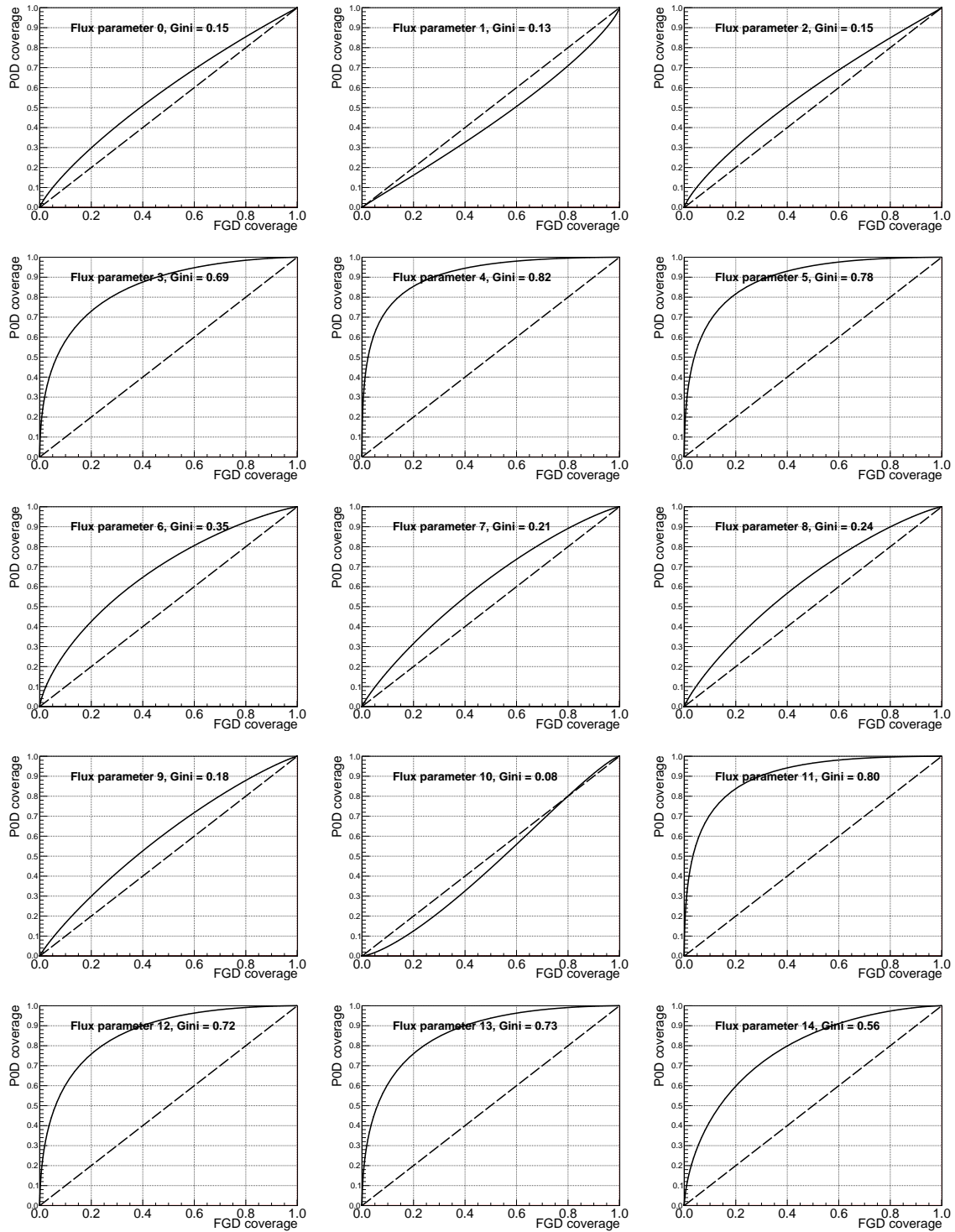
in area between the ROC curve and the diagonal (no-discrimination) line multiplied by two.

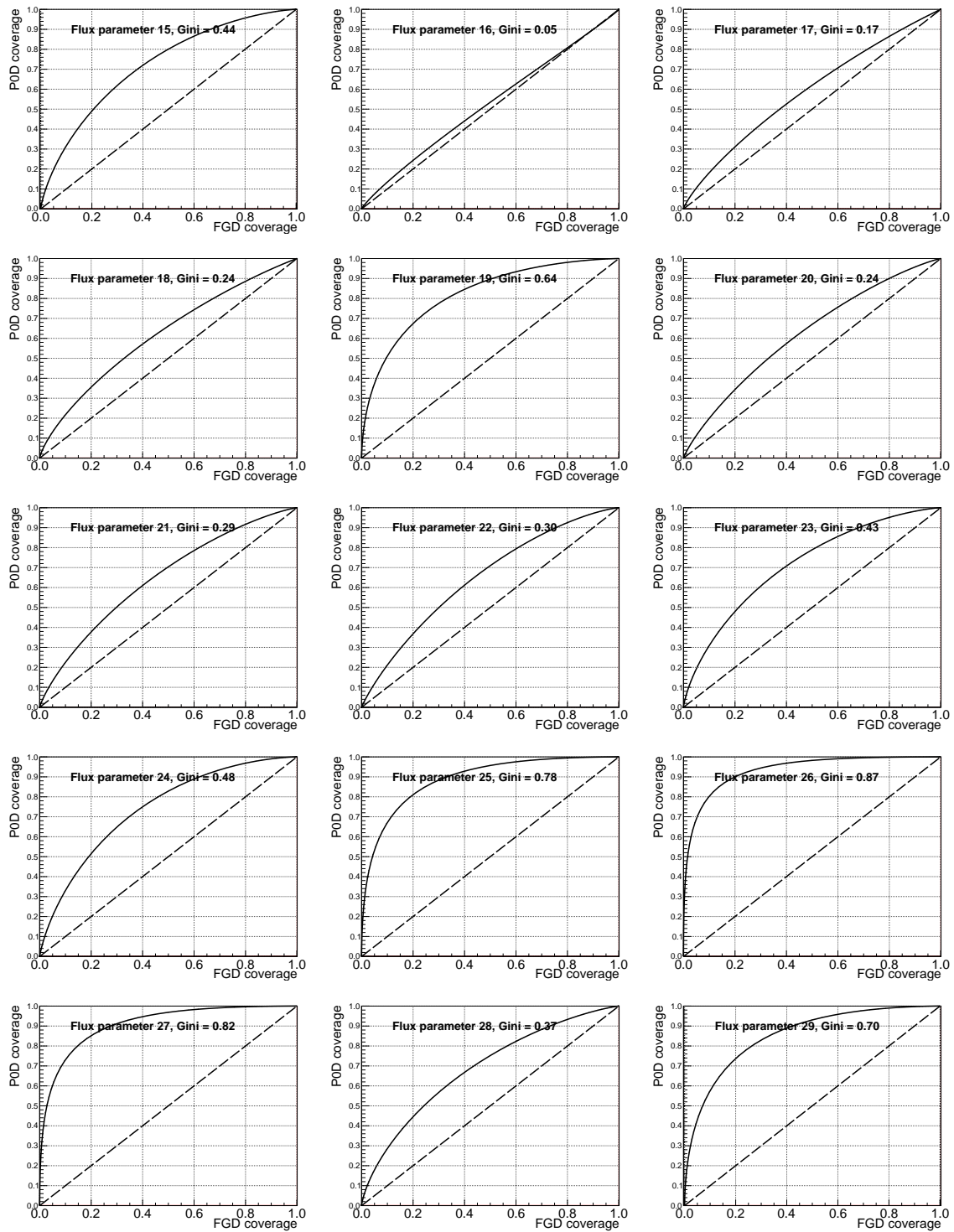
It is explicitly calculated as

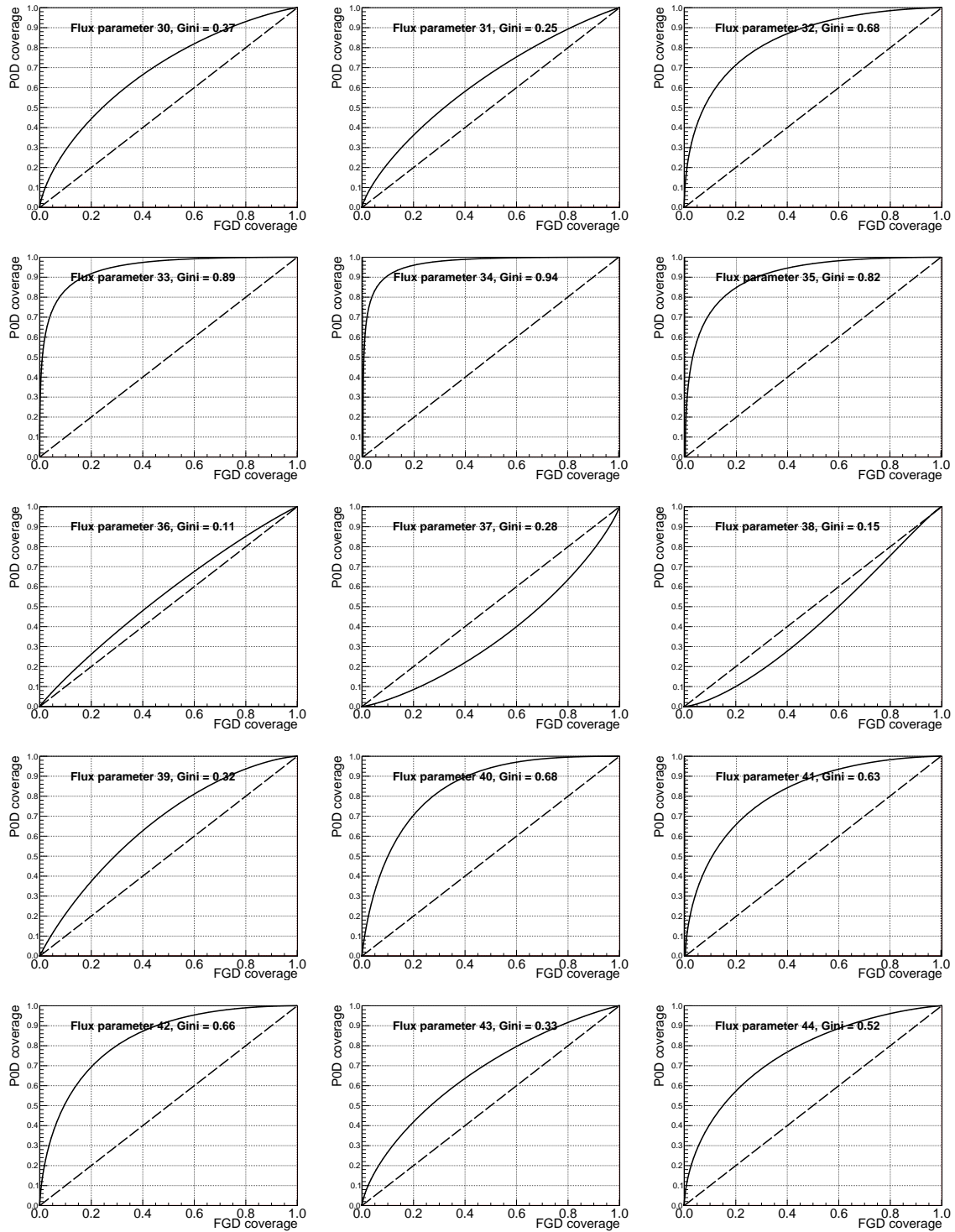
$$\begin{aligned}\text{Gini} &= 2 \left| \int_0^1 (\text{ROC}(x) - x) dx \right| \\ &= \left| 2 \int_0^1 \text{ROC}(x) dx - 1 \right|,\end{aligned}$$

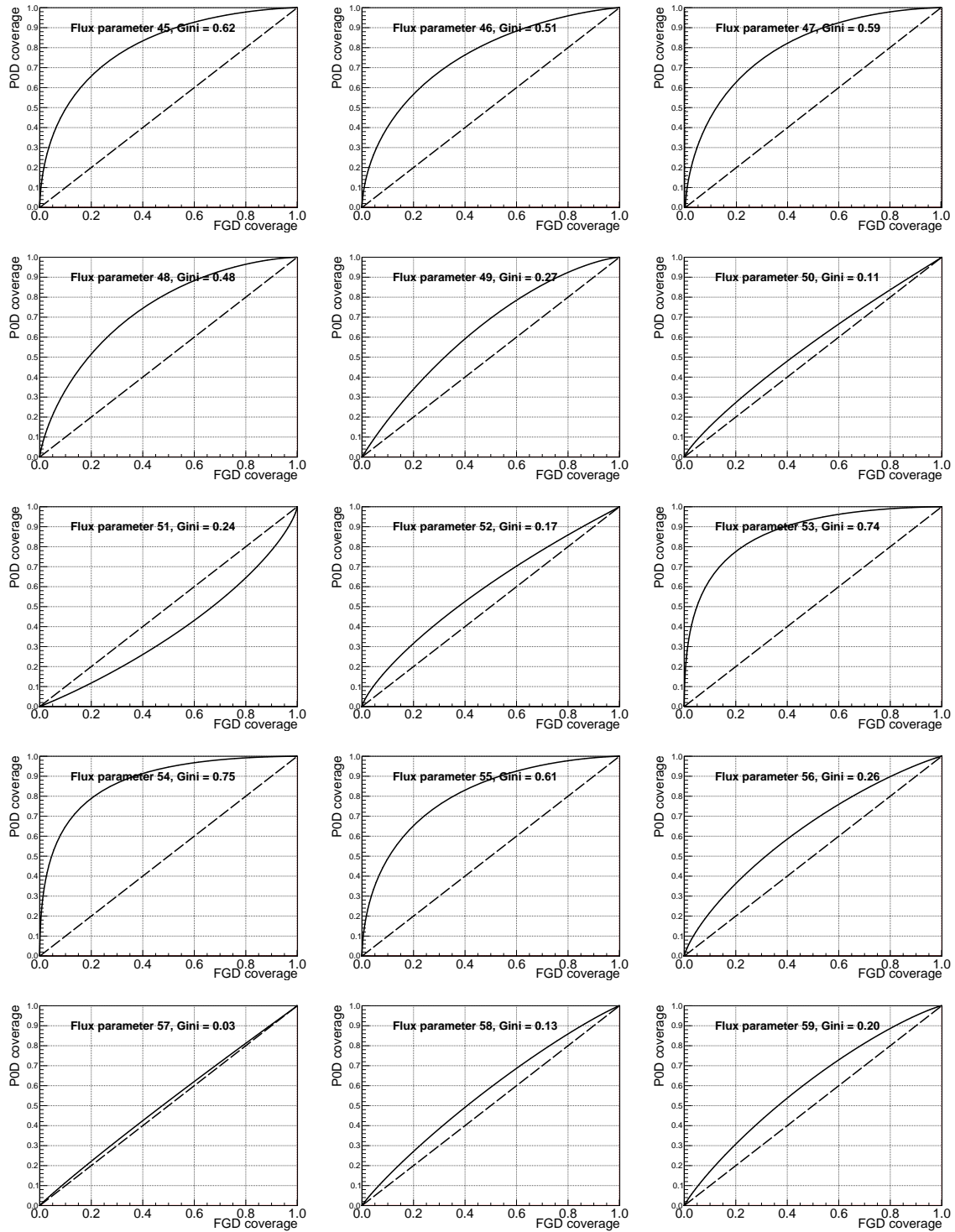
where  $\text{ROC}(x)$  is the PØD fit parameter space ROC curve as a function of the FGD fit parameter space coverage. This no-discrimination line is provided in each curve for the readers convenience.

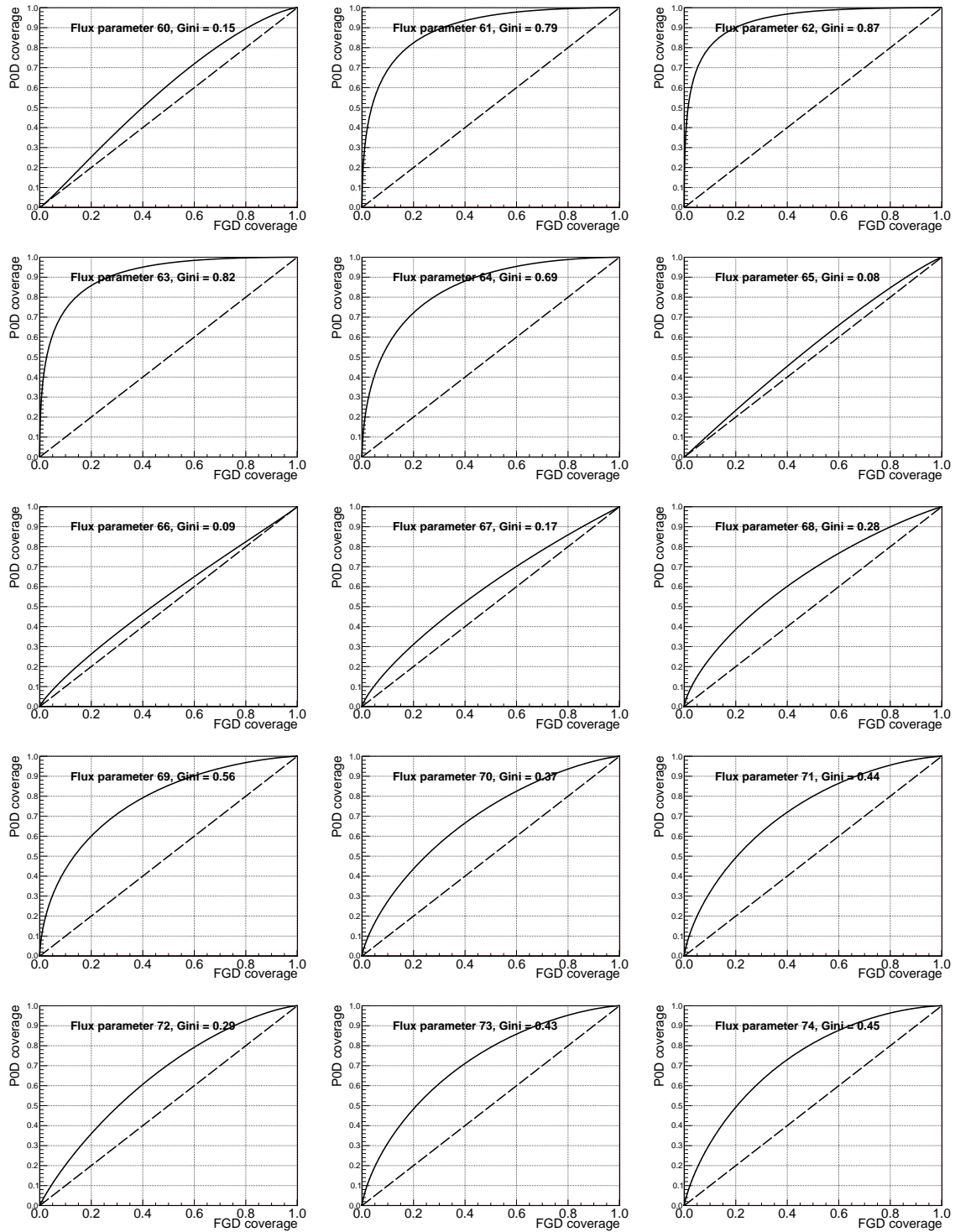
When the ROC curve is only above (below) the no-discrimination line, that means the PØD-only fit estimate prefers parameter values larger (smaller) than the FGD-only estimate. If the curve crosses the line once between  $(0, 1)$ , then the estimates are nearly identical and have a small Gini coefficient. If the ROC curve is diagonal, then the estimates are exactly the same with a Gini coefficient of zero. And finally, if the curve is a step function with the discontinuity at FGD coverage = 0, the parameter estimates are very different with a Gini coefficient of one.

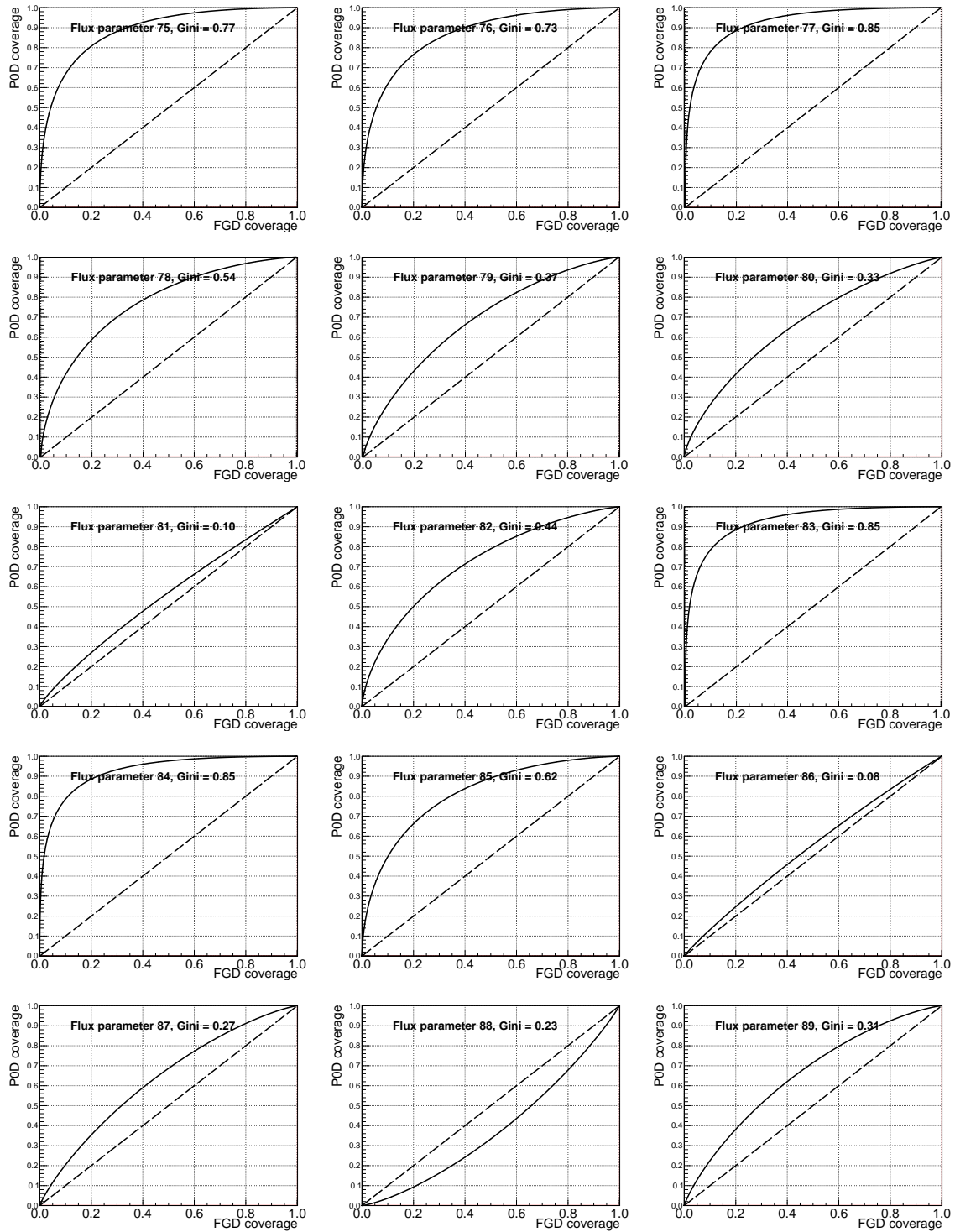


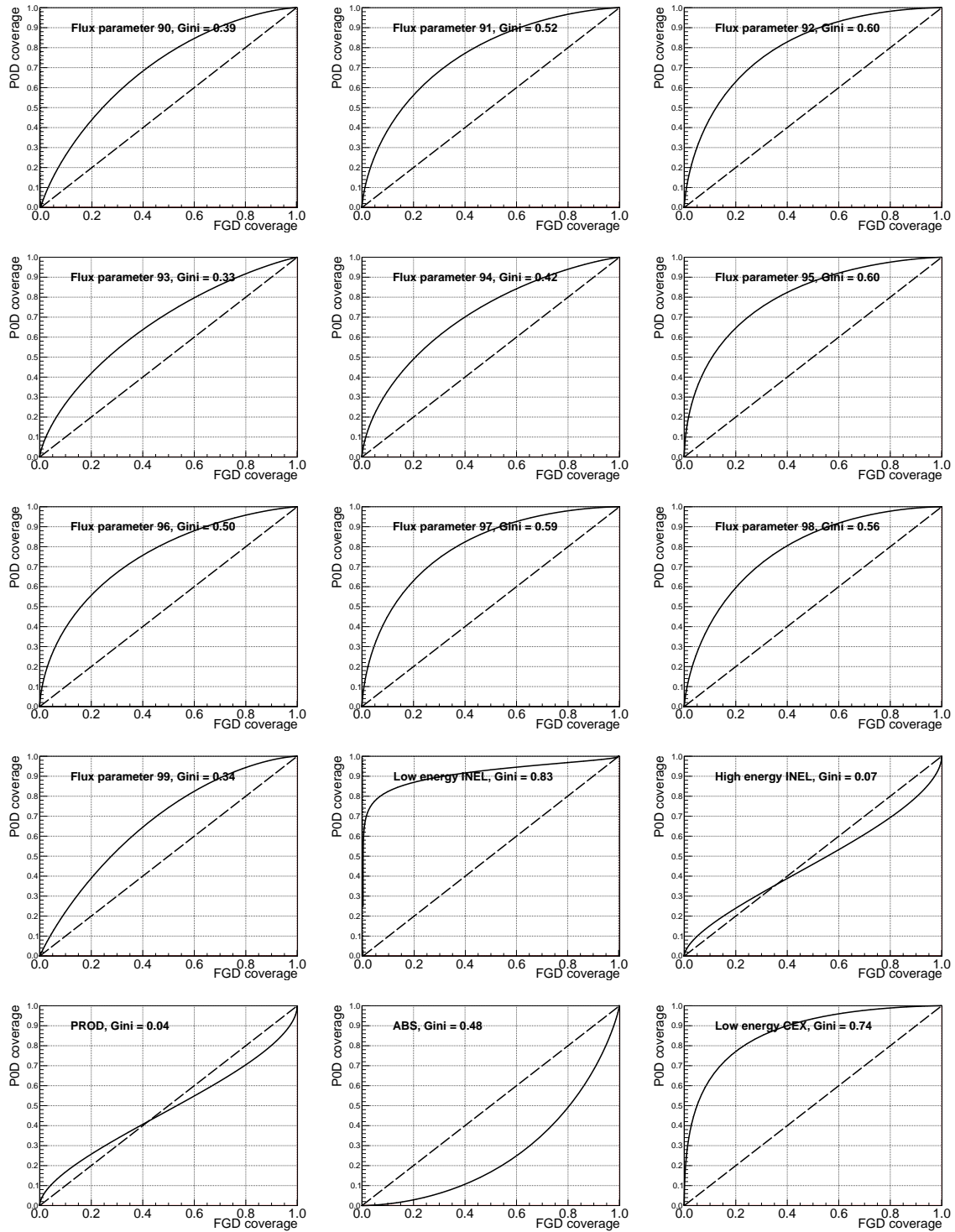


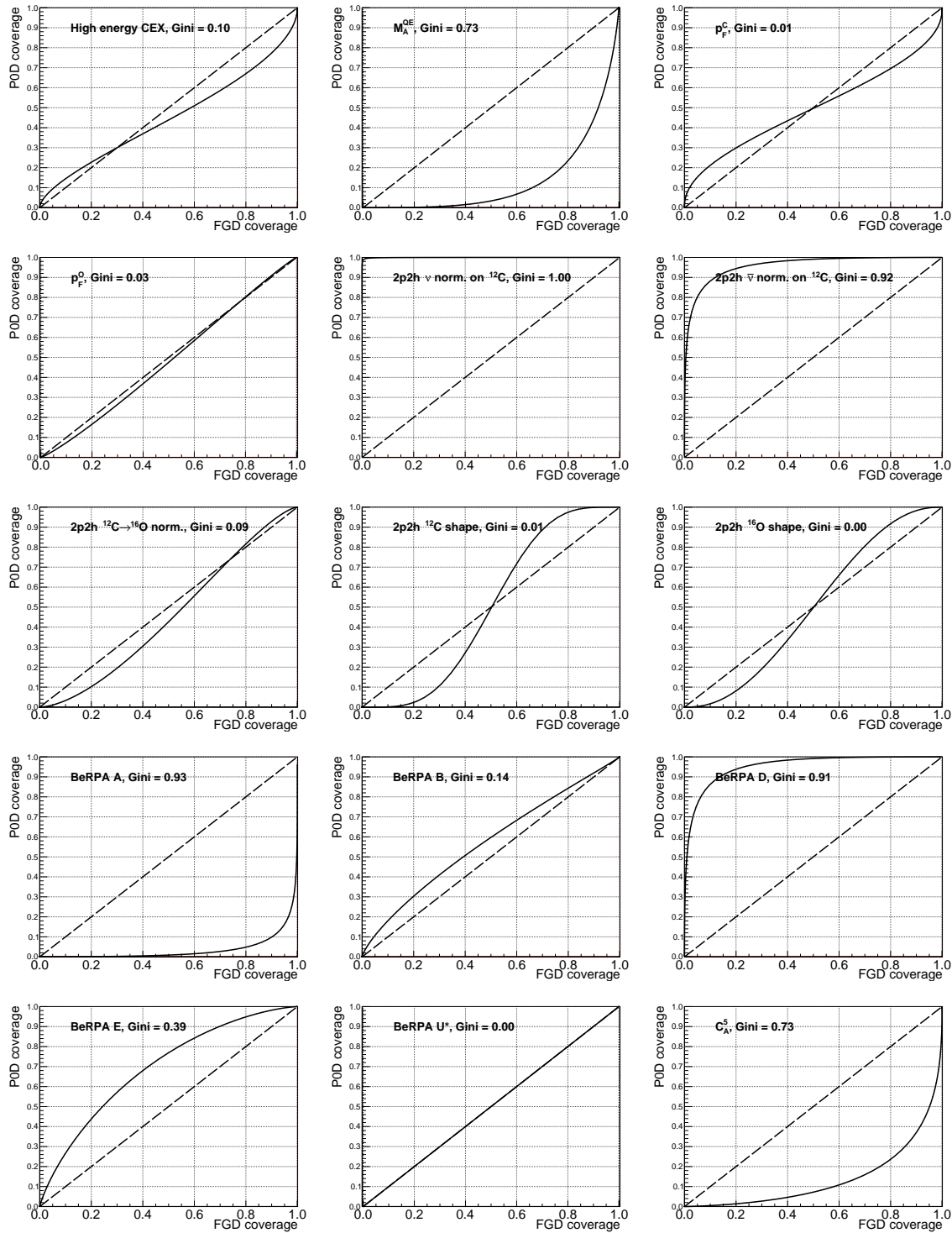


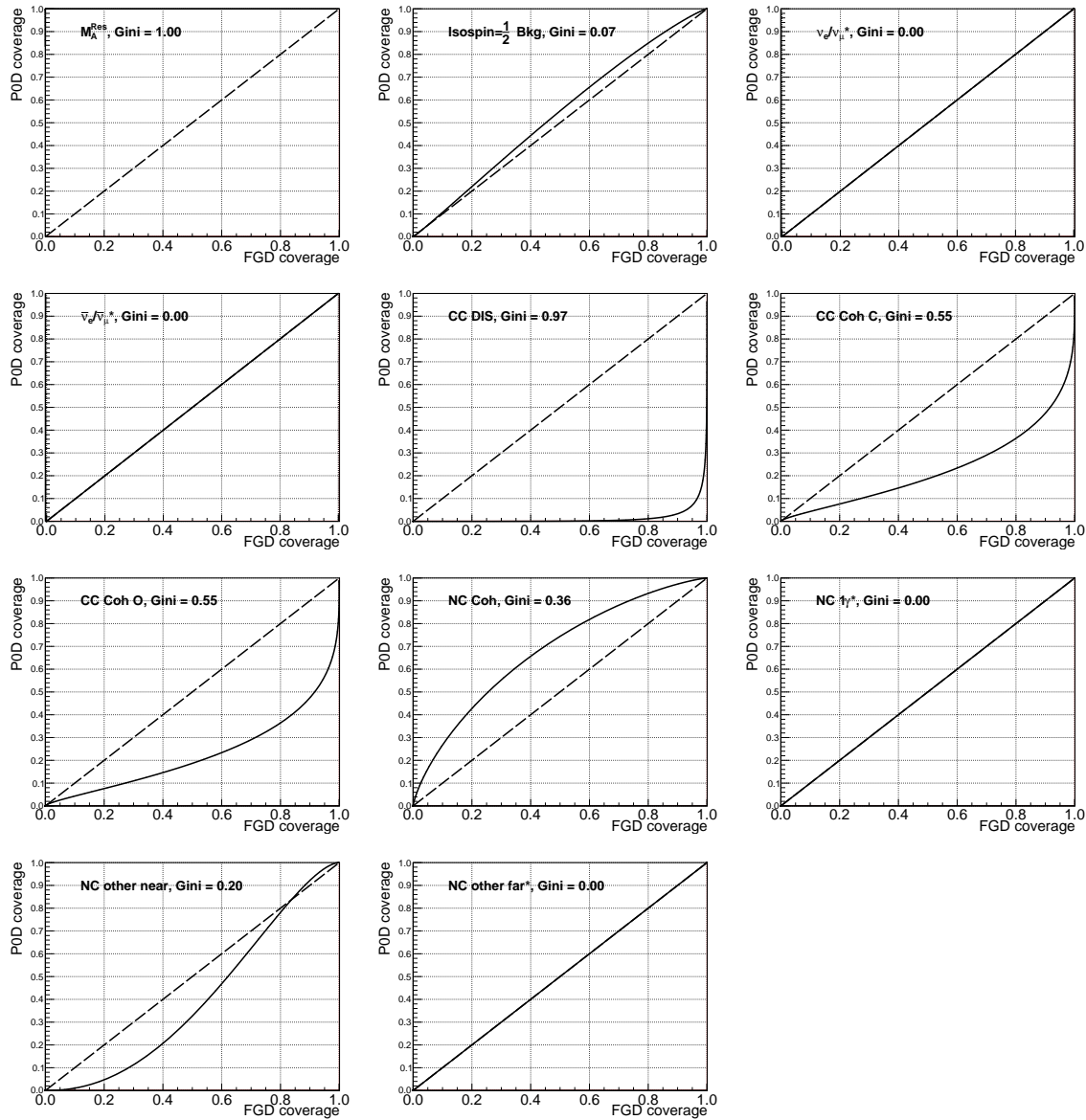












# Appendix J

## Cross-Validated PØD-Only BANFF Fit

This appendix shows the postfit results of cross validated PØD-only fit discussed in Chapter 7. The cross validation error Eqn. (1.42) was minimized with a regularization strength of  $\lambda = 1.4$ . That is to say the penalty term in the test statistic went from

$$\chi_{\text{Penalty}}^2 = (\Delta \vec{y})^T V^{-1} (\Delta \vec{y})$$

to

$$\chi_{\text{Penalty}}^2 = \lambda (\Delta \vec{y})^T V^{-1} (\Delta \vec{y}).$$

We generally see the flux parameters have a slightly larger bias, but reduced uncertainty. The cross section parameters are largely unchanged. The first eight figures are the ND280 flux parameters. The following eight are the unoscillated Super-Kamiokande (SK) flux parameters. The next five are the cross section parameters. The final two are the bin normalization parameters.

